ANARE RESEARCH NOTES 95

Australian atmospheric and space physics research in Antarctica, 1994–1995

Edited by R.J. Morris

Australian
National
Antarctic
Research
Expeditions

ANARE RESEARCH NOTES (ISSN 0729-6533)

This series allows rapid publication in a wide range of disciplines. Copies of this and other *ANARE Research Notes* are available from the Antarctic Division. Any person who has participated in Australian National Antarctic Research Expeditions is invited to publish through this series. Before submitting manuscripts authors should obtain advice from:

The Publications Office
Antarctic Division
Channel Highway
Kingston 7050
Australia

Published August 1996
ISBN: 0 642 25328 5

CONTENTS

AUSTRALIAN ATMOSPHERIC AND SPACE PHYSICS RESEARCH IN ANTARCTICA, 1994 – 1995

Edited by R.J. Morris

Antarctic Division

Department of the Environment Sport and Territories

Kingston Tasmania Australia

PREFACE

The papers in this anthology of middle and upper atmospheric physics, and cosmic ray physics were presented at either (i) 11th Australian Institute of Physics Congress, Solar and Terrestrial Physics Workshop, University of Queensland, Brisbane 4-8 July 1994, and/or the (ii) STEP 1995: Conference on Solar and Terrestrial Physics, University of Adelaide, 25-29 September 1995. Several additional papers were prepared by members of the Atmospheric and Space Physics group of the Antarctic Division and by members of ANARE.

The majority of papers are preliminary and are presented as an indication of the current direction of Australian atmospheric and space physics research in Antarctica. It is anticipated that several of the final results will be published in appropriate journals. The editor thanks the respective authors for their contributions, Judy Whelan for her excellent effort with the preparation of the manuscripts and Sandra Potter for arranging the final publication.

1. COSMIC RAY MODULATION – A REVIEW OF AUSTRALIAN RESEARCH

M.L. Duldig

Cosmic Ray Section
Antarctic Division
Kingston Tasmania 7050
Australia

ABSTRACT

Australian research into the modulation of galactic cosmic rays is concentrated in the Antarctic Division and the University of Tasmania. The shallow underground telescopes operated by these institutions are the sole source of such measurements in the southern hemisphere and, in the case of the Mawson observatory, the only such observations at polar latitudes in either hemisphere. The neutron monitors form a significant part of the world-wide neutron monitor network covering important latitude and longitude views which are otherwise inaccessible.

The unique combination of instruments has allowed Australian researchers to pursue a number of aspects of modulation research. Modelling of ground level enhancements has recently been developed to a stage where new insights are being revealed. Studies of solar and sidereal anisotropies are producing estimates of heliospheric cosmic ray transport parameters at higher energies than have been determined previously. The special significance of the heliospheric neutral sheet in cosmic ray modulation at low and moderately high energies (1 – 100 GeV) is also being demonstrated by these groups.

This review article introduces recent advances made in cosmic ray modulation research by Australian workers. Details of some of these advances are presented in following articles. It is hoped that this review will give readers the necessary background to understand and appreciate the status of cosmic ray modulation research, a field closely associated with solar terrestrial physics.

1.1 INTRODUCTION

Cosmic Rays are fully ionised nuclei of very high energy, typically $10^9 - 10^{20}$ eV. They arrive at the Earth almost isotropically and have elemental abundances similar to the observed galactic abundances, ~90% being protons. With the exception of cosmic ray particles accelerated on the Sun during solar flares all cosmic rays are non-solar in origin and some of the highest energy particles must be from extragalactic sources. The acceleration mechanisms responsible for these remarkable energies are poorly understood and at the highest energies are not consistent with our present understanding of particle acceleration.

Over the energy range 10^9–10^{12} eV (1–1000 GeV) solar influences on galactic cosmic rays are observed. These influences are collectively known as solar modulation of

galactic cosmic rays. The differential spectrum, for this energy range, is adequately described by a power law with an exponent of -2.6. At the lower end of the energy window solar processes dominate whilst at the upper end little, if any, solar influence remains and galactic phenomena are observed. Long-term anisotropies are indicative of solar magnetic and plasma structures and may be used to derive parameters of the modulation. Similarly, transient events carry information on the interplanetary magnetic field (IMF) through which they have passed and act as probes of the near Earth IMF structure. By considering both of these types of variation it is possible to build up a model of the IMF and of galactic cosmic ray modulation.

Before considering this research it is necessary to introduce the detection techniques and data corrections which must be included in such analyses so that the reader will have a greater understanding of the complexities involved. Section 1.2 discusses the detection techniques and data corrections involved in this energy window. In Section 1.3 transient phenomena are discussed and in Section 1.4 anisotropy studies are presented.

1.2 COSMIC RAY DETECTION

1.2.1 *Secondary particle production*

The atmosphere is an integral part of any cosmic ray detector. Figure 1 is adapted from Duldig (1994) and is a schematic representation of the low and moderately high energy-dependent processes that occur when an incident cosmic ray particle (primary cosmic ray) interacts with atmospheric nuclei to produce secondary products. It is these secondaries that are detected by ground-based and underground detectors.

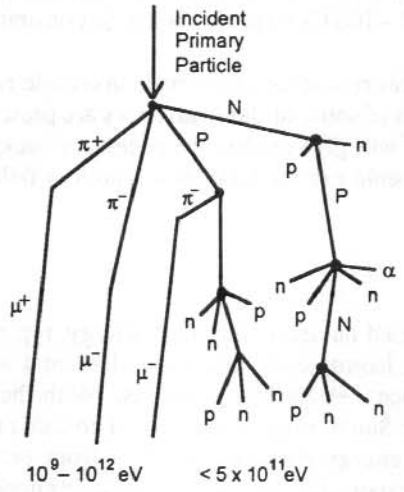

Figure 1. Schematic representation of the possible atmospheric interactions of primary cosmic rays of less than 10^{12} eV that lead to detected secondary particles. The approximate energy limits for neutron and muon production are shown. The horizontal scale is grossly exaggerated. Adapted from Duldig (1994).

Primary cosmic rays with energies less than about 1 GeV do not produce secondaries which penetrate to sea level. This is due to ionisation losses and eventual absorption in the atmosphere. For particles up to about 50 GeV and exceeding this threshold the initial atmospheric interaction may produce energetic nucleons which in turn collide with other atmospheric nuclei producing a cascade. The cascade eventually results in multiple neutrons and a few protons at sea level. These processes are highly relativistic and scattering from the initial direction of arrival of the primary during the cascade is small (less than a degree or two) so that directional information is not lost.

At higher energies of 1–1000 GeV the initial interaction can produce a π-meson (or pion) which rapidly decays into a μ-meson (or muon) of the same charge. There is an overlapping energy range where either of the two processes described above may occur. The charged muons generally do not decay into positrons or electrons before reaching the surface or underground detectors due to time dilation effects at such high energies. They are also highly penetrating and may be detected at depths in excess of 1 km underground.

1.2.2 *Neutron monitors*

Figure 2 is a schematic diagram of an NM64 (or IQSY) neutron monitor. The lead moderator and polyethylene *reflector* have been designed to *thermalise* incident neutrons through scattering and multiplication in nuclear collisions with lead nuclei.

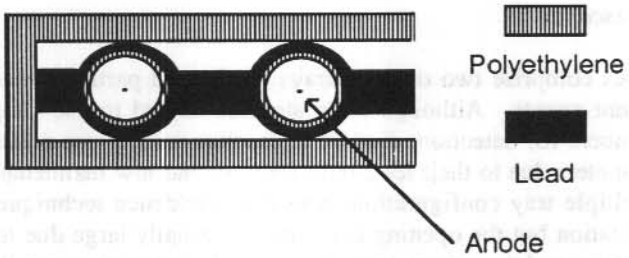

Figure 2. Schematic diagram of an NM64 neutron monitor. Adapted from Duldig (1994).

The thermalised neutrons enter the BF_3 proportional counters at the energy of maximum cross-section for the neutron capture reaction:

$$^{10}B + n \rightarrow {}^{7}Li + \alpha$$

The ionised Li atom and α particle then produce further ionisation in the proportional counter which produces a countable pulse. A complete description of this and earlier neutron monitor designs can be found in Hatton (1971).

The scattering in the lead moderator and subsequent nuclear reaction do not maintain any directional relationship to the incoming neutron and thus a neutron monitor is not strictly a telescope. However, the neutron monitor does have a restricted viewing aperture. Neutrons produced in the atmosphere by the nucleonic cascade will only have sufficient energy to reach the lower atmosphere if they arise from primaries incident within about 40° of the zenith. The geomagnetic field further restricts the incident primary directions that have access to the monitor. An energy dependent viewing window results which is known as the asymptotic cone of acceptance or the viewing cone.

At the equator particles travelling perpendicular to the magnetic field are deflected back into space unless their energies are above about 15 GeV. At mid-latitudes particles require less energy to penetrate the field, whilst at the magnetic poles, where particles can travel along the field lines, there is no minimum energy for access. Note that the 1 GeV atmospheric absorption will still be an effective lower cut-off. Thus there is a range of geomagnetic cut-off values which depend on the magnetic latitude of the observatory. It is possible to take advantage of this cut-off variation to determine spectral information about low energy cosmic ray phenomena. By employing observations from stations at varying geomagnetic cut-offs the maximum energy of certain phenomena or the low energy spectral variation of the effect can be derived. As the viewing cones also vary with longitude (see Section 1.2.5) it is necessary to site neutron monitors over a range of latitudes and longitudes to provide adequate coverage of free space directions and energy. It was this need that led to the establishment of the world-wide neutron monitor network which has operated since the International Geophysical Year, 1957.

1.2.3 *Muon telescopes*

Muon telescopes comprise two or more trays of charged particle detectors arranged to record coincident events. Although early systems tended to use Geiger counters and ionisation chambers for detection, modern telescopes usually use plastic scintillators or proportional counters due to their long-term stability and low maintenance requirements. The use of multiple tray configurations allows coincidence techniques to give arrival direction information but the opening apertures are usually large due to the low particle flux and need for good counting statistics. Counting statistics usually limit sampling times to a minimum of 5 minutes and for most studies hourly samples are used. The telescopes are fixed transit instruments. The soft (electron/positron) component of secondary radiation which arises from higher energy atmospheric cascades (>1000 GeV) is removed by placing absorbing material such as lead or iron between the trays of surface instruments. This is not necessary for underground installations where the overburden stops any soft component radiation in the first few centimetres.

Triple coincidence systems reduce the number of accidental triggerings caused when two or more cosmic ray secondaries enter the different trays at the same time, causing an apparently genuine coincident event. A two resolving time technique has been developed by the Antarctic Division researchers (Jacklyn and Duldig 1987) that allows two-tray telescopes to be effectively employed without significant accidental triggering contamination. These systems are of lower initial cost and require significantly less maintenance. The reduced maintenance of such telescopes is particularly advantageous

because the systems are often located at unstaffed, remote sites such as underground power stations or in the Antarctic.

There are two techniques employed for energy discrimination in muon telescopes. Placing telescopes underground allows the overburden to be used as absorbing material which removes lower energy particles. It is important to choose sites where the overburden material can be well determined (i.e. relatively homogeneous) and where seasonal changes such as water content are small. The second technique is to view at high zenith angles from the surface. The additional thickness of atmosphere acts as additional absorber and removes low energy particles. There are, however, some additional corrections which need to be considered when viewing at high zenith angles (see Section 1.2.6).

Because muon telescopes are directional greater coverage is possible from any site and fewer, well chosen, observatory sites are needed for good global coverage than with the lower energy neutron monitor network. Some observatory design considerations can be found in Mori et al. (1991), Duldig (1990) and Duldig et al. (1985a). Global coverage is still necessary, however, if anisotropies and transient variations are to be properly interpreted. The northern hemisphere has a reasonable coverage with muon telescope systems in North America, Japan, Europe and several states of the former Soviet Union. In the southern hemisphere muon telescopes are only located at Tasmania and Mawson, Antarctica, the latter being the only polar muon observatory in either hemisphere. Clearly the coverage is inadequate in the southern hemisphere, especially in longitude.

1.2.4 *Energy or rigidity–GeV or GV*

Although energy is the most useful unit when comparing with other branches of astronomy or radiation physics it is not the most appropriate reference unit for studies of charged particle propagation in a magnetic field.

The total energy of a relativistic particle is

$$E = m_o c^2 \gamma ,$$

where $\gamma = 1/(1-v^2/c^2)^{1/2}$ is the usual relativistic correction factor. The particle momentum is similarly $p = m_o v \gamma$ and as $v \rightarrow c$, $E \rightarrow pc$. The rigidity, or normalised momentum per unit charge, of a particle represents its tendency not to deviate from its path in a magnetic field (hence the name being related to a tendency not to bend) and is defined as

$$P = pc / q$$

where q is the charge of the particle. In a magnetic field B the particle gyroradius r is given by

$$Br = p / q$$

and the relationship can be rewritten as

$$r = P / 45B,$$

where r is in units of AU, B in nT, P in GV and the particles are assumed to have unit charge (i.e. protons). As can be seen from Table 1, proton energies in GeV and rigidities in GV have almost the same numerical values above ~2 GeV.

The gyroradius of a particle is a fundamental characteristic length in the study of cosmic ray modulation and thus rigidity, which is linearly related to the gyroradius, is the preferred unit. Note that the field strength has been assumed to have the average near Earth value for the IMF of 5 nT.

Table 1. Proton properties at high energies in a 5 nT field typical near the Earth.

Energy (GeV)	Rigidity (GV)	Speed (c)	Gyroradius (AU) (5nT)
1	0.35	0.35	0.004
2	1.77	0.88	0.009
3	2.85	0.95	0.013
5	4.91	0.98	0.022
10	9.96	0.996	0.044
100	99.996	0.99996	0.444

1.2.5 *Geomagnetic effects*

The geomagnetic field significantly distorts the viewing aperture of a cosmic ray detector. This is particularly true for neutron monitors with low cut-off values. Figure 3 shows the viewing direction in geocentric co-ordinates of vertically incident secondaries of several neutron monitors for undisturbed (Kp = 0) and moderately disturbed (Kp = 5) geomagnetic conditions. As the geomagnetic field is not spherically symmetric, being compressed on the sunward side and extended with a long tail on the night side, the viewing cones of neutron monitors also depend on time of day and date within the year. Only in recent times have corrections for these variations been incorporated into cosmic ray viewing cone calculations (Duldig et al. 1993; Cramp et al. 1993a, 1993b; Bieber et al. 1992; Flückiger and Kobel 1990; Kobel 1989) and then only by a few of the research groups world-wide.

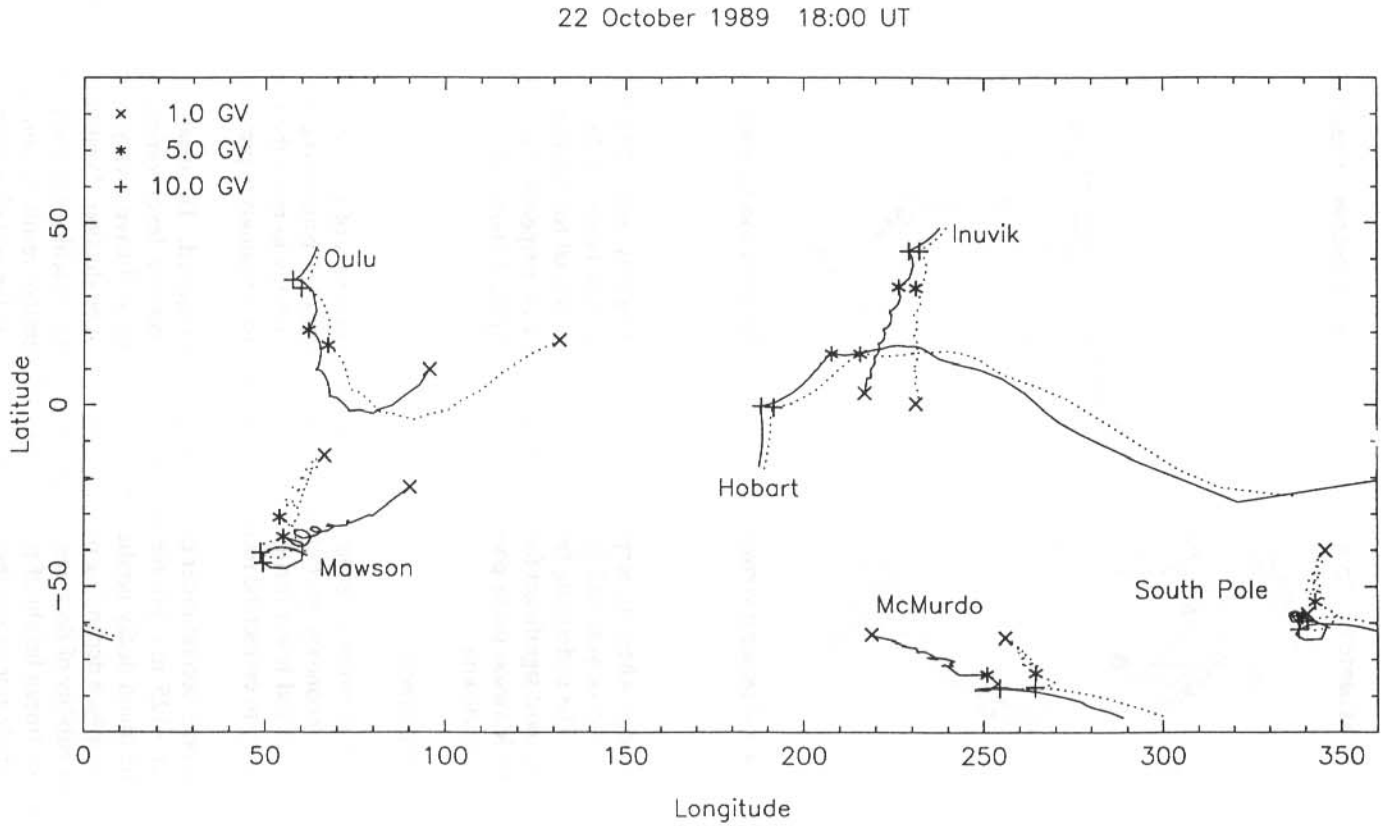

Figure 3. Vertical incident viewing directions of several neutron monitors for undisturbed (Kp = 0, dotted) and disturbed (Kp = 5, solid) geomagnetic conditions.

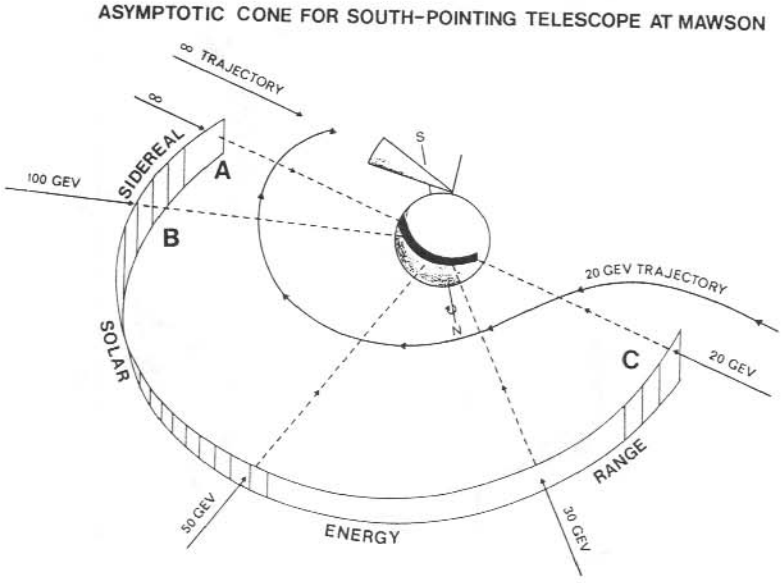

Figure 4. Rigidity-dependent viewing direction of the Mawson south-pointing telescopes.

For muon telescopes, where the response to particles of rigidity below 10 GV is small, the effect of time of day or year and level of geomagnetic disturbance on the viewing cones may be ignored. The underlying field must still be considered for rigidities below about 100 GV. This is most significant for telescopes which view perpendicular to the magnetic field such as the Mawson south-pointing telescope. Figure 4 shows this extreme case of rigidity-dependent viewing.

1.2.6 *Atmospheric effects*

An increase in air pressure at sea level indicates a greater mass of air over a site. This in turn means that secondary particles lose more energy in penetrating the increased absorbing material and fewer particles have sufficient energy to reach the detector. It is therefore necessary to correct the recorded count rates for variations in pressure.

For muon telescopes second-order corrections may be required. The mean production of pions occurs at ~125 mb but the height of this pressure level varies, particularly seasonally. The muon decay product from these pions will have a varying transit time through the atmosphere depending on the height of pion production. Positive muons have a significant probability of decaying into positrons before reaching sea level. An increase in the flight time (mean height of production) will therefore result in more muon decays and a lower particle rate at sea level. This is known as the negative temperature effect

because an increase in the atmospheric temperature leads to an expansion of the atmosphere and thus to a longer flight time for the particles which reduces the sea-level rate.

The temperature at the pion production level is also important. The air density at this level is inversely proportional to the temperature and also varies seasonally. At higher densities there is an increased probability of the pion interacting with an atmospheric nucleus before decaying into a muon. Thus lower temperatures result in higher densities and so fewer particles reaching sea level. This is known as the positive temperature effect. At moderate depths of absorbing material of about 40 hg cm^{-2} the energy of the particles is such that these two effects are equal but opposite and reduce to zero. This corresponds to surface zenith angles of view of ~64°. The atmospheric structures responsible for the temperature effects vary relatively slowly but have significant seasonal variations, especially at polar locations. Corrections for these atmospheric temperature effects are generally not necessary for short term transient studies but may be significant in long term studies such as investigation of anisotropies.

Radiosonde balloon measurements may be employed to determine the day-to-day values of these parameters and to correct the count rate for such variations. See Baker (1993), Baker et al. (1993) and Lyons (1981) for further discussion.

1.2.7 *Heliomagnetic effects*

The solar wind carries the solar magnetic field *frozen* within it as it streams radially from the Sun at an average speed of 400 km s^{-1}. The Sun also rotates with a 27 day period (as seen from the Earth) and so the field at equatorial latitudes forms an Archimedean spiral structure. Furthermore, the wind maintains a neutral sheet which separates the northern and southern solar magnetic fields. This neutral sheet is located at the solar magnetic equator and as the inclination of the solar dipole varies the neutral sheet becomes wavy as shown in Figure 5. The 11 year solar sunspot cycle is indicative of solar activity and at sunspot minimum the dipole field is relatively stable and closely aligned to the rotation axis producing a relatively flat neutral sheet. In contrast, at solar sunspot maximum the dipole tilt is highly variable producing complex magnetic structures and the neutral sheet has been known to extend to helio-latitudes in excess of 70°. Additionally, the solar magnetic field reverses every solar maximum resulting in a 22-year periodicity in the heliomagnetic field. Other variations are also present. For example, the strength of the solar field at the Earth is on average 5 nT but this can vary significantly with solar activity and extended periods of stronger fields may be observed around solar maximum.

The combined effect of these heliomagnetic variations can be seen in Figure 6, which shows the Mawson neutron monitor response plotted against time together with the smoothed monthly sunspot numbers. The clear anti-correlation with solar activity is due to the stronger field and wind acting as a more efficient barrier to galactic cosmic ray penetration into the inner solar system. The alternate sharp and flat topped peaks in the cosmic ray record have been attributed to the solar field reversals. More recent evidence and a re-evaluation of the scaling of early records from the 1940's and early 1950's suggests that this structure does not repeat, raising doubts about this interpretation (Pyle 1993).

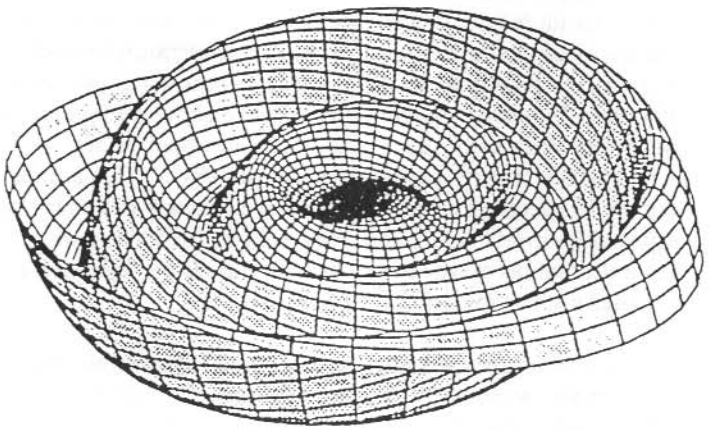

Figure 5. The heliomagnetic wavy neutral sheet (Flückiger 1991).

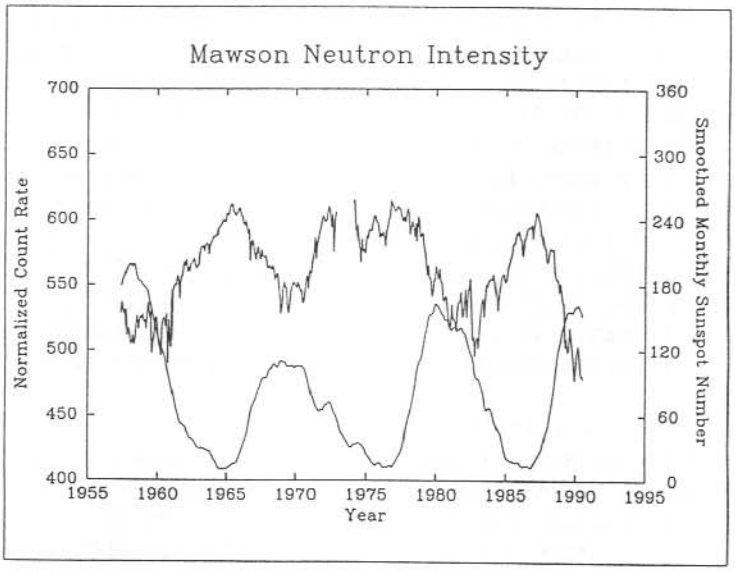

Figure 6. Mawson neutron monitor response compared with the smoothed monthly sunspot number.

1.3 COSMIC RAY TRANSIENT PHENOMENA

There are three broad categories of transient variation that ground based cosmic ray instruments observe.

(i) Forbush decreases – where the cosmic ray flux reduces by ~3-20% over timescales of hours or a few days and recovery takes days to weeks;

(ii) Ground level enhancements – where the cosmic ray flux increases by ~3-4500% over timescales of minutes to an hour or two and recovery is from a few hours to a day; and

(iii) Enhanced quasi-periodic variations – where the peak-to-peak flux variation is typically no greater than a few percent and lasts for several to 10 or 15 cycles, with periods related to either the solar or the Earth's rotation.

Each of these classes of events is attributed to different causes which are discussed below.

1.3.1 *Forbush decreases*

Forbush decreases may be divided into two types, rapid-onset, sometimes referred to as classical, and slow-onset. Very little work has been carried out in the study of slow onset Forbush decreases. By contrast the rapid-onset Forbush decrease has been extensively studied. Lockwood (1971) wrote an excellent review which has since become somewhat dated. Venkatesan and Badruddin (1990) reviewed cosmic ray intensity variations in the three-dimensional heliosphere, including a more up-to-date discussion of Forbush decreases.

Figure 7 shows observations by a range of neutron monitors of increasing cut-offs and one underground muon telescope of one of the largest Forbush decreases. The spectral response characteristics are evident simply by looking at these data. At Mawson the minimum particle rigidity observable is determined by the atmospheric absorption and is about 1 GV. At Mt. Wellington the geomagnetic cut-off is 1.9 GV whilst at Brisbane it is 7.2 GV and at Darwin it is 14.2 GV. The minimum rigidity of particles capable of producing a statistically significant observation in the Mawson underground north telescope is ~15 – 20 GV, depending on the spectrum of the event. Clearly there were few particles above ~25 – 30 GV that were modulated during this decrease. The solar flare that led to the decrease was located at E36° on the solar disk.

Figure 8 shows three further Forbush decreases observed by the Mawson neutron monitor and exhibiting some of the common features seen during such events. The top trace shows a two-step decrease which also indicates quite large diurnal variations before the event and during the recovery phase. Significant anisotropy of particle distribution is also evident, as demonstrated by the rapid initial recovery followed by at least one significant rise and fall. The *parent* flare for this disturbance was located at E33° on the solar disk. The middle trace shows a single step decrease with a slight pre-decrease enhancement, not in phase with the diurnal variation before the event. Note that the phase of the diurnal peaks has shifted after the event. This indicates an anisotropic particle density which is moving. The *parent* solar disturbance is unknown for this event. The lower trace shows

an event embedded within a cosmic ray storm. Complex anisotropies existed three to four days before and a distinct semi-diurnal variation can be seen for up to three days immediately prior to the decrease. This semi-diurnal variation most likely indicates a bidirectional flow of cosmic rays. Again a significant diurnal variation is seen in the recovery phase but the *parent* flare location is unusual being at W43° on the solar disk.

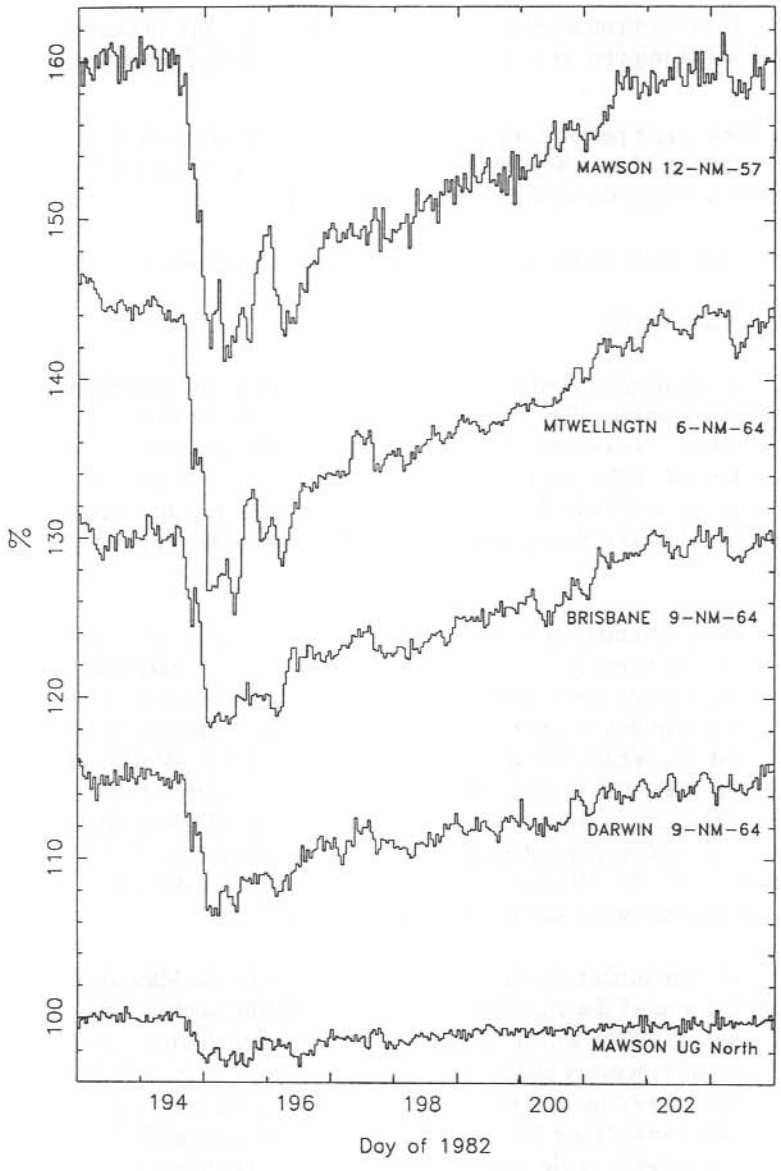

Figure 7. The Forbush decrease of July 1982 as observed by cosmic ray detectors of different low energy cut-off. The lowest cut-off is at the top.

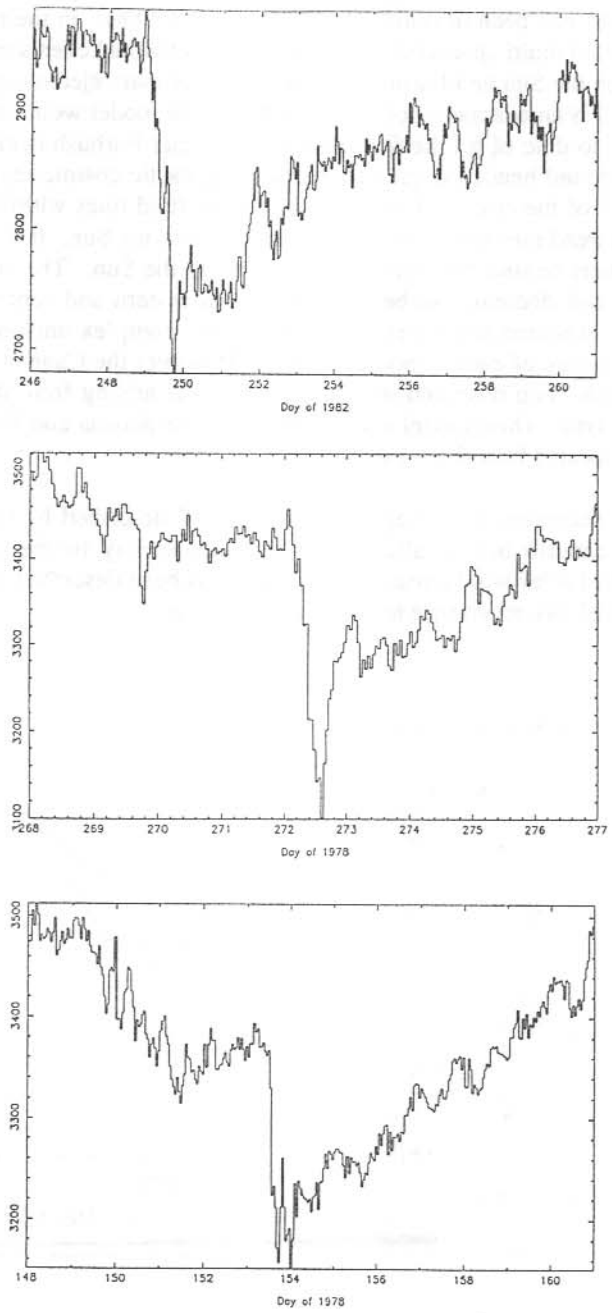

Figure 8. Three Forbush decreases observed by the Mawson neutron monitor. Each of the decreases shows specific features as described in the text.

Figure 9 summarises the features of a rapid-onset Forbush decrease. It is worth noting that there is sometimes a tendency for a recurrence of the decrease, though with a slower onset, after a solar rotation of 27 days. The most recent and compelling model to explain Forbush decreases has been developed by Cane et al. (1988). In their model, which is derived in part from multi-spacecraft observations of individual events made from several positions between the Sun and Earth, a flattened coronal mass ejection generates a driven shock. Figure 10 is an adaptation of their diagram. The model would appear to give the best explanation to date of all the features of rapid-onset Forbush decreases. The most compressed field, and hence the greatest barrier to galactic cosmic rays, is found to the west and in front of the ejecta. There may be closed field lines within the ejecta or the field lines may thread through the ejecta and back toward the Sun. It is unknown if these field lines or others behind the ejecta connect back to the Sun. The strong tendency of rapid-onset Forbush decreases to be associated with eastern and central meridian solar flares is clearly expected from this model as are the complex anisotropies during the decrease. This is true of earlier models as well. However the Cane et al. (1988) model explains the second step observed in some decreases as arising from the passage of the ejecta past the Earth. Their model also accounts for the plasma and field measurements from spacecraft located from 0.5 – 1 AU.

The slow-onset decreases do not appear to be as well described by this model. Some events fit the scenario but an alternative explanation may be the compressed field generated by a fast solar wind stream. This model has been described by Burlaga (1983) and explains the 27 day recurrence tendency quite nicely.

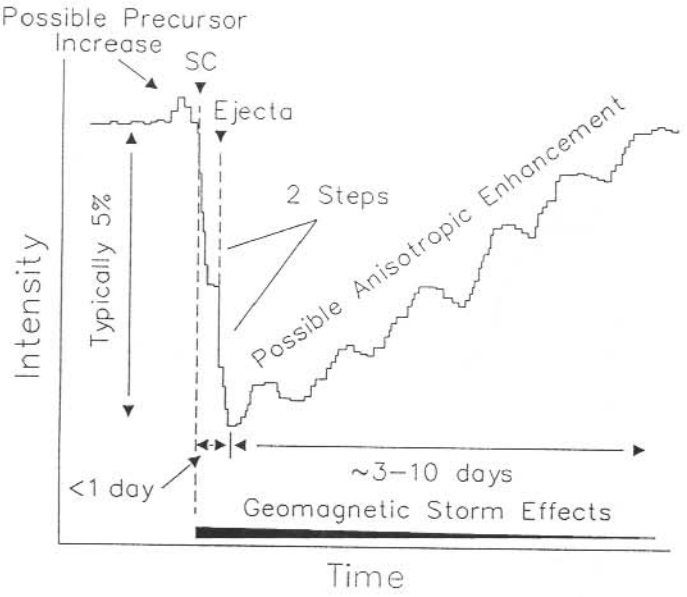

Figure 9. Idealised schematic of the features of rapid onset Forbush decreases.

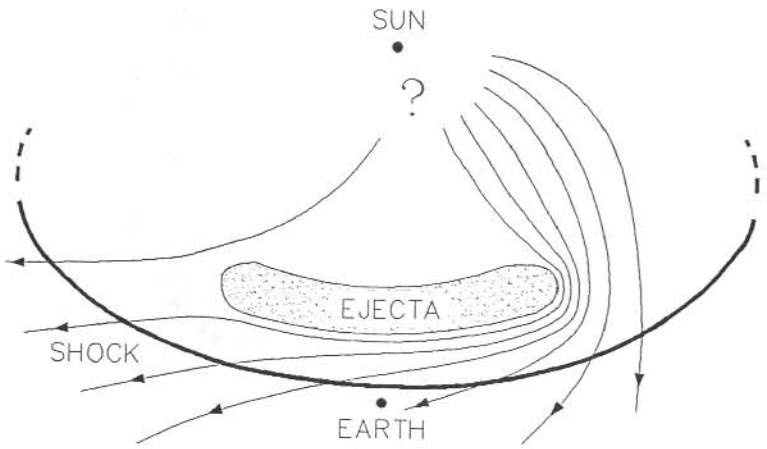

Figure 10. Schematic representation of the Cane et al. (1988) model of Forbush decreases.

The recurrence tendency of the rapid-onset decreases is still a mystery. After such a long time the original shock is far out in the solar system and can not, of itself, be responsible for the subsequent decreases. It is not yet clear how the region behind the shock behaves in the longer term and it may be that remnant structures capable of modulating galactic comic rays up to 10 GV rigidity are present for a few solar rotations. It may also be possible that fast solar wind streams form behind some shocks and that the Burlaga (1983) mechanism applies to the recurrence events.

1.3.2 *Ground level enhancements*

Ground Level Enhancements (GLEs) are rare events in which a sudden rise in the cosmic ray flux is followed by an approximately exponential decay back to pre-increase levels. There is a weak tendency for these events to occur around times of solar maximum but they can be observed at any time in the solar cycle. Recently Nagashima et al. (1991) proposed that no GLEs have been or should be observed at solar maximum whilst the solar polar field was reversing. This has been disputed by Shea and Smart (1995) who cite GLEs during the most recent solar field reversal in 1992.

Fifty-three GLEs have been observed since reliable observations began in the 1940's, but 13 of these were observed within a two-year period centred on the last solar maximum. For an excellent summary of GLE observations up to the end of the previous solar cycle see Shea and Smart (1990), whilst a more recent summary appears in Shea and Smart (1993).

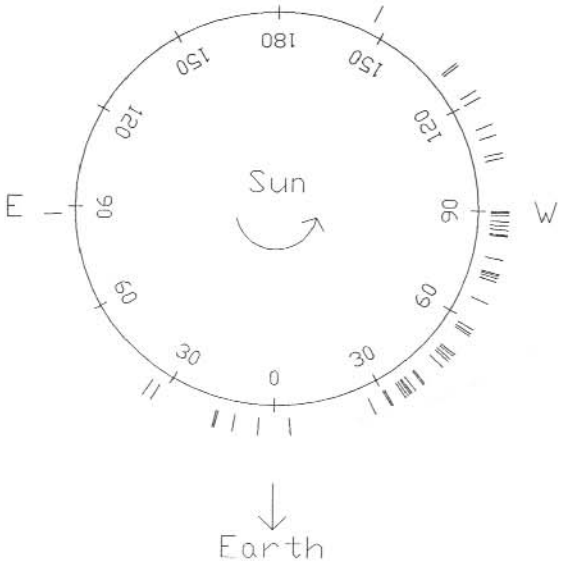

Figure 11. Parent flare locations on the Sun for all GLEs.

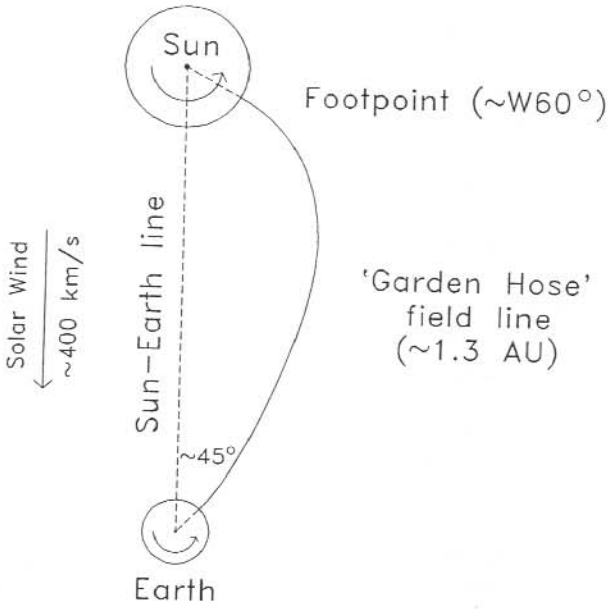

Figure 12. Nominal field line geometry connecting the Sun and Earth during a GLE.

The acceleration of protons to cosmic ray energies during solar flares is not well understood and no suitable model has been developed to explain the observed characteristics of the radio, optical, X-ray and particle emissions. The propagation of the solar accelerated protons to Earth is clearer. Figure 11 shows the *parent* flare location for all recorded GLEs. There is a clear tendency for *parent* flares to be located between 30°W and 90°W on the solar disk. In Figure 12 the typical geometry of the field line connecting the Sun and the Earth, the so-called *Garden Hose* field line, is shown. This geometry is highly variable, depending on solar activity, solar wind speed and the previous passage of shocks and coronal mass ejections. It does, however, explain the greater likelihood of a GLE being observed when the *parent* flare is located in the west. For these flares the protons have immediate access to the *Garden Hose* field lines and thus simply spiral along the field to the Earth. Distortions of the heliomagnetic field in interplanetary space closer to the Sun than 1 AU may explain the field connection to the Earth of flares located near the meridian or beyond the western limb. The explanation for significantly eastward *parent* flares generating a GLE is not at all apparent.

A standard technique for modelling GLEs has been developed over many years (Shea and Smart 1982; Smart et al. 1991). The analyses presented here are based on an extension of the standard technique. We have modified the modelling to allow a rigidity dependent pitch angle distribution for the particles and allowing reverse particle propagation. The pitch angle is the angle of gyration with respect to the direction of motion (i.e. the IMF direction). We have also enclosed the complete modelling software within a least-square framework to rapidly find the optimum solution in parameter space.

When modelling the neutron monitor response it is also useful to convert the observed increase to the increase that would be seen at sea-level. This involves comparing the responses of low and high altitude monitors which are geographically near to each other. An example is the Hobart and Mt. Wellington monitors which are separated by only 7 km but have altitudes of 10 m and 725 m respectively. Being geographically close means that the viewing cones are virtually identical and the different response will be solely due to the atmospheric absorption of particles between the higher and lower altitudes (and Poisson statistics). This will be related to the low energy cut-off and the spectrum of the GLE particles. An attenuation length can be calculated (McCracken 1962) for various pairs of suitable monitors in the world-wide network and the most consistent attenuation parameters can be employed to correct the monitor responses of all monitors in the network to a sea-level response.

For any GLE, the responses of the neutron monitors world-wide are used to determine the spectrum and spatial distribution of particles arriving from the Sun. The model for these responses is of the form

$$I_i = \sum_{P_{c,i}}^{\infty} J(\alpha, P)\, S_i(P)\, G(\alpha, P)\, \delta P,$$

where I_i is the recorded percentage increase at station i at the given time;

P is the particle rigidity in GV;

$P_{c,i}$ is the low energy geomagnetic cut-off for station i at the given time;

α is the pitch angle of the particles;

J is the differential interplanetary flux;

S_i is the specific yield function of the neutron monitor (including viewing cone);

and G is the particle pitch angle distribution around the arrival direction.

The specific yield function includes two components, the neutron monitor yield function (Debrunner et al. 1982), which gives the response of the neutron monitor to particles arriving at the top of the atmosphere (that have access to the detector) and the cones of view described earlier.

It should be noted that this is not a dynamic solution to the observed response profiles at the various neutron monitors but an '*instantaneous*' solution at a given time during the event. The term instantaneous is slightly misleading as data are collected for some time interval for each measurement (usually 5 minutes) to obtain adequate statistical accuracy. To understand the dynamic situation it is necessary to model the event at various times throughout its development.

The largest GLE in the space era was observed on 29 September 1989 by at least 42 neutron monitor stations in the world-wide network and a number of surface muon telescopes such as Mawson and Hobart. In addition, underground muons were observed at Embudo observatory (Swinson and Shea 1990). The detailed analysis of this event has already been reported (Duldig et al. 1993; Cramp et al. 1993a) and is not reproduced here. The least-squares technique has allowed a more rigorous coverage of parameter space. Figures 13, 14 and 15 show the recorded increases at various monitors and the improved spectra and pitch angle distributions derived for this GLE taking all available neutron monitor observations into account. The significant reverse particle propagation at 13:25–13:30 UT in Figure 15 is particularly interesting, implying scattering centres beyond the Earth's orbit which cause the particles to propagate back along the IMF toward the Sun. The origin and features of this scattering region are unknown. It should also be noted that the minimum pitch angle response on these curves represents the isotropic flux increase of the event and any anisotropy of the event must be considered with respect to this minimum. In the absence of any IMF data the zero of the pitch angle is assumed to lie in the IMF direction. Where IMF data are available the derived pitch angle can be compared with the field and used to help interpret the IMF structures present near the Earth.

Table 2 shows the improved determination of the pitch angle reference or *source* direction. Note that the longitude variation is partly due to the rotation of the Earth but still represents a significant deviation from the nominal *Garden Hose* field direction of W45° shown in Figure 11. No satellite field data are available for this time but the IMF direction at Earth was observed to be N16°, W6° three days before the event and N65°, W100° two days after the event. The derived *source* directions are thus not inconsistent with the possible field orientation during the GLE.

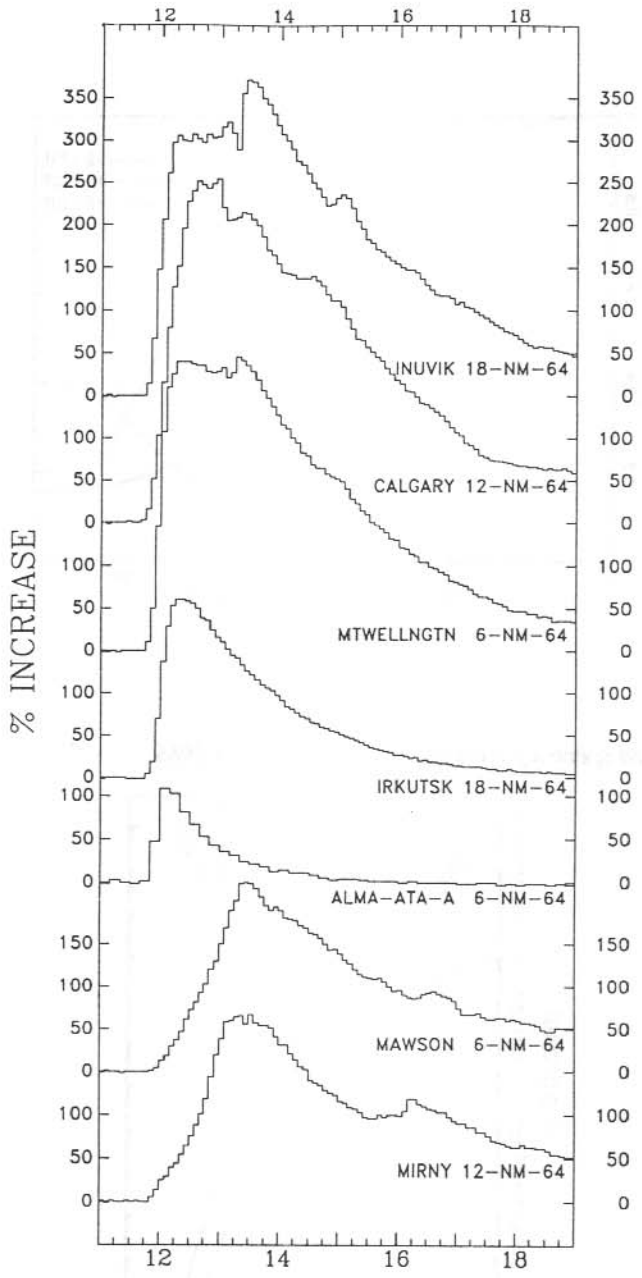

Figure 13. Count rate profiles at various neutron monitors for the large GLE of 29 September 1989.

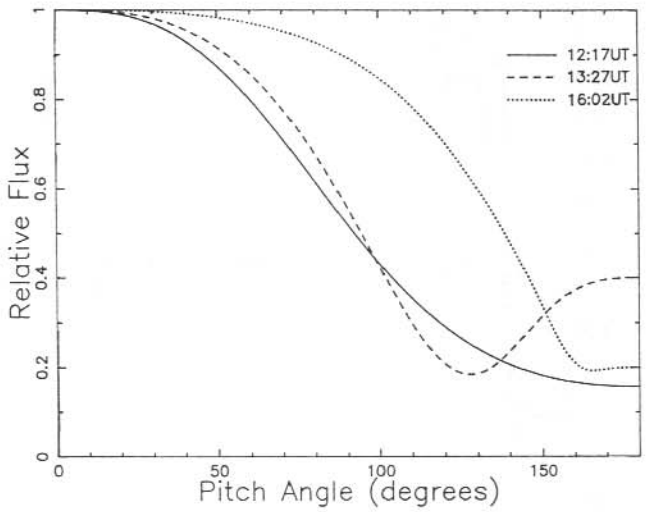

Figure 14. Derived spectra for the GLE of 29 September 1989.

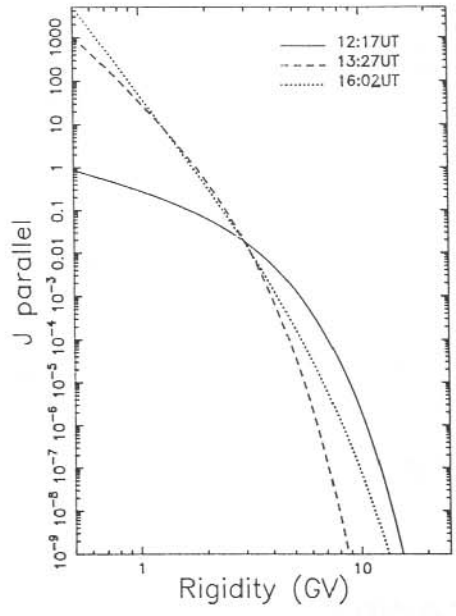

Figure 15. Derived pitch angle distributions for the GLE of 29 September 1989.

Table 2. Source direction parameters derived for the 29 September 1989 GLE.

Time UT	Source latitude	Source longitude	Angle to Sun-Earth line
12:15–20	N30°	237°	W117°
13:25–30	N24°	222°	W114°
16:00–05	N12°	190°	W108°

An interesting development over the last decade has been the discovery of solar flare accelerated neutrons. There is now clear evidence for the detection of neutrons accelerated at, or very near to, the Sun and propagating directly to the Earth (e.g. Shea et al. 1991a). These direct solar neutrons are associated with solar flares which also produce a subsequent GLE. Various models are being proposed to explain the production of the high-energy neutrons but no satisfactory model has yet been developed.

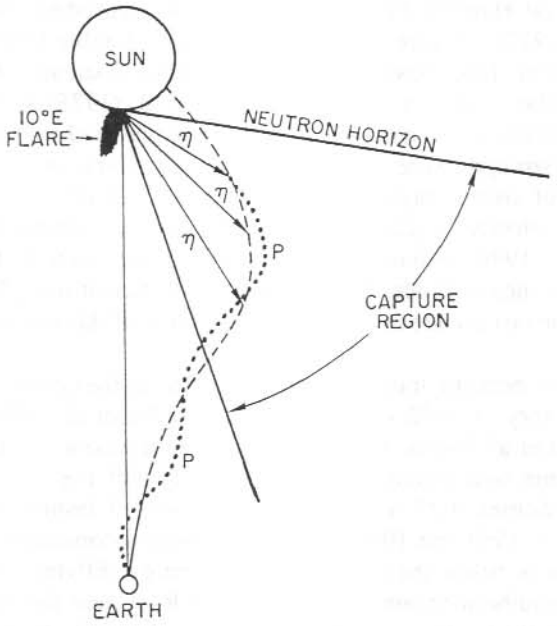

Figure 16. Proposed geometry for the neutron decay model of the 19 October 1989 GLE (from Shea et al. 1991b).

Perhaps even more exciting is the work of Shea et al. (1991b) where the decay of solar accelerated neutrons near the *Garden Hose* field line has been proposed to explain the very unusual onset of the 19 October 1989 GLE. Direct solar neutrons were also observed to arrive prior to the unusual onset. Figure 16, from Shea et al. (1991b), shows schematically the proposed geometry of the neutron decay process and subsequent GLE particle propagation.

The recent development of techniques to correct geomagnetic disturbance, together with improvements in modelling capability imply that we should progressively re-analyse earlier GLEs. Although this will be a computationally intensive undertaking, new insights into the distribution of the propagating particles will lead to a greater understanding of the interaction of the IMF with cosmic rays and may impose stringent new limits on solar particle acceleration models. Some new insights are already becoming apparent as reported in Duldig et al. (1996) in this issue.

1.3.3 *Quasi-periodic variations*

Quasi-periodic variations, lasting from a few to ten or so cycles, are indicative of short-term anisotropic structures in the cosmic ray distribution within the heliosphere. They have been associated with the rotation of the heliomagnetic field and its large-scale features such as the neutral sheet and with plasma features such as fast solar wind streams.

Periods of enhanced diurnal variation are observed by both neutron monitors and muon telescopes (Duldig and Humble 1990; Venkatesan and Badruddin 1990; Jacklyn and Humble 1981; Rao 1972). Figure 17 from Duldig and Humble (1990) shows such a period. Iucci et al. (1981, 1983) have proposed fast solar wind streams; Murayama (1981) suggested perpendicular cosmic ray gradients; Mori et al. (1975) and Swinson (1981) believed that enhancement of the north-south anisotropy due to changing radial gradients and/or varying field strength were possible causes; and Alania et al. (1981) proposed transverse diffusion of cosmic rays as the likely cause. All of these mechanisms can explain some of the enhanced diurnal variations but none are satisfactory for all cases. Duldig and Humble (1990) tentatively proposed that the neutral sheet may play a significant role during these periods. Unfortunately, insufficient interplanetary data have been collected over the last decade to make a detailed study of this proposal possible.

A second type of quasi-periodic transient was discovered in the cosmic ray records from the Mawson observatory in 1982 (Swinson 1993; Duldig et al. 1985a, 1985b, 1990; Duldig 1987; Jacklyn et al. 1984a, 1984b, 1987). Here intensity variations of isotropic nature and flat spectrum were found to correlate strongly with the neutral sheet structure near the Earth. Periodicities of 27 or 13.5 days were observed, lasting five or so cycles in the latter parts of 1982, 1983 and 1984. These periodicities correlated strongly with the Earth's position above or below the neutral sheet implying a different cosmic ray regime in the northern and southern heliomagnetosphere, at least near the neutral sheet. No mechanism for the relatively abrupt onset and the much slower decline of these waves of varying intensity has been found and the waves had not recurred up to the last solar maximum. Should these variations reappear it will again be essential to have high quality data on the IMF structure if our understanding of the phenomenon is to be advanced.

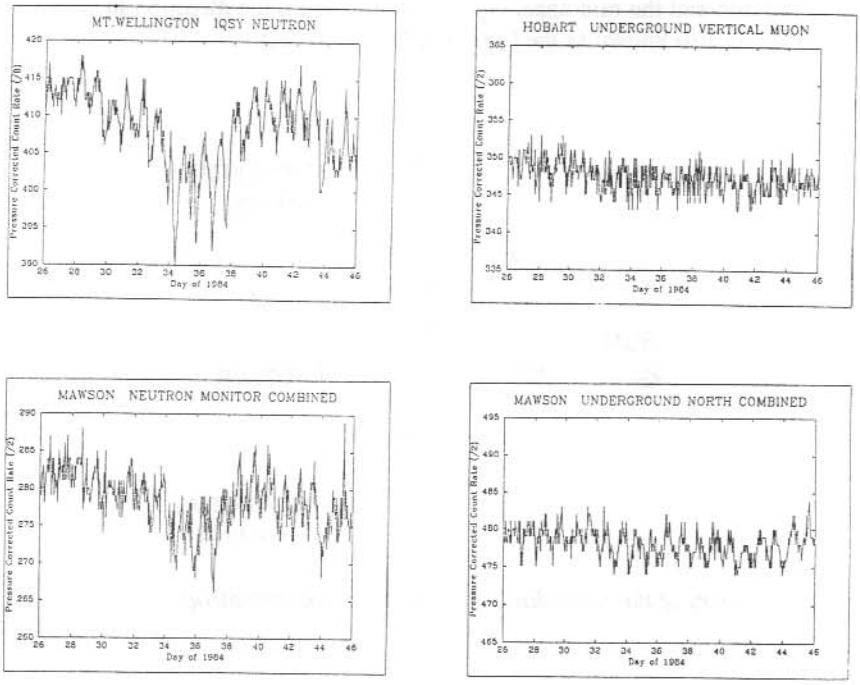

Figure 17. Enhanced diurnal variations observed at a number of cosmic ray observatories in 1984 (from Duldig and Humble 1990).

1.4 ANISOTROPIES

Various forms of long-term anisotropy are known to exist in the cosmic ray records of surface and underground detecting systems. At higher rigidities solar effects disappear and galactic phenomena may be observed in sidereal time.

1.4.1 *Heliospheric anisotropies*

Heliospheric anisotropies are those long-term anisotropies originating in the heliosphere due to solar influences. They arise from flows of the galactic cosmic rays that have propagated into the inner heliosphere.

The most significant anisotropy is the solar diurnal anisotropy. This anisotropy manifests itself as an apparent flow of cosmic rays from the 18 hour direction in local solar time. Figure 18 shows the geometry of the solar diurnal anisotropy. Cosmic rays of low rigidity

follow the rotation of the heliomagnetic field and thus sweep past the Earth in its orbit at ~400 km s^{-1}. The anisotropy is therefore sometimes referred to as the co-rotational solar anisotropy. A second effect is also present, namely the orbital Doppler effect which is due to the Earth's orbital motion (at 30 km s^{-1}) in the same direction as the heliomagnetic field is rotating and has the opposite sense to the solar diurnal anisotropy. It is the same as walking in the rain and the rain appears to be coming from the direction in which you are travelling. This is also known as the Compton-Getting effect.

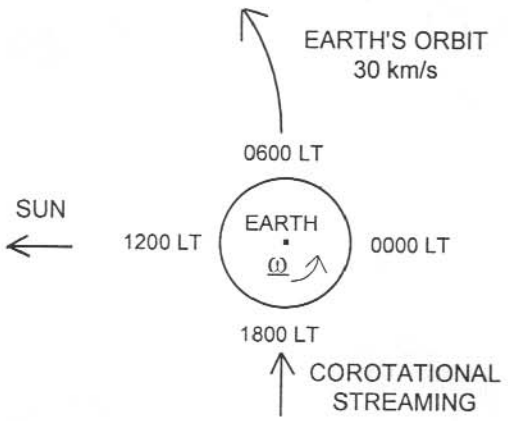

Figure 18. Geometry of the solar diurnal (or co-rotation) anisotropy.

A second solar anisotropy is the semi-diurnal anisotropy, caused by the bidirectional flow of galactic cosmic rays. This flow may be along the solar magnetic field but will also be influenced by gradient and curvature drifts.

Studies of both these solar anisotropies have in recent times considered north-south hemispheric differences in observed parameters in an attempt to separate the effects of the two anisotropies. This is best achieved by observations with identical equipment placed at similar longitudes and equal latitudes north and south. Hemispheric differences in the observed anisotropies arise because the bidirectional anisotropy changes phase between the hemispheres whilst the diurnal anisotropy does not. An experiment of this kind has been constructed with telescopes located at Nagoya and Hobart (Fujii et al. 1996). This experiment also uses multi-directional viewing to further differentiate the anisotropies.

As a result of solar modulation of galactic cosmic rays a radial density gradient which increases away from the Sun is established. An anisotropic flow is established perpendicular to the ecliptic plane. As shown in Figure 19, the greater density of particles at larger distances from the Sun spiral preferentially into the north or south pole of the Earth. As the solar magnetic field sweeps past the Earth the regime changes from a field toward or away from the Sun to the opposite sense and the net particle flow sways to the opposite pole.

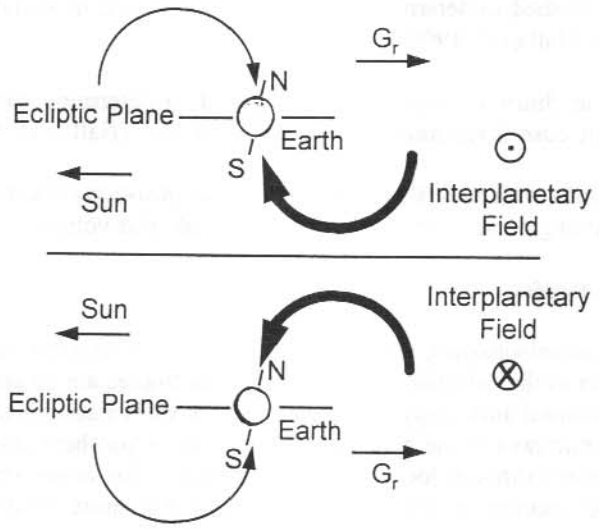

Figure 19. Schematic diagram of the north-south anisotropy. Note the reversal in direction with the changed magnetic field.

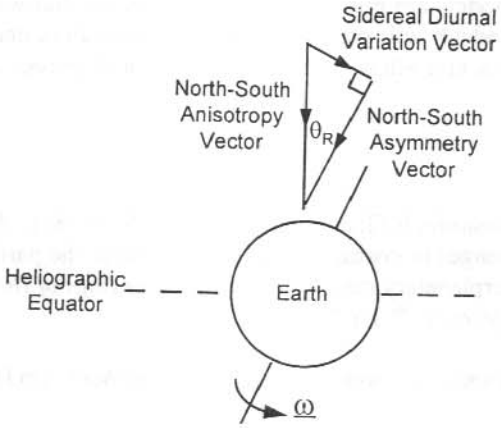

Figure 20. Observable components which make up the north-south anisotropy.

In Figure 20 it can be seen that the anisotropy expresses itself at the Earth with two components, one along the Earth's rotation axis (known as the north-south asymmetry) and the other expressing itself as a sidereal diurnal anisotropy. Either of these components can be studied to determine the radial gradient and its variation during the solar magnetic cycle (Hall et al. 1995).

Analysis of the solar diurnal anisotropy can be used to determine some modulation parameters of galactic cosmic ray transport in the heliosphere. (Hall et al. 1994a, 1994b).

Combining these results with analysis of the north-south anisotropy allows determination of many of the remaining parameters (Hall 1995; Hall et al., this volume).

1.4.2 *Galactic anisotropies*

As in the case of solar anisotropies, sidereal anisotropies result from particle flows which are fixed with respect to the celestial sphere. These anisotropies are measured in sidereal time. The sidereal diurnal anisotropy is believed to arise from a combination of the bulk flow of galactic cosmic rays in the neighbourhood of the heliosphere and the motion of the Sun and heliosphere through local region the galaxy. This anisotropy is not easily seen in lower energy neutron monitor measurements but is more clearly seen in high energy underground observations (Duldig 1991a, 1991b). Spurious sidereal anisotropies resulting from annual modulation of solar anisotropies must be removed in such analyses.

1.5 CONCLUSION

The study of cosmic ray modulation is a long term program which considers a large range of phenomena. The nature of the 22-year solar cycle means that a full understanding will not be possible for many years. However, through the varied range of studies of transients and anisotropies we are gradually building up an understanding of the cosmic ray regime near the Earth. Our models are now sufficiently developed that we are starting to build predictive techniques which will pre-warn spacecraft operators and crew of impending cosmic radiation storms and allow appropriate safety and preventative measures to be taken.

REFERENCES

Alania, M.V., Aslamazashvili, R.G. *and* Djapiashvili, T.V. (1981). A new type of the quasi periodic changes of cosmic ray anisotropy due to the particle drift in the sectors of the interplanetary magnetic field. *Proceedings of the 17th International Cosmic Ray Conference, Paris 4*:64 – 67.

Baker, C.P. (1993). *Cosmic ray modulation in the heliosphere*. Ph.D. Thesis, University of Tasmania.

Baker, C.P., Hall, D.L., Humble, J.E. *and* Duldig, M.L. (1993). Atmospheric correction analysis for Mawson muon telescopes. *Proceedings of the 23rd International Cosmic Ray Conference, Calgary 3*:753 – 756.

Bieber, J.W., Evenson, P. *and* Lin, Z. (1992). Cosmic ray trajectories in the Tsyganenko magnetosphere. Antarctic Journal, Review Issue 27. Pp 318–319.

Burlaga, L.F. (1983). Understanding the heliosphere and its energetic particles. *Proceedings of the 18th International Cosmic Ray Conference, Bangalore 12:* 21–60.

Cane, H.V., Reames, D.V. *and* Rosenvinge, T.T. (1988). The role of interplanetary shocks in the longitude distribution of solar energetic particles. *Journal of Geophysical Research 93:*9555–9567.

Cramp, J.L., Duldig, M.L. *and* Humble, J.E. (1993a). The GLE of 29 September 1989. *Proceedings of the 23rd International Cosmic Ray Conference, Calgary 3:*47–50.

Cramp, J.L., Duldig, M.L. *and* Humble, J.E. (1993b). The GLE of 22 October 1989. *Proceedings of the 23rd International Cosmic Ray Conference, Calgary 3*:51–54.

Debrunner, H., Flückiger, E.O. *and* Lockwood, J.A. (1982). *Eighth European Cosmic Ray Symposium, Rome*. (unpublished).

Duldig, M.L. (1987). Further observations of isotropic intensity waves. *Proceedings of the 20th International Cosmic Ray Conference 4*:75–78.

Duldig, M.L. (1990). The Mawson Automated Cosmic Ray Observatory (MACRO). *Proceedings of the 21st International Cosmic Ray Conference, Adelaide 7:* 288–291.

Duldig, M.L. (1991a). Underground observations of the sidereal diurnal variation at Mawson. *Proceedings of the 22nd International Cosmic Ray Conference, Dublin 3:*422–425.

Duldig, M.L. (1991b). Solar diurnal and semi-diurnal variations observed underground at Mawson. *Proceedings of the 22nd International Cosmic Ray Conference, Dublin 3:*437–440.

Duldig, M.L. (1994). Cosmic ray transient variations observed from the Earth. *Proceedings of the Astronomical Society of Australia 11:*110–125.

Duldig, M.L. *and* Humble, J.E. (1990). Enhanced cosmic ray diurnal variations in Mawson and Hobart neutron monitors and underground data records. *Proceedings of the Astronomical Society of Australia 8:*268–273.

Duldig, M.L., Jacklyn, R.M. *and* Pomerantz, M.A. (1985a). A medium rigidity muon experiment for South Pole station. *Proceedings of the Astronomical Society of Australia 6:*48–52.

Duldig, M.L., Jacklyn, R.M. *and* Pomerantz, M.A. (1985b). Isotropic intensity waves and features of their occurrence. *Proceedings of the 19th International Cosmic Ray Conference, La Jolla 5*:5 – 8.

Duldig, M.L., Baker, C.P. *and* Humble, J.E. (1990). Intensity waves and the neutral sheet structure. *Proceedings of the 21st International Cosmic Ray Conference, Adelaide 6*:291 – 294.

Duldig, M.L., Cramp, J.L. *and* Humble, J.E. (1996). Modelling some cosmic ray ground level enhancements. In: Morris, R.J. (Ed.) *ANARE Research Notes Number 95*. Pp. 34 – 52.

Duldig, M.L., Cramp, J.L., Humble, J.E., Smart, D.F., Shea, M.A., Bieber, J.W., Evenson, P., Fenton, K.B., Fenton, A.G. *and* Bendoricchio, M.B.M. (1993). The ground level enhancements of 1989 September 29 and October 22. *Proceedings of the Astronomical Society of Australia 11*:211–217.

Fujii, Z., Fujimoto, K., Sakakibara, S., Ueno, H., Munakata, K., Yasue, S., Kato, C., Akahane, S., Mori, S., Humble, J.E., Fenton, K.B., Fenton, A.G. *and* Duldig, M.L. (1995). Solar diurnal and semi-diurnal variations of cosmic rays observed by the north-south network of surface-level multi-directional muon telescopes. *Journal of Geomagnetism and Geoelectricity 47*:1079 – 1084.

Flückiger, E.O. (1991). Rapporteur paper on solar and terrestrial modulation. *Proceedings of the 22nd International Cosmic Ray Conference, Dublin 5*: 273 – 292.

Flückiger, E.O. *and* Kobel, E. (1990). Aspects of combining models of the Earth's internal and external magnetic fields. *Journal of Geomagnetism and Geoelectricity 42*:1123 – 1136.

Hatton, C.J. (1971). Neutron monitors. *Progress in Elementary Particle and Cosmic Ray Physics 20*. Pp. 1–100.

Hall, D.L., Duldig, M.L. *and* Humble, J.E. (1995). The north-south anisotropy and the radial density gradient of cosmic rays at 1 AU. *Publications of the Astronomical Society of Australia 12*:153 – 158.

Hall, D.L., Humble, J.E. *and* Duldig, M.L. (1994a). Radial and latitudinal gradients in galactic cosmic rays. *Proceedings of the Astronomical Society of Australia 11*: 170 – 174.

Hall, D.L., Humble, J.E. *and* Duldig, M.L. (1994b). Modulation of high energy cosmic rays in the heliosphere. *Journal of Geophysical Research 99*:1443 – 1457.

Hall, D.L., Duldig, M.L. *and* Humble, J.E. (1996). Combining the analyses of the sidereal and solar diurnal variations of galactic cosmic ray particles. In: Morris, R.J. (Ed.). *ANARE Research Notes Number 95*. Pp. 53 – 71.

Hall, D.L. (1995). *Modulation of high energy cosmic rays in the heliosphere*. Ph.D. Thesis, University of Tasmania.

Iucci, N., Parisi, M., Storini, M. *and* Villoresi, G. (1981). The behaviour of the cosmic ray equatorial anisotropy inside fast solar wind streams ejected by coronal holes. *Proceedings of the 17th International Cosmic Ray Conference, Paris 10:*238–241.

Iucci, N., Parisi, M., Storini, M. *and* Villoresi, G. (1983). The behaviour of the cosmic ray equatorial anisotropy inside fast solar wind streams ejected by coronal holes. *Proceedings of the 18th International Cosmic Ray Conference, Bangalore 3:* 354–357.

Jacklyn, R.M. *and* Duldig, M.L. (1987). The determination of the accidental coincidence rate in the output of a 2-tray gas counter telescope. *Proceedings of the 20th International Cosmic Ray Conference, Moscow 4:*380–383.

Jacklyn, R.M., Duldig, M.L. *and* Pomerantz, M.A. (1984a). Cosmic ray intensity waves and the north-south anisotropy. *Proceedings of the Astronomical Society of Australia 5:*581–586.

Jacklyn, R.M., Duldig, M.L. *and* Pomerantz, M.A. (1984b). Anisotropic and isotropic intensity waves. *Proceedings of the International Symposium on Cosmic Ray Modulation in the Heliosphere, Morioka.* Pp. 76–82.

Jacklyn, R.M., Duldig, M.L. *and* Pomerantz, M.A. (1987). High energy cosmic ray intensity waves. *Journal of Geophysics Research 92:*8511–8518.

Jacklyn, R.M. *and* Humble, J.E. (1981). A large enhancement of the solar diurnal variation observed underground and at the surface at southern latitudes in April 1980. *Proceedings of the 17th International Cosmic Ray Conference, Paris 4:* 134–137.

Kobel, E. (1989). *Determination of cutoff rigidities and asymptotic directions of cosmic rays for the solar proton event on 7–8 December 1982, allowing for the influence of the disturbed geomagnetosphere*. M.Sc. Thesis, University of Bern.

Lockwood, J.A. (1971). Forbush decreases in the cosmic radiation. *Space Science Review 12:*658–715.

Lyons, P.R.A. (1981). *Atmospheric effects of high energy cosmic rays*. Ph.D. Thesis, University of Tasmania.

McCracken, K.G. (1962). The cosmic-ray flare effect. 1. Some new methods of analysis. *Journal of Geophysical Research 67:*423–434.

Mori, S., Yasue, S., Ichinose, M. *and* Munakata, Y. (1975). 27-Day recurrences of enhanced daily variations in the cosmic ray intensity during 1973 – 1975. *Proceedings of the 14th International Cosmic Ray Conference, Munich 4:* 1463 – 1468.

Mori, S., Yasue, S., Munakata, K., Chino, K., Furuhata, M., Shiozaki, Y., Yokota, Y., Akahane, S., Fujii, Z., Morishita, I., Humble, J.E., Fenton, A.G., Fenton, K.B. *and* Duldig, M.L. (1991). Japan-Australia observations of the north-south sidereal asymmetry at ~10^{12} eV. *Proceedings of the 22nd International Cosmic Ray Conference, Dublin 2:*720 – 723.

Murayama, T. (1981). Cosmic ray flow in space and its relation to the structure of interplanetary plasma. *Proceedings of the 17th International Cosmic Ray Conference, Paris 4:*155 – 158.

Nagashima, K., Sakakibara, S. *and* Morishita, I. (1991). Quiescence of GLE - producible solar proton eruptions during the transition phase of heliomagnetic polarity reversal near the solar activity - maximum period. *Journal of Geomagnetism and Geoelectricity 43:*685 – 689.

Pyle, K.R. (1993). Private communication.

Rao, U.R. (1972). Solar modulation of galactic cosmic radiation. *Space Science Reviews 12:*719 – 809.

Shea, M.A. *and* Smart, D.F. (1982). Possible evidence for a rigidity-dependent release of relativistic protons from the solar corona. *Space Science Reviews 32:*251 – 271.

Shea, M.A. *and* Smart, D.F. (1990). A summary of major solar proton events. *Solar Physics 127:*297 – 320.

Shea, M.A. *and* Smart, D.F. (1993). History of energetic solar protons for the past three solar cycles including cycle 22 update. In: Swenberg et al. (Eds.). Biological Effects and Physics of Solar and Galactic Cosmic Radiation, Part B. Plenum, New York. Pp 37 – 71.

Shea, M.A. *and* Smart, D.F. (1995). Private communication.

Shea, M.A., Smart, D.F. *and* Pyle, K.R. (1991a). Direct solar neutrons detected by neutron monitors on 24 May 1990. *Geophysical Research Letters 18:*1655 – 1658.

Shea, M.A., Smart, D.F., Wilson, M.D. *and* Flückiger, E.O. (1991b). Possible ground-level measurements of solar neutron decay protons during the 19 October 1989 solar cosmic ray event. *Geophysical Research Letters 18:*829 – 832.

Smart, D.F., Shea, M.A., Wilson, M.D. *and* Gentile, L.C. (1991). Solar cosmic rays on 29 September 1989: An analysis using the world-wide network of cosmic ray stations. *Proceedings of the 22nd International Cosmic Ray Conference, Dublin 3:*97 – 100.

Swinson, D.B. (1981). Extended periods of enhanced solar diurnal variation. *Proceedings of the 17th International Cosmic Ray Conference, Paris 4:*138 – 141.

Swinson, D.B. *and* Shea, M.A. (1990). The September 29, 1989 ground level event observed at high rigidity. *Geophysical Research Letters 17:*1073 – 1075.

Swinson, D.B., Yasue, S. *and* Fujii, Z. (1993). Large amplitude 27-day waves in the cosmic ray north-south anisotropy. *Proceedings of the 23rd International Cosmic Ray Conference, Calgary 3:*671 – 674.

Venkatesan, D. *and* Badruddin. (1990). Cosmic ray intensity variations in the 3-dimensional heliosphere. *Space Science Review 52:*121 – 193.

2. MODELLING SOME COSMIC RAY GROUND LEVEL ENHANCEMENTS

M.L. Duldig[1], J.L. Cramp[2] and J.E. Humble[2]

[1] Cosmic Ray Section
Antarctic Division
Kingston Tasmania 7050
Australia

[2] Physics Department
University of Tasmania
Hobart Tasmania 7001
Australia

ABSTRACT

With the most advanced modelling technique available we have studied four Ground Level Enhancements (GLEs), namely those of 7/8 December 1982, 16 February 1984, 22 October 1989 and 24 October 1989. Scattering of cosmic rays in the near Earth environment by interplanetary magnetic field (IMF) irregularities has played an important role in the particle propagation of the latter two events. A spike in the response prior to the main GLE on 22 October 1989 showed extreme anisotropy indicating some form of focusing or channelling of the particles by the IMF. This may be related to the proximity of the wavy neutral sheet. The 16 February 1984 GLE also showed marked anisotropy throughout the event, in this case indicating very little scattering in the IMF. The rigidity dependence of the pitch angle distribution was studied for the 7/8 December 1982 event and showed that the higher rigidity particles had undergone less scattering than lower rigidity particles. This is the first time the rigidity dependence of the pitch angle distribution has been studied.

2.1 INTRODUCTION

Cosmic rays are fully ionised nuclei of high energy (10^9–10^{20} eV). Their distribution at the Earth is almost isotropic and they are principally of galactic or extra-galactic origin. The particles interact with atmospheric nuclei to produce secondary particles which are subsequently detected by ground based instruments. Directional information is maintained throughout these interactions due to the highly relativistic speeds of the particles. Occasionally, a solar flare will accelerate protons to sufficiently high energies for the secondaries to be detected at sea level. The arrival of these particles results in a sharp increase in the count rate of ground based cosmic ray detectors. These solar induced sharp increases are known as Ground Level Enhancements (GLEs). We have been progressively analysing the GLEs of the current and last solar cycles in an attempt to better understand the propagation of the particles through the interplanetary magnetic field (IMF) between the Sun and the Earth. In this paper we describe the results of modelling four GLEs, namely 7/8 December 1982, 16 February 1984, 22 October 1989 and 24 October 1989.

2.2 PARTICLE PROPAGATION

The solar wind plasma flows radially out from the Sun and carries the magnetic field with it. The field is said to be *frozen* into the solar wind. The solar rotation period of ~27 days results in field lines from the Sun's equatorial region forming an Archimedean spiral as they propagate into interplanetary space. The field line which connects the Earth to the Sun will, on average, leave the Sun at ~60°W of the Sun-Earth line (footpoint) and intersect the Earth at ~45° as shown in Figure 1. This field line is known as the garden hose field line. The precise arrangement of the garden hose field line may vary considerably and is strongly dependent on interplanetary conditions in the region between the Sun and the Earth.

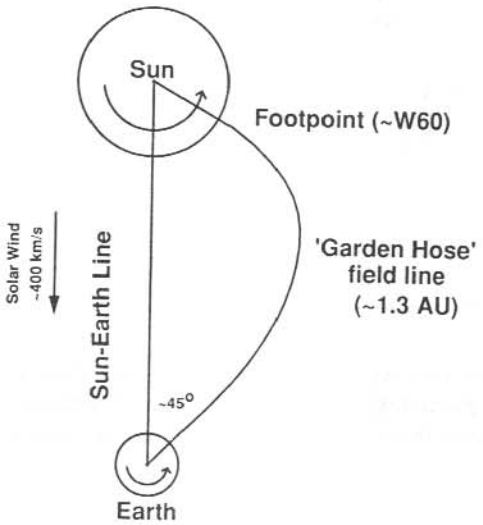

Figure 1. Schematic representation of the interplanetary magnetic field line connecting the Sun and the Earth.

Protons accelerated at the Sun near the footpoint of the garden hose field line will propagate easily to Earth, gyrating around the field line. Particles accelerated some distance from the footpoint must diffuse across field lines before they are able to propagate to Earth along the garden hose field line. It is not known if the particle acceleration takes place over a more extended region than the immediate vicinity of the solar flare site. This would make access to the garden hose field line easier for events where the parent flare is far from the footpoint of the garden hose field line.

When the protons encounter the Earth's magnetic field they undergo a rigidity (momentum per unit charge) dependent deflection as they cross the field. These deflections can be substantial (exceeding 180° of longitude in some special cases) and must be considered when modelling the arrival of the secondary particles at sea-level.

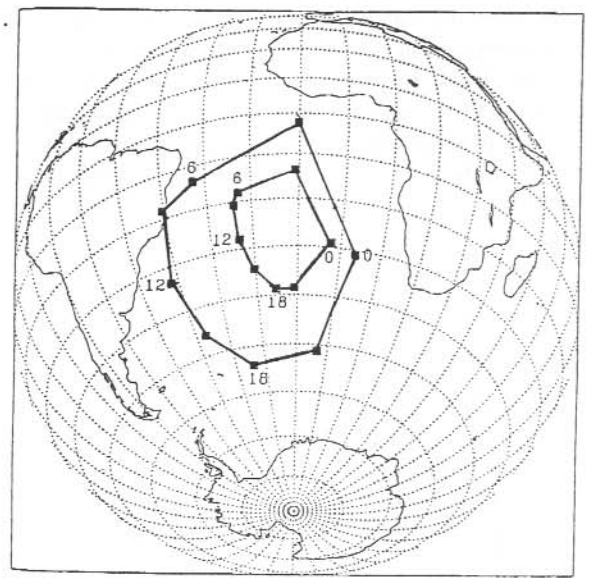

Figure 2. The change in viewing direction of the South Pole neutron monitor (for vertically incident 1 GV particles) with rotation of the Earth and disturbance of the geomagnetic field. The inner trace represents Kp = 0 and the outer trace Kp = 5 (Bieber et al. 1992).

The secondary particles, being created in the atmosphere, travel such short distances that their paths are effectively unchanged. To account for the bending of the paths of solar generated particles the viewing cones of the ground based instruments must be determined. For all but the most energetic GLEs the detecting systems will be neutron monitors. Computer techniques are used to calculate the regions of sky from which a particle has access to a given detector. Such corrections have, until recently, not included current systems in the Earth's field. However, as can be seen in Figure 2, the deflections can change significantly as the Earth rotates; the monitor looking either into the bow or tail field. Furthermore, the extent of geomagnetic disturbance, as represented by the geomagnetic index Kp, also changes the deflection of the incoming particles. Figure 3 shows the rigidity dependent effect on particles arriving vertically at a number of neutron monitors for disturbed and undisturbed geomagnetic conditions. Kobel (1989) developed software to calculate the viewing directions which he subsequently updated using the Tsyganenko (1989) long field model of the Earth's magnetic field (see also Flückiger and Kobel 1990). We have since updated the calculations incorporating aspects of a more recent field model of Peredo et al. (1993).

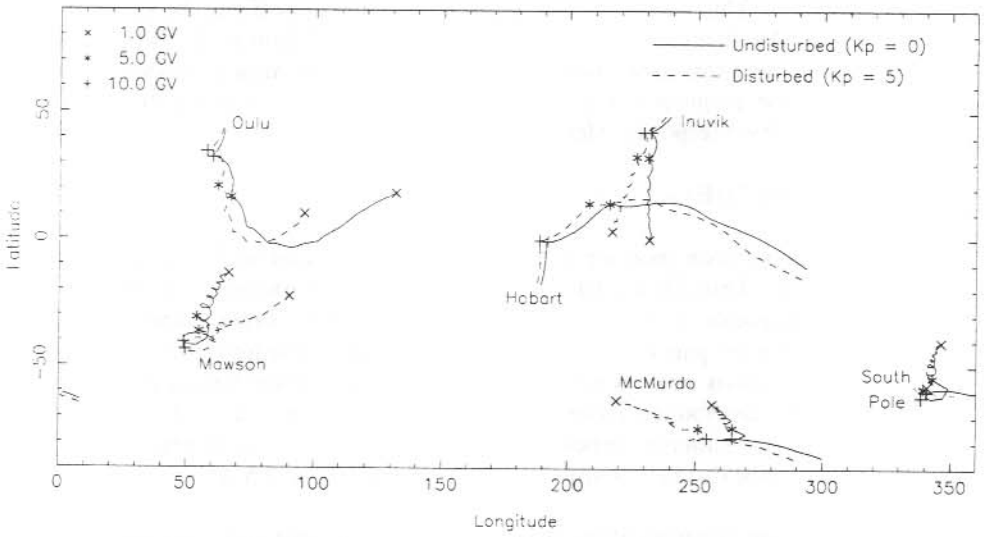

Figure 3. The change in viewing direction of various neutron monitors with geomagnetic disturbance at the time of the 22 October 1989 GLE.

Another feature of the particle deflections is that only particles which exceed a certain rigidity can reach a given monitor. For equatorial stations this low rigidity cut-off may be as high as 15 GV whilst polar monitor sites may have a zero cut-off. Secondary particles also lose energy in penetrating the atmosphere and the minimum proton energy capable of producing a sea-level response is ~0.5 GeV, equivalent to a rigidity of about 1 GV.

2.3 NEUTRON MONITOR RESPONSE

Neutron monitors respond in a predictable way to cosmic rays incident within their cones of view. The monitor response to these cosmic rays is called the specific yield function and includes two components. The first component is the cones of view discussed above, including the low rigidity cut-off. The second component is the neutron monitor yield function (Debrunner et al. 1982) which gives the response of the neutron monitor to particles arriving at the top of the atmosphere. This yield function includes terms to account for the GLE spectrum which is generally quite different from the usual galactic cosmic ray spectrum.

When modelling the neutron monitor response it is also useful to convert the observed increase to the increase that would be seen at sea-level. This involves comparing the responses of low and high altitude monitors which are geographically near to each other. An example is the Hobart and Mt. Wellington monitors which are separated by only 7 km but have altitudes of 10 m and 725 m respectively. Being geographically close means that the viewing cones are virtually identical and the different response will be solely due to the atmospheric absorption of particles between the higher and lower altitudes (and

poisson statistics). This will be related to the low rigidity cut-off and the spectrum of the GLE particles. An attenuation length can be calculated (Wilson et al. 1967) for various pairs of suitable monitors in the world-wide network and the most consistent attenuation parameters can be employed to correct the monitor responses of all monitors in the network to a sea-level response (McCracken 1962).

2.4 MODELLING THE GLE PROFILE

The world-wide neutron monitor network incorporates sites with various cut-offs as described earlier. This allows determination of spectral parameters of the GLE. The absence of a response at higher cut-off stations gives valuable information on the maximum rigidity of particles accelerated at the Sun. Furthermore the profiles of response at the various stations allows the determination of the arrival direction of the particles and their distribution about this arrival direction. The extent of isotropy and the presence of reverse scattered particles also carries important information about the IMF from the Sun to some distance beyond the Earth (perhaps up to 2.5 AU).

For some GLEs the direction of the IMF is known. In almost all these cases the arrival direction of the particles at the Earth has been found to match closely the field direction. All too often, however, details of the IMF are not known due to the paucity of spacecraft making the necessary measurements and the infrequent monitoring of IMP-8 data which records the appropriate parameters when it is clear of the geomagnetic tail.

A standard technique for modelling GLEs has been developed over many years (Shea and Smart 1982; Shea et al. 1991). The analyses presented here are based on an extension of the standard technique. We have modified the modelling to allow a rigidity dependent pitch angle distribution for the particles and allowing reverse particle propagation. The pitch angle is the angle of gyration with respect to the direction of motion (i.e. the IMF direction). We have also enclosed the complete modelling software within a least-square framework to rapidly find the optimum solution in parameter space.

For any GLE, the responses of the neutron monitors world-wide are used, after applying the correction for altitude described above, to determine the spectrum and spatial distribution of particles arriving from the Sun. The model for these responses is of the form

$$I_i = \sum_{P_{c,i}}^{\infty} J(\alpha,P)\, S_i(P)\, G(\alpha,P)\, \delta P,$$

where I_i is the sea-level corrected percentage increase at station i at the given time;
P is the particle rigidity in GV;
$P_{c,i}$ is the low rigidity geomagnetic cut-off for station i at the given time;
α is the pitch angle of the particles;
J is the differential interplanetary flux;
S_i is the specific yield function of the neutron monitor (including viewing cone);
and G is the particle pitch angle distribution around the arrival direction.

It should be noted that this is not a dynamic solution to the observed response profiles at the various neutron monitors but an 'instantaneous' solution at a given time during the event. The term instantaneous is slightly misleading as data are collected for some time interval for each measurement (usually 5 minutes) to obtain adequate statistical accuracy. To understand the dynamic situation it is necessary to model the event at various times throughout its development.

2.5 GENERAL FEATURES OF THE GLES AND THE INITIATING FLARES

2.5.1 *7/8 December 1982*

- The solar active region believed to be responsible for the flare and GLE was NOAA/USAF region 4007.
- At the time of this event the region was located at S19° W86° on the solar disk.
- X-ray emission lasting 4 hours commenced at 23:36 UT and reached its peak at 23:54 UT.
- H_α emission onset was observed at 23:41 UT and reached maximum intensity at 23:51 UT.
- Radio emission at 245–15400 MHz was observed from ~23:37 UT.
- The earliest GLE onset was measured at several stations at 23:55–24:00 UT.
- The GLE was observed by at least 44 stations with the largest response of 56% above normal background recorded at Kerguelen Island.
- The geomagnetic disturbance was Kp = 4 to 4+ throughout the event having reached a peak of 6+ during the geomagnetic storm prior to the GLE.

2.5.2 *16 February 1984*

- The solar active region believed to be responsible for the flare and GLE was NOAA/USAF region 4410.
- At the time of this event the region was located at approximately S19° W95° on the sun (behind the west limb).
- No X-ray or H_α emission were observed.
- Radio emission at 245–15400 MHz was observed from ~08:58 UT.
- The earliest GLE onset was measured at South Pole at 09:02–09:04 UT.
- The GLE was observed by at least 48 stations with the largest response of 209% above normal background recorded at South Pole.
- The geomagnetic disturbance was Kp = 1 to 2 throughout the event.

2.5.3 *22 October 1989*

- The solar active region believed to be responsible for the flare and GLE was NOAA/USAF region 5747.
- This region was also attributed as the source region for two other GLEs (Shea 1990) on 19 and 24 October 1989 (see below).
- At the time of this event the region was located at S27° W31° on the solar disk.
- X-ray emission lasting 4 hours commenced at 17:08 UT and reached a peak of X2.9 at 17:57 UT.
- H_α emission was recorded during the flare.
- Radio emission at 245–15400 MHz was observed from ~17:50 UT.
- The earliest GLE onset was measured at South Pole at 17:50 UT.
- The main GLE was observed by at least 18 stations with the largest response of 40% above normal background recorded at South Pole.
- An initial peak with extreme anisotropy was observed by only 6 stations of which the largest response was McMurdo at 193% increase above normal background at 18:06–18:08 UT.
- The geomagnetic disturbance was Kp = 5+ throughout the event.

2.5.4 *24 October 1989*

- The solar active region believed to be responsible for the flare and GLE was NOAA/USAF region 5747.
- At the time of this event the region was located at S30° W57° on the solar disk.
- X-ray emission lasting 7 hours commenced at 17:56 UT and reached a peak of X5.7 at 18:31 UT.
- Radio emission at 245–15400 MHz observed from ~17:35 UT peaked at ~18:10 UT.
- The earliest GLE onset was measured at Mt. Wellington at 18:15–18:20 UT.
- The GLE was observed by at least 31 stations with the largest response of 205% above normal background recorded at South Pole at 20:34–20:36 UT.
- The geomagnetic disturbance varied from K_p = 3+ to 4- during the event.

2.6 RESULTS OF THE MODELLING

2.6.1 *7/8 December 1982*

Figure 4 shows the profile of the GLE as observed at 6 stations. Flückiger et al. (1990) summarised the observations of the position of the IMF during this event. Table 1 shows the IMF direction in Earth based co-ordinates together with the fit to the source position

derived from modelling the particle arrival of the GLE. From the table it is clear that the direction of the IMF was highly variable. The derived particle arrival direction is certainly consistent with the IMF data.

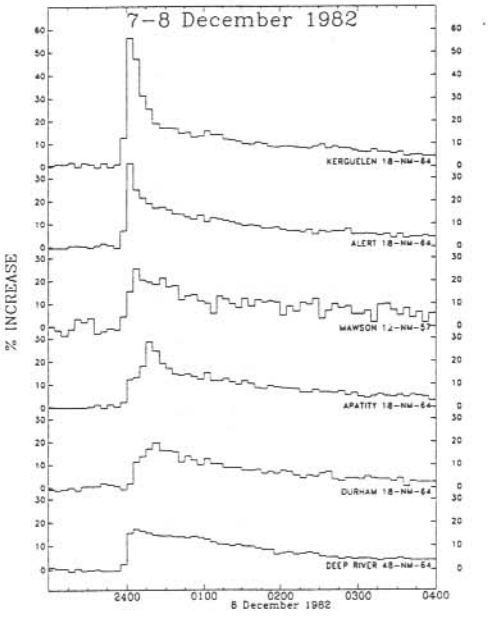

Figure 4. Pressure corrected count rates during the GLE of 7/8 December 1982.

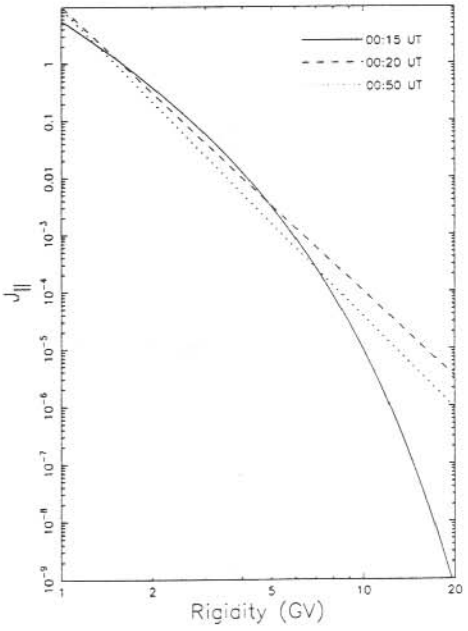

Figure 5. Derived spectra during the GLE of 7/8 December 1982.

Table 1. 7/8 December 1982 GLE particle arrival and IMF directions.

Time (UT)	Latitude	Longitude
00:15 – 00:20	32°	76°
00:20 – 00:25	27°	57°
00:50 – 00:55	-18°	30°
	IMF Latitude	IMF Longitude
00:01 – 00:07	25°	80°
00:08 – 00:11	50°	45°
00:12 – 00:31	40°	80°

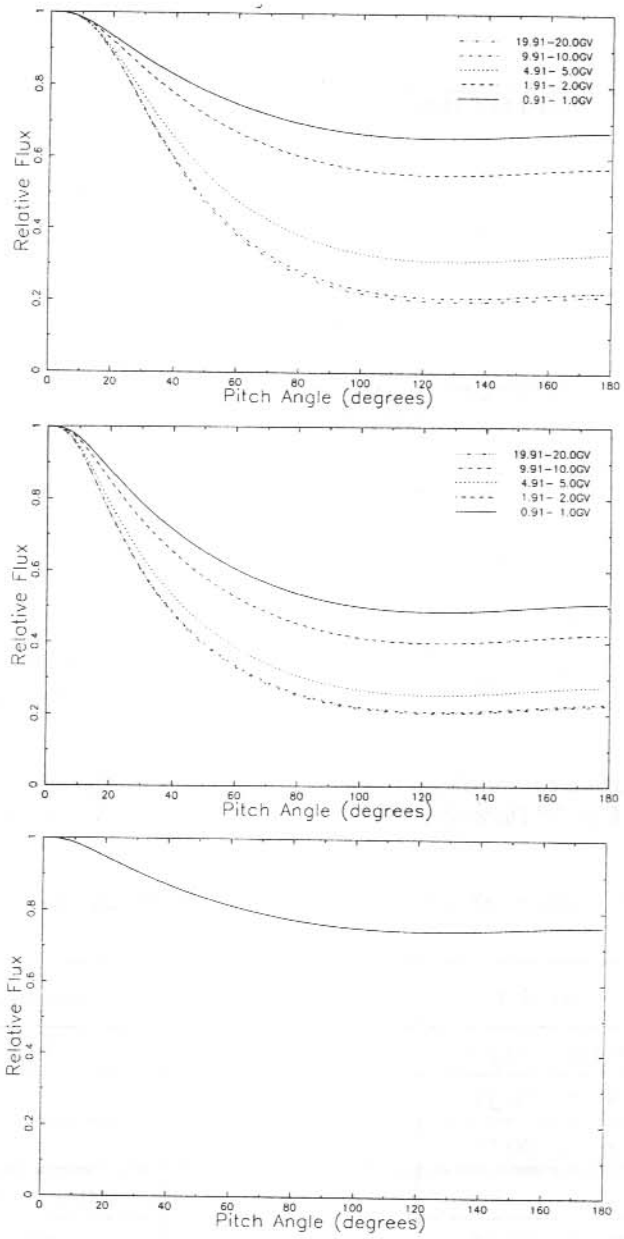

Figure 6. Derived energy dependent pitch angle distribution at 00:15 UT(top), 00:20 UT (middle) and 00:50 UT (bottom) on 7 December 1982 during the GLE. No energy dependence was found in the latter case.

In addition to the arrival direction the GLE spectrum and particle distribution about the arrival direction (pitch angle distribution) were also determined. Figure 5 shows the derived spectra for each of the times modelled. The spectrum initially showed significant bending at higher rigidities but later hardened to an unmodified power law form. The power law index is around 5 early in the event and steepens slightly to about 5.5 later. These spectral slopes are a little shallower (i.e. harder spectra) than most GLEs. The pitch angle distributions were modelled with a rigidity dependence and the results are shown in Figure 6. The earliest time showed a moderate anisotropy, indicated by the extent of the peak above the background and the width of the peak. By the second time the anisotropy had reduced significantly and by 00:50–00:55 UT the particle distribution was only very slightly anisotropic. The energy dependence of the pitch angle distributions shows that the higher rigidity particles have undergone less scattering and are thus more focused. It is also clear from a comparison of the top and middle panels of Figure 6 that the lower rigidities were becoming more isotropic earlier than the higher rigidities. By the last model time, seen in the bottom panel of Figure 6, no rigidity dependence was found in the pitch angle distribution. It is believed that this is the first quantitative observation of the rigidity dependence of the pitch angle distribution of GLE particles.

2.6.2 *16 February 1984*

Figure 7 shows the profile of the GLE as observed at 6 stations. We had no information on the position of the IMF during this event. Table 2 shows the sub-solar point in Earth based co-ordinates together with the fit to the source position derived from modelling the particle arrival of the GLE. Remembering that the nominal garden hose field direction is 45° to the Sun-Earth line (or sub-solar point) it is clear that the derived particle arrival direction is consistent with the most likely IMF direction.

Figure 8 shows the derived spectra for each of the times modelled. The spectrum was reasonably constant in shape throughout the event although there was some hardening around 09:20–09:25 UT from a power law index around 5.5 to around 5.0. Again these spectra are a little harder than for most GLEs. The pitch angle distributions are shown in Figure 9.

Table 2. 16 February 1984 GLE particle arrival and sub-solar point directions.

Time (UT)	Latitude (sub-solar = -13°)	Longitude (sub-solar)
09:05–09:10	-38°	8° (46°)
09:10–09:15	-38°	7° (43°)
09:15–09:20	-33°	1° (41°)
09:55–10:00	-40°	353° (38°)

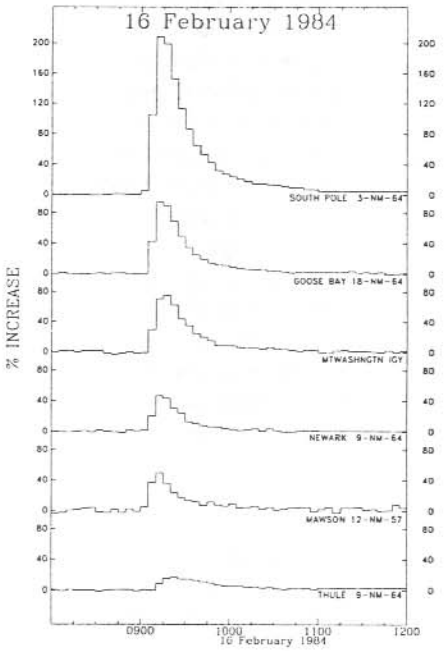

Figure 7. Pressure corrected count rate profiles during the GLE of 16 February 1984.

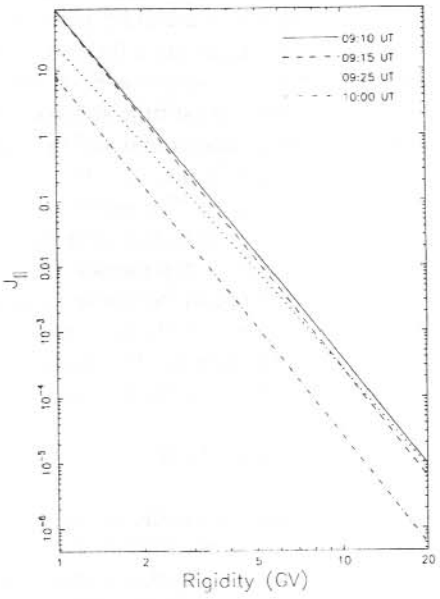

Figure 8. Derived spectra during the GLE of 16 February 1984.

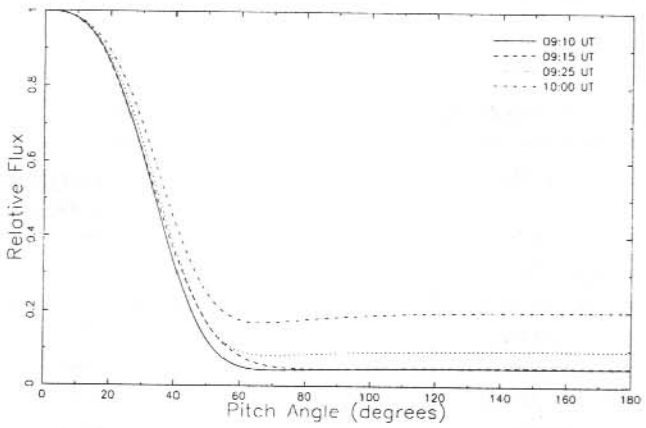

Figure 9. Derived pitch angle distributions during the GLE of 16 February 1984.

There was strong anisotropy at all modelled times with only a small rise in the isotropic component later in the event. It is very unusual for such strong anisotropy to remain indicating almost no scattering of the GLE particles.

2.6.3 *22 October 1989*

We had already analysed this event with a simpler version of the model employed here (Duldig et al. 1993). The results of this more recent study show some quantitative differences although the broad conclusions from the earlier study remain relatively unchanged. Figure 10 shows the sequence of three GLEs observed by the Mawson

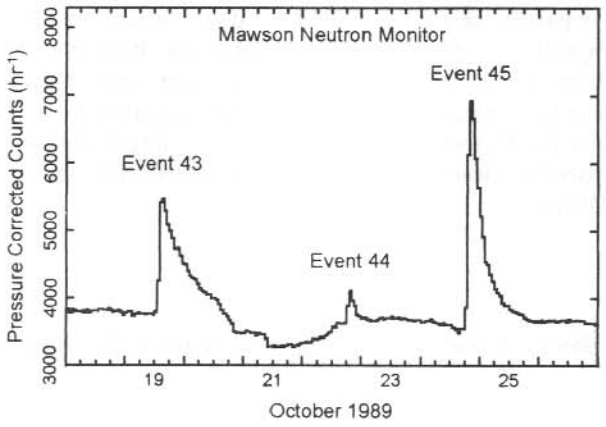

Figure 10. The count rate profile from the Mawson neutron monitor from 18 – 26 October 1989 showing the three GLEs which were attributed to the same solar active region.

neutron monitor during October 1989. All three of these events arose from the same active region on the Sun. Figure 11 shows the initial spike reported by only six stations in the world-wide network. Figure 12 shows other stations response to the main GLE. Table 3 shows the results of the modelling at various times. No field data were available for this event so the sub-solar direction is shown for comparison again. The table also shows details of the slopes of the spectra which are reproduced in Figure 13.

It is clear from the table that, excluding the spike, the particle arrival directions for the main GLE are initially closer to the Sun-Earth line than the nominal garden hose. They begin about 20° from the Sun-Earth line and have swung out to 32° by the end of the event.

The initial spike is very unusual. Its arrival direction is along the Sun-Earth line and its pitch angle distribution, shown in Figure 14, indicates extreme anisotropy. It is not clear why this has occurred. It would seem that the particles in this initial spike have been

focused or channelled, possibly by the heliomagnetic neutral sheet or some other IMF structure. This channelling along the Sun-Earth line results in a shorter distance of travel and thus an earlier arrival time than the more scattered particles. The spectra are fairly typical of GLEs with some spectral softening during the event. The initial spike is somewhat softer than earlier parts of the main GLE.

The pitch angle distribution also develops in a unique way during this GLE. As already noted the initial spike shows extreme anisotropy. With the arrival of the main GLE there is some evidence of reverse propagating particles. This become pronounced by 18:30 UT and remains significant until around 19:00 UT when the isotropic component begins to dominate as is seen in most GLEs. This reverse propagation implies a strong scattering region beyond the Earth's orbit which has caused particles to scatter back along the IMF. Such a region must have passed the Earth's orbit some days earlier. No candidate region could be found implying that the region did not cross the Earth. It seems that the particles arriving in the initial spike or those of the main GLE have been reflected back along the IMF. The arrival times of forward and reverse propagation indicate a distance beyond the Earth's orbit of the scattering region of 0.75 to 1.5 AU. The larger distance arises if the initial scattering is of particles from the spike whilst the nearer distance corresponds to scattering of the main GLE particles only.

Table 3. 22 October 1989 GLE particle arrival, sub-solar point directions and spectral slope.

Time (UT)	Latitude (sub-solar = -11°)	Longitude (sub-solar)	γ	$\delta\gamma$ GV^{-1} (>2 GV)
18:05 – 18:10	-49°	266° (265°)	-6.25	0.00
18:20 – 18:25	-53°	239° (261°)	-5.35	0.10
18:30 – 18:35	-48°	233° (259°)	-5.82	0.12
18:40 – 18:45	-45°	229° (256°)	-6.15	0.13
18:50 – 18:55	-40°	225° (254°)	-6.60	0.00
19:00 – 19:05	-40°	222° (251°)	-6.70	0.00
19:10 – 19:15	-35°	218° (249°)	-6.70	0.10
19:55 – 10:00	-31°	214° (246°)	-6.80	0.05

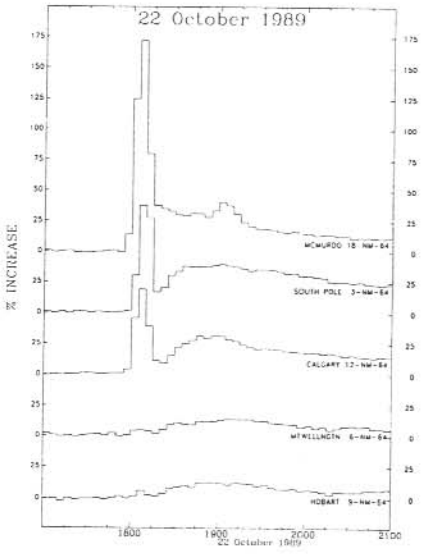

Figure 11. The pressure corrected count rate profiles of the initial spike during the 22 October 1989 GLE. Only six stations observed the spike. Note that the small rises at Mt. Wellington and Hobart are statistically significant.

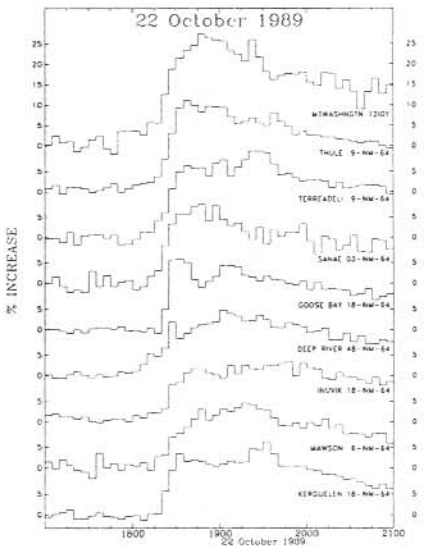

Figure 12. The pressure corrected count rate profiles from various other neutron monitors for the 22 October 1989 GLE.

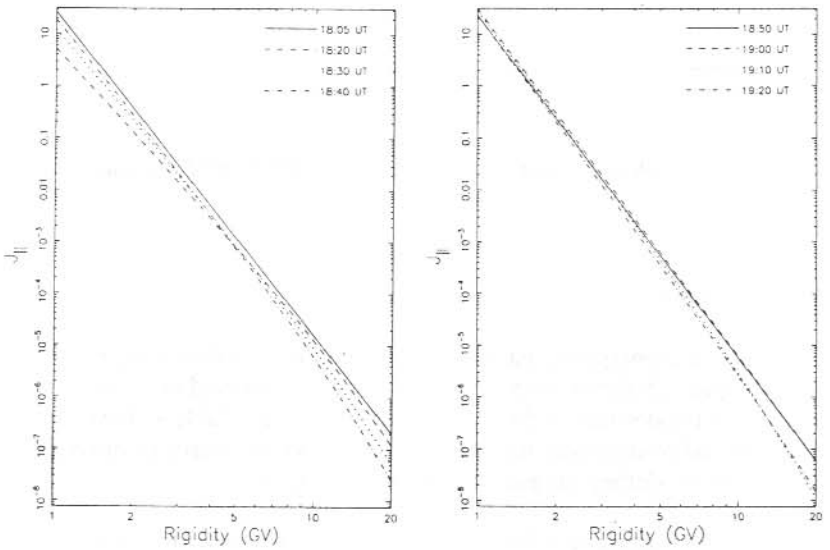

Figure 13. Derived spectra during the GLE of 22 October 1989.

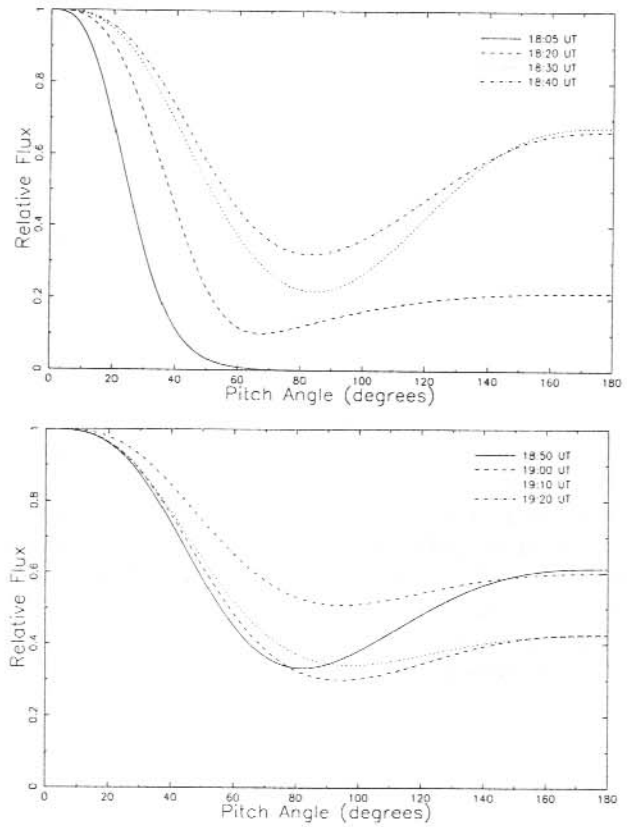

Figure 14. Derived pitch angle distributions during the GLE of 22 October 1989.

2.6.4 *24 October 1989*

Once again this is a re-analysis of earlier work (Cramp et al. 1994) using an updated form of the model. Figure 15 shows the profile of the GLE as observed at six stations. We had no information on the position of the IMF during this event. Table 4 shows the sub-solar point in Earth based co-ordinates together with the fit to the source position and spectral slope derived from modelling the particle arrival of the GLE.

The spectra and pitch angle distributions are shown in Figures 16 and 17 respectively. The spectra are unremarkable being power laws which soften throughout the event. The pitch angle distributions show remarkably little anisotropy, especially during the onset of

the GLE which is most unusual and indicates strong scattering between the Earth and the Sun. It is also notable that, throughout the event, the particle arrival direction (~65° to the Sun-Earth line) is significantly more westward than the nominal garden hose direction. This contrasts with the source region which is located very close to the nominal garden hose footpoint.

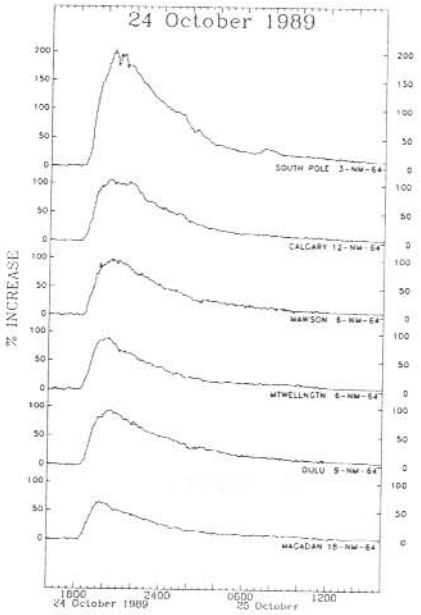

Figure 15. The pressure corrected count rates from various neutron monitors for the 24 October 1989 GLE.

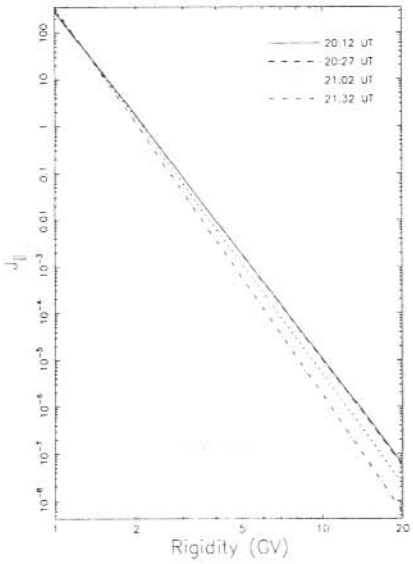

Figure 16. Derived spectra during the GLE of 24 October 1989.

Table 4. 24 October 1989 GLE particle arrival, sub-solar point directions and spectral slope.

Time (UT)	Latitude (sub-solar = -11°)	Longitude (sub-solar)	γ	$\delta\gamma$ GV^{-1} (>2 GV)
20:10–20:15	-19°	167° (234°)	-7.43	0.00
20:25–20:30	-22°	164° (230°)	-7.47	0.00
21:00–21:05	-22°	156° (220°)	-7.80	0.00
21:30–21:35	-24°	149° (213°)	-8.30	0.01

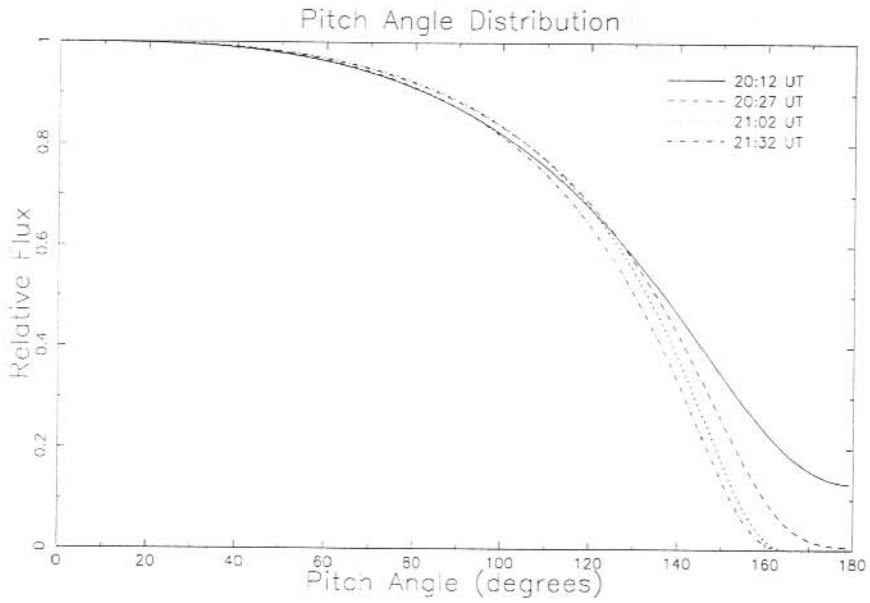

Figure 17. Derived pitch angle distributions during the GLE of 24 October 1989.

2.7 CONCLUSION

Using the most advanced modelling techniques for the arrival of GLE particles at the Earth we have shown that scattering in the IMF plays a crucial role in particle propagation from the Sun to the near Earth environment and beyond. It is clear from the analysis of the 22 October 1989 spike that the IMF is capable of either channelling or focusing the particle propagation. Furthermore, scattering beyond the Earth has resulted in particles being reflected back along the IMF during this GLE. The proximity of the neutral sheet may play an important role in such channelling but this possibility requires further study.

For the first time the rigidity dependence of the pitch angle distribution of arriving particles has been investigated. The 7/8 December 1982 GLE showed greater scattering of low rigidity particles and these particles became isotropically distributed earlier than particles of higher rigidity. Further investigation of this dependence should be carried out to determine if this is characteristic of most GLEs.

2.8 ACKNOWLEDGEMENTS

The authors wish to acknowledge all researchers who have made their data available to the GLE database held at the Philips Laboratory of the US Air Force Geophysics Directorate. J.L.Cramp acknowledges support of an ARC postgraduate research award

and J.E. Humble acknowledges support from the Australian Antarctic Division and from ARC research grants.

REFERENCES

Bieber, J.W., Evenson, P. *and* Lin, Z. (1992). Cosmic ray trajectories in the Tsyganenko magnetosphere. *Antarctic Journal, 1992 Review 27:*318–319.

Cramp, J.L., Humble, J.E. *and* Duldig, M.L. (1994). The cosmic ray ground-level enhancement of 24 October 1989. *Proceedings of the Astronomical Society of Australia 11:*28–32.

Debrunner, H., Flückiger, E.O. *and* Lockwood, J.A.(1982). *Eighth European Cosmic Ray Symposium, Rome,* (unpublished).

Duldig, M.L., Cramp, J.L., Humble, J.E., Smart, D.F., Shea, M.A., Bieber, J.W., Evenson, P., Fenton, K.B., Fenton, A.G. *and* Bendoricchio, M.B.M. (1993). The ground-level enhancements of 1989 September 29 and October 22. *Proceedings of the Astronomical Society of Australia 10:*211–217.

Flückiger, E.O. *and* Kobel, E. (1990). Aspects of combining models of the Earth's internal and external magnetic fields. *Journal of Geomagnetism and Geoelectricity 42:*1123–1136.

Flückiger, E.O., Kobel, E., Smart, D.F. *and* Shea, M.A. (1990). On the significance of the magnetospheric effects in the analysis of the ground-level solar cosmic ray event of 7 December 1982. *Proceedings of the 21st International Cosmic Ray Conference Adelaide 7:*22–25.

Kobel, E. (1989). *Determination of cutoff rigidities and asymptotic directions of cosmic rays for the solar proton event on 7–8 December 1982, allowing for the influence of the disturbed geomagnetosphere.* M.Sc. Thesis, University of Bern.

McCracken, K.G. (1962). The cosmic ray flare effect. 1. Some new methods of analysis. *Journal of Geophysical Research 67:*423–434.

Peredo, M., Stern, D. *and* Tsyganenko, N. (1993). Are existing magnetospheric models excessively stretched? *Journal of Geophysical Research 98:*15343–15354.

Shea, M.A. (1990). Solar cosmic rays. *Proceedings of the 21st International Cosmic Ray Conference Adelaide 12:*196–204.

Shea, M.A. *and* Smart, D.F. (1982). Possible evidence for a rigidity-dependent release of relativistic protons from the solar corona. *Space Science Reviews 32:*251–271.

Shea, M.A. Smart, D.F., Wilson, M.D. *and* Flückiger, E.O.(1991). Possible ground-level measurements of solar neutron decay protons during the 19 October 1989 solar cosmic ray event. *Geophysics Research Letters 18:*829–832.

Tsyganenko, N.A. (1989). A magnetospheric magnetic field model with a warped tail current sheet. *Planetary and Space Science 37:*5–20.

Wilson, B.G., Mathews, T. *and* Johnson, R.H. (1967). Intercomparison of neutron monitors during solar flare increases. *Physical Review Letters 18:*675–676.

3. COMBINING THE ANALYSES OF THE SIDEREAL AND SOLAR DIURNAL VARIATIONS OF GALACTIC COSMIC RAY PARTICLES

D.L. Hall[1], M.L. Duldig[2] and J.E. Humble[1]

[1] Physics Department
University of Tasmania
Hobart Tasmania 7001
Australia

[2] Cosmic Ray Section
Antarctic Division
Kingston Tasmania 7050
Australia

ABSTRACT

This paper reports on results which were presented at the Australian Institute of Physics National Congress in Brisbane during 1994. These results were part of the Ph.D. thesis submitted by D.L. Hall in March 1995 and were presented by Dr. M.L. Duldig at the congress.

The radial density gradient (G_r) of galactic cosmic rays in the ecliptic plane points outward from the Sun. This indicates an increasing density of cosmic ray particles beyond the Earth's orbit. Due to this gradient and the direction of the Sun's interplanetary magnetic field (IMF) above and below the IMF wavy neutral sheet, there exists an anisotropic flow of cosmic ray particles approximately perpendicular to the ecliptic plane (i.e. in the direction parallel to $B_{IMF} \times G_r$). This is called the North-South Anisotropy (ξ_{NS}) and manifests as a diurnal variation in sidereal time in the particle intensity recorded by a cosmic ray detector. By analysing the yearly averaged sidereal diurnal variation recorded by five neutron monitors and six muon telescopes from 1957 to 1990 we have determined yearly values of the amplitude and phase of ξ_{NS} to infer the magnitude of G_r for particles with rigidities in excess of 10 GV.

We have previously (Hall et al. 1994a) presented a report in which we derived the value of the coupled parameter $\lambda_{||}G_r$ (where $\lambda_{||}$ is the mean-free path of cosmic rays parallel to the IMF) from 1957 to 1985. The values of $\lambda_{||}G_r$ were obtained from observations of the solar diurnal variation in the counting rates of cosmic ray surface and underground muon telescopes. We have now extended our analysis up to the end of 1990 and have included in the calculations data from a further seven neutron monitors and another underground muon telescope. Thus, we have obtained the values of $\lambda_{||}G_r$ from 1957 to 1990 for particles with rigidities of about 10, 50, 100, 150 and 200 GV.

These results have been combined with the results from the analysis of the North-South anisotropy for the above rigidities and we have been able to examine any temporal and rigidity variations in the quantity $\lambda_{||}$.

3.1 INTRODUCTION

Galactic cosmic ray particles are high energy nuclei and exist in roughly the same relative galactic abundances as their corresponding atomic elements. Thus most of the galactic cosmic rays are protons. The energies of galactic cosmic rays range from about 10^8 eV to 10^{21} eV but the accelerating mechanisms of the highest energy galactic cosmic rays are not understood.

The heliosphere is the region of space where the interplanetary magnetic field (IMF) of the Sun dominates the galactic magnetic field. Outside the heliosphere, in the local inter-stellar region the distribution of galactic particles is considered almost isotropic in space and time. Due to random motion and collisions particles cross the heliospheric boundary and enter the heliosphere. These particles gyrate around the IMF but due to small scale irregularities in the IMF the particles are scattered from their gyro-orbits. The overall motion of the particles will be a diffusion from the boundary towards the Sun. Along their diffusive journey the particles also undergo gradient and curvature drifts in the IMF according to first order orbit theory (Isenberg and Jokipii 1979). The Sun also emits a solar wind plasma radially from its surface with the IMF *frozen* into it and convects particles back toward the heliospheric boundary. The overall result of these processes is the solar modulation within the heliosphere of the galactic distribution of cosmic ray particles (Forman and Gleeson 1975).

Solar modulation causes gradients in the number density of particles. Proof of the existence and knowledge of the magnitudes of these density gradients are key elements in discussing the validity of solar modulation models. Up to rigidities of 10 GV, modulation models predict 11 and 22 year cycles in the radial density gradient (G_r), and 22 year cycles in a latitudinal density gradient (G_θ), related to solar activity and solar magnetic cycles (for example – Jokipii and Kopriva 1979; Jokipii 1984; Potgieter and Moraal 1985; Jokipii 1989; Baker 1993).

Particle-streaming results from modulation in the heliosphere producing an anisotropy (ξ) of the galactic distribution. The streaming in the inner heliosphere can be decomposed into components in and perpendicular to the ecliptic plane. (For the sake of argument the ecliptic plane is taken to be approximately the solar equatorial plane). The streaming perpendicular to the ecliptic plane is observed as a sidereal diurnal variation in the count rate of a recording instrument. This streaming is known as the North-South Anisotropy (ξ_{NS}). The streaming parallel to the ecliptic plane is known as the Solar Diurnal Anisotropy (ξ_{SD}). Since the anisotropies are produced from solar modulation it is possible to derive solar parameters such as mean-free paths of particles and gradients in the number densities from observations of the anisotropies. For example, see the analyses by Yasue (1980) and Bieber and Chen (1991a).

Observations of parameters such as the radial density gradient (G_r), latitudinal density gradient (G_θ) and parallel and perpendicular diffusion coefficients ($\kappa_\parallel$ and $\kappa_\perp$, respectively) are important. Measurements of these parameters provide knowledge of the magnetic conditions and processes in interplanetary space. It is also the only way of supporting (or refuting) predictions made by theoreticians. Essentially, interplanetary space is a large

laboratory in which we can test the predictions of theories by direct and indirect observations of modulation parameters.

The majority of observations employed for these types of analyses have been obtained from northern hemisphere detectors, usually neutron monitors. Southern hemisphere observations and similar analyses at the same and higher primary rigidities may help to provide new insight into cosmic ray modulation.

3.1.1 *Sidereal diurnal variation*

Swinson (1969) proposed that the anisotropy responsible for the sidereal diurnal variation was IMF sector polarity dependent and was directed perpendicular to the ecliptic plane. The streaming of particles perpendicular to the ecliptic plane would have a component in the geo-equatorial plane which would be observed as a diurnal variation in data in sidereal time. The mechanics behind the anisotropy are presented in Figure 1 : the particles gyrate around a field line in the vicinity of the Earth and may be detected by Earth based instruments. The direction of flow can be represented as BxG_r. Due to the radial gradient in the number density of cosmic-rays, the flow of particles approaching from outside the Earth's orbit differs from the flow due to particles coming from inside the Earth's orbit. The two flows are in opposite directions and an Earth based instrument will record the excess streaming from the direction corresponding to the flow of particles which originated in the region of higher density. If the field line reverses direction (the Earth is in a different IMF sector) the excess streaming at Earth will reverse direction. Consequently, at times, a northern hemisphere telescope will detect a larger intensity of particles than a southern hemisphere telescope and vice-versa. This is ξ_{NS}. The effect was conclusively demonstrated by analysing underground muon data (Swinson 1971). In reality the streaming of particles perpendicular to the ecliptic plane is a net anisotropic flow caused mainly by curvature and gradient drifts in the IMF. These results suggested that the amplitude of ξ_{NS} was constant during the period 1965-68 and had an upper limiting rigidity (P_u) of about 75 GV.

Yasue (1980) derived the spectrum of ξ_{NS} for the combined years 1968 to 1972. He found that the anisotropy was weakly proportional to the rigidity of the particles ($P^{0.3}$) and that P_u was between 150 and 300 GV. He was the first to show conclusively that the anisotropy was from the direction perpendicular to the ecliptic plane. He did this by examining all three dimensions of the anisotropy relative to the Earth's equator (i.e. due to the ecliptic plane being tilted 23.5 degrees to the Earth's rotation axis). He examined both of the components of ξ_{NS} observable at Earth - a component in the geo-equatorial plane (sidereal diurnal intensity variation) and a component along the Earth's rotation axis (N-S asymmetry in particle intensity). ξ_{NS} can be derived from the measurement of either of these variations in intensity. His results were consistent with an invariant ξ_{NS}.

Bieber and Pomerantz (1986) examined the N-S asymmetry component of ξ_{NS} from 1961 to 1983 using data from polar based neutron monitors. They concluded that there was a variation in the magnitude of the anisotropy with a ten year period. No dependence of the anisotropy on the solar magnetic polarity was observed.

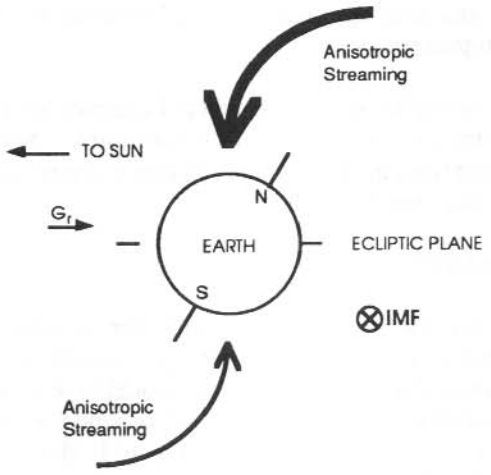

Figure 1. The North-South anisotropy in a towards interplanetary magnetic field (IMF) sector. The excess streaming will be from the northern hemisphere (see text).

Swinson (1988) found little variation in the sidereal diurnal variation recorded by underground muon telescopes from 1965 to 1985. He concluded that ξ_{NS} depends only weakly on the cycles in solar activity and magnetic polarity.

Inferences of G_r from Earth based cosmic ray data are made by measuring ξ_{NS}. Kudo and Wada (1977) examined ξ_{NS} of particles with rigidities ranging from 10 to 200 GV. They found that the G_r decreases with rigidity and is lower at solar minimum than at solar maximum.

Duggal and Pomerantz (1977) inferred G_r from examining ξ_{NS} derived from 12 years of neutron monitor data. They estimated that the average G_r was about 2% AU^{-1} at these rigidities from 1964 to 1975. Extending their analysis to the period 1961 to 1983, Bieber and Pomerantz (1986) showed that the average G_r of 10 GV particles was 1.6% AU^{-1} and G_r varied sinusoidally over this period, having lower values at solar minima. They found no dependence of G_r on the polarity of the IMF in agreement with spacecraft observations and verified at higher rigidities (Yasue 1980; Swinson 1988), although Yasue found no significant variation in G_r from 1968 to 1972.

We recently (Hall et al. 1994b; Hall 1995) derived ξ_{NS} from neutron monitor and muon telescope data and calculated G_r for cosmic rays with rigidities up to 200 GV in good agreement with the above studies. We derived yearly values of G_r from 1957 to 1990 and will use these results in this paper to investigate mean-free paths.

3.1.2 *Observations of modulation parameters such as diffusion coefficients, mean-free paths and density gradients*

There are two components of diffusion in the heliosphere - parallel (||) and perpendicular ($\perp$) to the interplanetary magnetic field (IMF) lines. These are caused by the random walk of particles in the heliosphere. The particles are scattered from their gyro-orbits by irregularities in the IMF and the bulk distribution essentially diffuses along and across field lines. As particles' rigidities increase, eventually the gyro-orbits are so large that particles will not be affected by the irregularities and regular particle motion will prevail (Erdös and Kota 1979). Regular motion is just the usual gyration of particles in the IMF combined with the curvature and gradient drifts of their trajectories.

The diffusion processes are characterised by parallel and perpendicular diffusion coefficients. These can be related to corresponding parallel and perpendicular mean-free paths (λ), interpreted physically as the average distance a particle will travel before being scattered by an irregularity in the Sun's magnetic field and prevented from travelling any further through the heliosphere in that particular direction. For example a small perpendicular mean-free path ($\lambda_\perp$) implies that the perpendicular velocity of a particle's gyration is often interrupted by irregularities in the IMF. This does not prevent parallel motion continuing and hence parallel diffusion dominates. Conversely, a large $\lambda_\parallel$ would imply that particles seldom have their parallel component of velocity *scattered*, hence limiting the relative amount of perpendicular diffusion. The theoretical expressions relating to anisotropies incorporate these mean-free paths. By analysing cosmic ray data for the relevant anisotropies, information about the corresponding mean-free path can be obtained.

One can determine the coupled parameter $\lambda_\parallel G_r$ from the solar diurnal variation in neutron monitor and ionisation chamber data. Bieber and Chen (1991a) have shown that this quantity is rigidity dependent and that it varies with an 11- and 22-year cycle. On the other hand Ahluwalia and Sabbah (1993) claim that $\lambda_\parallel G_r$ is independent of rigidity. These variations are related to the Sun which has an 11-year cycle in its observed number of sunspots and a 22-year cycle in its magnetic polarity. For a period of around 11 years the magnetic field of the Sun has northern magnetic polarity in its northern geographic hemisphere (termed the *$A > 0$ heliospheric magnetic polarity state*). At the end of this period (near the time of solar maximum) the solar magnetic polarity will reverse, over a period of, typically, a year. The new state is called the *$A < 0$ heliospheric magnetic polarity state* and will be the state of the solar magnetic field for a further 11 years until the magnetic poles reverse again. At times of solar minimum $\lambda_\parallel G_r$ of particles with rigidities between 17 and 70 GV is lower during $A > 0$ IMF polarity states than during $A < 0$ polarity states (Bieber and Chen 1991a). It has been shown that this occurs because $\lambda_\parallel$ of these cosmic rays depends upon solar polarity (Bieber and Chen 1991b; Chen and Bieber 1993). Ahluwalia and Sabbah (1993) also find that $\lambda_\parallel G_r$ is IMF polarity dependent but make no claims as to whether this is caused by a variation in $\lambda_\parallel$, G_r or both.

Earlier (Hall et al. 1994a), we derived the values of $\lambda_\parallel G_r$ for particles with rigidities between 50 and 195 GV, in good agreement with the lower rigidity results of the researchers above. We have recently extended this analysis to the entire rigidity range

between 17 and 195 GV by using the seven neutron monitors and five muon telescopes listed in Table 1.

Table 1. Stations and instruments used in the determination of the modulation parameters.

Station	Mnemonic	Data Availability	Pmed (GV)
Brisbane*	BRNM	1965 – 1990	28
Darwin	DNM	1978 – 1990	50
Deep River	DRNM	1965 – 1988	17
Embudo	EMBV	1965 – 1990	135
Hobart+	HNM	1968 – 1990	17
	HUV	1957 – 1989	185
	HUI	1973 – 1989	195
Kerguelen	KNM	1965 – 1988	17
Mawson#	MNM	1957 – 1990	17
	MSV	1957 – 1971	50
	MUN	1973 – 1990	165
Mt. Wellington	MTNM	1971 – 1990	17

\# 1973 missing (MNM only)
\+ Years 1975 and 1976 missing (HNM only)
* Years 1974, 1975 and 1976 missing

As noted earlier in the introduction knowledge of modulation parameters such as $\kappa_{\|}$, $\kappa_{\perp}$, $\lambda_{\|}$ and $\lambda_{\perp}$ is needed for more accurate numerical models and better understanding of modulation processes. In this paper we combine the results from our previous studies of $\lambda_{\|}G_r$ and G_r to determine $\lambda_{\|}$ from 1957 to 1990 at various rigidities from 17 to 200 GV.

3.2. DATA ANALYSIS

The data listed in Table 1 were Fourier (harmonically) analysed in solar, sidereal and 'anti-sidereal' time. Days with Forbush decreases and other transient phenomena were excluded. Anti-sidereal time is not physically meaningful, but is a useful mathematical concept which can be used for correcting the sidereal results. There are 364 anti-sidereal days in a year,

compared with 366 sidereal days in a year. All data were corrected for atmospheric pressure variations using well determined correction coefficients. First harmonics (diurnal) were averaged over the year and the uncertainties were taken to be the variance of the individual daily variations about the mean diurnal variation. The yearly averaged sidereal and anti-sidereal diurnal variation recorded by each instrument were separated according to the polarity of the IMF sector near the Earth when each measurement was made. The anti-sidereal results were then used to remove the unwanted spurious sidereal diurnal variation present in the sidereal time harmonics due to the annual modulation of the solar semi-diurnal anisotropy (Nagashima et al. 1985). The vector difference was used to produce the *towards minus away* diurnal variation vector ($D_{NS}^{T-A}(t)$) caused by the North-South anisotropy. This vector should be free from atmospheric effects and any other diurnal variations caused by anisotropies *which are modulated symmetrically with respect to toward and away sectors*, including true galactic anisotropies.

Figures 2 and 3 show the $D_{NS}^{T-A}(t)$ vectors (not corrected for geomagnetic bending) derived from the Deep River neutron monitor (DRNM) and the Hobart underground vertical muon telescope (HUV). These figures should illustrate to the reader the observed sidereal diurnal variation over the entire rigidity range being investigated here.

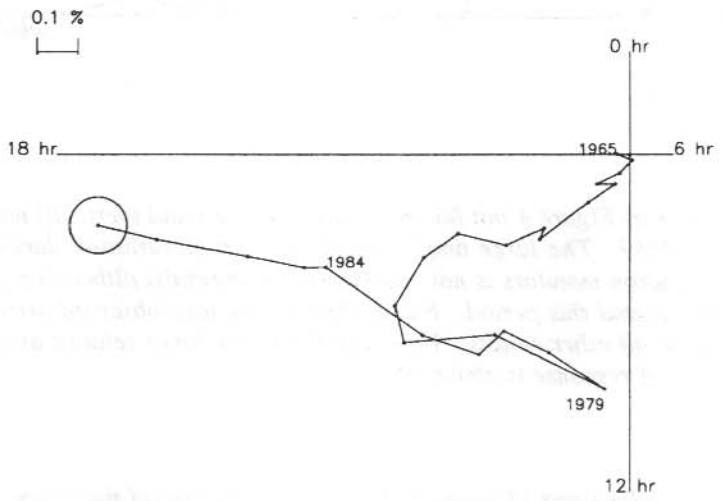

Figure 2. Yearly averaged toward - away sidereal diurnal variation (Nagashima et al. 1995 – corrected) observed by Deep River neutron monitor for 1965 to 1988. Error circles are derived from the combined uncertainties in the sidereal and anti-sidereal diurnal variation and are to 67% confidence. Year labels refer to the head of the corresponding vector. The median rigidity of response is about 17 GV. Significant phase changes are observed after 1965, 1976, 1979 and 1984. 1979 and 1984 are years of relatively large amplitudes.

All the neutron monitors have median rigidities about 17 GV and show the trends exhibited by DRNM. There are substantial phase changes around 1965, 1969, 1978 and 1985. The neutron monitors all record large amplitudes around 1978 and 1979, *unlike* the muon telescope observations at the same period. Large amplitudes are also recorded in the neutron monitor results in 1984 and 1990. From a comparison of all the observations it seems apparent that the vectors (uncorrected for geomagnetic bending) have a cyclic behaviour with a period about 20 years.

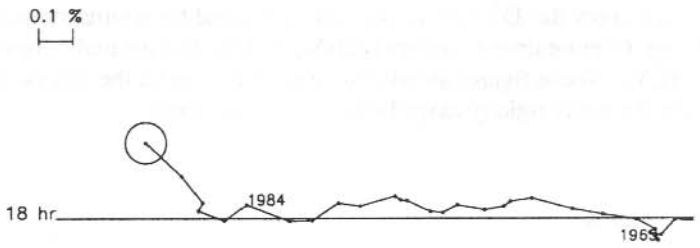

Figure 3. Same as Figure 4 but for the Hobart underground (vertical) muon telescope from 1957 to 1989. The large amplitude of the diurnal variation during 1978-1979 recorded by neutron monitors is not observed in these results although a phase change is observable around this period. Phase changes are also observed around 1965 and 1985, similar to all other results. 1984 and 1989 have large relative amplitudes. The median rigidity of response is about 185 GV.

The HUV vectors lie along 18 hours. Note that the amplitudes of the vectors for 1978 and 1979 are smaller than usual; a similar trend is seen by the Mawson underground north pointing muon telescope (MUN). The results from HUV and MUN suggest that after the period 1977 to 1979 the phase becomes a little earlier than during the previous period and that there are also phase changes around 1965 and after 1984. The median rigidities of the MUN and HUV underground muon telescopes are 165 and 185 GV respectively. This behaviour is also observed in the results of the Socorro underground muon telescope which has a median rigidity of response of about 300 GV.

The harmonics were analysed by the method described by Hall et al. (1994b) to derive the best-fit average rigidity spectrum and the best-fit yearly averaged values of the amplitude of ξ_{NS} (i.e. η_{NS}) and the phase (ϕ_{NS}).

The instruments in Table 1 have been used to obtain values of $\overline{\lambda_{\parallel} G_r}$. The details of the Hobart station have been described by Fenton et al. (1961) and Jacklyn (1970), the Mawson underground instruments by Duldig (1989) and the Mawson surface muon telescope by Parsons (1959). Minor parameters of the other instruments can be found in Fujimoto et al. (1984) and Yasue et al. (1982). The data obtained with the Embudo underground muon telescopes were kindly supplied by Professor D. B. Swinson of the University of New Mexico. Data from the neutron monitors at Deep River and Kerguelen were taken from the National Geophysical Data Centre CD-ROM data disc : NGDC-05/1. Many of these instruments were used to calculate G_r. The reader is directed to Bieber and Chen (1991a) and Hall et al. (1994a, 1994b) for a description of the derivation of these parameters.

Once $\overline{\lambda_{\parallel} G_r}$ and G_r have been calculated we can determine $\lambda_{\parallel}$ from

$$\lambda_{\parallel} = \frac{\left(\overline{\lambda_{\parallel} G_r}\right)}{G_r} \tag{1}$$

$\lambda_{\parallel}$ is actually an average of the parallel mean-free path on both sides of the neutral sheet. The two quantities in (1) are not independent and the relative error of the radial gradient will be more important than $\overline{\lambda_{\parallel} G_r}$ when calculating the error of $\lambda_{\parallel}$. We can examine the inverse of $\lambda_{\parallel}$ for its uncertainty and find that the error in $\lambda_{\parallel}$ is skewed about the value of $\lambda_{\parallel}$. We can calculate the minimum (+) and maximum (-) values of $\lambda_{\parallel}$ ($\lambda_{\parallel}^{\min}{}^{\max}$), within the 1σ error limits :

$$\lambda_{\parallel}^{\min}{}^{\max} = \frac{1}{\frac{G_r}{\left(\overline{\lambda_{\parallel} G_r}\right)} \pm \sigma_{\frac{1}{\lambda_{\parallel}}}} \tag{2}$$

where

$$\sigma_{\frac{1}{\lambda_{\parallel}}} = \frac{1}{\overline{\lambda_{\parallel} G_r}} \sqrt{\sigma_{G_r}^2 + \left(\frac{G_r}{\left(\overline{\lambda_{\parallel} G_r}\right)}\right)^2 \sigma_{\overline{\lambda_{\parallel} G_r}}^2} \tag{3}$$

$\lambda_{\parallel}$ was determined from Equations (1) to (3) for each year that the instruments in Table 1 were operating. In determining any yearly average value of $\lambda_{\parallel}$ from the neutron monitors with median rigidities of 17 GV all the values of $\overline{\lambda_{\parallel} G_r}$ for a particular year were averaged to produce only one (average) $\overline{\lambda_{\parallel} G_r}$ value (at 17 GV) for each year.

In the following, values of $\lambda_{\parallel}$ are determined from 1957 to 1990 for particles with rigidities of 17, 28, 50, 135, 165, 185 and 195 GV. Average values of $\lambda_{\parallel}$ are then determined for periods of distinct magnetic polarity to examine any magnetic polarity dependence of $\lambda_{\parallel}$.

3.3 RESULTS

3.3.1 *Average ξ_{NS}*

Yasue's (1980) spectrum was used to estimate η_{NS} as 0.087% and ϕ_{NS} as 19.2±0.2 hours^{SID} for the entire period. This value of η_{NS} is in excellent agreement with Yasue (1980) but slightly higher than Bieber and Pomerantz's (1986) which was 0.053%. Nagashima et al. (1983) considered the difference between the ecliptic and solar equatorial planes. The solar magnetic field is defined in the solar equatorial plane and the radial gradient is defined in the ecliptic plane. The predicted yearly averaged direction of the North-South anisotropy (BxG_r) was shown to be 18.57 hours^{SID}, similar to the derived averaged value of ϕ_{NS}. Note that the average ϕ_{NS} derived here contains twice as many years of negative heliospheric polarity in the derivation than of positive heliospheric polarity. If there are any differences in the phase of ϕ_{NS} related to the polarity of the heliosphere then the average will be slightly biased towards the results of the negative polarity state.

3.3.2 *Temporal variation of ξ_{NS}*

Figures 4 and 5 show the best fit η_{NS} and ϕ_{NS} of ξ_{NS} from 1957 to 1990. Note that there are definite variations in both η_{NS} and ϕ_{NS}.

3.3.2.1 *The amplitude η_{NS}*

The results shown in Figure 4 were derived under the assumption of Yasue's (1980) rigidity spectrum and fitted to a wave with arbitrary amplitude and phase and an 11-year period; that is, $\eta_{NS} = c_\eta + A_\eta \cos\omega(t - \phi_\eta)$. A statistical F test was performed to test the significance of the wave fitted to the amplitudes. This test compared the variance of the amplitudes from the fitted wave to the variance of the amplitudes from the mean η_{NS}. The F test indicated that there is only 34% probability that the wave is a better model to the amplitude variation than the mean. Attempts to fit waves of other periods yielded similar results with the most probable wave being one with a 15 year period (84% probability).

A 10-year wave in the amplitude of ξ_{NS} was reported by Bieber and Pomerantz (1986). Swinson (1988) observed the amplitudes of the sidereal variation vectors (uncorrected for geomagnetic effects) to have a small variation over a 20-year period. Swinson's (1988) analysis was similar to our analysis and is qualitatively in agreement with the results presented here. He did not derive the free-space anisotropy so direct comparison is impossible. The present results are directly comparable to those of Bieber and Pomerantz (1986) however, and are in reasonable agreement with their values although there is no definite cyclic variation in the results presented here. We previously suggested that our analysis is contaminated by another anisotropy which is damping out some of the variation in the results. This contamination can be discerned by examining the phase of the anisotropy more closely.

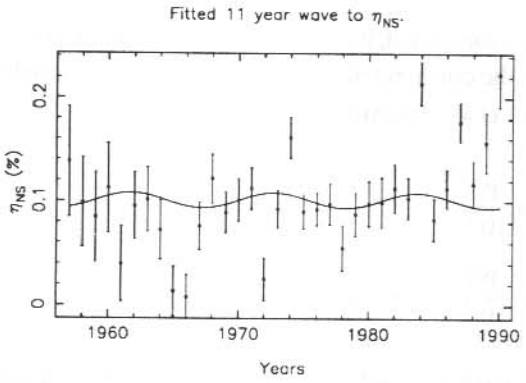

Figure 4. Fitted 11-year wave to η_{NS}. Uncertainties are to 67% confidence.

3.3.2.2 *The phase ϕ_{NS}*

In Figure 5 the phases were fitted to a 22-year wave; that is, $\phi_{NS} = c_\phi + A_\phi \cos\omega(t - \phi_\phi)$. Again an F test was performed to compare the variance from the fitted 22-year wave to the variance from the mean ϕ_{NS}. The test indicated a 99.99% probability that a 22-year wave is a better representation of the results than the mean. The wave has an amplitude of 1.6 hours and peaks during the years 1966 and 1988. We have previously speculated that this wave may exist and would be due to a contamination of the analysis by an asymmetric modulation (with respect to above and below the neutral sheet) of a true galactic anisotropy, predicted previously by Nagashima et al. (1982). Here we have shown that this contamination is real.

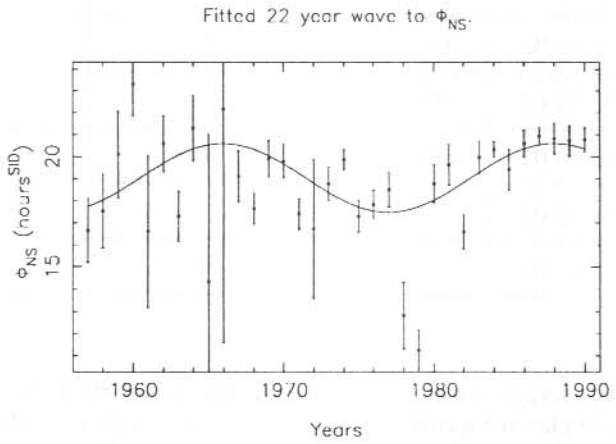

Figure 5. Fitted 22-year wave to ϕ_{NS}. Uncertainties are to 67% confidence.

3.3.3 *Radial gradient of galactic cosmic rays*

Since the analysis is contaminated, the radial density gradient (G_r) can only be inferred from ξ_{NS} by assuming that the contamination is small. G_r can be inferred from the amplitude of ξ_{NS} (Yasue 1980; Hall et al. 1994b) by :

$$G_r = \frac{4.5B}{\sin\psi}\eta_{NS}\left(\frac{P}{10}\right)^{\gamma-1}$$
$$= 31.82\eta_{NS}\left(\frac{P}{10}\right)^{-0.7} \quad P \leq 200 \text{ GV}. \tag{4}$$

The following results have assumed that the IMF strength (B) is a constant at 5 nT and that the angle at the Earth of the IMF to the Earth-Sun line (ψ) is constant at 45°.

Table 2. Values of the radial density gradient (G_r) calculated from Equation (2) and the North-South anisotropy assuming Yasue's (1980) rigidity spectrum. Previous determinations are included. Uncertainties are to 67% confidence.

P (GV)	G_r (%AU^{-1})	Yasue (1980)	Kudo and Wada (1977)	Bieber and Pomerantz (1986)
10	2.77±0.13	3.00± 1.10	–	2.0
20	1.70±0.08	1.85±0.68	0.9	–
50	0.90±0.04	0.97±0.36	–	–
80	0.65±0.03	0.70±0.26	0.4	–
100	0.55±0.03	0.60±0.22	–	–
150	0.42±0.02	0.45±0.17	0.3	–
200	0.34±0.02	0.37±0.14	–	–
230	0.31±0.01	–	0.2	–

Table 2 presents the average value of G_r (assuming Yasue's (1980) rigidity spectrum) for various energetic particles and a comparison of these values to previous determinations of the radial density gradient. All previous values, especially those presented by Yasue (1980), are in good agreement with those calculated in this paper.

3.3.4 *Parallel mean-free path*

Figure 6 contains the average values of $\overline{\lambda_{\|} G_r}$ calculated from 1957 to 1990 from observations with the five neutron monitors (median rigidities of 17 GV), determined in Hall (1995). Also shown is the yearly average value of G_r for 17 GV particles calculated in Hall et al. (1995). These two quantities were then used in Figure 6 to derive $\lambda_{\|}$ from Equations (1) and (3). Solid lines are three-point averages. Although the values have relatively large errors there is a hint that $\lambda_{\|}$ is suppressed during the 1970's in agreement with the observations of Bieber and Chen (1991b) and Chen and Bieber (1993).

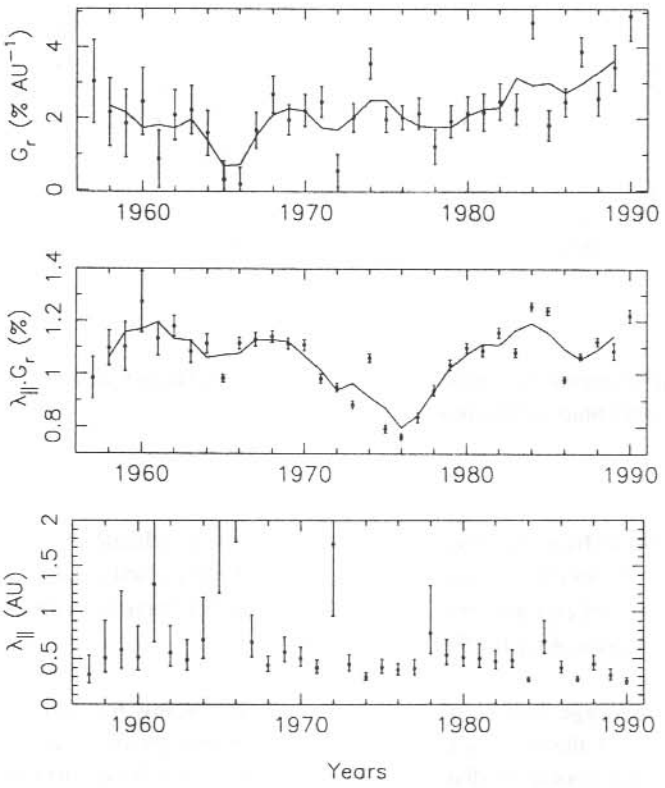

Figure 6. The radial gradient (G_r) of 17 GV particles determined from the North-South anisotropy by the method presented in Hall et al. (1995) from 1957 to 1990 is shown in the upper panel. The average product of the parallel mean-free path and the radial gradient ($\lambda_{\|} G_r$) determined from the solar diurnal anisotropy in Hall (1995) recorded by five neutron monitors is shown in the center panel. The solid lines are 3-point moving averages. The bottom panel is the determination of the parallel mean-free path ($\lambda_{\|}$) of 17 GV cosmic rays determined from Equation (1) and the results in the two upper panels. Note that the values of $\lambda_{\|}$ for 1965 and 1966 are off the scale at 3 and 5 AU respectively, with errors an order of magnitude larger.

Figures 7 and 8 contain the results of calculating $\lambda_{||}$ from the observations of $\overline{\lambda_{||}G_r}$ from EMBV ($P_{med} = 135$ GV) and HOBV ($P_{med} = 185$ GV) and the calculations of G_r from the North-South anisotropy. These higher rigidity calculations also indicate that $\lambda_{||}$ is reduced during the $A > 0$ polarity state.

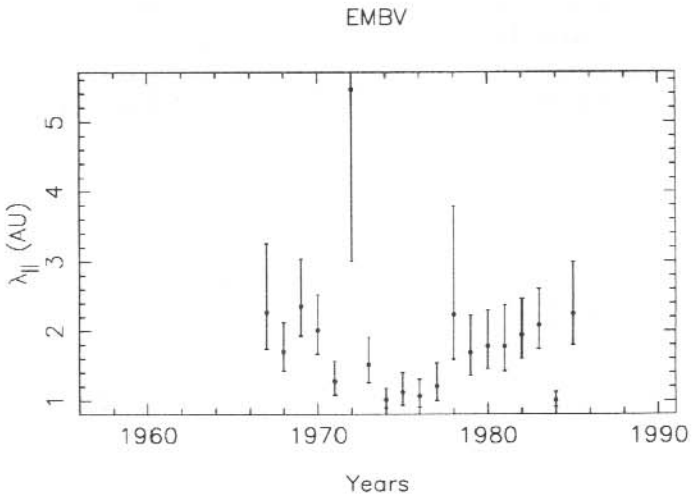

Figure 7. Parallel mean-free path ($\lambda_{//}$) of 135 GV particles determined from the Embudo underground muon telescope.

These results and those from the other instruments in Table 1 indicate that $\lambda_{||}$ could have a higher value around times of solar minimum during the $A < 0$ polarity state. Three notable exceptions to this hypothesis are 1984, 1987 and 1990 which have very low values of $\lambda_{||}$, due to the extreme values of G_r for these years.

Table 3 contains average values of $\lambda_{||}$ in order of increasing median rigidity of the instruments from which the value was obtained. The averages are over the entire period of data accumulation and epochs of distinct magnetic polarity. Each year has been weighted according to the largest error on $\lambda_{||}$, so one column of Table 2 has been attributed to the period 1981 to 1989 ($A < 0$) but excluding 1984 and 1987 since these years have relatively low values and small errors.

These average results suggest not only that the $\lambda_{||}$ has a linear relationship with rigidity but that there is also a very strong implication of a polarity dependence. This is clear if the column of averages which exclude 1984 and 1987 is considered, but even considering just the complete average values it is likely.

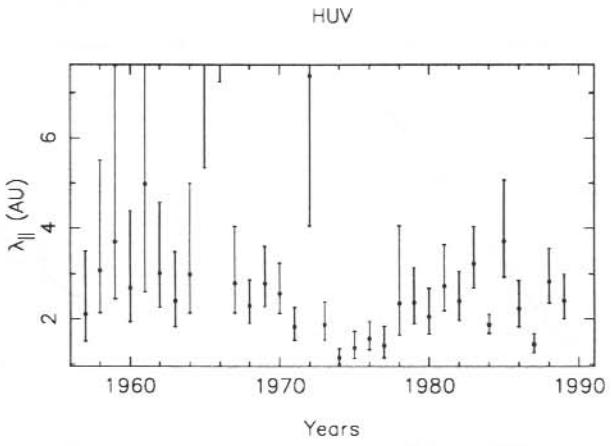

Figure 8. Same as Figure 2 except $\lambda_{//}$ is determined from the Hobart underground muon telescope from 1957 to 1989. The median rigidity is 185 GV.

Table 3. Average values of the parallel mean-free path $\lambda_{//}$.

Instrument	P_{med} (GV)	$\overline{\lambda_{\|}}$ (AU) Average	$\overline{\lambda_{\|}}$ (AU) 1959-68 A < 0	$\overline{\lambda_{\|}}$ (AU) 1972-79 A > 0	$\overline{\lambda_{\|}}$ (AU) 1981-89 A < 0	$\overline{\lambda_{\|}}$ (AU) 1981-89# A < 0
Neutrons	17	0.38 ± 0.03	0.48 ± 0.08	0.35 ± 0.03	0.30 ± 0.02	0.39 ± 0.05
BNM	28	0.73 ± 0.07	0.77 ± 0.17	-	0.48 ± 0.03	0.67 ± 0.06
DNM, MSV	50	-	0.96± 0.16	-	0.50 ± 0.03	0.76 ± 0.07
EMBV	135	1.21 ± 0.07	1.80 ± 0.39+	1.13 ± 0.11	1.15 ± 0.11	2.00 ± 0.29
MUN	165	1.41 ± 0.07	-	1.40 ± 0.14	1.45 ± 0.10	1.96 ± 0.19
HUV	185	1.73 ± 0.09	2.50 ± 0.42	1.37 ± 0.14	1.92 ± 0.14	2.61 ± 0.28
HUI	195	1.69 ± 0.10	-	1.39 ± 0.16	1.87 ± 0.14	2.36 ± 0.24

\# Not including 1984 and 1987
\+ 1965-1968 only.

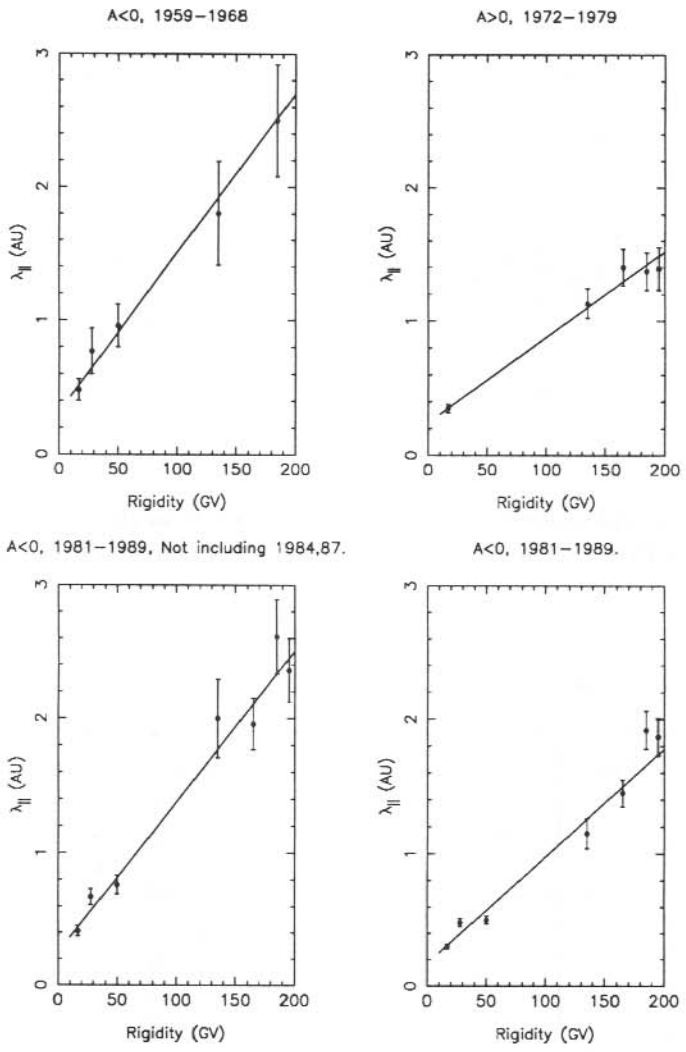

Figure 9. Average values of the parallel mean-free path as a function of rigidity. The lines of best-fit have similar slopes for the values calculated for the A < 0 magnetic polarity states, while the slope of the line for the A > 0 polarity state is about half the previous values.

The average results over distinct polarity states in Table 3 are presented graphically in Figure 9. The solid line is the line of best fit. It is fairly obvious that the relationship between $\lambda_{||}$ and rigidity is different for the A > 0 epoch and the A < 0 epochs. The slopes of the best fitted lines are 0.012 ± 0.002 AU $(GV)^{-1}$, 0.006 ± 0.001 AU $(GV)^{-1}$ and 0.008 ± 0.001 AU $(GV)^{-1}$ for the epochs 1959–68, 1971–72 and 1981–89 respectively. For the 1981 to 1989 epoch which excludes 1984 and 1987 from the averages, the line of

best fit has the same slope (0.011 ± 0.001) as the 1959–68 epoch. The trends of all the $A < 0$ polarity state plots are similar but are different to that of the $A > 0$ polarity state plot.

These results suggest strongly that $\lambda_{||}$ has a polarity dependence, with lower values being present during years of $A > 0$ magnetic polarity. This result is in agreement with neutron monitor studies by Bieber and Chen (1991b) and Chen and Bieber (1993) but observed here at rigidities an order of magnitude higher than before.

3.4 SUMMARY

By analysing the sidereal and solar diurnal variations in data recorded by instruments responding to primary cosmic ray particles with rigidities between about 10 and 300 GV one may conclude that between 1957 and 1990:

1. The amplitude of ξ_{NS} and hence the radial density gradient varies slightly, with smaller values around times of solar minima than around times of solar maxima.

2. There is some contamination to the analysis from another anisotropy which causes the phase of ξ_{NS} to vary with a 22-year period. This anisotropy is probably the asymmetric modulation (with respect to the neutral sheet) of a galactic anisotropy as predicted by Nagashima et al. (1982) and has a 22-year (solar magnetic) cycle.

3. The values of the radial density gradient of high rigidity galactic cosmic ray particles (between 10 and 200 GV) which have been presented here for the period 1957 to 1990 are in good agreement with investigations by Duggal and Pomerantz (1977); Kudo and Wada (1977); Yasue (1980) and Bieber and Pomerantz (1986).

4. $\lambda_{||}$ is dependent on the magnetic polarity of the heliosphere, with the value of $\lambda_{||}$ being lower during epochs when the interplanetary magnetic field of the Sun has northern magnetic polarity in its northern hemisphere.

3.5 ACKNOWLEDGMENTS

We thank the chief investigators for Deep River and Kerguelen for sending their data to the World Data Centre A. We would also like to thank D.B. Swinson for supplying us with the data from the Embudo and Socorro underground muon telescopes.

REFERENCES

Ahluwalia, H.S. *and* Sabbah, I.S. (1993). Cosmic ray diurnal anisotropy for a solar magnetic cycle. *Planetary and Space Science 41*:113–125.

Baker, C.P. (1993). *Cosmic ray modulation in the heliosphere*. Ph.D. Thesis, University of Tasmania, Australia.

Bieber, J.W. *and* Chen, J. (1991a). Cosmic ray diurnal anisotropy, 1936–1988: Implications for drift and modulation theories. *Astrophysical Journal 372*:301–313.

Bieber, J.W. *and* Chen, J. (1991b). Solar magnetic cycle variation of cosmic ray gradients and scattering mean free path. *Proceedings of the 22nd International Cosmic Ray Conference, Dublin 3*:525–528.

Bieber, J.W. *and* Pomerantz, M.A. (1986). Solar cycle variation of cosmic ray north-south anisotropy and radial gradient. *Astrophysical Journal 303*:843–848.

Chen, J. *and* Bieber, J.W. (1993). Cosmic-ray anisotropies and gradients in three dimensions. *Astrophysical Journal 405*:375–389.

Duldig, M.L. (1989). The Mawson automatic cosmic ray observatory (MACRO). *Proceedings of the 21st International Cosmic Ray Conference, Adelaide 7:* 288–291.

Duggal S.P. *and* Pomerantz M.A. (1977). Relationship between sector boundaries and polar nucleonic intensity variations: the heliocentric gradient during solar cycle 20. *Proceedings of the 15th International Cosmic Ray Conference, Plovdiv 3:* 215–220.

Erdös, G. *and* Kota, J. (1979). The spectrum of daily variations between 50 and 200 GV. *Proceedings of the 16th International Cosmic Ray Conference, Kyoto 4*:45–50.

Fenton, A.G., Jacklyn, R.M. *and* Taylor, R.B. (1961). Cosmic ray observations at 42 m.w.e. underground at Hobart. *Ill Nuovo Cimento, XXII(2):*3985–3996.

Forman, M.A. *and* Gleeson, L.J. (1975). Cosmic ray streaming and anisotropies. *Astrophysics and Space Science 32*:77–94.

Fujimoto, K., Inoue, A., Murakami, K. *and* Nagashima, K. (1984). Coupling coefficients of cosmic ray daily variations for meson telescopes. *Cosmic Ray Research. Laboratory Report No. 9*. Nagoya, Japan.

Hall, D.L. (1995). *Modulation of high energy cosmic rays*. Ph.D. Thesis. University of Tasmania, Australia.

Hall, D.L., Humble, J.E. *and* Duldig, M.L. (1994a). Radial and latitudinal density gradients in galactic cosmic rays. *Proceedings of the Astronomical Society of Australia 11(2)*:170-174.

Hall, D.L., Humble, J.E. *and* Duldig, M.L. (1994b). Modulation of high-energy cosmic rays in the heliosphere. *Journal of Geophysical Research 99:*1443–1457.

Isenberg, P.A. *and* Jokipii, J.R. (1979). Gradient and curvature drifts in magnetic fields with arbitrary spatial variation. *Astrophysical Journal 234*:746–752.

Jacklyn, R.M. (1970). Studies of the sidereal daily variation of cosmic ray intensity with particlular reference to observations at 40 m.w.e. underground. *ANARE Scientific Reports, Series C(II) Cosmic Rays, No.114*. Antarctic Divison, Melbourne.

Jokipii, J.R. (1984). The effects of heliospheric magnetic structure on the modulation of galactic cosmic rays. *Proceedings of International Symposium on Cosmic Ray Modulation in the Heliosphere*. Iwate University, Morioka, Japan. Pp. 27–38.

Jokipii, J.R. (1989). The physics of cosmic-ray modulation. *Advances in Space Research 9 (12)*:105–119.

Jokipii, J.R. *and* Kopriva, D.A. (1979). Effects on particle drift on the transport of cosmic rays. III. Numerical models of galactic cosmic-ray modulation. *Astrophysical Journal 234*:384–392.

Kudo, S. *and* Wada M,. (1977). Field dependent north-south anisotropy of cosmic rays in rigidities from 10 GV to 300 GV. *Proceedings of the 15th International Cosmic Ray Conference Plovdiv 3*:158–163.

Nagashima, K., Morishita, I. *and* Yasue, S. (1982). Modulation of galactic cosmic ray anisotropy in heliomagnetosphere: average sidereal daily variation. *Planetary and Space Science 30*:879–896.

Nagashima, K., Tatsuoka, R. *and* Matsuzaki, S. (1983). Spurious sidereal daily variation of cosmic rays produced from stationary anisotropy of solar origin. *Ill Nuovo Cimento Soc. Ital. Fis. C, 6*:550–565.

Nagashima, K., Sakakibara, S., Fenton, A.G. *and* Humble, J.E. (1985). The insensitivity of the cosmic ray galactic anisotropy to heliomagnetic polarity reversals. *Planetary and Space Science 33*:395–405.

Parsons, N.R. (1959). *Cosmic ray studies at high southern latitudes with special reference to the daily intensity variation*. Ph.D. Thesis, University of Tasmania.

Potgieter, M.S. *and* Moraal, H. (1985). A drift model for the modulation of galactic cosmic-rays. *Astrophysical Journal 294*:425–440.

Swinson, D.B. (1969). Sidereal cosmic ray diurnal variation. *Journal of Geophysical Research 74*:5591 – 5598.

Swinson, D.B. (1971). Solar modulation origin of 'sidereal' cosmic ray anisotropies. *Journal of Geophysical Research 76*:4217–4223.

Swinson, D.B. (1988). Long term variations of the cosmic ray north-south anisotropy and the radial cosmic ray gradient at high rigidity. *Journal of Geophysical Research 93*:5890–5896.

Yasue, S. (1980). North-south anisotropy and radial density gradient of galactic cosmic rays. *Journal of Geomagnetism and Geoelectricity 32*:617–635.

Yasue, S., Mori, S., Sakakibara, S. *and* Nagashima, K. (1982). Coupling coefficients of cosmic ray daily variations for neutron monitor stations. *Cosmic Ray Research. Laboratory Report No. 7*. Nagoya, Japan.

4. THE RELATIONSHIP BETWEEN MAGNETIC STORMS AND SOLAR WIND INPUT

Jiping Wu and P.J. Wilkinson

IPS Radio and Space Services
West Chatswood NSW 2057
Australia

ABSTRACT

In order to seek the possible scheme of magnetic storm forecasting, the relationship between the Dst and 16 solar wind – magnetosphere coupling functions was studied for the period of August 1978 to December 1979. Ten major storms (peak Dst <-100 nT) were identified during this period. It was found that:

1. If Dst indices are delayed one hour from the solar wind electric field Ey, the correlation coefficient between them is raised from 0.55 to 0.82, averaged over six events.

2. The interplanetary dawn-dusk electric field $E_y(= VB_z)$ and $E_y \cdot P^{1/2}$ $(P = NmV^2)$ are the best coupling functions in terms of magnetic storm forecasting. The correlation coefficients from linear fitting of one hour delayed Dst with E_y are 0.82, and with $E_y P^{1/2}$ are 0.73 averaged over six events.

3. The correlation would be improved further if a time-weighted accumulation of coupling function $-E_y(\tau_a)$ was used. The correlation between 1-hour delayed Dst with $E_{y(}\tau_a)$ would be raised from 0.82 to 0.93 on six events average, when the attenuation factor is $\tau_a = 0.6$.

4. The correlation depends strongly on individual events. While in most events, the averaged correlation between 1-hour delayed Dst and 16 coupling functions is around 0.70, in one example it was less than 0.20. Besides, the best coupling functions between the solar wind and the magnetosphere are different for individual events.

4.1 INTRODUCTION

It is now understood that coronal mass ejections (CMEs) cause most of the large geomagnetic storms during the more active part of the solar cycle. For example, of 37 major storms during August 1978 – October 1982, 27 were associated with the Earth passage of both a shock and the CME driving the shock. High flow speed and strong magnetic fields, often with a strong southward component, are features common to most interplanetary disturbances driven by CMEs. Many authors believe that, near the maximum of the solar cycle, CMEs are the most important source of magnetic storms (Gosling et al. 1991; Hoeksema 1992).

At present it is difficult to measure the occurrence of CMEs, although detecting the launch and outward speed of CMEs over the limb of the Sun is not difficult with spaceborne coronagraphs. Unfortunately, the CMEs that affect Earth originate near the centre of the disk and can only be observed from a spacecraft located 90 degrees away from the Earth. Such a spacecraft is not available at this time or in the near future. Besides, Garcia and

Dryer (1987) suggested that the dynamics of the interplanetary medium may also play an important role in the cause of magnetic storms.

So an interplanetary monitor, upstream from the Earth, will be a crucial issue in the practical forecasting of southward IMF events and, in turn, of magnetic storms. We noticed that WIND, a core satellite of the International Solar-Terrestrial Physics (ISTP)/Global Geospace Science (GGS) mission, data is available from 1995, followed by Atmospheric Composition Explorer (ACE) satellite in 1997, orbiting around L1 Lagrange point. Our goal is to understand the linkage between the magnetic storms and solar wind inputs by using currently available data, then develop an real-time prediction scheme that can be applied to data to be received from the WIND and ACE satellites.

4.2 THE Dst INDEX AND THE COUPLING FUNCTIONS

The most likely process of energy transfer from the solar wind into the magnetosphere is the field line reconnection between the IMF and the geomagnetic field. By reconnection, the kinetic energy of the solar wind plasma is first converted into magnetic energy and then stored in the magnetotail. This stored energy is then sporadically released into the inner magnetosphere, the ring current belt, and the polar ionosphere, as auroral particle energy and Joule heat energy of the auroral electrojets during substorms and storms. It is known that (Akasofu 1981) the ring current consumes much more energy than the polar ionosphere during substorms and storms, so that an intensification of the ring current belt, should indicate an increase in the energy input rate into the magnetosphere from the solar wind.

A magnetic storm is defined in general by the existence of a main phase during which the magnetic field at the Earth's surface is depressed. This depression is caused by a westward ring current in the magnetosphere and can be monitored by the Dst index. Dst is a measure of the worldwide deviation of the H component, caused by the global ring current system, at mid-latitude ground stations from their quiet day values. It is expected that there should be a close correlation between the Dst index and the solar wind energy input.

For a long time, a sudden storm commencement (SSC), due to the compression of the magnetopause by an interplanetary shock, was assumed to be an indicator of storm occurrence. People now realise that SSC is only related to a subset of the total number of storms and it is not a good indicator of the storm occurrence.

Here the storm onset (SO) suggested by Gonzalez et al. (1992) will be used as an indicator of storm occurrence. SO signals the start of a monotonic decrease of the magnetogram record that characterises the main phase of the storm. Figure 1 is a Dst plot for 24 – 31 August 1978, during which a storm is recognised. The SSC, SO and the typical phases of a storm (initial, main and recovery) are shown.

The solar wind interaction with the magnetosphere is extremely complex. In order to explore possible effective storm forecasts schemes, a number of coupling functions of the solar wind into the magnetosphere, recommended by many authors (Pudovkin et al. 1985; Bargatze et al. 1986; Murayama 1986; Gonzalez 1986; Gonzalez et al. 1989), listed in Table 1, are tested here. The optimum choice will lie in the success of their correlation with Dst.

Table 1. List of tested coupling functions.

1	$VB_z\ (= Ey)$
2	$P^{1/2}\ VB_z,\ P = NmV^2$
3	$P^{1/2}V\lvert B_z\rvert^{1/2}$
4	$P^{1/2}VB_z \cdot \sin(\frac{\Theta}{2})\ ,\quad \Theta = \tan^{-1}(\frac{B_y}{B_z})$
5	$VB_t \cdot \sin^2(\frac{\Theta}{2}),\qquad B_t = (B_y^2 + B_z^2)^{1/2}$
6	$P^{1/6}VB_t \cdot \sin^4(\frac{\Theta}{2})$
7	$P^{1/6}VB \cdot \sin^4(\frac{\Theta}{2})$
8	$VB^2 \cdot \sin^4(\frac{\Theta}{2})$

In Table 1, V is solar wind velocity, N the number density, m the proton mass, P the solar wind dynamic pressure, B the magnitude of IMF, B_y the dawn-dusk component of IMF, B_z the southward component of IMF, B_t the transverse component of IMF vector, and Θ the polar angle of IMF.

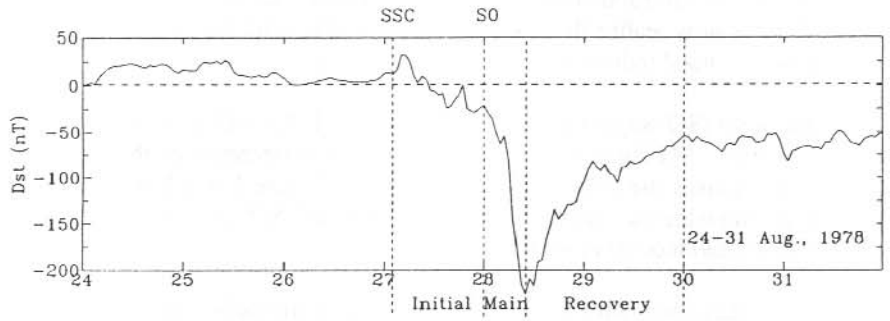

Figure 1. The Dst plot for 23–31 August 1978 during which a storm is recognised. SSC, SO and the typical phases of a storm, initial, main and recovery are shown.

4.3 DATA AND COORDINATES

The solar wind data from the ISEE-3 spacecraft were obtained on the CD_ROM NGDC01 (V2.0) from the National Geophysical Data Center, and the Dst index from the Solar Geophysical Data prompt reports. Both Dst index and solar wind data are hourly data.

The IMF data from ISEE-3 were organised in the Geocentric Solar Ecliptic system (GSE) or Geocentric Solar Magnetospheric system (GSM). GSM system is preferred here. The SM coordinates are useful for ordering data controlled by the Earth's dipole field, e.g. reconnection between IMF and geomagnetic field (Russell 1971). In order to find a better way to organise IMF data, the solar magnetic coordinates (SM) are also used here. Thus for each coupling function listed in Table 1, two formats are used, one for GSM and the other for SM coordinates. Altogether, 16 coupling functions are considered here.

Ten major storm events were identified during 1978 – 1979, in which the peak Dst value was less than -100 nT and solar wind data were available. An event is defined here as a period from SO to the maximum of main phase, as shown by the second and third dash lines in Figure 1. Table 2 gives some important features, e.g. event period, peak Dst and peak B_Z, of these 10 events.

Table 2. Summary of some features for 10 major events during 1978-1979.

No.	Event Start Date	Period of Dst Growth (UT/Day)	Peak Dst (nT)	Peak B_Z (nT)	Fully Studied
1	28 Aug 1978	00/28 – 09/28	-226	-22.78	Yes
2	29 Sep 1978	06/29 – 11/29	-224	-24.39	Yes
3	25 Nov 1978	12/25 – 18/25	-149	-15.25	Yes
4	21 Feb 1979	03/21 – 21/21	-107	-10.30	No
5	10 Mar 1979	17/10 – 23/10	-140	-14.10	Yes
6	29 Mar 1979	03/29 – 21/29	-129	-11.17	No
7	03 Apr 1979	15/03 – 03/04	-202	-16.89	Yes
8	25 Apr 1979	00/25 – 16/25	-149	-15.87	No
9	29 Aug 1979	08/29 – 18/29	-140	-11.28	No
10	17 Sep 1979	22/17 – 15/18	-129	-15.54	Yes

4.4 RESULT AND DISCUSSION

A regression analysis between Dst and the 16 coupling functions for each individual event was completed. The main results are summarised in Table 3, which lists the correlation coefficient r between Dst and the 16 coupling functions, for Event 3 and Event 9 and absolute value average of r on six events. The last column gives the absolute value average of r over the 16 coupling function for each case. Obviously, as shown in Table 3, there is no big advantage gained in the correlation analysis here by organizing the IMF data in SM, instead of GSM, coordinate systems.

The results are very dependent on individual events. The correlation over the 16 coupling functions average is 0.79 and 0.13 for Event 3 and Event 9, respectively, as listed in Table 3. It tells us that, maybe not only the magnitude but also the structure and characteristics of the interplanetary disturbance will play an important role in its coupling with the Earth's magnetosphere.

For simplicity, six events with reasonable values of r were selected (shown in Table 2 as 'Fully Studied') for further study.

Table 3. The correlation coefficient r between Dst and eight coupling functions (in both GSM and SM formats) for Event 3 and Event 9, and the absolute value average of r for six events.

1 Hour Delay	Event No	Format	Coupling Function 1	2	3	4	5	6	7	8	16 Function Average
Yes	3	GSM	.75	.82	-.80	-.97	-.85	-.72	-.72	-.69	
		SM	.73	.82	-.80	-.97	-.84	-.71	-.70	-.67	.79
Yes	9	GSM	.13	.03	-.06	.14	.06	-.02	-.01	.03	
		SM	-.33	-.40	.38	.20	.00	-.09	-.09	-.07	.13
Yes	6 events	GSM	.82	.73	.45	.53	.73	.68	.68	.63	
	average	SM	.78	.72	.44	.56	.71	.66	.66	.60	.65
No	6 events	GSM	.55	.38	.20	.36	.56	.54	.54	.53	
	average	SM	.53	.37	.22	.39	.54	.52	.51	.54	.45

If the Dst indices are delayed one hour with respect to the solar wind parameters, then the correlation is improved. The correlation for the six event average, improves from 0.55 to 0.82 if Dst indices are delayed 1 hour from the solar wind electric field E_y. The correlation for the six events and 16 functions average, improved from 0.45 to 0.65 if Dst indices are delayed one hour from the solar wind parameters.

This coincides with the correlation analysis of Arnolay (1971) and also confirms (Gonzalez et al. 1989) the suggestion that the average time lag for transmission of reconnection power, from the magnetopause to the inner magnetosphere, is about one hour during an intense storm.

Among the 16 tested coupling functions between solar wind and the magnetosphere, the simplest ones ($E_y(=V\cdot B_z)$ and $E_y\cdot P^{1/2}$ are the best. As shown in Table 3, the averaged r of six events for one hour delayed Dst to E_y are 0.82, and Dst to $E_y\cdot P^{1/2}$ they are 0.73, respectively, much better than the r value 0.65 on 16 coupling functions average. This indicates that interplanetary dawn-dusk electric fields E_y control the rate of transport of southward IMF field, which makes large scale magnetopause reconnection to the magnetosphere possible. The solar wind pressure P ($=NmV^2$) also plays an important role in causing magnetic storms.

It was also noticed that while on average E_y and $E_y\cdot P^{1/2}$ seem to be the best two coupling functions for most events, the best two coupling functions for event 3 are $P^{1/2}VB_z\cdot\sin(\frac{\Theta}{2})$ and $VB_t\cdot\sin^2(\frac{\Theta}{2})$.

The correlation between ionospheric disturbances and the time-weighted accumulation of magnetic indices, introduced by Wrenn (1987a, 1987b), has been shown to be better than the equivalent instantaneous indices at some Australian and European stations during the period September to October 1989 (Wu and Wilkinson 1993). We expected that it might be a good idea to explore the usefulness of the time-weighted accumulation of solar wind parameters here. As an example, the correlation between one hour delayed Dst and a time-weighted accumulation of coupling function E_y, $E_y(\tau_a)$, with $0 \le \tau_a < 1$ is examined.

$E_y(\tau_a)$ is defined as:

$$E_y(\tau_a) = (1-\tau_a)*\left(E_y + \tau_a * E_{y-1} + \tau_a^{\,2} * E_{y-2} + \ldots\right)$$

where $0 \le \tau_a < 1$ by definition and E_{y-1}, E_{y-2}, E_{y-3}, ... are E_y values for -1hour, -2 hours, -3 hours, etc. The factor $(1 - \tau_a)$ normalises the summation. Obviously $E_y(0)$ equals the instantaneous value of E_y. As an attenuation factor, τ_a determines how $E_y(\tau_a)$ will be averaging out rapid oscillatory changes in the E_y value.

The interplanetary dawn-dusk electric field, E_y, its time-weighted accumulation format, $E_y(\tau)_a$ with $\tau_a = 0.6$ and the Dst index for 1 – 8 April and 16 – 23 September 1979 are shown in Figure 2(a) and 2(b), respectively. With τ_a, the short-term variations in Ey are smoothed out within certain time-period in its integrating format $E_y(\tau)_a$. It is obvious that the Dst index follows the shape of $E_y(0.6)$ much better than $E_y(0)$'s. This is true for all 6 events examined.

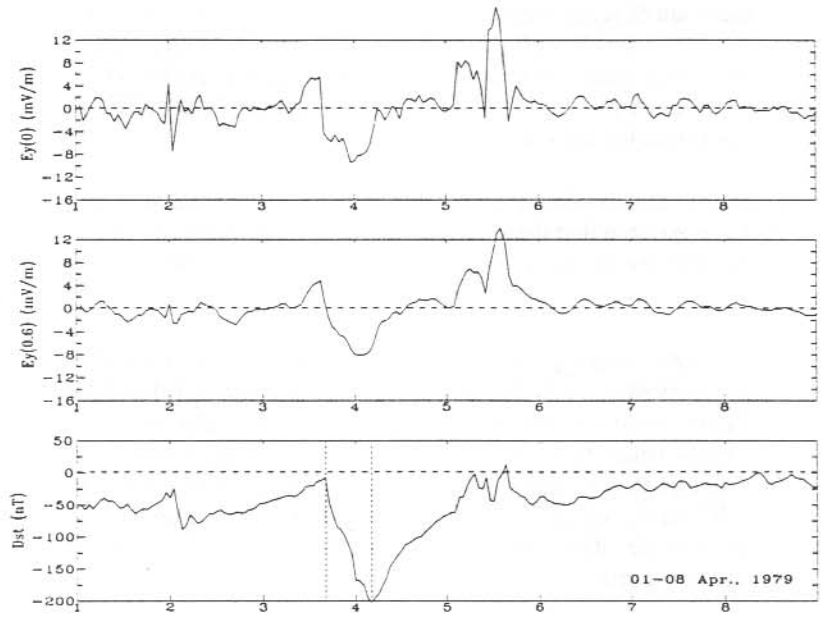

Figure 2a. The dawn–dusk interplanetary electric field $E_y(0)$, its time-weighted accumulation value, $E_y(0.6)$, and the Dst index for 1–8 April 1979. The period for Event 7 is indicated by the two dashed lines.

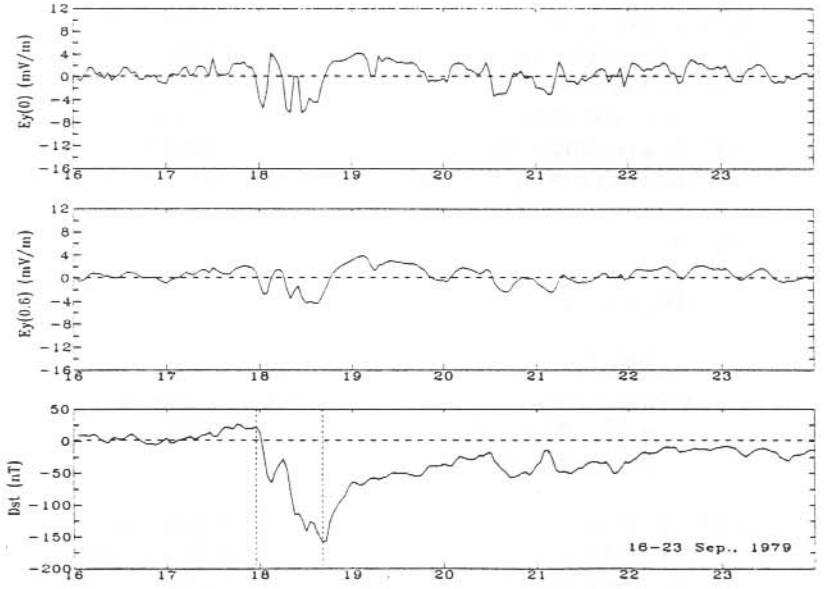

Figure 2b. The dawn–dusk interplanetary electric field $E_y(0)$, its time-weighted accumulation value, $E_y(0.6)$, and the Dst index for 16–23 September 1979. The period for Event 10 is indicated by the two dashed lines.

For $1 > \tau_a \geq 0$, it is found that the best correlation between Dst and $E_y(\tau)_a$ is attained when $\tau_a \approx 0.6$ which results in the r values being increased from 0.82 to 0.93 on the six events average.

The results above suggests that the magnetosphere does not respond to very rapid changes in the input of solar wind energy. From the τ_a value, when the best correlation between Dst and $E_y(\tau)_a$ is found, we can determine a characteristic response time of the magnetosphere to the solar wind inputs. The correlation coefficient r maximises at $\tau_a = 0.6$, corresponding to a response time of 2–3 hours ($1/(1-\tau_a)$, Wu and Wilkinson (1993). This provides a measure of the time-weighted smoothing extent of interplanetary effects on the magnetosphere. In other words, the magnetospheric condition at any time is controlled by the solar wind status averaged over the previous 2–3 hours, with more contributions from the most recent solar wind status.

4.5 CONCLUSION

There is certainly a good relationship between solar wind input and the corresponding magnetic storm, but further efforts are required to find an unique 'scheme' for quantitative magnetic storm forecasting if one exists.

REFERENCES

Akasofu, S.-I. (1981). Relationships between the AE and Dst Indices During Geomagnetic Storms. *Journal of Geophysical Research 86:*4820–4822.

Arnolay, R.L. (1971). Signature in the interplanetary medium for substorms. *Journal of Geophysical Research 71:*5189–5201.

Bargatze, L.F., Baker, D.N. *and* McPherron, R.L. (1986). Solar wind-magnetosphere energy input function. In: Kamide *and* Slavin, J.A. (Eds). *Solar Wind - Magnetosphere Coupling*. Terra, Tokyo, Japan. Pp. 101–109.

Garcia, H.A. *and* Dryer, M. (1987). The solar flares of February 1986 and the ensuing intense geomagnetic storm. *Solar Physics 109:*119–137.

Gonzalez, W.D. (1986). Electric field and energy transfer by magnetopause reconnection. In: Kamide, Y. *and* Slavin, J.A. (Eds). *Solar Wind - Magnetosphere Coupling*. Terra, Tokyo, Japan. Pp. 315–320.

Gonzalez, W.D., Tsurutani, B.T., Gonzalez, A.L.C., Smith, E.J., Tang, F. *and* Akasofu, S.-I. (1989). Solar Wind - Magnetosphere Coupling During Intense Magnetic Storms. *Journal of Geophysical Research 94:*8835–8851.

Gonzalez, W.D., Gonzalez, A.L., Mendes, O. *and* Tsurutani, T. (1992). Difficulties Defining Storm Sudden Commencements. *Eos Trans., AGU 73*. Pp. 180.

Gosling, J.T., McComas, D.J., Phillips, J.L. *and* Bame, S.J. (1991). Geomagnetic activity associated with Earth passage of interplanetary shock disturbances and Coronal Mass Ejections. *Journal of Geophysical Research 96:*7831 – 7839.

Hoeksema, J.T. (1992). Solar Sources of Geomagnetic Storms. *Eos Trans. AGU, 73.* Pp. 20.

Murayama, T. (1986). Coupling functions between solar wind and the Dst index, in Solar Wind. In: Kamide, Y. *and* Slavin, J.A. (Eds). *Solar Wind - Magnetosphere Coupling*. Terra, Tokyo, Japan. Pp. 119 – 126.

Pudovkin, M.I., Zaitseva, S.A. *and* Sizova, L.Z. (1985). Growth rate and decay of magnetospheric ring current. *Planetary and Space Science 33:*1097 – 1102.

Russell, C.T. (1971). Geophysical Coordinate Transformation. *Cosmic Electrodynamics 2:*184 – 186.

Wrenn, G.L. (1987). Time-weighted accumulations ap(τ) and Kp(τ). *Journal of Geophysical Research 92*:10125 – 10129.

Wrenn G.L., Rodger, A.S. *and* Rishbeth, H. (1987). Geomagnetic storms in the Antarctic F-region. 1. Diurnal and seasonal patterns for main phase effects. *Journal of Atmospheric and Terrestrial Physics 49:*901 – 913.

Wu, J. *and* Wilkinson, P.J. (1993). Time-weighted accumulation of ap index – a better indicator of magnetic disturbance. IPS Series TR-93-01.

5. COMPARISON OF HIGH RESOLUTION QUARTZ AND FLUXGATE MAGNETOMETER DATA RECORDED AT DAVIS, ANTARCTICA

V.O. Papitashvili [1], B.A. Belov [2], Yu.A. Burtsev [2], I.A. Pimenov [2], G.B. Burns [3], R.J. Morris [3], D.A. Neudegg [3] and L.P. Symons [3]

[1] Space Physics Research Laboratory
University of Michigan
Ann Arbor MI 48109
USA

[2] IZMIRAN
Troitsk Moscow Region 142092
Russia

[3] Atmospheric and Space Physics
Antarctic Division
Kingston Tasmania 7050
Australia

ABSTRACT

The results of geomagnetic observations at Davis, Antarctica (geographic $\phi = 68.60°S$ and $\lambda = 77.97°E$, corrected geomagnetic $\Phi = -74.48°$ and $\Lambda = 99.51°$), made in 1992 by digital quartz and fluxgate magnetometers are presented and discussed. Quartz variometers were designed at IZMIRAN and they measure H, D and Z components of the geomagnetic field with a one second sampling rate; their amplitude resolution is approximately 0.2 nT. The fluxgate magnetometer FM100C (EDA, Canada) is an observatory instrument at Davis operated with a ten second sampling rate measuring X, Y and Z components with a resolution of approximately 0.5 nT. Both magnetometers were deployed on concrete nonmagnetic pillars thermally isolated from the weather impact and separated by 30 m. A comparison shows excellent coincidence between geomagnetic variation records made by both instruments. Orientations of quartz sensors against the fluxgate magnetometer installation (i.e., 'quasi-true' direction of the geomagnetic field components) are defined and compared. The baseline/scale factor correction technique is discussed in order to determine the correct installation of these systems in severe conditions of the Antarctic continent.

5.1 INTRODUCTION

Due to the fact that the magnetosphere and ionosphere are electrically coupled by field-aligned currents and these currents close in the ionosphere, ground geomagnetic field observations made at high latitudes have become a focus for a variety of studies. On the Earth's surface, the 'electromagnetic weather' results from the energy and momentum transfer between the solar wind, magnetosphere and ionosphere. This can be easily monitored using ground magnetometers which sense the integrated effects of ionospheric currents from great distances.

Historically, magnetometer arrays have been the primary tool for investigations of the ionospheric electrical current systems responsible for electromagnetic weather. Much of our understanding of ionospheric and magnetospheric currents is based partly or fully on the analysis of data from ground magnetometers. This is largely because ground-based magnetic data collection systems are relatively inexpensive and simple devices and can therefore be widely deployed to provide measurements with nearly any desired temporal or spatial resolution. Analysis of data from ground magnetometers combined with radar and satellite measurements of ionospheric conductivities, electric fields, ion convection velocities, and high altitude magnetic fields (i.e., field-aligned currents) provides a powerful and robust capability for deriving real three-dimensional electric current systems in the entire magnetosphere (e.g., Kamide and Baumjohann 1993).

It is also well recognised that ground-based observations provide continuous time series for the main geomagnetic field and secular variation studies, and are important for analysing spacecraft data. Ground geomagnetic observations can be utilised to form a more global context within which to interpret the spacecraft measurements, for example. The worldwide network consists of more than 250 magnetic observatories and variation stations (Abston et al. 1985; McLean et al. 1994).

Antarctica is ideally situated for observing very high latitude upper atmosphere phenomena. Due to severe weather conditions on the Antarctic ice cap, most of the stations have been established along the continent coast. A number of inland stations have been operated from the 1950's through to the 1980's but only two stations survived until now: South Pole (from 1956) and Vostok (from 1957). Originally all of these stations had been equipped with analogue quartz magnetometers with photographic or paper-chart recording; later modernisation replaced them with modern fluxgate magnetometers and digital acquisition systems.

The Antarctic station Davis, managed under the auspices of the Australian Antarctic Division is uniquely located near the ionospheric projection of the southern magnetic polar cap statistical boundary (about $\Phi = -75°$). For example, magnetic field lines at these latitudes on the dayside map to the vicinity of the magnetopause where the solar wind first encounters the geomagnetic field. Phenomena observed at the ionospheric intersection of these geomagnetic field lines are likely to show manifestations of the coupling processes which occur between the solar wind and the Earth's magnetosphere.

Therefore we can utilise Davis magnetometer data for monitoring of the field lines which most likely connect with the near-magnetopause region and provide information on the position and dynamics of the polar cap boundary, especially combining magnetic measurements with the very low frequency (VLF) data. This was formulated as a scientific objective for the collaborative ASAC project 507 (funded in 1991 by the Australian Antarctic Foundation) between the Australian Antarctic Division and the Institute of Terrestrial Magnetism, Ionosphere, and Radio Wave Propagation (IZMIRAN). In the framework of this project IZMIRAN quartz magnetic sensors and VLF receiver (0.8 – 6.3 kHz) equipped with a digital acquisition system were deployed at Davis, during 1992. The Davis standard fluxgate magnetometer was also in operation and data from both the quartz and fluxgate magnetometers were collected. The purpose of this paper is to show a

comparison study of these observations and discuss some problems with sensor orientation under severe Antarctic conditions.

5.2 INSTRUMENTATION

Quartz variometers used in the study were designed at IZMIRAN in the 1950's and have demonstrated a remarkably successful and long history of magnetic measurements at magnetic observatories worldwide and in the field. This variometer consists of a quartz 'V-shaped' frame made from a melted optical quartz crystal, a thin (thinner than a human hair) quartz thread which connects the frame tips, and a small Vicalloy magnet (with an attached tiny quartz mirror) suspended on the thread (Bobrov and Burtsev 1977). An external compensating magnet (also with an attached tiny mirror) is fixed at a certain point on the quartz frame. This magnet compensates the main geomagnetic field and aligns the suspended magnet in the 'zero' position against the direction of the selected geomagnetic field component. As the geomagnetic field changes, the magnet rotates (oscillates) around the quartz thread and an incident light beam is reflected from the magnet mirrors, and split dual beams record geomagnetic variations on photographic paper.

A major advantage of the quartz magnetic system is its long-term stability, i.e., the baseline of the quartz sensor is stable during a year within $1-2$ nT because of a very low thermal coefficient of volume expansion of the quartz, and because two light traces (reflections from both the suspended and fixed mirrors) are recorded on photographic paper. A problem arose when an attempt was made to replace the photographic paper by a pair of differential photodiodes: here only the light beam reflected from the suspended mirror could be captured and digitised by the analogue/digital (A/D) converter.

Further development of the 'classic' quartz photo-variometer was made by Burtsev et al. (1977) and Belov et al. (1979). An optical system was invented where a corner reflector divided the incident light beam between the suspended and fixed mirrors, and the difference between these light beams is captured and digitised. Thus, the long-term stability of the new system is the same as for photo-recording. A special purpose balancing of the suspended magnet on the quartz thread provides the very low sensitivity of the system to micro-seismic vibrations (so-called 'anti-seismic' variometer) or to the pillar tilt ('anti-tilted' variometer). A differential electronic amplifier was designed with very strong negative feedback to reduce noise and expand the dynamic and frequency ranges of the quartz variometers. A small electric bulb or a light diode (LED) can be used to illuminate the mirrors.

Compensating coils are mounted around the variometer box to provide predetermined extra current to compensate the suspended magnet oscillations, and therefore, to measure the magnetic field variation magnitude proportional to the output voltage. These coils are also used for calibration of the system, i.e., sensitivity of the system is determined as a 'nanotesla per volt' ratio.

The quartz magnetometer system used at Davis measures H, D and Z components of the geomagnetic field with a one second sampling rate. The dynamic range of each sensor is about ± 4000 nT and the amplitude resolution is approximately 0.2 nT. The digital data acquisition system consists of a standard low rate 14 bit A/D converter connected to an

IBM-286 laptop computer via a serial RS232 port (three magnetic and three VLF channels). A dedicated console program runs the computer, collects data continuously, and stores them in hourly files on hard disk. Special-purpose software was designed to process stored files and provide ASCII output or graphic visualisation of the recorded variations.

A modified fluxgate magnetometer FM100C (EDA Canada) at Davis operated with a ten second sampling rate measuring X, Y and Z (geographic north, east and vertically downward) components (Burns and Klekociuk 1994). The modifications included provision for temperature stabilisation of the fluxgate sensor and daily calibration of the instrument at 1630 UT by means of a predetermined current fed to a coil mounted in the sensor unit. A further modification increased the sensitivity of the FM100C from 10000 nT/V to 200 nT/V; the amplitude resolution of the magnetometer sensor is approximately 0.5 nT for each component. Absolute calibration of the instrument is obtained by reduction of magnetic absolute measurements made by a QHM (quartz horizontal magnetometer – giving absolute H and D component values) and a PPM (proton precession magnetometer – giving F total field strength). Absolute observations of the geomagnetic field components are performed manually once approximately every ten days.

Both magnetometer systems were deployed on concrete non-magnetic pillars thermally isolated from the impact of weather and separated by 30 m. Thermal isolation was provided by a sensor enclosure box which incorporated a non-magnetic heating system that maintained the temperature in the box to within 1° of ambient (~20°C). The manufacturer specifies the FM100C temperature sensitivity as 1 nT/°C; the quartz system is specified for less than 1 nT/°C.

5.3 DATA COMPARISON

Davis geographic coordinates are $\phi = 68.60°S$ and $\lambda = 77.97°E$. The corrected geomagnetic coordinates computed for Epoch 1992 are $\Phi = -74.47°$ and $\Lambda = 99.44°$, an apex of the geomagnetic field line emanated from this point is on $L = 13.9R_E$, and local magnetic noon occurs at 1002 UT. The IGRF-based calculation of absolute values of the geomagnetic field components for Epoch 1992 yields H = 16734 nT, D = -77.574°, Z = -51750 nT, X = 3601 nT and Y = -16342 nT (Papitashvili and King 1993).

We selected 23 November 1992, for a detailed comparison of the quartz and fluxgate magnetometer measurements. This day was characterised by moderate geomagnetic activity with a clear large-amplitude, rapid change in all components at 0835 UT, connected with a sharp change in the interplanetary magnetic field (IMF) B_y, component from negative to positive values at 0815 UT (Papitashvili et al. 1994). Both pulsation and VLF activities were also observed during this day with Pc3 pulsations observed in the geomagnetic field as well as in VLF ranges.

Because both instruments were deployed on concrete pillars just 30 m apart, we can neglect the variation field gradient over that distance and assume that both instruments measured the same variations simultaneously. Both digital acquisition systems had separate electronic clocks but timing of the quartz system was checked everyday against GPS timing provided to the fluxgate system; no differences were recorded.

Two measurements around the step-like change in geomagnetic components have been selected and field values at that instance have been picked up for inter-instrumental calibration and comparison (note that fluxgate data are absolute and quartz data are variational):

Time = 0829 UT	X(D) nT	Y(H) nT	Z nT
Fluxgate (XYZ)	3637	-16699	-51966
Quartz (DHZ)	1606	-1928	1394
Time = 0845 UT			
Fluxgate (XYZ)	3088	-16195	-51631
Quartz (DHZ)	1057	-1424	1728

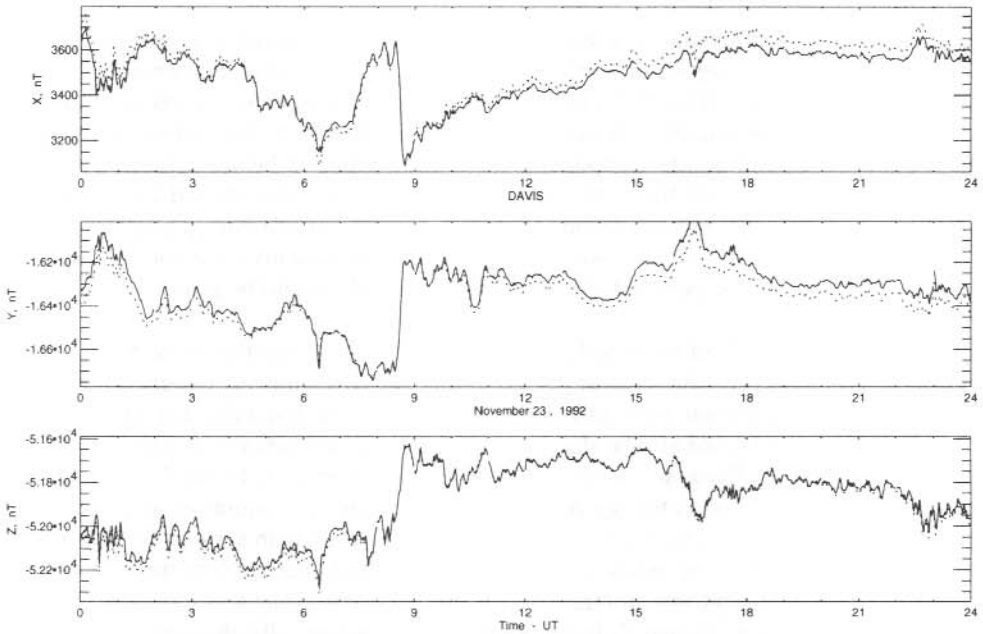

Figure 1. Magnetogram recording on 23 November 1992, made by fluxgate (solid lines) and quartz (dotted lines) magnetometers at Davis, Antarctica. The fluxgate magnetometer digital data are processed with absolute geomagnetic field component observations to obtain total values, and to compute baselines and scale factors for the quartz sensors by the use of sharp field changes at 0829-0845 UT.

Scale factors (nT/V ratios) for all quartz magnetometer components were obtained from these measurements and from corresponding calibrations made in accordance with the technique described above: the scale factors have been corrected to equalise differences (in nT) between two consecutive measurements from both instruments, and then baseline values for H, D and Z components for the quartz magnetometer were determined. Figure 1 shows an example of a daily variation recorded on 23 November 1992, by both instruments: quartz (solid lines) and fluxgate (dotted lines) magnetometers. One can see an

excellent coincidence between both traces at 0830–0845 UT but there are significant differences (up to 50–70 nT) between the two instruments during other parts of the day. Similar differences were also obtained for other days.

Because both instruments were well maintained during the field operation, we tried to consider what might be the source of these discrepancies. First, we analysed seasonal changes in air temperature, pressure and winds: none of these sources could cause such discrepancies. Possible irregular tilt of both concrete pillars were also considered but this could cause only a regular (seasonal) variation in the obtained differences. Finally, we agreed that only the orientation of both instruments against the 'true' direction of the geomagnetic field components could explain the behaviour of the measured magnetic field components.

5.4 CORRECTION TECHNIQUE

Let us consider the fluxgate magnetometer orientation as a reference and assume that its X sensors points to geographic north, Y – to east, and Z – to vertical downward direction (of course, a real orientation of the instrument was not so perfect but we do not know how much the orientation was off). Because the quartz magnetometer has been oriented in the direction of total horizontal component, the H-sensor has to be set approximately 78° anticlockwise (westward) from the X axis, i.e., this angle value should be an expected installation angle between orientations of H_{quartz} component and $X_{fluxgate}$ component (or between D_q and Y_f). In this case we assume that both instruments were oriented along the Z axis properly, i.e., the expected angle between Z_q and Z_f should be zero.

Taking into account all of these technical details, we can assume that these angles can be changed with time, i.e., due to changes in permafrost conditions of the gravel basement where both pillars are built, both instruments may have small (but different) tilts against the 'true' Z direction and could also be slightly rotated against each other and against axes in the 'true' X – Y plane. Because we do not know a 'true' reference frame for any of these instruments, we have accepted the orientation of fluxgate magnetometer as a 'quasi-true' reference and have correlated 1-minute averages obtained from both systems for all available data (we have data from the quartz system only for June and then for September – December periods because of equipment problems that occurred during spring and summer). All three angles (H_q to X_f, D_q to Y_f, and Z_q to Z_f) have been computationally changed in the range of ± 15° against the expected values with a step of 0.5°. We calculated correlation coefficients separately for each pair of components up to the fifth decimal point, to keep significance for the fourth digit, and in each case selected values for expected angles whose correlation coefficients were maximal (~0.99).

Table 1 shows the results for a number of days when absolute observations were made. One can see that in average the quartz Z variometer was aligned in the same vertical direction as the fluxgate instrument though local variations of the mutual vertical alignment vary from -6.5° to +5.0°. Despite some statistical scattering of orientation angles in the X-Y plane, average values for both inter-component angles (H_q to X_f and D_q to Y_f) are equal; therefore the platform with quartz sensors was installed (in fact) in the direction -83° anticlockwise from the X axis (i.e., from the geographic north direction) instead of the expected declination angle at Davis D = -78°.

Figure 2 shows the same magnetogram recording for 23 November 1992, as in Figure 1, but here the average baselines and scale factors are taken into account to simulate 'quasi-true' alignment of the quartz system with the 'quasi-true' orientation of the fluxgate instrument. One can see that data coincidence for both instruments is significantly improved after the use of the obtained 'real' orientation between the two systems, better baselines, and scale factors.

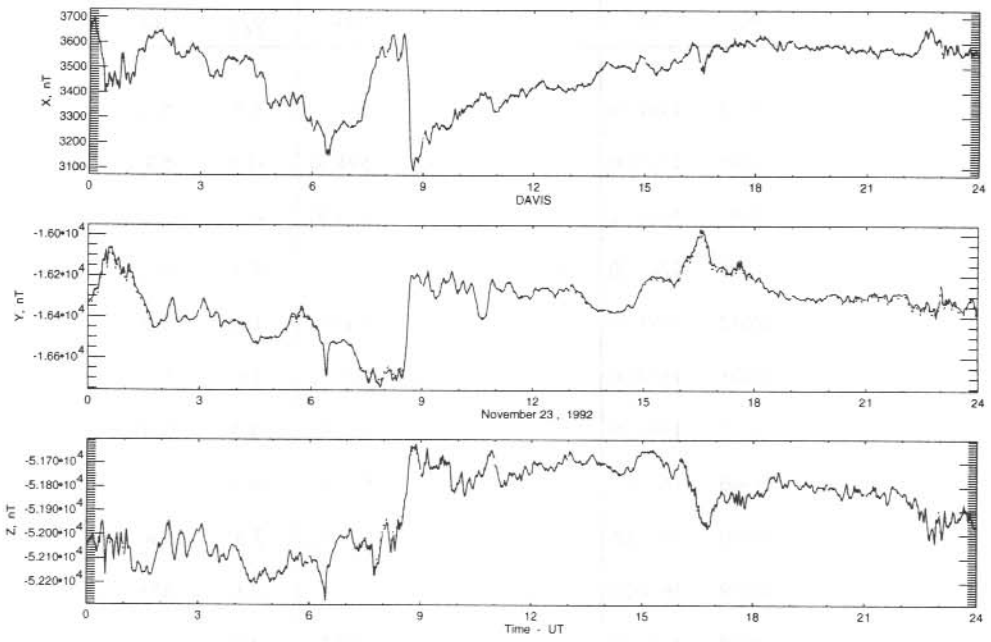

Figure 2. Same as in Figure 1 but the quartz magnetometer orientation is corrected against the 'quasi-true' direction of the fluxgate instrument, i.e., the average baseline and scale factor values from Table 1 are taken to simulate quasi-rotation of the quartz sensors of 7° anticlockwise to align with the X and Y geographic axes; no alignment is needed to adjust the quartz sensor vertical orientation.

5.5 HIGH RESOLUTION DATA COMPARISON

Figure 3 shows detrended (i.e., a linear trend within a given time interval is removed) 1 s geomagnetic data (upper panel) and original 1 s VLF data (lower panel) recorded by the quartz magnetometer and VLF receiver, during an interval of maximal change in the horizontal components corresponding to a steady re-orientation of the ionospheric current above Davis (Papitashvili et al. 1994). One can see clear Pc3 pulsations in all geomagnetic components as well as in the higher frequency ranges. This regime obviously changed at

0837 UT when the Y component of the geomagnetic field shows an intensification of Pcl pulsation activity. This time corresponds to a final establishment of the IMF B_y component in a positive direction 20 minutes earlier.

Table 1. Correlation analysis results for quartz and fluxgate magnetometers.

Date	H_q to X_f			D_q to Y_f			Z_q to Z_f		
mm/dd	γ_{HX}	BL	SF	γ_{DY}	BL	SF	γ_{ZZ}	BL	SF
06/01	-82.5	-14702	1441.39	-83.0	1813	1585.29	1.5	-53160	1360.62
06/10	-83.5	-14485	1516.06	-83.0	1795	1594.30	-1.5	-53090	1414.13
06/18	-81.5	-14357	1609.71	-83.0	1864	1539.00	-5.0	-53016	1292.54
06/24	-85.0	-14984	1240.10	-84.0	1857	1573.80	5.0	-53203	1263.95
06/29	-85.0	-14622	1471.31	-83.5	1862	1560.28	1.0	-53239	1412.29
09/11	-85.0	-14401	1579.00	-82.5	2277	1199.11	1.0	-53239	1412.29
09/17	-82.5	-14392	1544.30	-83.0	1920	1552.88	-1.5	-53138	1376.72
09/30	-81.5	-14446	1612.69	-85.0	1946	1623.13	-6.5	-53077	1258.35
10/06	-85.0	-14970	1411.06	-85.0	1940	1667.71	3.5	-53438	1364.62
10/17	-81.0	-14639	1624.31	-82.0	2005	1583.55	-1.0	-53305	1391.17
10/27	-84.5	-14688	1583.99	-83.0	2008	1577.27	-1.0	-53266	1389.32
11/03	-84.0	-14771	1562.34	-84.0	2017	1565.80	1.0	-53324	1382.32
11/09	-82.5	-14692	1555.02	-83.0	2003	1557.36	-1.0	-53169	1362.15
11/17	-80.0	-14823	1448.14	-83.0	2014	1571.81	-0.5	-53137	1194.99
11/23	-82.5	-14542	1657.80	-82.5	2033	1543.90	-2.5	-53149	1337.73
12/04	-83.0	-14569	1633.85	-82.5	2019	1541.85	-2.5	-53124	1295.25
Average values	-83.0	-14630	1530.69	-83.0	1961	1552.32	0.0	-53192	1344.28

Note: γ_{ss} are the obtained angles between the DHZ and XYZ instrument orientation axes; BL and SF stand for the baselines and scale factors obtained for maximal correlation between the corresponding instrument sensors data.

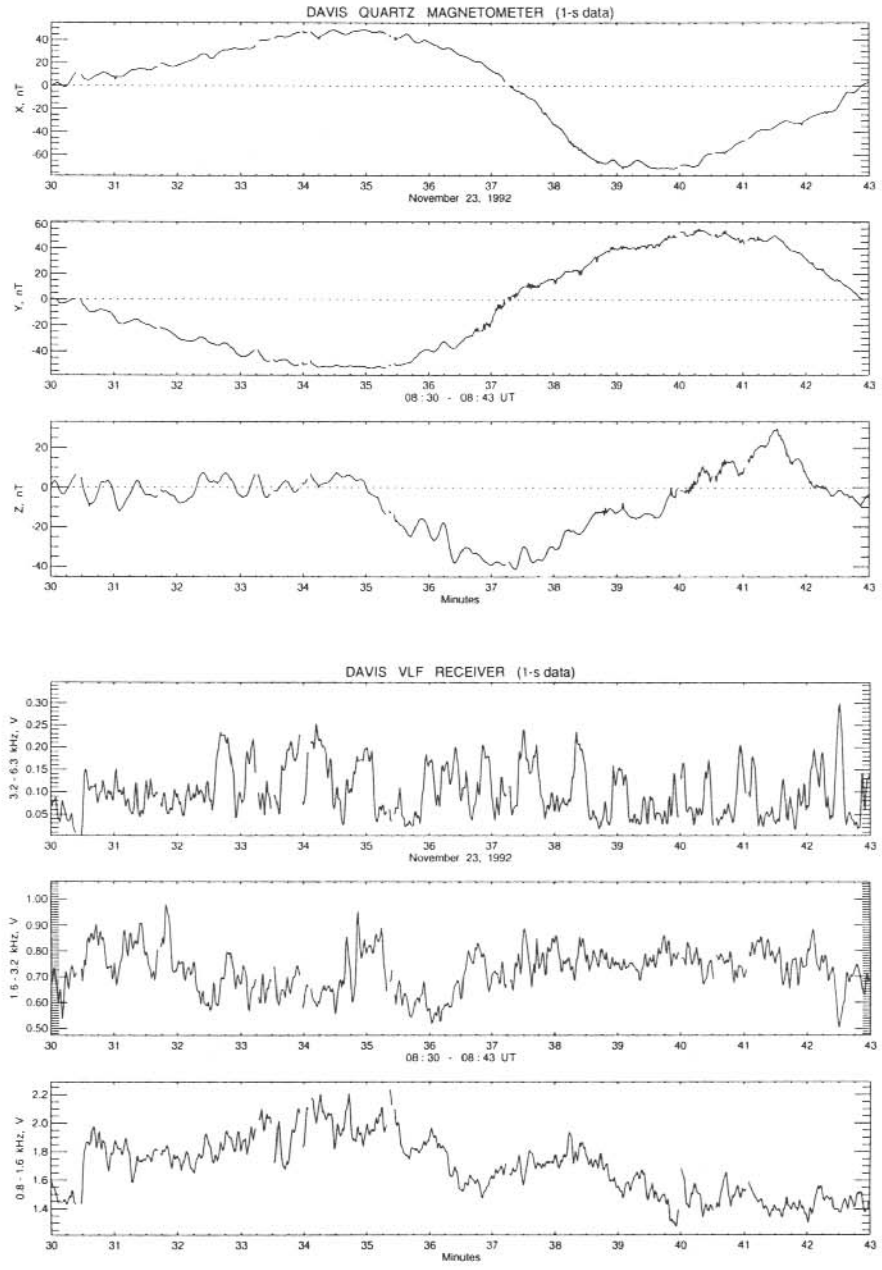

Figure 3. Detrended 1 s geomagnetic variations recorded at Davis on the quartz magnetometer (upper panel) and original 1 s VLF data (lower panel) for the 0830–0843 UT interval on 23 November 1992.

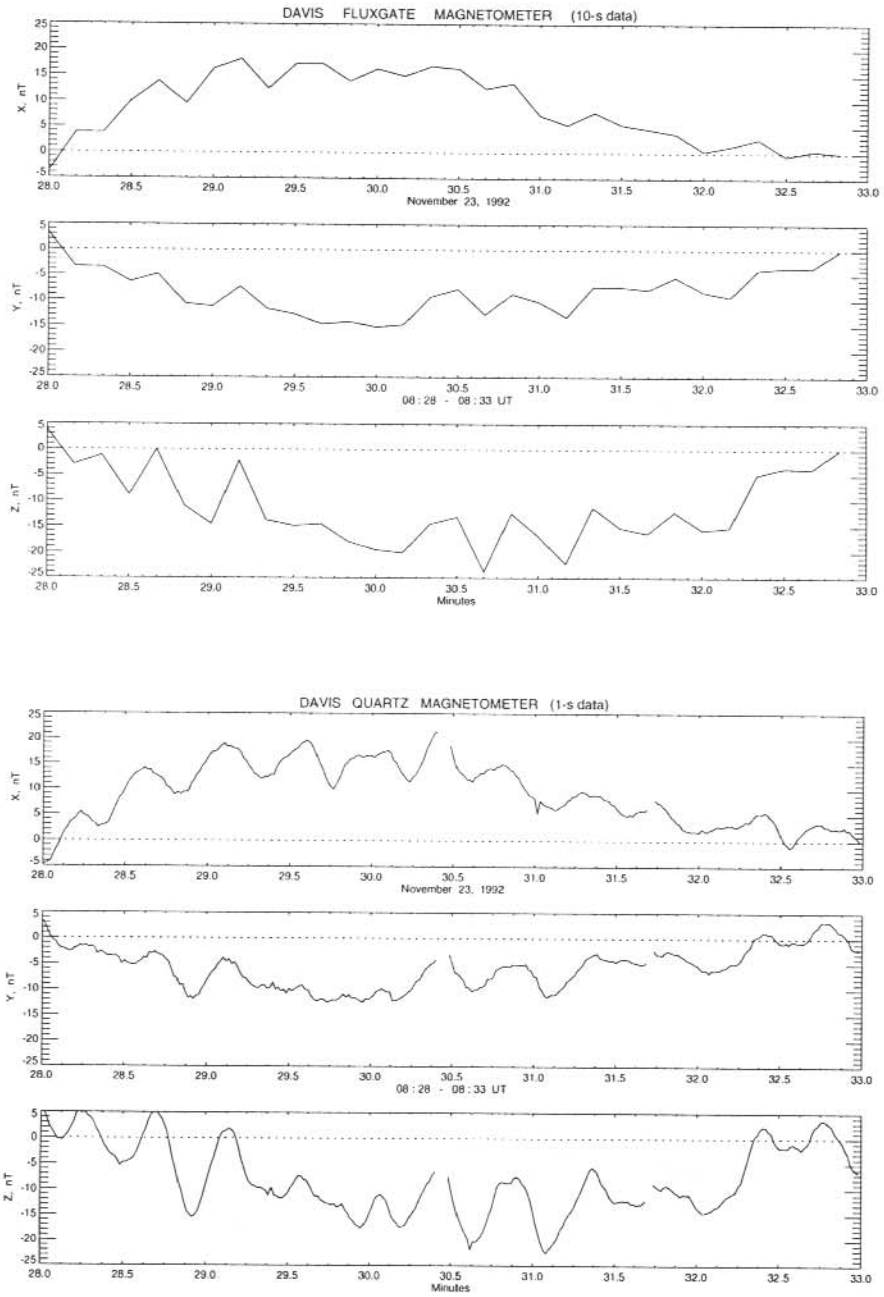

Figure 4. Comparison of detrended geomagnetic variations recorded on the fluxgate magnetometer (10 s sampling, upper panel) and quartz magnetometer (1 s sampling, lower panel) for the 0828–0833 UT interval on 23 November 1992.

Figure 4 shows a comparison of fluxgate and quartz magnetometer recordings on an initial phase of this ionospheric current re-orientation (0828–0833 UT) when Pc3 pulsations are most pronounced. One can see that the fluxgate magnetometer 10 s readings follow the 1 s sampled traces of the quartz magnetometer with a great deal of detail. We can conclude from these plots that 1 s sampling is much more informative for geomagnetic studies than 10 s sampling. Even though Pc3 pulsations can be filtered from 10 s data, the Pcl pulsations can be captured only from the 1 s data.

5.6 CONCLUSION REMARK

The data from the magnetometer array in Antarctica is an important component to complete the entire Antarctic instrumentation such as imaging riometers, digital all-sky cameras and VLF receivers deployed at manned and unmanned stations. Recent achievements with the deployment of US Automatic Geophysical Observatories a few hundred kilometers from South Pole station (Rosenberg and Doolittle 1994) and the joint project between the University of Michigan and Russian institutions AARI and IZMIRAN to deploy digital autonomous magnetometers at Komsomolskaya and Pionerskaya, significantly enhanced observational capabilities of the Eastern Antarctic manned station network (South Pole, Vostok, Mirny, Casey, Davis and Mawson). Two of these manned stations (Vostok and Mirny) are equipped with quartz variometers and digital data acquisition systems similar to the system studied in this paper, others have conventional or specially designed fluxgate magnetometers.

This paper shows that both types of magnetic instruments are capable of recording a wide range of geomagnetic variations with sufficient accuracy and resolution. It is shown also that 1 s resolution data are more useful for analysing high frequency phenomena as well as maintaining standard observatory measurements. The major problem studied in this paper was the correct orientation of magnetic instruments against geographic or geomagnetic axes, and to a local vertical line: large total values of the geomagnetic Z component in this area introduce significant errors in the horizontal field components if the local vertical line is not defined properly (e.g., about 90 nT for each 0.1° at Davis and 110 nT at Casey). We recommend installation of tiltmeters with an accuracy of about 0.01° on the concrete pillars at Davis and Casey inside the sensor enclosure box to monitor seasonal changes of the 'quasi-true' sensor orientation. The best possible orientation of the instrument to geographic north and east in the horizontal plane is also required. Absolute observations of the geomagnetic field component values (F with PPM, H and D with QHM or D and I with DIM theodolite) should be carried out once per week during quiet geomagnetic activity periods. Modern data acquisition systems allow visualisation of current geomagnetic field variations on the station-based computer display to help selection of appropriate quiet-time periods for absolute observations.

5.7 ACKNOWLEDGMENTS

Drs Papitashvili, Belov and Pimenov thank Robyn Graham at the Australian Antarctic Foundation for providing financial support and Ray Morris at the Antarctic Division for organising a successful winter for Igor Pimenov (1992 ANARE) at Davis and ensuing scientific studies. This work has been supported at the University of Michigan by the NSF

grant OPP-9318766, at the Antarctic Division by the AAF grant for ASAC project 507, and at IZMIRAN by the RFFI research grant 93-05-8722.

REFERENCES

Abston, C.C., Papitashvili, N.E. *and* Papitashvili, V.O. (1985). Combined International Catalog of Geomagnetic Data, Report UAG-92, 271 pp., WDC-A for STP, WDC-B2 and WDC-C, NOAA/NGDC, Boulder, Colorado, USA, 1985.

Bobrov, V.N. *and* Burtsev, Yu.A. (1969). Quartz Z-variometer for autonomous magnetic variation stations. Geomagnetism and Aeronomy, English Translation, 9, No. 3, 770.

Belov, B.A., Murashov, B.P. *and* Sizov, Yu.P. (1979). Magnetometer for registration of the MHD generator pulse fields and geomagnetic field variations in a frequency range from 0 to 10 Hz (in Russian), in Izmerenie i Obrabotka Odinochnix Signalov pri Geofizicheskix Issiedovaniyax s Impul'snimi Istochnikami (Measurements and Processing of the Single Pulse Signals for Geophysical Studies with the Pulse Generators), AN SSSR, Apatity. Pp.41-46.

Burns, G.B. *and* Klekociuk, A.R. (1994). Davis and Casey magnetic field data. In: Morris R.J. (Ed). *ANARE Research Notes Number 92*. Pp. 17–41.

Burtsev, Yu.A., Belov, B.A. *and* Murashov, B.P. (1977). Digital magnetic variation station, USSR Patent No. 577496 (in Russian), Patent Bulletin (Bulleten Izobretenii), 39.

Kamide, Y. *and* Baumjohann, W. (1993). Magnetosphere-Ionosphere Coupling, Springer-Verlag, Berlin Heidelberg. P. 178.

McLean, S.J., Davis, W.M., Morris, L.D. *and* Meyers, H. (1994). A Report on Geomagnetic Observatories and Observations, 1994, Report SE-52, WDC-A for SEG, NOAA/NGDC, Boulder, Colorado, USA. P. 143.

Papitashvili, N.E. *and* King, J.H. (1993). Corrected geomagnetic coordinate software at NSSDC, STEP International, 3, No. 11. P. 14.

Papitashvili, V.O., Clauer, C.R., Belov, B.A., Pimenov, I.A., Schekotov, A.Yu., Burns, G.B., Morris, R.J. *and* Friis-Christensen, E. (1994). Observations in both southern and northern dayside polar caps of solar wind-magnetosphere-ionosphere current coupling during the November 23, 1992 GEM interval, Eos Trans. AGU, 75(44), Fall Meeting Supplement. P. 550.

Rosenberg, T.J. *and* Doolittle, J.H. (1994). Studying the polar ionosphere and magnetosphere with Automatic Geophysical Observatories: The US program in Antarctica, Antarctic Journal, US, XXVIII, No. 5.

6. TSYGANENKO CONJUGACY PREDICTIONS FOR ANARE STATIONS

G.B. Burns[1,2], D.J. Hearn[1], R.D. Elphinstone[1], J.S. Murphree[1] and D.J. McEwen[3]

(1) Department of Physics and Astronomy
University of Calgary
Calgary Canada T2N 1N4

(2) Atmospheric and Space Physics
Antarctic Division
Kingston Tasmania 7050
Australia

(3) Institute of Space and Atmospheric Studies
University of Saskatchewan
Saskatoon Canada S7N 0W0

ABSTRACT

Improvements to the Tsyganenko (1987) 'long-field' model, which include an increase in the near-earth magnetotail $<B_z>$ values and the incorporation of 'tail warping' (see Peredo et al. 1993 for a recent discussion of Tsyganenko models), result in a magnetosphere 'closed' at higher latitudes than for earlier versions. Conjugacy predictions for the Australian National Antarctic Research Expedition (ANARE) stations using this recent model are presented.

Conjugate mapping of a closely spaced (25 km) array around each of the ANARE (Australian National Antarctic Research Expeditions) stations is used to examine model predictions of the stretching, contraction and twisting of auroral forms. The ANARE stations, Macquarie Island (magnetic latitude 64.3°S – PGM88), Mawson (70.5°S), Davis (74.6°S) and Casey (80.4°S) cover a useful range of magnetic latitudes. We have adopted this procedure to gain an indication of how the appearance of forms may alter between the hemispheres. There have been a limited number of attempts to experimentally determine conjugate links using VIKING images (Northern Hemisphere) and ground-based optical observations (Southern Hemisphere) (Burns et al. 1990, 1992). Difficulty was experienced in experimentally determining conjugate points, particularly in the post-noon region. This modelling approach gives some insight into possible interhemispheric variations in the appearance of auroral structures. At auroral latitudes, a measurable diurnal variation in the relative orientation of conjugate auroral arcs is predicted. At higher latitudes, significant variations in the inter-hemispheric ratio of the length and width of auroral patches are predicted, particularly at times of high dipole tilt (when the Earth's magnetic field is significantly off-perpendicular with respect to the sun-earth line).

Using a development of the Stenbaek-Nielsen et al. (1973) approximations, diurnal variations in the relative intensity of conjugate auroral forms are also presented.

Care must be taken in applying the conjugacy predictions to specific instances as small variations in the starting point of the field line traces can result in significantly different regions of the magnetosphere being traversed. The model conjugacy predictions in such cases would be significantly altered. The station array field line traces do however give a good idea of the range of conjugacy variations that are predicted by recent external field models.

6.1 INTRODUCTION

The geomagnetic field provides a link between the auroral regions of the Northern and Southern Hemispheres. Electrons of auroral energy can traverse the distance between the hemispheres along the magnetic field lines in the order of tens of seconds. Some similarity of auroral development and associated activity is expected for regions in opposite hemispheres linked by the geomagnetic field. Such regions are said to be 'conjugate'.

Full representations of the internal magnetic field of the Earth, such as provided by the IGRF/DGRF (International/Definitive Geomagnetic Reference Field) series can be used to determine the inter-hemispheric linkages that would exist in the absence of ionospheric and magnetospheric current systems. The inter-hemispheric linkages of internal field models are contained in the magnetic coordinate systems that are derived from full internal field models. These include the Corrected Geomagnetic Coordinate system (for example Gustafsson 1984) and derivative (Baker and Wing 1989) or revised systems (Gustafsson et al. 1992). Full internal field model conjugate locations provide a useful reference point from which experimentally determined displacements, or displacements implied by external magnetic field models, can be discussed. The measured or modelled displacements can be referenced to the ionospheric or magnetospheric current systems that have resulted in the displacement. Magnetic models that are analytic simplifications of a full internal field model, such as centred dipole or eccentric dipole models, are generally inappropriate for conjugacy studies because errors induced by the analytic simplifications are generally of a magnitude similar to expected conjugacy variations.

External field models have been used to estimate diurnal and seasonal variations in the conjugate locations of stations of particular interest (Stassinopoulos et al. 1984; Ono 1987). It is important to realise the model limitations when using them in this manner. There are large standard deviations in the satellite measurements of the magnetic field that are averaged to provide the input for determining the magnitude of the analytic current representations incorporated in the external field models (see for example Peredo et al. 1993). Calculations for an individual site at a particular time under specific geomagnetic conditions can at most represent an average of what is likely to be highly event specific variability. The current external field models do however provide the best available indication of the manner in which some of the major magnetospheric current systems may modify the field-line linkages. Determinations of conjugacy using such models can be discussed in terms of what current systems may or may not be well represented by the external model.

The Tsyganenko series of external magnetic field models (Tsyganenko 1987, 1989) have been most extensively used. Peredo et al. (1993) have reported on the incorporation of ISEE satellite magnetic observations into a re-evaluation of the Tsyganenko formulations.

The recalculations lead to a significant increase in $<B_z>$ in the near tail region (XGSM = -10 to -22 RE). B_z is crucial to the mapping between the equatorial magnetosphere and the polar ionosphere. A higher B_z leads to a more closed magnetosphere. We have chosen to use a modified Tsyganenko (1987) formulation that has incorporated the ISEE data into the determination of the coefficients and has tail warping effects incorporated self-consistently. We refer to this model as T87/93, or some variation of this formulation. The syntax indicates the Peredo et al. (1993) recalculation of the Tsyganenko (1987) model coefficients. This model is referred to by Peredo et al. (1993) as T87Wd. We chose a reformulation of the Tsyganenko (1987) model over the reformulation of the Tsyganenko (1989) model because comparisons of the Tsyganenko (1987) model with VIKING images have proved interesting (see for example Elphinstone et al. 1991).

The internal field model incorporated with the T87/93 model for the results presented in this paper is the 1985 IGRF model with secular variation extension to the 1986 dates indicated. The internal model used is of little importance if the results are referenced to variations from the conjugate point of the internal model. The specific reason for the dates chosen for the results presented in this paper is that the VIKING auroral imager was operational during 1986. All field line traces commence and conclude at an altitude of 120 km.

6.2 MACQUARIE ISLAND CONJUGACY PREDICTIONS – SEASONAL VARIATION, VARIATION WITH LEVEL OF ACTIVITY AND COMPARISON OF MODELS

Previous authors (Ono 1987; Burns et al. 1991) have shown that at auroral latitudes the diurnal variations predicted by the early Tsyganenko models are greater during the solstices than during the equinoxes, and that the higher the level of magnetic activity the larger is the predicted distance from the conjugate point determined using a full internal field model. These features are shown in Figures 1 and 2 using the T87/93 model for Macquarie Island (PGM-88 magnetic latitude 64.3°S, L = 5.3, magnetic midnight ~1215 UT). In these and subsequent Figures, a diamond is plotted at the model calculated conjugate point for each UT hour of the day for the level of magnetic activity (Kp) chosen. A cross indicates the location of the internal field conjugate point. A consistent feature of these plots is that the magnetic noon and midnight displacements from the internal field calculated conjugate point are significantly less that the displacement calculated at dawn and dusk.

Figure 3 shows a comparison of the conjugacy predictions of the T87/93, Tsyganenko – 1987 (T87) and Tsyganenko – 1989 (T89) models. A significant reduction in the range of the conjugacy variations calculated is apparent for the T87/93 model. For the June solstice, Kp 3 data presented, the range of the conjugate points are approximately: T87/93 – 400 km, T87 – 825 km and T89 – 715 km. The importance of the B_z value to the conjugacy mapping is readily apparent.

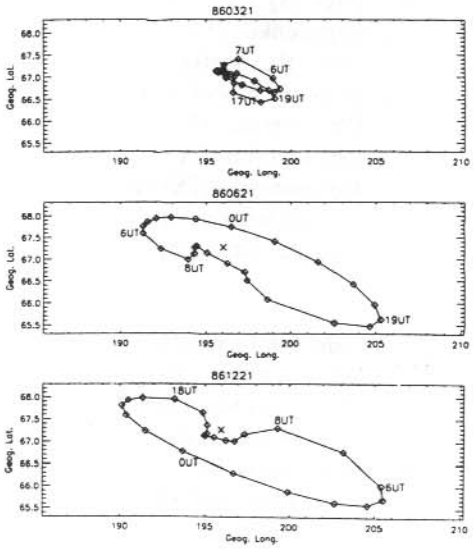

Figure 1. Macquarie Island conjugacy predictions using the T87/93 model, Kp = 5, for the March equinox and the June and December solstices.

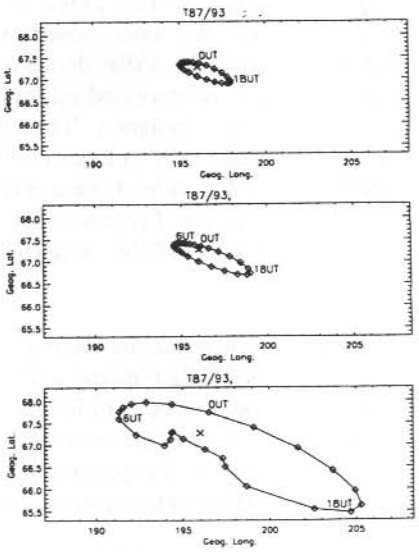

Figure 2. Macquarie Island conjugacy predictions using the T87/93 model, for the June solstice, for Kp = 0, 3 and 5.

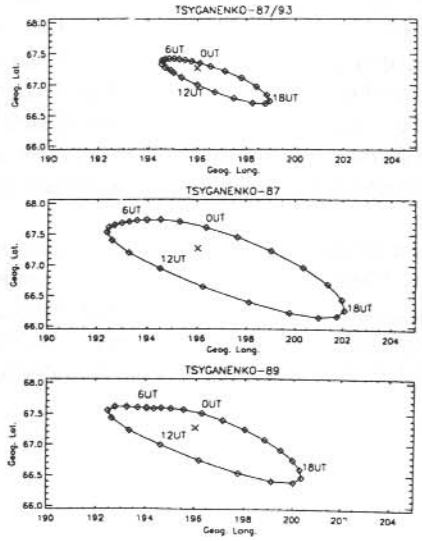

Figure 3. Macquarie Island conjugacy predictions for the June solstice, Kp = 3, for the T87/93, T87 and T89 models.

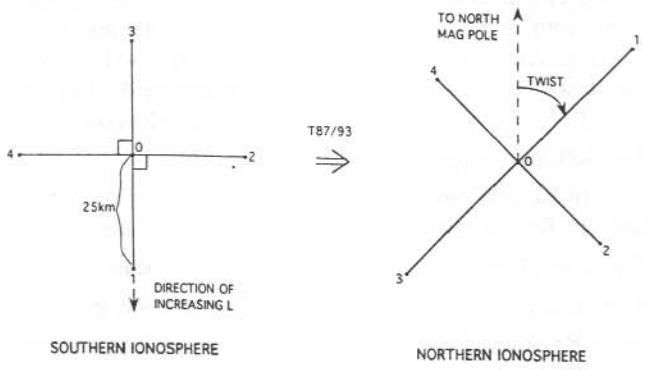

Figure 4. Representation of the interhemispheric grid mapping via the T87/93 model.

6.3 ARRAY MAPPING – STRETCHING, CONTRACTION AND TWISTING

A five-point, closely spaced (25 km) grid around the chosen starting site was mapped through the T87/93 model. The results of the mapping were used to calculate variations between the hemispheres. Figure 4 characterises the mapping.

Table 1 shows the features calculated from the grid mapping for Macquarie Island at the June solstice and a Kp = 3 level of magnetic activity. The last line gives the values calculated using the internal field model only.

The columns in Table 1 indicate:

The UT time of the calculation.

TILT is the dipole tilt, the angle the Earth's centred dipole makes to the perpendicular of the sun-earth line, in the plane defined by the Sun-Earth line and the dipole axis. A positive value indicates the Northern Hemisphere is tilted toward the sun. GLAT and GLON are the geographic latitude and longitude of the model calculated conjugate point.

Flat1 (N/S) is the ratio of the separation of the points 0 and 1 (see Figure 2) in the Northern Hemisphere to the distance of separation of these points in the Southern Hemisphere (=25 km).

Flat2 (N/S) is a similar ratio for points 0 and 3. The ratios are calculated separately to indicate when the variations are so great as to be inconsistent across the 50 km range of the grid. The average of Flat1 and Flat2 is taken as the model implied inter-hemispheric stretching/compression of the field lines across the latitudes.

Flon1 (N/S) is the inter-hemispheric distance ratio for the points 0 and 2 and Flon2 (N/S) is the ratio for the points 0 and 4. The average of Flon1 and Flon2, is taken as the

model implied inter-hemispheric stretching/compression of the field lines across the longitude meridians.

Farea (N/S) is the ratio of the areas defined by the grid in the two hemispheres. This is calculated as the sum of the 'plain' triangles defined by the points 124 and 234 (see Figure 4). The product of the average Flat and Flon values does not give the appropriate area when there are variation across the grid. For severe variations across the grid, the 'plain triangles' assumption also breaks down.

Twist is calculated as defined in Figure 4.

Equat is the distance, in Re (the radius of the Earth), from the centre of the Earth to the minimum magnetic field (Bmin) value along the field line trace.

Xgsm, Ygsm and Zgsm are the GSM coordinates of the Bmin location.

Bmin is the minimum magnetic field value along the field line trace, given in nanoteslas.

Dste is the distance, in Re, along the model field line from the Southern ionosphere to the Bmin (= geomagnetic equator) location.

Detn is the distance, in Re, along the model field line from the Bmin location to the Northern ionosphere.

Diff = Dste – Detn.

FBmag (N/S) is the ratio of the magnitude of magnetic field at 120 km in the Northern Hemisphere to its value at the same altitude in the Southern Hemisphere.

FBrad (N/S) is a similar ratio for the radial component of the magnetic field.

A*Br is the product of FBrad(N/S) and Farea(N/S). By the conservation of magnetic flux, if the assumptions involved in the area calculation are valid, A*Br will equal unity.

The 'twist' variations across the day presented are from -12° to +22° (see Table 1). A possible test of whether this average variation in the twisting of auroral forms occurs between Macquarie Island and its conjugate point near Kotzebue in Alaska would be to compare the average diurnal alignment of auroral arcs at the two sites. This seems to be the most readily measured signal of the average distortion of the internal field by the magnetospheric currents in the high tilt (solstice) periods. It may be possible to statistically test the predictions of stretching/contraction between the hemispheres by appropriately averaging distances from satellite particle observations.

6.4 CONJUGATE AURORAL INTENSITIES

We can use the results of the grid point external field mapping to modify and expand an approach developed by Stenbaek-Nielsen et al. (1973) for estimating intrinsic and photometric measured auroral brightness ratios between the hemispheres, for a range of assumptions. Differences in the approach presented here are that magnetic flux is balanced between the hemispheres as the product of the horizontal area in the ionosphere by the radial component of the magnetic field strength. In the Stenbaek-Nielsen (1973) paper the total field strength is substituted for the radial component. The approach we adopt estimates the intrinsic brightness in the zenith of the site. We believe, the approach by Stenbaek-Nielsen et al. (1973) ultimately gives the brightness ratio between the hemispheres for photometers of equal field-of-view, aimed at the magnetic zenith. The different off-zenith alignments of the photometers would compensate for the interhemispheric site-zenith intrinsic intensity

differences we calculate. The varying approaches make no difference to the interhemispheric ratios Stenbaek-Nielsen et al. (1973) derive for the area south of New Zealand and the conjugate area near Alaska. In this case the magnetic dip-angles of the conjugate regions are similar, rendering the ratio of total field component equivalent to the ratio of the radial component. We derive a interhemispheric intrinsic brightness ratio that is dependent on the ratio of the sine of the magnetic field dip-angles [$\sin(dip_N)/\sin(dip_S)$] of the conjugate regions. This makes a particular difference for the intrinsic brightness ratio between Mawson station and its conjugate.

Table 1. T87/93 conjugacy mapping information for Macquarie Island (-54.50°S, 158.95°E, geographic), June solstice, Kp = 3. The diurnal variation of features defined in Section 6.3. The last line gives the values calculated using the internal field model only.

Date: 860621 Macquarie Island (-54.50°S, 158.95°E)

TIME (UT)	TILT (Deg)	GLAT (Deg)	GLDN (Deg)	Flatl (N/S)	Flat2 (N/S)	Flonl (N/S)	Flon2 (N/S)	Farea (N/S)	Twist (Deg)	Fquat (Re)	Xgsm (Re)	Ygsm (Re)	Zgsm (Re)	Bmin (nT)	Dste (Re)	Detn (Re)	Diff (Re)	FBmin (NIS)	FBrad (NIS)	A*Br (NIS)
0	19.5	67.35	196.11	1.02	1.02	1.15	1.15	1.17	0.4	5.76	5.4	0.0	-1.9	168.2	6.75	6.99	-0.24	0.87	0.86	1.00
1	17.0	67.38	195.77	1.01	1.02	1.16	1.15	1.17	-1.3	5.76	5.3	1.5	-1.6	167.7	6.75	6.99	-0.24	0.86	0.86	1.00
2	15.0	67.40	195.50	1.01	1.01	1.16	1.16	1.17	-2.9	5.79	4.9	2.8	-1.3	164.0	6.78	6.98	-0.20	0.86	0.86	1.00
3	13.5	67.41	195.26	1.00	1.00	1.16	1.16	1.17	-4.5	5.83	4.1	4.0	-1.0	157.5	6.84	6.98	-0.13	0.86	0.86	1.00
4	12.6	67.42	195.05	1.00	1.00	1.17	1.16	1.17	-6.2	5.89	3.1	5.0	-0.7	148.8	6.87	7.04	-0.16	0.86	0.86	1.00
5	12.4	67.42	194.85	0.99	1.00	1.18	1.17	1.17	-7.9	5.96	1.8	5.7	-0.4	138.5	6.94	7.11	-0.17	0.86	0.86	1.00
6	13.0	67.41	194.68	1.00	1.00	1.18	1.18	1.17	-9.6	6.05	0.4	6.0	-0.1	126.9	7.00	7.16	-0.16	0.86	0.86	1.00
7	14.2	67.39	194.55	0.98	0.98	1.19	1.19	1.17	-11.2	6.15	-1.0	6.1	0.3	114.2	7.13	7.25	-0.12	0.86	0.86	1.00
8	15.9	67.34	194.54	0.96	0.97	1.21	1.21	1.17	-11.7	6.27	-2.5	5.7	0.7	100.3	7.19	7.32	-0-13	0.86	0.86	1.00
9	18.2	67.28	194.71	0.95	0.96	1.23	1.22	1.17	-9.4	6.40	-3.8	5.0	1.2	87.8	7.28	7.47	-0.18	0.86	0.86	1.00
10	20.9	67.24	194.92	0.96	0.96	1.22	1.22	1.17	-8.2	6.52	-4.9	3.9	1.8	80.4	7.38	7.56	-0.19	0.86	0.86	1.00
11	23.7	67.20	195.05	0.95	0.96	1.22	1.22	1.17	-8.5	6.59	-5.6	2.5	2.4	78.0	7.41	7.62	-0.21	0.86	0.86	1.00
12	26.5	67.12	195.37	0.94	0.95	1.24	1.24	1.17	-4.4	6.59	-5.9	1.0	2.8	78.5	7.41	7.62	-0.21	0.86	0.85	1.00
13	29.2	67.00	195.99	0.95	0.95	1.25	1.25	1.17	3.9	6.55	-5.8	-0.7	3.1	79.9	7.35	7.57	-0.22	0.86	0.85	1.00
14	31.5	66.88	196.72	0.97	0.97	1.24	1.24	1.17	10.4	6.47	-5.2	-2.4	3.0	83.0	7.28	7.52	-0.24	0.86	0.85	1.00
15	33.2	66.78	197.50	1.00	1.00	1.24	1.24	1.17	15.0	6.34	-4.2	-3.9	2.6	91.1	7.16	7.42	-0.26	0.86	0.86	1.00
16	34.2	66.70	198.26	1.04	1.04	1.24	1.23	1.17	20.3	6.20	-3.0	-5.1	1.9	104.9	7.06	7.29	-0.22	0.86	0.86	1.00
17	34.4	66.69	198.78	1.08	1.07	1.22	1.21	1.17	22.1	6.08	-1.6	-5.8	1.0	118.9	6.97	7.23	-0.26	0.86	0.86	1.00
18	33.8	66.73	198.97	1.09	1.08	1.20	1.19	1.17	21.3	6.00	-0.2	-6.0	0.0	130.6	6.94	7.13	-0.19	0.87	0.86	1.00
19	32.4	66.83	198.85	1.09	1.09	1.18	1.17	1.17	18.8	5.94	1.2	-5.7	-0.9	140.0	6.81	7.21	-0.40	0.87	0.86	1.00
20	30.4	66.97	198.42	1.07	1.07	1.16	1.15	1.17	14.8	5.89	2.6	-5.1	-1.6	147.9	6.81	7.16	-0.34	0.87	0.86	1.00
21	27.9	67.11	197.80	1.05	1.05	1.15	1.15	1.17	10.1	5.05	3.7	-4.1	-2.0	155.0	6.78	7.06	-0.28	0.87	0.86	1.00
22	25.1	67.22	197.14	1.04	1.04	1.15	1.15	1.17	5.8	5.81	4.6	-2.8	-2.2	161.1	6.75	7.03	-0.28	0.87	0.86	1.00
23	22.3	67.30	196.56	1.02	1.03	1.15	1.15	1.17	2.5	5.79	5.2	-1.4	-2.2	165.8	6.75	7.02	-0.27	0.87	0.86	1.00
0	19.5	67.27	196.01	1.00	0.99	1.18	1.18	1.17	0.0	5.50	5.2	0.0	-1.7	188.8	6.53	6.56	-0.03	0.86	0.86	1.00

The following is taken from the development by Stenbaek-Nielsen et al. (1973) with the incorporation of the modification to the magnetic flux balance mentioned above.

For a particle with pitch angle α in the equatorial plane

$$\sin^2\alpha = \frac{B_Q}{B_M}$$

where

B_O is the magnetic field strength at the equator and
B_M is the magnetic field strength at the 'mirror' point.

Since $B_O/B_M << 1$, then $\sin\alpha \approx \alpha$ and

$$\alpha_N = (B_O/B_N)^{1/2} \quad \text{and} \quad \alpha_S = (B_O/B_S)^{1/2}$$

where

B_N is the magnetic field strength at the mirror point in the northern hemisphere and
B_S is the magnetic field strength at the mirror point in the southern hemisphere.

Consider the case of *strong diffusion and an isotropic flux* (as per the development of Stenbaek-Nielsen et al. 1973).

Let j be the directional flux (the number of particles in a given direction per unit area, perpendicular to the direction of incidence, per unit time per unit solid angle) at the equator.

Let A_O be the equatorial cross-section of the flux tube containing the particles.

Then the number of particles, n, crossing the equatorial plane with pitch angles $< \alpha$, per unit time is

$$n = A_O \pi j \sin^2\alpha \approx A_O \pi j \alpha^2 .$$

Thus the ratio of the number of particles in the loss cone, at the equator, heading for the northern ionosphere (n_N) to the number of particles in the loss cone, at the equator, heading for the southern ionosphere (n_S) is

$$\frac{n_N}{n_S} = \frac{\alpha_N^2}{\alpha_S^2} = \frac{B_S}{B_N} .$$

Consider now the conservation of magnetic flux between the two hemispheres. Stenbaek-Nielsen et al. (1973) use

$$A_N B_N = A_S B_S$$

where A_N and A_S are the areas of the flux tube *perpendicular to the magnetic field direction,* in the respective hemispheres. In calculating the relative auroral brightness in the zenith above conjugate sites we need to consider the density of particles incident on a horizontal layer. Redefining A_N and A_S as *horizontal areas of the flux tube in the respective polar ionospheres*, the conservation of magnetic flux becomes

$$A_N B_N \sin(dip_N) = A_S B_S \sin(dip_S)$$

where dip_N and dip_S are the magnetic field dip angles in the respective hemispheres (see Figure 5). Let I_N, I_S be the brightness per unit area in the respective hemispheres. Then

$$\frac{I_N}{I_S} = \frac{n_N}{n_S}\frac{A_S}{A_N} = \frac{A_S B_S}{A_N B_N} = \frac{\sin(dip_N)}{\sin(dip_S)} .$$

Using the terminology introduced in Section 6.3 and used in Table 1

$$\frac{I_N}{I_S} = \frac{FBrad(N/S)}{FBmag(N/S)} .$$

The interhemispheric intrinsic brightness ratio calculated in this manner is essentially constant for conjugate sites. Some minor variability is possible in the results we present, as the location of the mapped conjugate point varies and consequently the magnetic field at the northern hemisphere changes slightly.

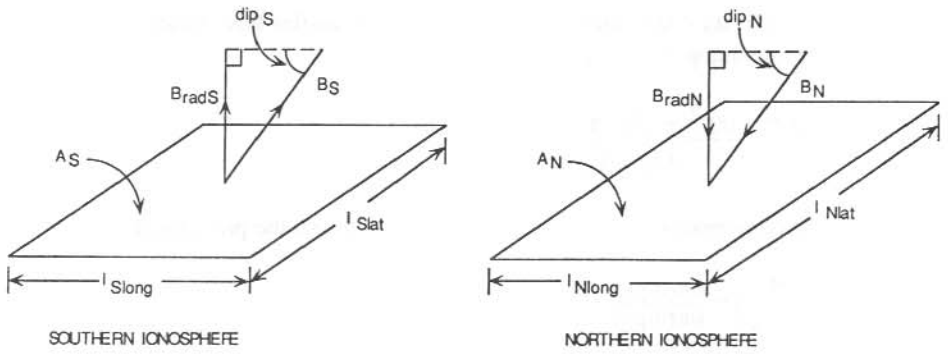

Figure 5. Conjugate flux areas. Defining terminology used in Section 6.4.

In determining a photometric intensity ratio, Stenbaek-Nielsen et al. (1973) note that auroral arcs are generally extensive in an East-West direction but relatively narrow in North-South extent. Stenbaek-Nielsen et al. (1973) postulate that a photometer with a significant field-of-view (fov) would generally see the North-South extent of an arc, but that the East-West component would likely extend beyond the fov. They also assume that the interhemispheric area ratio is divided equally between latitude and longitude. They propose

$$\frac{l_{Nlat}}{l_{Slat}} = \left(\frac{A_N}{A_S}\right)^{0.5}$$

where l_{Nlat} and l_{Slat} are the latitudinal widths of the flux tubes in the respective polar ionospheres (see Figure 5). We have shown that even for an internal field mapping the

interhemispheric stretching/contraction is not uniform across and along magnetic latitudes. See, for example, the last line of Table 1, where for the internal model mapping, Flat(N/S) is 1.00 and Flon(N/S) is 1.18. We can incorporate the modelled diurnal variations in the interhemispheric stretching and contraction. Thus for strong diffusion and an isotropic flux we derive a photometric measured interhemispheric intensity ratio

$$\frac{I_{Nphot}}{I_{Sphot}} = \frac{I_{Nlat}}{I_{Slat}} * \frac{I_N}{I_S} .$$

In the terms introduced in Section 6.3 and used in Table 1

$$\frac{I_{Nphot}}{I_{Sphot}} = \frac{[Flat(N/S)*FBrad(N/S)]}{Fmag(N/S)} .$$

Now consider the case of strong *diffusion and anisotropy* for the situation when $B_S > B_N$, as per Stenbaek-Nielsen et al. (1973). Under these conditions, although particles with pitch angles $\alpha < \alpha_S$ precipitate in both north and south polar regions, those with $\alpha_S < \alpha < \alpha_N$ are precipitated only in the northern hemisphere. If the directional flux in $0 < \alpha < \alpha_S$ is j, the directional flux in $\alpha_S < \alpha < \alpha_N$ is 2j, since these pitch angles have twice as much time to accumulate before dumping. Thus

$$\frac{n_N}{n_S} = \frac{A_O \pi j \alpha_S^2 + A_O \pi 2 j (\alpha_N^2 - \alpha_S^2)}{A_O \pi j \alpha_S^2} .$$

Incorporating the conservation of magnetic flux condition as per the previous development

$$\frac{I_N}{I_S} = \left(2 - \frac{B_N}{B_S}\right) * \frac{\sin(dip_N)}{\sin(dip_S)} .$$

In the terms introduced in Section 6.3 and used in Table 1

$$\frac{I_N}{I_S} = \left(\frac{2}{FBmag(N/S)} - 1\right) * FBrad(N/S).$$

If $B_N > B_S$, then the equation becomes

$$\frac{I_N}{I_S} = (2FBmag(N/S) - 1)^{-1} * FBrad(N/S).$$

We can incorporate the previous development for photometers which cover the latitudinal but not the longitudinal extent of auroral forms to determine the model predicted interhemispheric variation in photometer measured intensities.

$$\frac{I_{Nphot}}{I_{Sphot}} = \frac{I_N}{I_S} * Flat(N/S).$$

We use magnetic field ratios calculated at a 120 km altitude whereas Stenbaek-Nielsen et al. (1993) use the ratios at 300 km. For the models used, the differences in ratios so calculated is minimal.

It would be extremely unlikely if these model predictions could be effectively tested using ground observations, given the difficulty of making conjugate observations at high latitudes, particularly in the solstices when the greatest variations are predicted, and given the variability of factors such as atmospheric composition and transmission. An appropriate averaging of satellite particle observations may be able to test if variability of the nature predicted does exist.

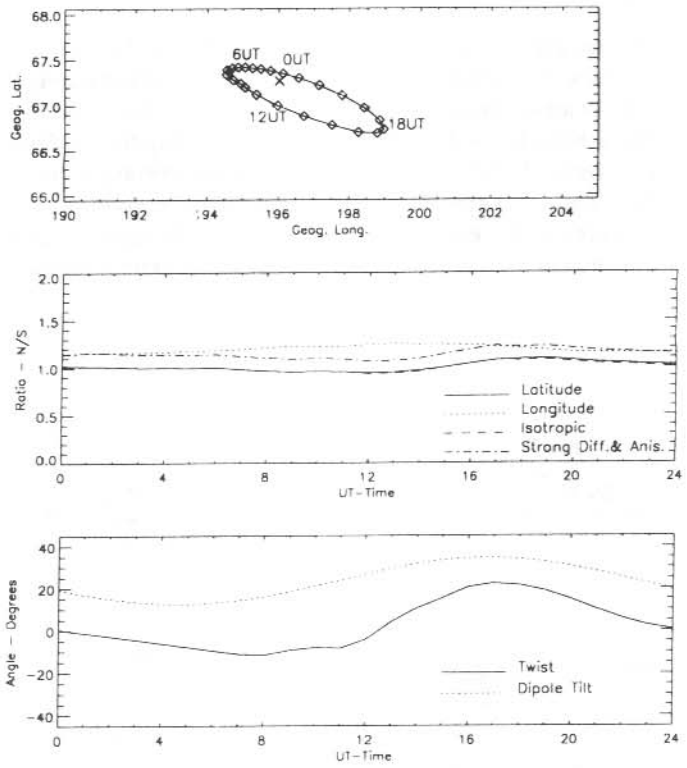

Figure 6. T87/93 conjugacy mapping for Macquarie Island, June solstice, Kp = 3. A development of some of the information contained in Table 1. The diurnal variation of the conjugate point, Flat(N/S), Flon(N/S), interhemispheric photometer measured intensity ratios for isotropic fluxes and for strong diffusion and anisotropic fluxes (see Section 6.4), twist and dipole tilt are shown.

Figure 6 diagrammatically represents some of the results presented in Table 1. Included in the plots are our evaluations of the diurnal interhemispheric *photometer measured* intensity ratios for the cases of *strong diffusion and isotropic flux* and *strong diffusion and anisotropy*. The respective values calculated using only the internal field model are 1.00

and 1.14. The Figure also includes plots of the calculated diurnal variation of the conjugate point, Flat(N/S) and Flon(N/S), *twist* and dipole tilt. Subsequent Figures contain similar information.

6.5 MAWSON CONJUGACY PREDICTIONS

Figures 7 and 8 show the T87/93 conjugacy predictions for the March equinox and the June solstice, for an activity level of Kp = 3, for Mawson station (PGM-88 magnetic latitude 70.5°S, L = 9.0, magnetic midnight ~2230 UT). The inter-hemispheric photometer measured intensity ratios caculated using the internal field only are 1.05 for strong diffusion and asotropic flux and 0.99 for strong diffusion and anisotropy. Tables 2 and 3 show the listings, as previously described, for these days.

Figures 7 and 8 show occasional large scale jumps apparent in the conjugacy locations between consecutive hours. From Table 3 it is apparent that the assumptions of uniformity over the 50 km grid point array break down around 5 UT and 17 UT. The Xgsm values in this Table indicate that at these times the field line trace is changing from a dayside trace to a nightside trace, or vice versa. Different current systems would dominate the field line trace either side of this boundary. At these times there are sharp discontinuities in the *twist* measurements (see Figure 8). Given the variability noted in the satellite data from which the model coefficients are derived, the model is unlikely to accurately measure the time at

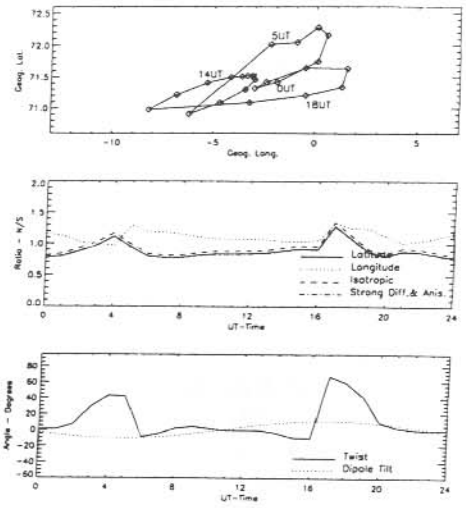

Figure 7. T87/93 conjugacy mapping for Mawson, March equinox, Kp = 3. As per Figure 6.

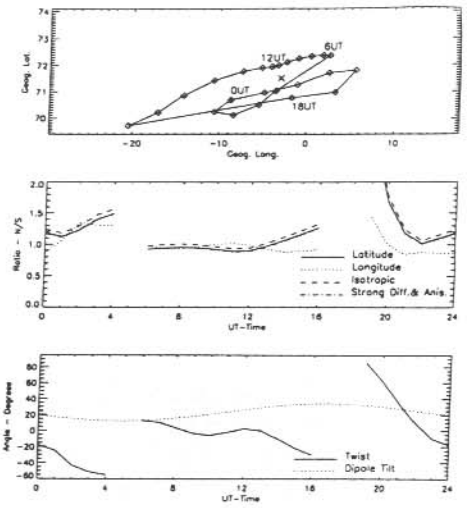

Figure 8. T87/93 conjugacy mapping for Mawson, June solstice, Kp = 3. As per Figure 6.

which the transition from dayside to nightside field lines occurs, or the magnitude of the changes involved. The change, however, appears to more dramatic at higher latitudes (where the field lines pass closer to the dawn-to-dusk dayside magnetopause current and the nightside dusk-to-dawn currents of the outer reaches of the magnetotail) and at times of high dipole tilt (compare the variations around 5 UT [dipole tilt = 12.4°] and 17 UT [dipole tilt = 34.4°] in Figure 8 and Table 3). At times when a small location change dramatically alters the field line trace, the small grid, individual station mapping does not provide much insight.

6.6 DAVIS AND CASEY CONJUGACY PREDICTIONS

At the higher latitude sites of Davis (PGM-88 magnetic latitude 74.6°S, L = 14.2, magnetic noon ~0950 UT) and Casey (PGM-88 magnetic latitude 80.4°S, L = 35.9, ~0615 UT) the T87/93 model predictions are very sensitive to small changes in starting location. Tables 4 and 5 list the predictions for the March equinox and June and December solstices, for a magnetic activity level of Kp = 3, for Davis and Casey respectively. The times when the model predicts an open field line or a field line that extends beyond the model limit of 70 Re in the magnetotail are indicated. The assumptions made with the use of the 25 km spaced grid fail most dramatically when there is a break-down in the calculation of the balance of magnetic flux (A*Br must equal 1; last column in the Tables). Uniformity across the 50 km range of the grid may break-down before this occurs and is apparent initially in the variation in the Flat1(2) and Flon1(2) determinations.

Table 2. T87/93 conjugacy mapping information for Mawson (-67.60°S, 62.87°E, geographic), March equinox, Kp = 3. The last line gives the values calculated using the internal field model only. As per Table 1.

Date: 860321 Mawson (-67.60°S, 62.87°E)

TIME (UT)	TILT (Deg)	GLAT (Deg)	GLDN (Deg)	Flat1 (N/S)	Flat2 (N/S)	Flon1 (N/S)	Flon2 (N/S)	Farea	Twist (Deg)	Fquat (Re)	Xgsm (Re)	Ygsm (Re)	Zgsm (Re)	Bmin (nT)	Dsto (Re)	Dstn (Re)	Diff (Re)	FBms (NIS)	FBrad (NIS)	A*Br (NIS)
0	-3.2	71.42	358.10	0.78	0.77	1.16	1.16	0.90	0.7	49.03	-49.7	-3.6	-0.4	1.5	51.45	51.09	0.36	1.06	1.11	1.00
1	-5.8	71.75	0.10	0.81	0.80	1.13	1.12	0.90	0.9	45.00	-44.5	-6.9	-0.7	1.4	47.28	46.68	0.59	1.06	1.11	1.00
2	-8.0	72.16	0.57	0.88	0.89	1.02	1.02	0.90	7.0	36.14	-34.7	-10.0	-0.6	1.9	39.27	38.67	0.60	1.06	1.11	1.00
3	-9.6	72.28	0.09	0.96	0.98	0.99	0.99	0.90	29.5	27.48	-24.5	-12.4	-0.4	3.7	31.42	30.73	0.69	1.06	1.12	1.00
4	-10.6	72.05	359.07	1.10	1.13	0.97	0.96	0.90	42.8	21.57	-16.4	-14.0	-0.3	5.9	25.96	25.38	0.58	1.06	1.11	1.00
5	-10.9	72.02	357.79	0.97	0.91	1.24	1.33	0.90	42.0	16.44	-8.0	-14.3	0.1	5.1	20.34	20.15	0.19	1.06	1.11	1.00
6	-10.4	70.91	353.77	0.80	0.80	1.18	1.19	0.90	-8.9	10.68	0.8	-10.6	1.2	25.7	14.19	12.82	1.37	1.06	1.11	1.00
7	-9.1	71.09	355.31	0.78	0.78	1.18	1.18	0.90	-5.2	9.58	3.6	-8.7	1.7	43.1	13.37	11.67	1.70	1.06	1.11	1.00
8	-7.3	71.30	356.55	0.79	0.78	1.15	1.15	0.90	1.9	8.92	5.6	-6.6	2.3	57.2	13.31	10.58	2.73	1.06	1.11	1.00
9	-4.9	71.46	357.03	0.83	0.81	1.11	1.10	0.90	4.0	8.43	6.7	-4.2	2.9	67.5	13.78	9.51	4.27	1.06	1.11	1.00
10	-2.2	71.52	356.92	0.84	0.84	1.08	1.08	0.90	1.4	8.14	7.4	-1.9	2.9	73.8	14.00	8.90	5.10	1.06	1.11	1.00
11	0.6	71.52	356.65	0.84	0.84	1.08	1.08	0.90	-0.9	8.06	7.6	0.3	2.5	77.0	14.03	8.76	5.27	1.06	1.11	1.00
12	3.5	71.51	356.37	0.85	0.84	1.08	1.08	0.90	-0.8	8.21	7.3	2.6	-2.7	73.0	9.04	14.03	-4.98	1.06	1.11	1.00
13	6.1	71.50	355.82	0.86	0.85	1.07	1.06	0.90	-0.8	8.58	6.5	4.9	-2.6	64.9	9.73	13.90	-4.17	1.06	1.11	1.00
14	8.3	71.41	354.69	0.89	0.89	1.04	1.04	0.89	-4.5	9.16	5.2	7.2	-2.1	53.4	10.89	13.60	-2.71	1.06	1.11	0.99
15	10.0	71.22	353.17	0.92	0.92	1.03	1.04	0.90	-9.9	9.87	3.2	9.2	-1.6	39.5	11.90	13.85	-1.95	1.06	1.11	0.99
16	11.1	70.98	351.79	0.91	0.91	1.05	1.06	0.90	-9.8	10.98	0.4	10.9	-1.1	23.3	13.03	14.69	-1.66	1.06	1.11	1.00
17	11.3	71.09	356.77	1.26	1.31	1.34	1.32	0.90	67.0	16.94	-9.6	13.9	0.1	5.9	20.18	20.97	-0.79	1.06	1.11	1.00
18	10.9	71.21	359.53	1.06	1.10	1.25	1.25	0.90	58.9	21.79	-17.6	12.8	0.4	5.3	24.96	25.86	-0.90	1.06	1.11	1.00
19	9.6	71.34	1.30	0.85	0.89	1.24	1.24	0.90	41.5	27.55	-25.4	10.6	0.7	3.1	30.10	30.95	0.84	1.06	1.11	1.00
20	7.8	71.64	1.56	0.81	0.81	1.13	1.12	0.90	9.9	37.79	-36.9	8.1	0.9	1.7	39.68	40.41	-0.73	1.06	1.11	1.00
21	5.5	71.65	359.52	0.89	0.88	1.02	1.01	0.90	2.9	47.70	-47.4	5.5	0.8	1.4	49.03	49.77	-0.74	1.06	1.11	0.99
22	2.8	71.42	357.59	0.88	0.86	1.05	1.05	0.90	0.2	50.86	-50.8	2.5	0.4	1.5	51.98	52.45	-0.47	1.06	1.11	1.00
23	0.0	71.32	357.02	0.83	0.82	1.10	1.10	0.90	-1.2	51.28	-51.3	-0.5	0.0	1.6	52.49	52.57	-0.09	1.06	1.11	1.00
0	-3.2	71.51	356.96	0.83	0.82	1.11	1.10	0.90	0.0	8.97	-8.6	-2.6	-0.3	41.5	11.43	11.46	-0.03	1.06	1.11	1.00

Table 3. T87/93 conjugacy mapping information for Mawson, June solstice, Kp = 3. The last line gives the values calculated using the internal field only. The last line gives the values calculated using the internal field model only. As per Table 1.

Date: 860621 — Mawson (-67.60°S, 62.87°E)

TIME (UT)	TILT (Deg)	GLAT (Deg)	GLDN (Deg)	Flat1 (N/S)	Flat2 (N/S)	Flon1 (N/S)	Flon2 (N/S)	Farea (N/S)	Twist (Deg)	Fquat (Re)	Xgsm (Re)	Ygsm (Re)	Zgsm (Re)	Bmin (nT)	Dste (Re)	Detn (Re)	Diff (Re)	FBma (NIS)	FBrad (NIS)	A*Br (NIS)
0	19.5	70.68	351.26	1.17	1.20	0.86	0.87	0.90	-17.8	39.93	-39.6	-4.0	2.8	1.9	40.49	43.06	-2.56	1.06	1.11	1.00
1	17.0	70.24	349.42	1.07	1.18	1.05	1.08	0.90	-24.8	37.92	-37.3	-6.6	2.1	1.8	39.14	41.09	-1.94	1.06	1.11	1.00
2	15.0	70.11	351.58	1.15	1.30	1.34	1.35	0.90	-43.0	30.10	-28.6	-9.2	1.3	2.5	32.11	33.52	-1.41	1.05	1.11	1.00
3	13.5	70.50	354.53	1.36	1.43	1.30	1.31	0.90	-51.2	24.09	-21.1	-11.7	0.7	4.1	26.84	28.09	-1.25	1.05	1.11	1.00
4	12.6	71.04	356.44	1.47	1.52	1.29	1.31	0.90	-54.9	19.90	-14.6	-13.5	0.4	6.0	23.23	24.33	-1.10	1.06	1.11	1.00
5	12.4	72.38	2.69	1.93	0.88	1.33	1.16	0.71	-74.1	12.72	-2.5	-12.5	-0.5	7.4	14.72	16.21	-1.49	1.06	1.12	0.80
6	13.0	72.39	1.84	0.93	0.92	0.98	0.97	0.89	13.0	10.56	1.4	-10.4	-1.5	28.3	12.46	14.65	-2.18	1.06	1.12	1.00
7	14.2	72.35	0.51	0.95	0.94	0.94	0.94	0.89	10.7	9.70	3.5	-8.7	-2.4	41.5	11.36	14.23	-2.86	1.06	1.12	1.00
8	15.9	72.26	359.02	0.96	0.95	0.94	0.94	0.90	4.1	9.11	5.0	-6.8	-3.4	51.3	10.33	14.34	-4.01	1.06	1.12	1.00
9	18.2	72.12	357.67	0.95	0.94	0.97	0.97	0.89	-2.9	8.71	5.9	-4.7	-4.4	56.9	9.54	14.46	-4.92	1.06	1.12	1.00
10	20.9	72.00	356.69	0.93	0.92	1.00	1.01	0.90	-5.5	8.51	6.3	-2.5	-5.2	58.5	9.13	14.49	-5.36	1.06	1.11	1.00
11	23.7	71.94	355.96	0.90	0.89	1.02	1.02	0.90	-1.9	8.50	6.3	-0.2	-5.7	57.3	9.07	14.49	-5.41	1.06	1.11	1.00
12	26.5	71.91	354.85	0.91	0.90	0.99	0.99	0.90	2.9	8.65	5.9	2.1	-5.9	54.3	9.26	14.58	-5.32	1.06	1.11	1.00
13	29.2	71.78	352.66	0.98	0.97	0.93	0.92	0.89	0.3	8.94	5.2	4.5	-5.8	49.9	9.70	14.71	-5.01	1.06	1.11	1.00
14	31.5	71.43	349.40	1.08	1.06	0.88	0.88	0.90	-9.9	9.35	4.0	6.7	-5.2	43.7	10.26	14.87	-4.61	1.06	1.11	1.00
15	33.2	70.86	345.93	1.17	1.16	0.89	0.90	0.90	-21.3	9.85	2.3	8.6	-4.2	35.5	10.86	15.08	-4.22	1.06	1.11	1.00
16	34.2	70.21	342.92	1.26	1.27	0.91	0.92	0.90	-29.8	10.59	0.1	10.1	-3.0	24.4	11.52	15.64	-4.12	1.06	1.11	1.00
17	34.4	69.72	339.56	23.77	1.09	2.13	19.99	14.13	97.7	13.68	-4.2	13.0	-1.0	1.3	14.35	18.25	-3.90	1.06	1.12	15.77
18	33.8	70.77	358.26	3.50	3.74	1.26	1.22	0.90	93.2	21.02	-17.2	11.9	1.5	4.8	23.07	26.33	-3.26	1.05	1.11	0.99
19	32.4	70.98	3.23	2.73	2.96	1.46	1.42	0.90	85.7	23.45	-21.5	9.1	2.7	4.0	24.80	28.00	-3.20	1.06	1.11	1.00
20	30.4	71.82	5.65	1.59	1.76	1.02	0.99	0.90	61.9	28.54	-27.6	6.2	3.7	3.1	29.32	32.71	-3.39	1.06	1.11	1.00
21	27.9	71.72	2.54	1.18	1.20	0.85	0.84	0.90	35.0	31.65	-31.2	3.6	3.9	2.8	31.92	35.39	-3.47	1.06	1.11	1.00
22	25.1	71.26	358.89	1.04	1.00	0.88	0.88	0.90	9.7	33.30	-33.1	1.1	3.6	2.6	33.34	36.64	-3.30	1.06	1.11	1.00
23	22.3	70.96	355.16	1.11	1.09	0.86	0.87	0.90	-9.8	36.46	-36.3	-1.4	3.2	2.3	36.60	39.64	-3.04	1.06	1.11	1.00
0	19.5	71.52	357.02	0.82	0.82	1.11	1.11	0.90	0.0	8.97	-7.8	-3.5	2.9	41.5	11.43	11.40	0.03	1.06	1.11	1.00

Table 4. T87/93 conjugacy mapping information for Davis, Kp = 3, for March equinox and June and December solstices. The last line gives the values calculated using the internal field model only. As per Table 1.

(a) Date: 860321 — Davis (-68.60°S, 77.97°E)

TIME (UT)	TILT (Deg)	GLAT (Deg)	GLDN (Deg)	Flat1 (N/S)	Flat2 (N/S)	Flon1 (N/S)	Flon2 (N/S)	Farea (N/S)	Twist (Deg)	Fquat (Re)	Xgsm (Re)	Ygsm (Re)	Zgsm (Re)	Bmin (nT)	Dste (Re)	Detn (Re)	Diff (Re)	FBma (NIS)	FBrad (NIS)	A*Br (NIS)
0	-3.2			EXITS	MODEL	LIMITS	TRACES	TO	BEYOND	70	Re									
1	-5.8	76.81	4.08	0.85	0.85	1.16	1.15	0.98	11.7	65.21	-63.4	-15.4	-0.2	1.7	70.44	69.26	1.19	0.99	1.02	1.00
2	-8.0	77.50	6.36	0.90	0.90	1.09	1.08	0.97	13.9	43.49	-39.9	-17.3	-0.2	3.8	49.72	48.58	1.14	0.99	1.02	1.00
3	-9.6	77.93	8.23	0.96	0.96	1.03	1.02	0.97	18.3	33.59	-27.8	-18.8	-0.2	6.8	40.49	39.77	0.72	0.99	1.03	1.00
4	-10.6	78.09	9.23	1.00	0.99	1.01	1.01	0.97	24.7	28.45	-20.4	-19.9	0.0	9.4	35.72	35.58	0.15	0.99	1.03	1.00
5	-10.9	78.12	10.30	0.89	0.89	1.13	1.14	0.97	27.6	24.74	-14.4	-20.1	0.2	10.6	32.14	32.67	-0.52	0.99	1.03	1.00
6	-10.4	79.73	23.16	2.85	4.38	3.78	4.83	0.94	-77.9	20.32	-7.0	-19.1	0.7	7.6	27.28	30.00	-2.72	1.00	1.04	0.98
7	-9.1	75.90	1.65	0.98	0.88	1.13	1.16	0.99	38.6	13.21	2.5	-12.8	2.0	23.0	20.15	18.38	1.77	0.98	1.02	1.00
8	-7.3	76.40	3.91	0.78	0.80	1.35	1.34	0.98	29.8	10.44	5.6	-5.8	6.6	37.2	24.01	10.88	13.13	0.98	1.02	1.00
9	-4.9	77.03	3.88	1.49	1.30	1.00	0.96	0.98	51.5	10.02	6.6	-2.6	7.0	29.0	23.45	9.87	13.58	0.99	1.02	1.00
10	-2.2	76.65	359.30	1.23	1.15	0.83	0.84	0.99	7.7	9.82	7.2	-0.4	6.7	26.8	22.63	9.54	13.09	0.98	1.02	1.00
11	0.6	76.27	359.22	0.83	0.86	1.18	1.19	0.98	2.7	9.56	7.2	2.2	5.9	36.6	22.88	9.48	13.41	0.98	1.02	1.00
12	3.5	76.48	0.66	0.92	0.90	1.10	1.10	0.98	22.6	10.18	6.1	5.2	-6.3	38.6	10.39	24.53	-14.14	0.98	1.02	1.00
13	6.1	76.58	359.38	0.96	0.92	1.12	1.13	0.97	40.9	13.18	3.1	12.7	-1.4	25.2	19.12	20.50	-1.38	0.98	1.02	0.99
14	8.3	76.56	18.10	3.14	9.45	1.04	0.62	2.60	-24.7	18.47	-5.7	17.5	-0.5	5.1	25.49	23.89	1.60	0.99	1.02	2.66
15	10.0	76.65	11.46	0.98	0.98	1.04	1.05	0.98	30.8	23.84	-14.0	19.3	-0.1	9.9	30.98	30.64	0.34	0.99	1.02	1.00
16	11.1	76.68	12.51	0.92	0.92	1.15	1.14	0.98	34.8	27.97	-20.5	19.0	0.1	8.5	34.40	34.68	-0.27	0.99	1.02	1.00
17	11.3	76.72	13.11	0.92	0.92	1.11	1.10	0.98	28.7	33.96	-28.9	17.8	0.3	5.8	39.43	40.38	-0.95	0.99	1.02	1.00
18	10.9	76.74	11.60	0.98	0.98	1.02	1.01	0.98	22.3	44.86	-41.8	16.4	0.4	3.2	49.28	50.88	-1.60	0.99	1.02	1.00
19	9.6	76.87	7.92	1.07	1.06	0.94	0.93	0.99	16.1	65.04	-63.3	15.0	0.4	1.7	68.62	70.61	-1.99	0.99	1.02	1.00
20	7.8			EXITS	MODEL	LIMITS	TRACES	TO	BEYOND	70	Re									
21	5.5			EXITS	MODEL	LIMITS	TRACES	TO	BEYOND	70	Re									
22	2.8			EXITS	MODEL	LIMITS	TRACES	TO	BEYOND	70	Re									
23	0.0			EXITS	MODEL	LIMITS	TRACES	TO	BEYOND	70	Re									
0	-3.2	76.33	360.00	0.90	0.90	1.10	1.11	0.98	0.0	14.45	-12.9	-6.5	-0.6	10.0	18.99	18.97	0.02	0.98	1.02	1.00

(b) Date: 860621 Davis (-68.60°S, 77.97°E)

TIME (UT)	TILT (Deg)	GLAT (Deg)	GLDN (Deg)	Flat1 (N/S)	Flat2 (N/S)	Flon1 (N/S)	Flon2 (N/S)	Farea (N/S)	Twist (Deg)	Fquat (Re)	Xgsm (Re)	Ygsm (Re)	Zgsm (Re)	Bmin (nT)	Dste (Re)	Detn (Re)	Diff (Re)	FBma (NIS)	FBrad (NIS)	A*Br (NIS)
0	19.5			EXITS MODEL LIMITS TRACES TO BEYOND 70 Re																
1	17.0	74.71	349.03	1.34	1.31	0.88	0.90	0.98	-19.0	69.98	-68.6	-13.9	0.7	1.5	72.83	76.54	-3.71	0.98	1.01	1.00
2	15.0	74.11	348.73	1.17	1.16	1.07	1.08	0.99	-23.0	48.66	-46.0	-15.9	0.6	2.7	52.61	55.12	-2.51	0.98	1.01	1.00
3	13.5	74.02	349.23	1.04	1.04	1.15	1.17	0.99	-25.5	36.19	-31.7	-17.4	0.4	5.0	41.34	42.78	-1.43	0.98	1.01	1.00
4	12.6	74.18	350.02	1.03	1.04	1.22	1.23	0.99	-30.3	29.57	-22.9	-18.7	0.2	7.7	35.72	36.39	-0.67	0.98	1.01	1.00
5	12.4	74.33	350.60	1.11	1.12	1.20	1.20	0.99	-34.0	25.43	-16.6	-19.3	0.0	9.5	32.33	32.45	-0.11	0.98	1.01	1.00
6	13.0	73.98	349.16	1.28	1.34	0.90	0.88	1.00	-17.2	21.70	-10.8	-18.8	-0.4	9.2	29.19	28.51	0.68	0.98	1.01	1.00
7	14.2	76.33	354.35	7.88	3.80	2.21	2.05	0.99	-97.2	15.67	-0.6	-15.5	-2.3	12.0	21.50	23.24	-1.73	0.98	1.02	1.01
8	15.9	77.72	354.81	1.65	1.31	0.90	0.88	0.96	-58.2	13.32	3.3	-12.3	-3.8	24.7	18.74	22.88	-4.14	0.99	1.03	0.98
9	18.2	77.00	348.70	2.30	2.21	0.52	0.55	0.96	-6.5	11.06	4.8	-4.7	-8.8	24.8	11.08	27.92	-16.84	0.99	1.02	0.98
10	20.9	75.38	347.24	9.19	4.92	1.96	2.31	2.65	-53.6	11.18	5.3	-1.8	-9.6	11.8	10.89	24.15	-13.26	0.98	1.02	2.69
11	23.7	79.31	15.21	8.69	6.47	0.94	0.70	1.98	31.5	11.47	4.7	2.5	-10.2	13.0	11.18	27.56	-16.38	1.00	1.04	2.05
12	26.5	79.50	2.16	5.19	2.40	0.55	0.55	0.93	92.1	14.02	2.8	12.4	-6.0	22.2	20.15	24.16	-4.01	1.00	1.03	0.97
13	29.2	79.60	6.34	11.35	6.01	1.43	1.40	1.16	114.8	15.84	-0.3	15.0	-5.2	14.2	21.35	24.54	-3.20	0.99	1.03	1.19
14	31.5	76.73	39.51	2.54	3.88	0.67	0.63	1.17	32.5	20.93	-10.9	17.9	-0.7	8.2	29.79	27.19	2.60	1.01	1.05	1.23
15	33.2	77.58	35.34	1.78	1.83	1.12	1.10	0.96	74.1	27.22	-19.5	19.0	0.2	7.8	34.37	34.66	-0.29	1.01	1.05	1.00
16	34.2	78.19	35.56	1.42	1.43	0.97	0.94	0.95	55.7	34.33	-29.1	18.3	0.9	5.5	39.87	42.94	-3.07	1.01	1.05	1.00
17	34.4	78.23	29.94	1.54	1.50	0.67	0.66	0.96	32.1	43.74	-40.6	16.2	1.3	3.3	47.59	53.03	-5.45	1.00	1.04	1.00
18	33.8	77.51	21.26	1.54	1.47	0.64	0.65	0.97	18.0	56.00	-54.4	13.2	1.6	1.9	58.42	64.79	-6.37	1.00	1.03	1.00
19	32.4			EXITS MODEL LIMITS TRACES TO BEYOND 70 Re																
20	30.4			EXITS MODEL LIMITS TRACES TO BEYOND 70 Re																
21	27.9			EXITS MODEL LIMITS TRACES TO BEYOND 70 Re																
22	25.1			EXITS MODEL LIMITS TRACES TO BEYOND 70 Re																
23	22.3			EXITS MODEL LIMITS TRACES TO BEYOND 70 Re																
0	19.5	76.33	0.08	0.90	0.89	1.10	1.10	0.98	0.0	14.45	-11.4	-7.8	4.2	10.0	18.99	18.99	0.01	0.98	1.02	1.00

(c) Date: 861221 Davis (-68.60°S, 77.97°E)

TIME (UT)	TILT (Deg)	GLAT (Deg)	GLDN (Deg)	Flat1 (N/S)	Flat2 (N/S)	Flon1 (N/S)	Flon2 (N/S)	Farea (N/S)	Twist (Deg)	Fquat (Re)	Xgsm (Re)	Ygsm (Re)	Zgsm (Re)	Bmin (nT)	Dste (Re)	Detn (Re)	Diff (Re)	FBma (NIS)	FBrad (NIS)	A*Br (NIS)
0	-26.7			EXITS MODEL LIMITS TRACES TO BEYOND 70 Re																
1	-29.4	78.38	17.52	0.68	0.68	1.71	1.71	0.96	45.3	62.14	-60.6	-13.7	-1.3	1.7	70.82	64.64	6.18	1.00	1.03	1.00
2	-31.6	79.72	29.70	0.95	0.97	1.36	1.33	0.95	49.5	41.52	-37.5	-17.7	-1.1	4.2	51.07	46.22	4.85	1.01	1.05	1.00
3	-33.3	80.78	36.59	1.32	1.34	1.15	1.13	0.94	58.3	33.19	-26.4	-20.0	-0.7	7.2	42.32	40.27	2.04	1.02	1.06	1.00
4	-34.3	91.61	46.04	1.68	1.68	1.30	1.30	0.94	82.1	28.52	-19.2	-21.1	0.0	9.5	38.98	36.27	-1.29	1.02	1.07	1.00
5	-34.4	-100.0		DOES NOT MAP TO NH EXITS MODEL AT Xgsm = 8.2, Ygsm = -1.4, Zgsm = 20.2																
6	-33.8	76.54	8.39	9.35	6.88	4.68	3.26	0.87	87.7	15.98	-1.8	-15.1	4.9	10.6	23.36	20.02	3.34	0.99	1.02	0.89
7	-32.3	74.26	358.92	0.74	0.70	1.65	1.67	0.99	50.6	12.11	2.4	-9.7	6.8	23.3	20.75	13.52	7.23	0.98	1.01	1.00
8	-30.3	75.62	7.80	1.46	1.31	1.76	1.72	0.98	75.3	10.97	4.2	4.8	8.9	24.2	21.53	11.25	10.29	0.98	1.02	1.00
9	-27.8	-100.0		DOES NOT MAP TO NH EXITS MODEL AT Xgsm = 12.0, Ygsm = -0.4, Zgsm = 19.0																
10	-25.0	-100.0		DOES NOT MAP TO NH EXITS MODEL AT Xgsm = 12.1, Ygsm = -0.3, Zgsm = 17.8																
11	-22.1	74.81	353.98	2.94	2.26	1.91	1.92	0.99	-60.0	10.75	5.2	2.8	8.9	20.0	22.26	10.68	11.58	0.98	1.01	1.00
12	-19.4	75.12	2.67	0.64	0.66	1.81	1.80	0.99	-15.9	10.85	4.7	6.8	7.0	31.9	21.66	11.53	10.13	0.98	1.01	1.00
13	-16.9	75.62	7.06	0.94	0.83	1.30	1.25	0.99	-22.1	12.86	2.5	12.1	3.6	23.4	20.37	16.17	4.20	0.98	1.02	1.00
14	-14.9	69.71	313.70	10.37	39.42	23.13	10.76	4.57	88.8	19.59	-4.5	19.0	1.7	7.1	26.37	32.65	-6.28	1.01	1.04	4.77
15	-13.4	74.92	345.02	1.01	0.99	1.30	1.28	0.99	-34.6	24.09	-13.4	20.0	0.3	10.5	31.52	32.13	-0.62	0.98	1.02	1.00
16	-12.6	75.15	346.15	1.16	1.17	1.06	1.06	0.98	-32.2	27.54	-18.9	20.0	0.0	9.8	34.91	34.76	0.15	0.98	1.02	1.00
17	-12.4	75.15	345.85	1.10	1.10	1.07	1.08	0.98	-27.5	31.68	-25.1	19.3	-0.2	7.7	39.89	38.08	0.81	0.98	1.02	1.00
18	-13.0	75.10	345.57	1.02	1.03	1.14	1.16	0.98	-25.2	38.41	-33..9	18.0	-0.4	5.1	45.39	43.84	1.55	0.98	1.02	1.00
19	-14.2	74.97	346.71	0.95	0.95	1.32	1.35	0.99	-26.4	51.50	-48.8	16.4	-0.5	2.7	58.20	55.58	2.62	0.98	1.02	1.00
20	-16.1			EXITS MODEL LIMITS TRACES TO BEYOND 70 Re																
21	-18.4			EXITS MODEL LIMITS TRACES TO BEYOND 70 Re																
22	-21.0			EXITS MODEL LIMITS TRACES TO BEYOND 70 Re																
23	-23.9			EXITS MODEL LIMITS TRACES TO BEYOND 70 Re																
0	-26.7	76.34	0.24	0.90	0.90	1.11	1.11	0.98	0.0	14.44	-11.8	-6.0	-5.8	10.0	18.96	18.98	-0.02	0.98	1.02	1.00

Table 5. T87/93 conjugacy mapping information for Casey (-66.30°S, 110.53°E, geographic), Kp = 3, for March equinox and June and December solstices. The last line gives the values calculated using the internal field model only.

(a) Date: 860321 — Casey (-66.30°S, 110.53°E)

TIME (UT)	TILT (Deg)	GLAT (Deg)	GLDN (Deg)	Flat1 (N/S)	Flat2 (N/S)	Flon1 (N/S)	Flon2 (N/S)	Farea (N/S)	Twist (Deg)	Fquat (Re)	Xgsm (Re)	Ygsm (Re)	Zgsm (Re)	Bmin (nT)	Dste (Re)	Detn (Re)	Diff (Re)	FBma (NIS)	FBrad (NIS)	A*Br (NIS)
0	-3.2	88.21	53.68	1.08	1.09	1.02	1.02	1.11	13.3	39.29	-31.4	-23.7	-0.1	10.4	51.39	50.94	0.45	0.89	0.90	1.00
1	-5.8	88.64	93.61	1.03	1.04	1.08	1.09	1.11	56.6	36.29	-26-5	-24.8	-0.1	13.2	49.25	49.19	0.07	0.90	0.91	1.00
2	-8.0	87.71	131.16	0.93	0.96	1.21	1.22	1.11	102.7	34.87	-23.4	-25.8	-0.1	15.4	48.81	49.61	-0.79	0.90	0.91	1.01
3	-9.6	85.47	139.08	0.78	0.87	1.70	1.78	1.10	136.0	34.49	-21.8	-26.7	0.0	17.2	49.66	52.15	-2.49	0.91	0.92	1.01
4	-10.6	-100.0	DOES NOT MAP TO NII EXITS MODEL AT Xgsm = 12.2, Ygsm = -1.4, Zgsm = 16.5																	
5	-10.9	-100.0	DOES NOT MAP TO NII EXITS MODEL AT Xgsm = 12.0, Ygsm = -1.4, Zgsm = 18.0																	
6	-10.4	86.73	2.42	8.03	9.22	15.52	16.48	5.35	-55.0	51.42	-43.8	-26.9	-0.6	9.6	81.81	73.24	8.57	0.89	0.89	4.77
7	-9.1	67.71	51.32	6.23	7.39	15.13	16.33	8.40	25.4	50.00	-42.0	27.1	-0.5	10.4	79.48	73.15	6.33	0.89	0.90	7.57
8	-7.3	-100.0	DOES NOT MAP TO NII EXITS MODEL AT Xgsm = 12.2, Ygsm = -1.3, Zgsm = 15.9																	
9	-4.9	83.90	27.17	0.76	0.71	1.60	1.55	1.13	-3.9	35.54	-22.7	27.4	0.0	18.0	52.61	54.32	-1.71	0.88	0.89	1.01
10	-2.2	86.38	28.20	1.04	1.04	1.09	1.10	1.12	-14.0	34.80	-22.8	26.3	0.0	16.5	49.63	49.98	-0.35	0.89	0.89	1.00
11	0.6	87.54	42.11	1.15	1.15	0.97	0.96	1.11	1.3	35.32	-24.7	25.2	0.0	14.4	48.56	48.53	0.04	0.89	0.90	1.00
12	3.5	87.90	64.22	1.22	1.21	0.91	0.91	1.11	23.2	37.29	-28.4	24.1	0.1	11.8	49.22	49.45	-0.23	0.89	0.90	1.00
13	6.1	87.93	79.63	1.27	1.27	0.88	0.69	1.11	36.3	41.42	-34.4	23.0	0.2	8.9	52.14	53.24	-1.10	0.90	0.90	1.00
14	8.3	88.21	83.66	1.39	1.37	0.83	0.83	1.11	35.4	48.91	-43.6	22.2	0.4	6.1	58.45	61.24	-2.79	0.90	0.90	1.00
15	10.0	89.28	40.76	1.74	1.69	0.93	0.93	1.11	-13.5	61.83	-57.9	21.6	0.4	3.7	70.38	75.76	-5.38	0.89	0.90	1.01
16	11.1	EXITS MODEL LIMITS TRACES TO BEYOND 70 Re																		
17	11.3	EXITS MODEL LIMITS TRACES TO BEYOND 70 Re																		
15	10.9	EXITS MODEL LIMITS TRACES TO BEYOND 70 Re																		
19	9.6	EXITS MODEL LIMITS TRACES TO BEYOND 70 Re																		
20	7.8	EXITS MODEL LIMITS TRACES TO BEYOND 70 Re																		
21	5.5	EXITS MODEL LIMITS TRACES TO BEYOND 70 Re																		
22	2.8	87.05	29.39	1.22	1.21	0.99	0.98	1.11	-8.5	55.77	-51.3	-21.8	0.1	4.6	65.83	67.07	-1.24	0.89	0.90	1.00
23	0.0	87.39	38.51	1.13	1.13	1.00	1.00	1.12	-2.0	45.10	-39.0	-22.6	0.0	7.4	56.19	56.15	0.04	0.89	0.90	1.01
0	-3.2	87.32	40.66	1.14	1.14	0.96	0.98	1.12	0.0	39.73	-5.5	-39.3	-0.4	0.5	53.80	53.73	0.07	0.89	0.90	1.00

(b) Date: 860621 — Casey (-66.30°S, 110.53°E)

TIME (UT)	TILT (Deg)	GLAT (Deg)	GLDN (Deg)	Flat1 (N/S)	Flat2 (N/S)	Flon1 (N/S)	Flon2 (N/S)	Farea (N/S)	Twist (Deg)	Fquat (Re)	Xgsm (Re)	Ygsm (Re)	Zgsm (Re)	Bmin (nT)	Dste (Re)	Detn (Re)	Diff (Re)	FBma (NIS)	FBrad (NIS)	A*Br (NIS)
0	19.5	83.73	358.00	1.74	1.70	0.95	0.98	1.14	-22.3	45.80	-39.8	-22.6	0.8	7.0	54.93	60.80	-5.87	0.88	0.88	1.01
1	17.0	83.26	0.05	1.61	1.59	0.86	0.88	1.14	-28.3	40.32	-32.8	-23.5	0.6	9.5	51.04	53.88	-2.84	0.87	0.88	1.01
2	15.0	83.19	356.65	1.63	1.62	0.78	0.78	1.15	-35.0	37.65	-28.7	-24.4	0.4	11.7	50.01	51.05	-1.04	0.87	0.88	1.01
3	13.5	83.18	348.64	1.66	1.67	0.68	0.68	1.14	-39.4	37.02	-27.0	-25.3	0.3	13.4	51.20	51.30	-0.10	0.87	0.88	1.00
4	12.6	83.15	335.80	1.60	1.63	O.85	0.88	1.14	-33.7	38.44	-28.1	-26.2	0.4	14.1	54.97	54.90	0.06	0.88	0.88	1.00
5	12.4	84.44	319.54	2.05	1.84	2.33	2.77	1.15	26.8	43.69	34.5	-26.8	0.6	12.6	63.50	65.76	-2.26	0.89	0.89	1.02
6	13.0	-100.0	DOES NOT MAP TO NII EXITS MODEL AT Xgsm = -60.3, Ygsm = -12.0, Zgsm = 30.1																	
7	14.2	-100.0	DOES NOT MAP TO NII EXITS MODEL AT Xgsm = 12.1, Ygsm = 0.6, Zgsm = 16.8																	
8	15.9	86.49	261.17	2.63	2.31	4.44	3.50	1.19	99.3	45.17	-36.4	26.8	0.8	11.7	64.54	68.96	-4.42	0.90	0.90	1.07
9	18.2	85.29	222.33	1.81	1.82	1.36	1.29	1.10	129.9	40.09	-30.5	26.0	0.7	12.6	56.03	57.49	-1.45	0.90	0.91	1.01
10	20.9	85.46	201.43	1.94	1.94	0.78	0.78	1.10	127.9	39.25	-30.2	25.0	0.7	11.5	52.67	54.67	-2.00	0.90	0.91	1.00
11	23.7	85.85	190.69	2.03	1.99	0.57	0.57	1.10	117.9	41.12	-33.3	24.1	0.9	9.5	52.42	56.75	-4.33	0.90	0.91	1.00
12	26.5	86.85	195.10	2.32	2.22	0.51	0.50	1.10	114.5	45.98	-39.7	23.2	1.2	7.1	55.41	63.97	-8.57	0.90	0.91	1.00
13	29.2	87.47	260.51	3.43	3.18	0.85	0.83	1.12	171.8	54.93	-50.2	22.4	1.4	4.7	62.50	78.81	-16.31	0.89	0.90	1.01
14	31.5	-100.0	DOES NOT MAP TO NII EXITS MODEL AT Xgsm = -48.1, Ygsm = 8.3, Zgsm = 30.0																	
15	33.2	-100.0	DOES NOT MAP TO NII EXITS MODEL AT Xgsm = -53.3, Ygsm = 8.1, Zgsm = 30.1																	
16	34.2	EXITS MODEL LIMITS TRACES TO BEYOND 70 Re																		
17	34.4	EXITS MODEL LIMITS TRACES TO BEYOND 70 Re																		
15	33.8	EXITS MODEL LIMITS TRACES TO BEYOND 70 Re																		
19	32.4	EXITS MODEL LIMITS TRACES TO BEYOND 70 Re																		
20	30.4	EXITS MODEL LIMITS TRACES TO BEYOND 70 Re																		
21	27.9	EXITS MODEL LIMITS TRACES TO BEYOND 70 Re																		
22	25.1	EXITS MODEL LIMITS TRACES TO BEYOND 70 Re																		
23	22.3	85.07	340.21	2.36	2.26	1.45	1.44	1.13	-29.0	55.69	-51.2	-21.9	1.0	4.6	63.22	74.49	-11.27	0.88	0.89	1.01
0	19.5	87.31	40.94	1.14	1.15	0.98	0.99	1.12	0.0	39.70	-1.4	-39.7	0.4	0.5	53.77	53.69	0.09	0.89	0.90	1.00

(c) Date: 861221 Casey (-66.30°S, 110.53°E)

TIME (UT)	TILT (Deg)	GLAT (Deg)	GLDN (Deg)	Flat1 (N/S)	Flat2 (N/S)	Flon1 (N/S)	Flon2 (N/S)	Farea	Twist (Deg)	Fquat (Re)	Xgsm (Re)	Ygsm (Re)	Zgsm (Re)	Bmin (nT)	Dste (Re)	Dein (Re)	Diff (Re)	FHma (NIS)	FBrad (NIS)	A*Br (NIS)
0	-26.7	83.77	194.55	0.58	0.65	2.23	2.27	1.10	143.3	38.86	-29.8	-24.9	-0.9	11.1	54.46	52.29	2.27	0.91	0.91	1.00
1	-29.4	-100.0	DOES NOT MAP TO NH EXITS MODEL AT Xgsm = 10.3, Ygsm = -0.6, Zgsm = 20.1																	
2	-31.6	-100.0	DOES NOT MAP TO NH EXITS MODEL AT Xgsm = 3.1, Ygsm = -2.8, Zgsm = 20.1																	
3	-33.3	-100.0	DOES NOT MAP TO NH EXITS MODEL AT Xgsm = 0.9, Ygsm = -4.6, Zgsm = 20.0																	
4	-34.3	-100.0	DOES NOT MAP TO NH EXITS MODEL AT Xgsm = 1.5, Ygsm = -5.6, Zgsm = 20.1																	
5	-34.4	-100.0	DOES NOT MAP TO NH EXITS MODEL AT Xgsm = 7.1, Ygsm = -3.9, Zgsm = 20.0																	
6	-33.8	-100.0	DOES NOT MAP TO NH EXITS MODEL AT Xgsm = 12.1, Ygsm = -1.0, Zgsm = 19.3																	
7	-32.3	-100.0	DOES NOT MAP TO NH EXITS MODEL AT Xgsm = 7.8, Ygsm = 3.8, Zgsm = 20.1																	
8	-30.3	-100.0	DOES NOT MAP TO NH EXITS MODEL AT Xgsm = 3.8, Ygsm = 4.2, Zgsm = 20.2																	
9	-27.8	-100.0	DOES NOT MAP TO NH EXITS MODEL AT Xgsm = 4.6, Ygsm = 3.1, Zgsm = 20.2																	
10	-25.0	-100.0	DOES NOT MAP TO NH EXITS MODEL AT Xgsm = 8.0, Ygsm = 1.8, Zgsm = 20.0																	
11	-22.1	-100.0	DOES NOT MAP TO NH EXITS MODEL AT Xgsm = 12.2, Ygsm = 0.5, Zgsm = 18.4																	
12	-19.4	80.69	346.25	0.82	0.89	1.94	1.93	1.15	-65.8	36.77	-26.5	25.5	-0.4	13.3	51.07	51.27	-0.19	0.87	0.87	1.00
13	-16.9	83.06	349.90	0.84	0.88	1.63	1.64	1.14	-48.4	39.37	-31.0	24.3	-0.5	10.7	53.49	51.31	2.18	0.87	0.88	1.00
14	-14.9	84.47	359.12	0.82	0.86	1.55	1.57	1.13	-32.1	44.07	-37.6	23.0	-0.6	7.9	58.01	54.06	3.95	0.88	0.88	1.00
15	-13.4	85.13	15.21	0.74	0.77	1.67	1.71	1.13	-10.2	52.82	-48.2	21.7	-0.5	5.0	66.49	61.01	5.48	0.88	0.89	1.00
16	-12.6	EXITS MODEL LIMITS TRACES TO BEYOND 70 Re																		
17	-12.4	EXITS MODEL LIMITS TRACES TO BEYOND 70 Re																		
18	-13.0	EXITS MODEL LIMITS TRACES TO BEYOND 70 Re																		
19	-14.2	EXITS MODEL LIMITS TRACES TO BEYOND 70 Re																		
20	-16.1	EXITS MODEL LIMITS TRACES TO BEYOND 70 Re																		
21	-18.4	86.13	102.33	0.58	0.60	2.21	2.18	1.10	44.5	67.58	64.6	-19.6	-0.6	2.5	81.55	72.80	8.76	0.90	0.91	1.00
22	-21.0	87.43	144.31	0.67	0.70	1.93	1.89	1.10	85.6	50.34	-45.4	-21.8	-0.9	5.4	65.92	58.05	7.88	0.90	0.91	1.00
23	-23.9	86.37	193.26	0.69	0.73	1.89	1.89	1.10	128.0	42.81	-35.8	-23.5	-1.0	8.3	58.64	53.03	5.61	0.90	0.91	1.00
0	-26.7	87.29	41.51	1.14	1.14	0.98	0.99	1.11	0.0	39.65	-6.3	-39.0	-3.2	0.5	53.68	53.63	0.05	0.89	0.90	1.00

For Davis station, and its conjugate point, the inter-hemispheric photometer measured intensity ratios calculated using the internal field only are 1.04 for strong diffusion and isotropic flux and 1.06 for strong diffusion and anisotropy.

Similar values for Casey are 1.03 and 1.00 respectively.

6.7 DISCUSSION

Our analysis of the conjugacy predictions of a Tsyganenko model is prompted by difficulties found experimentally determining interhemispheric optical conjugacy, particularly for a limited number of dayside oval VIKING and ground-based South Pole observations at times of high dipole tilt (Burns et al. 1990, 1992). Some aspects of interhemispheric asymmetry, most notably the implied extent of the auroral region (Burns et al. 1992) may be related to the large dipole tilt and is modelled by the Tsyganenko formulation.

We have undoubtedly extended the Tsyganenko models beyond the scope of their present development, but they remain the most appropriate and most used external model formulations for determining average behaviour as dipole tilt varies. The variation in the conjugacy predictions for Macquarie Island for the three Tsyganenko formulations examined (see Figure 3) indicates the uncertainty that should be associated with the magnitude of the predicted conjugacy displacements. Interhemispheric stretching/contraction and alignment twisting of auroral forms is a likely occurrence. Interhemispheric stretching/contraction of auroral forms is in fact inherent in internal field

formulations. While the magnitude of the variations and the exact timing of the changes are unlikely to be well determined, the model predictions that the most dramatic variability will be at times of high dipole tilt, at high latitudes, and when the field line traces are traversing the dayside/nightside boundary, are not unreasonable.

REFERENCES

Baker, K.B. *and* Wing, S. (1989). A new magnetic coordinate system for conjugate studies at high latitudes. *Journal of Geophysical Research 94:*9139 – 9143.

Burns, G.B., McEwen, D.J., Berkey, F.T., Murphree, J.S., Hearn, D. *and* Eather, R.A. (1992). Dynamics of the conjugate post-noon regions during an auroral enhancement. *Journal of Geomagnetism and Geoelectricity 44:*66 – 90.

Burns, G.B., McEwen, D.J., Eather, R.A., Berkey, F.T. *and* Murphree, J.S. (1990). Optical auroral conjugacy: Viking UV imager – South Pole station ground data. *Journal of Geophysical Research 95:*5781 – 5790.

Burns, G.B., McEwen, D.J., Steele, D. *and* Hearn, D. (1991). Optical auroral conjugacy: history and potential. In: Burns G. (Ed). *ANARE Research Notes Number 80.* Pp. 283 – 300.

Elphinstone, R.D., Hearn, D., Murphree, J.S. *and* Cogger, L.L. (1991). Mapping using the Tsyganenko long magnetospheric model and its relationship to the Viking auroral images. *Journal of Geophysical Research 96:*1467 – 1480.

Gustafsson G. (1984). Corrected geomagnetic coordinates for epoch 1980. *Magnetospheric Currents.* Geophys. Monograph. Ser., Vol 28, Thomas Potemra, AGU, Washington, D.C. Pp. 276.

Gustafsson, G., Papitashvili, N.E. *and* Papitashvili, V.O. (1992). A revised geomagnetic coordinate system for epochs 1985 and 1990. *Journal of Atmospheric and Terrestrial Physics 54:*1609 – 1631.

Ono, T. (1987). Temporal variation of the geomagnetic conjugacy of the Syowa-Iceland pair. *Memoirs of National Institute of Polar Research, Japan 48:*46 – 57.

Peredo, M., Stern, D.P. *and* Tsyganenko, N.A. (1993). Are existing magnetospheric models excessively stretched? *Journal of Geophysical Research 98:*15343 – 15354.

Stassinopoulos, E.G., Lanzerotti, L.J. *and* Rosenberg, T.J. (1984). Temporal variations in the Siple station conjugate area. *Journal of Geophysical Research 89:* 5655 – 5659.

Stenbaek-Nielsen, H.C., Wescott, E.M., Davis, T.N. *and* Peterson R.W. (1973). Difference in auroral intensity at conjugate points. *Journal of Geophysical Research 78:*659 – 671.

Tsyganenko, N.A. (1987). Global quantitative models of the geomagnetic field in the cislunar magnetosphere for different disturbance levels. *Planetary and Space Science 35:*1347 – 1358.

Tsyganenko, N.A. (1989). A magnetospheric magnetic field model with a warped tail current sheet. *Planetary and Space Science 37:*5 – 20.

7. POLARISATION CHARACTERISTICS OF LONG PERIOD GEOMAGNETIC PULSATIONS RECORDED AT ANTARCTIC STATIONS

S.T. Ables[1], B.J. Fraser[1], H.J. Hansen[1], F.W. Menk[1] and R.J. Morris[2]

[1] Physics Department
University of Newcastle
NSW 2304
Australia

[2] Atmospheric and Space Physics
Antarctic Division
Kingston Tasmania 7050
Australia

ABSTRACT

Induction magnetometer data acquired from four Antarctic stations (Mawson, Davis, Casey and Scott Base) during the period January – February 1993, have been analysed using pure state filtering techniques. Spectral characteristics of ULF power in the Pc5 band, such as broadband pre- and post-noon bursts, ellipticity reversals and resonances have been clearly identified. Concurrent events between Davis and Mawson in the 1 – 10 mHz band show evidence of azimuthal propagation with ground velocities of ~11 km s^{-1} predominantly westward in the pre-magnetic-noon sector and eastward in the post-noon sector. Days of low geomagnetic activity (Kp < 3) strongly exhibit these Kelvin-Helmholtz like characteristics. Systematic studies of cusp and near-cusp magnetometer data can provide insight into the dynamic topology of the outer magnetosphere, magnetopause and associated boundary layers.

7.1 INTRODUCTION

Quasi-periodic magnetic fluctuations of long period (100 – 1000 s), generally classified as Pc5 geomagnetic pulsations, have been extensively studied over the years, using both ground-based and satellite-borne magnetometers (see for example review by Samson 1991). Since relatively simple instrumentation is required for recording these signals, and the associated magnetohydrodynamic (MHD) modes are standing waves with spatial scales as large as the magnetosphere (wavelengths comparable to high latitude field line lengths), these pulsations provide useful diagnostics on the dynamic topology of the magnetosphere. The close association between the spectral characteristics of Pc5 pulsations and the structure of the magnetosphere was first effectively shown by Rostoker et al. (1972) in a ground based statistical study of Pc5 activity over a range of northern magnetic latitudes and local times. A roughly inverse linear relationship was found between pulsation frequency and latitude, and poleward of mlat ~75° the activity in the 1–10 MHz band was found to be more broadband around local magnetic noon. In a more extensive study of time series data, Troitskaya (1985) identified these as a high-latitude sub-class of pulsations, termed IPCL (Intervals of Pulsations Continuous Long), and their use as a cusp signature was argued.

sampled at a rate of 0.25 s^{-1} with the exception of a 10 day campaign period from 11 to 21 February, during which the data were sampled at a rate of 2 s^{-1}. To reduce the computing resources required for the analysis of the long period pulsations, all the data were resampled to 0.05 s^{-1} (20 s) after being low-pass filtered at the Nyquist frequency of 25 mHz.

7.4.2 *Pure state filtering*

Frequency domain representation of magnetometer data is often useful in distinguishing different pulsation types through the identification of distinct spectral characteristics. For example, Menk et al. (1992) performed FFTs on Antarctic data to generated grey-scale dynamic power spectra, and determined up to six different types of Pc1-2 pulsations (0.1 – 2.5 Hz). Dynamic spectra for the 1 – 10 mHz band can also show structure such as band limited pulsations and temporal bursts, although the trade-off between time and frequency resolution restricts the usefulness of such techniques. Cross-phase measurements between the X and Y channels of a single station or between common channels of different stations provide information about the polarisation state and phase lag respectively, of discrete pulsations. An extremely useful technique has been developed for detecting polarised waves (pure states) in geophysical data (Samson 1983, and references therein). The essence of pure state analysis is the decomposition of the spectral matrix of multi-channel data into eigenvectors and eigenvalues. The dominant polarisation properties of the data can then be characterised by eigenvectors with significantly large eigenvalues. This process removes noise which appears as unpolarised power. A particular application of this technique is demonstrated in Figure 2. The top panel shows the dynamic power spectrum of the X component at Davis on 24 February 1993, obtained by performing 256 point FFTs every 10 minutes. The next two panels show the polarised power and the degree of polarisation of pure states detected in the X and Y component data. Through masking the data by setting threshold levels on the degree of polarisation and power, significant events can be identified. For instance the bottom panel shows the phase between the X and Y components of events with at least 70% polarisation and polarised power greater than 0.8 of the maximum detected. Further analysis of the azimuth angle and ellipticity of the polarisation ellipse is possible. In this report, the sense of ellipticity (right-hand / left-hand) is inferred from the phase measurements (positive/negative). Pure state analysis of multi-station data has also been used to identify concurrent signals and associated phase lags.

7.5 OBSERVATIONS

The following observations were present to varying degrees in data recorded on magnetically quiet days (Kp < 3) in the 60 day period January – February 1993. Figure 3 shows the X component power recorded at Davis station over a representative 8 day period. Both 15 and 19 February meet our criterion for magnetically quiet days, and distinct similarities can be seen in their spectra. Days of higher Kp typically have more broadband activity above 10 mHz during the daytime (0400 – 1400 UT) and exhibit substorm activity in the night sector (e.g. 2130 – 2400 UT on 13 February 1993). The more temporal nature of signals on these days tend to mask the spatial structure associated with pulsations analysed in this study.

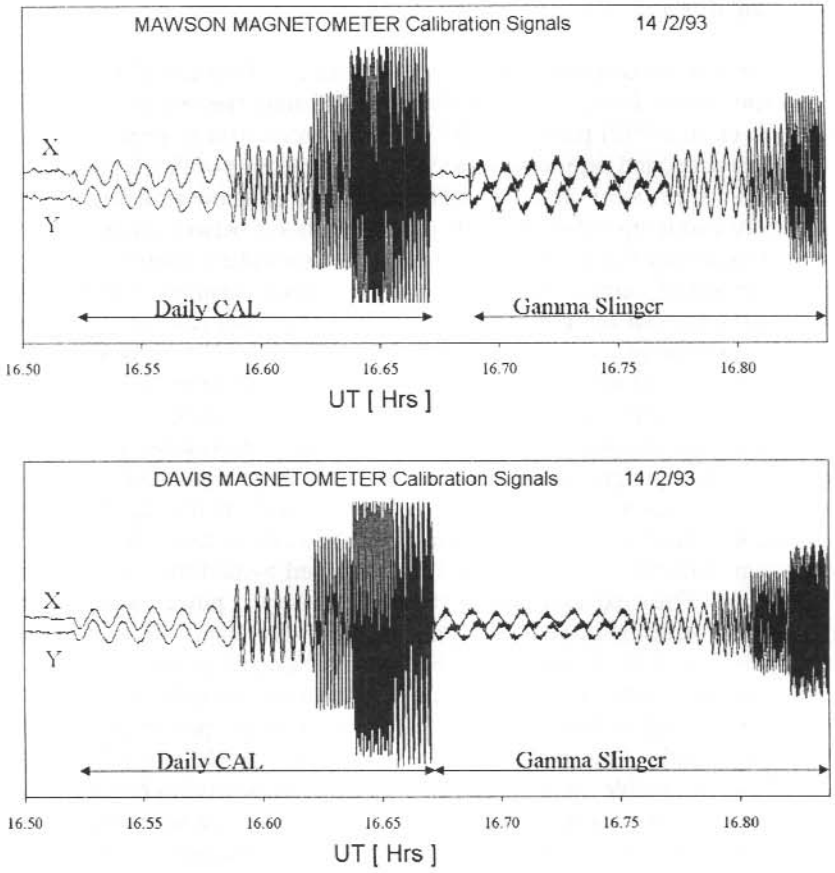

Figure 1. Daily calibration and gamma-slinger signals showing the frequency response and polarity with respect to ellipticity measurements of the magnetometers at Mawson and Davis stations during the present study.

7.4 POLARISATION ANALYSIS

7.4.1 *Data reduction*

During a sixty day period over January – February 1993 around 5 Mbytes of induction magnetometer data were collected from each station in the Antarctic array. The data were

At any instant, the location of the dayside magnetospheric regions which are magnetically linked to high latitude sites via field lines, depend on geomagnetic activity and the orientation of the Interplanetary Magnetic Field (IMF). For example, Newell et al. (1989) found that when IMF B_z is negative (southward) a negative IMF B_z can move the ionospheric projection of the cusp downwards. The present study concentrates on days of low geomagnetic activity (Kp < 3), predominantly northward IMF, and the IMF B_y effect is not considered. It is under these conditions that the regions listed in Table 1 are magnetically linked to the listed stations around local magnetic noon.

7.3 INSTRUMENTATION

7.3.1 *Data logging*

The solenoidal detection coils of the induction magnetometer systems are sited in interference free areas at each station. Two coils are oriented orthogonally in the horizontal plane in geomagnetic North-South (X) and East-West (Y) directions. The outputs from the coils are filtered and preampfified to give the time derivatives of the X and Y components of the local magnetic field. These signals are connected through ~100 m of shielded cabling to analogue-to-digital converters and sampling cards located in laboratory PC-XT/AT computers at each station (Fraser et al. 1991). The sensitivity of this system is 0.2 nT V^{-1} at 10 mHz, and sampling rates ranging from 0.25 to 16 s^{-1} can be selected. Suitable low pass anti-aliasing filters are applied to the data and varied according to the Nyquist frequency of the sampling rate.

7.3.2 *Calibration*

Meaningful interpretation of magnetometer data is only possible when thorough calibration techniques are employed. Additional concentric coils, magnetically coupled to the magnetometer sensing coils, allow known calibration signals to be injected simultaneously into both channels providing the following system parameters -

a. Amplitude response (gain and linearity),
b. Frequency response,
c. Absolute Phase (time lag) in both channels,
d. Relative phase between channels.

Small changes over time are expected in these parameters due to varying climatic conditions and the ageing of electronic components. An automatic daily calibration signal is generated at each station during the evening when local geomagnetic activity is generally at a minimum. In addition, a bar magnet which rotates in the horizontal plane (gamma-slinger) is activated every five days allowing the polarity of the complete system to be checked. Figure 1 shows the calibration signals recorded at Davis and Mawson on 14 February 1993. It is important to note that both stations show the same X-Y phase lag (+90°) in the gamma-slinger signals indicating the same polarity with respect to ellipticity measurements.

The local time occurrence of IPCL was related to where the ground based pulsation measurements were made with respect to the ionospheric footprint of the magnetospheric cusp, with peak IPCL activity occurring at local magnetic noon when the cusp was directly overhead. A later study by Dunlop et al. (1992) confirmed a cusp or boundary layer association using pulsation data, and energetic particle fluxes from DMSP satellite data (Newell and Meng 1988). The global nature of long period pulsations has been demonstrated in conjugate studies involving data from both northern and southern high latitude stations which show concurrent broadband Pc3-5 activity around local magnetic noon (e.g. Olson and Fraser 1994).

To further understand the physical significance of the latitudinal and local time dependence of Pc5 pulsations, a more complete analysis of the spectral characteristics is necessary. For instance, Samson (1972) analysed the three-dimensional polarisation ellipses obtained from a chain of magnetometers in Alberta, Canada, and found that in the H-D plane (horizontal components) the ellipticity of Pc5 undergoes a reversal around local magnetic noon. The current study uses similar sophisticated pure-state polarisation analysis to extend previous work which examined Pc5 activity at Mawson, Davis and Casey stations (Dunlop et al. 1992).

7.2 THE ANTARCTIC ARRAY

Unlike northern magnetometer chains such as those located in Canada (Samson 1972) and Scandinavia (Glassmeier 1988), the four Antarctic stations used in this study are located as a consequence of historical exploration rather than scientific objectives. Nonetheless a useful range of magnetic latitudes and a wide range of magnetic longitudes are covered, as can be seen in Table 1.

Mawson, Davis and Casey are Australian stations, supported through the Australian Antarctic Division, while Scott Base is a New Zealand station supported through the New Zealand Antarctic Program.

Table 1. Statistics of the Antarctic magnetometer sites used in this study.

Station Name	Geomagnetic Latitude *	Geomagnetic Longitude *	Local Magnetic Noon +	Magnetospheric Region
Mawson	-70.50°	92.10°	1019 UT	Auroral oval
Davis	-74.60°	102.30°	0920 UT	Cusp/cleft
Scott Base	-80.00°	329.20°	1847 UT	Polar Cap
Casey	-80.40°	156.10°	0526 UT	Polar Cap

* PGM 1988 coordinates (Burns and Beggs 1992)

\+ Annual average for 1977.25 epoch eccentric dipole model

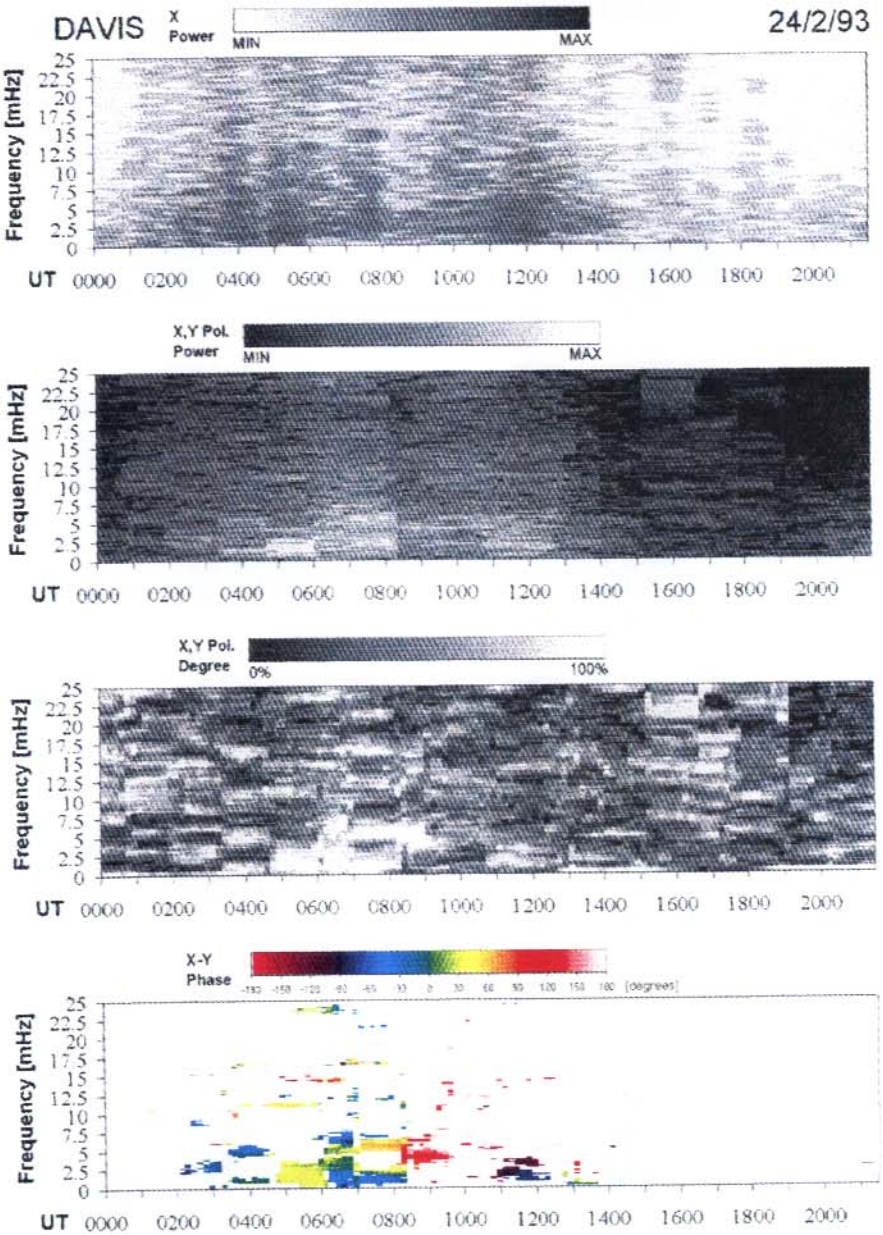

Figure 2. An example of pure state filtering of the Davis magnetometer data for 24 February 1993.

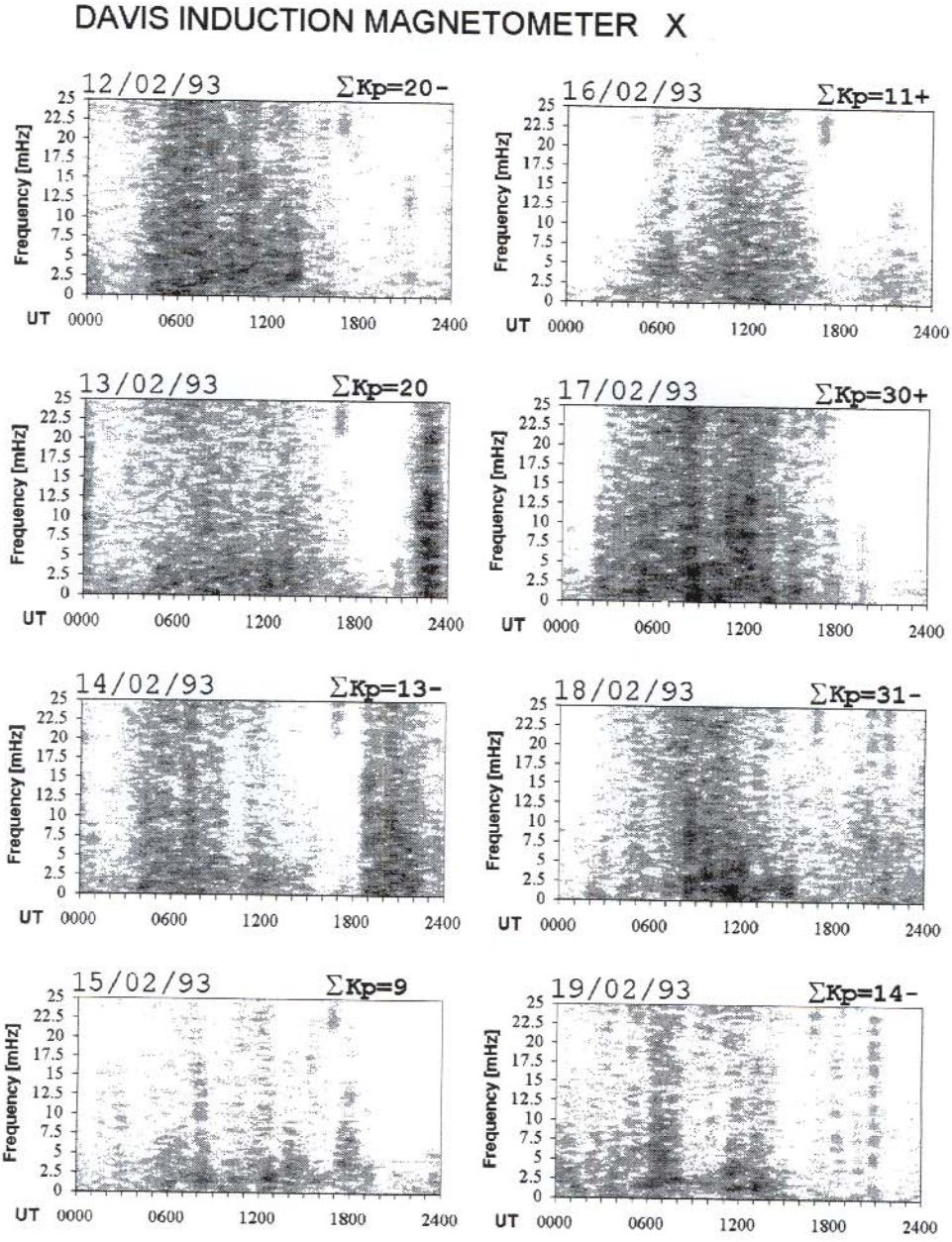

Figure 3. X-component (magnetic N-S) dynamic power spectra for Davis induction magnetometer data over a representative 8-day period. February 15 and 19 are typical quiet days. (note the calibration signals around 1630 UT at 22.5 mHz).

7.5.1 *Ellipticity*

It has been reported that the polarisation ellipticity of Pc5 pulsations reverses around local magnetic noon at northern high latitude stations (e.g. Samson 1972) This is also observed at Antarctic stations. In Figure 4 the phase between the X (N – S) and Y (E – W) components of the pure states on 15 February 1993 is shown as a function of time and frequency for the four stations in the Antarctic array. From careful examination of these dynamic phase plots, and those for the other days (not shown here), the following properties are deduced:

1. Significant polarised power (> 70% polarisation) occurs in the band from 1 to 5 mHz at all stations.
2. Distinct bursts of polarised power occur 2 to 4 hours before and after local magnetic noon.
3. The ellipticity of these bursts is right-hand before noon and left-hand after noon at all stations except Mawson.
4. The pre- and post-noon bursts start earlier and finish later at the more equatorward stations.

The reversal of the diurnal variation in ellipticity seen at Mawson compared with the more poleward stations is interesting. As mentioned earlier, stringent calibration techniques have been used to ensure that this effect is not instrumental. This may indicate that the ionospheric projection of the boundary layer and/or cusp lies between the geomagnetic latitudes of Davis and Mawson on such days, resulting in a distinctly different magnetospheric region being mapped to these stations. Indeed, Casey and Scott Base, being polar cap stations, generally lie under fieldlines which map to the magnetotail, whereas Mawson generally lies under field-lines which are closed in the day-side magnetosphere. The decrease in activity around local magnetic-noon at all stations (for instance 0800 – 1100 UT at Mawson in Figure 4) is another intriguing aspect of these data. These observations are consistent with emissions resulting from a Kelvin-Helmholtz (K-H) type excitation at the flanks of the magnetospheric boundary layer, where shear flows are maximised, and a stagnation point near the nose of the magnetopause. Furthermore, Lee et al. (1981) showed that both the magnetosheath-magnetopause interface, and the inner boundary between the magnetopause and the magnetosphere can be susceptible to K-H instability. This may explain the reversal in ellipticity at Mawson, the lowest latitude station.

7.5.2 *Azimuthal propagation*

The relatively close spacing of Davis and Mawson stations (~640 km) allows the propagation velocities of concurrent events to be estimated. Propagation analysis has been found to be a useful tool in characterising pulsations. For instance, by measuring the phase difference between signals recorded with longitudinally separated magnetometers, an estimate of the azimuthal wave number can be made, allowing propagation modes to be inferred (Olson and Rostoker 1978). Unfortunately, Davis and Mawson stations have similar latitudinal and longitudinal spacings, making the rigorous determination of propagation directions impossible. Nonetheless, interstation pure-states analysis does provide some information. Shown in Figure 5 is the polarity of the phase lag between the

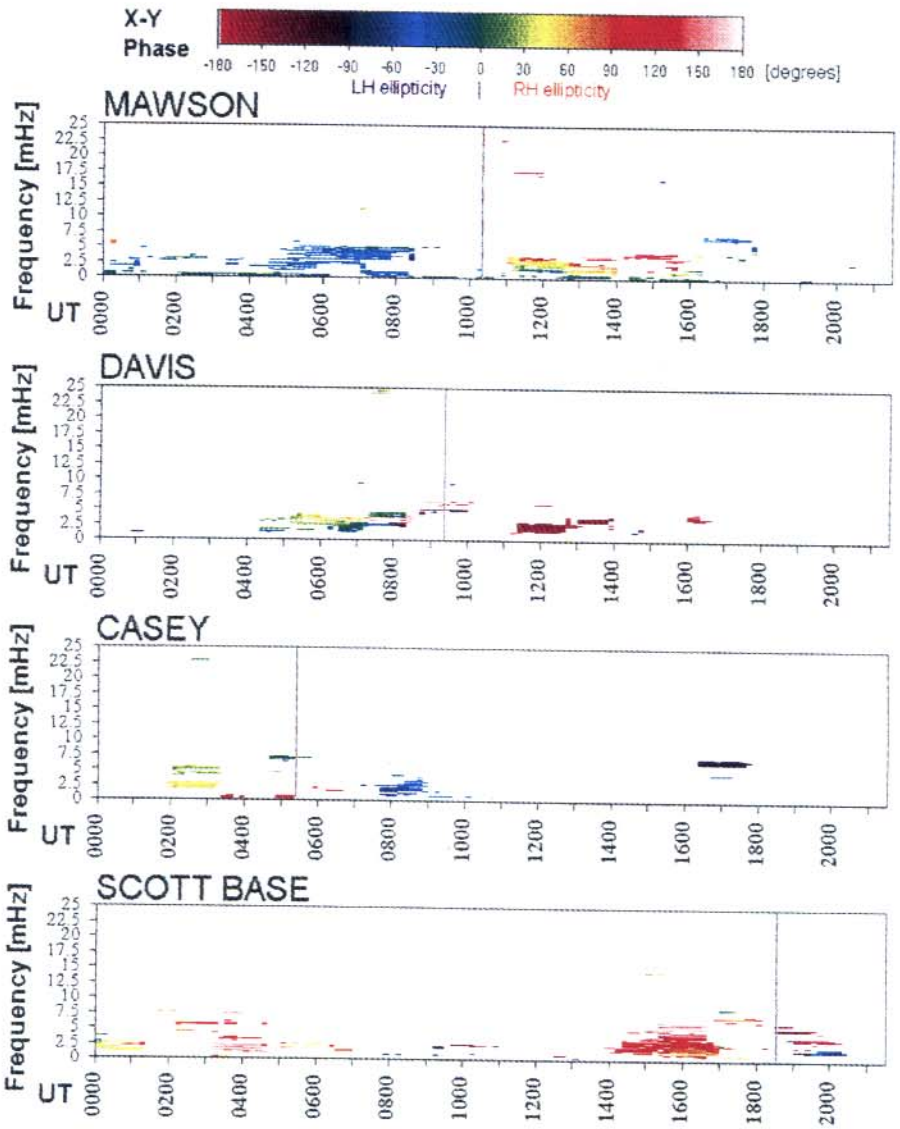

Figure 4. Dynamic phase spectra of Antarctic magnetometer data for 15 February 1993. Only events of > 70% polarisation and > 0.8 of the maximum power are shown. Vertical lines indicate magnetic storms.

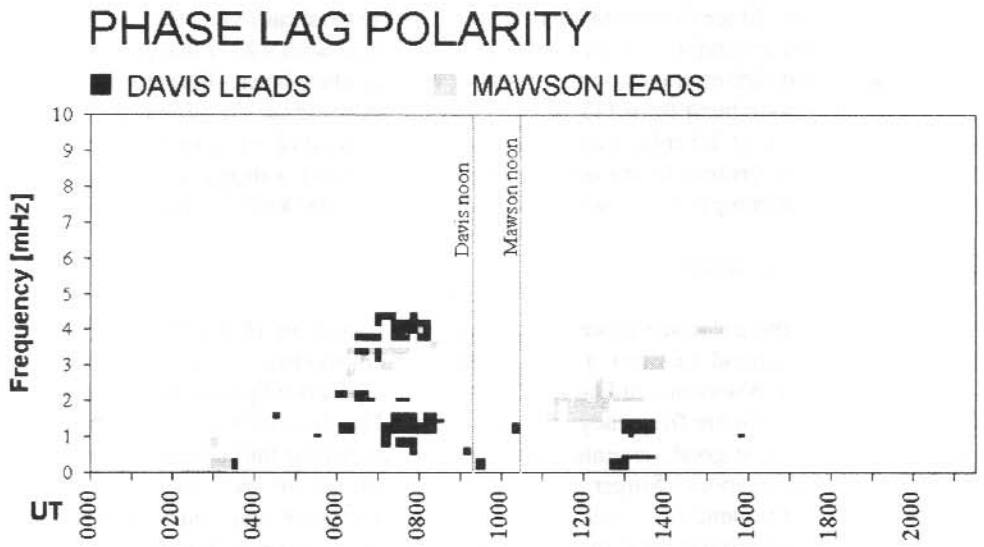

Figure 5. Dynamic plot of phase delays between Davis and Mawson on 15 February 1993, showing which station leads during significant concurrent events. Local magnetic noons are shown by vertical lines.

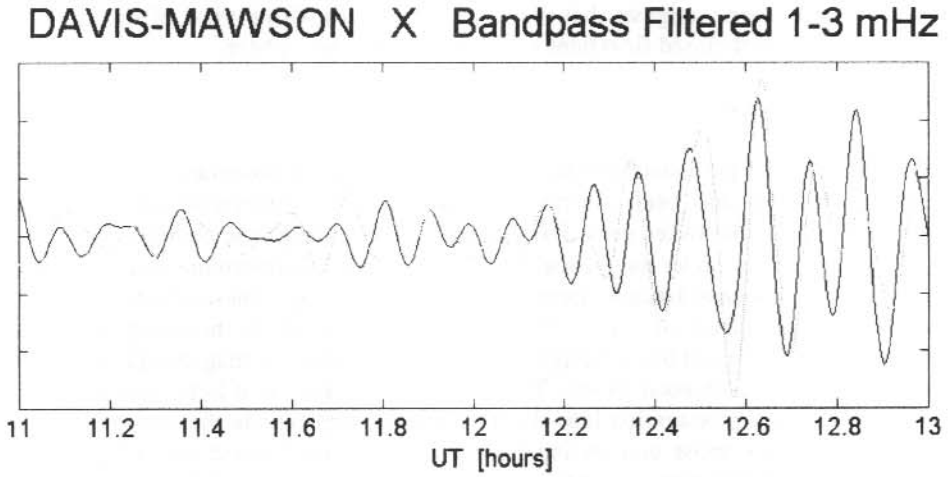

Figure 6. Filtered time series data from Davis and Mawson showing the event which occured around 1200 UT on 15 February 1993. The average frequency is 2.5 mHz, and the phase delay between Mawson and Davis is around 50 s.

X-components of Davis and Mawson data for concurrent Pc5 events on 15 February 1993. In the pre-noon sector Davis generally leads Mawson, while in the post-noon sector the opposite is the case. Since the azimuthal direction of shear flow caused by the solar wind is expected to reverse around local noon, this is also consistent with a K-H like interpretation where an instability drives waves on the flanks of the boundary layer. Filtered time series plots for the post-noon burst from 1120–1250 UT (Figure 6) show the propagation delay is around 50 seconds at 2.5 mHz yielding a propagation speed of ~11 km s^{-1}. Projecting this speed from the ground to the equatorial plane, assuming a dipole geometry, gives 290 km s^{-1}. This is comparable to solar wind speeds (300–800 km s^{-1} – Parks 1991).

7.5.3 *Field line resonance*

Figure 7 displays the polarised power spectra at each station on 15 February 1993 In a roughly 10 hour period centred around 1000 UT, individual events can be seen concurrently at both Mawson and Davis. The maximum polarised power for these events generally occurs at a higher frequency at Mawson (~4 mHz) than at Davis (~2 mHz). Both these frequencies are in good agreement with those predicted for the fundamental toroidal (field line resonance) mode (Singer et al. 1981). Sometimes an arch shaped local time dependence of the frequency of maximum polarised power can be seen, with the maximum frequency occurring around local magnetic noon (e.g. at Mawson in Figure 7). Similar local time dependence has been observed at northern high latitudes (e.g. Olson 1987), and at the northern cusp (McHarg et al. 1995). This is also in agreement with the diurnal variation of toroidal mode frequencies calculated by Singer et al. (1981) using a realistic magnetosphere geometry. A problem arises in explaining the resonant activity at Casey and Scott Base (Figure 7) since these stations are assumed to lie under open field fines. It is possible that distant resonating field lines are within the large apparent field of view of ground based magnetometers in the polar cap. Indeed, the fact that Davis, Casey and Scott Base data shows approximately the same frequency of maximum polarised power before and after local noon, suggests that these stations are all within view of the ionospheric projection of the last closed field lines in the dayside magnetosphere.

7.6 CONCLUSION

Through the use of pure-state spectral analysis a richer set of observations of high latitude Pc5 characteristics has been assembled than would have otherwise been achieved by inspection of the time series data. Distinct pre- and post-magnetic noon bursts of activity have been identified under magnetically quiet conditions. Furthermore, evidence for field line resonance is seen at latitudes extending into the polar cap. These observations support an interpretation based on Kelvin-Helmholtz excitation at the boundary layer of the magnetosphere, followed by coupling to Alfvén waves within the magnetosphere (Chen and Hasegawa 1974; Southwood 1974). The subsequent resonance of field lines via the shear Alfvén mode, and propagation into the inner magnetosphere via the fast compressional mode remains the most convincing model to date (Southwood and Hughes 1983). Furthermore, satellite-borne experiments have been most successful in establishing the locations at which energy from the solar wind is coupled into global MM modes (see Takahashi 1994 for a recent example using the AMTTE CCE satellite). Unfortunately, determining how these modes are manifested in ground based data remains problematic,

especially at stations that rotate under or near the ionospheric footprint of the cusp where the combined influences of external sources and internal resonances are evidently at play.

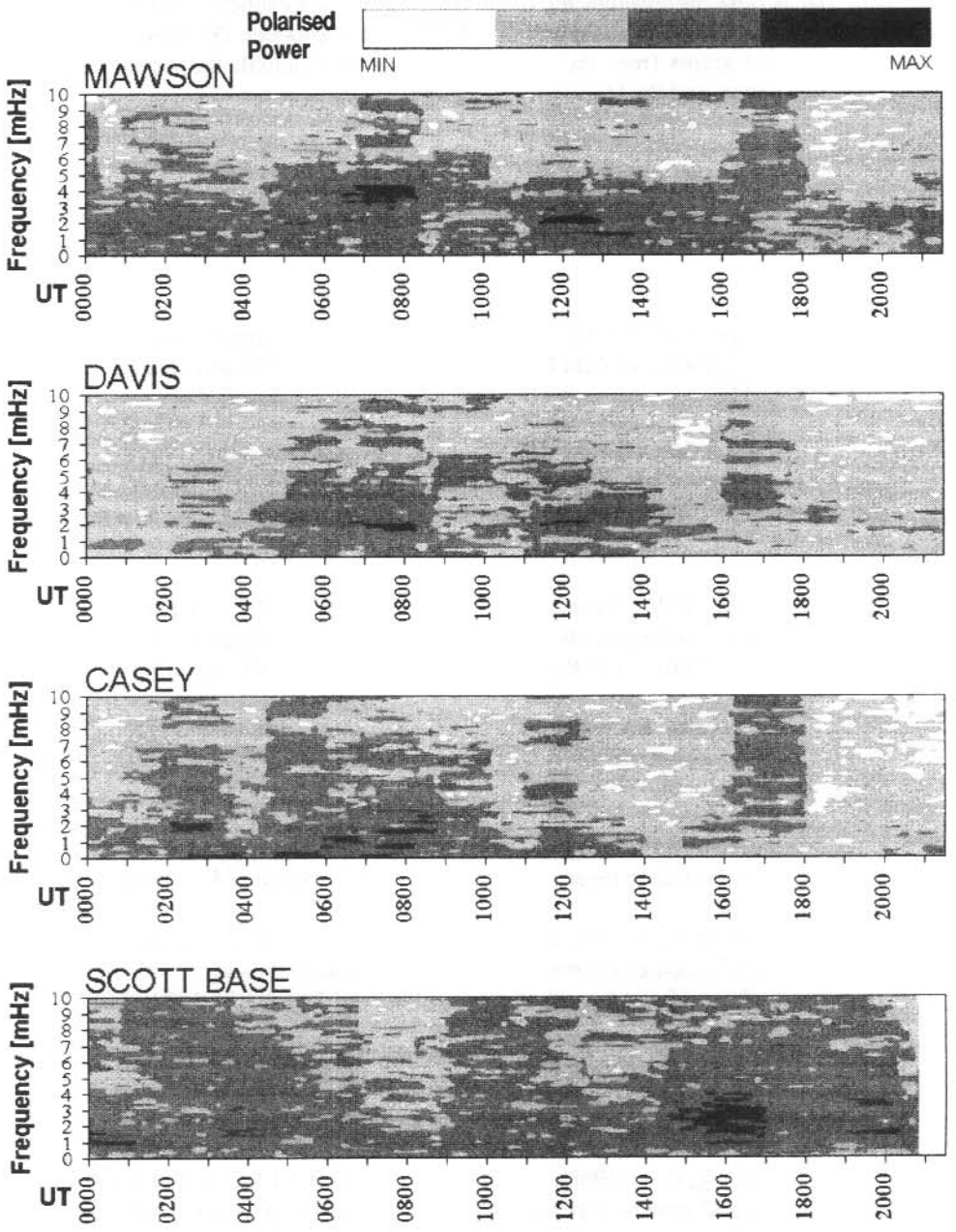

Figure 7. Polarised power directed in induction magnetometer data recorded at Antarctic stations on 15 February 1993.

7.7 ACKNOWLEDGMENTS

The continued maintenance of equipment, and collection of data from the Australian stations has been made possible through the dedication of the Atmospheric and Space Physics expeditioners and the logistical support of the Australian Antarctic Division. The research was supported by grants from the Australian Research Council, the Antarctic Science Advisory Committee, and the University of Newcastle.

REFERENCES

Burns, G.B. *and* Beggs, H.M. (1992). Magnetic time for Australia's Antarctic stations. In: Burns, G.B. *and* Duldig, M.L. (Eds). *ANARE Research Notes Number 88.* Pp. 99 – 111.

Chen, L. *and* Hasegawa, A. (1974). A Theory of long-period magnetic pulsations 1. Steady state excitation of field line resonance. *Journal of Geophysical Research* 79:1024 – 1032.

Dunlop, I.S., Menk, F.W., Hansen, H.J., Fraser, B.J. *and* Morris, R.J. (1992). A multistation study of long period geomagnetic pulsations in the polar cleft and cusp. In: Burns, G.B. *and* Duldig, M.L. (Eds). *ANARE Research Notes Number 88.* Pp. 29 – 41.

Fraser, B.J., McNabb, P.W., Menk, F.W. *and* Waters, C.L. (1991). A personal computer induction magnetometer system for recording geomagnetic pulsations. In: Burns, G.B. (Ed). *ANARE Research Notes Number 80.* Pp. 83 – 92.

Glassmeier, K.-H. (1988). Reconstruction of the ionospheric influence on ground based observations of a short duration ULF event. *Planetary and Space Science 36:* 801 – 817.

Lee, L.C., Albano, R.K. *and* Kan, J.R. (1981). Kelvin-Helmholtz instability in the magnetopause boundary layer region. *Journal of Geophysical Research 86:*54 – 58.

Menk, F.W., Fraser, B.J., Hansen, H.J., Newell, P.T., Meng, C.-I. *and* Morris, R.J. (1992). Identification of the magnetospheric cusp and cleft using Pcl-2 ULF pulsations. *Journal of Atmospheric and Terrestrial Physics 54:*1021 – 1042.

McHarg, M.G., Olson, J.V. *and* Newell, P.T. (1995). ULF cusp pulsations: diurnal variations and interplanetary magnetic field correlations with ground based observations. *Journal of Geophysical Research 100:*19729 – 19742.

Newell, P.T. *and* Meng, C.-I. (1988). The cusp and the cleft /LLBL: low altitude identification and statistical local time variation. *Journal of Geophysical Research 93:*14549 – 14556.

Newell, P.T., Meng, C.-I., Sibeck, D.S. *and* Lepping, R. (1989). Some low-altitude dependencies on the interplanetary magnetic field. *Journal of Geophysical Research 94:*8921 – 8927.

Olson, J.V. (1987). Diurnal characteristics of field line resonance at College, Alaska. *Journal of Geophysical Research 92:*8805 – 8811.

Olson, J.V. *and* Rostoker, G. (1978). Longitudinal phase variations of Pc4-5 micropulsations. *Journal of Geophysical Research 83:*2481 – 2488.

Olson, J.V. *and* Fraser, B.J. (1994). Conjugate ULF pulsations in the cusp. *Advances in Space Research* . Proceedings of COSPAR Conference, Washington DC.

Parks, G.K. (1991). Physics of space plasmas. Addison-Wesley Publishing Company, Redwood City, CA. Pp. 204 – 219.

Rostoker, G., Samson, J.C. *and* Hguchi, Y. (1972). Occurrence of Pc 4, 5 micropulsation activity at the polar cusp. *Journal of Geophysical Research 77:*4700 – 4706.

Samson, J.C. (1972). Three-dimensional polarization characteristics of high latitude Pc5 geomagnetic pulsations. *Journal of Geophysical Research 77:*6145 – 6160.

Samson, J. C. (1983). The spectral matrix, eigenvalues, and principle components in the analysis of multichannel geophysical data. *Annales Geophysicael 2:*115 – 119.

Samson, J.C. (1991). Continuous plasma waves and pulsations in the low-frequency band (1–10 mHz). In: Jacobs J.A. (Ed.) *Geomagnetism Volume 4*. Academic Press. Pp. 511 – 530.

Singer, H.J., Southwood, D.J., Walker, R.J. *and* Kivelson, M.G. (1981). Alfvén wave resonance in a realistic magnetospheric magnetic field geometry. *Journal of Geophysical Research 86:*4589 – 4596.

Southwood, D.J. (1974). Some features of field line resonance in the magnetosphere. *Planetary and Space Science 22:*483 – 491.

Southwood, R.J. *and* Hughes, W.J. (1983). Theory of hydromagnetic waves in the magnetosphere. *Space Science Review 35:*301 – 366.

Takahashi, K. (1994). Studies of magnetospheric ULF waves using active magnetospheric particle tracer explorers charge composition explorer. *Journal of Geomagnetism and Geoelectricity 46:*953 – 970.

Troitskaya, V.A. (1985). ULF wave investigations in the dayside cusp. *Advances in Space Research 5:*219 – 228.

8. DETERMINATION OF PC1-2 ULF WAVE VELOCITY AND DIRECTION USING A CLOSELY SPACED ANTARCTIC MAGNETOMETER ARRAY

D.A. Neudegg[1,2], G.B. Burns[2], B.J. Fraser[1], F.W. Menk[1], R.J. Morris[2], H.J. Hansen[1] and M.J. Underwood[2]

[1] Space Plasma Waves Group
University of Newcastle
Callaghan NSW 2308
Australia

[2] Atmospheric and Space Physics
Antarctic Division
Kingston Tasmania 7050
Australia

ABSTRACT

The group velocity and direction of ULF waves have been determined from induction magnetometer records at three closely spaced stations in an Antarctic array. The technique of wavefront reconstruction is used to determine the velocities and directions of the waves, and is the subject of this paper. It is believed that wave events observed in this study were propagating in the ionospheric waveguide and these are the first direct measurements of their velocity and direction at high latitudes. The array was deployed beneath the cusp projection near Davis station during the 1992 Antarctic winter to study the source regions and propagation of Pc1-2 (0.1 – 5 Hz) ULF waves. ULF waves are one of the processes by which high latitude magnetospheric energy sources link directly to the ionosphere in geospace coupling. The polar cusp regions are important in this coupling and are a major focus of the international Solar-Terrestrial Energy Program (STEP) and Geospace Environment Modelling (GEM) program.

8.1 INTRODUCTION

To determine the source location of a ULF wave and to then relate that to a high latitude feature in geospace requires determination of the wave's direction of propagation. Once the propagation direction and velocity of each wave event has been established it can be entered into a database of processed wave events. The variation in propagation direction of the waves in the database, and therefore their source direction, can be examined as a function of geophysical activity. This gives an indication as to the nature of the sources and will be described in a companion paper. The velocity measurements can be used to assist in assessing the mode of propagation of the ULF waves, believed to be propagating away from their sources in the ionospheric waveguide parallel to the Earths surface.

The temporary three station magnetometer array deployed in this experiment was based around the austral polar cusp latitude station Davis in Antarctica (74.6°S, 102.3°E in PGM-88 coordinates [Baker and Wing 1988]). A site on the polar plateau 150 km inland

from Davis and another site at Law Base, 120 km magnetically west of Davis were deployed for this study by vehicle traverse (Neudegg et al. 1994a). The the array is depicted in Figure 1. The coordinate system used for wavefront direction analysis has been superimposed on the array. This should be compared with the wavefront reconstruction geometry in shown Figure 5 and discussed in Section 8.2.4. The array deployment and data recording campaign were conducted during the austral winter (27 July to 8 August 1992) due to occurrence and amplitude maxima of Pc1-2 in winter at Davis (Morris and Cole 1991). The recording period encompassed a wide range of geomagnetic conditions from quiescent to active and then quiet recovery periods.

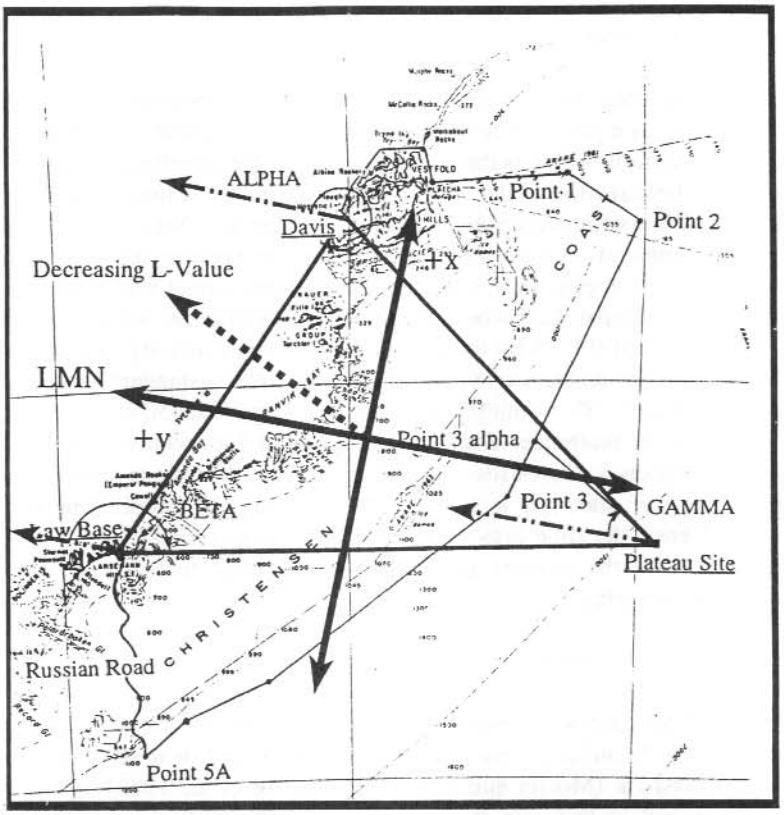

Figure 1. The coordinate system used for the wavefront reconstruction geometry superimposed on the magnetometer array and traverse route. Local magnetic north at Davis was chosen as the +y axis of a cartesian system whose origin is at the intersection of the bisectors of the three array legs. The angles alpha, beta and gamma represent the angles of the three array legs from LMN. The time lag for each leg of the array is translated into a velocity projection vector along the direction of that array leg. A rotation of 27° translates the coordinate system to one using decreasing L-value for north which is more globally oriented in terms of assessing the arrival angles for waves in comparison to geospace features.

The technique of wavefront reconstruction has been used to determine the direction and velocity of a wave that has passed across several spatially separated sensors. Correlation of the waveforms between each pair of sites, or leg of the array, allows determination of the time lag of the wavefront across that particular leg. The length of the array leg divided by the time lag represents the velocity projection of the wavefront along that particular leg of the array. A wavefront must be fitted to the various vectors representing the velocity projections along each leg of the array. The vector orthogonal to this wavefront represents the direction and group velocity of the wave itself.

8.2 EXPERIMENT

8.2.1 *Magnetometer array*

The geometry of the array is shown in Figure 1 with the wavefront reconstruction geometry superimposed. Angles alpha, beta and gamma represent the angle of each leg of the array from local magnetic north which is the chosen +y axis of the coordinate system. The dotted arrow represents the direction of decreasing L-value which is a more global indication of magnetic north. The coordinate system is described in detail in Section 8.2.4 and Figures 1 and 5 should be compared. At each site the magnetometer systems consisted of orthogonal, magnetic north-south and east-west, induction coils whose output was digitally sampled at 10 Hz. The analogue signal was recorded digitally and to chart records, both unfiltered and through a Pc1-2 filter of 0.1 – 5 Hz to isolate high frequency activity. Coordinated timing was supplied using chronometers set to HF time signals from a standard time reference on a known propagation path. This timing was accurate to better than 50 ms (0.05 s) at all three sites with respect to the reference. Each site was calibrated for relative and absolute phase, amplitude and frequency responses. Absolute phase calibrations established that the instrument lag between sites was less than 0.05 s, one half the sampling period (Neudegg et al. 1994a). Hence the time lags of waveforms between sites are not artifacts from differing responses of the sensors and have been assumed to be the result of a wave propagating across the array.

8.2.2 *Selection of wave events*

The methods used to select wave events are described in detail elsewhere (Neudegg et al. 1994b) and will only be outlined here. Pc1-2 wave events such as unstructured and discrete 0.15 – 0.4 Hz emissions (Morris and Cole 1985; Menk et al. 1992) were selected for propagation analysis from dynamic spectra on days of low geomagnetic activity. Examples of these bandlimited events can be seen in the waveforms and dynamic spectra displayed in Figures 2 and 3.

High frequency noise generally obscured band limited emissions across the Pc1-2 band in the spectra during days of high geomagnetic activity. Hence event durations on geomagnetically active days were obtained from the filtered Pc1-2 channel time series, and a fixed frequency width of 0.5 – 2 Hz within the Pc1-2 band was selected to perform propagation analysis. The frequency width was chosen due to the apparent non-propagation of the lower frequency Pc2 (0.1 – 0.2 Hz) component as described below in determination of time lags. The ionospheric waveguide is also predicted to have lower cutoff frequencies up

to 0.36 Hz depending upon ionospheric conditions (Greifinger and Greifinger 1968), so it was considered prudent to examine frequencies above this.

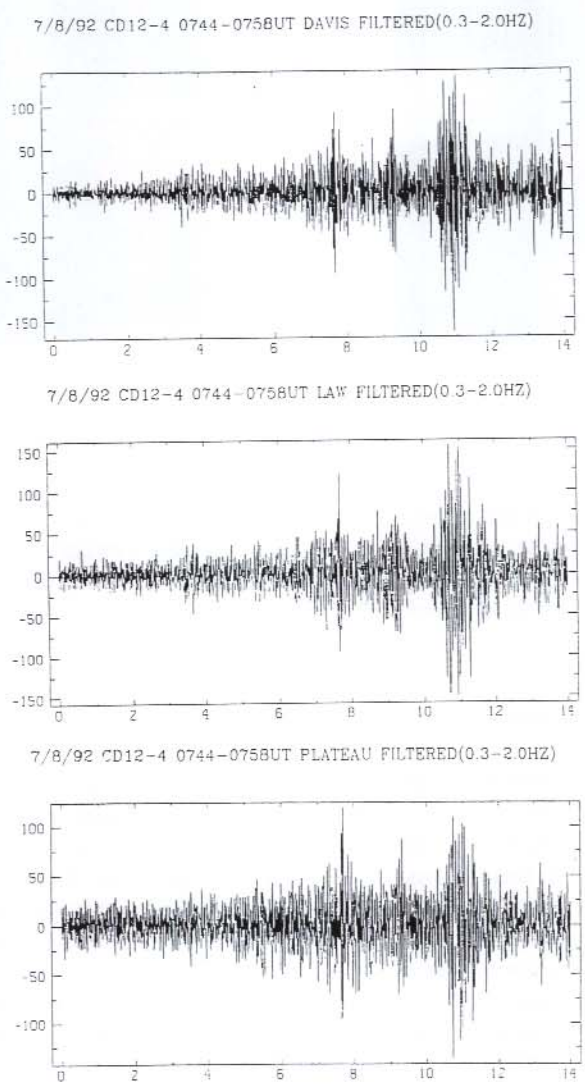

Figure 2. Typical filtered magnetic pulsation waveforms after selection from Pc1-2 filtered chart records during an active period. Three station, H channel (magnetic north-south) data from event CD12-4 (the 4th event selected from day 12 of the campaign) are shown for comparison. The time axis is scaled in minutes from the commencement of the event and the amplitude is in digital units. Data were sampled at 10 Hz with synchronised time error less than 50 ms.

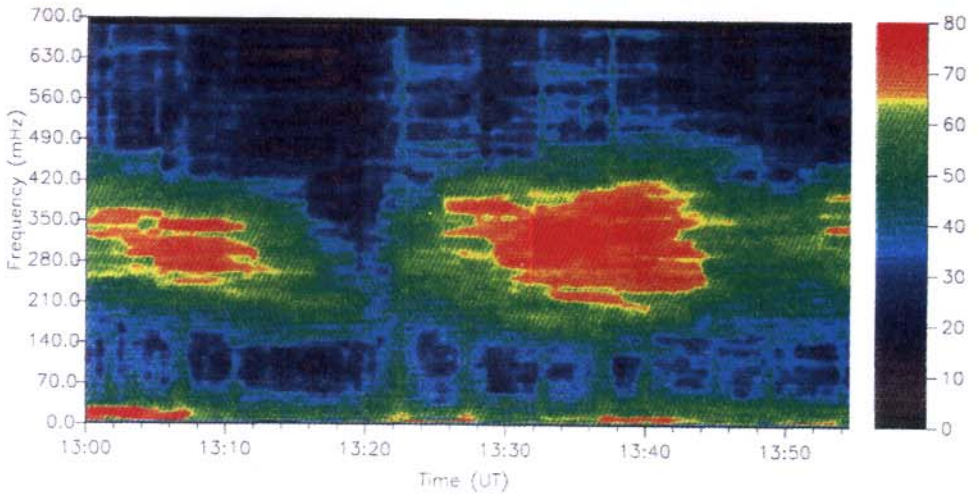

Figure 3. Dynamic spectra from a quiet period on 6 August 1992, day 11 of the recording campaign. The regions of enhanced power are typical Pc1-2 band limited events that were chosen for propagation analysis. The raw magnetic pulsation data were filtered for each event to isolate the region of enhanced power over its duration.

8.2.3 *Determination of time lags*

The bandpass filtered events selected using the above criteria, typically of 5 to 15 minutes duration, were divided into one minute time segments. For each segment a cross-correlation was performed between the pairs of sites comprising each of the three legs of the array. The three legs are Davis – Law Base, Davis – Plateau Site and Law Base – Plateau Site. For each array leg, every one minute waveform segment has a time lag between the sites and an associated correlation coefficient. The time lags of the segments from the cross-correlation were examined as a function of the magnitude of the correlation coefficient as shown in Figure 4. The wave activity chosen from either the dynamic spectra or the 0.5 – 2 Hz band within the Pc1-2 time series exhibited consistent time lags for signals between each pair of sites with correlation coefficients generally greater than 0.75. Both H and D channels showed similar time lags between each pair of sites. Hence a value for the lag of the wave along each leg of the array was established for propagating wave events.

The Pc2 (0.1 – 0.2 Hz) frequency component during an event period showed high values of correlation coefficient between pairs of sites but no consistency of lags amongst the waveform segments. This was interpreted as the Pc2 component not propagating between the sites but being recorded at different stations due to their overlapping field of view. The

magnetometer effective fields of view overlap for site separations of less than 200 km as the instruments respond to ionospheric currents within 100 km of the zenith (Olson and Fraser 1994). A minimum station separation of 100 km is therefore required for propagation studies of ULF waves. Hence these signals in the Pc2 range were not considered for propagation analysis. It has previously been established that common Pc1-2 wave activity is rare over the 630 km separating Davis and Mawson (Francke et al. 1993), setting an upper bound for site separation. The present study confirmed this with very few events seen at both Mawson and the triangular array. Therefore wave direction had to be established from three station analysis rather than point source location from four site analysis. It is intended that point source analysis will be performed on the few events that were observed at Mawson when advanced spectral processing techniques can be employed to enhance the signal common with the triangular array.

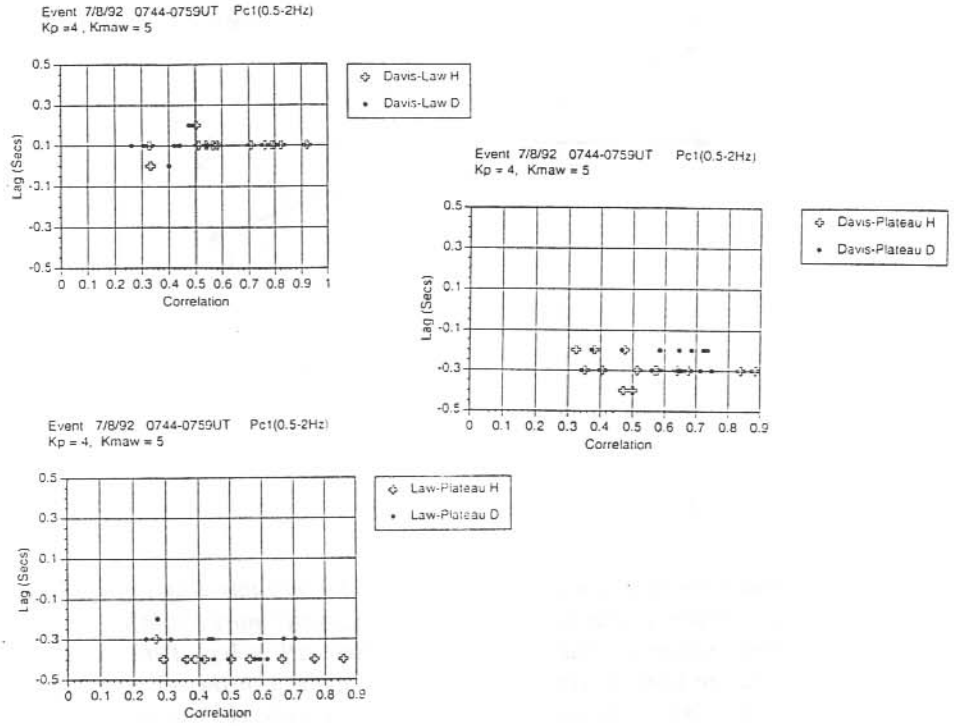

Figure 4. Time lag versus correlation plots for the waveforms shown from event CD12-4 in Figure 2. Each symbol represents the result from a cross correlation of a one minute waveform segment between the two sites shown. The crosses represent the H (magnetic north-south) sensor and the dots the D (magnetic east-west) sensor. The Davis-Law Base leg shows a lag of +0.1 s to +0.15 s, ie the wave moves from Law Base to Davis. The Davis-Plateau Site leg shows a lag of -0.3 s, ie. the wave moves from Davis to Plateau Site. The Law Base-Plateau Site leg shows a lag of -0.4 s, ie. the wave moves from Law Base to Plateau Site.

8.2.4 *Wavefront reconstruction geometry*

Wavefront reconstruction was used to establish the direction and velocity of events from the time lags of the waveform on each leg of the array. This is a common technique used in areas such as 3-field photometry (De Deuge 1990). The basic geometry is illustrated in Figure 5.

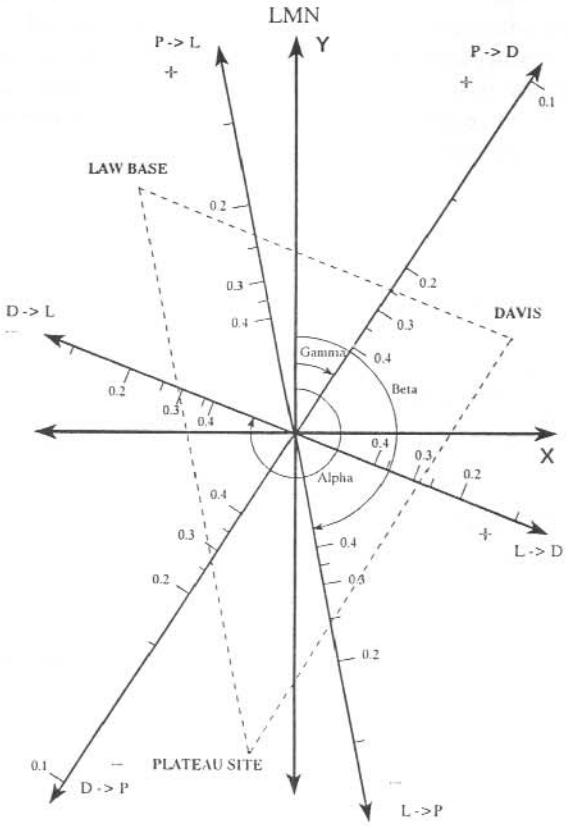

Figure 5. Wavefront reconstruction geometry. Cross reference this diagram with Figure 1. The coordinate system is cartesian with local magnetic north (LMN) as the +Y reference. The three reference lines are each parallel with a leg of the array. The reference lines make the same angles alpha, beta and gamma to the +Y axis that each array leg makes with LMN. The outline of the array to scale is superimposed on the geometry for reference. Each reference line is set to a velocity projection vector direction and length according to the waveform time lag along the corresponding array leg. The reference lines are marked with a wave direction according to the + or - sign at their tips. They are scaled with time lags from the waveform correlations. The distance of the scale marks from the origin represent the velocity projected along that array leg by a waveform with the corresponding time lag. The smallest scale divisions are 0.05 s. Refer to Appendix A for details concerning the mathematics for setting up the velocity projection vectors.

The origin of the coordinate system was chosen as the intersection of the perpendicular bisectors of the three array legs. The coordinate system is cartesian, chosen with positive Y in the direction of local magnetic north at Davis. A conversion can then be made to a propagation direction with respect to invariant magnetic north by a simple rotation of the coordinate system. Invariant magnetic north can be thought of as the direction of the largest decrease in L-value from a particular point, chosen in this case to be Davis. Invariant magnetic south points towards the south Invariant Pole near Vostok. We are interested in high latitude pulsation sources that can be linked to geospace features, which are themselves oriented about the invariant magnetic pole and move with reference to it. The magnetic declination at Davis is -77.5°and the direction of invariant magnetic south is 129.5° (Burns – private communication). Therefore local magnetic north lies at 282.5° geographic, invariant magnetic north at 309.5° geographic and the translation between the coordinate systems is a 27° rotation.

Three other reference lines are superimposed on this coordinate system. Each line is in the direction of a leg of the array and represents the velocity projection of the wavefront along that leg. The opposite ends of the line represent a velocity in either direction along the leg with corresponding values of time lag for scale. The less the time lag, the longer the velocity projection vector. Different separations between the scale markers on the various reference lines are due to the differing lengths of the array legs. The angle that each array leg makes with local magnetic north is also the angle that the associated reference line makes with the positive Y-axis. These angles are alpha for Davis – Law Base, beta for Law Base – Plateau Site and gamma for Davis – Plateau Site. The array outline, drawn to scale, is superimposed on the reconstruction geometry for reference.

The three lags are determined by the method previously described and their velocity vectors superimposed on the reference lines. The wavefront as it passes across the array can be thought of as connecting the tips of these vectors to cause the apparent velocities seen along each leg. Hence to actually reconstruct the wavefront requires fitting a line to the apparent velocity vector tips. The method should be applicable to any number of sensors in an array where the geometry is known. The mathematics and method for the calculation of the projection velocity vectors are outlined in Appendix A.

8.2.5 *Zero lag problem*

If the time lag for the correlation of the waveforms is zero along one of the array legs then a special case occurs. A lag of zero along a particular array leg means an infinite projection velocity which in turn implies that the wavefront is parallel to that leg. As the sampling frequency is 0.1 s and the timing at all the sites is accurate to at least 0.05 s it can be assumed that the uncertainty in the lag is no greater than 0.05 s. This means there is a possible range of lags between +0.05 s and -0.05 s. The method chosen to resolve which lag to use was to select the +0.05 s and the -0.05 s lag, and determine which solution has the velocity projection vector closest to those of the other two array legs. This is physically the most satisfying solution as it will produce the wavefront with the minimum amount of curvature. The concept is illustrated in Figure 6 where the two solutions are similar in magnitude but opposite in direction. This is event CD7-6, the 6th event chosen from campaign day 7. The wavefronts labelled -a and -b lead from the Plateau Site – Law Base

and Plateau Site–Davis velocity projection vector tips to the -0.05 s Davis–Law Base vector and those labelled +a and +b to the +0.05 s vector. The wavefront joining the Plateau Site–Law Base and Plateau Site–Davis velocity projection vector tips has been omitted for clarity. The total wavefront for the +0.05 s solution has the least separation between the velocity projection vector tips and wavefront fitting method 1 (refer Section 8.2.6) gives a velocity of 505 ±89 km s^{-1} and a direction of 9 ±4 degrees with respect to local magnetic north. The method and mathematics of deciding which velocity projection vector to use are outlined in Appendix A.

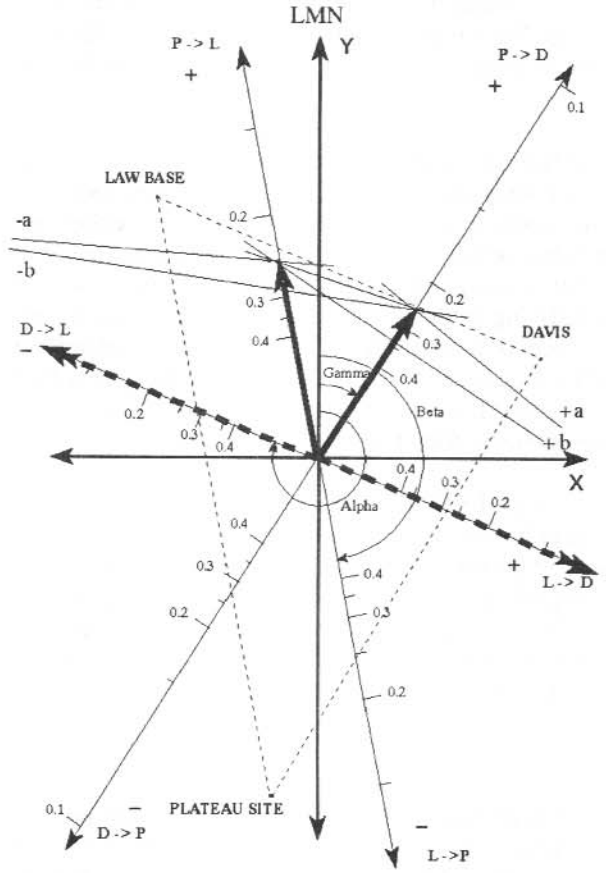

Figure 6. An illustration of a benign case of the zero lag problem from event CD7–6. The Davis–Law Base leg has a zero lag for the waveform, Plateau Site–Law Base leg has +0.25 s and Plateau Site–Davis also has +0.25 s. Wavefronts have been drawn from the Plateau Site–Law Base and Plateau Site–Davis velocity projection vectors to the possible vectors on the Davis–Law Base leg. Wavefronts +a and +b lead to the projection vector at +0.05 s and -a and -b lead to the vector at -0.05 s. The velocity projection vector tip for Davis–Law Base that is closest to the tips of the other two vectors will be the solution. In this case it is the +0.05 s vector. The mathematics for solving the zero lag problem are outlined in Appendix A.

In some events the velocity vector orientations produce a geometric solution which appears to be non-physical. Wavefront lines joining pairs of velocity projection vectors are used to illustrate the wavefronts for pairs of array legs. The total wavefront can be thought of as being represented by the combination of these three lines. The more linear the total wavefront becomes the closer the three lines are to coinciding. The three velocity projection vectors are oriented in such a way as to make the wavefront lines joining them form a triangle about the origin as shown in Figure 7 for the +0.05 s case. An alternative explanation would be for the source to be within the array boundaries but this solution is not considered here. The solution that would be chosen for this event is the -0.05 s case which gives a wide variation in the possible total velocity but at least appears to have a physical solution with a source direction in the first quadrant.

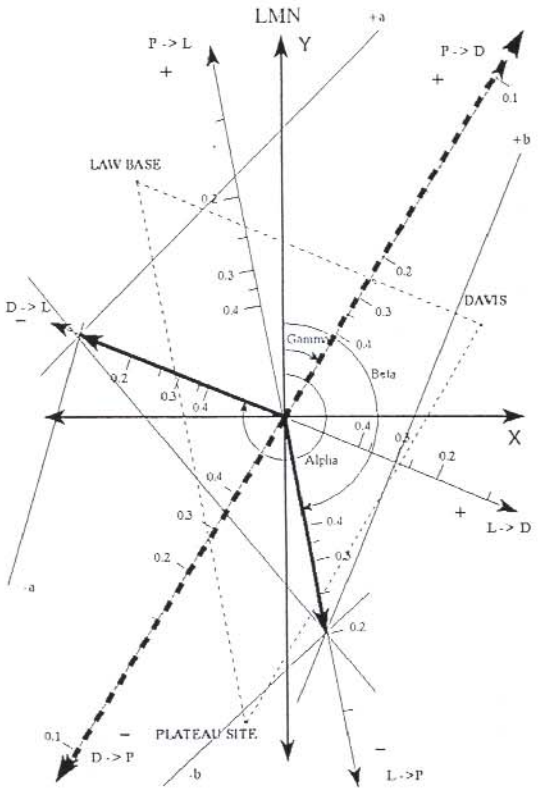

Figure 7. A difficult zero lag event. The Davis–Plateau Site leg has zero lag, the Law Base–Plateau Site leg has -0.2 s and the Davis–Law Base leg -0.15 s. As in Figure 6 pairs of velocity projection vectors have been joined by wavefronts with +a and +b leading to the +0.05 s solution, and with -a and -b leading to the -0.05 s solution. The +0.05 s solution is non-physical, wavefronts forming a triangle around the array origin. The solution selected here is the -0.05 s which has a large uncertainty in possible angles of arrival and velocity but appears to be physically viable.

8.2.6 *Wavefront fitting*

A plane wavefront passing across the array with the lags representing a projection of wave velocity on each array leg was assumed as a first approximation. It might be expected that a curved wavefront would be the best description for many events (Althouse and Davis 1978). However the curvature observed when the geometry is plotted for most wave events is slight and the difference in direction and velocity from a plane wavefront approximation is small. Two methods for fitting the plane wavefront were used:

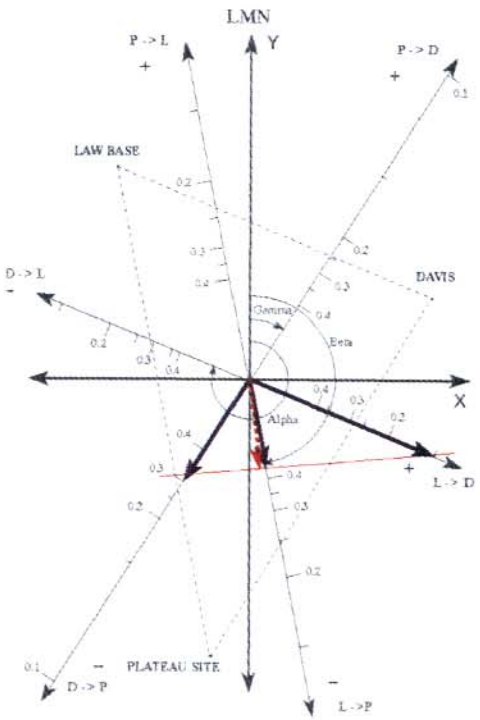

Figure 8. Wavefront reconstruction performed by method 1 on the waveforms shown in Figure 2 for event CD12-4. Each lag is represented as a velocity projection vector in purple along a reference line through the origin which is parallel to a given array leg. The sign of the lag determines the direction of the velocity vector. The wavefront that would cause all three velocity projection vectors to be observed is the line that passes though the tip of all three vectors. The aim is to find a line of best fit to these three points and this is shown in red. The velocity is the perpendicular to the wavefront from the origin and is the dotted red arrow. The wave angle of arrival is 355 ±1° (equatorward of the array) with a velocity of 331 ±7 km s^{-1} at a K_p value of 4. The cusp/boundary layer is predicted to be well equatorward of Davis during geomagnetically active conditions. Refer to Appendix B for an outline of the mathematics for this method.

Method 1 involved fitting a straight line to the three points representing the tips of the velocity vectors. This line was a least squares fit to three points with an associated uncertainty and is the total reconstructed wavefront. The total velocity vector is the perpendicular bisector of the wavefront from the origin. This method is illustrated in Figure 8 with event lags chosen from event CD12-4 (the 4th event chosen from campaign day 12). The results are a velocity of 331 ±7 km s^{-1} and an angle of arrival of 355 ±1 degrees which translates to a direction of propagation of 175 ±1 degrees. The general method and mathematics are described in Appendix B.

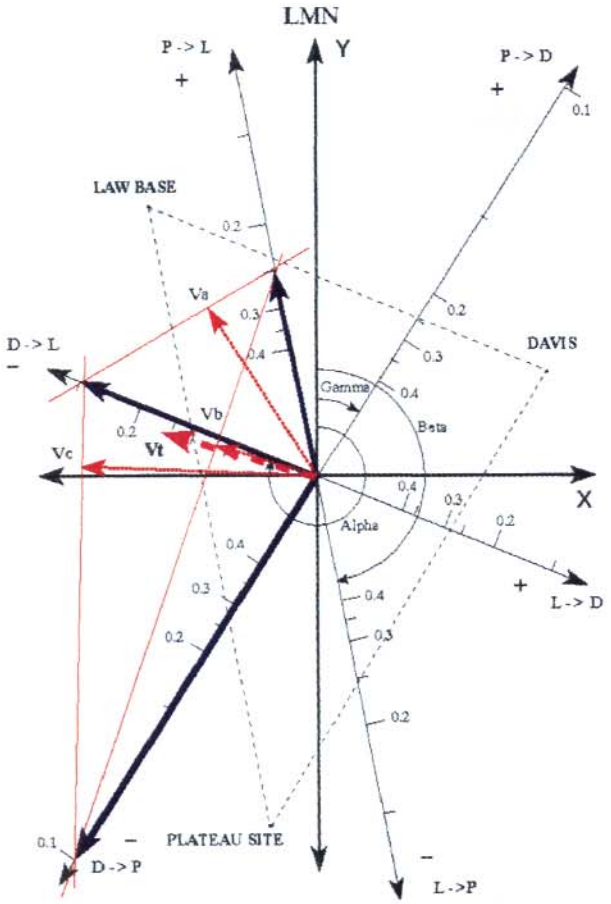

Figure 9. Wavefront reconstruction method 2 applied to event CD8-6 where the total wavefront is obviously less linear than in Figure 8. Here the tips of each pair of array leg velocity projection vectors (purple) are joined by a wavefront (red). The velocity vector of each wavefront is again the perpendicular from the origin (red dotted arrows). The total wavefront velocity is the average of the three wavefront velocities (dashed purple arrow). This method yields less spread in possible values than method 1 in Figure 8 for total wavefronts that depart significantly from linear.

Method 2 involved joining each of the three pairs of velocity vector tips with a straight line. The normal to each of these wavefronts is a velocity vector. These three velocity vectors were then 'averaged' to give a resultant velocity and direction. This method is illustrated in Figure 9. The event CD8-6 shown here is an example of the advantage of this method over method 1 for some events. The direction and velocity for this event is 116 ±33 degrees with respect to LMN and 459 ±213 km s^{-1} for method 2 compared with 120 ±91 degrees with respect to LMN and 396 ±1158 km s^{-1} for method 1. The method and mathematics are described in Appendix C.

8.2.7 *Geometry to computer code*

Rather than hand plotting the geometry for multiple events it is useful to code the mathematics into computer software for rapid calculation. By supplying the time lags for each leg of the array which have been selected from the correlation analysis the code performs all of the geometry outlined in the appendices. This includes and solving the zero lag problem and performing both methods 1 and 2 for wavefront fitting. The output includes the velocity and its uncertainty in km s^{-1}, the direction of the wave with respect to both magnetic north and increasing L-value with associated uncertainties. This enables large numbers of events to be processed contributing to a database covering a range of times and geomagnetic activities.

8.3 RESULTS AND DISCUSSION

8.3.1 *Technique applied to magnetic pulsation data*

A single case study has been used to illustrate the technique from the selection of the event through to determination of its velocity and direction. The event is CD12-4 selected from the Pc1-2 filtered time series during a geomagnetically active period with the waveforms shown in Figure 2. The lag versus correlation number plots are shown in Figure 4 from which the time lags on each leg were chosen. The lags are +0.15 s for the Davis–Law Base leg, -0.3 s for the Davis–Plateau Site leg and -0.4 s for the Law Base–Plateau Site leg. The wavefront reconstruction was shown in Figure 8 using method 1 with a resultant velocity of 331 ±7 km s^{-1} and direction of 175 ±1 degrees with respect to local magnetic north.

An initial database of 42 events were chosen from one active and three quiet days across a range of times around local noon when the cusp/cleft passes closest to the array. The two wavefront reconstruction methods work well for most of the events, giving acceptable variations in possible angle of arrival (less than ±15 degrees) and velocity (less than ±15%). Some events are more amenable to one method rather than the other depending on the geometry of the velocity projection vectors. The event database will be used in a companion paper for a synoptic study of wavefront angles of arrival and source directions with varying geomagnetic activity and time.

8.3.2 *Possible improvements to the technique*

There are obvious improvements that can be made to various stages in the technique. These will increase the yield of useable events from those initially selected for analysis to use in a

synoptic study. The current method supplies a sufficient number of events for an initial study of source location variation with high and low geomagnetic activity. For studies of source location direction with more subtle variations in geophysical parameters (ie. K_p, IMF B_z and B_y , PC index etc), more refined techniques may need to be employed to reduce the variation in possible angle of arrival. These could include improving the correlation method of waveforms between the sites to find the time lags beyond the simple but effective approach used here. A refinement is to manually inspect the correlation curve of each waveform segment correlated between pairs of sites. It can be compared with the others for that event and pair of sites to look for peaks at a common time lag that may have been overlooked in favour of one larger by the peak selection algorithm. This may reduce the spread of lags amongst the waveform segments and hence the error in selecting a lag for that leg of the array. Another refinement is to fit some form of elliptical wavefront to the velocity projection vectors for the events that clearly do not have linear wavefronts (Althouse and Davis 1978). These improvements are time consuming and will only be considered for events which have not proven easy to reduce by the current method and are also required for a synoptic study because of the unique geomagnetic conditions under which they occur.

8.4 SUMMARY AND CONCLUSIONS

Similar waveforms in the Pc1 (0.2 – 5 Hz) ULF frequency range observed on induction magnetometer records have an observable time lag between spaced sensors. It appears possible to reconstruct the velocity and direction of a plane wavefront passing across an array of closely spaced magnetometers (separation less than 500 km) at high latitudes. The time lags between the waveforms observed at the various sensors in the array have been interpreted as being due to the velocity projections of the wavefront along the line between the sensors. A plane wavefront can be used as an approximation to the actual wavefront that would cause the the observed velocity projections. The speed and direction of the reconstructed wave with their associated uncertainties can be calculated. A source direction with respect to the array can be inferred from the wave angle of arrival. The wave is believed to be propagating in the ionospheric waveguide parallel to the Earths surface. Wavefront velocities shown for example events in this paper and subsequent more comprehensive analysis presented in a companion paper support this. These are believed to be the first direct velocity measurements of duct propagating ULF waves at polar latitudes.

The technique itself becomes more powerful as a tool for polar geospace mapping when it is applied to multiple wave events. The variation of wave source directions can be examined as a function of time and geophysical activity in concert with intercalibrations performed against satellite and radar observations. It can then be determined if it is possible to match the behaviour of the ULF wave sources with the predicted behaviour and location of polar geospace features. If this is so, then a closely spaced magnetometer array is a viable tool for ground monitoring the mapping of high-latitude magnetospheric features onto the ionosphere. This has implications in assessing coupling of the polar atmosphere to the Earth's near space environment above. It is also important in understanding the global atmospheric energy budget beyond the immediate need to explore the dynamics of polar geospace above Antarctica.

8.5 ACKNOWLEDGMENTS

We would like to acknowledge the logistical support for data collection provided by the wintering ANARE (Australian National Antarctic Research Expedition) and CHINARE (Chinese Antarctic Research Expedition) expeditioners at Davis and Zhong Shan stations in 1992, as well as staff of the Antarctic Division. Additional analysis software was produced by M. Hesse of the Antarctic Division and C. Waters from the University of Newcastle. D.A.N would like to thank Prof. D. Southwood for a valuable discussion concerning plasma wave theory, and P. Greet, A. Klekociuk and D. Rasch for discussions regarding correlation and wavefront reconstruction techniques. Financial assistance from Atmospheric and Space Physics short research contracts, and casual employment with the Health Physics section of the Tasmanian State Government made this research possible.

REFERENCES

Althouse, E.L. *and* Davis, J.R. (1978). Five-station observations of Pc1 micropulsation propagation. *Journal of Geophysical Research 83*:132 – 144.

Baker, K.B. *and* Wing, S. (1988). A new magnetic coordinate system for conjugate studies at high latitudes. *Journal of Geophysical Research 80*:9139 – 9143.

De Deuge, M.A. (1990). *Optical observations of gravity waves in the high latitude thermosphere*. MSc Thesis. Mawson Institute of Antarctic Research, University of Adelaide, Australia.

Francke, M.H., Hansen, H.J., Menk, F.W., Fraser, B.J. *and* Morris, R.J. (1993). The propagation of Pc1 magnetic bursts across the polar cap region. In: Burns, G. *and* Duldig, M. (Eds). *ANARE Research Notes Number 88*. Pp. 82 – 88.

Greifinger, C. *and* Greifinger, P. (1968). Theory of hydromagnetic propagation in the ionospheric waveguide. *Journal of Geophysical Research 73*:7473 – 7490.

Menk, F.W., Fraser, B.J., Hansen, H.J., Newell, P.T., Meng, C.-I. *and* Morris, R.J. (1992). Identification of the magnetospheric cusp and cleft using Pc1-2 pulsations. *Journal of Atmospheric and Terrestrial Physics 54*:1021 – 1042.

Morris, R.J. *and* Cole, K.D. (1985). Pc1-2 discrete regular daytime pulsation bursts at high latitudes. *Planetary and Space Science 33*:53 – 67.

Morris, R.J. *and* Cole, K.D. (1991). High latitude day-time Pc1-2 continuous magnetic pulsations: a ground signature of the polar cusp and cleft projection. *Planetary and Space Science 39*:1473 – 1491.

Neudegg, D.A., Underwood, M.J., Burns, G.B., Fraser, B.J., Menk, F.W., Hansen, H.J. *and* Morris, R.J. (1994a). Deployment of a multi-station magnetometer array to examine source regions of ULF waves at southern cusp/cleft latitudes. In: Morris, R.J. (Ed). *ANARE Research Notes Number 92*. Pp. 135 – 143.

Neudegg, D.A., Burns, G.B., Fraser, B.J., Menk, F.W., Hansen, H.J., Morris, R.J. *and* Underwood, M.J. (1994b). Monitoring propagation of Pc1-2 ULF waves at southern cusp/cleft latitudes. In: Morris, R.J. (Ed). *ANARE Research Notes Number 92*. Pp. 144 – 160.

Olson, J. *and* Fraser, B.J. (1994). Conjugate ULF pulsations in the cusp. *The initial results from STEP facilities and theory campaigns*. COSPAR colloquia series, Vol. 5. Pp 205 – 212.

APPENDIX A.

SETTING THE VELOCITY PROJECTION VECTORS FOR EACH ARRAY LEG

(i) Calculation of projection velocities

For a particular leg of the array where ΔS_i is the array leg length for leg i in km.

$i = 1$	Davis – Law Base	$\Delta S_1 = 112$ km	(A1a)
$i = 2$	Davis – Plateau Site	$\Delta S_2 = 127$ km	(A1b)
$i = 3$	Law Base – Plateau Site	$\Delta S_3 = 148$ km	(A1c)

The time lag Δt_i of the waveform between two stations is decided by the correlation analysis and v_i is the projection velocity

$$\text{if} \quad \Delta t_i \neq 0 \text{ then } v_i = \frac{AS_i}{\Delta t_i}. \tag{A2}$$

The largest possible error in Δt is 0.045 s as the sampling rate is 0.1 s and the timing is accurate to 0.05 s. So the possible upper and lower values of the velocity projections are

$$v_{i+} = \frac{\Delta S_i}{(\Delta t_i - 0.045)} \tag{A3a}$$

$$v_{i-} = \frac{\Delta S_i}{(\Delta t_i + 0.045)} \tag{A3b}$$

for a positive Δt_i and the signs reversed for a negative Δt_i representing time lags in either direction along the array leg.

If $\Delta t = 0$ then

$$v_{i+} = v_{i-} = \frac{\Delta S_i}{(0.05)} \tag{A4}$$

with the direction of the velocity to be calculated later.

(ii) (x, y) components of each velocity projection vector tip

The angle that each array leg reference line makes with the +Y axis is converted to an effective angle with respect to the X axis for use in the trigonometry.

$$\alpha = 292.0° \quad \alpha_{eff} = 292.0 - 270.0 = 22.0° \text{ for Davis – Law Base} \tag{A5a}$$

$\beta = 169.0°$ $\beta_{eff} = 169.0 - 90.0 = 79.0°$ for Law Base – Plateau Site (A5b)

$\gamma = 33.3°$ $\gamma_{eff} = 90.0 - 33.3 = 56.7°$ for Plateau Site – Davis (A5c)

The sign of the x and y components of the velocity projection vector depends on the direction of propagation along each array leg which determines the quadrant that the velocity projection vector is in.

Davis → Law Base

$$\Delta t_{DL} < 0,\ x_1 < 0,\ \text{signx}_1 = -1,\ y_1 > 0,\ \text{signy}_1 = +1 \quad \text{(A6a)}$$

Law Base → Davis

$$\Delta t_{DL} > 0,\ x_1 > 0,\ \text{signx}_1 = +1,\ y_1 < 0,\ \text{signy}_1 = -1 \quad \text{(A6b)}$$

Davis → Plateau Site

$$\Delta t_{DP} < 0,\ x_2 < 0,\ \text{signx}_2 = -1,\ y_2 < 0,\ \text{signy}_2 = -1 \quad \text{(A6c)}$$

Plateau Site → Davis

$$\Delta t_{DP} > 0,\ x_2 > 0,\ \text{signx}_2 = +1,\ y_2 > 0,\ \text{signy}_2 = +1 \quad \text{(A6d)}$$

Law Base → Plateau Site

$$\Delta t_{LP} < 0,\ x_3 > 0,\ \text{signx}_3 = +1,\ y_3 < 0,\ \text{signy}_3 = -1 \quad \text{(A6e)}$$

Plateau Site → Law Base

$$\Delta t_{LP} > 0,\ x_3 < 0,\ \text{signx}_3 = -1,\ y_3 > 0,\ \text{signy}_3 = +1 \quad \text{(A6f)}$$

Hence

$$x_1 = v_{DL} \cdot \cos\alpha_{eff} \cdot \text{signx}_1 \quad \text{(A7a)}$$

$$y_1 = v_{DL} \cdot \sin\alpha_{eff} \cdot \text{signy}_1 \quad \text{(A7b)}$$

$$x_2 = v_{DP} \cdot \cos\beta_{eff} \cdot \text{signx}_2 \quad \text{(A7c)}$$

$$y_2 = v_{DP} \cdot \sin\beta_{eff} \cdot \text{signy}_2 \quad \text{(A7d)}$$

$$x_3 = v_{LP} \cdot \cos\gamma_{eff} \cdot \text{signx}_3 \quad \text{(A7e)}$$

$$y_3 = v_{LP} \cdot \sin\gamma_{eff} \cdot \text{signy}_3 \quad \text{(A7f)}$$

(iii) Zero lag problem

If $\Delta t_i = 0 \Rightarrow v_i \rightarrow \infty$ so the wavefront is nearly parallel to that leg of the array. Because of the sampling rate and the timing accuracy $\Delta t_i = 0 \Rightarrow \Delta t_i \leq 0.05$ s so we can set the lag to either + 0.05 s or -0.05 s. There is no information about which sign to use. The method selected is to choose the velocity vector tip (+ or -) that is closest to the tips of the other two velocity projections for geometric consistency.

For example if $\Delta t_{DL} = 0$ the distance between the possible tip of the velocity projection vector v_{DL} at point A (x_1, y_1) using -0.05 s and that at B $(-x_1, -y_1)$ using +0.05 s must be determined. The tip of v_{PD} is point 2 (x_2, y_2) and the tip of v_{PL} is point 3 (x_3, y_3).

Distance of point A from point 2 is

$$D1 = ((x_2 - x_1)^2 + (y_2 - y_1)^2)^{1/2}. \qquad \text{(A8a)}$$

Distance of point A from point 3 is

$$D2 = ((x_3 - x_1)^2 + (y_3 - y_1)^2)^{1/2}. \qquad \text{(A8b)}$$

Distance of point B from point 2 is

$$D3 = ((x_2 + x_1)^2 + (y_2 + y_1)^2)^{1/2}. \qquad \text{(A8c)}$$

Distance of point B from point 3 is

$$D4 = ((x_3 + x_1)^2 + (y_3 + y_1)^2)^{1/2}. \qquad \text{(A8d)}$$

If $D1 + D2 < D3 + D4$ then point A (Δt_{DL} = -0.05 s) is the best solution for the tip of vector v_{DL}.

If $D1 + D2 > D3 + D4$ then point B (Δt_{DL} = +0.05 s) is the best solution for the tip of vector v_{DL}.

This will represent the the most linear wavefront that it is possible to construct from the time lags.

(iv) Reconstructing the wavefront

The next step is to fit a wavefront to the tips of the three velocity projection vectors. The two methods for doing this are outlined in Appendices B and C.

APPENDIX B.

WAVEFRONT FITTING TO THE VELOCITY PROJECTION VECTORS

Method 1

Using a least squares fit for a linear wavefront to the tips of the three velocity projection vectors. Refer Figure 8.

(i) Calculate the (x, y) components of the upper and lower velocity projection vectors to find the uncertainties of the y data points to use in the linefit

The (x, y) components of the three velocity projection vectors (x_1, y_1), (x_2, y_2) and (x_3, y_3) are given by equations (A7a – f).

The (x, y) components of the possible upper and lower velocity projections $x_1\pm$ and $y_1\pm$ are given by

$$x_{1\pm} = v_1 \pm \cdot \cos\alpha_{eff} \cdot \text{signx}_1 \tag{B1a}$$

$$y_{1\pm} = v_1 \pm \cdot \text{cin}\alpha_{eff} \cdot \text{signy}_1 \tag{B1b}$$

$$x_{2\pm} = v_2 \pm \cdot \cos\beta_{eff} \cdot \text{signx}_2 \tag{B1c}$$

$$y_{2\pm} = v_2 \pm \cdot \sin\beta_{eff} \cdot \text{signy}_2 \tag{B1d}$$

$$x_{3\pm} = v_3 \pm \cdot \cos\gamma_{eff} \cdot \text{signx}_3 \tag{B1e}$$

$$y_{3\pm} = v_3 \pm \cdot \sin\gamma_{eff} \cdot \text{signy}_3 \tag{B1f}$$

where the upper and lower velocity projections $v_1\pm$ are given by equations (A3a-b) and the indices 1 to 3 describe the array legs as in equations (A1a-c).

The uncertainties in the y components required by the linefit routine are

$$\sigma_{y1} = (|y_{1^+} - y_1| + |y_1 - y_{1^-}|)/2 \tag{B2a}$$

$$\sigma_{y2} = (|y_{2^+} - y_2| + |y_2 - y_{2^-}|)/2 \tag{B2b}$$

$$\sigma_{y3} = (|y_{3^+} - y_3| + |y_3 - y_{3^-}|)/2 \ . \tag{B2c}$$

(ii) Least squares line of best fit

An algorithm is called in the computer software that performs a Bevington least squares fit of a line to the three points representing the tips of the velocity projection vectors. The modes that can be chosen for weighting the fit are instrumental, statistical or no weighting. No weighting has been used for the present.

The line is represented in the form

$$y = A + Bx \tag{B3}$$

with

A = y intercept of the fitted line

σ_A = the standard deviation of A

B = y intercept of the fitted line

σ_B = the standard deviation of B

R = The linear correlation coefficient,
how effectively the line fits the data with R=1 being a perfect fit.

(iii) Calculate the total velocity vector

To do this the equtaion of the wavefront must first be converted from the format of (B3) to the 'normal' form

$$Qx + Ry + S = 0\ . \tag{B4}$$

To do this two points are found on the line by setting x to +100 and -100 and finding y from equation (B3). If these two points are (x_A, y_A) and (x_B, y_B) then

$$Q = y_B - y_A \tag{B5a}$$

$$R = x_A - x_B \tag{B5b}$$

$$S = x_B . y_A - x_A . y_B\ . \tag{B5c}$$

The velocity is determined by

$$V_T = \left| \frac{S}{\sqrt{(R^2 + Q^2)}} \right| . \tag{B6}$$

The angle of the velocity to the vector to the x-axis is

If $Q \neq 0$ then

$$\theta_T = |\text{ArcTan}(R/Q)| \tag{B7a}$$

If $Q = 0$ then

$$\theta_T = \Pi/2 \tag{B7b}$$

and the quadrant can be found by examining the x and y intercepts of the wavefront from

equation (B4).

(iv) Uncertainties in the direction and velocity

The uncertainty in the velocity is found by determining the velocities when the wavefront is moved by σ_A. If x = +100 and -100 are substituted into equation (B3) firstly using $A + \sigma_A$ and then $A - \sigma_A$ in place of A. Thus Q, R and S are found for the $A + \sigma_A$ and $A - \sigma_A$ cases using equations (B5a-c) and the velocities $V_{\sigma+}, V_{\sigma-}$ for the two cases using equation (B6).

Then

$$\Delta V_T = \left| V_{\sigma+} - V_{\sigma-} \right| . \qquad \text{(B8)}$$

The uncertainty is found in a similar manner using equation (B3) again but varying B by σ_B. Then Q, R and S for the two cases are again found using (B5a-c) and the angles $\theta_{\sigma+}, \theta_{\sigma-}$ by (B7a-b).

Then

$$\Delta\theta_T = \left| \theta_{\sigma+} - \theta_{\sigma-} \right| . \qquad \text{(B9)}$$

APPENDIX C.

WAVEFRONT FITTING TO THE VELOCITY PROJECTION VECTORS

Method 2

Join each pair of velocity projection vector tips with a wavefront and average the three resultant wavefront velocities and directions. Refer Figure 9.

(i) Finding the equation of the line (wavefront) joining pairs of velocity projection vector tips

For each wavefront use the 'normal form' of the equation of a line

$$Ax + By + C = 0 \qquad \text{(C1)}$$

The parameters A, B and C can be calculated for each line by substituting the two velocity projection vector tips in the 'point form' equation of the line in equations (C2) and (C3).

e.g. The line joining the Davis – Law Base and Davis – Plateau Site velocity projection tips (x_1, y_1) and (x_2, y_2) is represented by

$$\frac{(y - y_1)}{(y_1 - y_2)} = \frac{(x - x_1)}{(x_1 - x_2)} \quad \text{point form of the linear wavefront equation} \qquad \text{(C2)}$$

$$\therefore (y - y_1)\cdot(x_1 - x_2) = (y_1 - y_2)\cdot x + (y_2 - y_1)\cdot x_1$$

$$\therefore (y_1 - y_2)\cdot x + (x_1 - x_2)\cdot y + (x_1 \cdot y_2 + x_2 \cdot y_1) = 0. \qquad \text{(C3)}$$

Equate this with the normal form to find the parameters A, B and C. (x_1, y_1) etc, are found in equations (A7a-f). Let the following indices represent the three wavefront lines joining pairs of velocity projection vectors.

I = Davis – Law Base/Davis – Plateau Site
II = Davis – Law Base/Law Base – Plateau Site
II = Davis – Plateau Site/Law Base – Plateau Site

So...

$$A_I = y_2 - y_1 \qquad \text{(C4a)}$$

$$B_I = x_1 - x_2 \qquad \text{(C4b)}$$

$$C_I = x_2 y_1 - x_1 y_2 \qquad \text{(C4c)}$$

$$A_{II} = y_3 - y_1 \qquad \text{(C5a)}$$

$$B_{II} = x_1 - x_3 \qquad \text{(C5b)}$$

$$C_{II} = x_3y_1 - x_1y_3 \tag{C5c}$$

$$A_{III} = y_3 - y_2 \tag{C6a}$$

$$B_{III} = x_2 - x_3 \tag{C6b}$$

$$C_{III} = x_3y_2 - x_2y_3 \tag{C6c}$$

So, for example the Davis – Law Base/Davis – Plateau Site wavefront can be represented by

$$A_I = y_2 - y_1 = v_{DP} \cdot \sin\beta_{eff} \cdot \text{signy}_2 - v_{DL} \cdot \sin\alpha_{eff} \cdot \text{signy}_1 \tag{C7a}$$

$$B_I = x_1 - x_2 = v_{DL} \cdot \cos\alpha_{eff} \cdot \text{signx}_1 - v_{DP} \cdot \cos\beta_{eff} \cdot \text{signx}_2 \tag{C7b}$$

$$\begin{aligned} C_I &= x_2y_1 - x_1y_2 \\ &= (v_{DP} \cdot \cos\beta_{eff} \cdot \text{signx}_2).(v_{DP} \cdot \cos\beta_{eff} \cdot \text{signx}_2) \\ &\quad -(v_{DL} \cdot \cos\alpha_{eff} \cdot \text{signx}_1) \cdot (v_{DP} \cdot \sin\beta_{eff} \cdot \text{signy}_2) \end{aligned} \tag{C7c}$$

etc.

(ii) Velocities and directions of the three wavefronts

So the velocity of each wavefront is the length of the normal to the wavefront from the origin and the direction is that of the normal.

$$V_I = \frac{C_I}{\sqrt{(B_I^2 + C_I^2)}} \tag{C8a}$$

$$\Theta_I = \text{Arc tan}(B_I / A_I) \tag{C8b}$$

and similarly for II and III.

The direction Θ is in an unknown quadrant and to find that quadrant we need to check the x and y axis intercepts of the wavefront. From the normal Equation (C1)

$$\text{x intercept, } y = 0 \;\Rightarrow\; x = \frac{-C}{A} \tag{C9a}$$

$$\text{y intercept, } x = 0 \;\Rightarrow\; y = \frac{-C}{B}. \tag{C9b}$$

If, for example, $A_1 = 0$ then $y_1 = y_2$ and the wavefront is parallel to the X axis making the velocity direction north or south, parallel to the Y axis. North or south velocity can be determined from the sign of the Y intercept. Similarly if $B_1 = 0$ then $x_1 = x_2$ and the wavefront is parallel to the Y axis making the velocity direction east or west, parallel to the

X axis. East or west velocity can be determined from the sign of the X intercept.

So if

Θ = angle of the propagation direction to the X axis in an unknown quadrant. (C10a)

Φ = direction of propagation with respect to LMN (C10b)

Φ' = wave source direction = $\Phi \pm 180°$ (C10c)

Examine the X and Y intercepts to determine the quadrant.

$y = 0,\ x > 0,\ x = 0,\ y > 0$ => 1st Quadrant

$$\therefore \Phi = 90 - \Theta,\ \Phi' = \Phi + 180 \quad \text{(C11a)}$$

$y = 0,\ x > 0,\ x = 0,\ y < 0$ => 2nd Quadrant

$$\therefore \Phi = 90 + \Theta,\ \Phi' = \Phi + 180 \quad \text{(C11b)}$$

$y = 0,\ x < 0,\ x = 0,\ y > 0$ => 3rd Quadrant

$$\therefore \Phi = 270 - \Theta,\ \Phi' = \Phi - 180 \quad \text{(C11c)}$$

$y = 0,\ x < 0,\ x = 0,\ y > 0$ => 4th Quadrant

$$\therefore \Phi = 270 + \Theta,\ \Phi' = \Phi - 180 \quad \text{(C11d)}$$

(iii) Finding the total velocity vector

To add the three velocity vectors from the wavefronts we require their x and y components as we have calculated them in (V, Θ) form. These are simply

$$V_x = V.\cos\Theta \quad \text{(C12a)}$$

$$V_y = V.\sin\Theta \quad \text{(C12b)}$$

for V_I to V_{III} with the $\pm$ sign depending on the quadrant of the velocity vectors.

Adding the components of the three wavefront vectors gives the components of the total velocity vector.

$$V_{Tx} = (V_{Ix} + V_{IIx} + V_{IIIx})/3 \quad \text{(C13a)}$$

$$V_{Ty} = (V_{Iy} + V_{IIy} + V_{IIIy})/3 \quad \text{(C13b)}$$

$$V_t = \sqrt{V_{Tx}^2 + V_{Ty}^2} \qquad \text{(C13c)}$$

$$\Theta_T = \left|\text{Arc}\tan(V_{Ty}/V_{Tx})\right| \qquad \text{with respect to LMN} \qquad \text{(C13d)}$$

Calculate Φ_T from the quadrant of Θ_T obtained from the signs of V_{Tx} and V_{Ty} in a manner similar to equations (C11).

A rotation by $\varepsilon = 27°$ converts the directions to those with respect to decreasing L-value.

Finally, the uncertainties are

$$\Delta V_T = ((V_T - V_I)^2 + (V_T - V_{II})^2 + (V_T - V_{III})^2)^{1/2} \qquad \text{(C14a)}$$

$$\Delta\Theta_T = ((\Theta_T - \Theta_I)^2 + (\Theta_T - \Theta_{II})^2 + (\Theta_T - \Theta_{III})^2)^{1/2}. \qquad \text{(C14b)}$$

9. SOURCES AND PROPAGATION OF ULF WAVES NEAR THE AUSTRAL POLAR CUSP: IMPLICATIONS FOR MAPPING THE DYNAMICS OF HIGH LATITUDE GEOSPACE

D.A. Neudegg[1,2], G.B. Burns[2], B.J. Fraser[1], F.W. Menk[1], R.J. Morris[2], H.J. Hansen[1] and M.J. Underwood[2]

[1] Space Plasma Waves Group
University of Newcastle
Callaghan NSW 2308
Australia

[2] Atmospheric and Space Physics
Antarctic Division
Kingston Tasmania 7050
Australia

ABSTRACT

The polar cusp regions are important in coupling high latitude magnetospheric energy sources directly to the ionosphere. ULF waves are one of the processes by which this coupling is realised. To study the source regions and propagation of Pc1-2 (0.1 – 5 Hz) ULF waves at cusp latitudes an array of closely spaced induction magnetometers was deployed beneath the average cusp projection during the 1992 Antarctic winter. Analysis of the magnetic pulsation data shows that wave sources are poleward of the array at low geomagnetic activity and equatorward at high activity. The source locations show east to west motion with time, centred on local noon, evolving with time and magnetic activity in a similar manner to that expected of the cusp and boundary layer. The pulsation event directions have been intercalibrated with PACE radar and DMSP satellite cusp signatures. Group velocities in the range 300 – 800 km s^{-1} with a mean of 450 km s^{-1} and strong attenuation of the waves over 650 km are consistent with wave propagation in the ionospheric duct. These results indicate cusp or boundary layer sources of Pc1-2 ULF waves which propagate away from the source in the ionospheric F_2 waveguide. A closely spaced (< 200 km) magnetometer array, measuring the arrival angles of propagating Pc1-2 waves, is therefore a feasible ground based technique for monitoring the location of the cusp and boundary layer projections over short time scales (of the order of tens of minutes) with varying geomagnetic parameters.

9.1 INTRODUCTION

The projection of magnetospheric features onto the polar ionosphere, particularly the cusp and boundary layer, has long been associated with various frequency components in the spectrum of high latitude Pc1-2 (0.1 – 5 Hz) ULF wave activity. Studies have associated the occurrence of Pc1-2 waves with the proximity of the polar cusp (Heacock 1974; Bolshakova et al. 1980; Morris and Cole 1991; Menk et al. 1992). These waves have a peak occurrence near local noon, maximum amplitude under or near the average cusp location, and a source region that appears to move equatorward with increasing

geomagnetic activity.

The cusp and boundary layer are not the only possible sources of Pc1-2 wave activity observed at high latitudes. A study of 0.1 – 0.4 Hz pulsations classified as Pc1/2 at cusp and plasmapause latitude stations indicated source region locations between the plasmapause and the auroral zone, equatorward of the cusp/boundary layer projections (Popecki et al. 1993). Pc1 >0.4 Hz observed in the same study are believed to have originated near the plasmapause, also equatorward of polar magnetospheric projections.

The aim of this investigation was to study Pc1-2 ULF wave source regions and propagation characteristics near the polar magnetospheric cusp with high temporal and spatial resolution (Neudegg et al. 1995). Measurements that resolve the direction of arrival of the waves as shown in this study can be used to distinguish between possible source regions. The distribution of event velocities and general wave attenuation can be compared to predictions for pulsation propagation in the ionospheric duct.

It is believed that Pc1-2 ULF waves observed in this study propagate away from their sources by ducting in the ionospheric waveguide. Previous observations have been made of Pc1 waves in the 0.2 – 5 Hz frequency range propagating at middle and low latitudes in the ionospheric duct (Fraser 1975; Manchester 1970) and it is an accepted mechanism for propagation of ULF wave energy. Velocities, lower cutoff frequencies and attenuation factors for hydromagnetic waves propagating in the duct have been modelled for a variety of ionospheric conditions (Greifinger and Greifinger 1968) enabling predictions to be made concerning high latitude propagation. These compare favourably with the results presented here.

9.2 EXPERIMENT

9.2.1 *Magnetometer array*

The three station magnetometer array deployed in this experiment was based around the Antarctic cusp latitude station Davis (74.6°S, 102.3°E in PGM-88 coordinates, Baker and Wing 1988). A site on the polar plateau 150 km inland from Davis and another site at Law Base, 120 km magnetically west of Davis were deployed for this study by vehicle traverse (Neudegg et al. 1994a). The array deployment and data recording campaign were conducted during the austral winter (27 July to 8 August 1992) due to occurrence and amplitude maxima of Pc1-2 in winter at Davis (Morris and Cole 1991). A fourth station, at Mawson (70.5°S, 92.1°E in PGM-88 coordinates), 630 km magnetically north-west of Davis, allowed comparison of event waveforms and amplitudes over larger separations. The magnetometer array itself has been described in detail in an earlier publication (Neudegg et al. 1994a). The magnetometer effective field of view overlap for site separations of less than 200 km as the instruments respond to ionospheric currents within 100 km of the zenith (Olson and Fraser 1994). A minimum station separation of 100 km is therefore required for propagation studies of ULF waves. It has previously been established that common Pc1-2 wave activity is rare over the 630 km distance between Davis and Mawson (Francke et al. 1993), setting an upper bound for site separation.

9.2.2 *Data coverage*

During the course of the campaign, data was recorded continuously at all three sites in the triangular array with occasional gaps for disk changes and equipment malfunctions. Timing was maintained at the required level of accuracy for the majority of the campaign, and intervals with incorrect timing were noted. Further data gaps were caused by precipitation static at the Plateau site, and Law Base manifested high frequency noise caused by snow blowing across the plastic induction coil covers during blizzards. This was solved by burying the coils in hard snow. Despite these gaps, enough data was collected at all three sites with good timing to enable a study to be conducted across a wide range of geomagnetic activities and times, which is necessary for the work described here. For a true synoptic study of the variation of wave source location with varying geomagnetic conditions, data must be recorded across the spectrum of conditions at each time of day. This data coverage can be built up over several days to fill in each time and geomagnetic activity combination. The index chosen for this broad study of wave source location variation is K_p but this applies to the range of geomagnetic indices (i.e. IMF B_z, AE). A range of K_p values from 1^- to 6^- were covered during the campaign. The interval 0400 – 1500 UT where pulsations associated with the cusp and boundary layers are most likely to be found have a good spread of low, medium and high K_p data. Data during periods of $K_p < 3^-$ are the most common, little data for $K_p = 3, 3^+$, good representation at $K_p = 4^-, 4$, no data for $K_p = 4^+, 5$ and some coverage at $K_p = 5, 5^+$. This enabled the current study focusing on the high and low ends of the K_p spectrum during cusp/cleft transit periods to be performed.

9.2.3 *Data analysis*

The methods used are described in detail elsewhere (Neudegg et al. 1994b) and will only be outlined here. ULF wave events were chosen from three quiet and one active day, 4 – 5 hours either side of local noon. Pc1-2 wave events such as unstructured and discrete 0.15 – 0.4 Hz emissions (Morris and Cole 1985; Menk et al. 1992) were selected for propagation analysis from dynamic spectra on days of low geomagnetic activity. High frequency noise generally obscured band limited emissions in the spectra during days of high activity. Hence event durations on active days were obtained from the filtered Pc1-2 channel time series, and a frequency band of 0.5 – 2 Hz within the Pc1-2 range was selected to perform propagation analysis.

The bandpass filtered events selected using the above criteria, typically of 5 to 15 minutes duration, were divided into one minute time segments. Each segment was cross-correlated between the pairs of sites comprising each of the three legs of the array. The time lags of the segments from the cross-correlation were examined as a function of the magnitude of the correlation coefficient. The wave activity chosen from either the dynamic spectra or the 0.5 – 2 Hz band within the Pc1-2 time series exhibited consistent time lags for signals between each pair of sites with correlation coefficients generally greater than 0.75. Both H and D channels showed similar time lags between each pair of sites. Hence a value for the lag of the wave along each leg of the array was established for propagating wave events.

Wavefront reconstruction was used to establish the direction and velocity of events

(Neudegg et al. 1996). A plane wavefront passing across the array with the lags representing a projection of wave velocity on each array leg was assumed as a first approximation. Although it might be expected that a curved wavefront would be the best description for many events (Althouse and Davis 1978), the observed curvature for most wave events is slight and the difference in direction and velocity from a plane wavefront approximation is small.

On days of high activity the Pc2 (0.1 – 0.2 Hz) frequency component during an event period showed high values of correlation coefficient between pairs of sites, but no consistency of lags amongst the waveform segments. This was interpreted as the Pc2 component not propagating between the sites, but being recorded at spaced stations due to their overlapping field of view. Hence these signals were not considered for propagation analysis.

9.3 RESULTS

9.3.1 *Wave angle of arrival variation with geomagnetic activity*

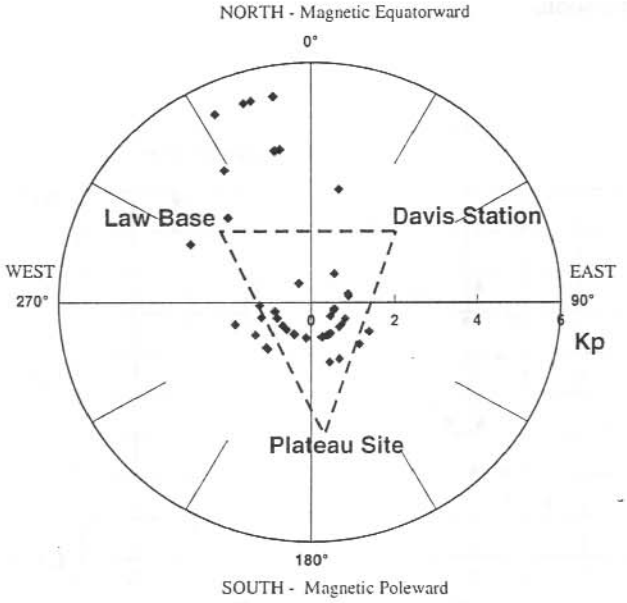

Figure 1. Angle of arrival of Pc1-2 events as a function of K_p. Events were taken from the 1st to the 3rd and the 7th of August 1992. The 1st to the 3rd August were days of low K_p and the 7th was high K_p. The events were of varying bandwidths in the 0.15 – 2 Hz band from the 0500 – 1300 UT interval with local magnetic noon at 0945 UT. The average uncertainty of arrival angles from the wavefront reconstruction is eight degrees. The co-ordinate system is array centred; North is invariant magnetic equatorward, South or poleward refers toward the south invariant pole. A rotation of 27 degrees anticlockwise for the zero degrees reference converts the co-ordinate system to local magnetic north.

A total of 42 propagating wave events, spanning a range of K_p from 1^- to 5^+ and local daytime from 0900 – 1700 MLT, with high interstation correlations and distinct waveform lags, were chosen to perform a synoptic analysis of event velocities and angles of arrival. Arrival angles for these events are shown as a function of planetary magnetic activity index K_p in Figure 1. The coordinate system is centred on the array, and uses the invariant magnetic equatorward direction as a north reference. Array geometry is superimposed on the coordinate system for orientation. Angles of arrival were found to be poleward of the array for low planetary magnetic activity and equatorward for high activity. It is assumed that the pulsation sources lie in the direction of the angle of arrival, 180° from the wave propagation direction.

9.3.2 *Wave angle of arrival variation with time*

The relationship between arrival angles of events with the time of the observation is shown in Figure 2. Only events with $K_p < 2$ have been used and were selected from three days of data. This places all the sources in a southerly direction (magnetically poleward) of the array. There is a general east to west motion of the wave arrival angles with time, with sources due south (poleward) of the array between 0700 – 1000 UT, encompassing both local solar and magnetic noons.

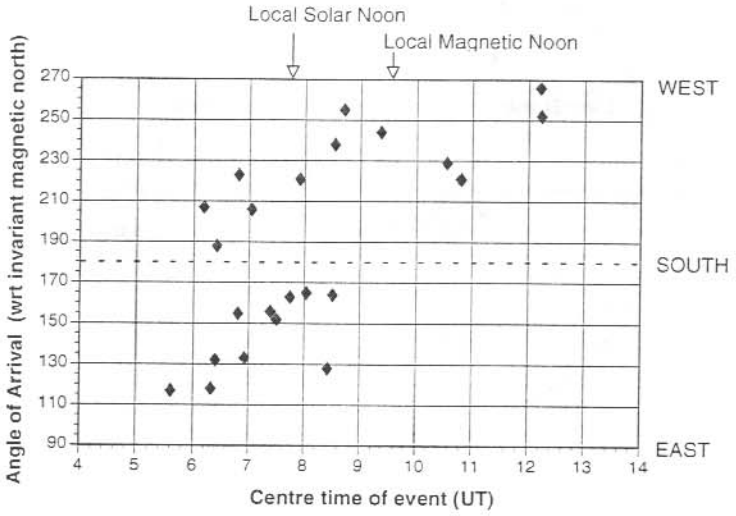

Figure 2. Angle of arrival of Pc1-2 events as a function of the centre time of the event (UT). The events are usually of 10 – 20 minutes duration and are a subset of those in Figure 1 taken from periods of low geomagnetic activity. $K_p < 2$ and all angles of arrival are poleward of the array. There is a progression of source direction from east to west with time and the source(s) pass south or poleward of the array around noon. This is the general behaviour expected of the cusp/boundary layer projections as they remain in the Sun-Earth line and the Earth rotates beneath them in a manner similar to the sub-solar point.

9.3.3 *Wave velocity measurements*

Interstation group velocities of events are shown by the histogram in Figure 3. These have been binned in 50 km s^{-1} columns, an interval typical of the velocity uncertainties from the wavefront reconstruction technique. The velocities range from 150–750 km s^{-1} with a significant peak at 350–400 km s^{-1} and a mean of 450 km s^{-1}.

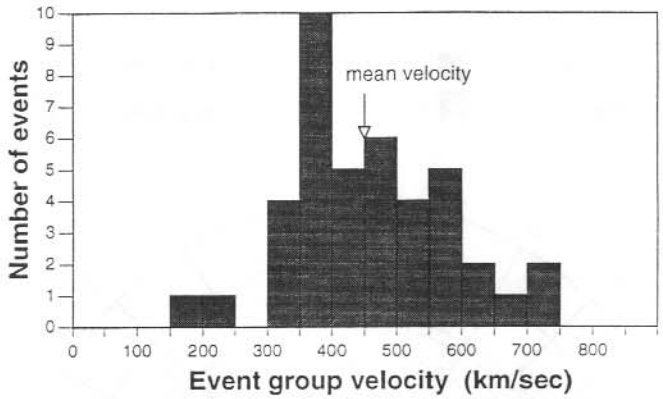

Figure 3. Histogram of event velocities. The events are those used in Figure 1. The average percentage uncertainty in the velocities from the wavefront reconstruction is 13% of the calculated velocity. The average uncertainty is 58 km s^{-1} (ie, about one bin size). These velocities are typical of waves propagating in the ionospheric F_2 duct parallel to the Earths surface. Predicted wave velocities vary with ionospheric conditions for day/night and solar maximum/minimum. The recording campaign was conducted across both day and night due to the short winter days, and the velocities encompass those predicted for the various ionospheric conditions.

9.3.4 *Intercalibration with spacecraft and radar data*

A trial comparison was performed between ULF wave source directions from the magnetometer array data and accepted signatures of high latitude geospace features from spacecraft and radar. The intercalibration of spacecraft and ground based data, particularly radar, is now an accepted method of maximising the different and complementary aspects of each platform (Baker et al. 1990; Watermann et al. 1994a, 1994b). This allows simultaneous examination of phenomena in the magnetosphere and their effects on the ionospheric projections below. The database of propagating wave events is a unique set of ground based measurements to compare with those from spacecraft. In this case the satellite and radar measurements of the cusp and boundary layers are used as a reference to compare with the wave angle of arrival.

Defence Meteorological Satellite Program (DMSP) is a series of United States satellites with charged particle flux and energy detectors. The particle spectra from these satellites have been used to determine the location of distinct high latitude plasma environments – regions

of the magnetosphere around 800 km altitude – just above the ionosphere (Newell and Meng 1988, 1992). As these regions are dynamic in time, the spacecraft provides snapshots of where these regions are as it passes through them, but lacks the ability to track them with time. The topology of these regions is believed to remain constant, although their shape may alter with varying geomagnetic conditions. The map of these high latitude projections onto the ionosphere is shown for average conditions in Figure 4.

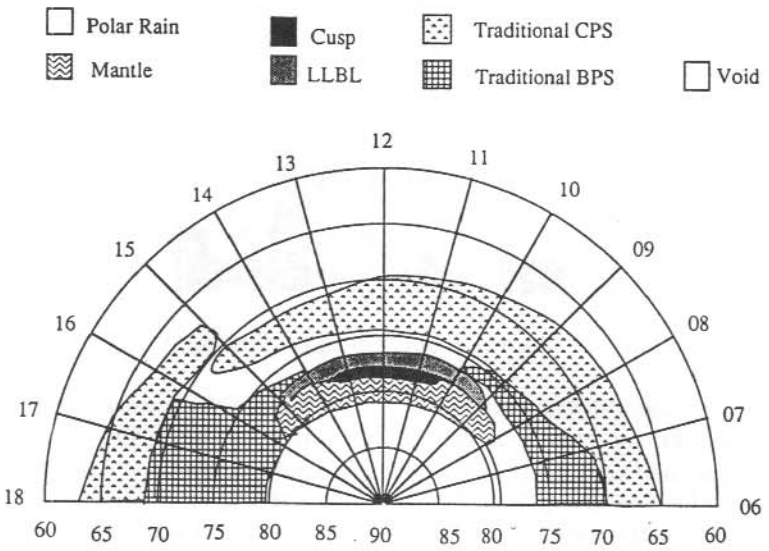

Figure 4. A map of the ionosphere to the magnetosphere based on plasma characteristics. The radial axis represents geomagnetic latitude and the angular axis local geomagnetic time. LLBL = Low Latitude Boundary Layer, CPS=Central Plasma Sheet, BPS = Boundary Plasma Sheet. Refer to the geospace topology in Figure 8. This is an average over all interplanetary magnetic field and geomagnetic activity conditions. (After Newell and Meng 1992.)

Polar Anglo-American Conjugacy Experiment (PACE) is an HF coherent backscatter radar measuring 10 m scale ionospheric electron density irregularities located at Halley Bay, Antarctica. A typical PACE scan containing what is believed to be a cusp signature is shown in Figure 5. A typical cusp signature has a broad spectral width and significant velocities away from the radar. The radar coverage is shown in Figure 6 and includes the important high latitude projections of the magnetosphere onto the ionosphere. The location of the 1992 temporary magnetometer array is shown for comparison. It should be noted that the fields of view do not overlap, hence the need for interpolation of the cusp signature position backwards in time from where it was observed in beam 8 of the radar. Approximate position of the beam 8 scan is shown by the twin lines in the centre of the radar coverage. Presumed motion of the cusp about the invariant pole is outlined by the

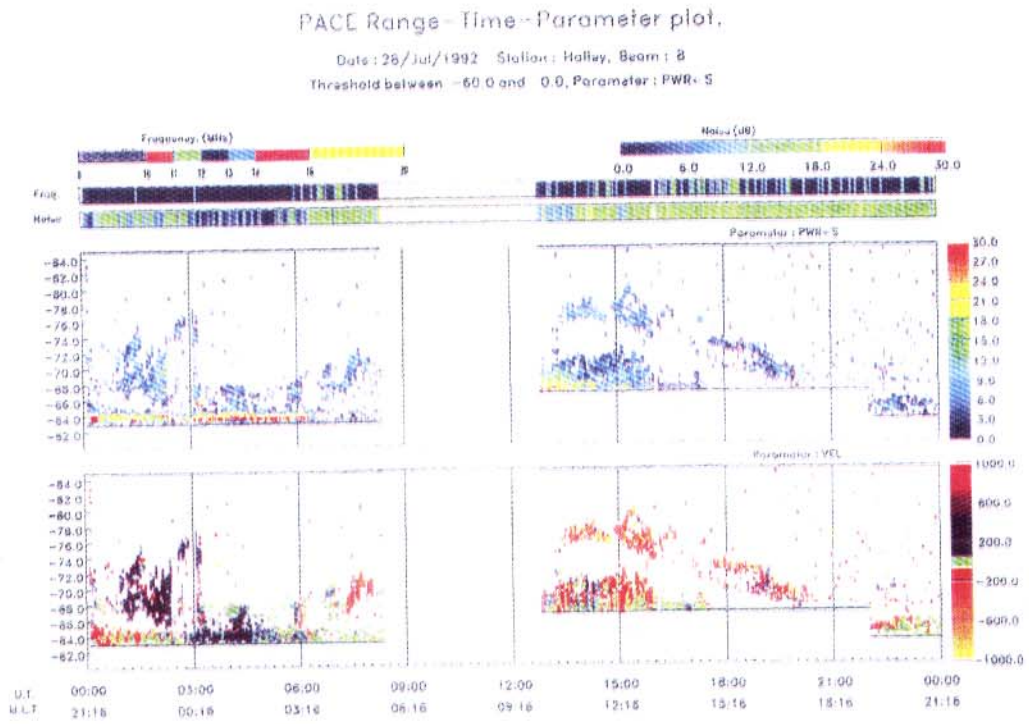

Figure 5. A PACE radar range-time-parameter plot of 28 July 1992 for beam 8, the central beam. The radar scans were performed using frequencies of 12 and 13 MHz. This day was chosen to display the prominent backscattered power from 1300 – 1600 UT between -74 and -80 degrees geomagnetic latitude which is believed to be cusp scatter. This scan is more illustrative of cusp scatter than the signature used for the intercalibration with pulsation direction in Figure 7. It has high backscattered power (6 – 9 dB) from the upper plot and significant negative velocities (-500 to -1000 m s^{-1}), away from the array, in the lower plot. Diagram courtesy of Alan Rodger, Geospace Coupling Group, British Antarctic Survey.

dotted line from the interpolated position near the magnetometer array to the position it was observed in beam 8 of the radar. This is obviously a simplified picture as the motion will be affected by changes in K_P and IMF B_y during this period. The interpolation is discussed in greater depth in the next paragraph.

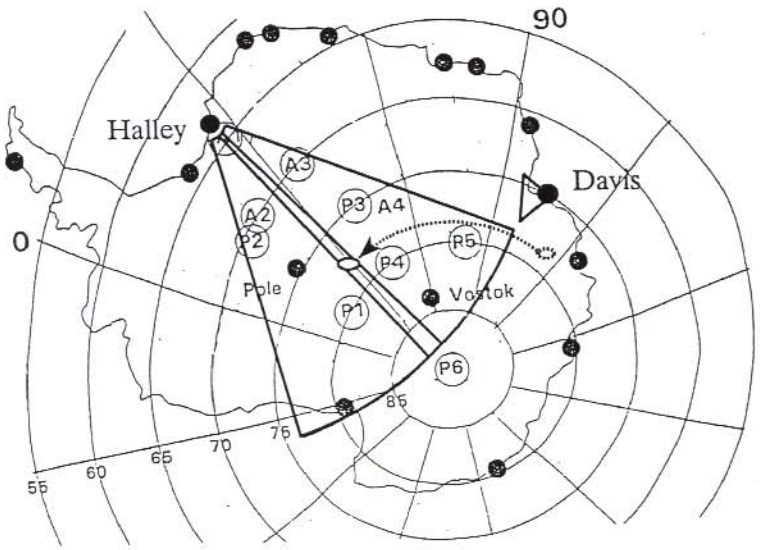

Figure 6. The Halley Bay PACE radar field of view and the 1992 Davis winter temporary magnetometer array. The field of view for the two instruments do not overlap, hence the need for interpolation of the cusp signature position backwards in time from where it was observed in beam 8 of the radar. Approximate position of the beam 8 scan is shown by the twin lines in the centre of the radar coverage. Presumed motion of the cusp about the invariant pole is outlined by the dotted line from the interpolated position near the magnetometer array to the position it was observed in beam 8 of the radar. This is a simplified picture as the motion will be affected by changes in K_P and IMF B_y during this period. The circles represent planned locations of British and American Automated Geophysical Observatories. (After Dudeney 1993.)

Figure 7 shows an intercalibration of angles of arrival for selected events with DMSP satellite and PACE radar cusp and boundary layer signatures from campaign day 8, (3 August 1992). The pulsation events had angles of arrival of 106°-128° with respect to invariant magnetic north and centre times of 0915–0945 UT when the K_p was 1^-. The DMSP regions identified in Figure 7 are an approximation to average magnetospheric projections from particle signatures fitted to measurements from a DMSP F8 satellite pass near 0950 UT. The PACE radar cusp signature was observed at 1300–1400 UT ($K_p = 1^+$) and 75–77° magnetic latitude which is poleward of the magnetometer array latitude.

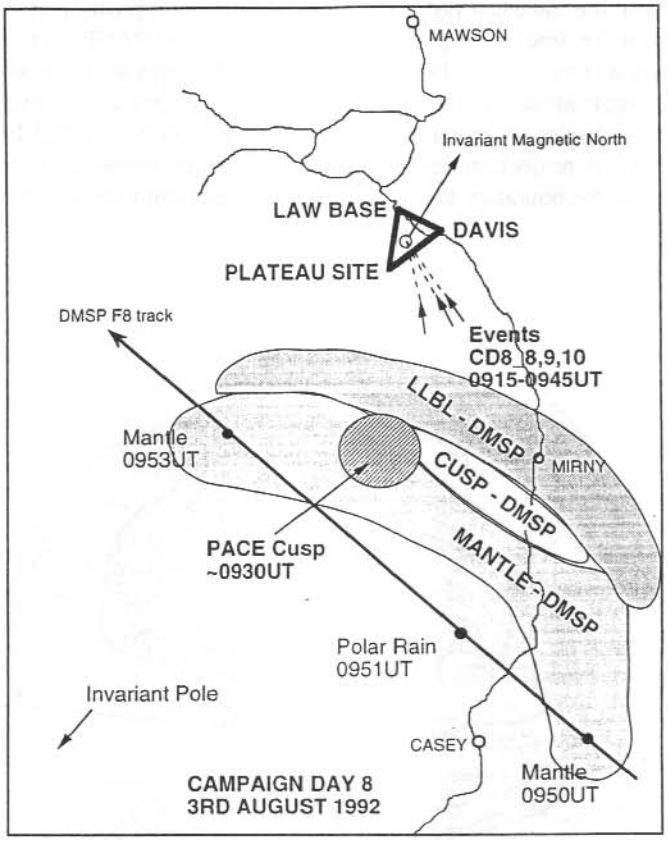

Figure 7. Intercalibration of angles of arrival for three Pc1-2 events with inferred magnetospheric projections from PACE radar and DMSP satellite data on campaign day 8 (3 August 1992). The three pulsation events are CD8–8, 9, 10 from 0915–0945 UT when the K_p value is 1⁻. DMSP average projection shapes and sizes according to Figure 4 have been fitted to a single pass of the DMSP F8 satellite. The times of various samples and the projections observed are shown on the satellite track. The PACE cusp diameter is ~2° based on the original observation at 1300–1400 UT when K_p was 1 and the cusp was in the radar field of view at -77 geomagnetic latitude to the west of the array and poleward of its latitude. As the K_p value was low from 0900–1400 UT it was assumed the PACE cusp signature would have also been poleward of the array at 0930 UT and so it was rotated by 15° per hour east about the invariant pole to interpolate where it may have been at 0930 UT. The three events have source directions that coincide with the assumed position of the DMSP LLBL and cusp projections, and the boundary layer/cleft that is presumed to be equatorward of the PACE cusp interpolated signature.

As the field of view of the radar and the magnetometer array do not overlap, it is necessary to interpolate the position of the PACE cusp signature back in time to where it is likely to have been at the time of the pulsation events. The signature was rotated eastward by 60° (15° per hour) about the invariant pole back to its approximate position at 0930 UT. The K_p value was less at the time of the pulsation events than at the PACE cusp observation so the cusp projection was assumed to be also poleward of the array at the time of the events. Considering these approximations the two inferred cusp locations are relatively close. The pulsation events have angles of arrival in the direction of the DMSP cusp/LLBL projections, and the boundary layer projection that is presumed to be equatorward of the PACE cusp from the topology of the boundary layers and their mapping onto the ionosphere shown in Figure 8.

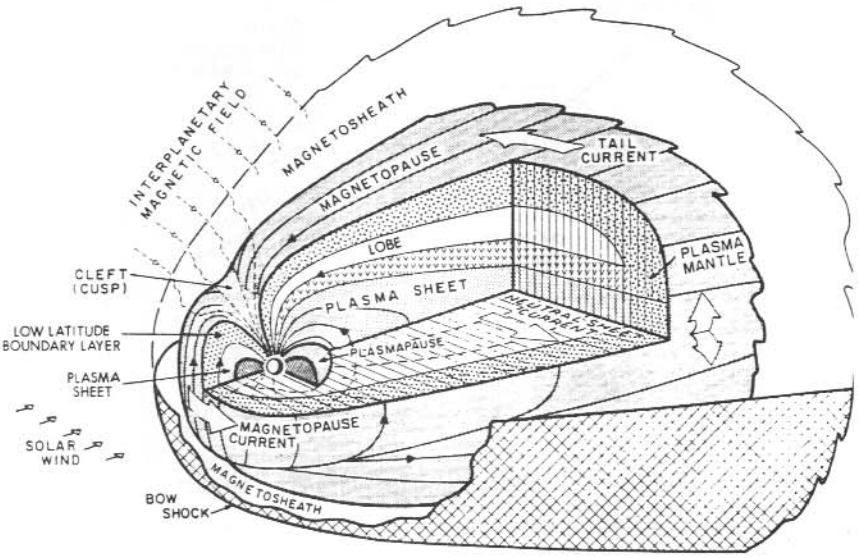

Figure 8. Schematic of geospace topology. This should be cross referenced with Figure 4 and illustrates the fixed topology of the various regions and their mappings onto the ionosphere. Although variations in shape occur with geomagnetic activity, they preserve their relative position with respect to one another.

9.4 DISCUSSION

9.4.1 *Wave angle of arrival variation with K_p*

The latitudinal dependence of the pulsation sources with K_p in Figure 2 shows sources to be equatorward of the array at times of high planetary geomagnetic activity and poleward for low activity. Davis station is expected to be beneath the average cusp location and Pc1-2 occurrence is a maximum at the mid-range K_p value of 2^- (Morris and Cole 1991). The cusp and boundary layer are known to move equatorward of their average location with increased magnetic activity (Meng 1982). The observed wave source locations are

consistent with dynamic variations in cusp/boundary layer location with K_p. Several pulsation events occur when $K_p < 2$ but the local magnetic activity at Mawson measured by K_{maw} is 5. So these events still have sources poleward of the array complying with the general pattern observed for K_p dependence. Thus while local ionospheric current sources in the instrument field of view cause the recorded pulsation's, they appear to be driven by Alfvén wave packets from the magnetosphere.

9.4.2 *Wave angle of arrival variation with time*

The east to west motion of the low K_p, poleward sources shown in Figure 2 is typical of a feature with motion similar to the sub-solar point at 15° in longitude per hour. The fact that the sources pass due south, poleward of the array around local noon strongly implies a connection with the cusp and boundary layer. Particle signatures (Newell and Meng 1988) show the cusp projection maximises in occurrence at local magnetic noon and the low latitude boundary layer (LLBL) projection equatorward of the cusp is longitudinally centred around local noon.

9.4.3 *Intercalibration with spacecraft and radar signatures*

DMSP particle and PACE radar backscatter signatures of magnetospheric projections are accepted references against which to compare pulsation arrival angles (Newell and Meng 1988, 1992; Baker et al. 1990). The basic topology of the boundary layers and their projections shown in Figures 4 and 8 is believed to remain constant as is the overall motion westward with time with respect to the Earth's surface, and equatorward with increasing planetary activity. It appears from Figure 6 that for the wave events considered, the arrival angles align with the cusp/LLBL. The plasmapause would not move poleward of a typical cusp latitude station at times of quiet activity. The cusp/LLBL regions are of limited longitudinal extent but this is not the situation for the plasmapause and plasmatrough. Hence the latter would not be expected to produce a time varying source direction at the array as seen in Figure 2. The observed angles of arrival are not consistent with source regions near the plasmapause or between the plasmapause and the boundary layer.

9.4.4 *Ionospheric duct propagation*

The group velocities shown in Figure 3 are comparable to those expected for ducting in a wave guide mode between the ionospheric F_2 and E layer. Mid-latitude studies have determined a range of velocities, 400–745 km s^{-1} (Manchester 1968, 1970), 540–2500 km s^{-1} (Fraser 1975) and 440–1520 km s^{-1} (Althouse and Davis 1978). Theory predicts group velocities of 360 to 720 km s^{-1} (day-night, sunspot minimum) and 190–400 km s^{-1} (day-night, sunspot maximum) at mid-latitudes (Greifinger and Greifinger 1968). The recording campaign was conducted halfway between sunspot maximum and minimum. Events were selected from hours centred on local noon which had both day and night conditions due to the short winter days. The observed velocities of 300–600 km s^{-1} with a 350–400 km s^{-1} peak from Figure 3 agree reasonably well with the spread predicted across day and night for a mid sunspot cycle. Latitudinal differences in waveguide properties have not yet been investigated in this study.

The low number of observations over the 630 km Davis to Mawson separation found by Francke et al. (1993) is also seen in the lack of common wave activity at these two stations in the present study. This suggests the attenuation to be high over this distance, of order 10 dB/100 km, comparing favourably with amplitude studies performed at high northern latitudes (Hayashi et al. 1981). Previously predicted attenuation lengths are 650 – 950 km and lower cutoff frequencies for the F_2 duct are expected to be 0.13 – 0.36 Hz (Greifinger and Greifinger 1968). Observed lower bounds of Pc1-2 events from the dynamic spectra in this study are in the range 0.13 – 0.35 Hz. The apparent non-propagation between sites of the Pc2 (0.1 – 0.2 Hz) band described in the data analysis may be due to these signals lying below the duct cutoff frequency. The propagating waves observed have properties compatible with hydromagnetic waves in the ionospheric waveguide.

9.5 SUMMARY AND CONCLUSIONS

A closely spaced magnetometer array has been deployed at cusp latitudes during the austral winter and a two week campaign conducted recording magnetic pulsations across a wide range of geomagnetic activity. A database of bandlimited Pc1-2 pulsation wavepackets has been isolated for propagation analysis. The observed wave directions are compatible with sources at or near the cusp and low latitude boundary layer. Local ionospheric sources and other magnetospheric projections seem unlikely to produce the same observations. The propagation velocities of 300 – 600 km s^{-1} and cutoff frequencies of 0.13 – 0.35 Hz for the waves are compatible with hydromagnetic waves propagating in the ionospheric duct. The comparison of PACE radar and DMSP satellite projections with pulsation source directions for selected events shows a coincidence of cusp/LLBL locations with event angles of arrival.

These observations suggest a mechanism whereby Pc1-2 ULF waves, possibly from the boundary layer or exterior cusp, propagate along magnetic field lines down to the low altitude cusp. Some of the energy in the Pc1-2 band above the cutoff frequency is accepted into the ionospheric F_2 region duct and propagates away from the source. The possibility arises of using the direction of arrival of such waves from a closely spaced magnetometer array as a ground based monitor of the location of the cusp and low latitude boundary layer. Future work will probably include monitoring source location variations assumed to be co-located with the cleft over variations in interplanetary magnetic field B_z, B_y components and more subtle graduations in K_p.

9.6 ACKNOWLEDGMENTS

We would like to acknowledge the assistance of the wintering ANARE (Australian National Antarctic Research Expedition) and CHINARE (Chinese Antarctic Research Expedition) expeditioners at Davis and Zhong Shan stations in 1992, and staff of the Australian Antarctic Division for the large logistics program involved in the winter vehicle traverse for the magnetometer data collection. The PACE radar data were kindly supplied by A.S. Rodger of the British Antarctic Survey and the DMSP satellite data by P.T. Newell of John Hopkins University Applied Physics Laboratory. Analysis software was produced by M. Hesse of the Australian Antarctic Division and C. Waters from the University of Newcastle. Financial assistance for this research from an Atmospheric and Space Physics group short contract is gratefully acknowledged.

REFERENCES

Althouse, E.L. *and* Davis, J.R. (1978). Five-station observations of Pc1 micropulsation propagation. *Journal of Geophysics Research 83:*132 – 144.

Baker, K.B. *and* Wing, S.(1988). A new magnetic coordinate system for conjugate studies at high latitudes. *Journal of Geophysics Research 80:*9139 – 9143.

Baker, K.B., Greenwald, R.A., Ruohoniemi, J.M., Dudeney, J.R., Pinnock, M., Newell, P.T., Greenspan, M.E. *and* Meng, C.-I. (1990). Simultaneous HF-radar and DMSP observations of the cusp. *Geophysics Research Letters 17:*1869 – 1872.

Bolshakova, O.V., Troitskaya, V.A. *and* Ivanov, K.G. (1980). High latitude Pc1-2 geomagnetic pulsations and their connection with the location of dayside polar cusp. *Planetary and Space Science 28:*1 – 7.

Dudeney, J.R. (1993). Signatures of dayside solar wind/magnetosphere/ionosphere coupling as revealed by the PACE HF radars and associated experiments. *Proceedings of the NIPR Symposium on Upper Atmospheric Physics 6:*25 – 35.

Fraser, B.J. (1975). Ionospheric duct propagation and Pc1 source regions. *Journal of Geophysics Research 80:*2790 – 2796.

Francke, M.H., Hansen, H.J., Menk, F.W., Fraser, B.J. *and* Morris, R.J. (1993). The propagation of Pc1 magnetic bursts across the polar cap region. In: Burns, G. *and* Duldig, M. (Eds). *ANARE Research Notes Number 88.* Pp. 82 – 88.

Greifinger, C. *and* Greifinger, P. (1968). Theory of hydromagnetic propagation in the ionospheric waveguide. *Journal of Geophysics Research 73:*7473 – 7490.

Hayashi, K., Kokubun, S., Oguti, T., Tsuruda, K., Machida, S., Kitamura, T., Saka, O. *and* Watanabe, T. (1981). The extent of Pc1 source region in high latitudes. *Canadian Journal of Physics 59:*1097 – 1105.

Heacock, R. R. (1974). Midday Pc 1-2 pulsations observed at a subcleft location. *Journal of Geophysics Research 79:*4239 – 4245.

Manchester, R. N. (1968). Correlation of Pc 1 micropulsations at spaced stations. *Journal of Geophysics Research 73:*3549 – 3556.

Manchester, R.N. (1970). Propagation of hydromagnetic emissions in the ionospheric duct. *Planetary and Space Science 18:*299 – 307.

Meng, C.-I. (1982). Latitudinal variation of the polar cusp during a geomagnetic storm. *Geophysical Research Letters 9:*60 – 63.

Menk, F.W., Fraser, B.J., Hansen, H.J., Newell, P.T., Meng, C.-I. *and* Morris, R.J. (1992). Identification of the magnetospheric cusp and cleft using Pc1-2 pulsations. *Journal of Atmospheric and Terrestrial Physics 54:*1021 – 1042.

Morris, R.J. *and* Cole, K.D. (1985). Pc1-2 discrete regular daytime pulsation bursts at high latitudes. *Planetary and Space Science 33:*53 – 67.

Morris, R.J. *and* Cole, K.D. (1991). High latitude day-time Pc1-2 continuous magnetic pulsations: a ground signature of the polar cusp and cleft projection. *Planetary and Space Science 39:*1473 – 1491.

Neudegg, D.A., Underwood, M.J., Burns, G.B., Fraser, B.J., Menk, F.W., Hansen, H.J. *and* Morris, R.J. (1994a). Deployment of a multi-station magnetometer array to examine source regions of ULF waves at southern cusp/cleft latitudes. In: Morris, R.J. (Ed). *ANARE Research Notes Number 92.* Pp. 135 – 143.

Neudegg D.A., Burns, G.B., Fraser, B.J., Menk, F.W., Hansen, H.J., Morris, R.J. *and* Underwood, M.J. (1994b). Monitoring propagation of Pc1-2 ULF waves at southern cusp/cleft latitudes. In: Morris, R.J. (Ed). *ANARE Research Notes Number 92.* Pp. 144 – 160.

Neudegg, D.A., Burns, G.B., Fraser, B.J., Menk, F.W., Hansen, H.J., Morris, R.J. *and* Underwood, M.J. (1995). Sources and velocities of Pc1-2 ULF waves at austral polar cusp latitudes. *Geophysical Research Letters 22 (21):*2965 – 2968.

Neudegg, D.A., Burns, G.B., Fraser, B.J., Menk, F.W., Hansen, H.J., Morris, R.J. *and* Underwood, M.J. (1996). Determination of Pc1-2 ULF wave velocity and direction using a closely spaced Antarctic magnetometer array. In: Morris, R.J. (Ed). *ANARE Research Notes Number 95.* Pp. 126 – 151.

Newell, P.T. *and* Meng, C.-I. (1988). The cusp and cleft/boundary layer: low altitude identification and statistical local time variation. *Journal of Geophysical Research 93:*14549 – 14556.

Newell, P.T. *and* Meng, C.-I. (1992). Mapping the dayside ionosphere to the magnetosphere according to particle precipitation characteristics. *Geophysical Research Letters 19:*609 – 612.

Olson, J. *and* Fraser, B.J. (1994). Conjugate ULF pulsations in the cusp. The initial results from STEP facilities and theory campaigns. *COSPAR Colloquia Series Vol 5:* 205 – 212.

Popecki, M., Arnoldy, R., Engebretson, M.J. *and* Cahill Jr. L.J. (1993). High latitude ground observations of Pc 1/2 micropulsations. *Journal of Geophysics Research 98:*21481 – 21491.

Watermann, J., Lummerzheim, D., de la Beaujardiere, O., Newell, P.T. *and* Rich, F. (1994a). Ionospheric footprint of magnetosheathlike particle precipitation observed by an incoherent scatter radar. *Journal of Geophysics Research 99:*3855 – 3867.

Watermann, J., de la Beaujardiere, O., Lummerzheim, D., Woch, J., Newell, P.T., Rich, F.J. *and* Shapsak, M. (1994b). The dynamic cusp at low altitudes: a case study utilizing Viking, DMSP-F7, and Sondrestrom incoherent scatter radar observations. *Ann. Geophys. 12:*1144 – 1157.

10. ANALOGUE DATA ACQUISITION SYSTEM FOR ANARE STATIONS

L.P. Symons

Atmospheric and Space Physics
Antarctic Division
Kingston Tasmania 7050
Australia

ABSTRACT

During 1994, the Atmospheric and Space Physics section installed a new general purpose data acquisition system at all ANARE stations. The new ADAS (Analogue Data Acquisition System) is specifically designed to replace a number of existing data logging systems collecting data from a variety of experiments.

The new ADAS systems are all connected to the ANARE Inter-Station Wide Area Network through the ANARESAT system. Through this network, the ADAS systems perform automatic daily transfers of data without interruption to data collection.

Each station's ADAS system can also be reconfigured through the network on a daily basis thus allowing data campaigns to cordinated from Kingston.

10.1 INTRODUCTION

Of the wide variety of experiments operated by the Atmospheric and Space Physics section at ANARE stations, many have broadly similiar features in common. These include:

- One or more channels of analogue output data (generally in the form of a slowly varying voltage).
- The requirement for an accurate time base against which to record the data.
- The need to record data continuously (preferably) without interruption for long periods of time (often years!).

With these common requirements in mind, it seems that a single data acquisition system might be used to collect data from a number of different experiments. This has the practical advantages of simplifying hardware, reducing costs and taking up less space in crowded laboratories! One disadvantage of this approach is that all the experimental eggs are gathered into a single basket. However with the reliablity of modern computing equipment this is not seen as a major concern. This is particularly true if the system can be constructed cheaply enough to allow a complete spare system to be kept at every station.

During the 1980's, steps had already been taken in this direction with the development by Antarctic Division Staff of the LOGIT data acquisition system which was employed up until the the end of 1994 to log data from such diverse experiments as Magnetometers, Riometers and Electric Field Mills on a single computer system.

However, the LOGIT system had a number of disadvantages.

1. It was based on 1970's computing technology in the form of PDP-11 microcomputers which made finding spare parts an expensive and (increasingly through later years) difficult task. The annual turnover of staff also caused problems since few people are familiar with PDP-11 computers and training was often a time consuming and frustrating task.

2. The LOGIT software needed modification every time an experiment was added to, or deleted from, the system. This meant delving into the source code, making appropriate (or perhaps inappropriate!) modifications and recompiling. Consequently, every station had a different version of the LOGIT software and confusion sometimes resulted.

3. LOGIT could not interface to the ANARE Wide Area Network directly. This led to inefficiencies in data transfers and more than a few quirks which annually had to be mastered by new expeditoners.

4. LOGIT could not log data at sample rates greater than 1 Hz. This limited the type of experiments which could be logged on this system.

For all these reasons, it was decided in 1992 to begin work on a new data acquisition system which would address these problems and provide a more efficient means of data collection in Atmospheric and Space Physics laboratories. One of the principal objectives of this project would be to allow expeditioners to spend more time on major research projects and less time on routine observatory work.

10.2 THE ADAS SYSTEM

One precept of the new system was that it should be based on IBM compatible computers. This decision was based on cost effectiveness, the ability of these computers to perform the task and the wide spread use of these computers throughout industry.

This latter factor should not be underrated since it reduces the learning curve associated with the new system.

A further objective was to use commercially available components as far as possible in order to minimise the engineering effort required to develop and maintain the system.

It was also decided that the new system would need to interface with the existing equipment designed for use with the LOGIT system. This equipment included the 'Analogue Conditioner Rack' which amplifies and buffers analogue signals from experiments as well as the 'Laboratory Chronometer' and 'Time Code Buffer Rack'.

A commercial 'Analogue-to-Digital' converter card was selected to give 16 channels at 12 bits resolution. 12 bits was deemed adequate for current purposes although a 16 bit A/D card could be added to the system with minimal software modifications.

The ADAS system design is depicted in block diagram form in Figure 1.

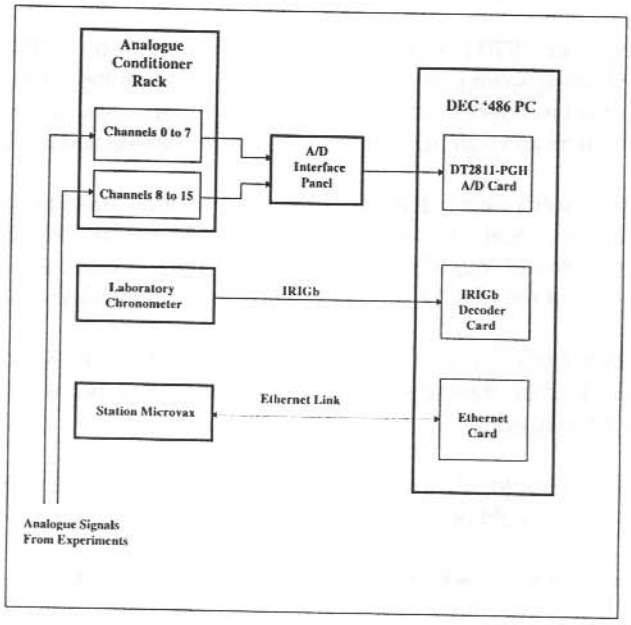

Figure 1. The ADAS system.

The computer is a DEC 80486 33MHz IBM compatible personal computer equipped with a 200 Mbyte hard disk, VGA Colour Graphics and a mouse. It is equipped with the following plug in cards:

- Data Translation DT2811 16 channel, 12 bit Analogue-to-Digital converter.
- ANARE IRIGb Time Decoder.
- DEC Ethernet Adaptor.

Analogue signals from the experiments are first buffered and amplified by the 'analogue conditioner rack' to bring them up to the ±5 Volt levels required by the DT2811 A/D card. The 'analogue conditioner rack' was originally developed by the Antarctic Division for use with the LOGIT system and operates in the same way with the ADAS system.

Apart from amplifying and buffering the signals, the rack also applies a 10 Hz low pass filter to eliminate 'high frequency' noise. This can have a detrimental effect on data being collected at higher rates, so the 'analogue conditioners' should be bypassed when using sampling rates higher than 5 Hz.

An A/D interface panel (also manufactured by Antarctic Division) simply adapts the signals from the 'analogue conditioner rack' to a connector suitable for plugging into the DT2811 A/D card.

Computers of any sort are not reknowned for accurate internal clocks, so it is essential to provide an accurate time signal to the PC to synchronise data collection. In the ADAS system, this signal is provided using IRIGb serial time code which is generated by an external chronometer. The IRIGb is decoded within the PC using a specially designed decoder card.

Network connection is provided by a DEC ethernet card. The computer is configured with DEC PATHWORKS software which allows it to access other computers on the network as virtual disk drives. For the normal ADAS configuration, the station microvax is configured as a remote drive which the ADAS system can copy data to and from.

10.3 SOFTWARE DEVELOPMENT

In the early stages of this project, efforts were made to find a commercial software package that would perform the task, however it soon became clear that the requirements were too specialised for all the selection criteria to be met.

Consequently, the data acquisition and supporting software was all developed from scratch using Borland C++ version 3.1. At present, the software consists of 3 programs.

- ADAS – The actual logging software.
- SETUP – A configuration program for defining experiments.
- VIEW – A data file plotting and inspection program.

10.4 FEATURES

ADAS provides 16 channels of 'analogue input' at 12 bit resolution. Using a configuration program, an operator may define and save a number of experiments in a configuration file. Each experiment definition includes the following information:

Item	Example
Experiment Title:	'Fluxgate Magnetometer'
No of Channels:	4
Channel Names:	'X Component', 'Y Component', 'Z Component', 'Temperature'
Sample Rate:	0.1 Hz
A/D Channels:	0, 1, 2, 3

The range of available sample rates is as follows: 0.1 Hz, 0.2 Hz, 0.5 Hz, 1 Hz, 2 Hz, 5 Hz, 10 Hz, 20 Hz and 50 Hz.

An experiment may contain from between 1 and 16 channels. There may be up to 16 separate experiments defined simultaneously, although since there are only 16 channels available, these would necessarily be limited to being single channel experiments. A typical ANARE station configuration would be:

Riometer:	1 channel logged at 0.1 Hz
Fluxgate Magnetometer:	4 channels logged at 0.1 Hz
Magnetic Pulsations:	2 channels logged at 0.5 Hz

Data from each experiment is recorded in daily files starting at 0000 UT and containing 24 hours of data. A separate file is produced for each experiment with the file names formatted as follows:

SSSEEEYY.DDD

where SSS denotes the station, EEE denotes the experiment, YY denotes the year and DDD denotes the day number.

So a Casey Fluxgate Magnetometer file recorded on Day 339 of 1995 would have the file name CASMAG95.339 (see Figure 2).

In addition, each file contains a 500 byte header containing the following information:

Station Name:	Casey
Experiment Name:	Magnetic Pulsations
No Of Channels:	4
Channel Names:	H-Dot, D-Dot
Sample Rate:	2 Hz
Day Number:	97
Year Number:	1995

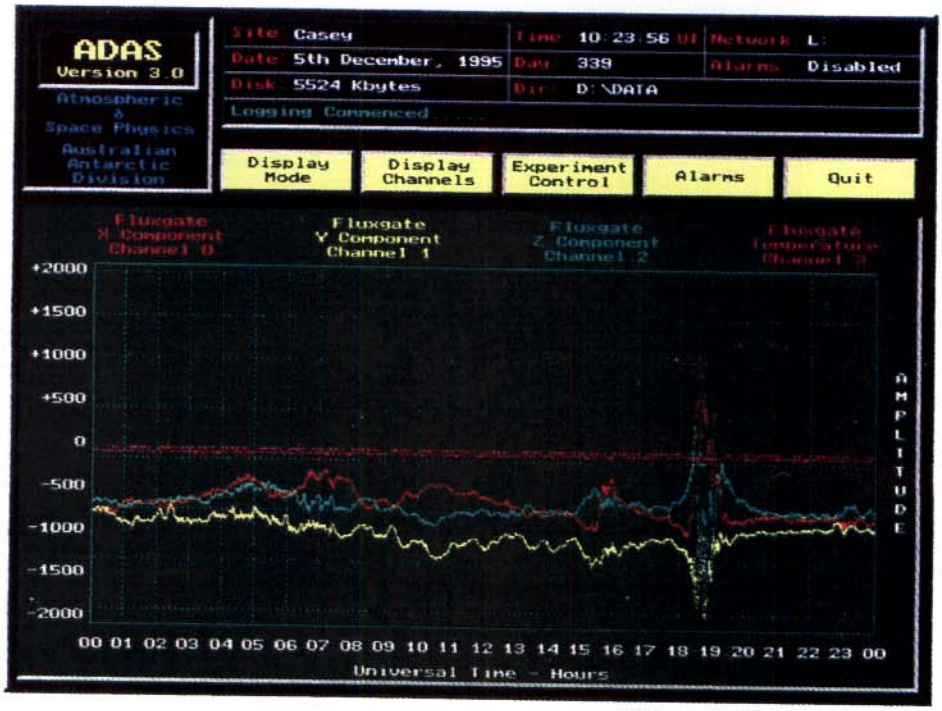

Figure 2. Casey fluxgate magnetometer file.

10.5 TIMING SYSTEM

It was always considered desirable to use IRIGb serial time code as the means of getting timing information to the ADAS system. IRIGb code consists of binary time code modulated onto a 1 kHz carrier and can be distributed via twisted pair over long distances (several kilometres) without degradation of timing accuracy.

Using IRIGb time code therefore not only simplifies wiring but it allows the ADAS system to be remotely located from the laboratory chronometer. (Very useful if the experiments that being logged happen to located at a distance.)

Early versions of ADAS employed a parallel interface card to accept BCD encoded data from a 'laboratory chronometer'. This method was only employed as a stop gap measure until an IRIGb decoder card could be purchased or designed in house.

During 1994, the decision was made to proceed with design and construction of an IRIGb decoder card. Commercial units were available but were priced at several thousand dollars each. The ANARE versions were much cheaper and because they were specifically designed for the job, more suited to the task.

The ANARE IRIGb card has two functions within the ADAS system:

1. It provides time data to the CPU via internal registers accurate to better than a millisecond.

2. It provides a 50 Hz interrupt to the PC CPU that is used to provide accurately aligned data acquisition to the external clock.

Although developed with ADAS in mind, the ANARE IRIGb card will have many other applications in future projects.

The source of IRIGb time code may be either a GPS Truetime Model 800 or an Austron 8120 Chronometer. The objective is to provide IRIGb code which is accurate to ± 1 ms.

10.6 DATA TRANSFERS VIA THE NETWORK

During 1994/1995, Mawson became the final station to be linked into the ANARE Wide Area Network. Each station now has it's own microvax which acts as a local file server for personal computers at each station and as a gateway to the computing facilities at Kingston.

ADAS is able to take advantage of the network using DEC PATHWORKS software which allows each station ADAS PC to connect the local microvax as though it were an extended disk drive of the PC.

Special ADAS file areas have been set aside for the ADAS systems. Into these areas at 0000 UT, each morning, the previous days data files are automatically transferred without interruption to the data acquisition process.

The ADAS file areas are accessible from Kingston and so it is possible to inspect data collected at the Antarctic bases within 24 hours of them having been collected. This normally requires no operator intervention at the station and is a fully automatic procedure.

10.7 REMOTE CONTROL VIA THE NETWORK

As previously mentioned, an operator can define and save a number of experiments using the SETUP program. ADAS is programmed to automatically look for a new configuration file in the ADAS file area at 0000 UT. If it finds such a file, it is copied across to the ADAS system, which loads the new file and reconfigures itself accordingly.

In this way, it is possible to alter the sample rate of an experiment at one or all of the stations from Kingston without requiring any local operator intervention. Similiarly, experiments can be deleted or added at will.

10.8 FILE FORMAT

The move to a new data acquisition system has resulted in a lot of changes to data handling procedures. One of the biggest impacts has been the need to change file formats to one that is suitable for a wide range of experiments.

A particular problem was finding a format which could cope with widely varying sample rates ranging from 0.1 Hz to 50 Hz.

One contender which emerged was CDF (or Common Data Format) a file format developed by NASA for storing a wide range of data in a standard format. While CDF has considerable merit as a long term storage format, it was decided that it was unrealistic to try and store the data in CDF format as it was being collected.

Ultimately, it may be worthwhile to produce software that will convert ADAS format data into a suitable CDF format. Especially since CDF seems to be gaining momentum as a world wide data storage standard.

The format which was finally settled on is based on time stamping data in 10 second blocks. Obviously the number of data points in each block depends on the number of channels and the sample rate being employed.

A 0.1 Hz single channel experiment will have one data point per 10 second block while a 16 channel, 50 Hz experiment would have 8000 data points per block.

This strategy is effective in keeping the size of data files under control since the proportion of data space taken up with timing information is reduced as the sample rate increases.

The ADAS file format has been designed to be as flexible as possible. To this end, four ADAS file types have been defined. The file type is contained in the Header.

ADAS (12 bit signed)
ADAS (16 bit signed)
ADAS (12 bit unsigned)
ADAS (16 bit unsigned)

The ADAS logging system currently only produces '12 bit signed' files however it is conceivable that in the future the system could be fitted with a 16 bit A/D card and be modified to produce '16 bit signed' files.

The 12 and 16 bit unsigned formats are intended for files produced by counting systems (for example photometers). In fact such ADAS compatible files have already been produced by new acquisition systems using adapted ADAS software.

10.9 DATA FILE INSPECTION AND MANAGEMENT

Obviously there's not much point in collecting data if you can't look at it afterwards ! The VIEW program was developed with this problem in mind and it allows ADAS data files to be displayed, plotted and edited.

Specifically it provides the following functions:

1. On screen display of data files (up to four channels simultaneously).
2. Graph plotting to a HPGL compatible plotter.
3. ADAS binary to ASCII conversion of data.
4. Recovery of corrupted data files.
5. Inspection of file headers.
6. Editing of files.
7. Averaging functions.

Figure 2 illustrates a displayed Fluxgate Magnetometer file using VIEW for Day 339 at Casey.

VIEW is most definitely not designed as an analysis tool. Such tasks are most efficiently performed by analysis languages such as IDL.

10.10 CURRENT APPLICATIONS

ADAS is currently installed at Davis, Casey, Mawson and Macquarie Island. It is being used to log Riometer and Magnetic Pulsations data at all four stations. At Davis and Casey it is also being used to log Fluxgate Magnetometer data.

During the 1994/1995 summer at Davis, the ADAS system was also employed to data from a Ultra Violet Biometer experiment.

At each station it has successfully managed to replace three individual logging systems. The LOGIT slow logging system, EARS fast logging system and the Newcastle magnetic pulsations computer have all been replaced with a single computer system running ADAS.

10.11 FUTURE DIRECTIONS

While the ADAS acquisition software is still undergoing minor upgrades, the basic functions are already in place. Two possible areas where improvements might be made are:

1. Producing a 16 bit version of ADAS. This would require relatively simple software modifications and a new A/D card.

2. Porting VIEW to WINDOWS. While all of the ADAS software operates under MSDOS, there would be considerable benefits in porting VIEW to the WINDOWS environment. This would allow use of a wider range of plotting/printing devices and prolong the useful life of the software.

10.12 ACKNOWLEDGEMENTS

A project such as this only comes as a result of contributions by many people. The following Antarctic Division personnel deserve specific mention. Ray Morris for instigating the project. Brad Phillips for the IRIGb Decoder card design. Mike Dymond for the Analogue Conditioner rack design. Peter Yates for ongoing support and many valuable discussions. In addition, the Engineering Staff of the Division should be commended for their efforts in commissioning the Inter Station Wide Area Network which has immeasurably improved communications between Kinsgton and the Antarctic stations.

REFERENCES

Dymond, M. (1991). Analogue conditioner rack manual. Australian Antarctic Division. (internal report).

Phillips, B. (1994). IRIGb decoder card: operation and maintenance manual. Australian Antarctic Division. (internal report).

Symons, L.P. (1995). Users guide to ADAS 2.00. Australian Antarctic Division. (internal report).

Symons, L.P. (1995). Users guide to VIEW 3.03. Australian Antarctic Division. (internal report).

11. COMPARISON OF EMPIRICAL MODEL PREDICTIONS WITH AUTOMATICALLY AND MANUALLY SCALED IONOSPHERIC PARAMETERS FOR THE POLAR CAP STATION, CASEY

M. Dubovinsky[1], D.P. Monselesan[1], P.J. Wilkinson[2], P.L. Dyson[3], P.R. Smith[4,3], D. Schneider[1] and R.J. Morris[1]

[1] Atmospheric and Space Physics
Antarctic Division
Kingston Tasmania 7050
Australia

[2] IPS Radio and Space Services
PO Box 5606
Chatswood NSW 2057
Australia

[3] School of Physics
La Trobe University
Bundoora Victoria 3083
Australia

[4] School of Electrical Engineering
La Trobe University
Bundoora Victoria 3083
Australia

ABSTRACT

ARTIST scaled ionograms collected by a Digisonde Portable Sounder (DPS-4) at Casey, Antarctica (-80.84 CGM) have been analysed over a period of three years since its installation in 1993. Of the numerous parameters routinely recorded by the DPS-4 at Casey, four important characteristics, f_0F2, M(3000)F2, f_0F1 and f_0E, are compared with model calculations, and manually scaled data collected by traditional analogue ionosondes. The diurnal and seasonal variations of scaled ionospheric parameters are presented. An assessment of ARTIST performance compared with standard manual reduction methods was undertaken. This aspect of the DPS-4 operation is crucial for automatic drift measurements, necessary to determine accuarately the location and velocities of ionospheric echoes. A comparison between data collected during low and high solar activity was also performed. The three years of data reduction using ARTIST automatic scaling software gives results which in most instances generally agree with expected average results, giving some confidence in its use for scaling some parameters under Antarctic high latitude ionospheric conditions.

11.1 INTRODUCTION

During the 1992/1993 austral summer a Lowell Digital Portable Sounder (DPS-4) was installed at Casey (alternate name, Wilkes), Antarctica (66.3°S, 110.5°E geographic coordinates, 80.84°S Centred Geomagnetic Coordinates). Casey is essentially a polar cap ionospheric station.

To date the instrument has been used primarily to study the behaviour of the ionosphere from routine measurements of the electron density profile and ionospheric drifts associated with large-scale convection of the F-region plasma (Monselesan et al. 1993). This research note reports the analysis of vertical incidence ionograms using ARTIST software (Reinisch and Huang 1982; Reinisch 1986).

Of the many parameters routinely recorded by the DPS-4 at Casey, four important characteristics, f_0F2, M(3000)F2, f_0F1 and f_0E, are compared with model calculations and manually scaled data collected by the traditional analogue ionosondes.

11.2 ANALYSIS

The new data analysed covers the first three years of operation of the DPS-4, from April 1993 until July 1995. The DPS-4 system records scaled ionogram characteristics for the standard scaling parameters recommended by URSI (Piggott and Rawer 1978). Similar sets of manually scaled data obtained at Casey between 1957 and 1991 have also been used for comparison.

The DPS-4 began operation in April 1993 and initial observations were made using a standard observing routine, in which a sequence of ionograms followed by a period of drift measurements was repeated every 15 minutes. Since the end of August 1993, the sequence has been repeated every 5 minutes. This data has been examined in several ways.

The first uses a scatter diagram, or mass plot, of a particular parameter in which all the data obtained over a certain interval (e.g. month or season) is plotted as a function of, for example, universal time. These plots show the dispersion of the data and hence give an indication of the daily variability of the ionospheric parameters, and an indication of gross errors produced by the automatic or manual scaling procedures.

The second method is a long standing one used to indicate the average behaviour of the ionosphere and its variability. For each parameter, a value is determined at each hour of the day. These daily values for each month are then used to determine the median, upper decile and lower decile.

Third is to use surface plots based on hourly mean values of selected parameters, and contour plots based on monthly medians of hourly means. These plots show the diurnal and seasonal variations very clearly.

11.3 RESULTS

Wilkes and Casey stations are a few kilometres apart and we will refer to them both as Casey station. The Casey analogue ionosonde was operated over almost two complete solar cycles and manually scaled parameters reveal the typical behaviour of the Casey ionosphere during increasing and decreasing solar activity, see Figure 1.

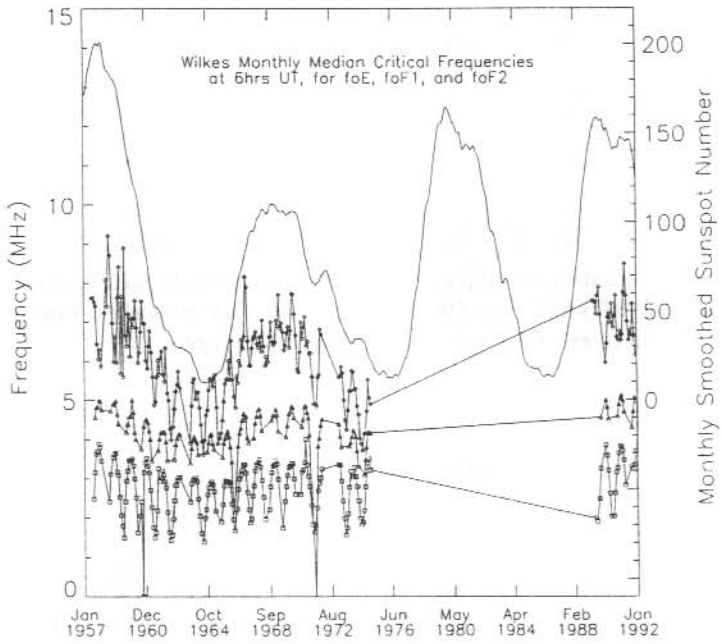

Figure 1. Monthly median critical frequencies at 6 UT for f_oE, f_oF1 and f_oF2 over the period from 1957 until 1992, and the monthly smoothed sunspot number. Squares – E layer, triangles – F1 layer and diamonds – F2 layer.

The DPS 4 was operating in a period of decreasing solar activity in 1995, the third year of operation, with solar minimum approaching. We have compared the DPS automatically scaled data (April 1993 until July 1995) with the manually scaled data from a decreasing period and similar range of sunspot numbers (1961 until 1963), see Figures 2 and 3. From visual comparison it is evident that there is good agreement between the manually and automatically scaled parameters for similar solar conditions. A later comparison will use manually scaled DPS 4 data.

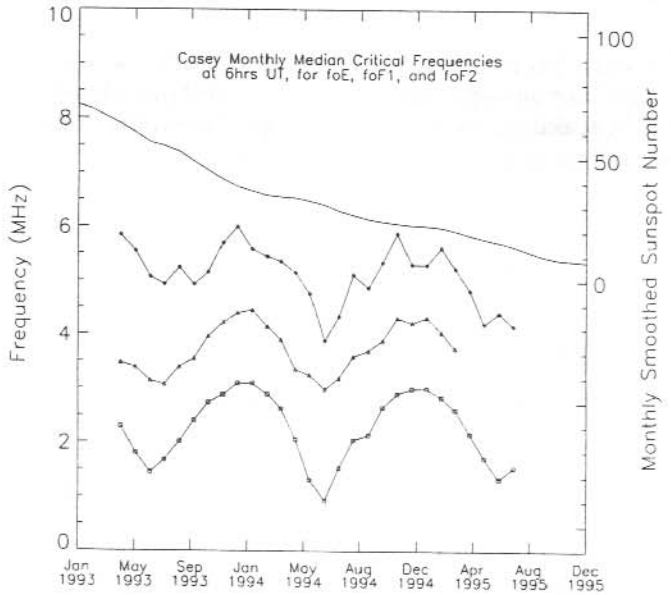

Figure 2. Monthly median critical frequencies at 6 UT for f_oE, f_oF1 and f_oF2 over the period from April 1993 until July 1995, and the monthly smoothed sunspot number. Squares – E layer, triangles – F1 layer and diamonds – F2 layer.

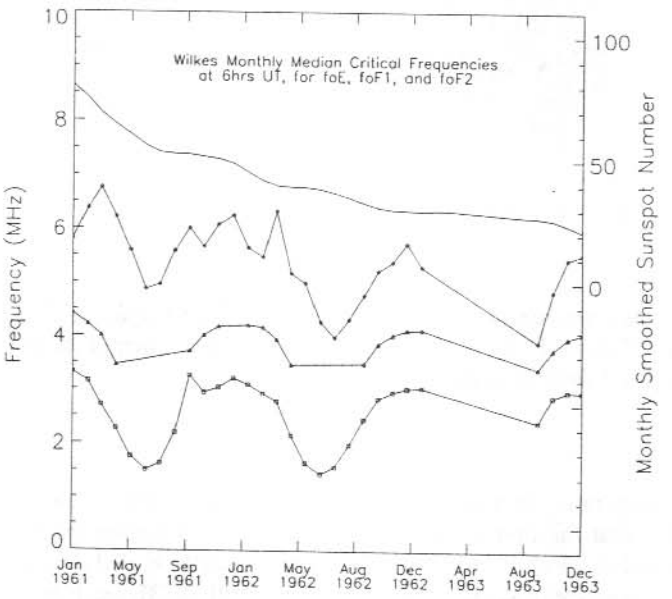

Figure 3. Monthly median critical frequencies at 6 UT for f_oE, f_oF1 and f_oF2 over the period from 1961 until 1963, and the monthly smoothed sunspot number. Squares – E layer, triangles – F1 layer and diamonds – F2 layer.

E layer. Experimental data is compared with Muggletons formula as implemented in the IRI (International Reference Ionosphere) using monthly 10.7 cm flux values. The comparison shows good agreement, with the residuals of (f_0E - prediction) being less than 0.5 MHz. The seasonal and diurnal variations show strong solar correlation, with a flat maximum of 3.5 to 4 MHz during summer around noon. When ARTIST software is unable to scale a value of f_0E a predicted value is added to the database, suitably flagged so that scaled and predicted values can be distinguished if required. Figure 4(a) shows typical behaviour of the E layer with combined experimental and predicted values. Figure 4(b) shows only the scaled values. ARTIST scaled values are in good agreement with manually scaled data for the same solar conditions during the summer time.

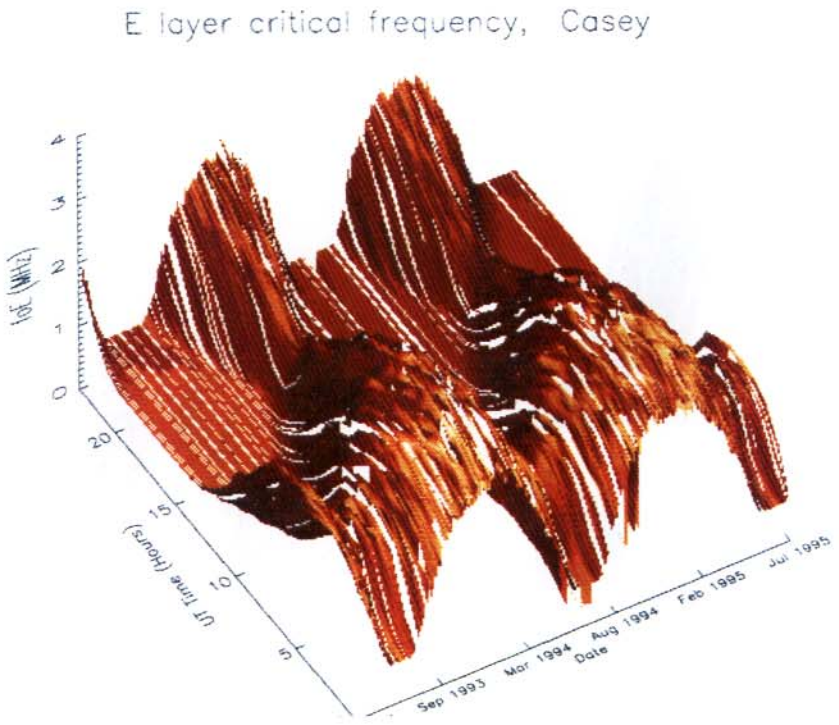

Figure 4(a). E layer critical frequency over the period from April 1993 until July 1995 – combined experimental and predicted values.

F1 layer. Experimental data is compared with du Charma's formula as implemented in the IRI using monthly 10.7 cm flux values. The model predicts the F1 region to be present only during the summer daytime, but ARTIST scales values during summer nighttime as well. These nighttime values are typically 3 MHz whereas the model predict that the F1 layer is not present.

ARTIST also finds values for f_oF1 at most other seasons and times, see Figure 5. A detailed inspection of ARTIST and manually scaled data shows that ARTIST scales f_oF1 incorrectly during the winter time.

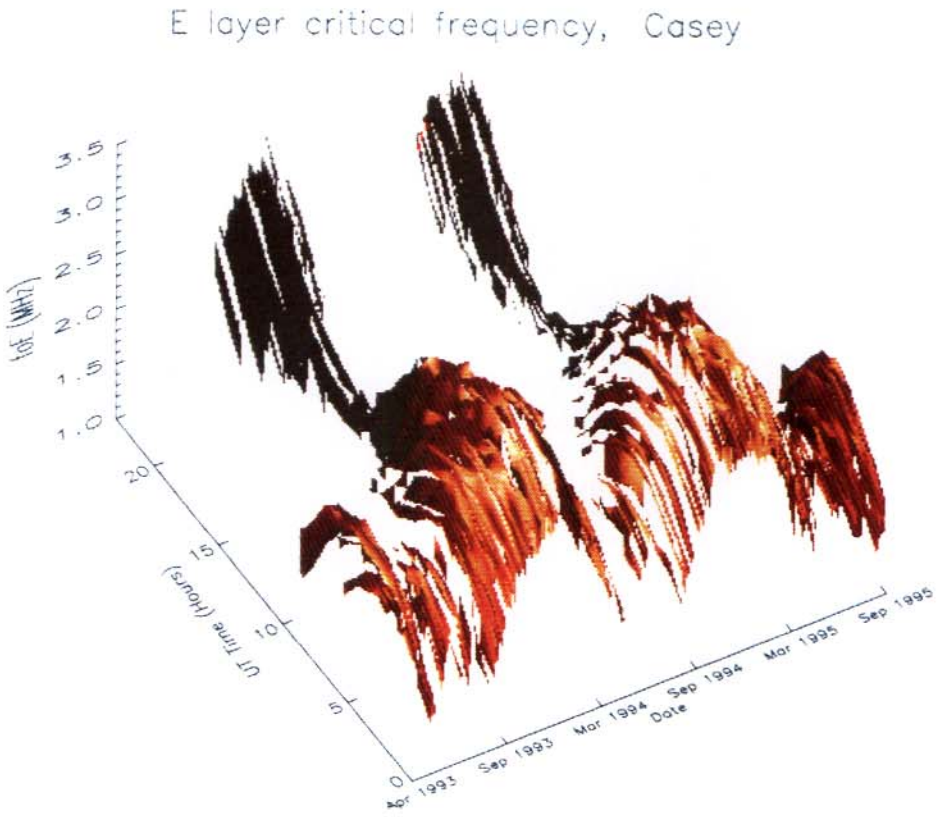

Figure 4(b). E layer critical frequency over the period from April 1993 until July 1995 – experimental data only.

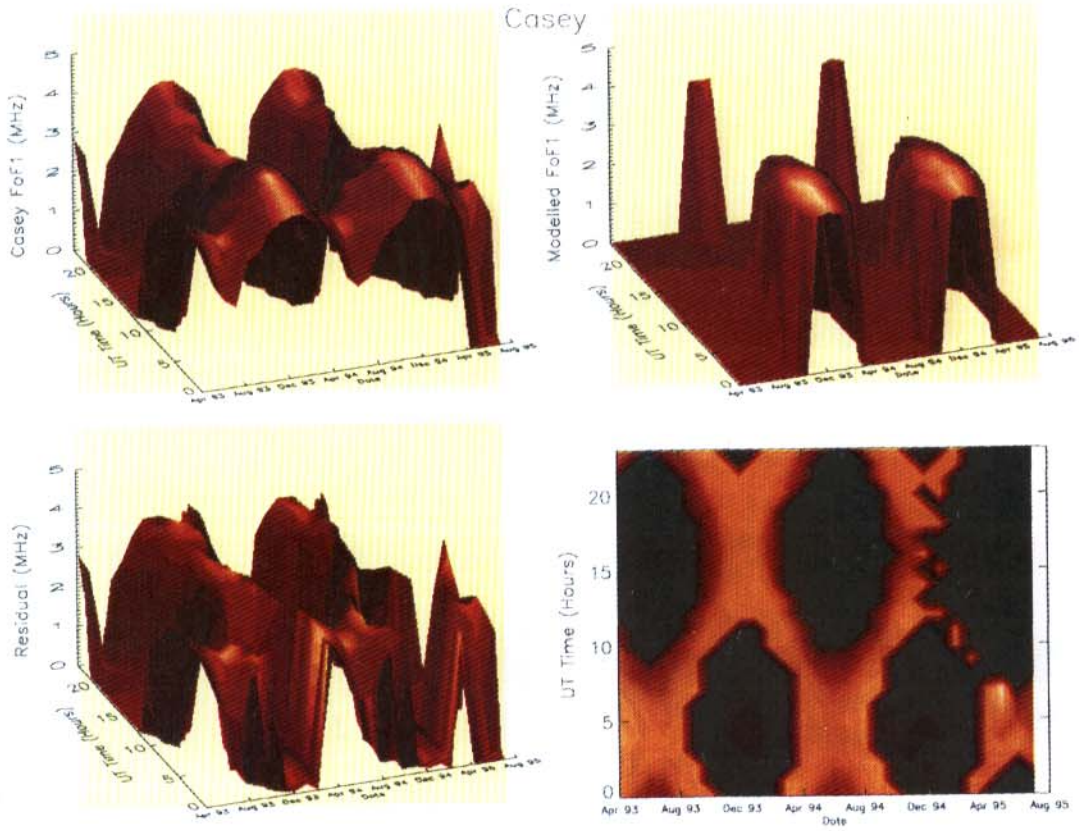

Figure 5. F1 layer critical frequency, the model, residual and contour of the residual for the period from April 1993 until July 1995.

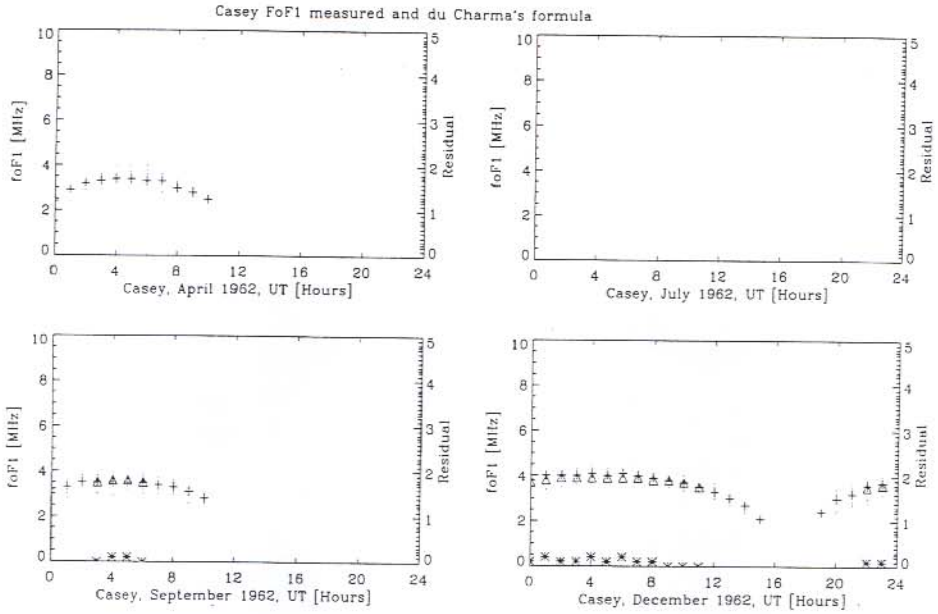

Figure 6. F1 layer critical frequency for four seasons – 1962 manually scaled data. Pluses – experimental data, triangles – model and stars – residual values.

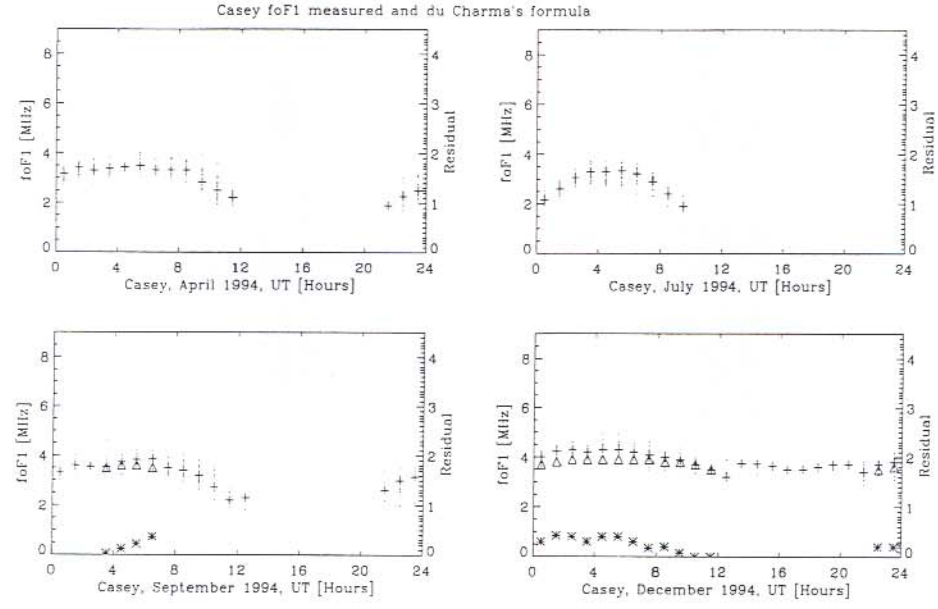

Figure 7. F1 layer critical frequency for four seasons – 1994 ARTIST scaled data. Pluses – experimental data, triangles – model and stars – residual values.

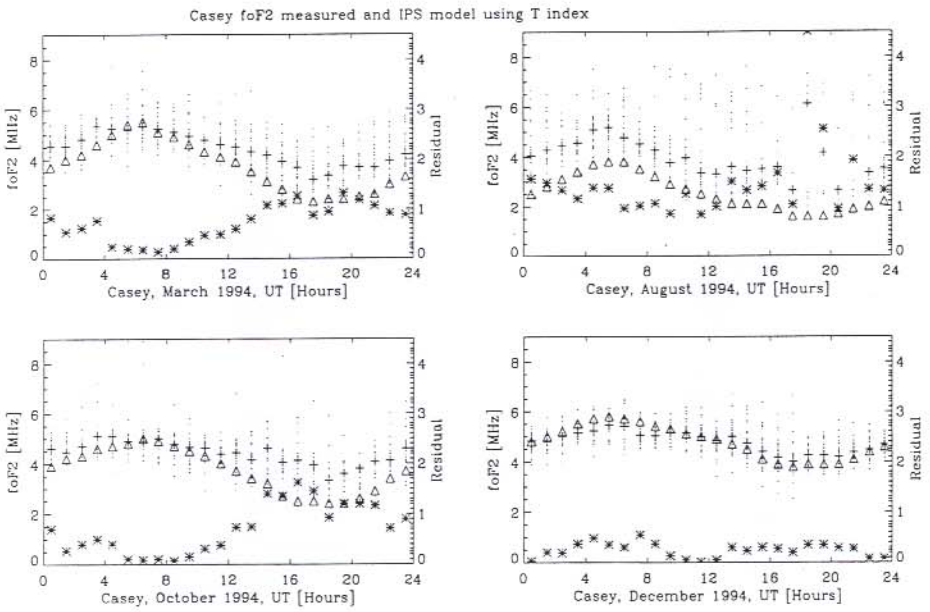

Figure 8. F2 layer critical frequecy for four seasons – 1994 ARTIST scaled data, the model and residuals. Pluses – experimental data, triangle – model and star – residual values.

We compared the manually scaled values obtained from ionograms recorded by traditional ionosondes with values automatically scaled from DPS ionograms obtained during similar solar conditions. For example, Figures 6 and 7 show the F1 layer critical frequencies obtained using manual and automatic scaling. They show that ARTIST scaled f_0F1 in July when the model predicts that there is no F1 layer present, and the absence of the F1 layer is supported by the manual scaling of the 1962 data when no values of f_0F1 were scaled during July. In December 1994 ARTIST scaled values of f_0F1 throughout the day, contrary to the manually scaled results for the period 1957 to 1962, which produced scaled values of f_0F1 only during daylight hours.

We found ARTIST scaled f_0F1 incorrectly during winter time.

F2 layer. Experimental data is compared with the CCIR, IRI and IPS models. For each hour the absolute value of (data-prediction) was calculated and the largest residual (worst) and the smallest (best) was found. The noon/midnight plots of parameters versus time were analysed to highlight the discrepancies between the experimental data and the models. The comparison has shown that the IPS model has the best agreement ahead of the CCIR and IRI models.

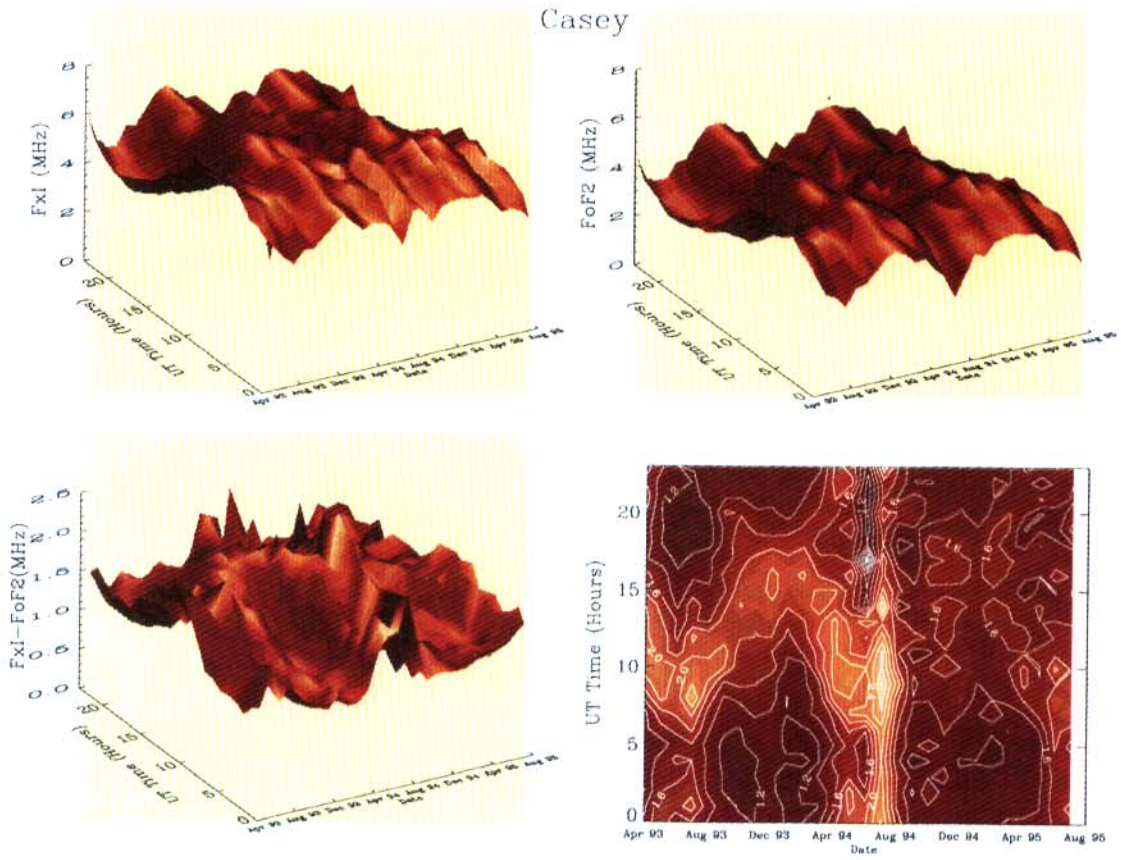

Figure 9. F2 layer critical frequency, the fxI and residual with the corresponding contour plot.

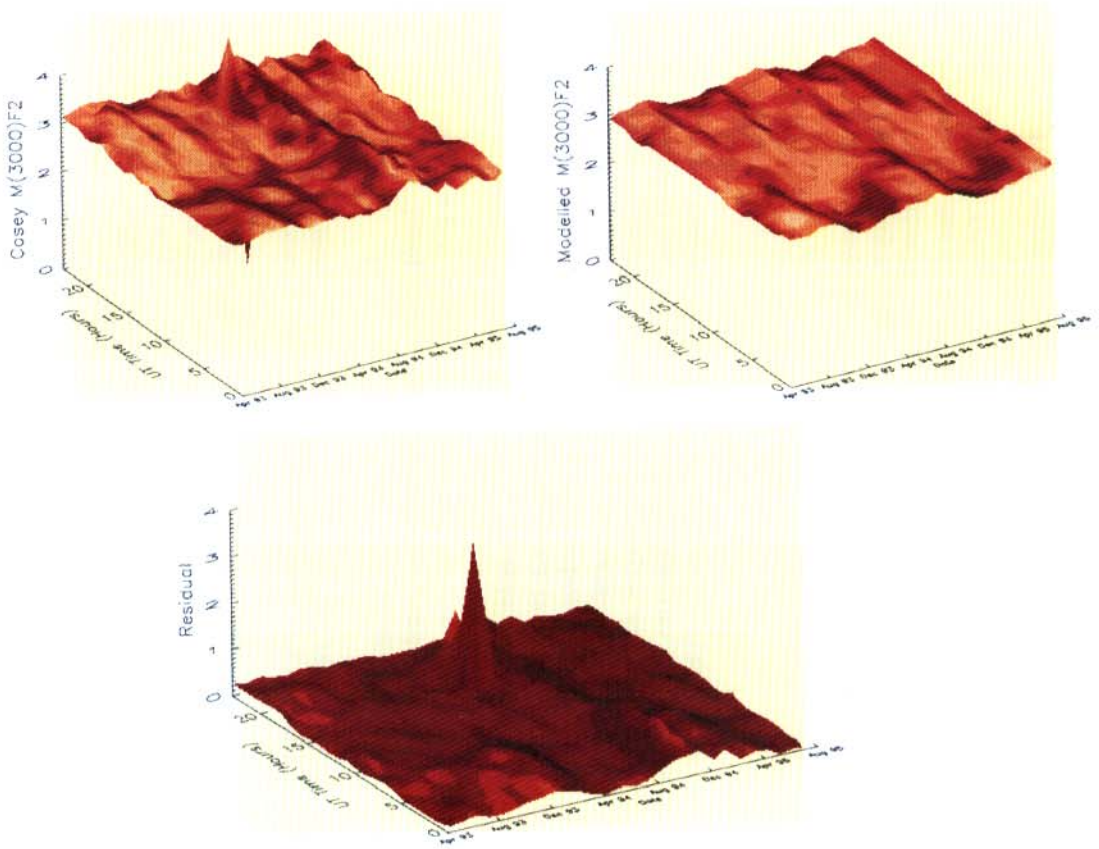

Figure 10. M(3000)F2, the model and residual for period from April 1993 until July 1995.

At times ARTIST chose values which varied wildly from ionogram to ionogram, even for ionograms at five minutes intervals. Figure 8 shows that the largest residuals occurred in August and October. Preliminary analysis indicates that these are associated with magnetic activity.

(fxI-f_oF2). Another way of testing the quality of data is to find the difference between fxI and f_oF2. Figure 9 shows the F2 layer critical frequency for Casey, fxI and the residuals with the corresponding contour plot. The bulk of the data (fxI-f_oF2) fall in the expected range, around 1.6 MHz, with extremes occurring during the winter months around 10 UT.

M(3000)F2. Figure 10 shows a comparison of ARTIST scaled data, the CCIR model predictions and the residuals. The comparison shows good agreement between the automatically scaled data and the CCIR model. The main discrepancies occur between August 94 and December 94 corresponding to increased magnetic activity and special data campaigns, when ionograms suitable for automatic scaling were obtained less frequently during this period.

11.4 SUMMARY

The analysis using automatically scaled ionospheric parameters reveals quite clear solar controlled diurnal and seasonal variations of the E and F1 layer. The three years of data reduction using ARTIST automatic scaling software gives results which in most instances agrees generally with expected average results, giving some confidence in its use for scaling some parameters under Antarctic ionospheric conditions. Comparisons with published data at Wilkes during the IGY (Penndorf 1965) and other manually scaled data from Wilkes (1957 – 1991) generally show good agreement.

However a detailed comparison between models and manually scaled data has revealed some difficulties with ARTIST, particularly in scaling the F1 layer during the winter period and also during the summer nighttime.

Scaling of the F2 layer was more variable, but the average data is consistent and comparable to empirical model predictions for Casey. Comparisons agreed best with the IPS model.

An important feature of the DPS-4 is a mode which automatically selects a suitable frequency for ionospheric drift measurements. This frequency is selected using parameters automatically scaled from standard ionogram modes of operation. The frequency used for drift measurements is selected according to the formula (Reinisch and Huang 1982),

$$\text{fdrift} = \text{fmin} + (f_oF2 - \text{fminF})/3.$$

Since installation, the DPS-4 has been quite reliable in obtaining drift measurements automatically, indicating that ARTIST automatic scaling procedures are adequate for this purpose.

Further analysis will include comparisons between manual and automatic scaling of the same ionograms. This work will give a clearer picture of the accuracy of present empirical maps of the ionosphere above Casey.

11.5 ACKNOWLEDGEMENTS

This work has been supported by the Australian Research Council and the Antarctic Science Advisory Committee Grants Scheme.

REFERENCES

Monselesan, D.P., Smith, P.R., Morris, R.J. *and* Dyson, P.L. (1993). Deployment of a digisonde portable sounder-4 at Casey station, Antarctica. In: R.J. Morris (Ed). *ANARE Research Notes Number 92*. Pp.115 – 134.

Penndorf, R. (1965). The average ionospheric conditions over the Antarctic. Antarctic Research. Geomagnetism and Aeronomy. A.H. Waynick, Vol.4, of Antarctic Research Series, 1 – 45.

Piggott, W.R. *and* Rawer, K. (1978). U.R.S.I. Hand-Book of ionogram interpretation and reduction. Report UAG 23A: 1978.

Reinisch, B.W. *and* Huang, X. (1982). Automatic calculation of electron density profiles from digital ionograms. *Radio Science 17:*421 – 434.

Reinisch, B.W. (1986). New Techniques in ground-based ionospheric sounding. *Radio Science 21:*331 – 341.

12. OBSERVATIONS OF AURORAL BACKSCATTER, FIELD-ALIGNED IRREGULARITIES, AND OBLIQUE SPREAD-F ASSOCIATED WITH THE MID-LATITUDE TROUGH DURING GEOMAGNETIC STORMS

M.L. Parkinson, A.T.D. Quach and P.L. Dyson

School of Physics
La Trobe University
Bundoora Victoria 3083
Australia

ABSTRACT

A modern digital ionosonde (Digisonde 256) recording the amplitude, phase, Doppler shift, angle-of-arrival, and polarisation of HF (0.5–30 MHz) echoes from the ionosphere is operated by La Trobe University at the mid-latitude station of Beveridge (144.9°E, 37.5°S; Λ = -48.0°), located 40 km north of Melbourne, Australia. We have adapted this radar to alternate between recording near-vertical angle-of-arrival ionograms and monostatic, oblique 'poleward-bound' Doppler ionograms. This is accomplished by separately transmitting with a vertical delta antenna with broad overhead beam, and a horizontal rhombic antenna which projects a main beam at intermediate elevation angles towards the south. In the oblique mode at 5 MHz, the effective radar beam has a geographic azimuth ≈190° (magnetic South is at 191°), an elevation angle ≈36°, and a half-power full-width ≈21°. It is this beam which permits observations of ionospheric irregularities associated with the poleward wall of the mid-latitude trough normally located far to the south of mainland Australia; indeed we can routinely record auroral backscatter out to the maximum digisonde range limit of 2940 km. Experimental ionograms recorded during the storm period 22 and 23 August 1990 (days 234 and 235 during which ΣK_p = 40 and 46, and R_i = 262 and 281 respectively) are presented, and the various forms of spread-F are described, including normal frequency and range spread-F attributed to atmospheric gravity-wave activity, slant-F patches attributed to small-scale irregularities associated with the mid-latitude trough, oblique quasi-horizontal traces at great ranges tentatively attributed to field-aligned auroral irregularities in the poleward wall of the trough and beyond, and distinctive oblique spread-F (OS-F) patches located in proximity to the equatorward boundary of the auroral zone. This preliminary study shows how during geomagnetic storms monostatic, oblique sounding from Beveridge permits us to study the ionospheric dynamics normally only observed by vertical incidence sounders at subantarctic stations such as Macquarie Island (Λ = -64.4°).

12.1 INTRODUCTION

The mid-latitude station of Beveridge (Λ = -48.0°, L = 2.2) is located 40 km north of Melbourne, Australia (see Figure 1). A Digisonde 256 manufactured by the University of Massachusetts Lowell Center for Atmospheric Research (UMLCAR), Massachusetts (Bibl et al. 1981) was installed at Beveridge during 1984, and we are still realising the full experimental capability of this advanced, digital HF (0.5–30 MHz) sounder. The instrument can be programmed to record the amplitude, phase, angle-of-arrival, Doppler

shift, and polarisation of echoes produced by 10 kW phase-coded transmitter pulses (Reinisch et al. 1989), though usually some of the observables are rejected to reduce the data to manageable quantities. Moreover, our particular Digisonde is an especially sophisticated instrument because of the innovative antenna design (to be explained further in Section 12.2).

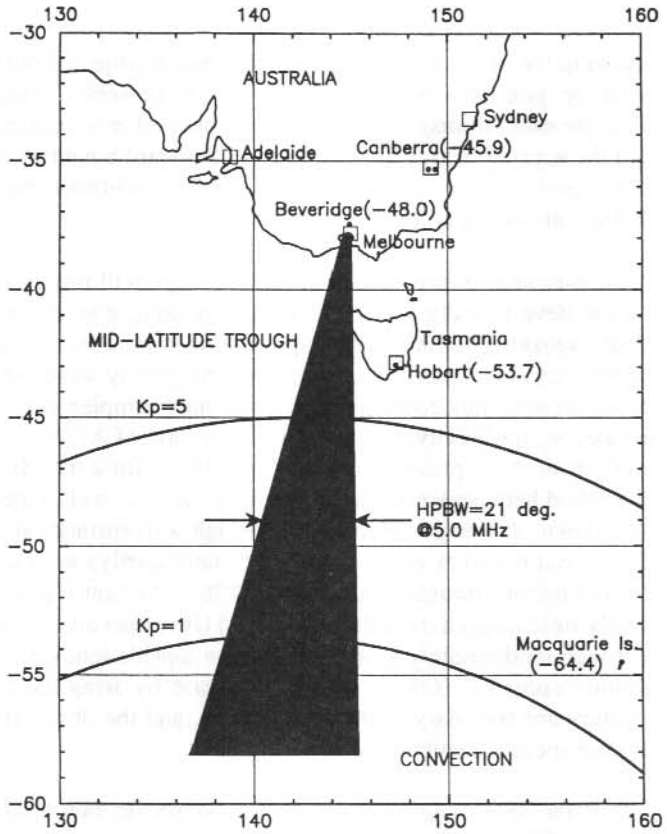

Figure 1. A geographic map of southern Australia showing major cities (squares), relevant ionospheric research stations (dots, magnetic latitudes in brackets), and the Beveridge Digisonde 256 radar beam (60 to 2620 km range gate) looking obliquely towards the subantarctic. Approximate equatorward boundaries of the auroral zone (for K_p = 1 and 5) are also shown.

Basically, by using relays we can digitally switch between a vertical delta transmitter antenna with broad overhead beam and a horizontal rhombic transmitter antenna (Kjaersgaard 1984) with a broad beam at intermediate elevation angles along the magnetic meridian towards the south (i.e. optimum for the backscatter cross-section of field-aligned auroral irregularities). Side lobes also permit fair sensitivity to echoes from all other directions, though especially the zenith. Different lengths of coaxial cables feeding the

seven elements of our antenna receiver array can be switched digitally by use of other relays so as to steer the receiver beam into alignment with either the near-vertical beam of the delta antenna (in which case there are 12 possible azimuths at an off-vertical angle of ≈8°), or the oblique beam of the rhombic antenna. Thereby we have adapted our digisonde to electronically alternate between recording near-vertical angle-of-arrival ionograms and monostatic, oblique, southward-looking Doppler ionograms. Presently, we are recording six of each per hour.

Figure 1 is a map showing the oblique southward-looking beam projected out to a nominal range limit using a range gate from 60 to 2620 km (we are presently using ray-tracing techniques to establish the exact limits). Also shown are some other important ionospheric research stations, and the approximate latitudes of the equatorward boundary of the auroral zone for magnetically quite (K_p = 1) and active (K_p = 5) conditions, based upon the statistical results of Gussenhoven et al. (1983).

In Section 12.3 we will present an experimental sea-echo ionogram illustrating the excellent oblique sensitivity of the Beveridge digisonde, and then more oblique ionograms illustrating the five forms (broadly speaking) of subauroral spread-F that we observe including: (1) classical range and frequency spread attributed to atmospheric gravity wave (AGW)-induced distortions of isoionic surfaces (this continuum of sometimes complex spread-F forms is included in a single category for brevity), (2) a more subtle form of AGW-induced spread-F known as day-time second-hop spread-F (see Bowman 1992a for a true daytime study), and in the examples studied here, apparent on the first-hop traces as well, especially during the F-region dusk and dawn, (3) range spread due to trough wall surfaces at high altitude, (4) range spread due to radio aurora often (though not necessarily) associated with the poleward wall of the mid-latitude trough (Rodger et al. 1986), (5) slant-F patches attributed to small-scale, probably field-aligned irregularities (FAIs) (Bowman and Hajkowicz 1991) associated with the trough (and possibly extending into the topside ionosphere), and (6) a special kind of oblique spread-F (OS-F) which is caused by irregularity patches in proximity to the equatorward boundary of the auroral zone, and the observation of which may be dependent on our special antenna design.

Figure 2 is a plot of all the 1990 magnetic midnight equatorward boundaries of diffuse aurora deduced from DMSP satellite measurements of precipitating particles using the computational method of Gussenhoven et al. (1983) (and obtained here via the SPAN computer network from Fred Rich). These sunspot maximum results are presented to investigate the times when the before-mentioned phenomena are likely to be observed at high mid-latitudes. For example, Scali (1989) has shown that OS-F is most likely observed during the austral autumn equinox, consistent with the more equatorward location of auroral boundaries at this time which is evident in Figure 2 (this figure also suggests that there may be a second, lesser peak in OS-F occurrence during the spring equinox). Minimum occurrence of OS-F, and possibly also the mid-latitude trough and related spread-F forms arriving near to Beveridge, occurs near both solstices. These occurrence statistics are the same as those for F-layer patches in the polar ionosphere (Alan Rodger, private communication 1995), and possibly also boundary-layer blobs. Quach and Dyson (1992) have shown that the diurnal occurrence of OS-F peaks at around 16–17 UT, consistent with the most equatorward displacement of the auroral zone after magnetic midnight (statistically speaking).

The purpose of this scientific note, therefore, is to introduce the high-latitude researcher to the oblique pointing capabilities of the digisonde, its advanced experimental capability, and to emphasise the importance of stations such as Beveridge for studying the ionospheric dynamics occurring from subauroral latitudes poleward into the auroral zones (normally accessible only to high-latitude research bases), and especially during geomagnetic storms, the impact of the dynamics upon the greater region of the mid-latitude upper atmosphere. To this end, in Section 12.4 we discuss the early results of a case study of ionospheric dynamics on 23 August 1990 when $\Sigma K_p = 46$ and $R_i = 281$. On this night, radio aurora and OS-F patches were first seen to the south of Beveridge at great range, subsequently converging upon the near-vertical ionospheric traces. Preceding their arrival, the characteristic perturbations of the ionosphere attributed to the passage of large-scale travelling ionospheric disturbances (LSTIDs) were observed (Bowman 1992b). After their arrival, there were major spread-F events with ionisation depletions and slant-F traces suggesting the arrival of the mid-latitude trough. The OS-F patches were seen during the early morning hours, and presumably in proximity to the boundary of the auroral zone.

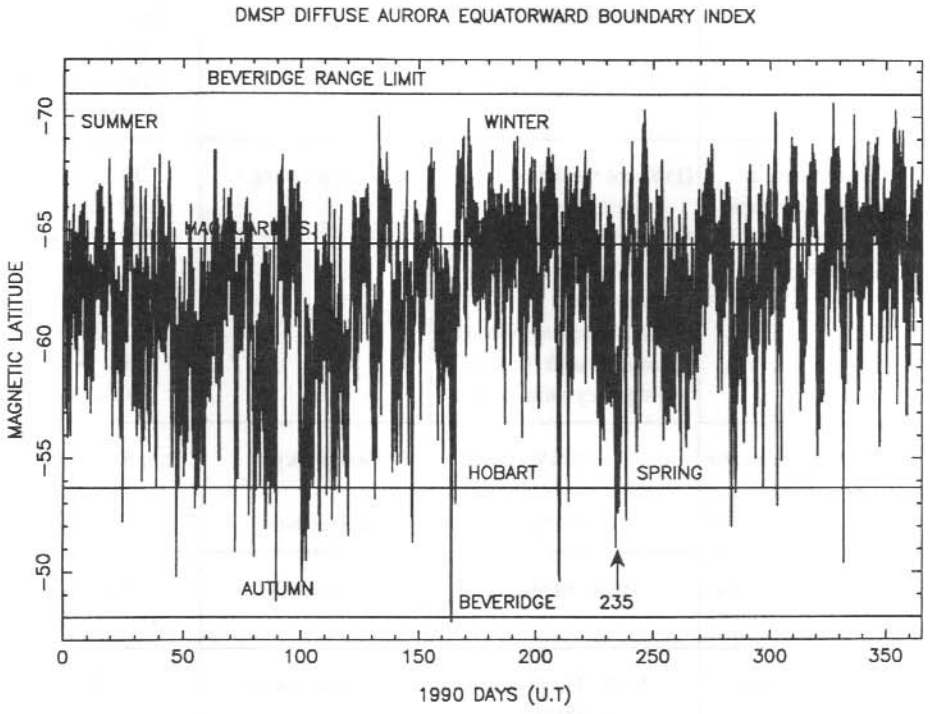

Figure 2. Magnetic midnight equatorward boundaries of the diffuse auroral zone inferred from DMSP precipitating electron measurements for the year 1990. The magnetic latitudes of Beveridge (-45.0°), Hobart (-53.7°), and Macquarie Island (-64.4°) stations, and the nominal range limit of the digisonde oblique radar beam (60 to 2620 km range gate) are also shown.

Table 1. Digisonde 256 ionospheric sounder operating parameters.

Geographic coordinates	144.9°E, -37.5°S	Spatial half-power pulse widths	≈9.9 or 20.0 km
Corrected geomag. coordinates	219.4°E, -48.0°S	Beam steering	Selectable from 25 directions (max. of 8 per CIT)
Conjugate Point	Sea of Okhotsk (Kumchatka Peninsular)	Half-power beam widths	≈20° at 5 MHz
L-Shell	2.2	Wave polarisation	O & X tagging of received signals
Dip angle	68.5°	Receiver bandwidth	20 kHz
Electron gyrofrequency	1.1 MHz @ 200 km	Doppler lines	Max. of 8/CIT in modes (1), (2) Max. of 256/CIT in mode (3)
Near-vertical & oblique, monostatic backscatter sounder modes	(1) Swept-frequency phased array (2) Fixed-frequency phased array (max. of 4 frequencies) (3) Fixed-frequency spaced-antenna drift (max. of 4 frequency-range bins)	Range gates (eg.)	10 – 330 km 60 – 380 km 60 – 700 km 60 – 1340 km 760 – 2040 km 60 – 2620 km 1400 – 2680 km 380 – 2940 km
Peak transmitter power	≈ 10 kW	Range steps	2.5, 5.0 or 10.0 km
Transmitter bandwidth	≈ 200 kHz	Range bins	128 or 256
Operating frequencies	0.5 – 30 MHz	Samples/CIT	2^{N+1}, N = 2, 3,...,9 (8, 16,...,1024)
Frequency steps	5, 10, 25, 50, 100 or 200 kHz	Dynamic range	90 dB
Pulse repetition rates	50, 100, 200 Hz	Amp. resolution	2/8 or 3/8 dB
Phase coding	Inter- & intra-pulse 180° phase codes	Phase resolution	1.4°

12.2 THE BEVERIDGE DIGISONDE 256

12.2.1 *Operational parameters*

Table 1 is a summary of the Digisonde 256 operating parameters. Although most entries are self-explanatory, consider the following points: (1) because of the offset between geographic and geomagnetic poles, Beveridge is at a fairly high magnetic latitude, despite its geographic mid-latitude, this being a favourable circumstance for auroral studies, (2) in the so-called fixed-frequency mode the coherent integrations (CITs) can be performed on up to four multiplexed frequencies simultaneously (with tape dump of spectral amplitudes and phases), (3) in the spaced-antenna drift mode the o- and x-mode echoes for up to eight antennas at four frequency-range bins can be multiplexed during each CIT, (4) in the swept- and fixed-frequency beam-steering modes a maximum of eight directions (including o- and x-mode vertical beams) can be multiplexed, (5) the Doppler spectral resolution is necessarily crude in the rapid, swept-frequency mode and, (6) each CIT may consist of any value from 8 to 1024 samples. Consult Bibl et al. (1981) for more insights into the operational capabilities of this instrument.

12.2.2 *Vertical delta radiation distribution patterns*

The vertical delta (ie. a vertical half-rhombic antenna) consists of two radiating wires each of length about 57 m and with elevation (tilt) angles of $\Phi_0 = 47°$ converging to form an apex. The plane of the delta is orientated at a geographic azimuth of $\theta_0 = 146°$. Here the antenna pattern was modelled as that due to the sum of two nonresonant wires pointing towards (θ_0, Φ_0) and $(\theta_0 + \pi, \Phi_0)$. The formula for the antenna pattern of a nonresonant wire is radially symmetric (see Terman 1943), simplifying the calculation across all (θ, Φ). Since the delta antenna is approximately a vertical element, vertically-polarised emissions should dominate; hence the positive image factor was used to allow for ground-plane reflections (Hall, 1991). A dielectric constant of 13 and a conductivity of 0.005 S m^{-1} were used to model the surrounding Earth. Figure 3(a) is the model radiation pattern at a representative frequency of 5 MHz, and showing substantial side lobes at low elevation angles. All such patterns in this note are plotted as energy patterns ($\propto$ amp^2) using a normalised grey scale.

Figure 4 is a plan view of the seven-element receiver antenna array orientated towards magnetic (compass) north. It is a form of the standard design at Millstone Hill, Massachusetts by UMLCAR. Each antenna consists of a crossed loop (for discrimination of circular polarisation) about 1.5 m across, which at the HF frequencies normally used (1 – 10 MHz) are adequately modelled as isotropic sources (however, side lobes develop by 30 MHz). The array factor derived by Scali (1989) for this elegant, spatial drift array was used, except again the effects of ground-plane reflections were modelled. Figure 3(b) is the antenna pattern for phase-delay cables of equal electrical length at 5 MHz, and Figure 3(c) is the effective radar pattern given by the product of the two preceding patterns. The half-power beam width (HPBW) is about 18° which means that the diametrical region of the overhead ionosphere illuminated is about 79 km across at an altitude of 250 km. By digitally selecting appropriate lengths of coaxial cable, this vertical beam can be tipped through about 8° from zenith at up to 12 possible azimuths; by multiplexing six of these partially overlapping beams separated by 60° in azimuth (i.e. 360° coverage), plus a vertical

beam, a 130 km swathe of the ionosphere is effectively illuminated at an altitude of 250 km.

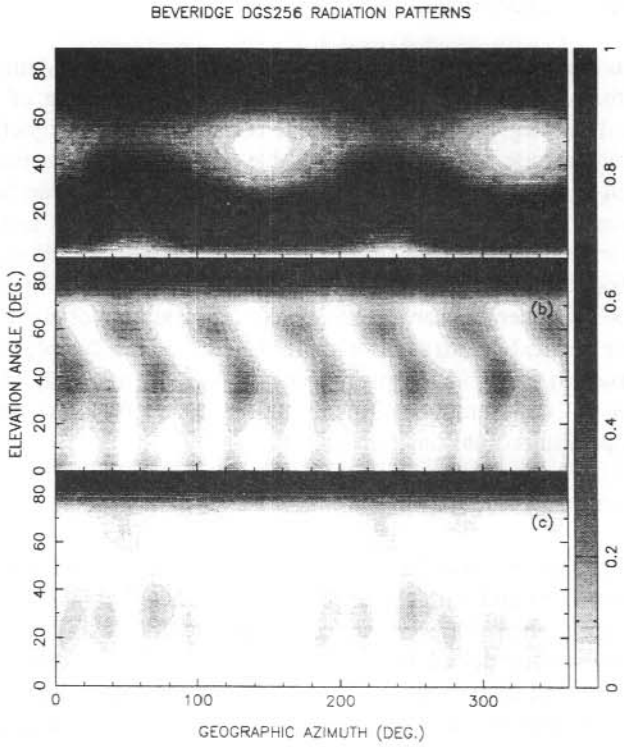

Figure 3. Model 5.0 MHz radiation distribution patterns plotted using a linear, normalised grey scale for (a) the vertical delta transmitter antenna, (b) the seven-element receiver array with equal lengths of phase-delay cable, and (c) the effective radar pattern.

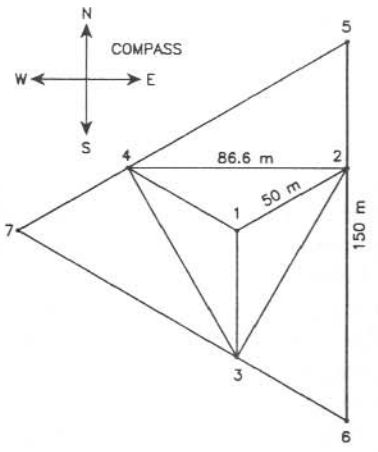

Figure 4. Plan view of the Beveridge Digisonde 256 seven-element receiver antenna array.

12.2.3 *Horizontal rhombic radiation distribution patterns*

We have implemented this nonstandard digisonde antenna design. The horizontal rhombic transmit antenna (e.g. see Terman 1955) consists of four horizontal radiating wires, in our case each of length about 105 m, and with the major axis of the rhombic aligned close to magnetic south. The one-half included side angle of our rhombic is $\chi = 55°$, with the first wire pointing towards azimuth $\theta_0 = 151°$, and the height of all wires above ground about 14 m. Here the antenna pattern was modelled as that due to the algebraic sum of four nonresonant wires, two of each pointing towards infinity at $(\theta_0, 0°)$ and $(\theta_0 + \pi - 2\chi, 0°)$ respectively (i.e. the four wires form two parallel pairs). The horizontal rhombic antenna is essentially a horizontal element, so the negative image factor was used to model ground-plane reflections.

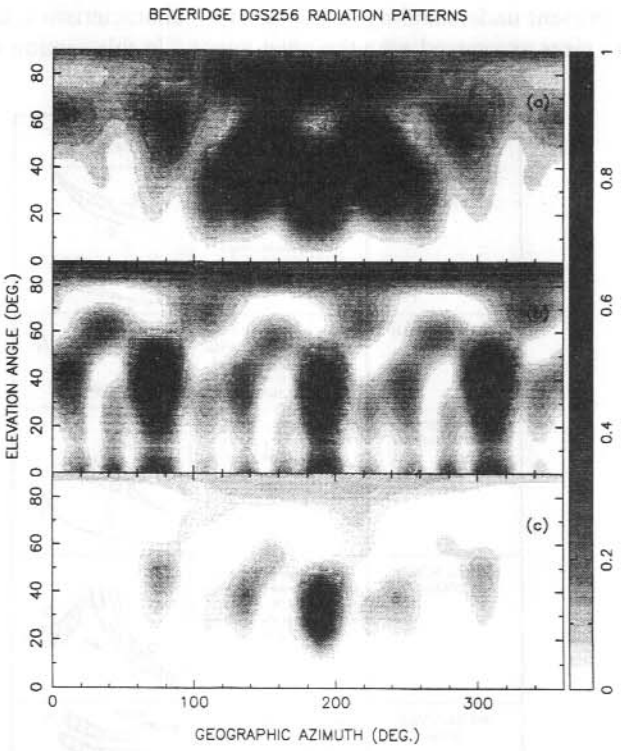

Figure 5. Model 5.0 MHz radiation distribution patterns for (a) the horizontal rhombic transmitter antenna, (b) the seven-element receiver array with large phase delays chosen to produce oblique beams, and (c) the effective radar pattern.

Figure 5(a) is the transmitter pattern calculated at 5 MHz, and it shows substantial, adjacent side lobes. Figure 5(b) is the receiver array pattern using the long lengths of coaxial cable required to tip the principal beam down to an intermediate elevation angle. Figure 4 shows that there is symmetry hidden within this double triangular array, and Figure 5(b) shows

that there are actually three principal beams for large lengths of phase-delay cables. The product of transmitter and receiver patterns (Figure 5(c)), however, results in a single, dominant beam of HPBW ≈21° centred at an elevation angle of 36°, and pointing towards the magnetic meridian. Note that the difference between geographic south (180°) and magnetic south is about 11° (1994 epoch) at Beveridge.

Obviously, as frequency increases, the HPBW of principal beams decreases, and more side lobes develop. The elevation angle of the oblique beam also decreases with frequency, and we expect that this will prove to be a useful design feature for probing the aspect sensitivity of field-aligned structures.

12.3 EXPERIMENTAL DIGITAL IONOGRAMS

Consider Figure 6 which summarises schematically the prevalent spread-F types observed at Beveridge, our present understanding of the spread-F characteristics, and the probable dominant structure sizes associated with the phenomena. In this section we illustrate the

DOMINANT STRUCTURE SIZE	CHARACTERISTICS	EXAMPLE O-RAY IONOGRAMS
LARGE SCALE (AGWs)	Range (top) & frequency (bottom) spread-F & intermediate forms: duplicate traces associated with oblique echoes and horizontal electron-density gradients.	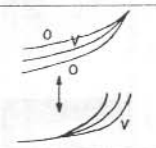
MEDIUM SCALE (AGWs)	Slightly range spread-F form associated with increasing (decreasing) obliquity of echoes during the F-region dusk (dawn).	
LARGE SCALE (Trough Surfaces) & SMALL SCALE (Slant-F)	Oblique trough surface traces at long ranges with slant-F (faint spread patches with straight undersides).	
SMALL SCALE (FAIs)	Oblique spread-F at long ranges & spread in frequency and range. Retardation observed at initial frequency of trace.	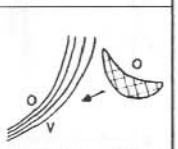
SMALL SCALE (FAIs)	Curtains of auroral echoes at great ranges attributed to backscatter from E-Region/lower F-Region irregularities.	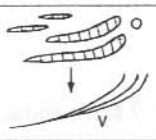

*Figure 6. Summary of ionospheric irregularities observed using the Beveridge digisonde (Λ = -48.0°). **V** characters represent near-vertical traces, **O** characters represent oblique traces, and arrows indicate the typical direction of movement of traces with time (except in the first schema where the double-headed arrow symbolises a continuum of spread-F forms between two extremes).*

various high-latitude phenomena observed from Beveridge by presenting experimental digital ionograms plotted using colour-coded optifont (Bibl and Reinisch 1978). Basically, the echo amplitudes are represented by a 16 character optically-weighted font (thereby encoding a 64 dB dynamic range using 4 dB resolution in these ionograms), with the angle-of-arrival and Doppler information represented using different colour palettes.

First, though, consider Figure 7(a) which is a high-integration gain Doppler ionogram demonstrating the enhanced sensitivity to oblique echoes recorded at great ranges achieved with the horizontal rhombic antenna design. Apparent are the leading edges of backscatter from the Southern Ocean due to signals propagated via the ionosphere on their outward and return paths, hence extending from the second-hop near-vertical traces (M condition F-layer traces are also present). Sea echoes are clearly visible from 7–13 MHz forming sloping traces from 250–400 km (Es propagation, trace A) and 600–1300 km (F-layer propagation, trace B).

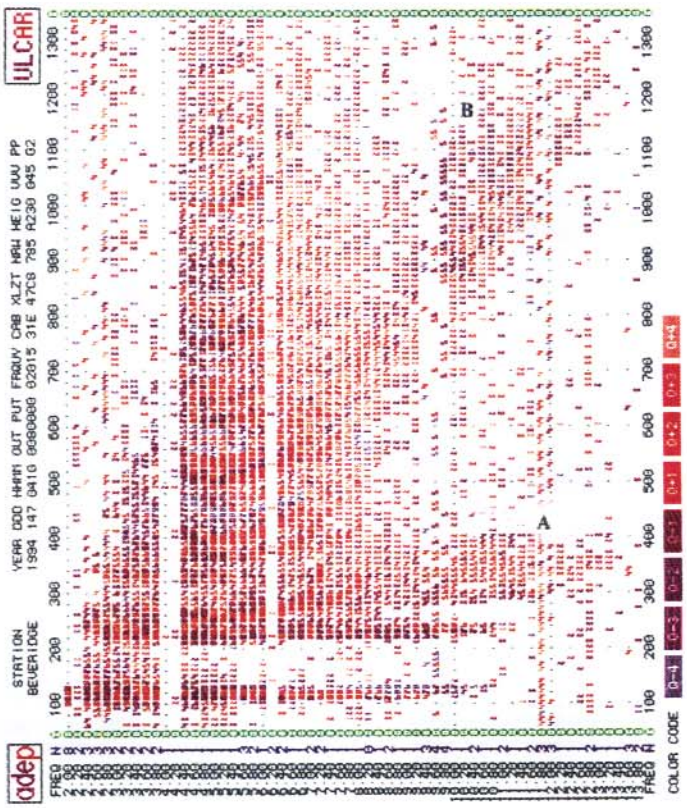

Figure 7(a). Sea-backscatter Doppler ionogram recorded on 04:10 UT day 147 1994. Doppler information is encoded with eight different colours representing frequency shifts of -0.684 Hz (grey blue; receding from station) through to +0.684 Hz (flesh) in 0.196 Hz steps.

Digisondes are extremely versatile instruments and programming them usually involves a complex set of trade-offs. The oblique sensitivity of Figure 7(a) was achieved by applying minimum automatic attenuation to the receiver, using a wide pulse width (133 s) to increase the backscattering volume, a long CIT (5.12 sec/frequency) to increase the spectral resolution attained by DFT-hardware (hence also the amplitudes of Doppler-binned echoes), whilst only integrating on a single beam to increase the Nyquist frequency in spectra and also the ionogram sweep rate so as to minimise the potential interference caused to other users of the HF spectrum. For auroral backscatter, however, it is probably not useful to multiplex different beams and thereby extend the CIT beyond several seconds because the maximum Doppler number will be too low for the very high Doppler shifts encountered in the auroral regions. This is because hardware constraints in the digisonde cause the actual cut-off frequency in spectra to be constrained by the CIT, not the Nyquist frequency.

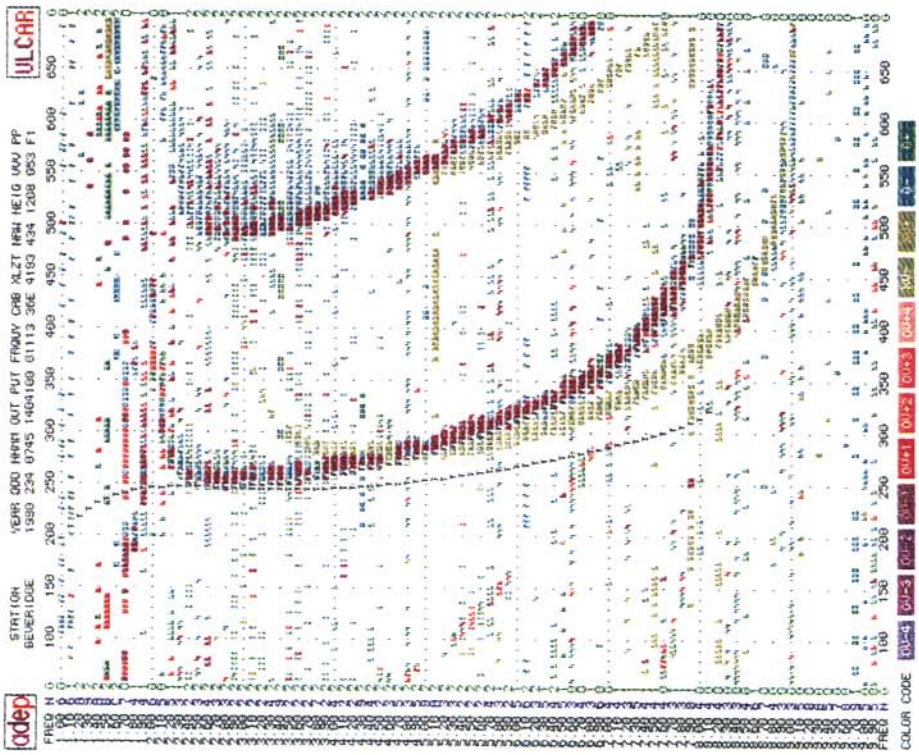

*Figure 7(b). Daytime first-hop spread-F ionogram with second-hop amplification of spread recorded on 07:45 UT day 234 1990. The first-hop F-layer trace was manually scaled (**F** characters) and inverted to yield an estimate of the true-height profile (**T** characters).*

Figure 7(b) is a daytime ionogram showing a narrow envelope of range-spread oblique echoes (green) which are found to increase (decrease) in number during the F-region dusk (dawn). The spread is amplified on the trailing edge of the second-hop trace, and has been associated with the passage of medium-scale AGWs (Bowman 1992a).

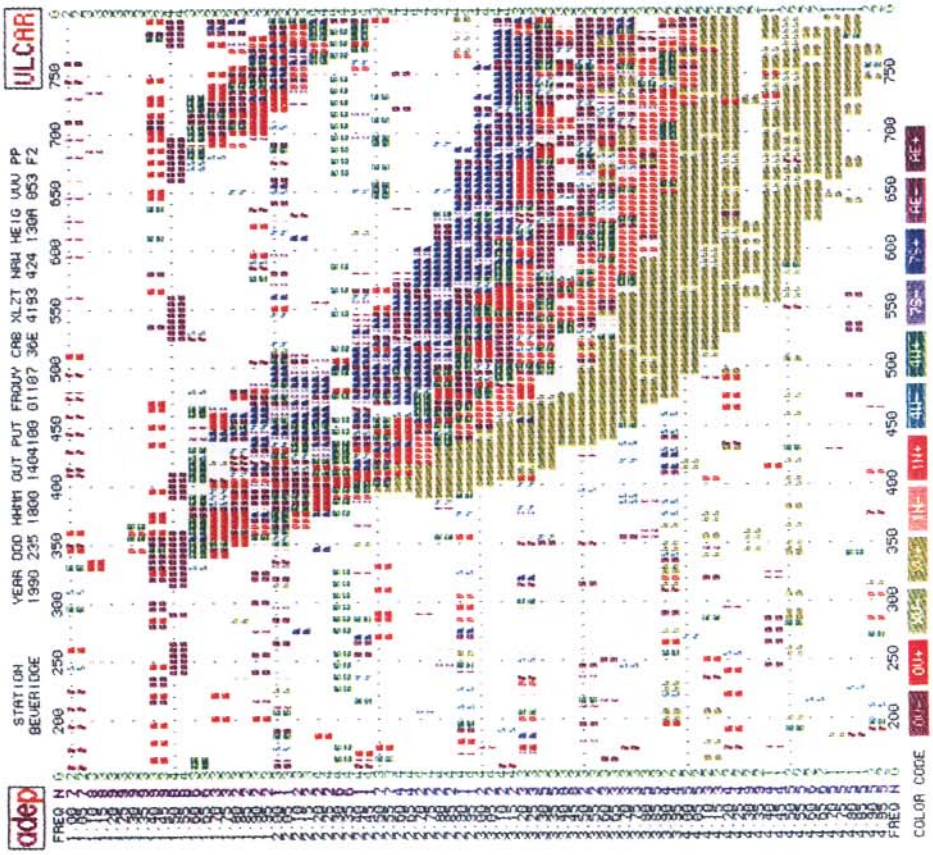

Figure 7(c). Ionogram recorded during severe spread-F conditions on 18:00 UT day 235 1990. The colour-coded key (right) shows that the spread is resolved into a number of reflection surfaces with different angle-of-arrivals. A digisonde with narrower radio beams would, presumably, resolve these reflection surfaces into still more angle-of-arrivals.

Figure 7(c) is an ionogram showing severe spread in range (160 km @ 2.5 MHz) and frequency (f_0F2 ranges from 3.00 to 4.05 MHz) recorded during the early morning hours (18:00 UT) when the mid-latitude trough was still near to overhead (as we show in Section 12.4). In a conventional ionogram recording this may have been classified as a case of unresolved spread-F; here the digisonde has resolved at least five dominate reflection surfaces, including those towards the south (blue), west (green), vertical (red), east (purple) and north (yellow red), and mostly with positive Doppler (ie. approaching surfaces). We interpret this ionogram in terms of the classical spread-F events associated with troughs and described by Bowman (1990).

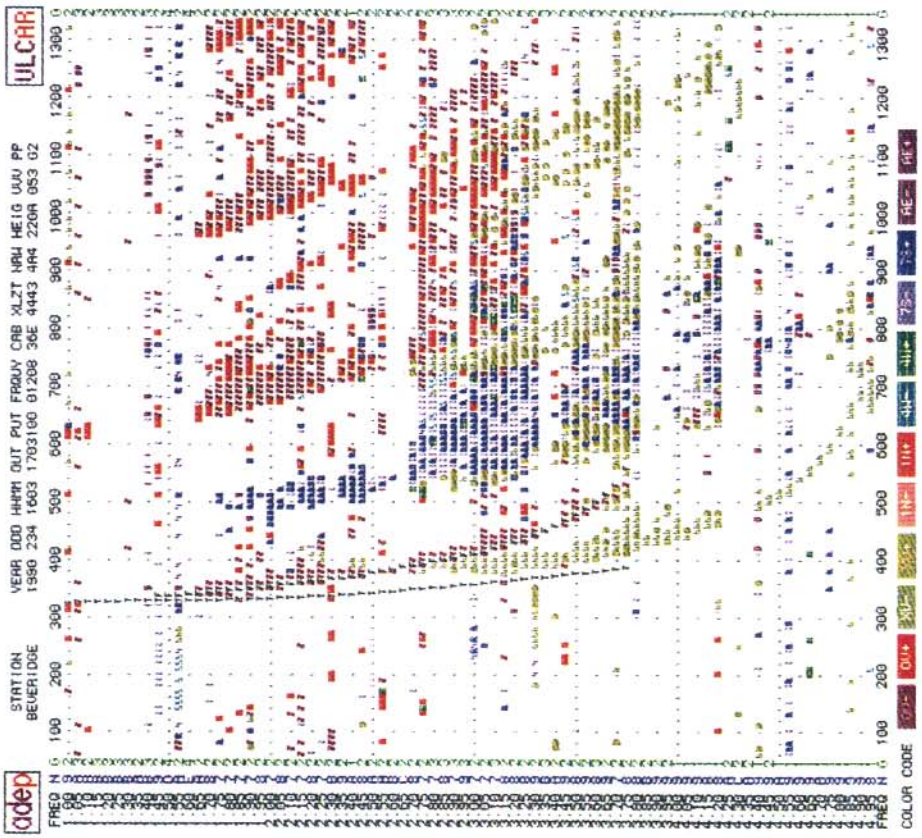

Figure 7(d). Echoes from an upper poleward trough surface exhibiting strong slant-F (blue echoes from the south) recorded on 16:03 UT day 234 1990.

Figure 7(d) was recorded on day 234 when the mid-latitude trough was approaching Beveridge from the south. Echoes from an elevated, poleward trough surface (trailing blue echoes with f_0F2 as low as 2.75 MHz) were accompanied by strong slant-F echoes (leading edge echoes extending out to as far as 4.60 MHz). It is uncertain whether incidences of trough wall detections with no slant-F occurrence are partly due to the poor signal-to-noise discrimination of ionograms. It is interesting that although the trough wall and slant-F echoes are dominated by large amplitude +ve Dopplers (dark blue), many of the weaker slant-F echoes have -ve Dopplers (light blue). This suggests that though the bulk motion of trough structures is towards the north, numerous small-scale structures migrate to the south (ie. there is a complete spectrum of irregularity wave numbers). However, Doppler aliasing is more likely to be the cause because the cut-off velocity for spectra in this digisonde mode was only ± 312.5 m s^{-1} @ 3.0 MHz, compared to the $1-3$ km s^{-1} often encountered at high latitudes (ie. the -ve Dopplers may have actually been due to echoes from sources moving at great speed towards the north).

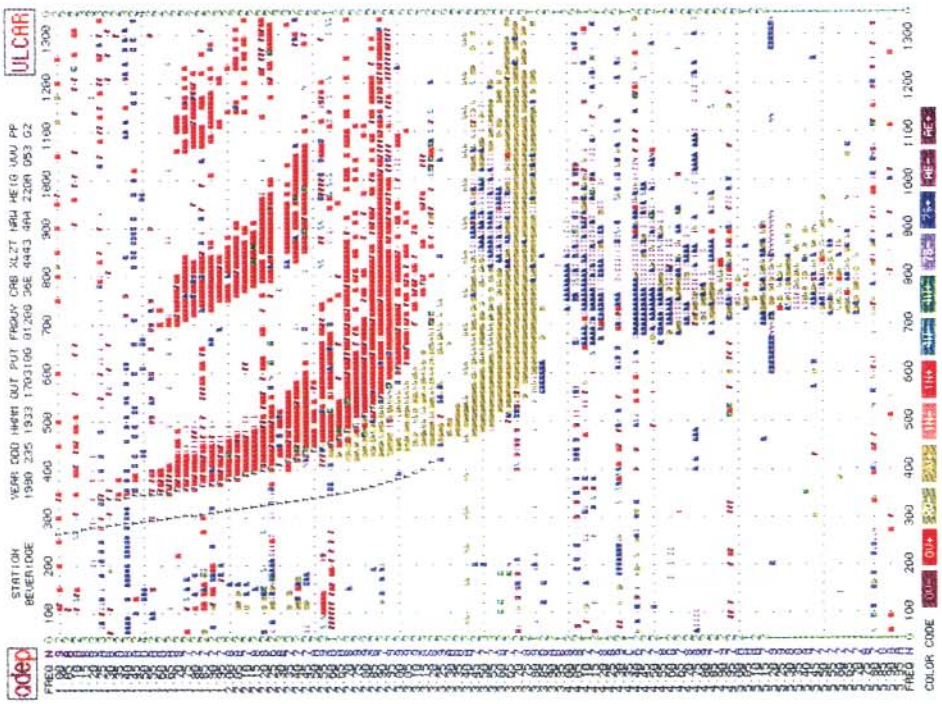

Figure 7(e). OS-F patch (blue echoes) recorded 19:33 UT day 235 1990.

Figure 7(e) shows an example of an OS-F patch (blue echoes) spread in frequency from 3.50 to as far as 5.65 MHz and range from 660 to about 1000 km. This patch approached and merged into the near-vertical ionosphere during the early morning hours, producing a unique form of spread-F. We are presently investigating the possibility that OS-F is caused by highly field-aligned irregularity patches extending into the topside ionosphere, and that these patches are related in some way to other high-latitude phenomena such as boundary-layer blobs or SAR-arcs (Rodger 1984).

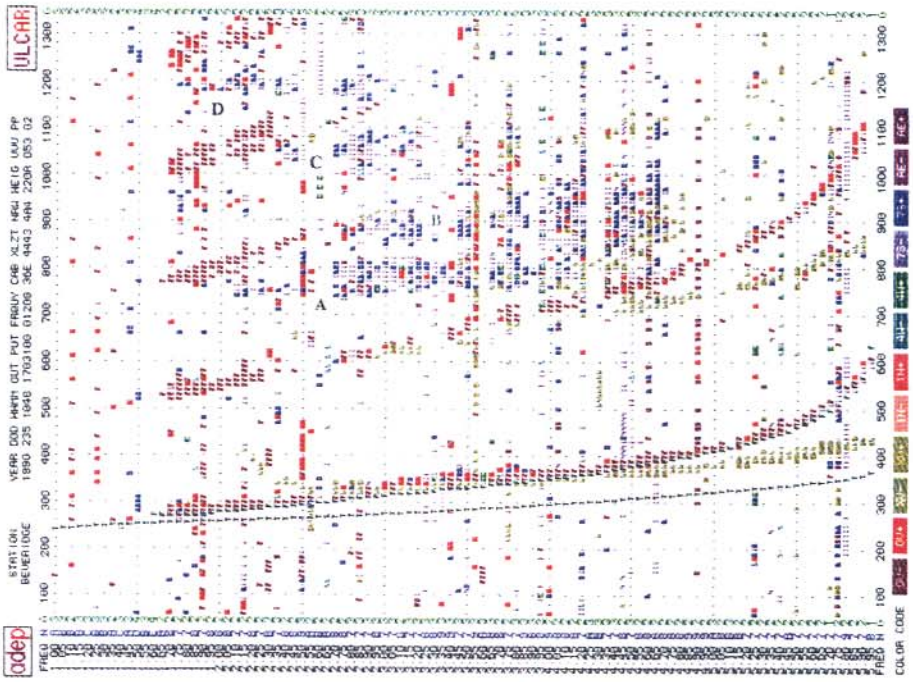

Figure 7(f). A curtain of radio aurora (i.e. blue echoes) recorded at great range on 10:48 UT day 235 1990.

Figure 7(f) is an example of an ionogram showing a curtain of radio aurora (Bates et al. 1966), a phenomena observed about every second night at Beveridge (albeit at ranges greater than those observed here; we are presently compiling occurrence statistics in the dimensions of time, range, and frequency), and in this instance converging upon the near-vertical ionosphere, thereby causing a major spread-F event. In this instance the leading edge of the blue echoes was probably coincident with the steep, field-aligned wall of the mid-latitude trough. Here, auroral traces are seen roughly from frequency 2.00 – 4.70 MHz and range 740 – 820 km (A), from 2.75 – 4.70 MHz and 850 – 1000 km (B), from 2.35 – 3.15 MHz and 1010 – 1100 km (C), and from 1.70 – 2.95 MHz and 1160 – 1260 km (D).

12.4 THE GEOMAGNETIC SUBSTORMS OF AUGUST 23 1990

Here we present the early results of manual ionogram scalings in time series form for the disturbed night ($\Sigma K_p = 46$) of 23 August 1990 (day 235) revealing the complex upper-atmosphere dynamics that can occur in the vicinity of the transition between the high- and mid-latitude ionospheres during geomagnetic substorms. Figure 8 presents (a) the variation of frequency parameters f_oF2, f_oE, $f_{o,x}Es$ (i.e. the top frequency whether it corresponds to an o- or x-mode echo) and $f_{min}F$, and (b) the results of ARTIST true-height profile analysis (Reinisch and Xueqin 1983; Gamache et al. 1992) applied to near-vertical ionogram traces for the period 9 – 21 UT (7 pm – 7 am LT). Two major disturbances arrived above Beveridge during this evening. At about 11:33 UT the ionosphere had completed a sudden drop in true height of about 85 km (3.0 MHz contour) which was followed by a dramatic height rise ($\approx$ 145 km) finishing at about 12:00 UT. A strong dip in f_oF2 by about 1.6 MHz also occurred at 11:45 UT. The passage of this LSTID (Bowman 1992b) was accompanied by an episode of blanketing Es which may have been caused by wind shears (Whitehead 1989) associated with the arrival of the LSTID, or, as shall be seen, by the arrival of aurora.

Figure 9 presents the results of further manual vertical and oblique ionogram scalings (8 h^{-1}), including (a) the width of range spread at frequency 2.5 MHz (chosen to yield consistent results throughout the evening) as an index of near-vertical spread-F activity throughout the same period as Figure 8. It can be seen that a substantial range-spread event (reaching 60 km of spread at 11:45 UT) accompanied the arrival of the disturbance at about 11:33 UT (estimates of this index were unreliable for some ionograms because of blanketing Es, hence the missing values).

The arrival of a second TID of somewhat different character occurred at about 14 UT, as shown by the second minimum in Figure 8(b) tagged '14:15 UT'. The height rise following this event was about 135 km (3.0 MHz contour), but was much slower, reaching 430 km at about 16:30 UT. Figure 8(a) shows that f_oF2 dropped to about 3.7 MHz at this time. However, this is an upper estimate of the actual values occurring within the volume of ionosphere above Beveridge selected by the radio beams. As Figure 9(a) shows, an intense episode spread-F accompanied the height rise, well developed by 14:30 UT and reaching values of over 250 km in spread at 3.0 MHz. This large index of spread-F is partly the result of range-spread, but it is also a consequence of intense frequency spread. Figure 7(c) showed one of these highly spread ionograms recorded at 18:00 UT in which f_oF2 was actually as low as 3.1 MHz; earlier at 16:03 UT f_oF2 was as low as 2.4 MHz. The F-layer heights at 16:30 UT were 50 km greater than those of the previous day at the

same time (which we believe were becoming trough-like anyway), and the f_0F2 values dropped to values comparable to those observed at Hobart when the mid-latitude trough is overhead. It seems reasonable to conclude that on this night of high geomagnetic activity the mid-latitude trough drifted over Beveridge shortly after the arrival of the TID at 14:15 UT.

Figure 9(b) shows that auroral backscatter traces were first observed at great ranges (on oblique ionograms) near to 10:10 UT, then rapidly converged towards Beveridge, but disappeared in ionograms at 11:18 UT. If they had reached Beveridge it would have been shortly after the arrival time of the LSTID at 11:33 UT (tagged in Figures 8 and 9). The appearance of these backscatter traces in ionograms was illustrated in Figure 7(f).

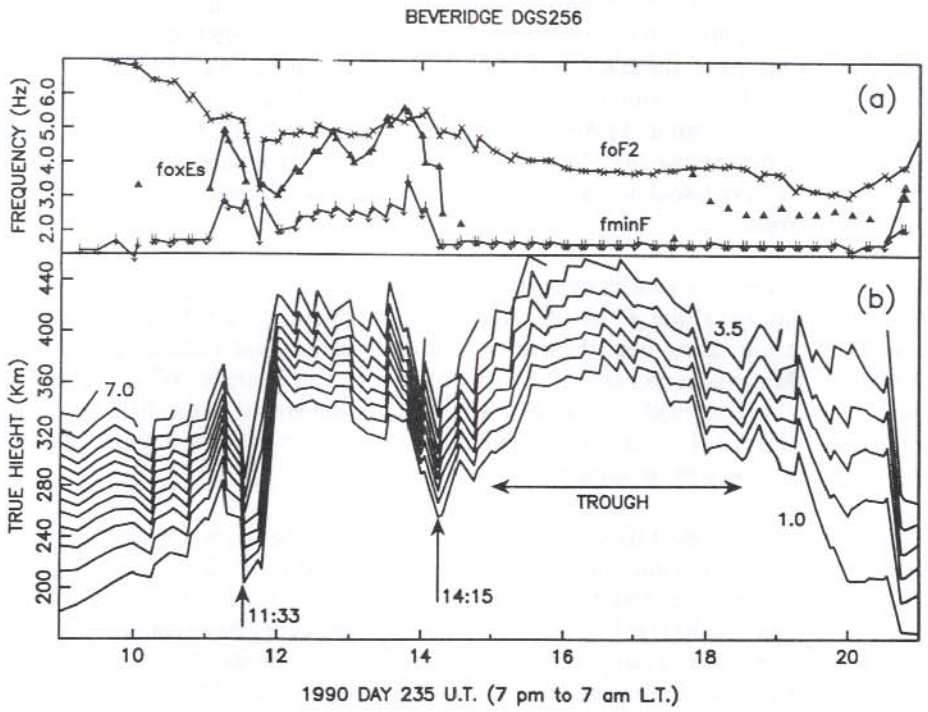

Figure 8. (a) Variation of frequency parameters f_oF2 (×), f_oE (Δ), $f_{o,x}Es$ (Δ), and $f_{min}F$ (↓) and (b) the results of true-height profile analyses for the period 9–21 UT day 235 1990 at Beveridge. Isoionic contours from 1.0 to 7.0 MHz are plotted in 0.5 MHz steps. Ninety-two ionograms were used for this manual analysis.

Another episode of auroral backscatter appeared at great range (≈1330 km) on ionograms just before 12 UT. D. Ward (personal communication 1994) observing near Melbourne, first noticed an optical aurora at 12:00 UT located towards magnetic south at low to medium elevation. The radio aurora arrived near Beveridge shortly after the arrival of the second TID at around 14:15 UT (tagged in Figure 8(b)), and lingered to the south of the station at close range (Figure 9(b)) throughout the period of trough-like conditions, directly contributing to the overall spread-F event. The appearance of these spread-F traces was illustrated in Figure 7(c).

A reflection point in the ionosphere which passes overhead with a uniform speed will exhibit a characteristic U-shaped trace in a h't plot (Macdougall and Grant 1994). Separate U-shaped curves for reflection points passing overhead were calculated and fitted to the two episodes of auroral convergence. These curves are shown in Figure 9(b), but they are truncated by the edges of the plot. The first curve is for a reflection point moving at horizontal speed of 150 m s^{-1}, and passing overhead with arbitrary, though plausible, values of h' = 150 km and time 12:30 UT; the second curve uses a speed of 125 m s^{-1}, and passes overhead with h' = 150 km and at time 15:15 UT.

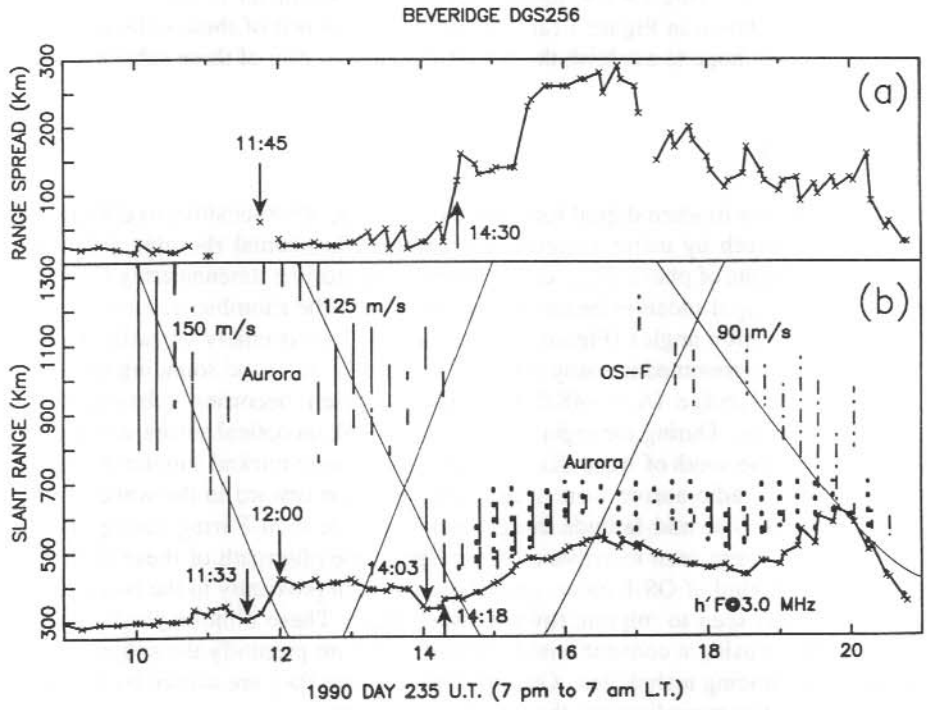

Figure 9. Results of further manual scalings of Figure 8 data. (a) Range spread @ 2.5 MHz. (b) Slant range of auroral traces in oblique ionograms @ 3 and 4 MHz (——), range of auroral traces in near-vertical ionograms @ 3.0 MHz (• • • • •), OS-F traces @ 4.0–4.8 MHz (• — • — •), and h'F @ 3.0 MHz (×–×–×–×). Parameters used to calculate the truncated U-shaped curves are explained in the text.

A third kind of disturbance arrived just before F-region sunrise. To our knowledge this special kind phenomena that we call OS-F is not completely understood. A tenuous OS-F patch first appeared in ionograms at 17:03 UT at range ≈1200 km. The patch slowly converged in range upon Beveridge (and down in radio frequency), beginning to merge into the overhead ionosphere just before 20 UT and causing another near-vertical spread-F event, then was lost at F-region sunrise. The disappearance of F-layer ionogram traces during 20:30 to 21:00 UT showed that a D-region absorption event occurred above Beveridge then. The appearance of this OS-F patch in ionograms was illustrated in Figure 7(e).

A third U-shaped curve (Figure 9(b)) was fitted to the OS-F patch convergence above Beveridge. A reflection point moving at a horizontal speed of 90 m s^{-1} and passing overhead with h' = 400 km and at time 21:22 UT gave a plausible fit. This speed is for the front wall of the irregularity patch since the fit was to the leading edge of the ionogram traces (echoes from which experienced the least retardation). The leading edge of auroral traces was not used for speed estimates because the trend for the auroral zone was sought (as opposed to individual, sometimes diffuse traces).

We are presently studying routine ionograms and magnetometer records recorded at the research stations shown in Figure 1 (and others) in the context of these oblique ionosonde measurements. We hope to establish the propagation and impact of these substorm events at true mid-latitudes.

12.5 SUMMARY

We have rendered a modern digital ionosonde (Digisonde 256) sensitive to oblique echoes from magnetic south by using a specially configured horizontal rhombic antenna. We increased the lengths of phase-delay cables driving the receiver antenna array (Figure 4) so as to form a principal receiver beam in alignment with the rhombic transmitter beam at intermediate elevation angles (Figure 5). The sounder is extremely versatile, having the capability to be programmed in many different modes (Table 1) and sounding schedules. It is located at Beveridge (Λ = -48.0°), a station which becomes subauroral during geomagnetic storms. During the night of 23 August 1990, an optical aurora was reported to have occurred to the south of Australia, and radio aurora were tracked simultaneously by the digisonde. These radio aurora were seen to migrate equatorward in the wake of LSTIDs passing overhead. The mid-latitude trough, and fine-scale slant-F irregularities associated with this trough, were seen to arrive at Beveridge in the aftermath of these disturbances. Finally, a special kind of OS-F patch, probably located in proximity to the boundary of the auroral zone, was seen to migrate towards Beveridge. These oblique patches would be difficult to detect using a conventional ionosonde, and are presently the subject of further study using ray-tracing techniques. One possibility is that they are caused by highly field-aligned irregularities extending into the topside ionosphere.

Clearly, the oblique sensitivity of our digisonde makes it especially useful for surveying the ionospheric dynamics occurring over much larger atmospheric regions than are accessible to conventional ionosondes. Indeed, new kinds of spread-F only become fully accessible in the oblique sounding mode (e.g. distant trough surfaces and OS-F). Beveridge is an important ionospheric research station because of these reasons, and because of its strategic

location in the transition region between the high- and true mid-latitude ionospheres, where, especially during periods of high solar activity, we can expect to record the impact of substorm events (including mid-latitude dynamo electric fields driven by joule heating in the auroral zone) upon the greater global region covered by the mid-latitude ionosphere. Expanded high-latitude convection patterns also offer the possibility for convection-corotation transition effects to be investigated. The results indicate some of the phenomena which could be studied in detail by a SuperDARN backscatter radar (Greenwald et al. 1985) located near, say, Hobart. With such a facility Beveridge would become an even more important station supporting the interpretation of measurements obtained by a SuperDARN type radar.

12.6 ACKNOWLEDGMENTS

This research is supported by a grant from the Australian Research Council. Jim Scali is thanked for his pioneering work establishing the Beveridge digisonde. Alan Rodger of the British Antarctic Survey is thanked for stimulating discussions about trough physics. Fred Rich is thanked for providing access to DMSP electron boundary files over the SPAN computer network. The receiving antenna design for low-angle reception was provided by Bodo Reinisch of UMLCAR.

REFERENCES

Bates, H.F., Belon, A.E., Romick, G.J. *and* Stringer, W.J. (1966). On the correlation of optical and radio auroras. *Journal of Atmospheric and Terrestrial Physics 28*: 439–446.

Bibl, K. *and* Reinisch, W. (1978). The universal digital ionosonde. *Radio Science 13*:519–530.

Bibl, K., Reinisch, B.W. *and* Kitrosser, D.F. (1981). Digisonde 256 – general description of the compact digital ionospheric sounder. University Lowell Center for Atmospheric Research Technical Manual.

Bowman, G.G. (1990). A review of some recent work on mid-latitude spread-F occurrence as detected by ionosondes. *Journal of Geomagnetism and Geoelectricity 42*:109–138.

Bowman, G.G. *and* Hajkowicz, L.A. (1991). Small-scale ionospheric structures associated with mid-latitude spread-F. *Journal of Atmospheric and Terrestrial Physics 53*:447–457.

Bowman, G.G. (1992a). Some aspects of mid-latitude daytime ionospheric disturbances. *Journal of Atmospheric and Terrestrial Physics 54*:1513–1521.

Bowman, G.G. (1992b). Some aspects of large-scale travelling ionospheric disturbances. *Planetary and Space Science 40*:829–845.

Gamache, R.R., Reinisch, B.W. *and* Kersey, W.T. (1992). ARTIST electron-density profile algorithm. University of Massachusetts Lowell Center for Atmospheric Research, Scientific Report No. 468.

Gussenhoven, M.S., Hardy, D.A. *and* Heinemann, N. (1983). Systematics of the equatorward diffuse auroral boundary. *Journal of Geophysical Research 88*:5692–5708.

Greenwald, R.A., Baker, K.B., Hutchins, R.A. *and* Hanuise, C. (1985). An HF phased-array radar for studying small-scale structure in the high-latitude ionosphere. *Radio Science 20*:63–79.

Hall, G. (Ed) (1991). *The ARRL Antenna Book*. The American Radio Relay League, Newington, CT 06111, U.S.A.

Kjaersgaard, H. (1984). Radio antenna for off-vertical ionospheric echoes. Research Report, Department of Electrical and Computer Systems Engineering, Monash University, Australia.

Macdougall, J. *and* Grant, I. (1994). Polar cap patches by a pair of polar cap digital ionosondes. Second Joint Workshop for CEDAR HLPS/STEP GAPS near Boulder, Colorado, June 27 to 29.

Quach, A.T.D. *and* Dyson, P.L. (1992). Severe spread-F events at the mid-latitude station of Beveridge. In: Essex, E.A. *and* Whitehead, J.D. (Eds). *South Pacific STEP Workshop Proceedings*, Melbourne, Victoria, February 10–14.

Reinisch, B.W. *and* Xueqin, H. (1983). Automatic calculation of electron density profiles from digital ionograms 3. Processing of bottomside ionograms. *Radio Science 18*:477–492.

Reinisch, B.W., Bibl K., Kitrosser, D.F., Sales, G.S., Tang, J.S., Zhang, Z-M., Bullett, T.W. *and* Ralls, J.A. (1989). The Digisonde 256 ionospheric sounder. In: Liu, C.H. (Ed). *World Ionosphere Thermosphere Study Handbook 2*:1–33.

Rodger, A.S. (1984). Spread-F ionospheric irregularities and their relationship to stable auroral red arcs at magnetic mid-latitudes. *Journal of Atmospheric and Terrestrial Physics 46*:335–342.

Rodger, A.S., Brace, L.H., Hoegy, W.R. *and* Winningham, J.D. (1986). The poleward edge of the mid-latitude trough – its formation, orientation and dynamics. *Journal of Atmospheric and Terrestrial Physics 48*:715–728.

Scali, J.L. (1989). *A study of spread-F irregularities at mid-latitudes*. Ph.D. Thesis, La Trobe University, Australia.

Terman, F.E. (1943). *Radio Engineer's Handbook*. McGraw-Hill, New York. Pp.795–797.

Terman, F.E. (1955). *Electronics and Radio Engineering*. McGraw-Hill, New York. Pp. 880–882.

Whitehead, J.D. (1989). Recent work on mid-latitude and equatorial sporadic-E. *Journal of Atmospheric and Terrestrial Physics 51*:401–424.

13. SPREAD E – A SURVEY OF THE AUSTRALIAN STATIONS

P.J. Wilkinson

IPS Radio and Space Services
P 0 Box 5606
West Chatswood NSW 2057

ABSTRACT

Spreading in the F region, thought due to irregularities in the ionisation, is easily recognised on ionograms and statistics of its occurrence are familiar in the literature. Spreading is also observed on ionogram returns from the sporadic E and the normal E region but has attracted much less systematic attention. At Australian ionosonde stations, since 1983, spreading in the E region has been scaled regularly.

Generally, spreading is more common at higher latitudes and in winter. It is least common at the equinoxes, and least of all during the southern hemisphere, spring equinox. There is a diurnal change in spreading occurrence, with a maximum towards dawn. There is a good amount of year-to-year variability, making it difficult to decide whether there is also solar cycle variability present. There is also station-to-station variability, making it hard to identify more subtle trends in the appearance of spreading. Spreading in the normal E region is far less common than when sporadic E is present. When spread sporadic E is present, the blanketing frequency, fbEs, can differ significantly from the penetration frequency for the layer (foEs).

13.1 INTRODUCTION

Night-time spread-F in the ionosphere has been studied extensively, studies outlining its morphology and phenomenology. The cause of the spread traces has been attributed to various ionisation gradients from small scale irregularities to travelling ionospheric disturbances. Much of this work has been based on ionograms collected in the world-wide ionosonde network. At stations in this network, a set of standard parameters is scaled and when spreading in the F region exceeds 0.5 MHz, a descriptive letter, F, is scaled with foF2 (UAG-23A, Piggott and Rawer 1972). These data have proved to be a valuable resource in delineating the nature of spread F.

Although spreading in the E region is not uncommon, no similar convention exists for scaling its presence. Consequently, mid-latitude E region spreading has attracted much less attention. Bowman (1985), in possibly the only work of any note on spread Es morphology, used data from the Japanese network scaled before the International Geophysical Year (IGY). In preparation for the IGY, ionogram scaling rules were standardised and, unfortunately, E region spreading was not included among the common set scaled from that time, presumably because it is a gain sensitive parameter.

Spreading seems to affect both the normal E layer as well as the sporadic E layer although it is more common in the latter. An example of sporadic E spreading is shown in Figure 1. Whatever the process, the irregular, but common appearance makes the phenomenon worthy of more detailed analysis.

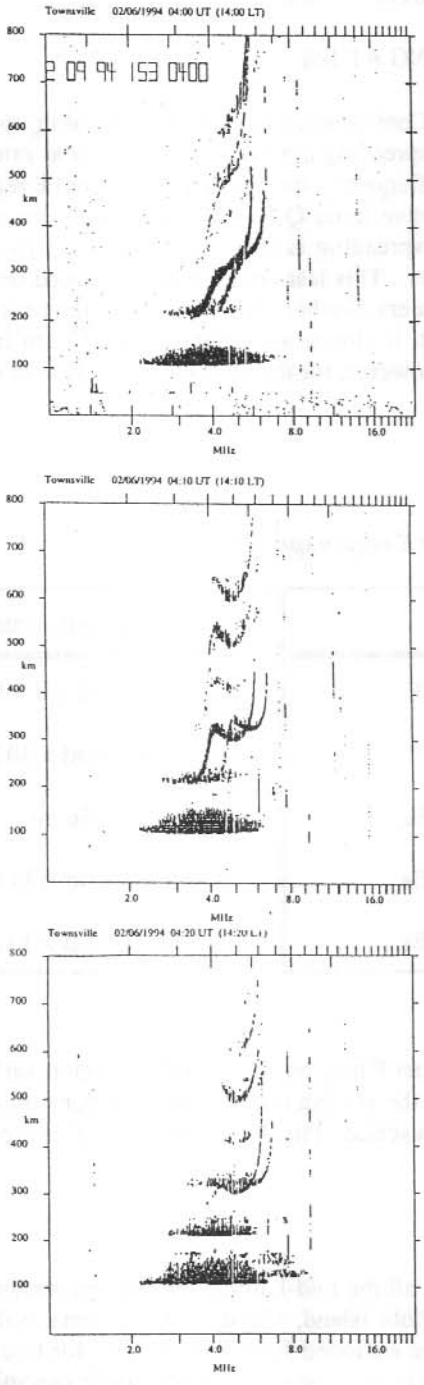

Figure 1. Examples of spread Es.

IPS therefore introduced new scaling rules in 1984 for scaling spreading in the E region. The first preliminary results based on this are reported here.

13.2 E REGION SCALING AT IPS

At the 1984 IPS Scalers' Conference, IPS commenced scaling spread in the E region using several flags. Since the spreading almost always formed as range spreading, there being too little turn-up to show frequency spreading in the normal E region anyway, the presence was noted with a descriptive letter Q on h'E and h'Es whenever there is 30 km or more range spreading. When spreading is present, but does not exceed 30 km, an F may be scaled on either parameter. This last option was introduced on an experimental basis at Hobart and Vanimo. Scalers at other stations felt the distinction was too small and that when spread was present, it almost always exceeded 30 km in range. These rules are summarised in Table 1. However, for the analysis, Q and F were usually treated together.

Table 1. Scaling ruler for E region spreading.

	Descriptive letter
foE	F is spread ≥ 0.3 MHz
h'E	Q is spread > 30 km
foEs	Nothing
h'Es	F if spread < 30 km
h'Es	Q if spread > 30 km

In addition, the scaling letter F may be scaled in the E region, on foE, if there is significant spreading there affecting the scaling of foE. This happens on occasions and affects the accuracy of the parameters scaled. Finally, when particle E is present, then a K is scaled on foE and foEs, as usual.

13.3 RESULTS

Data were collected from all the mid-latitude ionospheric stations. These were Vanimo, Townsville, Darwin, Norfolk Island, Mundaring, Canberra, Salisbury and Hobart. The high latitude stations were excluded from this analysis for two reasons. First, E region spreading at high latitudes is very common due to particle precipitation and is scaled using the particle E notation together with the auroral type Es classification. Second, at the time

this study was started, high latitude data were being scaled by a variety of people and it was unrealistic to add the additional rules. In retrospect, it is unfortunate this decision was not reviewed when the high latitude scaling task was stabilised around 1989 – 1990.

The analysis presented here uses the percentage occurrence of spread Es throughout. This is calculated as follows. Sporadic E is judged present if h'Es $\neq 0$, and the value is counted. When h'Es = 0, sporadic E is not present, although its appearance may have been obscured by some form of equipment m (descriptive letter C is used), interference (S) or a major absorption increase (B). If any of these descriptive letters was used, that datum was discarded. The percentage occurrence was then defined as the number of times the descriptive letter F or Q was scaled divided by the number of times it could have been scaled times 100.

13.3.1 *Normal E region spreading*

Very little spreading was observed in the normal E region that was not accompanied by sporadic E. Overall, E region spreading occurred roughly 20% as often as sporadic E spreading.

Spreading was more likely to be scaled as an F on foE, indicating frequency spreading near the critical frequency, than as a Q on h'Es, indicating at least 30 km of range spread.

Spread E is most prominent at Hobart, diminishing in importance with decreasing latitude and is most common in winter. Since spreading is gain sensitive, this trend may be linked to changes in absorption. This will be worth investigating further.

13.3.2 *Diurnal occurrence of spread Es – Figure 2*

All mid-latitude stations show a marked diurnal variation in spread Es. There is a broad minimum near local noon and a maximum prior to dawn. The nighttime maximum reaches 25% occurrence at Norfolk, Townsville and Darwin.

There are local variations from this general pattern. Norfolk Island has a broader nighttime maximum while Mundaring, Townsville and Darwin have a secondary maximum near 22 LT (12 UT). Vanimo differs, having a clear maximum prior to 22 LT. Generally, the occurrence maximum increases as latitude decreases.

Bowman (1985) reported similar results for the Japanese stations, although the occurrence peak was closer to 8%. The difference could be linked to equipment sensitivity.

13.3.3 *Seasonal occurrence of spread Es – Figure 3*

Occurrence of spread Es is lowest at the equinox; the spring minimum being deepest. The minimum occurrence is greater at lower latitudes.

A winter maximum in occurrence appears at all stations, with the peak shifting towards autumn as latitude decreases.

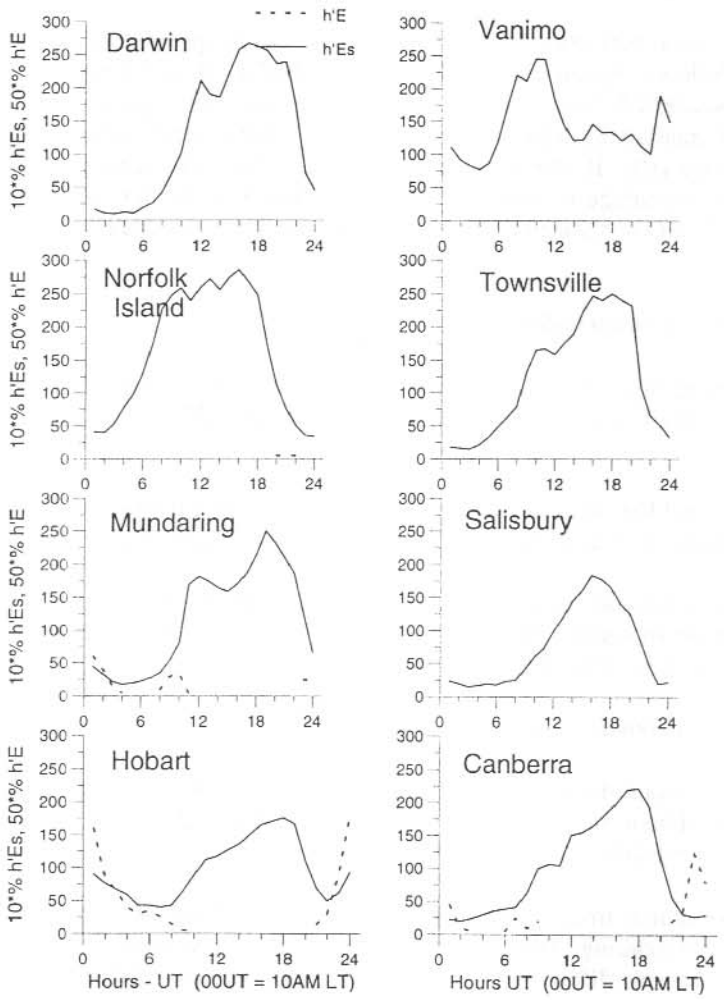

Figure 2. The diurnal percentage occurrence of spread Es and spread E for Australian stations. Note that the scales are adjusted. Spread Es increases by a factor of 10 and spread E by a factor of 50.

13.3.4 *Yearly occurrence of spread Es – Figure 4*

No obvious relationship was found between the different stations when accumulative yearly statistics were inspected. Partly, this could be due to missing data (e.g. Darwin lost 8 months following a lightning strike) and is worth further analysis.

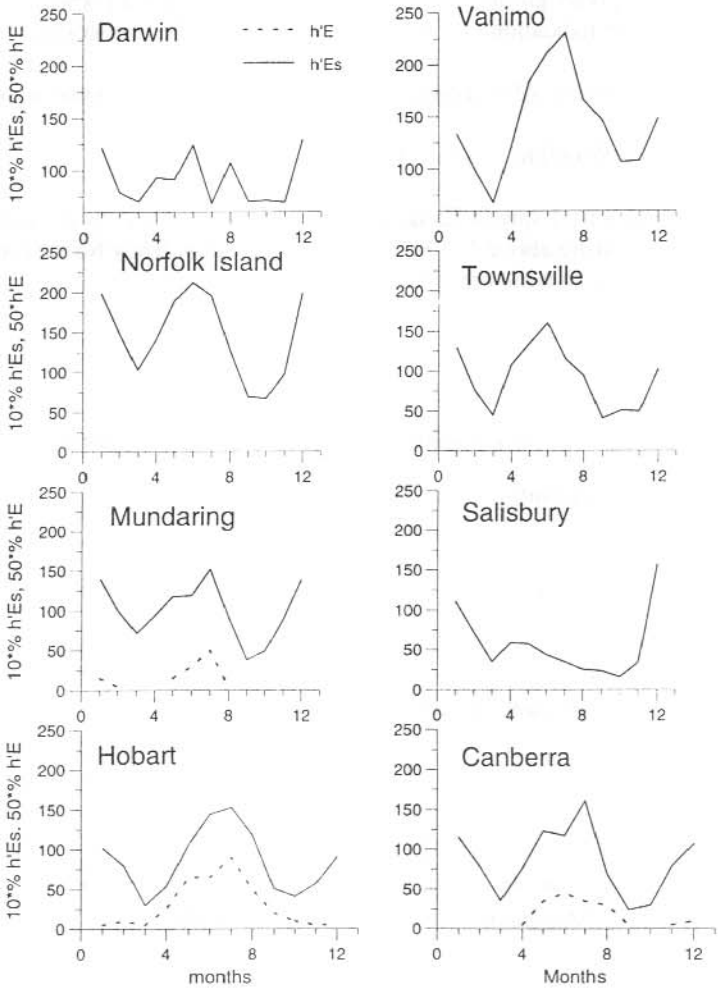

Figure 3. The seasonal percentage occurrence of spread Es and spread E for Australian stations. Note that the scales are adjusted.

13.3.5 *Comparison with (foEs-fbEs) in the presence of spread Es – Figure 5*

The presence of spread Es affects the difference between the penetration frequency (foEs) and blanketing frequency (fbEs) for a layer. This is clear from inspection of just a few examples and would be expected to show up in a statistical samples. In Figure 5, Δf = (foEs-fbEs) is split into two samples – those where spread Es is present and those where it isn't - and histograms of Δf are calculated. As Figure 5 shows, there is a significant difference between these samples with the most common value of Δf being

0 MHz for the no-spread group and $\Delta f \approx 1$ MHz when spread is present for all stations. The error bars give an indication of the yearly differences in the histograms.

When spread Es is present, Δf is larger, on average, than when no spread is present.

13.3.6 *Variation with height of spread Es*

The height distribution of spread Es is narrower than when there is no spread, with few spread Es layers occuring above 125 km. Thus there is a tendency for spread Es to have a lower average height than non-spread Es.

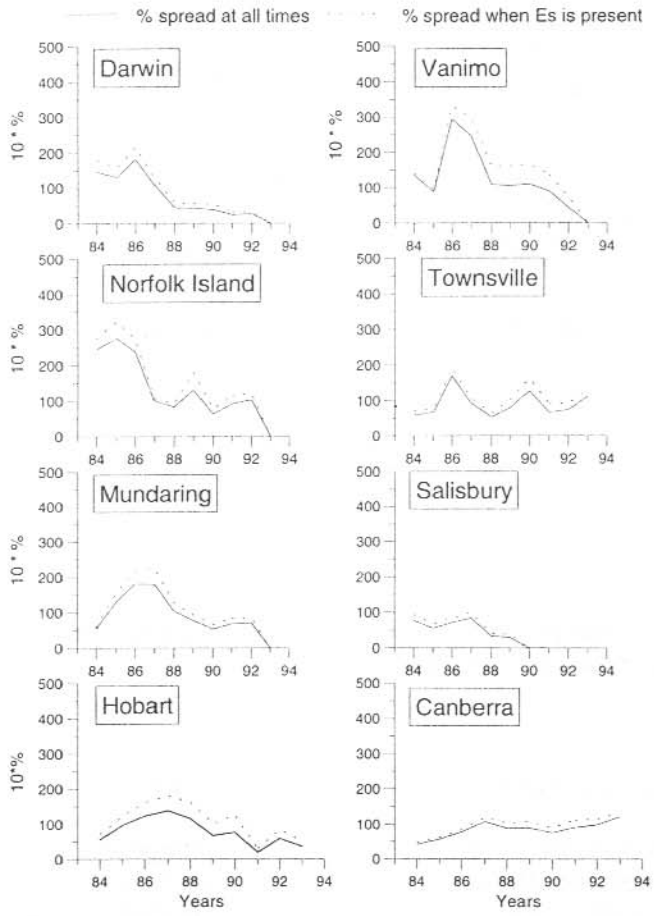

Figure 4. The yearly percentage occurrence of spread Es and all E region spreading for Australian stations. Here, the E region spreading has been added to the sporadic E spreading. The two distributions are relatively similar from one year to the next.

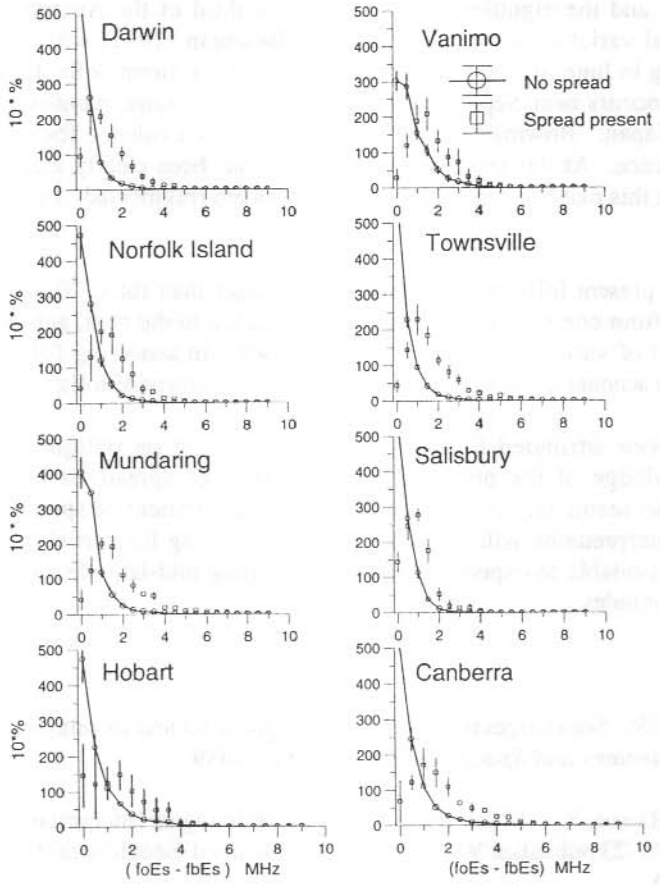

Figure 5. The percentage occurrence of (foEs-fbEs) for spread and non-spread conditions. The length of the error bars shows the yearly variation.

13.4 SUMMARY

Spread E is much less common than spread Es. Whitehead (private communication) has suggested the E region spreading could be a gradient instability, in which case there will always be some sporadic E present, although it may be obscured by the normal E region. It will be worth checking the occurrence of sporadic E in association with spread E. Spread E is less common at lower latitudes. This may be real, or due to observational bias. E region spreading appears to be a gain sensitive parameter and the increased solar induced absorption associated with lower latitudes could cause the apparent decrease in occurrence. However, it seems unlikely given the seasonal and diurnal characteristics.

The morphology of spread Es is similar to Bowman (1985) having the same shaped diurnal curve. However, the daytime occurrence rate in Japan is roughly half that observed for the Australian stations and the nighttime rate is roughly a third of the Australian stations. Oddly, the seasonal variation appears the same as Bowman (1995) with the principal maximum occurring in June (winter for the Australian stations, summer for Japan) and the deepest minimum occurs near September-October, again the same months as Bowman (1995) found for Japan. Bowman (1995) also found weak evidence for a solar cycle variation in occurrence. At this stage, no similar trend has been clearly identified in the Australian data, but this maybe because the data samples are fragmented. Further analysis will be worthwhile.

When spread Es is present foEs may be significantly larger than fbEs. The difference is reasonably similar from one year to the next, and one season to the next, although there is still a good amount of variation for any one observation. In analysing foEs, spread Es should be taken into account as it can clearly affect the measurement of foEs.

Scintillation has been attributed to spread Es as has fading on oblique HF circuits. Therefore, a knowledge of the presence and properties of spread Es has important applications. It also seems reasonable to extend the measurement of spread Es to high latitudes. While interpretation will be more complex, allowing for particle precipitation effects, it seems reasonable to expect the processes forming mid-latitude spread Es to be effective at higher latitudes.

REFERENCES

Bowman, G.G. (1985). Some aspects of mid-latitude spread-Es and its relationship with spread-F. *Planetary and Space Science 33:*1081 – 1089.

Piggott, W.R. *and* Rawer, K. (1972). URSI handbook of ionogam interpretation and reduction. UAG23 published WDC-A for STP. National Geophysical Data Center, Boulder, USA.

14. FINESSE MEASUREMENTS OF THE MAWSON HIGH RESOLUTION FABRY-PEROT SPECTROMETER

D.J. Murphy

Atmospheric and Space Physics
Antarctic Division
Kingston Tasmania 7050
Australia

ABSTRACT

Finesse is an important quantity in the determination of temperature from Fabry-Perot spectrometer observations of atmospheric airglow. A set of finesse measurements were carried out during the 1994/95 summer on the FPS at Mawson, Antarctica. Reflective, etalon and defect finesse at wavelengths ranging from 546.1 nm to 842.5 nm were measured or inferred. Some evidence of ageing of the coatings was found but this result was made uncertain by some inconsistencies in the measurements. The methods used to make these measurements are presented.

14.1 INTRODUCTION

This note describes a set of measurements, made by the author, of the finesse of the high-resolution Fabry-Perot spectrometer at Mawson, Antarctica during November and December of 1994. Finesse measurements were made at a number of wavelengths in the visible and near infra-red parts of the spectrum. The results can be used to calculate temperatures from observations of atmospheric airglow emanating from species such as oxygen and hydroxyl.

Some theoretical aspects of Fabry-Perot spectrometers are presented before the method used to obtain the finesse measurements is described. After the results are presented and summarised, they are compared with previous measurements of this quantity.

14.2 THEORY

A brief description of the theory of Fabry-Perot spectrometers, that is relevant to measurements of finesse, is presented here. This description is meant to be an overview and is based on Jacka (1984). The symbol convention used by Jacka is used here. For further information, the reader is referred to that paper and to Wilksch (1985).

The phase difference between successive multiply reflected wavefronts emerging from an ideal etalon is $2\pi m$ where m is defined by

$$m\frac{\lambda}{2} = \mu t_g \cos\theta + \frac{\lambda\phi}{2\pi} \qquad (1)$$

where μ is the refractive index of the medium between the reflecting surfaces, θ is the angle of incidence of the ray, λ is the wavelength of the light, ϕ is the phase change on reflection at each surface and t_g is the geometrical distance between the reflecting surfaces.

Constructive interference, and therefore maximum transmission, occurs when m is integral. The transmission as a function of m, for an etalon consisting of perfectly flat plates is given by the Airy function

$$A'(m) = \frac{\tau_A}{1 + F \sin^2(\pi m)} \tag{2}$$

where $\tau_A = \frac{T^2}{(1-R)^2}$ and $F = \frac{4R}{(1-R)^2}$,

and T and R are the transmittance and reflectance of the reflecting surfaces respectively. This function has a period of unity in m and for most applications, coatings are chosen so that τ_A is close to 1.

For values of R large enough, the Airy function peaks at integral m with a width at half maximum of

$$\delta_A(m) = \frac{1-R}{\pi\sqrt{R}}. \tag{3}$$

The ratio of the width of these peaks to the spacing between them is known as the 'reflective finesse' of the coatings N_A. In terms of m, the spacing between the peaks is one so

$$N_A = \frac{1}{\delta_A(m)} = \frac{\pi\sqrt{R}}{1-R}. \tag{4}$$

This parameter describes the width (in m) a transmission peak would have when parallel light of a single (Delta function) wavelength is passed through an ideal etalon. Note that order (m) is not the parameter that is scanned by a Fabry-Perot spectrometer (although it is proportional to it). When manipulating the above equation, care must be taken to ensure that an equivalent definition, in terms of the parameter being scanned, is used.

For a real etalon, physical factors other than the plate coating reflectance R contribute to the width of maxima in the etalon transmission. The result is a broadening of the transmission feature causing the overall finesse of the system to decrease. This can be attributed to the fact that in a real etalon, a range of m values are present simultaneously. The physical processes that bring about this decrease in finesse are indicated by the expression for order

$$m = \frac{2\mu t_g \cos\theta}{\lambda} + \frac{\phi}{\pi}. \tag{5}$$

A variation in any of the parameters in the above expression over the surface of the plates will bring about a range of m values and broaden the transmission feature. If the plates are not perfectly flat, a range of t_g values will be present. This kind of broadening is described by a parameter called the 'defect finesse'. A variation in the phase change on reflection (ϕ) over the plates can be thought of as being equivalent to a variation in t_g, as the etalon gap acts as a phase shifter that is linear with distance. Thus, if a variation in ϕ is present, this will be included in measurements of defect finesse. Variations in the refractive index, although unlikely, could be considered in the same way. In a real system, an aperture of finite width is used to admit light to the etalon. The result of this is that a range of angles of incidence are present. This maps to a range of m values via θ. The source used to illuminate the etalon may be subject to broadening of the wavelength. A real source emits a finite range of wavelengths, this range being determined by factors such as the temperature of the emitter. This is usually one of the parameters that is to be measured and is not described as a finesse.

Combinations of some of the above effects can be measured and are given the following terms. The width of the Airy function of a real etalon, combined with the defect function, is described through the 'etalon finesse'. This combination is represented mathematically by a convolution so that, to a good approximation

$$\frac{1}{N_E^2} \approx \frac{1}{N_D^2} + \frac{1}{N_A^2} \tag{6}$$

where N_D is the defect finesse and N_E is the etalon finesse. In combination with the effect of the aperture, the finesse measured is that of the instrument function. The instrument finesse N_I is given by

$$\frac{1}{N_I^2} \approx \frac{1}{N_E^2} + \frac{1}{N_F^2} \tag{7}$$

where N_F is that component of finesse due to the aperture.

14.3 MEASUREMENT TECHNIQUE

Jacka (1984) presents a method by which finesse can be measured and those principles are followed here.

1. A small plate spacing is selected giving a small order m and large free spectral range.
2. A small aperture is placed near the plane of the etalon to ensure that the variation in the etalon gap is small and the defect finesse is large.
3. A small field stop is selected to give a small field of view and a large N_F.
4. Profiles spanning two orders are collected and analysed to give the finesse.

This process yields the reflective finesse; etalon finesse can be measured by omitting step 2 above. Details of how these tasks were carried out are now presented.

Routine operation of the Mawson Fabry-Perot spectrometer utilises an etalon gap of

approximately 5 mm. The gap required for finesse measurements was approximately 0.1 mm. At small separations, the contribution of the source width to the overall width of the observed transmission feature is small. Thus it was necessary to make a change in plate separation. This process is made somewhat daunting by the fact that if the plates were touched together, they could 'optically contact' and would be damaged irreparably.

The task of changing plate separation was carried out in two stages. It was known that a single step of the lower plate support stepper motors yielded a change in separation of 208 nm, however the precision of this figure was not known. Thus, to ensure that the plates were not driven too far, it was decided to aim for 0.3 mm and make a precise determination of the separation there. Thus the plates were driven closer together by 25339 steps and the system was made parallel. It was found that the spacing was now 0.3123577 mm suggesting that 1021 steps were required to get to 0.1 mm. After taking 1002 steps, the separation was measured to be 0.1034821 mm and this separation was used for the finesse measurements. This corresponds to an order of approximately 328 at λ 630 nm.

The wavelengths at which finesse measurements were made depended on the previous measurements and the sources available. These are presented in Table 1. Except where otherwise stated, the sources were hollow cathode lamps.

Table 1. Wavelengths at which finesse was measured and the sources used.

Wavelength (nm)	Source	Intensity
546.1	Mercury RF discharge lamp	Weak
557.0	Krypton Phillips discharge lamp	Weak
630.5	Neon	Medium
632.8	Frequency stabilised He-Ne laser	Strong
834.7	Xenon	Medium
842.5	Argon	Medium

In the Mawson instrument, the etalon finesse, which describes the combined effects of coating reflectance and plate defects, can be measured without disturbance. Once at the appropriate separation, all that is required is a change in field stop to limit the range of angles with which rays pass through the etalon. Because of this, etalon finesse measurements were made first.

To make a finesse measurement, the appropriate field stop and filter are set in place and the

plate separation is set so that a 256 channel scan spans two orders in such a way that both transmission maxima are sampled down to the noise level on both sides of the peak. The number of channels that separate the two peaks (one order) is calculated using the CHORD program. The full width at half maximum of the peaks (in channels) is calculated from the e^{-1} width produced by CHORD by multiplying it by 2ln2. The ratio of this to the number of channels per order gives the finesse.

The maximum distance over which the Mawson FPS plates can be scanned is of the order of 450 nm. To measure a channels per order profile of a spectral line, it is necessary to scan in separation by more than $\lambda/2$ so that the shape of the wings of the transmission feature is recorded. This means that it is not possible to record an adequate channels per order profile for the Xe line at 834.68 nm and the Ar line at 842.46 nm. If finesse is to be calculated for these wavelengths, the channels per order must be predicted in some other way and then used with a profile width. To make this prediction, the linear relationship of channels per order to wavelength is used. The ratio of channels per order to wavelength for all the lines where it was possible to measure channels per order is calculated and averaged. This is then multiplied by the wavelength for Ar and Xe.

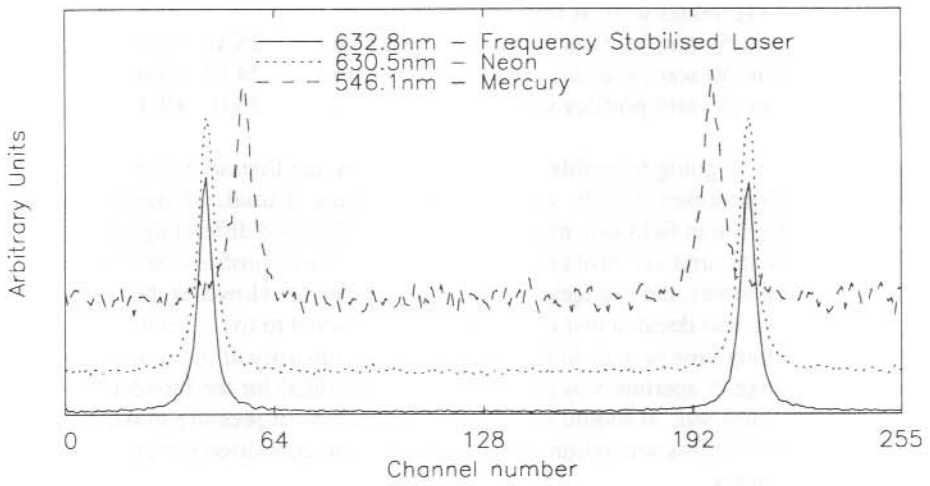

Figure 1. Examples of channels per order profiles collected during finesse measurements.

The change in channels per order with wavelength is demonstrated in Figure 1. Example channels per order profiles for Neon, Mercury and the frequency stabilised laser are presented. Note that the profiles have been scaled and shifted for clarity.

Normal operation of the Mawson FPS system utilises a field stop of 4.5 mm diameter. This can be changed, without major disturbance to the instrument, to 2 mm and 1 mm. It should be noted, however that in going from a 4.5 mm to a 2 mm field stop, the light intensity decreases by a factor of 5. A 1 mm field stop represents a light intensity decrease of 20 when compared to a 4.5 mm field stop. For some of the weaker sources used, a 1 mm field stop yielded profiles of poor signal to noise ratio. Integration over longer time periods could compensate for the decrease in light intensity in the absence of drift, however this may not be feasible using the Mawson system. Movement of the position of the peak of a spectrum due to mechanical variations during the integration of a profile would smear out the width and yield a lower finesse. (However the distance between the peaks would not be effected.) Thus an investigation of the effect of drift and of different field stops was carried out.

The frequency stabilised laser was used to illuminate the etalon using both 1 mm and 2 mm field stops, and profiles of short duration (5 scans, approximately 33 s) and longer duration (50 scans, approximately 5 minutes) were collected. The effect of drift should be greater in the later profiles. It was found that, during this series of measurements, the peak positions drifted by up to approximately 0.3 channels during the course of a long duration profile. The amount of drift varies from day to day depending on the laboratory and instrument temperature stability.

The resulting finesse values were as follows:

Short duration (5 scan) profiles with 1 mm field stop...	25.10 ±0.05
Long duration (50 scan) profiles with 1 mm field stop...	24.93 ±0.08
Short duration (5 scan) profiles with 2 mm field stop...	25.0 ±0.1

It can be seen that by going to profiles of longer duration, the finesse is decreased slightly. The finesse also decreases slightly when a larger aperture is used. (Note that the errors associated with the 2 mm field stop measurement were calculated differently to those for the other measurements, and are probably larger because fewer profiles contributed to the result). Given the errors, the changes are almost insignificant. However, because drift can be unpredictable, it was decided that it would be more prudent to use a 2 mm field stop than to integrate over long time periods in the cases where the intensity of the source is low. The effect of this change in aperture was minimal and the potential for the broadening effect of drift would be minimised. It should be noted that variations in pressure make a negligible contribution to drift at this separation. Hence the pressure correction system was not used in these measurements.

Where possible, the following sequence of profiles was collected to measure finesse. A set of 256 channel profiles of channels per order was obtained, followed by a set of 128 channel profiles of a single transmission feature. Finally, another set of channels per order profiles was collected. This gave estimates of channels per order both before and after the widths were determined and ensured that the widths were obtained using a shorter integration time.

14.4 ETALON FINESSE

The etalon finesse measurements presented below were calculated as described in the previous section. The errors given are the result of propagating the standard deviations of the width and the channels per order through the appropriate quadrature error formula.

Table 2. Etalon finesse measurement.

Wavelength (nm)	Source	Etalon Finesse	Notes
546.1	Hg	19.9 ±0.3	
557.0	Kr	21.6 ±0.3	
630.5	Ne	24.7 ±0.1	
632.8	He-Ne laser	25.1 ±0.1	
834.7	Xe	25.5 ±0.4	Ch/ord inferred
842.5	Ar	24.4 ±0.1	Ch/ord inferred

For most of the above measurements (and the reflective finesse measurements that follow), the system was operated with the temperature control system off. Access to the inside of the instrument was required to check the plate position during the separation change and this would have caused a loss of thermal stability. Thus the temperature control system was not used and the consequence of increased drift was tolerated. One exception to this was in the case of the Xe line at 834.7 nm. The filter used for this line was nominally centred on 834.5 nm and did not provide a large throughput for the Xe line when the system was at room temperature. On restarting the temperature control system at the end of the measurement series and warming the instrument, it was found that the Xe throughput improved and the etalon finesse for the Xe line was measured again.

14.5 REFLECTIVE FINESSE

The reflective finesse does not contain a contribution due to the variation in the plate separation over the area of the plates, i.e. there is no component of the defect finesse in it. To remove the effects of plate defect, it is assumed that variations in plate separation only occur over larger spatial scales. This assumption is reasonable given the high quality fused silica and the grinding method used to make the plates. A mask is used to isolate a small area of the plates so that the defect finesse is negligible over the part of the etalon being used. This mask was placed above the aspheric lens at the base of the etalon chamber. Here it was in the parallel part of the light path but would not damage the coatings on the etalon plates themselves. The mask used holes of 20 mm diameter and the plate areas it sampled are described in Figure 2.

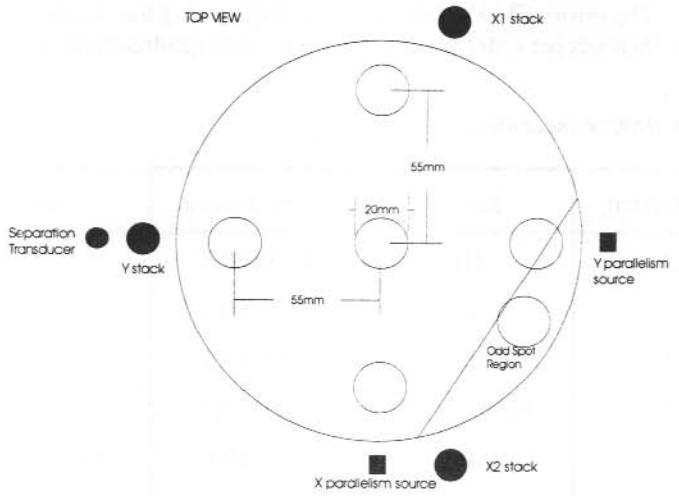

Figure 2. Mask configuration used in measurements of the reflective finesse. The region known as the 'odd spot' is also shown.

The sequence used for etalon finesse measurements was repeated for the five central mask positions described in Figure 2. In addition, measurements were made in the 'odd spot'. It is noted in the FPS logs (see 1984 FPS log, DOY256, p83) that a region of poorer finesse existed on the plates. A hole in the mask was cut so that this region was sampled and the resulting finesse is given below.

The throughput of the system is significantly decreased by the inclusion of the mask. As a result, the signal to noise ratio for the Kr and Xe lines was such that reflective finesse measurements could not be made.

Table 3. Reflective finesse.

Wavelength (nm)	Source	Reflective Finesse (averaged over five positions)	In 'odd spot'
546.1	Hg	21.7 ±0.6	19.9 ±0.6
630.5	Ne	26.2 ±0.2	25.3 ±0.2
632.8	He-Ne laser	26.80 ±0.09	26.0 ±0.2
842.5	Ar	25.3 ±0.9	25.7 ±0.2

The above measurements were made using a 1 mm field stop in the case of the He-Ne laser and Ar, and a 2 mm field stop for Hg and Ne. Once again the number of channels per order had to be inferred for Ar as it was not possible to measure it. The argon measurement presented another challenge due to the parallelism light source. One of the mask positions fell below the parallelism light source transmitter and the light was getting through the parallelism cut off filter at that wavelength. This meant that the backgrounds of the Ar profiles were distorted and the quality of the width estimate was degraded. To overcome this, the system was operated with the parallelism system switched off for this particular case. Preliminary trials where the parallelism light source was switched on but not active, showed that the parallelism was holding quite well during the scans and that little parallelism correction was being applied. The system was then run with the parallelism light source switched off and the appropriate profiles gathered.

14.6 DEFECT FINESSE

Although the defect finesse was not measured, it could be inferred from the reflective and etalon finesse values using Equation (6) above. The results are presented below.

Table 4. Defect finesse.

Wavelength (nm)	Source	Defect Finesse
546.1	Hg	50 ±4
630.5	Ne	74 ±2
632.8	He-Ne laser	72 ±1
842.5	Ar	92 ±12

It should be noted that although the variation in the etalon gap over the plates is independent of wavelength, the proportion of a wavelength that these variations represent does vary with wavelength and so too does the defect finesse. The defect finesse is in fact proportional to wavelength. Thus the results given above should fall on a straight line in a wavelength against defect finesse plot. Unfortunately, they do not do this and the fact that two data points are close together makes it impossible to make a meaningful fit to the data. The defect finesse results are presented in Figure 3.

It is possible to infer the reflective finesse for cases where the etalon and defect finesses are available. In the measurements presented here, it is possible to do this for Krypton (557.0 nm) and for Xenon (834.7 nm). As the Krypton measurements were of poor signal to noise, only the Xenon line is used to infer reflective finesse. The defect finesse was interpolated from the Argon line at 842.5 nm to the average of the Neon and frequency stabilised laser lines near 630 nm and a defect finesse of 91 ±12 was obtained. This produces a reflective finesse value of 27 ±1.

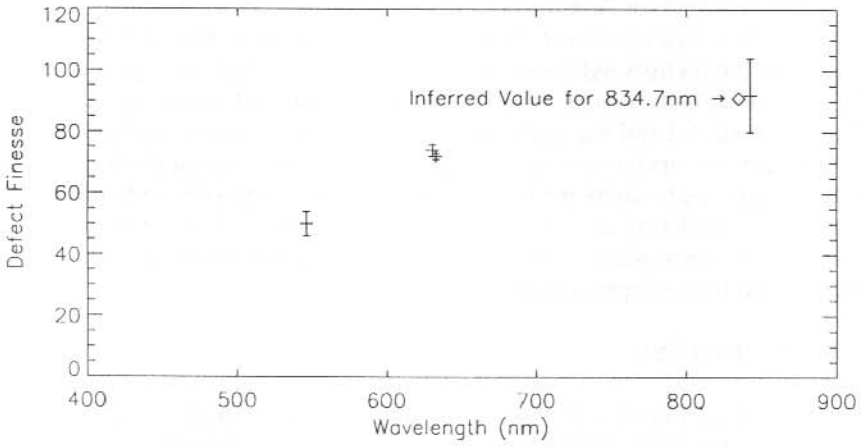

Figure 3. Defect finesse results. The diamond denotes the inferred value of defect finesse for 834.7 nm.

14.7 COMPARISON WITH PREVIOUS MEASUREMENTS

Finesse measurements have been carried out on the Mawson instrument on three previous occasions. In 1983, Norm Jones and Paul Wardill made the first set of measurements, Mark Conde made some in 1984, and in 1989, Pene Greet and Mark Conde repeated them. More recently, a 'problem' with the separation control system brought to light the necessity to apply a correction factor to the 1984/1989 finesse measurements.

The size of the steps in separation that are taken during a scan is set by a parameter called the 'scan attenuation'. Possible settings are 1, 2, 4 and 8 and it has always been assumed that changing the scan attenuation brings about a change in the step size that is consistent with these settings. Recently, it has been found that this is not the case. This affects the historical measurements in that they used a scan attenuation of 8 to obtain the width of the transmission feature but a scan attenuation of 2 to measure the number of channels per order. The factor used to account for these settings has been found to be incorrect. As part of this set of measurements, scans of the frequency stabilised He-Ne laser were made at different scan attenuations in order to ascertain the change in step size that resulted. The results are presented in Table 5. The widths of laser scans for three scan attenuations are given as well as their ratio when compared to a scan attenuation of 2. Finally, the correction factors required to compare a finesse measurement made using scan attenuations of 2 and 8 with one made using a scan attenuation of 2 only are presented.

Table 5. Scan attenuation correction factors.

Scan Attenuation	2	4	8
He-Ne laser width (Channels)	4.74	7.97	15.01
Ratio	1.0	1.68	3.17
Finesse correction factor	1.0	0.84	0.79

The measurements made by Paul Wardill in 1983 (see log book entries on 13 October 1983 for etalon finesse and 30 October 1983 for reflective finesse and telexes MAU/83/64 and MAU/83/68) are presented in Table 6. The scan attenuation values are also presented along with corrected results on the basis of the above factors. It is assumed that the channels per order was measured using a scan attenuation of 2. The measurements were made with a 2 mm field stop and a 1 mm plate spacing.

Table 6. Wardill's 1983 etalon finesse values.

Wavelength (nm)	Etalon Finesse	Scan Attenuation	Corrected Etalon Finesse
546.1	21.6 ±0.4	4	18.1 ±0.3
577.0	25.6 ±0.9	4	21.5 ±0.8
632.8	24.3 ±0.5	4	20.4 ±0.4
690.7	23.5 ±1.2	4	19.7 ±1.0

Reflective finesse measurements utilised a 10 mm mask aperture at plate centre and at three positions 120° apart and 40 mm off-centre (toward each ceramic stack). It is expected that this mask layout will avoid the 'odd spot' discussed above. The average values of the four positions are presented. Note that the range of the values contributing to the average is larger than the error associated with each value. The errors presented in Table 7 reflect that range.

Table 7. Wardill's 1983 reflective finesse values.

Wavelength (nm)	Reflective Finesse	Scan Attenuation	Corrected Reflective Finesse
546.1	27 ±3	4	23 ±3
579.1	35 ±3	4	29 ±3
632.8	34 ±2	4	29 ±2

During 1984, Mark Conde repeated the measurements at a spacing of 0.1 mm. The result presented in telex MAU/84/27 is (uncorrected) 33 ±0.5 for laser illumination. This seems inconsistent with the values presented in the log book. These show the finesse at different positions on the plates and identify the 'odd spot' for the first time. It is these results that are presented in Table 8. Values for both outside and inside the 'odd spot' are presented. The correction factor appropriate for a scan attenuation of 8 is applied.

Table 8. Conde's 1984 reflective finesse values.

Wavelength (nm)	Reflective Finesse		Scan Attenuation	Corrected Reflective Finesse	
	Non-Odd Spot	Odd Spot		Non-Odd spot	Odd Spot
632.8	32 ±2	28 ±1	8	25 ±2	22 ±1

Analysis of the etalon finesse results was not carried out until 1986 (see FPS log book entries around day 259, 1986). It is assumed that the 1984 etalon finesse results were taken using a scan attenuation of 4 although this has been difficult to verify as it is not clear which profiles were used in the finesse calculation. Note that Conde measured the effect that changes in the scan attenuation had on the gain of the separation control circuit but found gain changes that were close to 2 and 4. These are in contrast to the findings, using peak widths, presented above. The results the 1986 analysis are given in Table 9.

Table 9. Conde's 1984 etalon finesse measurements.

Wavelength (nm)	Etalon Finesse	Scan Attenuation	Corrected Etalon Finesse
546.1	25.3	assumed to be 4	21.3
630	31.0	assumed to be 4	26.0

Table 10. Greet and Conde reflective finesse measurements.

Wavelength (nm)	Reflective Finesse	Scan Attenuation	Corrected Reflective Finesse
546.1	28.7 ±1.4	8	22.7 ±1.1
589	38.4 ±0.5	8	30.3 ±0.4
632.8	38.3 ±0.9	8	30.3 ±0.7

Table 11. Greet and Conde etalon finesse measurements.

Wavelength (nm)	Etalon Finesse	Scan Attenuation	Corrected Etalon Finesse
546.1	25.3 ±0.3	8	20.0 ±0.3
589	31.6 ±0.7	8	25.0 ±0.6
632.8	31.8 ±0.1	8	25.1 ±0.1

Table 12. Summary of etalon finesse measurements.

Wavelength	Etalon Finesse			
(nm)	1983	1984	1988/89	1994
546.1	18.1 ±0.3	21.3	20.0 ±0.3	19.9 ±0.3
557.0				21.6 ±0.3
577.0	21.5 ±0.8			
589			25.0 ±0.6	
630.5				24.7 ±0.1
632.8	20.4 ±0.4	26.0	25.1 ±0.1	25.1 ±0.1
690.7	19.7 ±1.0			
834.7				25.5 ±0.4
842.5				24.4 ±0.1

An extensive set of measurements was carried out by Mark Conde and Pene Greet in the summer of 1988/89 at a separation of 0.12 mm (see telex MAU/89/011). A mask with a 20 mm diameter hole on the optical axis or 40 mm away from the optical axis was used for the reflective finesse measurements, once again, avoiding the odd spot. The average reflective finesse for the four positions used, and the etalon finesse are presented in Table 10. The correction factors appropriate to a scan attenuation of 8 are applied.

It is now possible to compare all the measurements taken so far. The correction factors that have been applied make this comparison appropriate.

Note that the value in brackets in Table 13 was inferred using an interpolated defect finesse and Equation (6). The defect finesse value used is indicated on Figure 3.

Table 13. Summary of reflective finesse measurements.

Wavelength (nm)	Reflective Finesse 1983	1984	1988/89	1994
546.1	23 ±3		22.7 ±1.1	21.7 ±0.6
579.1	29 ±3			
589			30.3 ±0.4	
630.5				26.2 ±0.2
632.8	29 ±2	25 ±2	30.3 ±0.7	26.80 ±0.09
690.7				
834.7				(27 ±1)
842.5				25.3 ±0.9

Where both etalon and reflective finesse measurements are available, it is possible to calculate the defect finesse. The results are presented in Table 14.

The etalon finesse results presented show a good degree of consistency when the scan attenuation correction factors are taken into account. The exceptions are largely confined to the 1983 data set. The log books for that time note that there was some difficulty with drift in the system and this would explain the smaller values of etalon finesse. In contrast, the defect finesse results are rather inconsistent with time. There must be some doubt about the 1983 results for the reason noted above and because the inferred values, for two different wavelengths, are the same. This should not be the case.

Table 14. Summary of inferred defect finesse values.

Wavelength (nm)	Defect Finesse 1983	1984	1988/89	1994
546.1	29 ±5		42 ±4	50 ±4
630.5				74 ±2
632.8	29 ±2	91	45 ±2	72 ±1
842.5				92 ±12

If the reflection coefficient of the plate coatings is changing as the coatings age, then a change in reflective finesse will occur. This is evident in the last two sets of reflective finesse measurements but should also be evident in the etalon finesse results. The different mask configurations used in the measurements taken over the years may explain the variation in reflective finesse. It is known that there is some variation in finesse over the plates. Perhaps the region, identified as the 'odd-spot' is expanding.

14.8 CONCLUSION

The finesse of the Mawson FPS system has been measured at a number of wavelengths. These measurements should allow the determination of temperatures from Oxygen red and OH airglow observations. Although some evidence of degradation in the coatings with age is present, there are some inconsistencies that make it difficult to determine if this is in fact the case.

14.9 ACKNOWLEDGEMENTS

Discussions with Pene Greet during the collection of the above measurements were valuable as was her proof reading of this document. Thanks also to Micheal Manion, 1994 Mawson ASP engineer for his help.

REFERENCES

Jacka, F. (1984). Application of Fabry-Perot spectrometers for measurement of upper atmosphere temperatures and winds. *Handbook for MAP 13*:19 – 40.

Wilksch, P.A. (1985). Instrument function of the Fabry-Perot spectrometer. *Applied Optics 24*:1502 – 1511.

15. OBSERVATIONS OF THE OXYGEN 630 NM EMISSION IN THE VERTICAL DIRECTION ABOVE MAWSON, ANTARCTICA, IN 1993

J.L. Innis[1], P.A. Greet[1,2] and P.L. Dyson[3]

[1] Atmospheric and Space Physics
Antarctic Division
Kingston Tasmania 7050
Australia

[2] IASOS
University of Tasmania
Hobart Tasmania 7001
Australia

[3] Physics Department
La Trobe University
Bundoora Victoria 3083
Australia

ABSTRACT

Observations of the oxygen 630 nm auroral/airglow emission in the vertical direction were obtained with the Mawson Fabry-Perot spectrometer during three observing campaigns in 1993. These data were collected in order to search for the presence of tides, gravity waves, and aurorally induced effects. A diurnal variation of the zenith wind was seen, of amplitude ~5 m s^{-1}, similar to that detected in 1992 (Conde and Dyson 1995). A spectral analysis of the data revealed five nights when a frequency common to the wind, temperature, and relative intensity time series was present. The periods found are consistent with the gravity waves seen in photometric data above Mawson (De Deuge et al. 1994), but there is no consistent phase relationship between the wind, temperature and intensity variations from night to night. It is possible that these periodic variations are caused by gravity waves. We are undertaking further analysis in order to provide a more rigorous test of this hypothesis.

15.1 INTRODUCTION

The Mawson Fabry-Perot spectrometer (FPS) was developed by the Mawson Institute for Antarctic Research (MIAR), University of Adelaide, under the leadership of Fred Jacka, as a research instrument to study the winds and temperatures of the Antarctic upper atmosphere (Jacka 1984). The spectrometer was installed at Mawson station in 1980, and has been operated in every year since then, except for 1987. Following the closure of the Mawson Institute, the FPS was placed on permanent loan to La Trobe University. The FPS is currently operated as a collaborative project between La Trobe University and the Antarctic Division.

The FPS is a dual-etalon, separation-scanned instrument. For the night time observations reported here, the low resolution etalon was swung out of the optical path, and only the high resolution etalon plates (diameter 150 mm) were used. The spectral resolution is of order 2×10^5. The parallelism of the plates and their separation are under active servo control. The instrument is located in a thermally-insulated, temperature-controlled cabinet, which is mechanically isolated from the laboratory. The optical path length change from atmospheric pressure variations is also corrected, by adjusting the plate separation. Even with all these precautions, the instrument was still subject to drift over an observing night. This was measured by the use of a laboratory spectral lamp, as noted below, and the effect removed during data reduction.

A roof-mounted periscope allows observations to be obtained in any direction above the horizon. The field of view of the sky through this periscope is approximately 1 degree. The detector is a cooled photomultiplier tube, which measures the light transmitted through a small aperture centred on the optical axis of the instrument.

During 1993 the FPS was used to observe the oxygen 630 nm auroral/airglow emission line. Each observation of the sky was followed by an observation of a hollow cathode mercury lamp, which provided a reference in order to monitor instrumental drift. Data were obtained on 140 nights (including part nights) from late February to mid October.

In 1993 the FPS was operated in two modes, the first was zenith only observations. These took place in three campaigns: February 24 – April 15; July 1 – July 31; and September 15 – October 15. One observation of the vertically overhead sky was obtained approximately every eight minutes, being a five minute observation of the sky, and a two minute observation of the spectral lamp, with the remainder of the cycle time required for logging the data to a PC, changing the optical path from lamp to sky, and associated tasks. These data are to be used for a study of tides, aurorally induced events, and as a search for gravity waves. This paper presents the preliminary findings of the analysis of these zenith observations.

The second mode of operation was cardinal point observations, which consisted of a cycle of measurements (taking approximately 40 minutes) in the directions of North, South, East, West (at 60 degrees zenith distance), and the zenith. Cardinal point data were collected from April 16 to June 30, and from August 1 to September 15. These data form part of a continuing study of the dynamics of the thermosphere over Mawson. The results will be presented elsewhere at a later date.

In 1992, the Mawson FPS was used in cardinal point mode only. As noted above, zenith observations are still obtained in this case, although only once every 40 minutes or so. An analysis of the 1992 zenith observations was given by Conde and Dyson (1995). The work reported here follows in part from the stimulus of this earlier work, as well as that by others (e.g. Hernandez 1982; Wardill and Jacka 1986; Crickmore et al. 1991).

15.2 RESULTS

Zenith observations were obtained on a total of 54 nights during the three campaign intervals, resulting in over 3300 individual spectra of the oxygen 630 nm profile.

The raw spectra obtained were processed to yield vertical winds (velocities) and temperatures. The effects of instrumental broadening were removed by deconvolving an instrument function obtained from observations of a frequency-stabilised laser, assumed to have zero Doppler width. The peaks and widths of Gaussians fitted to the processed profiles were used to derive the winds and temperatures. The effects of instrumental drift were removed by reference to the peak positions of the mercury lamp observations.

We cannot derive absolute values of the wind velocity, as we have no absolute wavelength reference for the 630 nm line. (Ideally we would use an oxygen 630 nm calibration lamp, but these are not obtainable.) We have adopted the usual approach of assuming that the mean vertical wind observed on any given night is zero. This is clearly an approximation to reality – even if the mean wind over any given 24 hour interval is zero, observations taken over part of a day are unlikely to yield a zero mean. The assumption that the zenith wind has a nightly mean of zero has been widely used, and for the spectral analysis (described in the next section) where we are looking for effects within one night the actual value of the mean wind is of secondary importance. (See Crickmore et al. 1991; Conde and Dyson 1995; Aruliah and Rees 1994; for further discussion regarding the mean value of the vertical wind.) We follow the usual convention that positive winds are directed upwards (away from the observatory).

Relative intensities were also determined, by a summation of the counts obtained in each profile.

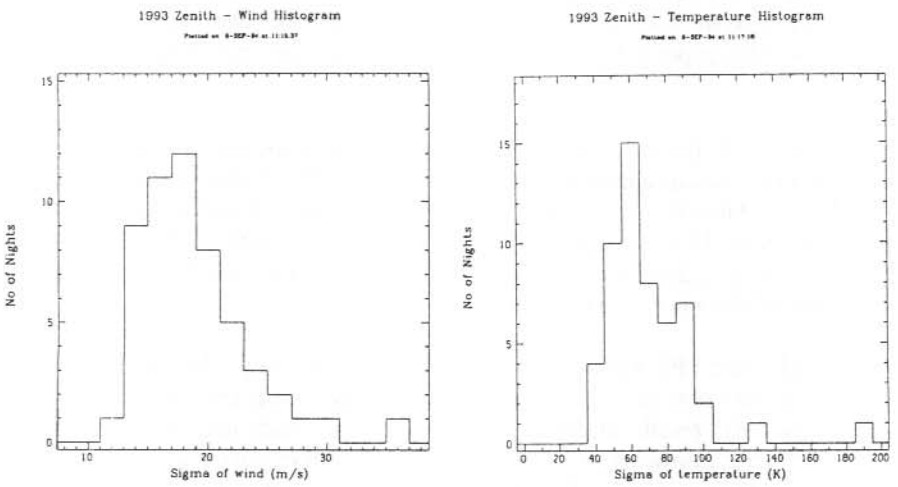

Figure 1. (a) Histogram of the nightly standard deviations in the vertical wind observations for the Mawson 1993 zenith oxygen 630 nm data. (b) As for (a), but for the nightly standard deviations in temperature.

To assess the variability in the vertical wind and temperature, we have calculated standard deviations for the wind and temperatures for each of the 54 nights on which zenith data were obtained. We have plotted histograms for both the wind and temperature nightly standard deviations in Figure 1(a) and (b) respectively. Such plots identify nights of high standard deviation, and also show a fairly well defined lower limit, of ~13 m s^{-1} for the wind, and ~40 K for temperature.

In their analysis of zenith data taken with the Mawson FPS, Conde and Dyson (1995) express the observed distribution of the zenith winds as a convolution of the intrinsic (actual) distribution with the uncertainties due to the fitting procedure and the incomplete cancellation of wavelength drift (as the observations of the mercury lamp are not of course taken exactly simultaneously with the OI observations). Using the reasonable assumption that all four quantities are normally distributed, they calculate that the intrinsic zenith wind distribution was 14.3 and 18.7 m s^{-1} for quiet (local 3-hourly K less than 3) and moderately disturbed times respectively, although they noted that the difference may not be significant. For our 1993 data, we do not see a significant variation with the level of magnetic activity, but for the entire data set we obtain a value of around 11 m s^{-1} for the intrinsic distribution of zenith winds. There is probably no significance to the lower value we obtained, although of course the geomagnetic activity was lower in 1993 compared to 1992, being further advanced on the declining phase of the solar cycle. (The average Ap index for the months of March to October – the observing season at Mawson – for 1992 is 15.8, while for the same interval in 1993 the corresponding value is 14.8.)

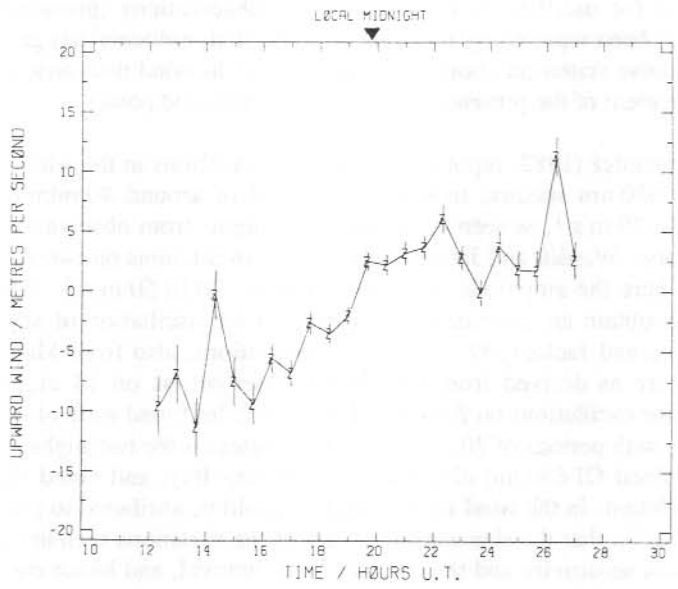

Figure 2. 1993 zenith wind observations averaged over the entire observing season. The diurnal variation of around 5 m s^{-1} is apparent, as seen in the 1992 Mawson observations (Conde and Dyson 1995).

We have searched for correlations between the nightly standard deviations in wind, temperature, and relative intensity, with each other, and with geomagnetic indices such as the local K index. No obvious correlations were apparent, although generally speaking a high value of the standard deviation in wind was associated with a high value for the standard deviation in temperature. We also searched for correlations between the individual measurements of wind, temperature and relative intensity (e.g. to see if upward winds were associated with a given sense of temperature change). Again, no obvious correlations were found when comparing the data set as a whole, although certain individual nights indicated some relationship. (See the next section.)

Conde and Dyson (1995) found a diurnal variation in the zenith wind, of amplitude ~5 m s^{-1} (the actual size showed a dependency on magnetic activity), with downward winds up to around local magnetic midnight, then positive winds afterwards. We have averaged our data, without reference to geomagnetic activity, into ~40 minute wide bins in order to look for a diurnal change. The resulting plot is shown in Figure 2. This shows a variation similar to that found by Conde and Dyson (1995), both in phase and amplitude. The large excursions from a smooth curve near the beginning and end of the data series are probably not of significance, but are likely to be due to the fact that data are only collected at these times for a few weeks around the middle of the austral winter, and hence there is less smoothing of the curve here when averaging the data.

15.3 SPECTRAL ANALYSIS – THE SEARCH FOR GRAVITY WAVES

Possible evidence for oscillations in vertical wind observations (presumably due to gravity waves) has been reported by previous workers. This evidence has generally been limited to a qualitative statement about the appearance of the wind time series, rather than a quantitative statement of the presence of given frequencies and power.

For example, Hernandez (1982) reports evidence for oscillations in the wind times series derived from OI 630 nm spectra, indicating a period of around 40 minutes, with an amplitude of 10 to 20 m s^{-1}, as seen on two separate nights from observations at a mid-latitude observatory. Wardill and Jacka (1986), report oscillations on two nights of data from Mawson, where the amplitude of oscillation was ~30 to 50 m s^{-1}. (On one night they were able to obtain an estimate of the period of the oscillation of approximately 30 minutes.) Price and Jacka (1991) obtained observations, also from Mawson, of the lower thermosphere as derived from OI 558 nm observations on 14 nights in 1985, finding evidence for oscillations on 2 nights. The amplitudes found were of the order of a few tens of m s^{-1}, with periods of 20 to 30, and 50 minutes on the two nights. Crickmore et al. (1991) obtained OI 630 nm observations at Halley Bay, and noted that they see evidence for oscillations in the wind time series that could be attributed to gravity waves. However, they caution that the size and time scale of the variations seen are close to the limits of instrument sensitivity and the data sampling interval, and hence do not claim a detection.

Our time series data of the vertical winds also show evidence for oscillatory behaviour. For example, Figure 3 shows the wind data obtained on the night of DOY 067 (8 March 1993), where there is a suggestion of some sort of quasi-periodic variation of period ~0.6 h during most of the night. In an attempt to provide a quantitative measure of the

presence of periodicities in our data, we have performed a spectral analysis for each of the 54 nights of zenith data. Our approach follows that of Hoegy et al. (1979), in their spectral analysis of neutral atmospheric waves as determined from measurements obtained with the Atmospheric Explorer satellite.

We acknowledge that there will be difficulties with our analysis: the noise levels are relatively high compared to a possible signal, the data sets are often only a few hours in duration, any 'wave' may be present for only part of a night, the possible presence of more than one wave may confuse the interpretation of the results, and only the vertical component of any wave is measured. However, as a first step such an analysis has proved instructive.

We have assumed that the presence of a gravity wave in the observing volume will have an observable effect on all of the wind, temperature and intensity measurements, although not necessarily with zero phase lag between each quantity. Hence, the spectral analysis took the following form: for each day, the frequency spectrum for the wind, the temperature, and the intensity time series was calculated. As well, the cross spectra between each of the wind and temperature, the wind and intensity, and the temperature and intensity time series pairs were found. (We calculated the frequency and cross spectra by two independent methods, one using subroutines from the Numerical Algorithms Group (NAG) library, the other using a Maximum Entropy Method (MEM) routine based on that presented by Dyson and Hoegy (1978). The results from these two approaches were almost indistinguishable for the five nights chosen for the comparison.)

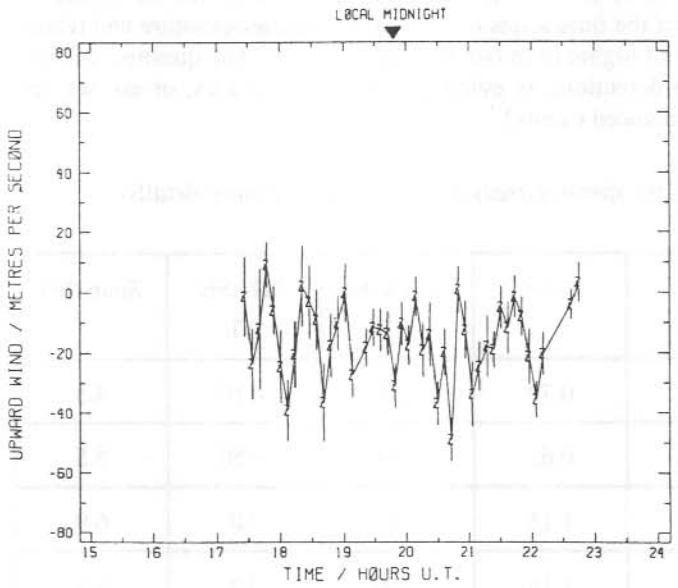

Figure 3. Zenith wind time series for DOY 067 (8 March 1993), showing evidence for a periodic oscillation.

We then looked for days in which a statistically significant signal (greater than 95% confidence level) was seen in all of the wind, temperature, and intensity spectra, as well as in all of the cross spectra (i.e. wind x temperature, wind x intensity, and temperature x intensity). From the total data set of 54 nights, only five nights were found which satisfied our criteria of significant power at a frequency common to all of the spectra. These nights are listed in Table 1, along with the period (in hours) corresponding to the frequency detected, the phase difference (in degrees, rounded to the nearest 10 degrees) between wind and temperature, and temperature and intensity (in the sense of a positive phase meaning the first named quantity leads the second), and the length of the data train (in hours), for reference.

Hence, on less than 10% of nights do we see evidence for a signal at a frequency common to all of the wind, temperature, intensity and cross spectra. The requirement that the signal be seen in all of these spectra may seem to be unnecessarily strict, as any signal present in all three univariate spectra (wind, temperature, intensity) would be expected to be seen in the cross spectra as well. It does, however, ensure that the detections are consistent with the hypothesis that they are due to coherent waves. It also provides us with a measure of the phase relationships between each of the three observables.

If we broaden our criteria, and only require a statistically significant detection (as defined above) in the three univariate spectra only, and not in the cross spectra as well, we increase the number of detections to around 10 separate nights (including the 5 listed in Table 1). A discussion of this increased data set will be the subject of a later paper. For the present we confine our remarks to the detections listed in Table 1.

Our findings (Table 1) are strong evidence for the detection of signals of common frequency in each of the time series of the zenith wind, temperature and relative intensity on a small number of nights from our total data sample. The question still to be asked is can we take these detections as evidence for gravity waves, or are we seeing quasi-periodic aurorally-induced events?

Table 1. Results of the spectral analysis (see the text for more details).

Day	P (hr)	PHASE WT	PHASE TI	Span (hr)
059	0.79	10	-110	4.5
067	0.62	-50	-150	5.5
073	1.13	-70	10	6.9
091	1.16	-100	80	9.2
094	2.46	-20	120	8.8

A photometric study of gravity waves over Mawson was reported by De Deuge et al. (1994). Their analysis suggested that, for their data at the oxygen 630 nm wavelength, waves were detected ranging in period from the Brunt-Vaisala limit of ~12 minutes up to ~300 minutes, but with a well marked peak in the relative frequency of occurrence in the range from 30 to 60 minutes. (The 60 to 90 minute period range was the next most frequent.) Hence the periods we have found from our analysis are consistent with the findings of De Deuge et al. (1994), although our sample is of course of limited size. This may be regarded as evidence to support the suggestion that we have detected gravity waves in our zenith FPS data.

There is no clear phase relationship between the observables of wind, temperature, and intensity on the five different nights. A common phase difference may be expected from simplified theoretical considerations – the temporal development of the wave (assuming an adiabatic process in an isothermal horizontally stratified atmosphere) would have the wind lagging temperature by 90 degrees. We do see the wind lagging the temperature on four out of the five detections listed in Table 1, but the mean value is not near 90 degrees.

Effects of gravity waves on ground-based airglow emissions have been investigated by a number of authors, including Porter et al. (1974), Tarasick and Hines (1990). Porter et al. (1974) demonstrated that the presence of a gravity wave in the F-region can produce a strong correlation between the OI 630 nm emission and the negative of the time derivative of the total electron content, and hence simultaneous observations of the emission intensity and ionospheric parameters can help identify the occurrence of waves. They do not however extend their treatment to the effects of the wave on the observed winds and temperatures.

Tarasick and Hines (1990) investigated the behaviour of intensity and temperature fluctuations due to the presence of gravity waves in the observing volume and concluded that the phase lag between temperature and intensity should be around zero in most cases. Table 1 also lists our results for this measurement, which are clearly non-zero in four of the cases. However, the work of Tarasick and Hines (1990) is concerned with the processes of the neutral atmosphere, and hence does not take account of the role of the F-region electron density profile in the production of O (1D). Furthermore, Porter et al. (1974) show that a phase shift of the OI 630 nm emission, relative to the time derivative of the total electron content, results from the effect of nitrogen quenching of the O (1D), due to a change in the effective height of the emission layer. Hence we feel that, at present, our observations of a non-zero phase lag between temperature and intensity are not necessarily evidence against the suggestion that we have detected gravity waves in our data.

A more detailed comparison with theory requires further modelling of the influence of gravity waves on the OI 630 nm emission intensity, winds, and temperatures at auroral latitudes. We are continuing the analysis, including a search for (quasi-periodic) auroral signatures co-incident with the variations detected in the FPS observations using simultaneous data from other instruments operating at the Mawson geophysical laboratory. At present though, we have positively identified periodic signals in the FPS observations. We believe that a probable cause of these periodicities is gravity waves.

15.4 CONCLUSIONS

Fabry-Perot spectrometer observations of zenith winds, temperatures and relative intensities of the OI 630 nm emission were obtained on 54 nights at Mawson in 1993. We find evidence for a diurnal variation in the wind data, of amplitude ~5 m s^{-1}, similar to that seen from observations in 1992 (Conde and Dyson 1995).

A spectral analysis of the zenith data indicates that on 5 nights out of the 54 we have good evidence for a periodic signal common to the wind, temperature and intensity data for that night. The periods of these oscillations are similar to those seen from a photometric study of gravity waves above Mawson (De Deuge et al. 1994), but there is no clear phase relationship between the signals seen in each of the wind, temperature and intensity from night to night. It is possible that these periodic variations are caused by gravity waves. We are undertaking a further analysis of the data, in order to provide a more rigorous test of this suggestion. The final results will be submitted for publication in the *Journal of Atmospheric and Terrestrial Physics.*

15.5 ACKNOWLEDGMENTS

Funding for this work came from the Australian Antarctic Division, and through ARC and ASAC grants to Peter Dyson at La Trobe University. Pene Greet acknowledges support from an ARC post-doctoral fellowship. Technical support for the operation of the Fabry-Perot spectrometer at Mawson in 1993 was provided by Atmospheric and Space Physics (ASP) engineer Martin Tait. John Innis wishes to thank all members of the 1993 Australian National Antarctic Research Expedition who wintered at Mawson station for their assistance and support of all aspects of the ASP program.

REFERENCES

Aruliah, A.L. *and* Rees, D. (1995). The trouble with thermospheric vertical winds: geomagnetic, seasonal and solar cycle dependence and high latitudes. *Journal of Atmospheric and Terrestrial Physics 57:*597–609.

Conde, M. *and* Dyson, P.L. (1995). Thermospheric vertical winds above Mawson, Antarctica. *Journal of Atmospheric and Terrestrial Physics 57:*589–596.

Crickmore, R.I., Dudeney, J.R. *and* Rodger, A.S. (1991). Vertical thermospheric winds at the equatorward edge of the auroral oval. *Journal of Atmospheric and Terrestrial Physics 53:*485–492.

De Deuge, M.A., Greet, P.A. *and* Jacka, F. (1994). Optical observations of gravity waves in the auroral zone. *Journal of Atmospheric and Terrestrial Physics 56:*617–629.

Dyson, P.L. *and* Hoegy, W.R. (1978). Spectral analysis of atmospheric waves using the maximum entropy method. *NASA Technical Memorandum 79687.*

Hernandez, G. (1982). Vertical motions of the neutral thermosphere at midlatitude. *Geophysical Research Letters 9:*555–557.

Hoegy, W.R., Dyson, P.L., Wharton, L.E. *and* Spencer, N.W. (1979). Neutral atmospheric waves determined from atmospheric explorer measurements. *Geophysical Research Letters 6:*187–190.

Jacka, F. (1984). Application of Fabry-Perot spectrometers for measurement of upper atmosphere temperatures and winds. In: Vincent, R.A. (Ed). *Handbook for MAP 13:*19–40.

Porter, H.S., Silverman, S.M. *and* Tuan, T.F. (1974). On the behaviour of airglow under the influence of gravity waves. *Journal of Geophysical Research 79:*3827–3833.

Price, G.D. *and* Jacka, F. (1991). The influence of geomagnetic activity on the upper mesosphere/lower thermosphere in the auroral zone. I. Vertical winds. *Journal of Atmospheric and Terrestrial Physics 53:*909–922.

Tarasick, D.W. *and* Hines, C.O. (1990). The observable effects of gravity waves on airglow emissions. *Planetary and Space Science 38:*1105–1119.

Wardill, P. *and* Jacka, F. (1986). Vertical motions in the thermosphere over Mawson, Antarctica. *Journal of Atmospheric and Terrestrial Physics 48:*289–292.

16. LOOKING FOR CORRELATIONS BETWEEN THE NEUTRAL WIND IN THE MESOSPHERE-LOWER THERMOSPHERE REGION ABOVE MAWSON AND THE INTERPLANETARY MAGNETIC FIELD

D.J. Murphy[1], V.O. Papitashvili[2], B.A. Belov[3], R.A. Vincent[4] and R.J. Morris[1]

(1) Atmospheric and Space Physics
Antarctic Division
Kingston Tasmania 7050
Australia

(2) Space Physics Research Laboratory
University of Michigan
Ann Arbor Michigan
USA

(3) Institute of Terrestrial Magnetism
Ionosphere and Radio Wave Propagation
Troitsk Moscow Region
Russia

(4) Department of Physics and Mathematical Physics
University of Adelaide
Adelaide SA 5000
Australia

ABSTRACT

A method of analysis which parameterises the effect of the interplanetary magnetic field (IMF) on the neutral winds in the mesosphere-lower thermosphere region is presented and described. This analysis, which sorts the wind and IMF data according to certain criteria and then assesses the correlation between them, was then applied to neutral wind velocity observations over Mawson, Antarctica, during 1985 – 1988 at an altitude of 98 km and the interplanetary magnetic field (IMF) magnitude and direction. A regression model of the lower thermospheric and mesospheric winds over Mawson is constructed and compared with modelling of the global ionospheric convection patterns obtained from the IZMIRAN Electrodynamic Model (IZMEM) for the altitude 120 km. It was found that the resulting neutral wind velocity vectors at 98 km altitude show striking agreement with the ionospheric convection patterns for changing IMF conditions.

16.1 INTRODUCTION

An interaction of the solar wind plasma flow and the interplanetary magnetic field (IMF) with the Earth's magnetosphere is a major driving force of the global magnetospheric plasma convection. Magnetospheric convection electric fields map down into the high-latitude ionosphere along equipotential geomagnetic field lines and force charged particles there into motion. Birkeland currents flow along field lines, therefore three-dimensional

high-latitude current systems link key magnetospheric regions (magnetopause, low latitude boundary layer, magnetotail lobes, ring current region) with the polar ionosphere in both the northern and southern hemispheres. As a result, the magnitudes and directions of the ion convection velocities at ionospheric F- and E-layer levels depend strongly on the energy and momentum transfer between the magnetosphere and ionosphere, i.e., on the orientation and strength of the IMF and solar wind velocity and density. (Friis-Christensen and Wilhjelm 1975; Maezawa 1976; Levitin et al. 1982; Banks et al. 1984; Heelis 1984; Friis-Christensen et al. 1985; Feldstein and Levitin 1986; Hairston and Heelis 1990; Papitashvili et al. 1994a, 1994b, 1995).

It is well-established that the neutral air in the polar thermosphere is primarily driven by momentum transfer from convective ions via ion-drag forcing and Joule or collisional heating (see for example, Killeen et al. 1984, 1991). At altitudes 120–350 km the ionospheric plasma convection plays a leading role dragging the neutral particles though, due to the 'flywheel' effect, the neutral winds can also drive the ionospheric convection, especially after geomagnetic storms (see for example, Deng et al. 1991, 1993; Thayer and Vickrey 1992).

The relationships between the IMF and thermospheric winds at altitudes of few hundred kilometers are studied relatively well (see for example, Killeen et al. 1985; McCormac et al. 1985; Niciejewski et al. 1992), but the IMF influences on the lower thermospheric and mesospheric neutral wind patterns at altitudes 90–120 km are still poorly understood. In this paper we utilise an interdisciplinary approach to study an influence of the IMF on the neutral wind velocities at an altitude of 98 km over the Antarctic station Mawson for all seasons of a year. This study can explain how the lower thermosphere couples with the middle atmosphere layers on a long-term scale, i.e., independently of magnetic storms.

16.2 TECHNIQUE

In this study, we assume that the magnetosphere-ionosphere coupling link can be considered as a 'black box' which accepts changes in the IMF components (B_x, B_y and B_z) as input signal, and produces ground-based geomagnetic perturbations as output signal (see details in Papitashvili et al. 1994b). Because these geomagnetic perturbations are caused by corresponding ionospheric currents (i.e., ionospheric ion convective motion), we assume that neutral winds below the ionospheric E-layer can also be driven by the ionosphere-lower thermosphere coupling via ion-drag forcing and heating due to various mechanisms. The aim then, is to look for correlations between the magnetospheric and atmospheric parameters available to us.

Assuming that the response of this 'black box' to its inputs is linear, it is appropriate to use linear regression analysis to obtain information about the character of this response. This approach provides a parameterisation of ground-based geomagnetic or neutral wind variations in terms of the IMF direction and magnitude. Therefore, a model of such responses can be easily constructed for the Earth's polar regions or, through extension of the analysis to other sites, on a global scale.

16.2.1 *Neutral wind data*

A medium frequency (2 MHz) spaced antenna radar system was established at Mawson (gg: 67.60°S, 62.87°E; corrected geomagnetic, $\Phi = -70.19°$, $\Lambda = 89.84°$, local magnetic noon at 1043 UT) during 1984 and operated almost continuously by the Mawson Institute for Antarctic Research, and the University of Adelaide, Department of Physics (and Mathematical Physics) until late 1993. Pulses transmitted from a square antenna array were reflected from the neutral atmosphere producing an electric field pattern on the ground. Complex samples of this pattern were taken at three antennas so that the motion and scale of the pattern could be measured and the wind speed and direction at the reflection level inferred. The full correlation analysis (Briggs 1984) was used to calculate the horizontal wind velocity over the height range that was sampled.

The radar generally received signals of suitable 'signal to noise' ratio over a range of heights from 70 to 108 km. Samples were taken at 2 km intervals within this range. The correlation analysis routines used to calculate wind velocities took 2 – 3 minutes to complete. This delay, combined with the time spent transmitting (just under 2 minutes) gave wind measurements every 5 minutes or so. The full correlation analysis method includes a series of rejection criteria. The rejection of data due to these and due to factors such as poor 'signal to noise' ratio resulted in a data acceptance rate that was lower than the optimum of every 2 km and every 5 minutes.

The data for altitude 98 km obtained during 1985 – 1988 and used in this analysis have been averaged into bins of one hour duration. This was partly to improve the quality of estimates and partly to match the one hour mean values of interplanetary magnetic field strength.

The Mawson radar system used universal time to tag the data it produced. The averaged data, however, was stored with local time tagging the beginning of the hour. It was necessary to convert the time associated with the hourly averages of the radar data back to UT and this was done using $T_{UT} = T_{LT}$-4 hours.

16.2.2 *IMF data*

The data on the interplanetary magnetic field was obtained from the NSSDC data base (King 1989). Hourly values of B_y and B_z for 1985, 1986 and 1987 were extracted for this study. A three day section of the raw IMF and wind data files is presented in Figure 1.

16.2.3 *The regression analysis*

The zonal (V_E) and meridional (V_N) wind velocities are defined in neutral atmosphere studies as being positive toward the east and north respectively. The zonal wind is also assumed to lie on the x-axis giving it an eastward orientation. These definitions differ from those used in magnetospheric physics and are not appropriate in studies where the Earth's magnetic field has a significant effect on the dynamics of the atmosphere. Consequently, the horizontal neutral wind vectors have been transformed into the corrected geomagnetic (CGM) frame using the angle $\alpha = 44.15°$ between geographic and geomagnetic meridians at Mawson (in the CGM system the x-axis is directed toward geomagnetic north and the y-axis

toward the east). The transformation equations used on the hourly averaged components of the wind vectors were

$$V_x = V_n \cos\alpha + V_E \sin\alpha \quad \text{and}$$

$$V_y = V_E \cos\alpha - V_N \sin\alpha. \tag{1}$$

The resultant velocity values of the (geomagnetically) meridional V_x and zonal V_y winds and the hourly mean values of the components of the IMF, B_y and B_z are thought to be correlated in accordance with the equations

$$V_x = K_{xB_y} B_y + K_{xB_z} B_z + V_{x_o} \tag{2}$$

$$V_y = K_{yB_y} B_y + K_{yB_z} B_z + V_{y_o}. \tag{3}$$

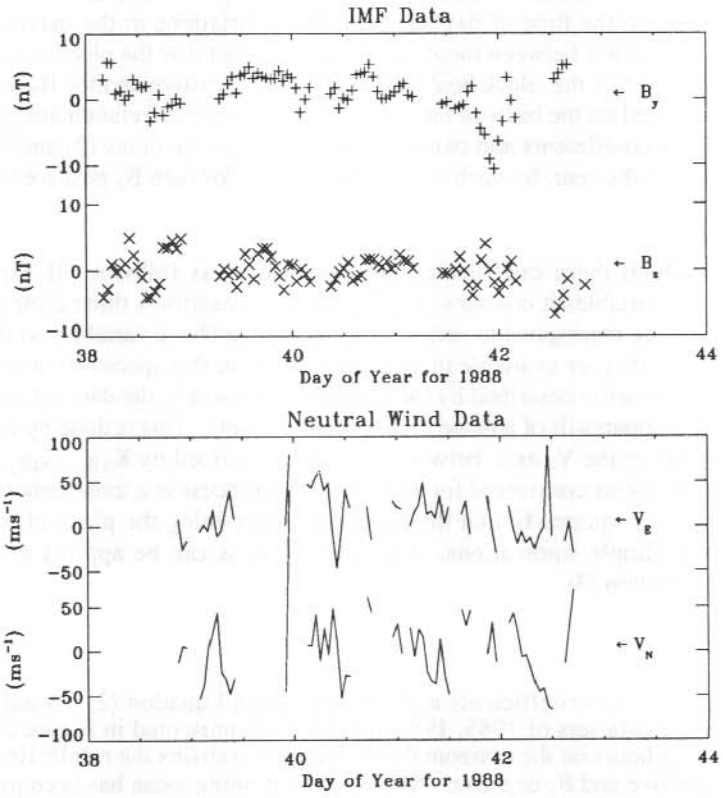

Figure 1. A section of the IMF and wind raw data for three days in 1988. The upper panel shows the B_y and B_z values of the IMF. The lower panel contains eastward V_E and northward V_N wind values.

Papitashvili et al. (1994b) suggests that correlations with the IMF component B_x can be neglected due to the inefficiency with which it produces significant geomagnetic disturbances at high latitudes. Hence B_x is not included in the above correlation equations. It is also expected that the correlation between neutral wind velocity and the IMF will vary as a function of season and of time of day. Thus, in order to prevent a possible relationship being 'washed out', it is necessary to presort the data before relationships between V_x, V_y, B_y and B_z are sought.

The data are first split up into seasons using the following start and end dates:

Summer Solstice	Oct 23 – Feb 22
Autumn Equinox	Feb 23 – Apr 22
Winter Solstice	Apr 23 – Aug 22
Spring Equinox	Aug 23 – Oct 22

The equinoctal periods are much shorter than those around the solstices but are often combined to improve statistics. The data for these periods in each of the three years of the study can also be combined to increase the number of points available. The data is also sorted according to the time of day so that diurnal variations in the parameters will not degrade the correlation between them. It is also expected that the physics associated with the mechanisms inside the 'black box' will differ for B_z positive and for B_z negative. Thus the data is presorted on the basis of the sign of B_z before the correlation analysis is applied. In summary, the coefficients and constants described by Equations (2) and (3) are sought for each season of the year, for each hour of the day and for both B_z positive and negative at each height.

The way in which these coefficients are obtained is as follows. If Equation (2) is considered, the variables it contains (V_x, B_y and B_z) describe a three dimensional space. Points in that space correspond to cartesian triplets of the above variables so that the hourly mean data points that are available to us form a 'cloud' in that space. To assess the degree to which the correlation described by the equation is present in the data set, it is possible to carry out a least squares fit of a plane to the cloud of points. This is done by minimising the distance, parallel to the V_x axis, between the plane described by K_{xB_y}, K_{xB_z} and V_{x_0}, and each of the data points considered for analysis. This process is a three dimensional analog of a standard least squares fit and the parameters describing the plane of best fit can be obtained using simple summations. The same process can be applied to the variables contained in Equation (3).

16.3 RESULTS

Plots of the correlation coefficients and the constant in Equation (2) (zonal case) for the summer solstice data sets of 1985, 1986 and 1987 are presented in Figure 2. Each panel has time (UT) in hours on the horizontal axis and each contains the results for the presorted cases of B_z positive and B_z negative. A three-point running mean has been passed over the data and the end points have been wrapped around. The upper three panels contain K_{xB_y}, K_{xB_z} and V_{x_0}, where the fourth panel presents the number of points that contributed to the fit. Although both the IMF and radar data sets have good temporal coverage, simultaneous

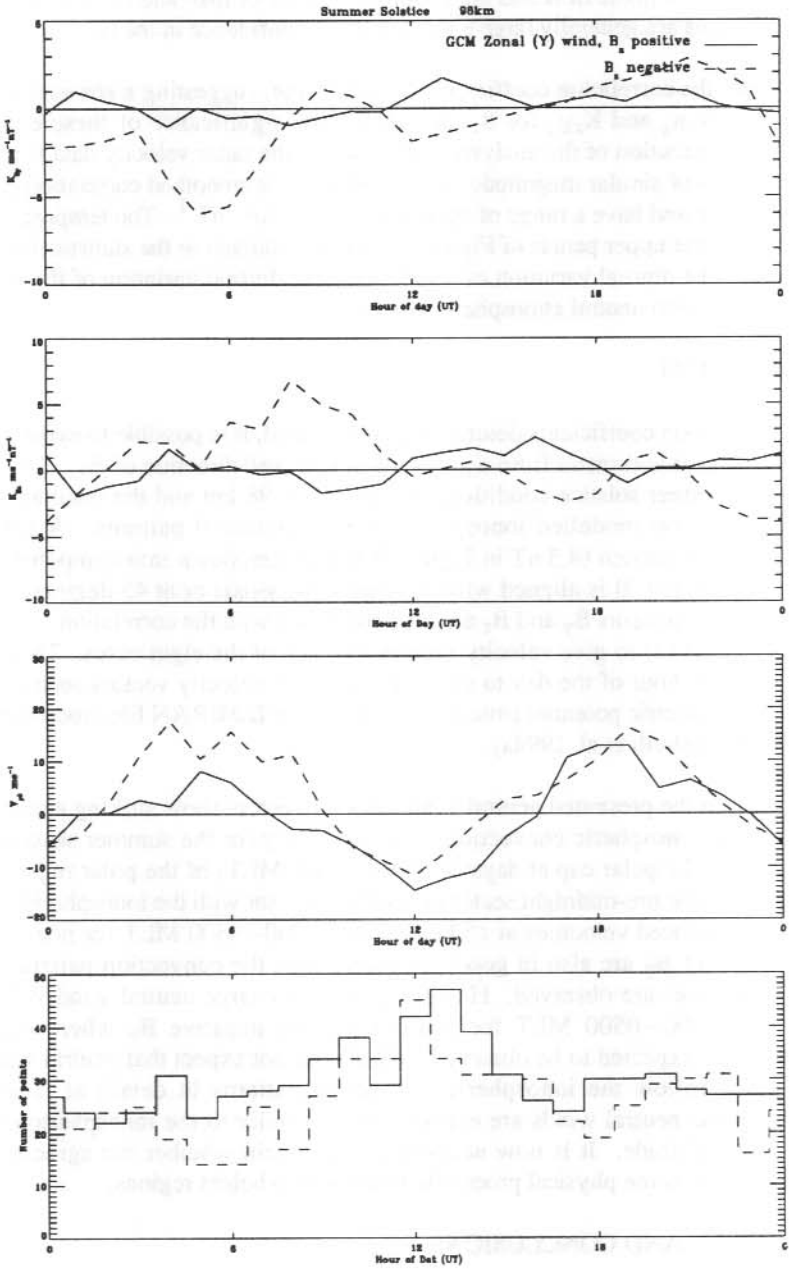

Figure 2. Constants and correlation coefficients given in Equation (3) for summer solstice data at a height of 98 km. The parameters represented are K_{yB_y}, K_{yB_z}, V_{y_0} and the number of points contributing to the fit. The horizontal axis of all the panels is UT and the two lines in each panel represent the B_z positive and B_z negative cases.

radar and IMF data points are needed for this analysis. Hence the number of points contributing to each plane fit is less than both the number of IMF and radar data points. The numbers of points are generally large enough to have confidence in the fit.

Periods where the correlation coefficients become large, suggesting a stronger correlation, occur in both K_{xB_y} and K_{xB_z} for B_z negative. The significance of these excursions is verified by an execution of the analysis routine where the radar velocity data is replaced by random numbers of similar magnitude. It is found that the smoothed correlation coefficients vary around zero and have a range of approximately ± 3 $ms^{-1}nT^{-1}$. The temporal coherency of the results in the upper panels of Figure 2 is also a testament to the statistical significance of the result. The diurnal variation of V_{x_0} reflects the diurnal variation of the background wind at 98 km due to neutral atmosphere solar tides.

16.4 DISCUSSION

With the correlation coefficients described above in hand, it is possible to make predictions of the velocity that will result from a given magnitude and direction of B_z. This is done in Figure 3 for summer solstice conditions at a height of 98 km and the resultant velocities aresuperimposed on modelled ionospheric electric potential patterns. A value of the magnitude of B is chosen (4.3 nT in Figure 3) and broken down into components in eight different ways, where B is aligned with the *z*-axis, the *y*-axis or at 45 degrees to the axes. The resulting components B_y and B_z are then combined with the correlation coefficients of Equations (2) and (3) to give velocity vectors for each of the eight cases. This process is repeated for each hour of the day to give the sets of 24 velocity vectors seen in Figure 3. The underlying electric potential patterns come from the IZMIRAN Electrodynamic Model (IZMEM) (Papitashvili et al. 1994a).

One can see that the presented neutral wind velocity vectors show striking agreement with the background ionospheric convection cells, especially for the summer season. Neutral winds flow into the polar cap at dayside (0900 – 1000 MLT) of the polar region and flow out of the cap in the pre-midnight sector in good agreement with the ionospheric convection patterns. The reduced velocities at 1800 MLT and 0300 – 0500 MLT for negative B_z and both directions of B_y are also in good agreement with the convection pattern where the reversal boundaries are observed. However, unusually large neutral wind velocities are obtained near 0300 – 0500 MLT for positive B_z and negative B_y where the reversal boundary is also expected to be observed. We should not expect that neutral winds above Mawson must follow the ionospheric convection patterns in detail; at least, general circulation of the neutral winds are expected to be similar to the ionospheric convection patterns at this altitude. It is now necessary to ascertain whether the agreement that is observed is due to some physical process linking the two height regions.

16.5 SUMMARY AND CONCLUSIONS

In this paper, the methods used to investigate correlations between the IMF and mesospheric-lower thermospheric-neutral wind data over Mawson are described. These methods are applied to data taken during 1985, 1986 and 1987. The results described above demonstrate that the lower thermospheric/mesospheric neutral wind circulation over

Mawson, Antarctica depends on the IMF conditions at some heights and during some seasons of the year. The wind patterns show a cellular type of circulation at 98 km altitude.

This preliminary study suggests that the analysis should be extended. The correlation coefficients associated with wind data at heights other than 98 km would be of interest as would other possible presorting conditions. These will be the basis of future work.

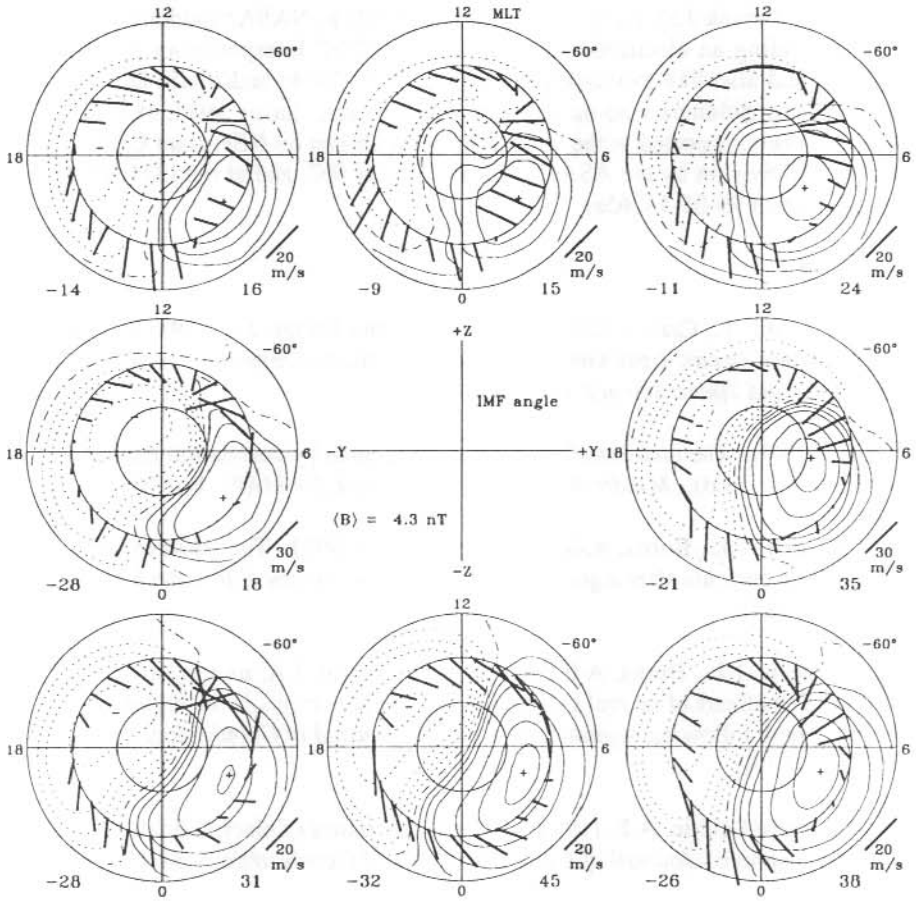

Figure 3. Neutral wind horizontal velocities over Mawson (98 km altitude, bold vectors plotted at $\Phi = -70.2°$ corrected geomagnetic latitude) during summer, superimposed over the ionospheric electric potential patterns modelled by IZMEM for different orientations of the IMF angle and for $|B| = 4.3$ nT. The numbers at the bottom of each plot indicate the minimum and maximum potential values in kV. Contours equal 0, ±3, ±6, ±10, ±20, ±30, ..., ±90 kV. The scale factor is an amplitude of the neutral wind velocity.

We conclude from the results presented that the neutral winds at -70° geomagnetic latitude and 98 km altitude tend to follow the two-cell ionospheric convection pattern defined by the corresponding IMF conditions. If a link exists it is likely to be ion-drag forcing from above, i.e., from the ionospheric E-layer convection, although we do not exclude a possibility that the pressure or temperature gradients also influence the neutral circulation at this altitude.

16.6 ACKNOWLEDGEMENTS

We would like to thank J.H. King and N.E. Papitashvili at NASA/Goddard Space Flight Center for providing an electronic version of the NSSDC Interplanetary Medium Data Book. We would also like to thank Gina Price, Mark Conde and Maria De Deuge, the Mawson ASP expeditioners who operated the MFSA radar during 1985, 1986 and 1987. This work has been supported at the University of Michigan by NSF grant OPP-9318766, at the Antarctic Division by the ASAC grant for project 507, and at the IZMIRAN by the RFFI research grant 95-05-15265a.

REFERENCES

Banks, P.M., Araki, T., Clauer, C.R., Maurice, J.P. *and* Foster, J.C. (1984). The interplanetary electric field, cleft currents and plasma convection in the polar caps. *Planetary and Space Science 32:*1551–1557.

Briggs, B.H. (1984). The analysis of spaced sensor records by correlation techniques. In: Vincent, R.A. (Ed). *Middle Atmosphere Handbook for MAP*. Pp. 166–186.

Deng, W., Killeen, T.L., Burns, A.G. *and* Roble, R.G. (1991). The flywheel effects: ionospheric currents after a geomagnetic storm. *Geophysical Research Letters 18:*1845–1848.

Deng, W., Killeen, T.L., Burns, A.G., Roble, R.G., Slavin, J.A. *and* Wharton, L.E. (1993). The effects of neutral inertia on ionospheric currents in the high-latitude thermosphere following a geomagnetic storm. *Journal of Geophysical Research 98:*7775–7790.

Feldstein, Ya.I. *and* Levitin, A.E. (1986). Solar wind control of electric fields and currents in the ionosphere. *Journal of Geomagnetism and Geoelectrticity 38:*1143–1182.

Friis-Christensen, E. *and* Wilhjelm, J. (1975). Polar cap currents for different directions of the interplanetary magnetic field in the Y-Z plane. *Journal of Geophysical Research 80:*1248–1260.

Friis-Christensen, E., Kamide, Y., Richmond, A.D. *and* Matsushita, S. (1985). Interplanetary magnetic field control of high-latitude electric field and currents determined from Greenland magnetometer data. *Journal of Geophysical Research 90:*1325–1338.

Hairston, M.R. *and* Heelis, R.A. (1990). Model of high-latitude ionospheric convection pattern during southward interplanetary magnetic field using DE 2 data. *Journal of Geophysical Research 95*:2333 – 2343.

Heelis, R.A. (1984). The effects of interplanetary magnetic field orientation on the dayside high-latitude convection. *Journal of Geophysical Research 89*:2873 – 2880.

King, J. H. (1989). Interplanetary Medium Data Book, Suppl. 4, 1985 – 1988, NSSDC/WDC-A-R&S 89-17, NASA Goddard Space Flight Center, Greenbelt, Maryland.

Killeen, T.L., Hays, P.B., Carignan, G.R., Heelis, R.A., Hanson, W.B., Spencer, N.W. *and* Brace, L.H. (1984). Ion-neutral coupling in the high-latitude F region: evaluation of ion heating terms from Dynamic Explorer 2. *Journal of Geophysical Research 89 (No. A9)*:7495 – 7508.

Killeen, T.L., Heelis, R.A., Hays, P.B., Spencer, N.W. *and* Hanson, W. B. (1985). Neutral motions in the polar thermosphere for northward interplanetary magnetic field. *Geophysical Research Letters 12*:159 – 162.

Killeen, T.L., McCormac, F.G., Burns, A.G., Thayer, J.P, Johnson, R.M. *and* Niciejewski, R.J. (1991). On the dynamic and composition of the high-latitude thermosphere. *Journal of Atmospheric and Terrestrial Physics 53*:797 – 815.

Levitin, A.E., Afonina, R. G., Belov, B. A. *and* Feldstein, Ya. I. (1982). Geomagnetic variations and field-aligned currents at northern high-latitudes and their relations to solar wind parameters. Phil. Trans. R. Soc. London, Ser. A 304. Pp 253 – 301.

Maezawa, K. (1976). Magnetospheric convection induced by the interplanetary magnetic field: quantitative analysis using polar cap magnetic records. *Journal of Geophysical Research 81*:2289 – 2303.

McCormac, F.G., Killeen, T.L., Gombosi, T.I., Hays, P.B. *and* Spencer, N.W. (1985). Configuration of the high-latitude thermospheric neutral circulation for IMF B_y negative and positive. *Geophysical Research Letters 12*:155 – 158.

Niciejewski, R.J., Killeen, T.L., Johnson, R.M. *and* Thayer, J.P. (1992). The behavior of the high-latitude F-region neutral thermosphere in relation to IMF parameters. *Advances in Space Research 12, 6*:215 – 218.

Papitashvili, V.O., Belov, B.A., Faermark, D.S., Feldstein, Ya. I., Golyshev, S.A., Gromova, L.I. *and* Levitin, A.E. (1994a). Global modelling of high-latitude geomagnetic variations. In: Baker, D.N., Papitashvili, V.O. and Teague, M.J. (Eds.). Solar-Terrestrial Energy Program: The Initial Results from STEP Facilities and Theory Campaigns. *COSPAR Colloquia Series, Vol. 5, Pergamon Press*. Pp. 739 – 750.

Papitashvili, V.O., Belov, B.A., Faermark, D.S., Feldstein, Ya.I., Golyshev, S.A., Gromova, L.I. *and* Levitin, A.E. (1994b). Electric potential patterns in the northern and southern polar regions parameterized by the interplanetary magnetic field. *Journal of Geophysical Research 99:*13251 – 13262.

Papitashvili, V.O., Clauer, C.R., Levitin, A.E. *and* Belov, B.A. (1995). Relationship between the observed and modeled modulation of the dayside ionospheric convection by the IMF B_y component. *Journal of Geophysical Research 100:*7715 – 7722.

Thayer, J. P. *and* Vickrey, J. F. (1992). On the contribution of thermospheric neutral wind to high latitude energetics. *Geophysical Research Letters 19:*265 – 268.

17. FABRY-PEROT SPECTROMETER CALIBRATIONS FOR MESOSPHERIC SODIUM TEMPERATURE MEASUREMENTS

P.A. Greet, D.J. Murphy and W.J. French

Atmospheric and Space Physics
Antarctic Division
Kingston Tasmania 7050
Australia

ABSTRACT

Determination of aeronomic quantities from optical high-resolution Fabry-Perot spectrometer measurements requires special attention and care. Observations of the mesospheric sodium emission from Mawson, Antarctica (67.6°S, 62.9°E) are used to illustrate some of the difficulties that can be encountered in the calibration process. The use and drawbacks of frequency-stabilised lasers, radio-frequency excited ^{198}Hg isotope discharge lamps, and sodium hollow-cathode lamps as reference sources in these mesospheric sodium observations are discussed.

17.1 INTRODUCTION

Fabry-Perot spectrometers (FPS) have traditionally been used for observations of the thermospheric oxygen λ 630 nm emission (Jacka 1984). In recent years high-resolution FPSs have been adapted for observations of mesospheric emissions. Mesospheric temperatures are in the range 150–250 K and winds are a factor of 10 less than thermospheric winds. There are a number of mesospheric emissions which could be observed including the sodium λ 589.0/589.6 nm doublet (Plane 1990) and lines in the OH and O_2 molecular emission spectra. The twilight emission of the sodium doublet was first investigated (Sipler and Biondi 1978; Hernandez 1975) but difficulties and limitations inherent in twilight observations and improvements in near-infra-red wavelength detectors have directed recent interests towards the OH and O_2 emissions.

The work presented here developed out of recent investigations into the sodium emission (Greet and Jacka 1994a). During the day and at twilight, resonant excitation by sunlight produces an emission which is an order of magnitude brighter than an exothermic photochemical emission. The night-time emission is solely photochemical in origin and thus thermally broadened and not indicative of atmospheric temperatures. Each line of the sodium doublet has hyperfine structure due to Zeeman splitting in Earth's magnetic field. Analysis of sodium observations made at Mawson, Antarctica, has highlighted the importance of FPS calibration for mesospheric measurements.

17.2 INSTRUMENTATION AND OBSERVING PROCEDURES

The Mawson FPS was developed and run by the Mawson Institute for Antarctic Research. It is described in detail by Jacka (1984). The instrument can be used to scan through a wavelength range, typically about 25 pm, by varying the voltage applied to piezoelectric

ceramic supports of the etalon plates. A single scan, of 128 steps or channels, is obtained in 6.4 s and a number of scans are summed to give a profile with adequate signal-to-noise. When observing the sodium twilight emission useful profiles can be obtained in 4 minutes. In mid-winter twilight observations were possible for up to three hours each day. Observations were interspersed with sodium lamp profiles to monitor small drifts in the etalon separation.

When analysing Fabry-Perot profiles the instrument response must be allowed for. This can be done using a calibration line, providing the source function for the calibration line is well known. A ^{198}Hg isotope discharge lamp has been used for this purpose and was thought to operate at a temperature near 375 K (Wilksch 1975). Allowance must also be made for variations in reflective finesse of the etalon between calibration and observing wavelengths (Jacka 1984).

Laboratory sources for the sodium emission are readily available. This has the potential advantage that the instrument function can be directly calculated at the wavelength of observation and a direct measurement of the rest wavelength for the emission is available (Greet and Jacka 1994b). We used a sodium hollow-cathode lamp which operates at about 500 K. Discharge lamps are also readily available however these operate at high temperatures and suffer self-absorption. We originally thought that the hollow-cathode lamp would not suffer significant self-absorption. Although the profiles do not show reversal they do show self-absorption with a departure from the theoretical ratio of the intensity of the hyperfine components and non-Gaussian emission profiles (Greet and Jacka 1994a).

Routine calibrations for sodium observations at Mawson included high signal-to-noise mercury and hollow-cathode sodium lamp profiles, a profile spanning more than one order to determine the channels per order, and a dark count record.

17.3 CALIBRATIONS

At first observations of the D1 emission were made. These were analysed using the sodium hollow-cathode lamp to determine the instrument profile and rest wavelength (Greet and Jacka 1994b). The D2 line is twice as bright as the D1 line and suffers twice as much self-absorption. In subsequent observations of the D2 emission, departure of the hollow-cathode lamp from Gaussian became apparent. As we could now not easily describe the sodium hollow-cathode lamp source function it was not possible to use these profiles to determine the instrument function. We still had the option of using the mercury lamp to do this.

In 1992 a frequency-stabilised laser was installed at Mawson for a program of thermospheric λ 630 nm observations. This has permitted a thorough comparison of the mercury lamp and frequency-stabilised laser. In Figure 1, recorded laser and nightly mean mercury lamp profile widths are plotted for data obtained in 1994. The profile width includes both the source function width and the instrument profile width. The mean mercury-lamp profile width varies in a very similar fashion to the frequency-stabilised laser width, which should be indicative of the instrument profile variation. Figure 2 shows individual values of profile width.

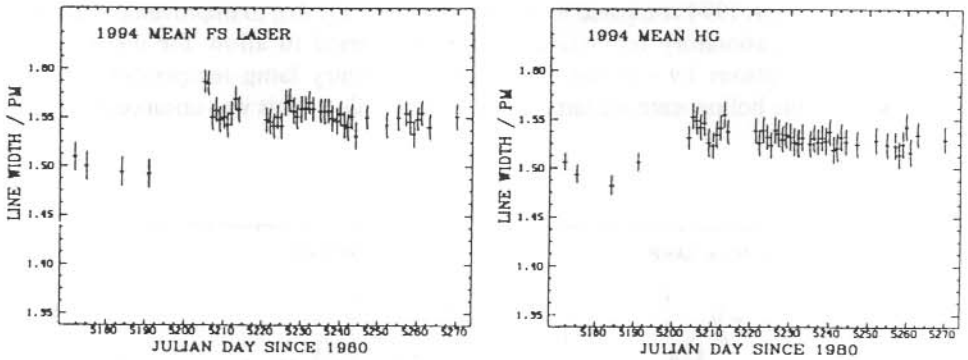

Figure 1. Mean mercury lamp and frequency-stabilised laser widths from calibration profiles obtained in 1994. The width is the sum of the instrument and source function widths.

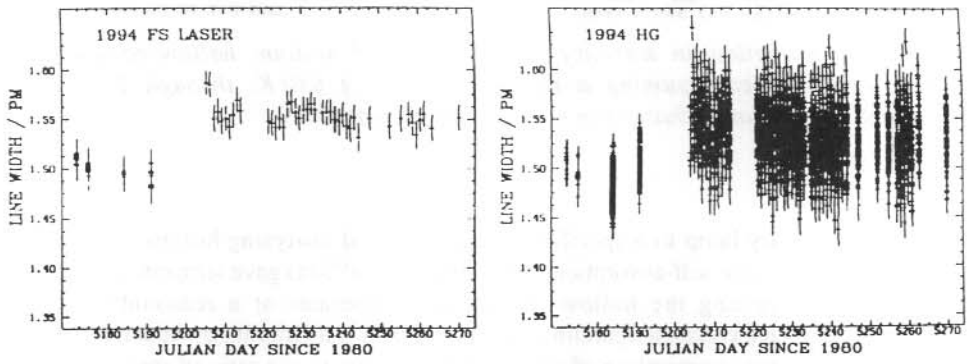

Figure 2. As for Figure 1 except each individual profile is plotted.

There is considerable variation in the mercury lamp. On four days when more than one frequency-stabilised laser profile was collected the laser is less variable than the mercury lamp. We have so far only been collecting one frequency-stabilised laser profile for each observing session. We are instigating a program where on cloudy nights a frequency-stabilised laser profile will be collected once every seven minutes.

The effective temperature of the mercury lamp can be determined using the frequency-stabilised laser to define the instrument profile. The mean of 49 nightly mean mercury temperatures is 1390 K; significantly greater than expected. The standard deviation is 907 K; also much larger than expected. The mean of nightly mean uncertainty in the fitting process is 110 K.

Returning to 1990 when the sodium data were collected, Figure 3 shows variation in width of the mercury lamp profile through 1990. Considerably less variation in the mercury lamp width can be seen in 1994 compared to 1990. This is mainly due to improvement in control of the Mawson laboratory temperature. We have tried to allow for mercury lamp temperature variations by varying the assumed mercury lamp temperature until the temperature of the hollow-cathode lamp had a defined value. This was unsuccessful.

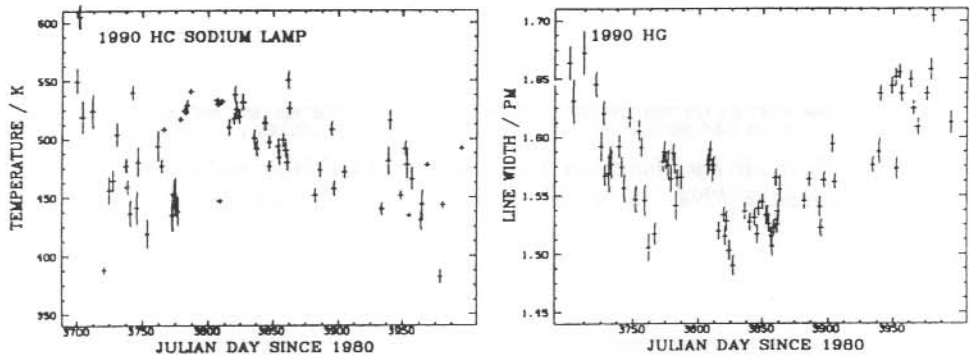

Figure 3. Variation in mercury lamp width and sodium hollow-cathode lamp temperature derived assuming a Hg temperature of 630 K, through 1990. These variations suggest large changes in mercury lamp temperature.

Setting the mercury lamp to a specified temperature and analysing hollow-cathode lamp variations, allowing for self-absorption (Greet and Jacka 1994a) gave temperature variations of ~150 K. Assuming the hollow-cathode lamp operates at a reasonably constant temperature, given a constant operating current of 5 mA, this implies an apparent variation in the mercury lamp temperature of about 1200 K. (Due to the ratio of mercury mass to sodium mass a 1 K change in sodium temperature is equivalent to ~10 K change in the mercury temperature). Over shorter time periods the lamp is more stable. Large changes appear to have occurred in the transition from summer to winter conditions.

Thus measurements in both 1994 with the frequency-stabilised laser and 1990 with the hollow-cathode lamp imply instability in the ^{198}Hg lamp. Possible explanations of these instabilities include profile broadening due to the Stark effect and/or localised heating within the mercury discharge. This apparent variation in the mercury lamp temperature precludes the determination of mesospheric temperatures using currently available analysis techniques. Cross comparison of calibrations shows that, in this case, what was considered to be a reliable calibration source, the ^{198}Hg single-isotope discharge lamp, is not performing as expected. A single-mode or frequency-stabilised laser is often considered a reliable calibration source. We would caution against relying solely on this. By routinely monitoring and comparing two calibration sources, their stability can be checked. This will allow for a more robust determination of the FPS instrument profile.

17.4 CONCLUSIONS

Particular care is required in calibrating an FPS for mesospheric observations. The results presented here illustrate the importance of developing more than one calibration procedure as part of routine operation of high-resolution Fabry-Perot spectrometers.

Mercury lamp observations at Mawson are, at present, not sufficiently repeatable to be used to determine FPS instrument profiles for mesospheric observations. The mercury lamp is still a useful wavelength reference. Without developing a more sophisticated analysis, accounting for self-absorption of the hollow-cathode lamp profiles, we cannot determine mesospheric temperatures from the sodium data obtained to date. It may be worthwhile investigating sodium absorption cell technology in the quest for a reliable sodium source suffering minimum self-absorption and operating at a defined temperature. Frequency-stabilised lasers should be able to provide adequate calibration for future mesospheric observations but cross comparison with another source is advised.

17.5 ACKNOWLEDGEMENTS

This work has been partly funded by the Australian Research Council, by the Antarctic Science Advisory Committee and the Australian Antarctic Division. We acknowledge discussions with Prof. P. Dyson, from La Trobe University, Dr M. Conde now at the Geophysical Institute, University of Alaska, and Dr J. Innis from the Australian Antarctic Division. 1994 observations and calibrations have been performed by M. Manion, Atmospheric and Space Physics engineer at Mawson.

REFERENCES

Jacka, F. (1984). Application of Fabry-Perot spectrometers for measurement of upper atmosphere temperatures and winds. *MAP Handbook 13:*19–40.

Plane, J.M.C. (1990). The chemistry of meteoric metals in the Earth's upper atmosphere. *International Review of Physics and Chemistry 10:*55–106.

Sipler, D.P. *and* Biondi, M.A. (1978). Interferometric studies of the twilight and night glow sodium D-line profiles. *Planetary and Space Science 26:*65–73.

Hernandez, G. (1975). Reaction broadening of the line profiles of atomic sodium in the night airglow. *Geophysical Research Letters 2:*103–105.

Greet, P.A. *and* Jacka, F. (1994a). Analysis of high-resolution mesospheric sodium twilight spectral emission profiles. *Journal of Atmospheric and Terrestrial Physics 56:*603–616.

Wilksch, P.A. (1975). *Measurement of thermospheric temperatures and winds using a Fabry-Perot spectrometer.* Ph.D. Thesis, University of Adelaide.

Greet, P.A. *and* Jacka, F. (1994b). Observations of the sodium layer using a Fabry-Perot spectrometer: twilight temperature variations. *Journal of Atmospheric and Terrestrial Physics 51*:91–99.

18. ENHANCEMENTS TO AN ALL-SKY VIDEO IMAGER FOR AIRGLOW MONITORING

D.J. Rasch and M.J. Underwood

Atmospheric and Space Physics
Antarctic Division
Kingston Tasmania 7050
Australia

ABSTRACT

An all-sky imaging video camera system has been modified to allow the imaging of structure within airglow emissions. The imaging wavelength is determined by computer selection of one of six optical filters mounted on a rotating platter. Noise has been reduced in the image intensifier by Peltier device cooling. Some preliminary results are presented and some techniques for enhancing structure within the airglow images discussed.

18.1 INTRODUCTION

Gravity waves appear to play a significant role in energy transport and coupling at high latitudes. Sources of gravity waves at these latitudes are diverse, and include orographic sources (below 10 km altitude), wind shear and convective sources (up to 100 km altitude), and may include auroral heating and neutral-plasma shear (source above ~90 km). A manifestation in all-sky images is the occurrence of periodic variations in airglow emission intensity of a few percent due to disturbance to the emitting layer by the wave (Taylor et al. 1987).

Imaging of airglow variations at different altitudes is made possible by selecting wavelengths associated with emissions that occur principally at the altitude of interest. For example, emissions in the 750 nm–950 nm range (molecular OH bands) are attributed to altitudes around 87 km, while 630 nm emissions are, in the absence of auroral activity, allied with dissociative plasma recombination above 200 km. Observations on 428 nm can serve to identify the presence or absence of auroral contamination within the 630 nm images.

The Atmospheric and Space Physics (ASP) group has operated three all-sky auroral video cameras in Antarctica for about five years. These instruments replace the older All-Sky Cameras which were operated at one or more of the Australian Antarctic bases until 1993. The main advantage of upgrading to the video cameras has been the elimination of time-consuming and potentially hazardous film processing, as well as facilitating computerised image processing and analysis.

The Imagers were originally designed to collect short exposure (1 second) all-sky images of auroral forms and record these images in analogue form on video tape. Camera operation is programmed using an interpretive 'script' language which is loaded prior to

camera operation. The use of these scripts allows a high degree of flexibility in the image collection modes, as well as providing a degree of automation in the post-analysis of images. A number of extra script commands have also been written (in C language), and incorporated into the software at runtime to enhance the instrument's capabilities and drive additional external hardware.

18.2 MODIFICATIONS TO THE AURORAL VIDEO SYSTEM

18.2.1 *Reduction in equipment noise*

The two active elements in the Imager are a gain-adjustable 'second generation' image intensifier, followed by an integrating CCD camera. With the intensifier operating at its minimum gain setting, the unmodified camera responds to a 1 second exposure of a whole-sky 115 Rayleigh emission at 557.7 nm (a typical airglow intensity) with a greyscale value of ~16 and a standard deviation (assuming $\sqrt{N}$ (Poisson) counting statistics) of 4, with an additional contribution due to equipment noise.

With 'ion events' effectively eliminated in the 'second generation' design, intensifier noise is principally thermal in origin. The CCD response also includes a thermal noise component, and both active elements contain blemishes in response, appearing on the image as gradients in sensitivity, as well as 'hot' and 'dead' pixels.

While an obvious reduction in system noise could be obtained by cooling the sources of thermal noise, the effects of temperature on 'hot' pixels and other blemishes was less clear. The Antarctic Division's temperature-controlled chamber was therefore used to quantify the relative contributions to overall system noise by the CCD and image intensifier as a function of temperature by performing long exposures with the lens cap in place and the instrument shrouded. Figure 1 illustrates the variation in mean greyscale counts per second obtained as a function of instrument temperature.

Intensifier noise was found to dominate the 'dark image' counts, being approximately 10 times greater than CCD noise at any given temperature. By reducing the temperature of the intensifier from room temperature to around +10°C, total noise generated within the image intensifier was found to reduce by a factor of ~10.

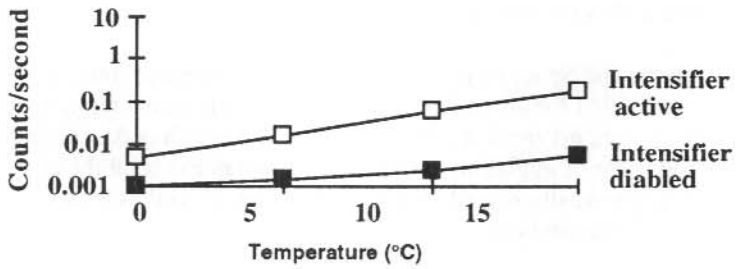

Figure 1. A plot of typical measured pixel count rates due to system noise as a function of temperature, measured both with the intensifier active (□) and with it disabled (■).

Cooling of the image intensifier was achieved using two Peltier cells. Other methods of cooling (e.g. circulating cooling water) were rejected because they compromised the ability of the instrument to operate at field sites without support facilities. Peltier cells were thermally connected to either side of the intensifier housing using metal saddles and heat conductive paste (see Figure 2). Each Peltier cell operates from an independent temperature controller circuit, operating to minimise the thermal gradient across the intensifier. The proportional temperature controllers adjust power to the Peltier cells without creating electrical switching transients, by passing or blocking individual half cycles of rectified 60 VAC. The heat energy, the bulk of which is generated by the Peltier cells themselves, is dissipated using two fan-forced heatsinks. The final electrical and mechanical arrangement allows the image intensifier to be cooled to its +10°C setpoint for ambient temperatures between +10°C and +30°C. Further cooling of the intensifier below 10°C was found to introduce problems with condensation on the image intensifier and adjacent lenses.

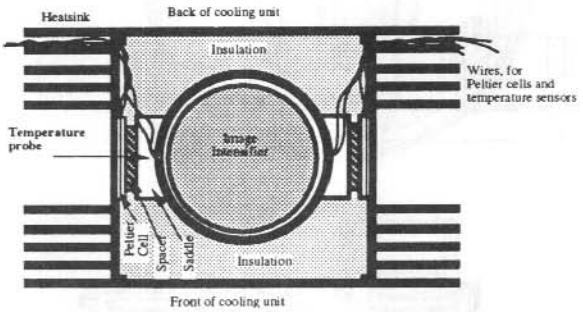

Figure 2. Cross-section of the image intensifier cooling assembly.

18.2.2 *Optical filter selection*

To enable image collection at several wavelengths of interest in an automated fashion, a mechanism was required which could locate a number of narrowband filters sequentially into position. The mechanism was also required to be easily installed in place of the existing single filter chamber without affecting camera focus or f-stop, or allowing light leakage into the instrument. The temperature of the optical filters had to be maintained in the range +20°C – +30°C.

A filter wheel platter was designed and manufactured by the Antarctic Division's Instrument Workshop which allows the use of up to six 2 inch optical filters mounted in a circular arrangement (see Figure 3). In the original design, the filters were to be mounted in tiltable cradles to fine tune their centre frequency, but there was insufficient room for this to be achieved without moving nearby lens elements. The filters are individually mounted in brass holders using threaded mounting rings then placed into the platter and held in position with grub screws. The filter wheel is rotated using a small electric motor and gearbox driving a six-pole Geneva cross mechanism. This arrangement ensures

precise positioning of the filters. The time required to move a particular filter into position with this arrangement varies from 5–15 seconds depending on the initial position of the required filter within the platter. Beneath the filter platter is a printed circuit board containing a network of surface-mounted resistors which are used to uniformly heat the filters and platter to 20°C in conjunction with a commercial temperature controller.

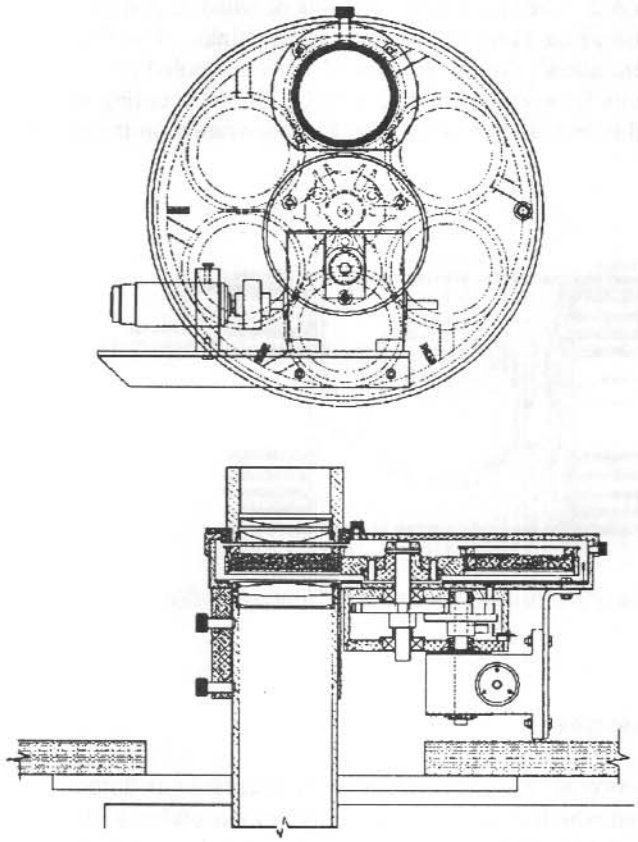

Figure 3. Plan and side views of the filter wheel mechanism.

The position of the platter is encoded using four Hall effect sensors (see Figure 4). One sensor is located beneath the Geneva cross mechanism to sense when a filter is in its 'home' position. Three other sensors are mounted around the circumference of the platter at 60° increments, with small magnets imbedded within the platter in adjacent positions. Whenever the first sensor indicates a filter is in the 'home' position (i.e. every 60°), the remaining three sensors provide a unique three bit code to the controlling computer that allows the platter orientation to be determined.

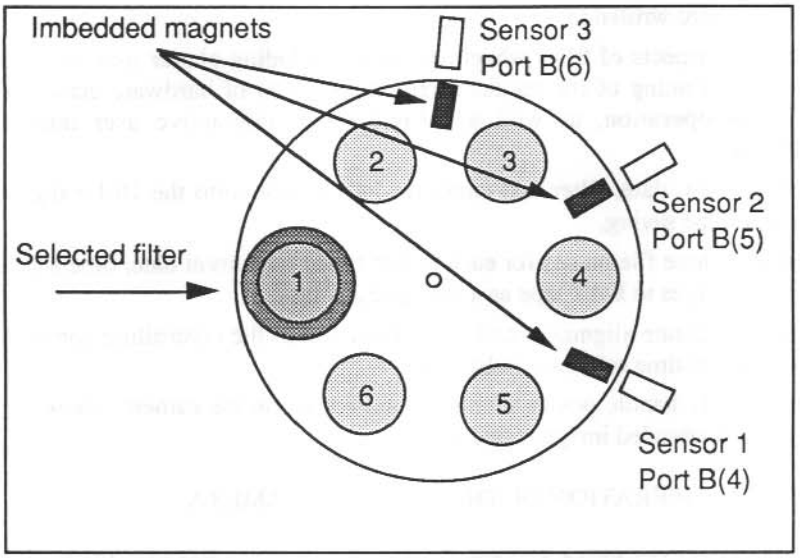

Figure 4. Filter wheel sensor placement.

18.2.3 *Digital image storage*

At the termination of each exposure, the image is downloaded once from the CCD camera to the controlling computer using a commercial video 'frame-grabber' card. In the unmodified Imager, each image was then converted back to a continuous PAL video signal and recorded for a brief period of time onto video tape using a commercial time-lapse VCR. Unfortunately, the signal subsequently recovered from the video tape recorder was susceptible to variations in brightness, contrast and general quality due to factors such as video recorder head wear and internal gain drifts. For this reason, digital storage of the airglow images was deemed desirable. With up to six airglow filters available, however, a single 'round' of airglow images yields approximately 2.4 MB of data which would rapidly fill hard disk storage in the controlling computer. A DAT tape drive was interfaced via the computer's SCSI port, allowing up to 8000 images to be digitally stored on a small data cassette. The DAT controller software actually performs the 'write' some time after that requested by the 'script' by stealing CPU time for several seconds. This behaviour requires some care to be taken during script development to ensure that control is not lost during other vital functions, such as, filter platter rotation or during short exposures.

18.2.4 *Controlling software*

New software routines in the form of 'script' commands were required to control the newly developed hardware described in Sections 18.2.1 – 18.2.3 above. The additional script commands are automatically incorporated at run time into the commercial application that controls image acquisition.

New routines were written to:

(a) control all aspects of filter wheel operation, including platter rotation direction for fastest positioning of the requested filter, detection of hardware errors or unusual delays in operation, as well as providing an interactive user interface filter description,

(b) annotate time, date, filter and exposure information onto the 16-bit digital images prior to image saving,

(c) generate unique file names for each image based on current date, time and filter, and store the images to DAT tape as a 'background' task,

(d) maintain accurate alignment and auto-correction of the controlling computer's clock to an external time reference pulse, and

(e) automatically handle power shutdown and restart on the camera, allowing multiple nights of unattended image collection.

18.3 TYPICAL OPERATION OF THE MODIFIED CAMERA

Long exposures of the broad 830 nm airglow spectrum are not possible because of the limited (8-bit) resolution of our 'frame-grabber' card. The instrument therefore accumulates a series of exposures into an unsigned 16-bit array. Exposure time for each image is adjusted for a typical mean greyscale value ~100 with a standard deviation of ~10 greyscales (assuming Poisson-distributed photon counting statistics for each pixel). The accumulation of M similar, consecutive images, each with Poisson-distributed counting statistics, results in a 'composite' image with a greyscale standard deviation which is $M^{-0.5}$ times that for a single image (the same result that would be obtained by exposing the image M times longer). Typically, 25 images are accumulated over a period of six minutes, with the 16-bit array easily accumulating the 25 x 255 = 6375 greyscale counts without overflowing. The resulting image has a signal-to-noise ratio of ~50.

The long net exposure results in some 'blurring' of moving structure. The upper limit on the net exposure time is that required for a periodic structure to drift approximately half a wavelength across a given pixel. Thus moving structure with periodicity (with respect to a particular pixel) shorter than about 12 minutes is essentially lost during the accumulating process.

Information including exposure time, time of day and the selected filter is annotated digitally onto each 'composite' image in graphical form, as well as encoding the information as greyscales into the first few pixels of each image. This latter encoding technique allows subsequent analysis software to read the exposure parameters. The image is then stored to DAT tape. Following storage, the image is contrast stretched and recorded to video tape using a 'one-shot' time-lapse recorder which is slaved to the controlling computer.

Contrast stretching involves 'histogram equalisation', where a histogram of greyscales within a circular region of the image (with presettable centre and radius) is generated, followed by the application of a mapping function derived from scaling the integrated histogram to the range 0 – 255 to generate the lookup table values. This technique applies

the largest greyscale range to the most common intensity values. Figure 5 shows the assembly of the modified camera.

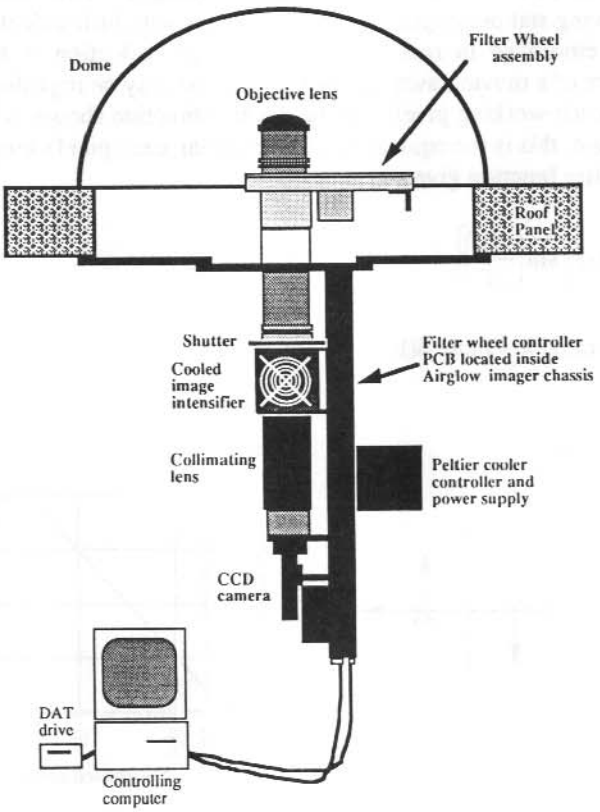

Figure 5. The modified camera assembly.

18.4 ANALYSIS OF IMAGES

Image analysis of the composite airglow images is still under development. It has not at this stage been found necessary to eliminate 'hot' or 'dead' pixels from the images due to their low density and good image signal-to-noise ratio.

Post-analysis seeks to identify the presence of long duration drifting waves within a portion of the image. The airglow modulation due to these wave structures may represent only a few percent variation in the overall airglow. Unfortunately, greyscale assignment using histogram equalisation tends to be dominated by the largest scale structures on the image, which are often not due to airglow, but to the presence of aurora, intensifier gain variations, backscatter from terrestrial light sources or the van Rijn effect. Such large

scale gradients must be removed, or accounted for in some fashion, before the smaller scale structure can be seen.

A technique currently popular with airglow imaging investigators is to render as an image the arithmetic difference between two consecutive images. This technique has the advantage of removing stationary gradients in the images with little calculation overhead, allowing it to be employed in real time during image collection if desired. Image subtraction is a form of a moving average (MA) filter, and may be regarded as convolving the time series for each working pixel with the discrete function shown in Figure 6(a). In the frequency domain, this is the equivalent of multiplying each pixel's temporal spectrum with a sinusoidal filter function given by:

$$A\,(\mathrm{dB}) = 20\log\left[\sin\left(\frac{\pi}{2T}\right)\right]$$

whose form is illustrated in Figure 6(b).

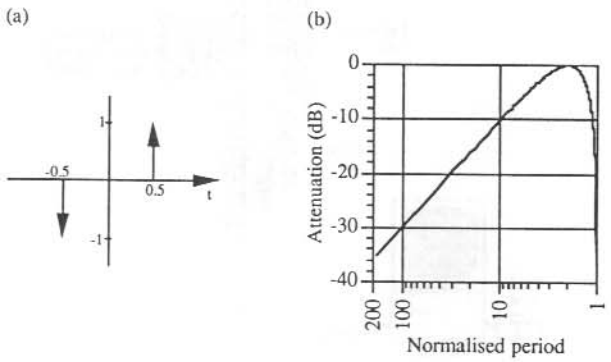

Figure 6 (a). Image subtraction as a convolution filter applied to the pixel time series. (b). Filter transfer function, normalised to image time separation.

For pixel variations with period slower than twice the image time separation, subtraction therefore equates to a high pass filter operation where the least attenuated period is twice the time separation between images, and the corner (-3 dB) period is one quarter of the time separation between images. This filter is quite selective, and biased heavily towards pixel variations with short period (including noise). Thus the 'subtracted' image will mainly display structure with pixel variation period twice the image time separation. There is the temptation with this technique to try and 'match' the image time separation to the periods one is seeking. However, as a consequence of the periodic nature of the filter function, there is the possibility of seriously aliasing shorter period pixel variations with little attenuation. For example, structure with pixel variation period 0.75 times the image time separation will pass through completely unattenuated. Typical effects of aliasing are the creation of large scale structure in the 'subtracted' image that is not present in either of

the individual images, or the apparent motion of structure in the opposite direction to that which is actually taking place. It is imperative therefore to analyse separately the individual images to ensure aliasing does not occur.

A result that is less selective toward pixel periodicity could be obtained by applying a filter of the general class of autoregressive-moving average (ARMA) filters of the general form:

$$y_n = \sum_{k=0}^{M} c_k x_{n-k} + \sum_{j=1}^{N} d_j y_{n-j}$$

where the first summation represents the moving average part (applied to unfiltered values), while the second autoregressive term is applied to previous filtered values. For example, a suitable bandpass filter may be constructed using the following coefficients:

$$c_0 = 0.408 \quad c_1 = 0 \quad c_2 = -0.408 \quad d_1 = 1.0974 \quad d_2 = -0.1487.$$

The transfer function and impulse response of this filter is shown in Figure 7. The horizontal wavelength axis has been normalised to the pixel resolution which, at zenith and using the 180° field of view lens, is approximately 600 metres at 85 km altitude.

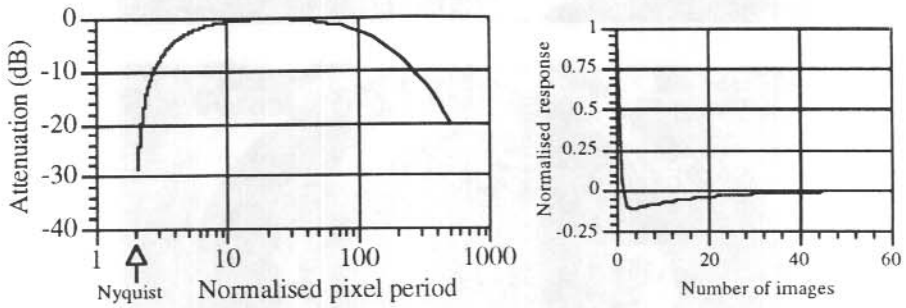

Figure 7. Transfer function and impulse response for the ARMA filter example with coefficients shown above.

The use of this filter requires, in addition to the current image, one previous unfiltered image and two filtered images to be utilised. The impulse response of the filter takes approximately 20 images to settle, so the first few filtered images would display some transient behaviour. This technique would perhaps be better applied to the individual rather than the 'composite' images. Importantly, the impulse response displays no oscillatory behaviour that might introduce artefacts that could be mistaken for periodic airglow structure.

The use of this filter for flat-fielding may be illustrated spatially by first converting the byte image to floating point, applying the recursive filter from left to right across the image, then rescaling the data values to byte, based on highest and lowest values within the area of interest. Larger and smaller greyscale values that may occur outside the region of interest are set to zero or 255. A comparison between Figures 8(a) and (b) illustrates the improvement in detail that can be obtained by flat-fielding. Since the filter has in this case been applied horizontally across the image, the image has acquired the

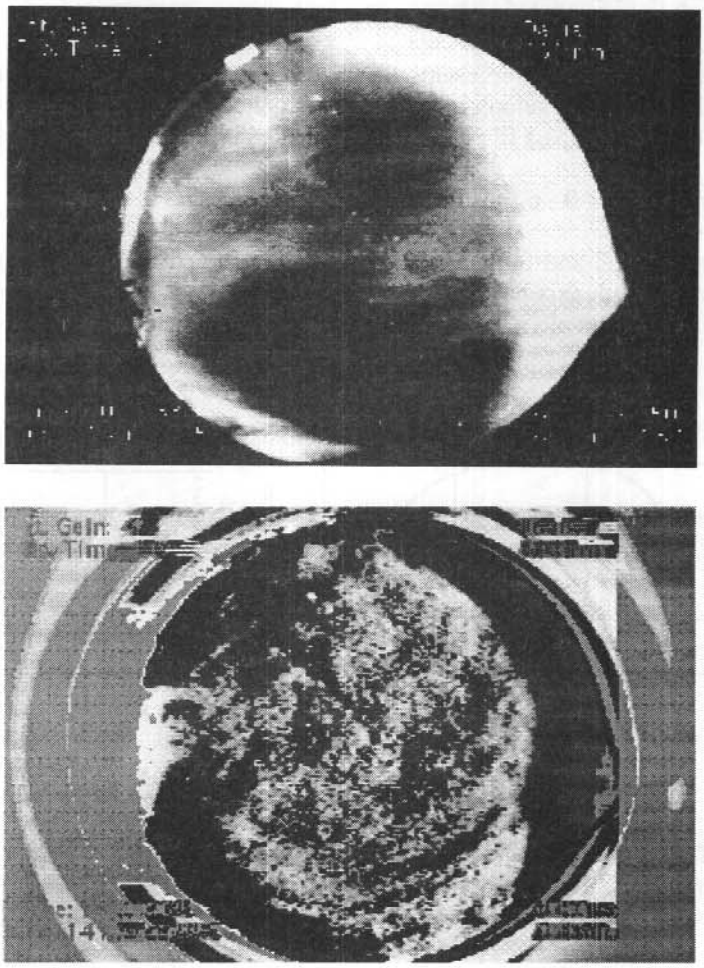

Figure 8 (a) [top]. Airglow image contrast stretched via histogram equalisation without flat-fielding. Note the loss of image information at lower centre due to a trend in the overall intensity. (b) [bottom]. Same airglow image filtered to remove trends then contrast stretched using histogram equalisation. Note the reappearance of image information at lower centre.

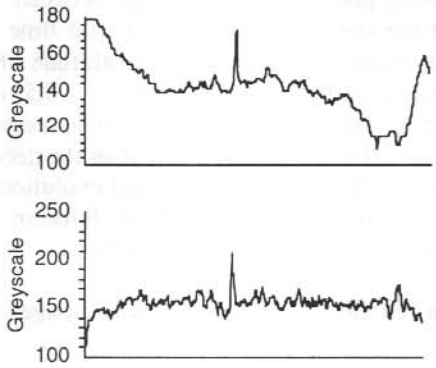

Figure 8 (c). Same vertical slice through the image centre before [top] and after [bottom] application of the filter (not to same scale).

appearance of surface texture that has been illuminated from the left. Although the filter is only applied horizontally, a vertical slice through the centre of the images shows that the image is effectively filtered in this direction also, by virtue of the structural correlation that exists between adjacent rows of the image. Because structure has finite correlation scale both spatially and temporally, applying the filter in the time domain also results in structure being filtered spatially.

From this point, images are analysed visually to directly scale structure, wavelength and direction of motion. When viewing structure that may be partially obscured by noise, cloud or aurora, it quickly becomes apparent that the structure is rendered more visible when viewed as a time sequence of images. During this process, the human brain (being an excellent image analyser) attempts to correlate regions within consecutive images with the following characteristics:

structure that is much larger than the pixel separation,
structure that is highly anisotropic,
structure that is periodic over several cycles,
structure that has steady drift motion normal to its direction of anisotropy,
structure with similar characteristics in consecutive frames.

Clearly, image history plays an important part in the visual identification of structure – a strongly periodic and anisotropic structure that appears only in a single frame of an image sequence should probably be rejected (or at least treated separately).

Visual identification of periodic structure is also possible by plotting greyscale value along an arbitrary one-dimensional linear slice through the image, although one must be careful not to mis-interpret stars as periodic airglow variations. Also, wavelengths cannot be reliably scaled in this fashion.

There has been some initial investigation of the use of correlation techniques for measuring structure wavelength. The term 'structure' implies a degree of correlation both spatially between neighbouring pixels, and temporally between consecutive images. Structure which is both drifting spatially and evolving with time will be successfully imaged if the adjacent pixel separation (referred to the altitude of the structure) is no greater than about half the characteristic correlation scale ($\rho = 0.5$) of the structure being imaged. Likewise for the time evolution of the structure to be recorded successfully, the time separation between adjacent images must be less than the decorrelation time scale for any given pixel due both to spatial drift and temporal evolution of the structure. In both spatial and temporal domains, equipment noise, Poisson counting noise and malfunctioning pixels act to decorrelate the adjacent images.

The spatial cross-correlation function for a region of two images can be conveniently calculated by:

$$\mathrm{IFFT}\left[\mathrm{FFT}(\mathrm{Image1}) \cdot \mathrm{FFT}^{*}(\mathrm{Image2})\right]$$

where the * denotes the complex conjugate of the Fast Fourier Transform (FFT).

An example of a periodicity in spatial correlation function calculated from two 558 nm images collected at Adelaide on 12 September 1993 is shown in Figure 9. Maximum cross-correlation between images appears slightly offset from centre (zero lag) indicating the presence of drift motion.

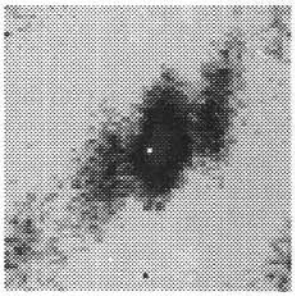

Figure 9. Spatial correlation function.

Given that the presence of drifting structure has been positively identified by other techniques (e.g. visually), a rectangular region of interest containing the structure could be defined, and a three-dimensional array (two spatial and one temporal) of greyscale values used to derive a 3-dimensional correlation function. A least-squares linear fit to the major axis of the correlation function should then yield the drift velocity (from the zenith angle of the linear fit relative to the temporal axis) and the direction of drift (from the azimuth angle of the linear fit) as well as providing a goodness of fit parameter to accept or reject the measurement. Furthermore, the least-squares fitting of an ellipsoid to

the correlation values (say $\rho = 0.5$) could yield a spatial scale size and the direction of anisotropy, while the major axis scale of the ellipsoid could yield the decorrelation time of the moving pattern (neglecting the decorrelating effect of the arrival and disappearance of 'new' structure from the edges of the image). A more accurate estimate of the decorrelation time scale could then be obtained by repeating the above procedure using data loaded from a region of interest which is moving with the calculated speed and direction obtained above. This should yield a correlation function whose major axis is oriented along the time axis.

There are a number of problems with the technique outlined above. The 180° fisheye lens distorts the image so that data is not evenly sampled in latitude and longitude (in which domain the waves are expected to show maximum linearity). Parallel wavefronts in a (N, E) coordinate system will therefore appear bent and the wavelength scaled from the image or correlation function must be corrected for zenith angle. Moving structure may also decorrelate more rapidly due to zenith angle variation of the structure. Correlation techniques are also sensitive to the presence of bright stars which are slowly rotating in the image view. The most useful analysis techniques will emerge as more experience is gained working with the airglow images.

18.5 ACKNOWLEDGMENTS

This equipment was developed under contract to the Antarctic Division. Thanks are due to Andrew Fleming and the Division's Instrument Workshop for mechanical design and construction, and to members of the ASP group for their support in this project.

REFERENCES

Taylor, M.J., Hapgood, M. A. *and* Rothwell, P. (1987). Observations of gravity wave propagation in the OI(557.7 nm), Na(589.2 nm) and the near infrared OH nightglow emissions. *Planetary and Space Science 35*:413–427.

19. DOPPLER PERFORMANCE OF THE LIDAR FOR DAVIS, ANTARCTICA

A.R. Klekociuk and J.L. Innis

Atmospheric and Space Physics
Antarctic Division
Kingston Tasmania 7050
Australia

ABSTRACT

A novel Doppler lidar is under development by the Australian Antarctic Division and the University of Adelaide for the study of the structure and dynamics of the middle atmosphere. The capabilities of the system will be established during test observations to be conducted from Tasmania during mid 1996 and early 1997. The lidar will be relocated to Davis, Antarctica (68.6°S, 78.0°E) during the 1997/98 austral summer as part of Australia's program of climate change studies.

The Davis lidar will have three important capabilities in comparison with existing Antarctic lidars. Firstly, its transmitter and receiver share a common field-of-view which can be rapidly moved in azimuth and zenith angle. Secondly, the receiver incorporates a high-resolution Fabry-Perot spectrometer which directly measures the Doppler characteristics of atmospheric molecules and aerosols as a function of range. Thirdly, the lidar will be capable of probing the upper mesosphere by virtue of its comparatively large 'power-aperture' product.

Simulations of the lidar's Doppler performance are described. The simulations have enabled the accuracy of temperature and wind measurements to be estimated as a function of temporal and spatial resolution and operating conditions. Importantly, it is shown that the presence of aerosols may significantly influence the recovery of temperatures using the Doppler technique, particularly in the lower stratosphere.

19.1 INTRODUCTION

The Davis lidar will undertake measurements relating to the structure, dynamics and climatology of the Antarctic atmosphere, from the upper-troposphere (~10 km altitude) to the mesopause region (~95 km altitude). The instrument and its scientific aims have previously been described by Jacka and Argall (1987), Klekociuk et al. (1994a, 1994b) and Morris et al. (1995). Its operating wavelength is that of the second harmonic of the Nd:YAG laser line, namely 532.1 nm.

The lidar will have two measurement modes. In 'total power' mode, laser light backscattered by gases and aerosols will be integrated over a fixed spectral bandpass as a function of range. When calibrated by balloon-borne radio-sonde data in the lower atmosphere, these observations will provide density profiles, from which molecular temperatures and aerosol loading will be inferred. In 'high spectral resolution' mode, a

separation-scanned Fabry-Perot spectrometer (FPS) will measure the spectrum of the backscattered laser light. Deconvolution of the 'instrument response' will yield Doppler-inferred wind speed, molecular temperature and possibly aerosol loading. Wind velocity information will be obtained from density and Doppler measurements made at several 'cardinal point' viewing directions.

Preliminary measurements in total power mode were undertaken at Buckland Park (South Australia) during 1992 and 1993 (Argall 1993). Further observations will be conducted at Antarctic Division Head Office (Tasmania) during 1996 and 1997. At this time, the high spectral resolution mode will be tested.

This paper describes simulations of the high spectral resolution mode which were undertaken to assess the performance of the lidar under typical atmospheric and operating conditions.

19.2 HIGH SPECTRAL RESOLUTION LIDAR

19.2.1 *The wavelength-dependent lidar equation*

Lidar performance is assessed via the 'lidar equation' which estimates the output signal as a function of range given certain instrumental and atmospheric parameters. In this section, a realisation of the wavelength-dependent lidar equation is described. Because the Davis lidar operates in a region of the spectrum where the scattering and absorption properties of the atmosphere are well-behaved, some simplifying assumptions can be made to the general formalism (see, for example, Measures 1984).

The Davis lidar has a coaxial mono-static design, and under the assumption of optimum optical alignment, the volumes probed by the transmitter and the receiver are identical. The detector is a photomultiplier tube (PMT) operating in 'photon-counting' mode. The photomultiplier pulses are accumulated in contiguous range-interval bins synchronously with the firing of the laser.

Both elastic and inelastic scattering processes take place in the atmosphere. However, in terms of the normal operation of the Davis lidar, the influence of inelastic scattering processes (such as Raman and Brillouin scattering) can be neglected. The lidar response is suitably modelled by applying standard Rayleigh and Mie elastic scattering theory to the molecular and aerosol components of the atmosphere, respectively.

For a single laser pulse, the total photomultiplier count associated with range interval Δr centred at range r_0 may be expressed as

$$N_L = \frac{\Delta r A_r}{r_0^2} \varepsilon_t \varepsilon_r T^2(\lambda_0, r_0) \eta \left(\frac{\lambda_0 E_t}{hc \int I_r(\lambda) d\lambda} \right) \cdot \left[\sigma_m(\lambda_0) \rho_m(r_0) \int \{ G_m(\Delta\lambda) * G_I(\lambda) \} I_r(\lambda) d\lambda + \right.$$

$$\left. \beta_a(r_0) \int \{ G_a(\Delta\lambda) * G_I(\lambda) \} I_r(\lambda) d\lambda \right] \qquad (1)$$

where A_r is the effective area of the receiving telescope, ε_t and ε_r are the wavelength-independent efficiencies of the transmitting and receiving optics, T is the one-way atmospheric transmission coefficient between the lidar and the scattering region, η is the quantum efficiency of the photomultiplier, λ_0 is the observing wavelength (532.1 nm), E_t is the total energy of the laser pulse, c is the speed of light, h is Planck's constant, σ_m is the molecular differential scattering cross-section (evaluated for linearly polarised incident radiation at a scattering angle of π radians), ρ_m is the molecular number density, and β_a aerosol volume scattering coefficient. The functions G_m and G_a are the unit-area thermal and Doppler response functions for molecules and aerosols, respectively (Section 19.2.2), G_l is the unit-area spectral distribution of the laser emission, and I_r is the spectral transmission function of the lidar receiver (Section 19.2.3). The operator '*' denotes convolution. In this realisation the terms T, ρ, and G are assumed constant over the range interval Δr.

In the atmosphere below about 100 km (where the mean molecular weight is independent of altitude), $\sigma_m \approx 4.99 \times 10^{-57} \lambda^{-4}$ $m^2 sr^{-1}$ (Measures 1984), or $\sim 6.22 \times 10^{-32}$ $m^2 sr^{-1}$ at $\lambda_0 =$ 532.1 nm. The aerosol volume scattering coefficient β_a varies considerably with altitude, geographic location, season, and weather conditions. Values of β_a may be conveniently obtained from experimental databases such as the LOWTRAN atmospheric model (Kneizys et al. 1988).

The one-way atmospheric transmission coefficient may be calculated from

$$T(\lambda_0, r_0) = \exp\left(-[\sigma_{mt} \int_0^{r_0} \rho_m(r) dr + \int_0^{r_0} \beta_t(r) dr] \right) .$$

Here σ_{mt} is the total scattering cross section for molecules (i.e. the backscatter cross section integrated over 4π steradians) with $\sigma_{mt} \approx 4.18 \times 10^{-56} \lambda^{-4}$ m^2, or $\sim 5.21 \times 10^{-31}$ m^2 at $\lambda_0 =$ 532.1 nm. The quantity β_t is the aerosol extinction coefficient, which may be obtained from an atmospheric transmission model.

The total number of photomultiplier pulses is given by

$$N_t = N_l + N_b + N_d \qquad (2)$$

where N_b is the contribution from background scattered light and N_d represents 'counting noise' in the detector. Each term is governed by Poisson statistics. The background signal may be written as

$$N_b = \varepsilon_r A \pi \frac{\alpha^2}{4} \frac{B_c \lambda_0}{hc} \frac{2\Delta r}{c} \int I_r(\lambda) d\lambda \qquad (3)$$

where B_c (expressed in units of $Wm^{-2}nm^{-1}sr^{-1}$) is the flux of the background light, and α is the full-angle field-of-view of the receiver.

It should be noted that 'pulse pile-up' in the photomultiplier and 'dead time' in the counting electronics may influence estimation of the true signal when the level of backscattered light is sufficiently high (Donovan et al. 1993).

19.2.2 *The atmospheric response function*

For purely elastic scattering, the wavelength-dependant scattering response function for a particular atmospheric constituent may be expressed as

$$G(\lambda) = G_T(\Delta\lambda) * G_t(\Delta\lambda) * D_D(\Delta\lambda) \quad (4)$$

where, respectively, the terms describe 'broadening' functions associated with random thermal motion and turbulence, and the Doppler shift induced by bulk motion of the scattering medium. Here, $\Delta\lambda = \lambda - \lambda_0$, where λ_0 is a reference wavelength (for example, the central wavelength of the laser line).

For purely elastic scattering, the width of the backscatter line is dictated by the kinetic behaviour of the scattering species. For a particular molecule, the thermal broadening function G_T is a Gaussian with a full width at half maximum (FWHM) of

$$\delta_T = 2\frac{2\lambda_0}{c}\sqrt{\frac{2\ln(2)\,kT}{M}} \quad (5)$$

where T and M are the kinetic temperature and mass of the molecule, respectively. The leading factor of 2 arises from reference frame considerations. For the molecular atmosphere, the actual broadening function results from the superposition of the Gaussians associated with each constituent. However in the atmosphere below the mesopause we can conveniently approximate the width of the actual broadening function by substituting a mass value equivalent to 29.964 amu in Equation (5). As an example, for T = 140 K (of the order of the expected summer mesopause temperature above Davis) and λ_0 = 532 nm, δ_T = 1.7 pm.

The thermal distribution function for aerosols of a particular mass may be approximated by a Lorentzian which accounts for translational and rotational Brownian motion (Fiocco and DeWolf 1968);

$$G_{T,a}(\Delta\lambda) = \frac{1}{\pi}\frac{\Gamma_a}{\Gamma_a^2 + \Delta\lambda^2} \quad (6)$$

where Γ_a is the FWHM of the distribution. Using Equation (6), the form of G_T was evaluated for λ_0 = 532.1 nm assuming a particle population with a log-normal size distribution characterised by a geometric mean diameter of d_g. For d_g ~0.5 μm, typical of recent post-volcanic stratospheric conditions (Kaufman et al. 1994), G_T is found to be essentially Lorentzian with Γ_a ~0.5 fm. For d_g ~0.1 μm (a reasonable value for stratospheric sulphate aerosols), Γ_a ~2.5 fm. Note that the thermal profile for aerosols is considerably narrower than that for molecules. For a given particle distribution, Γ_a is not significantly dependent on altitude.

The Doppler response G_D is described by a Delta function displaced from the rest wavelength by

$$\Delta\lambda_\Delta = 2\frac{\lambda_0 v_p}{c} \quad (7)$$

where v_p is the mean bulk velocity of the scatterers parallel to the line-of-sight. Here, the leading factor of 2 again arises from reference frame considerations. As an example, a 30 m s^{-1} horizontal wind (which is expected to be typical for the Davis stratosphere) blowing across a line-of-sight with a zenith angle of 45° results in a Doppler shift of ~0.1 pm at $\lambda_0 = 532$ nm. Viewing in three linearly independent (preferably mutually orthogonal) directions yields the complete relative velocity vector under the assumption that there is negligible velocity gradient between the range intervals under study.

The turbulence response G_t represents the superposition of Doppler shifts arising from variation in wind velocity. Turbulence arises as a consequence of heat diffusion due to radiative processes (important in the troposphere) and gravity wave 'breaking' (important in the mesosphere). The associated velocity and temperature fluctuations will in general influence the width of the backscatter spectrum. The amount of this effect depends on the volume and timescale over which the lidar data are accumulated. Turbulence has been neglected in this analysis as it is likely to have a second-order influence on the recovery of lidar temperature and wind estimates (see, for example, Vincent and Fritts 1987). However, further investigation of this area is recommended.

19.2.3 *Fabry-Perot spectrometer response*

In this section, the response function for the lidar receiver is described. The two etalons comprising the spectrometer each consist of a pair of flat and parallel glass plates which have a semi-transparent mirror coating on their inner surfaces. The plates have reflectance R, absorptance A, and transmittance T. Light from an extended source passes through the etalon where multiple reflection occurs. Rays are recombined by a focussing lens to generate circular interference fringes. The interference pattern within the radius of a field stop placed on the optical axis at the focal plane of the lens is passed through a narrow-band interference filter and is then admitted to the detector.

The wavelength transmission characteristic of a single etalon is usually expressed as

$$I(\lambda) = A(\lambda) * D(\lambda) * F(\lambda)$$

where $A(\lambda)$, $D(\lambda)$ and $F(\lambda)$ are termed the 'Airy', 'defect' and 'aperture' functions of the etalon, respectively (Wilksch 1975; Hernandez 1986; Jacka 1984). The function $I(\lambda)$ is termed the 'instrument' function.

The Airy function is given by

$$A(\lambda) = \frac{\tau_A}{1+\frac{4R}{(1-R)^2}\sin^2\left(\frac{2\pi\mu l\xi}{\lambda}\right)} \qquad (8)$$

where l is the separation of the etalon plates, μ the refractive index of the spacing medium, $\xi = \cos\theta$ where θ is the angle of incidence between the plates. The transmission coefficient τ_A is given by

$$\tau_A = \frac{T^2}{(1-R)^2}$$

with $T = 1 - R - A$.

For a given λ, Equation (8) is at a maximum when

$$m = \frac{2\mu l \xi}{\lambda} + \frac{\phi}{\pi}$$

is integral. Here ϕ is the phase change on reflection at each plate surface. For a given l and ξ, the etalon has a multiple bandpass transmission profile. The spacing between the transmission peaks is termed the free spectral range;

$$\Delta\lambda_{fsr} = \frac{l}{m}.$$

In the lidar spectrometer, the central wavelength of each transmission peak is scanned by adjusting l in discrete steps. The FWHM of the Airy function is approximately given by

$$\delta\lambda_A = \frac{\lambda(1 - R)}{m\pi\sqrt{R}}.$$

The unit area defect function $D(\lambda)$ accounts for changes in the optical path length over the area of the etalon. These changes occur in practice due to variation primarily of the physical separation between the plates and non-uniformities in their reflective coatings. If the distribution of path length defects has a characteristic width δx_D, then the characteristic width of $D(\lambda)$ is

$$\delta\lambda_D = \frac{\lambda}{l}\delta x_D.$$

The unit area aperture function $F(\lambda)$ accounts for variation in the angle of incidence θ across the aperture of the etalon;

$$F(\lambda_\xi) = \frac{1}{\delta\lambda_F} \qquad (-\delta\lambda_F \le \lambda_\xi \le 0)$$

$$F(\lambda_\xi) = 0 \qquad \text{otherwise,}$$

where

$$\delta\lambda_F = \frac{\lambda}{2}\left(\frac{r}{f}\right)^2,$$

with r the radius of the field stop, and f the focal length of the imaging lens.

The FWHM of the 'instrument' function for a particular etalon is given by

$$\delta\lambda_I \approx \sqrt{\delta\lambda_A^2 + \delta\lambda_D^2 + \delta\lambda_F^2}$$

and the instrument finesse is defined by

$$N_I = \frac{\Delta\lambda_{fsr}}{\delta\lambda_I}.$$

For the purposes of simulation, the response function of the dual etalon arrangement in the lidar spectrometer may be conveniently expressed as

$$I_r(\lambda) = I_{HRE}(\lambda)\, I_{LRE}(\lambda)\, I_{fil}(\lambda) \qquad (9)$$

where the terms describe the transmission characteristics of the high and low resolution etalons and the interference filter respectively. Here it is assumed that there is negligible angular cross-coupling between the interference patterns of the two etalons, which is reasonable given that the ratio of plate spacings (high resolution etalon to low resolution etalon) is approximately 15:1. The narrow-band interference filter prior to the PMT has an approximately Gaussian transmission function.

19.3 DOPPLER SIMULATION TECHNIQUE

19.3.1 *Choice of spectrometer response*

The wavelength response of the Fabry-Perot spectrometer was simulated using Equation (9). The aim in selecting the plate separation for each etalon was to obtain a suitably high spectral resolution while at the same time obtaining tolerable sideband levels. The free spectral range of the low resolution etalon, $\Delta\lambda_{LRE}$, was selected so that transmission peaks at $\lambda_0 \pm \Delta\lambda_{LRE}$ corresponded to 0.5% of the peak transmission for the interference filter.

Table 1. Specifications for the Fabry-Perot etalons.

Parameter	High Resolution Etalon	Low Resolution Etalon
Plate spacing, l	4.055 mm	0.265 mm
Plate reflectivity, R	0.905	0.905
Plate absorption, A	0.010	0.010
Order, m	15241	998
Free spectral range, $\Delta\lambda_{fsr}$	34.9 pm	533.2 pm
Airy function width, $\delta\lambda_A$	1.1 pm	17.0 pm
Defect function width, $\delta\lambda_D$	0.8 pm	12.6 pm
Aperture function width, $\delta\lambda_F$	1.3 pm	1.3 pm
Instrument function width, $\delta\lambda_I$	2.0 pm	24.0 pm
Instrument function finesse, N_I	17.5	22.2
Peak transmission	0.54	0.63

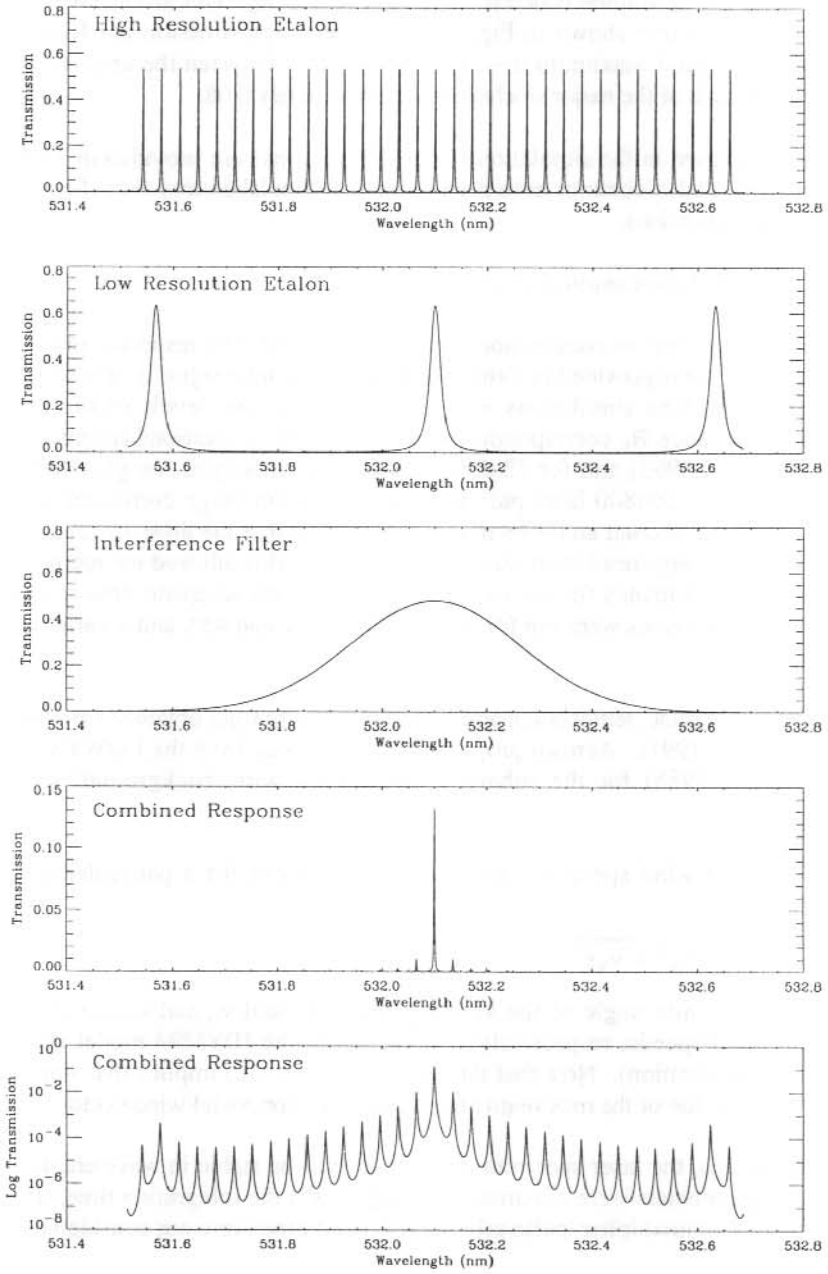

Figure 1. Simulated response of the lidar Fabry-Perot spectrometer. The etalon plate spacings have been selected so that the central wavelength of the instrument response matches that of the nominal laser wavelength.

Here λ_0 is the minimal wavelength of the laser. Similarly, $\Delta\lambda_{HRE}$ was chosen so that the transmission peaks of the high resolution etalon at $\lambda_0 \pm \Delta\lambda_{HRE}$ corresponded to 0.5% of the peak of the low resolution etalon transmission peak at λ_0. This arrangement resulted in the instrument function shown in Figure 1. The peak transmission is ~13%, while the FWHM of the central maximum is ~2.0 pm. The ratio between the areas of the central maximum and each of the major sidebands is approximately 0.08.

The parameters used in the simulation of the FPS response are provided in Table 1. The properties of the etalon coatings have been estimated from laboratory tests (Schaeffer 1994, personal communication).

19.3.2 *Simulated photomultiplier output*

Equation (1) was used in conjunction with the simulated FPS response and the general instrument parameters provided in Table 2 to estimate the lidar signal as a function of range and wavelength. The simulations were performed for two levels of the background continuum irradiance B_c corresponding to night and day conditions (using values from Meriwether et al. 1993) and for 13 different integration lengths, ranging from 50 laser pulses to $50 \times 2^{12} = 204800$ laser pulses. This integration range corresponds to elapsed times of between 1 second and ~ 68 minutes (assuming that the lidar operates with 100% duty cycle). The range resolution was chosen as 1 km. This allowed the recovery of wind and temperature estimates for the lower mesosphere with adequate time resolution. In addition, the simulations were run for zenith angles of 0°and 45°, and a variety of aerosol loading conditions.

For a particular altitude, temperature and molecular density were obtained from the MSISE-90 model (Hedin 1991). Aerosol properties were obtained from the LOWTRAN7 model (Kneizys et al. 1988) for the subarctic atmosphere with 'background' stratospheric conditions.

The line-of-sight wind speed assumed in the simulations for a particular altitude was obtained from

$$v = \sin(\theta) \sqrt{v_u^2 + v_v^2} \qquad (10)$$

where θ is the zenith angle of the viewing direction, and v_u and v_v are the zonal and meridional wind speeds, respectively, obtained from the HWM93 model (Hedin 1995, personal communication). Note that the use of Equation (10) implies that simulated lidar views in the direction of the maximum projection of the horizontal wind vector.

In the simulations, the laser spectrum was assumed to be stable in wavelength, while the atmospheric parameters were assumed to be stable over the integration time. In addition, the effects of photomultiplier 'pulse pile-up' and 'dead time' were not considered.

During observations, the FPS will continuously scan over a wavelength interval equivalent to approximately half the free spectral range of the high resolution etalon. The backscatter spectrum will be sampled at 128 points within this interval, with each wavelength 'bin' of a particular scan cycle corresponding to one laser pulse. A scan cycle will therefore last

128/50 = 2.6 seconds. The time required to reset the etalon plate separations for the start of a new scan cycle may necessitate missing a few laser pulse periods. The data for several scans will be integrated before being stored. When undertaking 'cardinal point' observations for wind vector measurements, the telescope will be moved in azimuth after a suitable number of integrations. The frequency of movement of the telescope at the sequence of viewing directions will be a compromise between minimising the 'dead time' between observations (i.e. the time required to slew the telescope and wait for vibrations in the system to die out) and the desired measurement accuracy (which is governed by the integration time and the level of bias introduced by variations in wind velocity over the integration time).

Table 2. Parameters of the lidar system used in the performance simulations.

Parameter	Value
Central wavelength, λ_0	532.1 nm
Laser pulse energy, E_t	0.6 J
Laser pulse repetition rate	50 Hz
Laser linewidth FWHM	0.13 pm
Full angle field of view of receiver, α	0.16 mrad
Interference filter peak transmission	0.48
Interference filter FWHM	0.38 nm
Efficiency of transmitting optics, ε_t	0.27
Efficiency of receiving optics, ε_r	0.12
Efficiency of each switching mirror	0.95
PMT quantum efficiency, η	0.14
Telescope collecting area	0.79 m^2
FPS field stop radius, r	1.0 mm
FPS imaging lens focal length, f	450.0 mm

It is intended to measure the instrument response of the system concurrent with operation of the spectrometer. A small amount of light from the laser will be 'temporally stretched' (by passing it though different lengths of optical fibre) and injected into the receiver, possibly by scattering from the face of the Blanking Shutter (see Klekociuk et al. 1994a). The amount of this 'calibration light' reaching the PMT will be a measure of the throughput of the system for the prevailing FPS configuration. In this way, it is possible that one calibration data point will be obtained for each laser pulse. This information would be stored in the first few bins of each range vector. It will probably be necessary to monitor the intensity of the laser output independently during the calibration measurements. In the simulations presented here, the instrument response was simulated using the calibration scheme described above. The energy of the calibration illumination was assumed to be 10 nJ.

The ability to measure the instrument response in 'real time' is a key aspect of the recovery of wind and temperature data where the accurate measurement of relative wavelength changes is required. If the instrument response cannot be obtained for each laser pulse, then the frequency of calibration measurements must be sufficient to remove the effects of the drifts that are inherent in the characteristics of the laser and spectrometer. It will be important to obtain calibration information with high signal-to-noise ratio in order to minimise statistical effects in the analysed data.

In practice, operation of the PMT in 'photon-counting' mode will be unsuitable for altitudes below about 25 km owing to the high signal levels. Instead, sampling of the anode current from the PMT (i.e. analogue detection) will be required, possibly in combination with a logarithmic preamplifier stage. In addition, range-dependant attenuation of the received signal (similar to that performed in the current system using a profiled shutter aperture) may be necessary.

19.3.3 *Estimation of temperature and wind speed*

The first step in the analysis procedure was to recover the 'backscatter' response by deconvolving the 'instrument' response from the simulated backscatter spectrum. A 'maximum likelihood' deconvolution procedure (Lucy 1974) was used for this purpose. A Gaussian function was then fitted to the backscatter response via an iterative generalised non-linear least-squares technique (Bevington 1969). The width and central wavelength of the fitted Gaussian were obtained, together with the associated standard errors. The width was converted to a temperature estimate using Equation (5).

In practice, the instrument response will be asymmetric. A suitable definition of the reference wavelength, λ_0, is the wavelength at which the areas under the function on either side are equal. The difference between the central wavelength of the fitted Gaussian and λ_0 was used to calculate wind speed using Equation (7). Error estimates were calculated by standard propagation formulae.

It should be noted that alternate methods of analysis are available (see Conner et al. 1993) and it would be useful to apply these to the simulated data to evaluate the most robust technique.

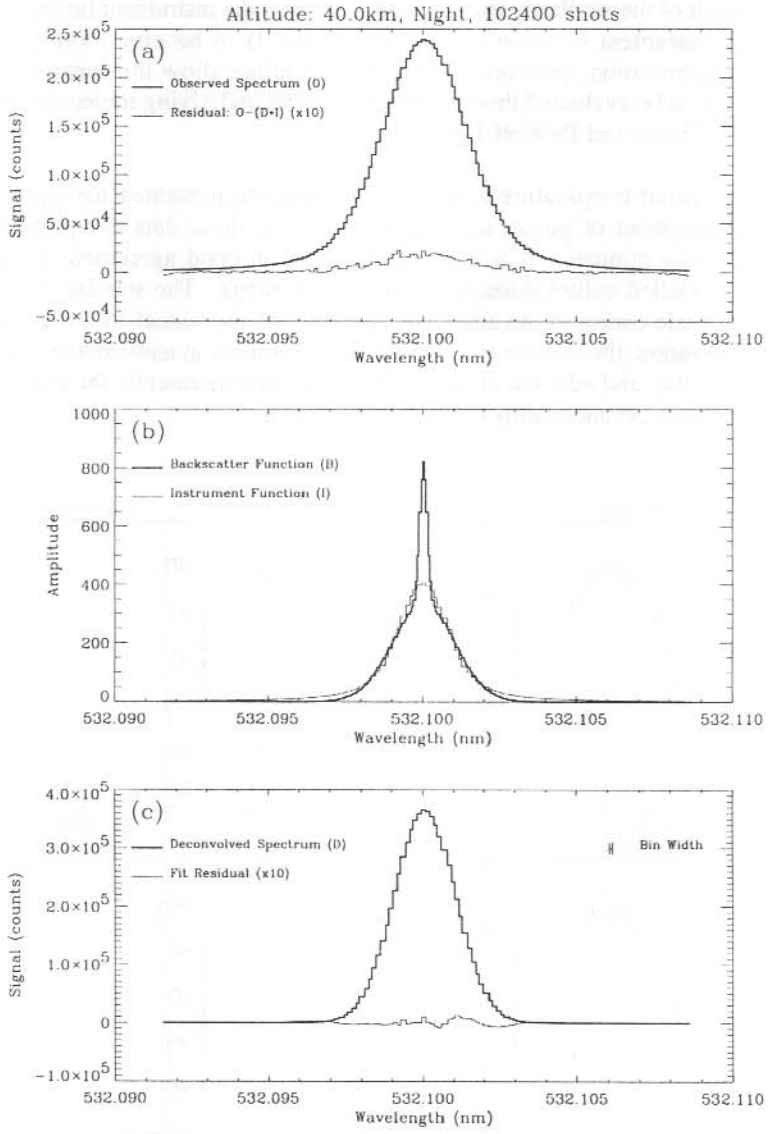

Figure 2. Example of a lidar simulation for $\theta = 45°$ and $\Delta r = 1$ km. (a) Raw 'observed' (simulated) spectrum (thick line) and 'convolution residual' (thin line) scaled by a factor of 10. (b) Unit area response for molecular and aerosol backscattering of the laser spectrum (solid) and unit area instrument function (dashed). In calculating the backscatter function, the following values were used; $T = 275$ K (Equation (5)), $\Gamma_a = 0.5$ fm, (Equation (6)), and $\beta = 0.19$ (Equation (11)). (c) Deconvolved backscatter spectrum (solid) and residual of fitted Gaussian (dashed; scaled by a factor of 10).

The recovery of a typical backscatter response function is shown in Figure 2. Both the 'observed spectrum' O and the recovered backscatter response D appear Gaussian, showing no obvious indication of the aerosol signature present in the 'backscatter function' B. This is mainly the result of the similarity in half-widths between the instrument function I and B. Narrowing the instrument function causes both O and B to become more peaked. A sufficiently high resolution spectrometer could in principle allow the aerosol scattering response function to be evaluated through removal of the underlying molecular scattering function from D (Fiocco and DeWolf 1968).

In Figure 3, recovered temperature and wind estimates are presented for night and day conditions. The number of pulses integrated to produce these data is equivalent to an elapsed time of ~34 minutes. It is evident that there is good agreement between the recovered and modelled values throughout the altitude range. The standard error values increase with altitude owing to the associated decrease of the 'signal-to-noise' ratio. For this integration duration, the altitude at which the 2σ uncertainty in temperature exceeds 2 K is ~45 km during day and ~55 km at night. For wind measurements, the day and night 'ceiling' altitudes for a 2σ uncertainty of 4 m s^{-1} are similar.

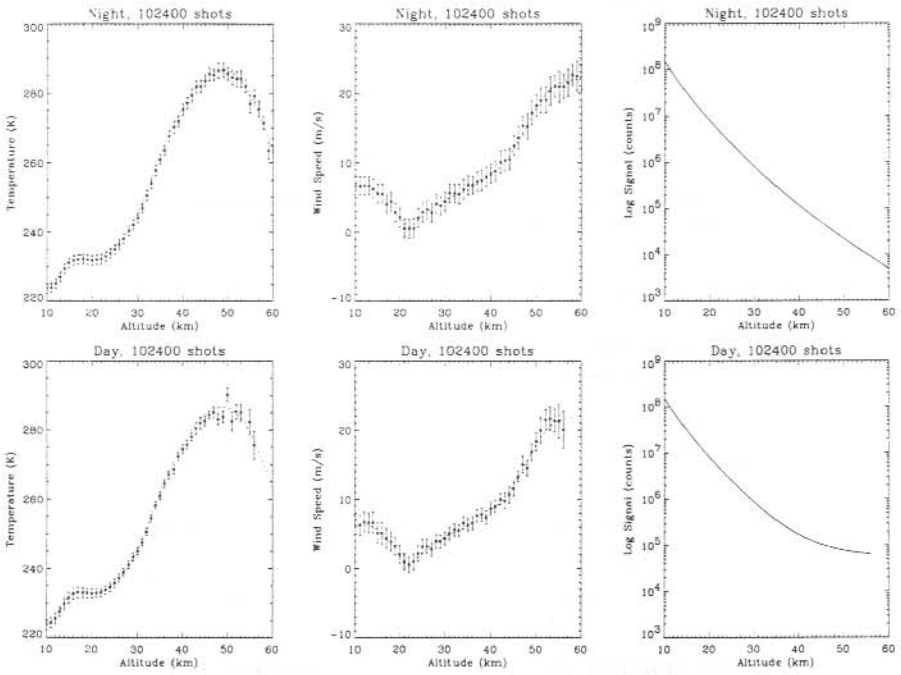

Figure 3. Results of lidar simulations for a $\theta = 45°$ and $\Delta r = 1$ km. Plotted in the horizontal panels are temperature, wind speed and total signal as a function of altitude. The recovered temperature and wind values (filled circles) are plotted together with their modelled variation (dashed curve). The error bars are $\pm 2\sigma$. Note that the recovered temperatures are generally lower than the modelled values, particularly below 35 km altitude at night.

A close inspection of the temperature plots in Figure 3 reveals that there is a systematic offset between the recovered and modelled values that varies with altitude. For the night-time data (where the background signal level is low), the offset is ~0.5 K at 20 km, and decreases to the point where it is dominated by 'noise' at about 35 km. For day-time measurements, the offset is near zero at low altitudes and increases with altitude to be about 1 K at 45 km. The offset behaviour is evidently dependent on the influence of aerosol scattering is discussed in the following section. The wind data do not show a systematic offset.

19.4 DISCUSSION

19.4.1 *The influence of aerosols on temperature measurements*

As noted by Jacka and Argall (1987), the estimation of temperatures obtained using a high spectral resolution lidar may be underestimated in the presence of aerosols. This is because the backscatter spectrum obtained through deconvolution of the instrument response from the measured spectrum is more 'peaked' than a simple Gaussian. As a result, the width δ_T assumed for the recovery of T by Equation (5) is underestimated. It is entirely reasonable to assume that aerosols and molecules will have identical wind velocities, so wind speed measurements will not be influenced by the level of aerosol loading.

The difference between the recovered and model temperatures was plotted as a function of altitude. For both night and day conditions, the variation closely matched the behaviour of the assumed aerosol loading factor defined by

$$\beta(r) = \frac{\beta_a(r)}{\sigma_m(r)\rho_m(r)}. \qquad (11)$$

Here β is 1- R_l, where R_l is termed the lidar backscattering ratio. The correlation between the temperature offset and β is shown in Figure 4. The data presented in this figure were obtained for simulations where the assumed value of β for each altitude was multiplied by factors of 0, 0.5, 1, 2 and 4. The integration time was chosen as 102400 pulses. This gave suitably small statistical uncertainties for the stratosphere where β maximises. In Figure 4, only those data in the altitude range 10 km to 30 km are shown. Above this height, the correlation becomes less pronounced due to decrease of the signal-to-noise ratio.

The offsets for the day-time data were consistently 0.25 K lower than those for the night-time data. This effect has been removed from the data presented in Figure 4. This small residual is apparently introduced by the presence of a significant background signal. Further evaluation of this effect is required.

The relationship shown in Figure 4 has an important bearing on the operation of the Davis lidar. The level of aerosol loading in the stratosphere can be highly variable. Values of β in excess of 2 were observed at a range of latitudes following the 1991 eruption of Mt. Pinatubo in the Philippines (Uchino et al. 1995). From Figure 4, a β of 2 would imply a temperature offset of 30 K. The mesosphere is much 'cleaner', with β typically

0.06 (Kneizys et al. 1988). However, this corresponds to a temperature offset of ~8 K based on Figure 4.

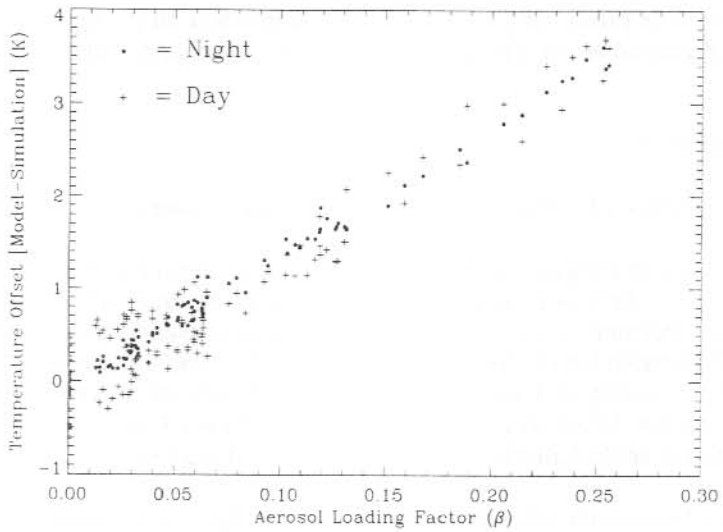

Figure 4. Plots of altitude against the estimated equivalent integration time required to achieve (a) a 2σ temperature accuracy of 2 K and (b) a 2σ wind speed accuracy of 4 ms^{-1}. Data are provided for night (solid) and day (dashed) conditions for zenith angles (ZA) of θ = 0° and θ = 45°. In all cases, the range resolution is Δr = 1 km.

It would seem important to have *a priori* knowledge of aerosol loading when recovering temperatures from backscatter spectra, particularly when long term climatological studies are being undertaken. Lidar density profiles are commonly used to infer the backscatter ratio R_l (and hence β) as a function of altitude. This involves using a model of the molecular density variation calibrated with in-situ radiosonde measurements (Measures 1984). Two other approaches to the measurement of β could in principle be applied for the recovery of temperatures from lidar backscatter spectra;

(a) a sufficiently high resolution spectrometer could be employed so that the aerosol effect can be accounted for in the fitting of the thermal broadening function, and

(b) the ratio between the total intensities of the rotational-vibrational bands of the Raman backscatter spectra for molecular oxygen and nitrogen could be measured.

The latter option, which is under evaluation, would allow relative changes in molecular density to be inferred as a function of altitude.

It may be possible in practice to achieve a narrower FPS instrument function than that modelled in the simulations. This would be achieved by increasing the order m of each etalon, and at the same time replacing the interference filter with one of narrower bandwidth in order to maintain the sideband rejection tolerance. Fischer et al. (1995) have employed a dual etalon imaging FPS for lidar wind studies. They use a temperature-controlled birefringent filter with a FWHM of 50 pm prior to the spectrometer. From the instrument parameters given in their paper, $\delta\lambda_I$ is calculated as ~0.1 pm, which is comparable with the width of their laser spectrum. As noted by Meriwether et al. (1993), the use of a birefringent filter in a lidar receiver in combination with a half-wave plate following the laser can be used to improve the signal-to-noise performance of the detected signal through polarisation rejection of background continuum light.

19.4.2 *Maximum effective altitude*

The altitude at which the uncertainty in temperature and wind speed estimates exceed 2 K and 4 m s^{-1}, respectively, are plotted in Figure 5 as a function of effective integration time (assuming a 100% duty cycle) for nominal aerosol loading and four observing situations. The value of the uncertainty for each measurement type was defined as

$$\delta_{temp} = 2\sigma_{temp} + \Delta_{offset}$$

$$\delta_{wind} = 2\sigma_{wind}$$

where the subscripts 'temp' and 'wind' identify quantities associated with temperature and wind measurements, respectively, σ are the standard errors obtained from the least-squares fitting procedure, and Δ_{offset} is the difference between the modelled and recovered temperature. In obtaining these plots, the variation of δ with altitude was fitted with spline approximation for each integration length. Where the least-squares fitting procedure did not converge, values of δ were omitted. The altitude A_δ at which δ exceeded the required threshold for the particular integration length T_δ was retained. An order 1 Gaussian smoothing filter was passed over each set of A_δ versus T_δ.

The variations shown in Figure 5 are a guide only. Small variations are due to uncertainties introduced by the analysis method. As expected day-time measurements have a lower altitude limit than night-time measurements due to the influence of background (non-laser) light. The zenith observations reach the greatest altitude as atmospheric extinction is least in this direction.

Figure 5 indicates that high spectral resolution measurements appear feasible in the lower mesosphere. This is an improvement on the capabilities of other equivalent systems (see Fischer et al. 1995), due mainly to the high power of the laser.

19.5 CONCLUSIONS

Atmospheric aerosols may significantly influence the recovery of temperature estimates using a high spectral resolution lidar, particularly where the resolution of the spectrometer is of the order of the molecular thermal broadening function. For the Davis lidar configured with an instrument function width of ~2 pm, Figure 4 indicates that recovered temperatures may be underestimated by on the order of ~15β(r) K, where β(r) is a measure of the aerosol loading at altitude r, at least for β in the range 0 to 0.3. Turbulence will tend to reduce the

apparent magnitude of this effect. Wind estimates are not likely to be strongly influenced by aerosol loading.

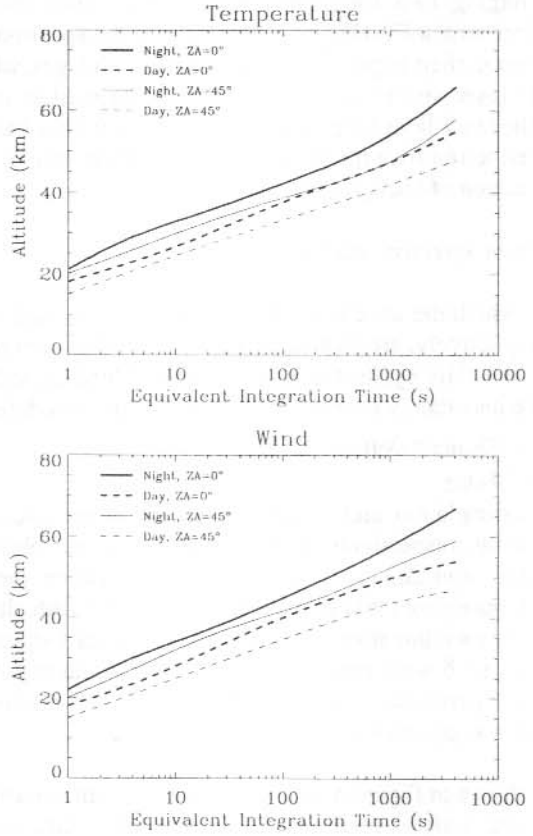

Figure 5. Temperature difference (model-simulation) as a function of backscatter ratio for night and day conditions at three altitudes, with $\theta = 0°$ and $\Delta r = 1$ km.

Improvement of the resolution of the Davis lidar FPS should be considered in order to better examine the influence of aerosol scatter, particularly in the stratosphere. This could be achieved by increasing the operating order of each etalon, and incorporating a filter having a narrower bandwidth following the FPS. The practical limitation to the resolution of the spectrometer will be dictated by the trade-off in throughput, and the constraints imposed by the efficiency of the plate coatings and the widths of the defect and aperture functions.

For a nominal level of aerosol loading and a reasonable integration time, the maximum effective altitude of the system (as summarised in Figure 5) should reach the top of the

stratosphere for a viewing direction of 45°, and possibly extend into the lower mesosphere for vertical observations. These limits depend to some extent on the stability of the spectrometer and laser, the accuracy of the calibration measurements, and the ability to account for aerosol and turbulence effects. As indicated in Klekociuk et al. (1994b), 'total-power' measurements of density are likely to reach the mesopause.

Further refinement of the simulation technique presented here would be useful in order to more fully explore the capabilities and limitations of the lidar system. The suggested developments are;

(a) simulation of analogue detection mode for high signal levels,

(b) allowance for 'pulse pile-up' effects in the photomultiplier system (Donovan et al. 1993), simulation of 'dead-time' in the counting electronics, and allowance for the enhanced photomultiplier 'noise' that is expected following high illumination levels,

(c) further analysis of the effects of background signal level on the recovery of temperature estimates,

(d) incorporation of drift in the power level and spectral characteristics of the laser output,

(e) allowance for variation of the modelled temperature and wind values during an integration, including turbulence effects,

(f) investigation of the effects of enhanced aerosol backscatter, particularly at stratospheric altitudes,

(g) incorporation of Brillouin and Raman scattering terms in the backscatter response, and in particular, examination of whether Raman scattering can be exploited in the measurement of aerosol loading, and

(h) development of an approach for optimisation of the FPS response function, particularly with regard to improving measurement accuracy for a given range and time resolution, and to allow separation of the molecular and aerosol components of the backscatter function.

19.6 ACKNOWLEDGEMENTS

The lidar was originally conceived and designed by the late F. Jacka, and its initial development was largely due to the efforts of P.S. Argall. Significant contributions to the design of the FPS have been made by D. Creighton. We thank members of the lidar project team (R. Morris, D. Murphy, P. Greet, I. Reid, R. Vincent, A. Fleming and P. Yates) for their efforts in the development of the instrument and its scientific program. The additional involvement by P. deVries, W. Hocking, D. White and S. Whiteside is gratefully acknowledged. Funding for the lidar project has been provided by the Australian Antarctic Division, the University of Adelaide, and the Australian Research Grants Scheme.

REFERENCES

Argall, P.S. (1993). *Lidar studies of the middle atmosphere*. Ph.D. Thesis, University of Adelaide.

Bevington, P. (1969). Data reduction and error analysis for the physical sciences. McGraw-Hill, New York, 235.

Conner, J.F., Smith, R.W. *and* Hernandez, G. (1993). Techniques for deriving Doppler temperatures from multiple-line Fabry-Perot profiles: an analysis. *Applied Optics 32*:4437 – 4444.

Donovan, D.P., Whiteway, J.A. *and* Carswell, A.I. (1993). Correction for nonlinear photon-counting effects in lidar systems. *Applied Optics 32*:6742 – 6753.

Fiocco, G. *and* DeWolf, J.B. (1968). Frequency spectrum of laser echos from atmospheric constituents and determination of the aerosol content of air. *Journal of the Atmospheric Sciences 25*:488 – 496.

Fischer, K.W., Abreu, V.J., Skinner, W.R., Barnes, J.E., McGill, M.J. *and* Irgang, T.D. (1995). Visible wavelength Doppler lidar for measurement of wind and aerosol profiles during day and night. *Optical Engineering 34*:499 – 511.

Hedin, A.E. (1991). Neutral atmosphere empirical model from the surface to the lower exosphere. *Journal of Geophysical Research A96*:1159 – 1172.

Hernandez, G. (1986). Fabry-Perot interferometers. Cambridge Studies in Modern Optics 3. Cambridge University Press, England.

Jacka, F. (1984). Application of Fabry-Perot spectrometers for measurement of upper atmosphere temperature and winds. *Middle Atmosphere Program - Handbook 13:*19 – 40.

Jacka, F. *and* Argall, P.S. (1987). A lidar system for stratosphere studies - performance simulation. In: Burns, G.B. *and* Craven, M. (Eds). *ANARE Research Notes Number 48*. Pp. 226 – 235.

Kaufman, Y.J., Gitelson, A., Karnieli, A., Ganor, E., Fraser, R.S., Nakajima, T., Mattoo, S. *and* Holben, B.N. (1994). Size distribution and scattering phase function of aerosol particles retrieved from sky brightness measurements. *Journal of Geophysical Research D5*:10341 – 10356.

Kneizys, F.X., Shettle, E.P., Abreu, L.W., Chetwynd, J.H., Anderson, G.P., Gallery, W.O., Selby, J.E.A. *and* Clough, A.A. (1988). Users guide to LOWTRAN7. Technical Report AFGL-TR-88-0177, Air Force Geophysics Laboratory, Massachusetts.

Klekociuk, A.R., Argall, P.S., Morris, R.J., Yates, P., Fleming, A., Vincent, R.A., Reid, I.M., Greet, P.A. *and* Murphy, D.J. (1994a). A lidar for the study of the atmosphere above Davis Antarctica. In: Morris, R.J. (Ed). *ANARE Research Notes Number 92*. Pp. 42 – 52.

Klekociuk, A.R., Argall, P.S., Morris, R.J., Yates, P., Fleming, A., Vincent, R.A., Reid, I.M., Greet, P.A. *and* Murphy, D.J. (1994b). The Australian Antarctic lidar facility. In: Wang, J. *and* Hays, P.B. (Eds). *Proceedings SPIE 2266 Optical Spectroscopic Techniques and Instrumentation for Atmospheric and Space Research*. The International Society for Optical Engineering. Pp. 624–634.

Lucy, L.B. (1974). An iterative technique for the rectification of observed distributions. *The Astronomical Journal 79*:745–754.

Measures, R.M. (1984). Laser Remote Sensing: Fundamentals and Applications. Kreiger, Malabar, FL.

Meriwether, J.W., Farley, R., McNutt, R. *and* Dao, P.D. (1993). Application of the Rayleigh lidar to observations of noctilucent clouds. *Journal of Geophysical Research D98*:14979–14989.

Morris, R.J., Monselesan, D.P. *and* Klekociuk, A.R. (1995). Australian Antarctic middle and upper atmosphere physics - a new direction. *Advances in Space Research 16*:151–162.

Uchino, O., Nagai, T., Fujimoto, T., Matthews, W.A. *and* Orange, J. (1995). Extensive lidar observations of the Pinatubo aerosol layers at Tsukuba (36.1°N), Naha (26.2°N), Japan and Lauder (45.0°S), New Zealand. *Geophysical Research Letters 22*:57–60.

Vincent, R.A. *and* Fritts, D.C. (1987). A climatology of gravity wave motions in the mesopause region at Adelaide, Australia. *Journal of the Atmospheric Sciences 44*:748–760.

Wilksch, P.A. (1975). *Measurements of thermospheric temperatures and winds using a Fabry-Perot spectrometer*. Ph.D. Thesis. University of Adelaide.

20. EXTENSION OF DENSITY PROFILES OBTAINED BY RAYLEIGH LIDAR INTO THE LOWER STRATOSPHERE USING RAMAN SCATTERING

A.R. Klekociuk

Atmospheric and Space Physics
Antarctic Division
Kingston Tasmania 7050
Australia

ABSTRACT

A method is described by which Raman vibrational-rotational scattering from molecular nitrogen (N_2) or oxygen (O_2) may be utilised by a conventional Rayleigh lidar to profile density as a function of altitude in the stratospheric aerosol layer. Incorporation of a Raman channel in the lidar system being developed by the Australian Antarctic Division and the University of Adelaide should allow the collection of density profiles with adequate resolution between altitudes of 10 km and 30 km without requiring first-order correction for the effects of aerosol scattering.

20.1 INTRODUCTION

The Rayleigh lidar technique, which is based on the backscattering of a pulsed laser beam by atmospheric molecules, provides a well established means of profiling atmospheric density and temperature. The temporal analysis of the laser echo provides molecular density as a function of altitude. The profile is usually referenced to an assumed density value at a particular height obtained from an atmospheric model, or measurements of density over a certain altitude range inferred from in-situ radiosonde measurements of pressure and temperature. By assuming that the atmosphere obeys the perfect gas law and is in hydrostatic equilibrium, the density information can be used to recover the temperature profile (in absolute units) by an iterative method which works down in altitude from a level of known or assumed atmospheric pressure (Hauchecorne and Chanin 1980; Chanin and Hauchecorne 1984).

The lower limit of lidar-derived density and temperature profiles is generally in the range 30 km to 35 km (Hauchecorne and Chanin 1980). This is set by the relative significance of Mie scattering from aerosols compared with Rayleigh scattering. The upper altitude limit for density measurements is determined by the strength of the received backscatter signal in comparison with detector noise and background light. This depends primarily on the laser power, the collecting area of the receiver and the temporal and spatial integration scales of the measurements. Modern Rayleigh lidar systems are generally able to reach altitudes in the range 70 km to 100 km.

A primary aim of the lidar system being developed by the Australian Antarctic Division and the University of Adelaide is to examine the structure and dynamics of the middle atmosphere above Davis, Antarctica (Klekociuk and Innis 1996; Morris et al. 1995). An

important focus of international studies of the Antarctic atmosphere relates to the stratosphere. Of relevance to the modelling of this region, particularly in regard to the concerns and uncertainties relating to the ozone chemistry, are detailed measurements of density, temperature, wind velocity and aerosol loading. The break up of the southern polar vortex takes place over Davis during the austral spring. The ability to undertake accurate molecular density profiling in the stratospheric aerosol regime would be of importance in studying the thermodynamics of the vortex and the associated influence on aerosol loading.

Gravity waves are recognised as playing a central role in determining the structure and circulation of the middle atmosphere. The extension of lidar density and temperature profiling in the lower stratosphere is of relevance to studies of wave generation and growth processes. It will also provide greater opportunity for the comparison of wave parameter information obtained by lidar and radiosonde techniques.

In this paper, a method by which Raman vibrational-rotational scattering from molecular nitrogen (N_2) or oxygen (O_2) may be used to extend the lower altitude limit of density profiles obtained by Rayleigh lidar is investigated. Performance simulations appropriate to the Davis lidar are presented, and the feasibility of using the Raman technique is discussed.

20.2 ATMOSPHERIC SCATTERING

When monochromatic light is incident on a molecular gas or liquid, both elastic and inelastic scattering processes take place. These processes are described by Raman scattering theory. The elastic scattering process is usually referred to as Rayleigh scattering. The spectrum of Rayleigh scatter results essentially from the convolution of the source spectrum with Doppler functions due to thermal agitation of the scatterers and relative motion between the source and the scattering medium. Where the density of the scattering medium is sufficiently high, the Rayleigh spectrum acquires a symmetrically doublet due to Brillouin scattering. The Brillouin doublet is the result of scattering from acoustic phonons associated with propagating pressure fluctuations in the medium. Brillouin scattering is only of consequence for high spectral resolution lidar studies in the troposphere.

The inelastic scattering process described by Raman scattering theory produces a characteristic spectral signature that is shown for N_2 and O_2 in Figure 1. The discrete spectral features accompanying the Rayleigh line are due to the interaction of the incident radiation with particular quantised rotational and vibrational energy levels of the molecules. The displacement of a particular spectral feature relative to the Rayleigh line is said to be in the Stokes or anti-Stokes direction depending on whether the relative wavelength of the radiation is increased or decreased.

For simple linear molecules such as N_2 and O_2, the allowed changes in the rotational quantum state associated with Raman scattering are $\Delta J = -2, 0$ or $+2$, which give rise to the O, Q, and S spectral branches respectively. The Q branch contains a number of degenerate lines, and as a result has a higher total cross section than that of the O and S branches combined. A change in the vibrational quantum number ν of ± 1 gives rise to the rotational-vibrational spectrum. Anti-Stokes rotational-vibrational scattering requires the molecule to

initially be in an excited state (Banwell 1983). The cross section for this type of scattering in the middle atmosphere is negligible compared with the Stokes branches.

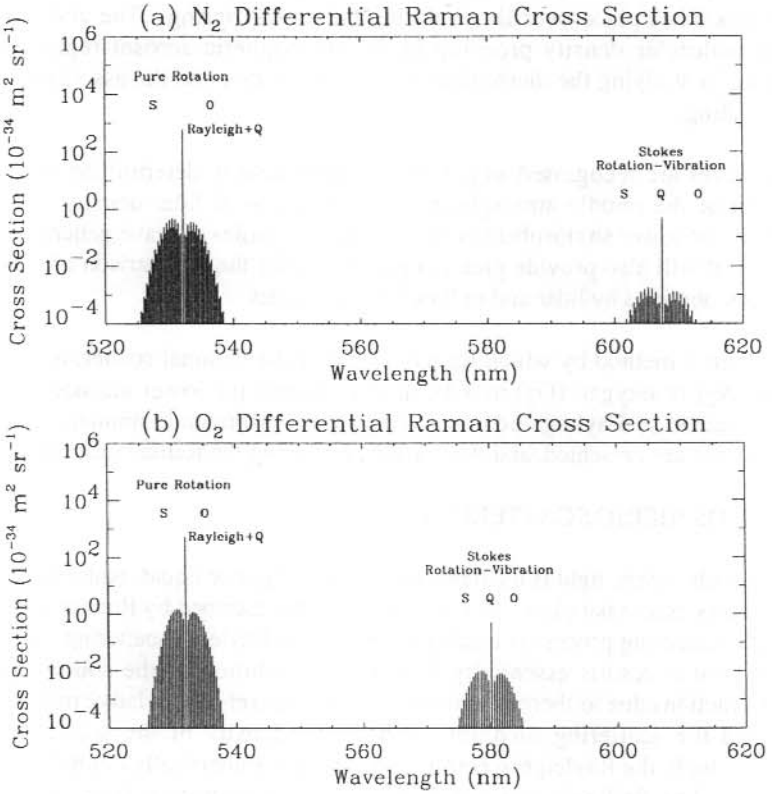

Figure 1. Differential Raman backscatter cross sections for (a) N_2 and (b) O_2, calculated for excitation at λ = 532 nm and for a temperature of 250 K (as discussed in Section 20.3). The O, S and Q spectral branches are indicated.

An important aspect of Raman scattering is that the relative spectral shift of the scattered radiation is characteristic of the structure of the scattering molecule. The wavelength of the scattered radiation is given by

$$\lambda' = \frac{10^7}{\frac{10^7}{\lambda_0} - \delta\nu} \quad \text{nm}$$

where λ_0 is the wavelength of the incident radiation (nm) and $\delta\nu$ is a characteristic spectral shift (cm^{-1}). For N_2 and O_2, the value of $\delta\nu$ associated with rotational-vibrational

scattering is approximately 2331 cm^{-1} and 1556 cm^{-1} respectively. The individual lines in the O and S branches for N_2 and O_2 are separated by approximately 8 cm^{-1} and 5.6 cm^{-1} respectively.

Of practical importance is the fact that inelastic scattering in the atmosphere is purely molecular in origin; there is no component of aerosol backscatter. This property has found recent application in ozone differential absorption lidar (DIAL) systems (McGee et al. 1995; D. Swart 1994, personal communication) as means of determining relative molecular density profiles in the stratospheric aerosol regime. The technique used in these systems is relatively straightforward, and involves measuring backscatter in the Stokes rotational-vibrational Q branch. For middle atmosphere studies, this approach is less difficult than measuring pure rotational backscatter, despite the fact that rotational-vibrational cross section for the major molecular species, namely N_2 and O_2, is less by about three orders of magnitude.

Pure rotational backscatter is difficult to measure owing to the fact that the elastic scattering has a significantly greater cross section (the difference is about three orders of magnitude in the case of N_2 and O_2) and may contaminate the measurements if care is not taken. However, the advantage in pursuing such measurements is that the scattering species involved can be deduced from the spacing of the Raman lines, and the temperature and density of the scatterers can be obtained from the relative strengths of the lines. This approach forms the basis of the Raman lidar technique, and generally involves using a high resolution spectrometer with a suitable level of discrimination against out-of-band light. Note however, that when there is more than one scattering species, the Raman spectra will overlap in the vicinity of the Rayleigh line.

In the following section, the feasibility of using Raman scattering to measure molecular densities in the stratosphere is examined through simulations involving the lidar equation.

20.3 LIDAR RESPONSE TO ROTATIONAL-VIBRATIONAL RAMAN SCATTERING

The most efficient method of making Raman scatter observations with the Davis lidar will be to conduct 'total power' measurements by placing an appropriately chosen bandpass filter in the lidar receiver to isolate the backscatter from either N_2 or O_2. Flexibility in the choice of filter will be provided by a rotating filter wheel. An important practical requirement of the filter wheel will be to ensure that filter placement in the optical train is reproducible so that throughput variations are minimised. As positioning of a particular filter should require at most a few tens of seconds, it will be feasible to conduct a sequence of multiplexed Raman and Rayleigh measurements. It turns out that Raman profiles with the Davis lidar will be restricted to altitudes below about 30 – 35 km for reasonable spatial and temporal resolutions. Some measure of overlap with the Rayleigh profiles will be important in relating the Raman observations to remainder of the atmosphere.

We now introduce the lidar equation in order to evaluate the expected performance of the Raman measurements. The expected signal returned from an altitude interval Δz centred at altitude z for a single laser pulse may be expressed as

$$N_l(z) = \frac{\Delta z A_r}{z^2} \varepsilon_t \varepsilon_r T(z)^2 \eta \frac{\lambda_R E_t}{hc} \cdot \{\varepsilon_f(\lambda_R)\sigma_{R\text{-}V}(\lambda_R)\}\rho_R \qquad (1)$$

where A_r is the effective collecting area of the receiver, ε_t and ε_r are the wavelength-independent efficiencies of the transmitting and receiving optics, T is the one-way atmospheric transmission coefficient between the lidar and the scattering region, η is the quantum efficiency of the photomultiplier, λ_R is the Raman-shifted wavelength of the backscatter, E_t is the total energy of the laser pulse, c is the speed of light, h is Planck's constant, ε_f is the wavelength-dependent transmission coefficient of the optical filter employed in the receiver, $\sigma_{R\text{-}V}$ is the wavelength-dependant Raman rotational-vibrational total differential scattering cross section (evaluated for linearly polarised incident radiation at a scattering angle of π radians) and ρ_R is the number density of the particular molecular species under investigation.

Our aim is to determine the variation of density of the scattering species ρ_R with altitude. Because the volume mixing ratios of N_2 and O_2 are essentially constant with altitude below the upper mesosphere, either species can be utilised by the Raman technique to infer total molecular density. The main consideration is normally that of signal return. The ozone lidars which observe Raman backscatter in the UV rely on scattering from N_2 in preference to that from O_2 mainly because N_2 has a higher volume backscatter coefficient (β) at these wavelengths. While this is also true in relation to scattering of 532 nm laser light ($\beta(N_2)/\beta(O_2)$ is about 3.4), measurement of the Raman signal from both N_2 and O_2 may provide useful information of the wavelength dependence of atmospheric transmission.

The terms T and $\sigma_{R\text{-}V}$ in Equation (1) are determined by the atmosphere. All of the terms in Equation (1) except T and ρ_R are independent of altitude, and once the bandpass of the receiver is set, they should be reasonably constant during the course of an observing session. Fluctuation in the laser power is likely to produce the largest range-independent variation.

Knowledge of the spectrum of Raman rotational-vibrational scatter is important in the choice of receiver bandpass. Calculation of $\sigma_{R\text{-}V}$ for an incident wavelength of 532 nm (the primary wavelength of the Davis lidar) was undertaken using methods described in Penney et al. (1974), Measures (1984) and Berens et al. (1981). As shown in Table 1, the total cross section of the Q branch dominates over that for the combined O and S branches. It is feasible to restrict the bandpass of the optical filter employed in the lidar receiver to transmit only the Q branch without compromising the signal level. For this application, the half-width of the optical filter was chosen as about 1 nm; this was regarded as providing a suitable level of discrimination against background light. Filters of this bandwidth are relatively easy to manufacture with both high peak transmission and off-band rejection. Given the spectrum of the Raman backscatter, such a filter will not be sensitive to potential movement in central wavelength due to the anticipated level of thermal and mechanical changes.

The total signal output by the lidar has terms associated with the background light level (N_b) and photomultiplier dark count (N_d). We can write

$$N_t = N_l + N_b + N_d \,. \qquad (2)$$

Klekociuk and Innis (1996) provide an expression for N_b. In the case of Raman measurements, the background signal will also contain a range dependent term due to

leakage of Rayleigh scattered light at the laser wavelength (532 nm) by the optical filter. In order to provide a suitable level of discrimination against this signal, the Rayleigh blocking level of the filter (specified by T(532 nm)/T(λ_R)) has been selected as 10^{-7}.

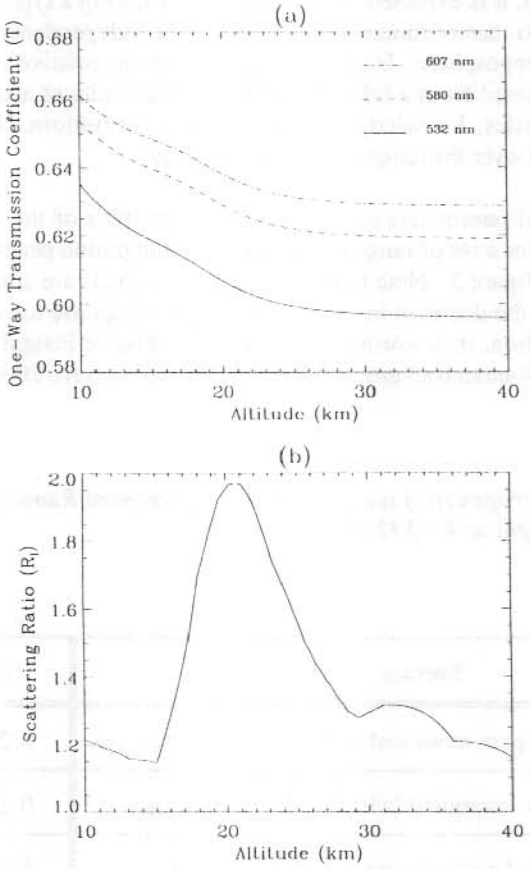

Figure 2. (a) Model of the one-way atmospheric transmission coefficient T as a function of vertical path length for the laser wavelength (532 nm) and the associated Q-branch Raman rotational-vibrational scattering wavelengths for O_2 (580 nm) and N_2 (607 nm). (b) Assumed backscatter ratio profile used in (a). The volume backscatter ratio (R_l as defined in Klekociuk and Innis 1996) is a measure of the significance of the backscatter coefficient for aerosols relative to that for atmospheric molecules. The profile of the R_l was obtained using the LOWTRAN7 atmospheric model (Kneizys et al. 1988) for moderate aged volcanic aerosol loading in the stratosphere, and subarctic tropospheric conditions. The tropopause height was assumed to be 15 km. The modelled variation of R_l with altitude is comparable to profiles inferred by lidars at Syowa and Dumont d'Urville, Antarctica (Iwasaka et al. 1986; Stefanutti et al. 1992). The assumed molecular density profile required in the calculation of T was obtained from the MSISE-90 model (Hedin 1991).

Evaluation of the atmospheric transmission coefficient T involves knowledge of both the molecular and aerosol volume backscatter coefficient as a function of altitude (see Klekociuk and Innis 1996). It is apparent from simulations of atmospheric conditions (an example of which is shown in Figure 2) that the largest influence on T is provided by the troposphere. In general, it is expected that variations of T during a typical lidar integration period (from minutes to tens of minutes duration) will be independent of altitude, at least above the bulk of the troposphere. Under this assumption, the relative variation of density with range can be obtained from a lidar profile within the limits of accuracy imposed by photon counting statistics, knowledge of the signal contributions N_b and N_d and the estimated variation of T over the range interval under study.

Using Equation (2) and parameters in Tables 2 and 3, profiles of the lidar signal versus range were calculated for a set of range resolutions and integration periods. Typical signal profiles are shown in Figure 3. Note that the N_2 and O_2 signals are similar in magnitude. This is partially due to the decrease in the photomultiplier response towards the red end of the spectrum. In addition, it is worth pointing out the relative insignificance of the λ = 532 nm leakage to the Raman background signal, particularly above 20 km.

Table 1. Molecular nitrogen (N_2) and oxygen (O_2) differential Raman backscatter cross sections for incident light at λ =532 nm.

Species	N_2	O_2
Rayleigh + Q branch pure rotational ($x10^{-32}$ m^2 sr^{-1}), $\sigma_{R+Q(R)}$	6.29	5.28
O + S branch pure rotational ($x10^{-32}$ m^2 sr^{-1}), $\sigma_{O+S(R)}$	0.20	0.32
Rayleigh + total pure rotational ($x10^{-32}$ m^2 sr^{-1})	6.49	5.60
Ratio $\sigma_{R+Q(R)}/\sigma_{O+S(R)}$	30.8	16.5
Q branch rotational-vibrational ($x10^{-32}$ m^2 sr^{-1}), $\sigma_{Q(R-V)}$	$3.94x10^{-3}$	$4.65x10^{-3}$
O + S branch rotational-vibrational ($x10^{-32}$ m^2 sr^{-1}), $\sigma_{O+S(R-V)}$	$0.62x10^{-3}$	$1.88x10^{-3}$
Total rotational-vibrational ($x10^{-32}$ m^2 sr^{-1})	$4.55x10^{-3}$	$6.53x10^{-3}$
Ratio $\sigma_{Q(R-V)}/\sigma_{O+S(R-V)}$	6.36	2.48
Ratio $\sigma_{R+Q(R)}/\sigma_{Q(R-V)}$	$1.60x10^{3}$	$1.13x10^{3}$

As discussed in the following section, the Raman lidar simulations were used to examine their potential benefit in middle atmosphere studies, particularly in regard to improving the potential for the absolute calibration of lidar density profiles, accurately inferring the backscattering ratio in the stratosphere, and investigating stratospheric gravity waves.

Table 2. Specifications for the Raman filters.

Species	N_2	O_2
Central wavelength	607.0	579.8
FWHM bandwidth	0.9 nm	1.2 nm
Peak transmission	0.74	0.67
Nominal transmission at 532 nm	10^{-7}	10^{-7}

Table 3. Parameters of the lidar system assumed in the performance simulations.

Parameter	Value
Laser wavelength, λ_0	532 nm
Laser pulse energy, E_t	0.6 J
Laser pulse repetition rate	50 Hz
Full angle field of view of receiver, α	0.16 mrad
Efficiency of transmitting optics, ε_t	0.35
Efficiency of receiving optics, ε_r	0.28
PMT quantum efficiency, η	0.14
Telescope collecting area	0.79 m^2

20.4 DISCUSSION

20.4.1 *Atmospheric density profiles*

By rearranging Equation (1), atmospheric density in absolute units, ρ_a, can be obtained from an individual lidar measurement using

$$\rho_a(z) = C\frac{N_l(z) - N_b(z)}{r^2\, T^2(z\rightarrow\infty)} \qquad (3)$$

where C is a normalisation constant and $T(z\rightarrow\infty)$ is the one-way transmission coefficient between a measurement altitude z and the top of the atmosphere. Here, the dark count contribution to the signal (N_d), which is normally negligible, has been ignored. The constant C depends on the instrumental parameters in Equation (1), as well as T(z), and may vary with time. For a particular observation interval, C is usually calculated so that at some reference altitude ρ_a equals the density obtained from an atmospheric model or inferred from radiosonde measurements.

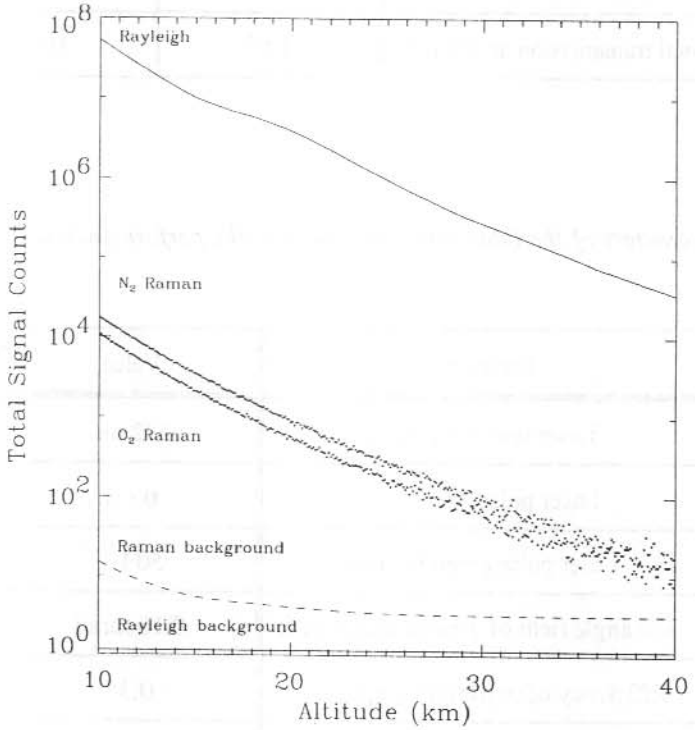

Figure 3. Simulated lidar signal profiles for the Davis lidar operating in Rayleigh and Raman modes for an altitude resolution of 100 m and a total observing time of 10 minutes. The aerosol profile shown in Figure 2 was assumed. Note the enhanced signal for Rayleigh mode near 20 km due to Mie scattering.

An important assumption in Equation (3) is that the signal N_l is not significantly contaminated by scattering from aerosols at the altitude where C is evaluated. The variability of stratospheric aerosol loading, combined with the inherent variation of balloon flight ceilings normally restricts the opportunity for using radiosonde-inferred densities for calibrating lidar data. However, Raman backscatter measurements (for which aerosol scattering is not an issue) have the potential to extend the overlap region.

The Australian Bureau of Meteorology (BoM) conducts a program of upper-air measurements using balloon-borne Väisälä RS80 radiosondes at several sites including Davis and Hobart, Tasmania (B. Copplestone 1996, personal communication). The radiosondes are normally released twice daily. They typically reach altitudes of 25-30 km, which is near the top of the stratospheric aerosol layer. Data archived by the BoM consist of pressure, temperature and humidity measured at 10 s intervals during the balloon's ascent. The typical one-sigma accuracy of the pressure and temperature measurements is 0.5 hPa and 0.2 K respectively.

Absolute atmospheric density can be calculated from the radiosonde data using the perfect gas law. In these calculations, the mean molecular weight can be considered constant with altitude, with a value of 28.964 kg $kmol^{-1}$. The correction of density due to the presence of water vapour (using the method in Kyle 1991) is negligible above the tropopause. The expected relative error in radiosonde-inferred densities varies approximately exponentially with altitude, and is ~1% at 20 km and ~4% at 30 km.

Using the Davis lidar, it should be feasible to directly compare the Raman lidar measurements with radiosonde density profiles above an altitude of 10 km (this limit is imposed by the mechanical shutters in the lidar). This will have the advantage of allowing a 'best fit' calibration constant to be obtained over a range of altitudes in order to constrain uncertainties in the inferred absolute densities.

Two important aspects should be borne in mind when comparing the radiosonde and lidar data. Firstly, the ascent rate of the balloons is typically 5-6 m s^{-1}, and so a balloon may potentially take an hour to rise from the tropopause to its maximum altitude. Secondly, winds may carry the balloon tens to hundreds of kilometres away from the release site, although its position at any particular time is known with good accuracy through use of radar or the Digicora system. For high resolution studies, it may also be necessary to consider the temporal response of the temperature sensor.

Using Equation (3), relative uncertainty in the calibration constant obtained using the signal in an individual lidar range bin can be expressed as

$$\left(\frac{\Delta C}{C}\right)^2 \sim \left(\frac{\Delta \rho_c(z)}{\rho_c(z)}\right)^2 + \left(\frac{\Delta \rho(z)}{\rho(z)}\right)^2 \qquad (4)$$

where ρ_c is an associated density estimate obtained from a recent radiosonde flight,

$$\frac{\Delta \rho(z)}{\rho(z)} = \frac{\sqrt{N_l(z)}}{N_l(z) - N_b(z)} \qquad (5)$$

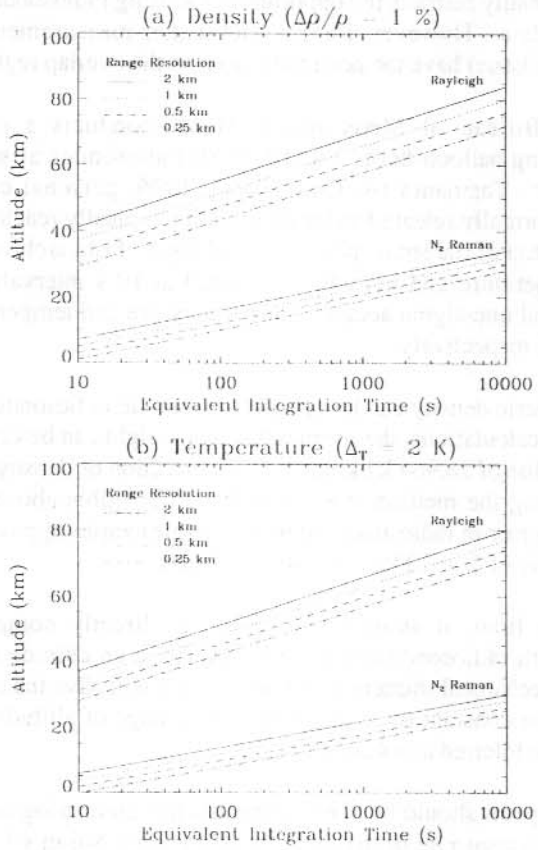

Figure 4. Summary of spatial and temporal resolution for measurements of Rayleigh backscatter and N_2 rotational-vibrational Raman backscatter with the Davis lidar. For various range resolutions, plots are provided of altitude against approximate minimum equivalent integration time (elapsed observing time for contiguous laser firing) required to achieve (a) a one-sigma relative error of 1% in density (evaluated using Equation (5)) and (b) a one-sigma absolute error of 2 K in temperature (evaluated using the method described in Chanin and Hauchecorne 1984). The corresponding performance profiles for O_2 Raman measurements are displaced approximately 2 km below those of the N_2 Raman measurements, and have been excluded for clarity.

and Δ denotes the statistical uncertainty of the associated quantity. Here it is assumed that fluctuations in N_b and T as a function of z can be neglected. The first term in Equation (4) will dominate for Raman lidar observations involving dwell times of tens of minutes or

more. This can be gauged from Figure 4 where the potential of the Raman measurements is summarised. As an example, an equivalent integration period of about 20 minutes or more and an altitude resolution of 1 km will yield density measurements with a relative uncertainty of 1% or less above an altitude of about 20 km. Note in Figure 4 the considerably shorter dwell times required for the Rayleigh measurements. An important aspect of the Raman calibrations will be their transfer to concurrent Rayleigh measurements. A suitable range of overlap in altitude is desirable so that a calibration constant for densities derived from the Rayleigh scatter profile can be evaluated if suitable radiosonde data is not available.

The main benefit of the calibration procedure will be to provide density profiles that are referenced to in-situ measurements of prevailing conditions, rather than model predictions. This will be particularly important when determining diurnal and seasonal behaviour of the middle atmosphere at Davis, where limited information is presently available.

20.4.2 *Temperature profiles and aerosol loading*

As shown in Figure 4, temperature profiles inferred from the Raman-derived density data are likely to have an uncertainty of less than 2 K below an altitude of about 30 km for reasonable integration parameters. The performance is compared with Rayleigh measurements of similar accuracy. In evaluating temperature errors, the reference altitude was chosen as 40 km, and the relative uncertainty in pressure at this altitude was assumed to be 1%. This value was based on the expected accuracy of the temperature and density at this height inferred from concurrent Rayleigh measurements.

Improved temperature estimates below 30 km should be possible by using the density profile inferred from the λ = 532 nm measurements, after correcting for the effects of aerosol scatter using the Raman measurements. This procedure will provide the backscatter coefficient as a by-product, and will assume knowledge of the wavelength dependence of atmospheric transmission in order to compare profiles at the different wavelengths.

20.4.3 *Gravity wave measurements*

The estimated vertical wavelength resolution of the Raman measurements to gravity waves was calculated using a method described by Gardner et al. (1989), and is shown in Figure 5. This figure provides the approximate minimum vertical wavelength that can be resolved for a particular integration time.

Gravity waves in the lower stratosphere have typical dominant vertical wavelengths of a few kilometres (Meriwether 1993; Allen and Vincent 1995; Hostetler and Gardner 1994). As indicated in Figure 5, the Raman measurements will require in excess of an hour of contiguous integration time to adequately investigate gravity wave spectra. While the resolution of the Rayleigh measurements in the upper stratosphere and mesosphere is similar to that of the Raman measurements (as shown in Figure 5), the dominant wavelength in this region is on the order of 10 km (Chanin and Hauchecorne 1981; Shibata et al. 1986). For these measurements, significantly lower integration times will be required.

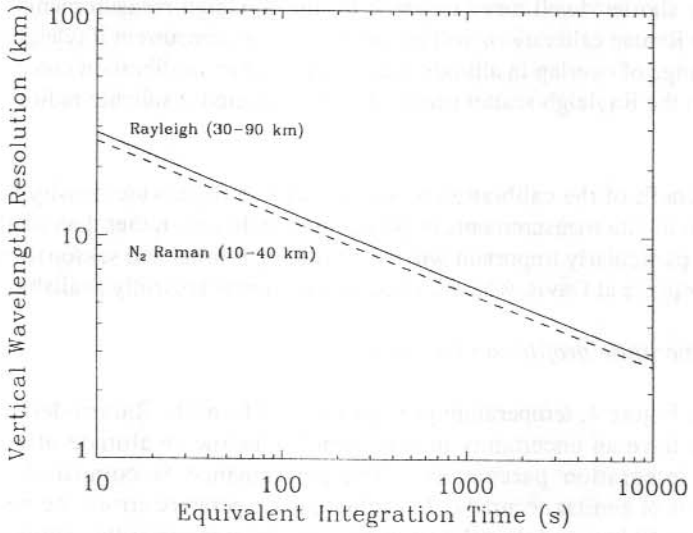

Figure 5. Estimated vertical wavelength resolution of gravity waves as a function of equivalent integration time (elapsed time for contiguous laser firing) for Rayleigh and N_2 rotational-vibrational Raman observations with the Davis lidar.

20.5 CONCLUSIONS

Based on the simulations presented here, it would seem that the Davis lidar will be capable of detecting adequate vibrational-rotational Raman backscatter from N_2 or O_2 for useful studies of the lower stratosphere. The Raman lidar measurements should provide an important means of deriving absolute density profiles through calibration with in-situ radiosonde observations.

In practice, it remains to be decided whether Raman backscatter from O_2 or N_2 will be preferentially measured by the Davis lidar. It may be more suitable to observe the O_2 scatter, as the wavelength shift may pose less of a problem for the optics in the receiver.

Improvement in the Raman backscatter signal level could be achieved by transmitting the laser beam directly to the sky (via a beam expander to control divergence) thereby avoiding one component of the losses associated with the lidar telescope. These observations would be restricted to the zenith. An improvement in signal by of a factor of about 2.5 could be expected.

An additional means of determining temperature in the lower atmosphere (as noted in Section 20.2) involves measuring the spectrum of pure rotational Raman backscatter. The

feasibility of conducting this type of measurement with the Davis lidar is under investigation.

20.6 ACKNOWLEDGEMENTS

The lidar being developed by the Australian Antarctic Division and the University of Adelaide was originally conceived and designed by the late F. Jacka, and its initial development was largely due to the efforts of P.S. Argall. Dan Swart provided information on the N_2 Raman measurements made with the ozone lidar operated by the National Institute for Public Health and Environment Protection, The Netherlands, at Lauder, New Zealand. Bruce Copplestone of the Australian Bureau of Meteorology kindly provided information on the program of radiosonde measurements at Davis. We thank R. Morris, D. Murphy and J. Whelan for assistance in the preparation of this paper. Funding for the lidar project has been provided by the Australian Antarctic Division, the University of Adelaide, and the Australian Research Grants Scheme.

REFERENCES

Allen, S.J. *and* Vincent, R.A. (1995). Gravity wave activity in the lower atmosphere: seasonal and latitudinal variations. *Journal of Geophysical Research 100*: 1327 – 1350.

Banwell, C.N. (1983). Fundamentals of Molecular Spectroscopy. Third Edition, McGraw-Hill, London.

Berens, P.H., White, S.R. *and* Wilson, K.R. (1981). Molecular dynamics and spectra. II. Diatomic Raman. *Journal of Chemical Physics 75*:515 – 529.

Chanin, M-L. *and* Hauchercorne, A. (1981). Lidar observations of gravity and tidal waves in the stratosphere and mesosphere. *Journal of Geophysical Research 86*:9715 – 9721.

Chanin, M-L. *and* Hauchercorne, A. (1984). Lidar studies of temperature and density using Rayleigh scattering. *Middle Atmosphere Program - Handbook 13*:87 – 98.

Gardner, C.S., Miller, M.S. *and* Liu, C.H. (1989). Rayleigh lidar observations of gravity wave activity in the upper stratosphere at Urbaba, Illinois. *Journal of the Atmospheric Sciences 46*:1838 – 1854.

Hauchecorne, A. *and* Chanin, M-L. (1980). Density and temperature profiles obtained by lidar between 35 and 70 km. *Geophysical Research Letters 7*:565 – 568.

Hedin, A.E. (1995). Neutral atmosphere empirical model from the surface to the lower exosphere. *Journal of Geophysical Research 96*:1159 – 1172.

Hostetler, C.A. *and* Gardner, C.S. (1994). Observations of horizontal and vertical wavenumber spectra of gravity wave motions in the stratosphere and mesosphere over the mid-Pacific. *Journal of Geophysical Research 99*:1283 – 1302.

Iwasaka, Y., Ono, T. *and* Nonura, A. (1986). Changes in aerosol content and temperature in the Antarctic spring stratosphere: lidar measurements at Syowa station (69° 00'S, 39°35'E) in 1983, 1984 and 1985. *Geophysical Research Letters 13*:1407 – 1410.

Klekociuk, A.R. *and* Innis, J.L. (1996). Doppler performance of the lidar for Davis Antarctica. In: Morris, R.J. (Ed). *ANARE Research Notes Number 95*. Pp. 276-295.

Kneizys, F.X., Shettle, E.P., Abreu, L.W., Chetwynd, J.H., Anderson, G.P., Gallery, W.O., Selby, J.E.A. *and* Clough, A.A. (1988). Users guide to LOWTRAN7, Technical Report AFGL-TR-88-0177, Air Force Geophysics Laboratory, Massachusetts.

Kyle, T.G. (1991). Atmospheric Transmission, Emission and Scattering. Pergamon, Oxford.

McGee, T.J., Gross, M.R., Upendra, N.S., Butler, J.J. *and* Kimvilakani, P.E. (1995). Improved stratospheric ozone lidar. *Optical Engineering 34*:1421 – 1430.

Meriwether, J.W.Jr. (1993). Lidar observations of atmospheric dynamics in the troposphere and lower stratosphere over Arecibo. *Journal of Geophysical Research 98*:20713 – 20723.

Measures, R.M. (1984). Laser Remote Sensing: Fundamentals and Applications. Kreiger, Malabar, FL.

Morris, R.J., Monselesan, D.P. *and* Klekociuk, A.R. (1995). Australian Antarctic middle and upper atmosphere physics - a new direction. *Advances in Space Research 16*: 151 – 162.

Penney, C.M., St. Peters, R.L. *and* Lapp, M. (1974). Absolute rotational Raman cross sections for N_2, O_2, and CO_2. *Journal of the Optical Society of America 64*: 712 – 716.

Shibata, T., Kuduka, T. *and* Maeda, M. (1986). Density fluctuations in the middle atmosphere over Fukuoka observed by XeF Rayleigh lidar. *Geophysical Research Letters 13*:1121 – 1124.

21. REPORT ON SOLAR RADIATION AND AEROSOL EXPERMENT AT CASEY, ANTARCTICA, JANUARY-FEBRUARY 1993

A. Leyva-Contreras

Universidad Nacional Autónoma de México
Instituto de Geofisica
Observatorio de Radiación Solar
Ciudad Universitaria
Coyoacán 04510
México DF

ABSTRACT

The results of a radiative-aerosol experiment, performed during January and February 1993 at Casey, Antarctica, are reported here. They consist of (a) irradiances of solar fluxes, total and those obtained by means of five broadband glass filters and a pyrheliometer with internationally validated response, and (b) number concentrations of particles of the surface air layer in twelve radius ranges. The preliminary analysis of results showed that the optical depth of the observed atmosphere has two maxima in the visible and in the near-infrared region, respectively. The first maximum is related to the accumulation mode, with modal radius 0.26 μm determined in the monitored aerosol by fitting the size distribution function with the aid of three log-normal distributions. The second maximum is explained by the attenuation of the solar flux by the atmospheric water vapour. The average of the total concentration of particles was 0.59 (±0.47) particle cm^{-3} and is similar to values obtained by other authors in 1983 at Mirny Station on the Antarctic coast, but the size distribution function shows an increase of the concentration of the accumulation mode, with modal radius equal to 0.26 μm. The obtained integral transparency of the atmosphere was significantly low, at 68% instead of 80–85% obtained by other authors for similar environments. This last mentioned result is still under evaluation.

21.1 THE INSTRUMENTS

The equipment employed in the experiment consists of:

(a) A pyrheliometer 'Sonntag', based on a thermopile with temperature dependent response $K(t_p)$:

$$K(t_p) = 3.373[1 + 0.002(t_p - 20)], \text{ mVW}^{-1}\text{m}^{-2} \quad (1)$$

where t_p is the thermopile temperature, in degrees Celsius, measured during the observation. The pyrheliometer is provided with five glass filters with the following characteristics:

Filter #1 (OG1): 530–3000 nm (1.07)

Filter #2 (RG2): 625–3000 nm (1.09)

Filter #3 (WG1): 350 – 3000 nm (1.08)
Filter #4 (WG7): 275 – 3000 nm (1.07)
Filter #5 (RG8): 710 – 3000 nm (1.02)

The reduction factor (Kondratyev 1976) is given for each filter in brackets. The readings were made with a HP 3478A multimeter, with a resolution of ±0.5 mV. The direct solar irradiances E_i were calculated as:

$$Ei = \frac{Li}{(fi\ K(tp))}, \quad Wm^{-2} \qquad (2)$$

where Li is the thermopile voltage generated by illumination through the i-the filter and f_i the corresponding reduction factor; for total irradiance i = 0 is used.

(b) A photoelectric counter of aerosol particles AZ-5, 1983 model, which determines the total amount of particles in 12 ranges; i.e. with radius greater than 0.20, 0.25, 0.30, 0.35, 0.40, 0.45, 0.50, 0.75, 1.0, 2.0, 3.5 and 5.0 microns, respectively. The readings are in particles $litre^{-1}$ and are reported here in particles cm^{-3}.

21.2 THE DATA VALIDATION

The response of the solar radiation sensor is checked periodically against the standard pyrheliometer of the IGf Observatory of Solar Radiation and is determined with an accuracy of ±3%. The resolution of the multimeter affect the irradiance values by ±0.1 Wm^{-2}. The reduction factors were obtained with the aid of a spectrophotometer in the Laboratory of Atmospheric Pollution of the Center of Atmospheric Sciences, Mexico City.

The AZ-5 counter was calibrated in March 1992 against a counter used only for intercomparisons in the Laboratory of Physics and Chemistry of Atmospheric Aerosols of the Saint Petersburg State University.

21.3 THE OBSERVATION SITE

The site to perform solar radiation and aerosol measurements was selected within Casey station environs on its east side. It is important to take into account the location of the site, since station activities are also a source of aerosol particles, besides the natural ones. Regarding the solar radiation measurements, the horizon from the east and west sides were free enough in order to permit the observation of the direct solar radiation for air masses up to 5.

21.4 DATA STORAGE

The resulting data were stored on magnetic diskettes, in ASCCI code. Here, these data are listed in the following form:

(a) The table of solar irradiances contains 8 columns; the first two refers to the local time in hours and minutes; the following 6 columns are the total irradiance and the irradiances of the filters OG1, RG2, WG1, WG7 and RG8 respectively; the last column indicates cloud interference of the solar disk at the time of observation ('1': low level clouds; '2': mean level clouds; '3': high level clouds; '0' means no cloud interference).

(b) The table of aerosol concentrations contains 14 columns: the first two refer to the local time, in hours and minutes; the following 10 columns refer to the number concentration of aerosol particles (particles cm^{-3}) for the first 10 of the 12 ranges mentioned above; the readings of the two last channels were systematically equal to 0. The last two columns contain the observed wind velocity (in m s^{-1}) and wind direction; only four directions are discriminated; N (1), E (2), S (3) and W (4).

21.5 PRELIMINARY ANALYSIS OF RESULTS

21.5.1 *Solar radiation data*

One of the main objectives of the experiment was to estimate the levels of transparency of the Antarctic atmosphere. The observed irradiancies were fitted with the following linear regression:

$$\ln\left(\frac{E_i}{f_{es}E_{0i}}\right) = a_i - \tau_i m \qquad (3)$$

where index i refers to the number of the filter, E_i is the measured irradiance, E_{0i} is the irradiance for the same spectral interval at the top of the atmosphere at the mean Earth-Sun (ES) distance, f_{es} is the correction factor for the ES distance variation, and m is the air mass. Parameters a_i and τ_i are calculated for each morning or afternoon series in order to prevent significant variations in the atmospheric optical state which can lead to a variable slope in Equation (3). The parameter τ_i is similar to the optical depth of the Bouguer-Beer law and here the name is retained. However, it must be kept in mind that in this case, with broadband actinometric glass filters, Equation (3) has an empirical meaning seeing that the mentioned law is valid only for strictly monochromatic radiative fluxes and thin layers of propagation medium. Nevertheless, the differences of the filter irradiances can be used for the estimation, in a first approximation, of the atmospheric spectral transparency. In the table given below, the bands W43, W31, W12 and W25 are defined by means of the corresponding differences (see Figure 1):

band	limits (nm)	characteristic wavelength (nm)
W43	275 – 350	310
W31	350 – 530	425
W12	530 – 625	575
W25	625 – 710	670

The characteristic wavelength λ^* is defined by:

$$I_0(\lambda^*) = (\lambda'' - \lambda')^{-1} \int_{\lambda'}^{\lambda''} I_0(\lambda)\, d\lambda \qquad (4)$$

where $I_0(\lambda)$ is the spectral distribution of the solar irradiance; λ' and λ'' are the limits of the corresponding band. The results of 14 series of observations, with correlation coefficients greater than 0.98 are shown in the following table:

	W43	W31	W12	W25
τ	0.283	0.368	0.985	0.685
σ	0.067	0.056	0.022	0.102

Here, τ and σ are the average optical depths and their standard deviations, respectively. These results are shown graphically in Figure 2, where for comparison the spectral aerosol optical depth measured in summer at Mirny station in 1982 and 1983 is also provided. The values obtained represent the optical depth of both the gaseous and particle components of the atmosphere, and because of that, they are higher than the aerosol one. However, it is interesting that, in general, they have a similar behaviour to the aerosol optical depth, with a maximum in the visible and another in the near-infrared spectral regions. This indicates the important role of aerosol particles in the attenuation of solar radiative fluxes, the presence of an important aerosol fraction with characteristic radii around 0.25 μm (Leyva and Vasilyev 1996) and the influence of the water vapour in the attenuation of the solar flux. The value of the optical depth for the RG8 filter is shown in Figure 2. It is included because, in spite of its large band width (710 – 3000 nm) it is defined in a region with comparatively low irradiance and soft spectral dependence.

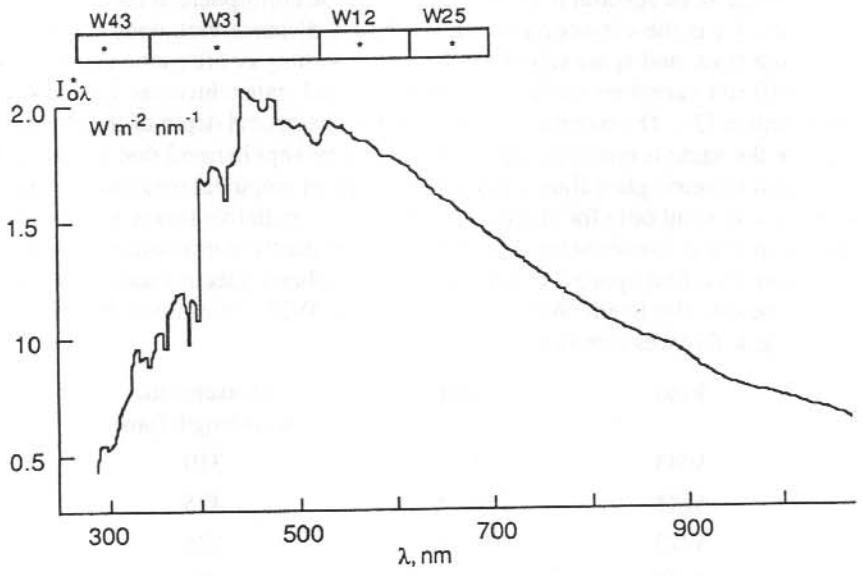

Figure 1. The spectral distribution of the astronomical flux of solar radiation.

An unexpected result is the low transparency values of total irradiance defined as $\exp(-2\,\tau_0)$, i.e. the transparency referred to air mass 2. According to Marshunova (1980), cited in (Barteneva et al. 1991), for Mirny station in summer (1983–1984) this parameter was around 0.83. In our experiment this parameter has varied very little around a lower value: 0.68 (±0.03). It will be necessary to perform estimations of the amount of precipitable water and ozone content in order to estimate the role of gases in the attenuation of the radiative solar fluxes during the experiment and to find the origin of the unusual low transparency values.

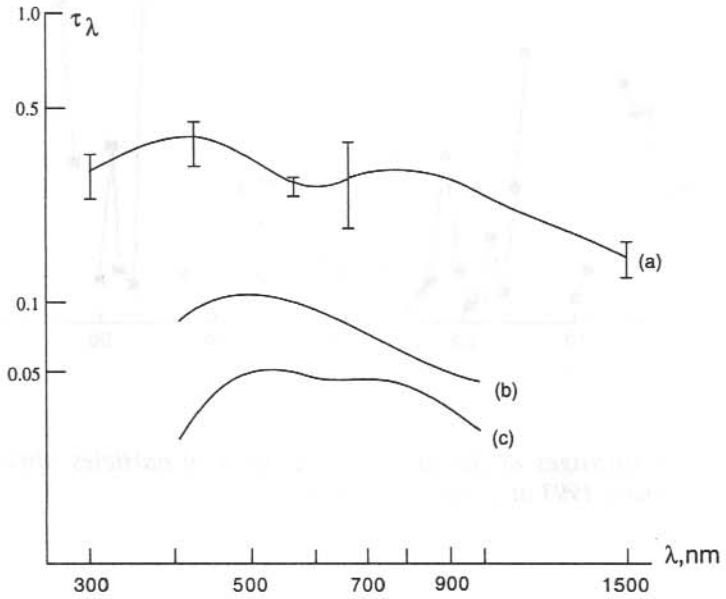

Figure 2. The spectral dependence of the optical depths. (a) Total (gases and particles) optical depth as obtained at Casey, January–February 1993; (b) and (c) aerosol optical depths obtained at Mirny station during summer 1982–1983 and 1983–1984, respectively (after Barteneva et al. 1991).

21.5.2 *Aerosol data*

With regard to acquired data on number concentration of aerosol particles, the exceptionally clean conditions of the Antarctic air enabled us to detect when local pollution had affected the measurements: the proximity of the main source of local pollution (the powerhouse) caused an instability in the readings when it was in the path of air currents flowing toward the observation site . However, there is no doubt that a local, not natural background effect is included in the observed concentrations, but it must be more or less constant and negligible, and it cannot explain the strong variability observed in the measured parameters. Figure 3 shows the evolution of the daily average of total concentration of particles N_t ($r > 0.2\ \mu m$), the mean value being 0.590 (±0.471) particles cm^{-3} with a maximum of 2 and a

minimum of 0.086 corresponding to 15 February and 24 January, respectively, in the same units.

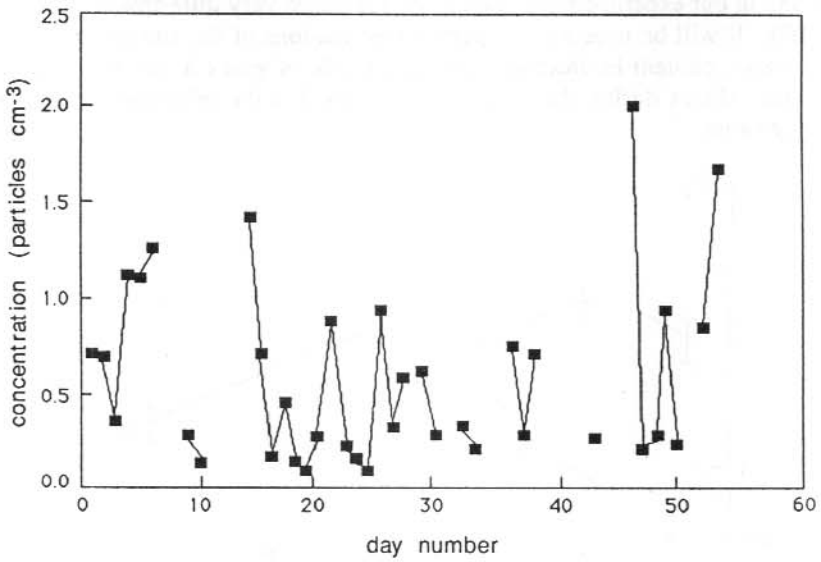

Figure 3. Daily averages of the total concentration of particles obtained during January and February 1993 at Casey, Antarctica.

The strong variability of N_t (see Figure 3) can be explained only by the strong variability of the weather conditions at Casey during the experiment: active processes of cloud formation and periods of strong wind (mainly easterlies) with velocities of 50 to 60 knots. On the other hand, regarding the behaviour of aerosol parameters, it was not an exceptional Antarctic summer: in cited work (Barteneva et al. 1991) it is reported for Mirny station, also for summer, the average concentration of particles as 0.332 (±0.282) particles cm^{-3}, with a maximum of 1.6 and a minimum of 0.050 in the same units. In Figure 4 the frequency distribution of N_t is shown; the observed two-modality is only apparent and caused by the reduced number of monitored days. Nevertheless, we can affirm that the more probable value of N_t is near to 0.4 particles cm^{-3}.

The variability of the aerosol system is reflected also in its size distribution function (SDF). In Figure 5 the SDF´s of days with the highest (15 February 1993) and the smallest (24 January 1993) total concentration are plotted. In the first case, a general increase of concentration, specially in the coarse and in the mean fractions, is observed. In the second case, there is a general reduction in the concentration with respect to the average, particularly in the coarse fraction which practically disappeared. Figure 5 shows the average SDF for Casey (January – February 1993) and Mirny (January – March 1983). As it can be seen, in the case of the average Casey SDF, the coarse fraction ($r > 1.0$ μm) seem

to be similar, the fine fraction ($r < 0.1$ μm) seem to be reduced, and the mean fractions ($r \sim 0.3$ μm) increased with respect to the Mirny SDF of 1983.

It is possible to reproduce the Casey SDF by means of the sum of three log-normal functions with the following parameters (at 60% of relative humidity):

N particles cm^{-3}	s	r' μm
50	0.35	0.02
0.3	0.12	0.26
0.05	0.26	0.50

where N is the total concentration, s the standard deviation and r' the modal radius of the corresponding mode, for a dry aerosol (0% of relative air humidity). The modal radii 0.02 and 0.26 μm coincide approximately with those reported by different authors for the transient nuclei and accumulation modes of the aerosol of the boundary layer of the atmosphere (continent). The third mode (modal radius of 0.50 μm) is an extremely reduced coarse mode, which usually has a modal radius close to 4 μm.

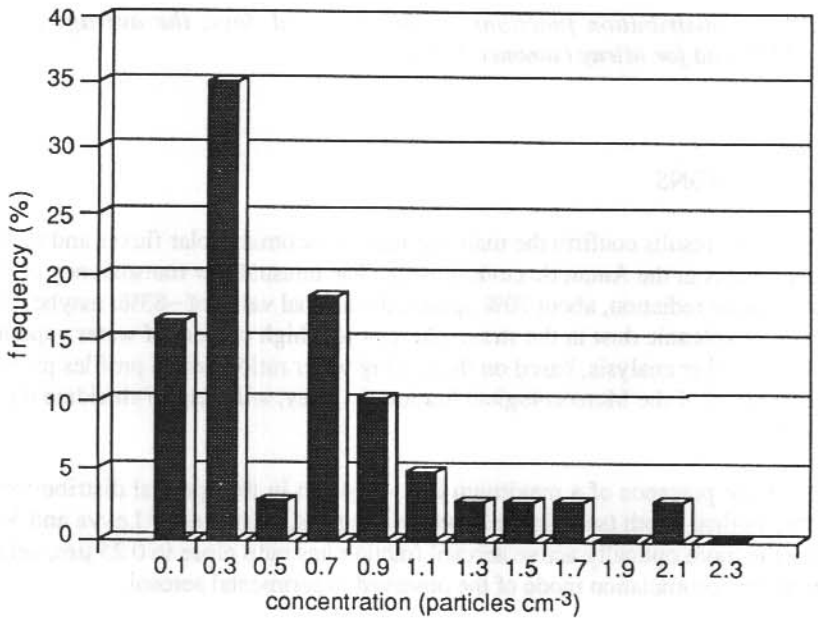

Figure 4. Frequency distribution of daily averages of total concentrations observed from 1 January until 22 February, 1993, at Casey, Antarctica.

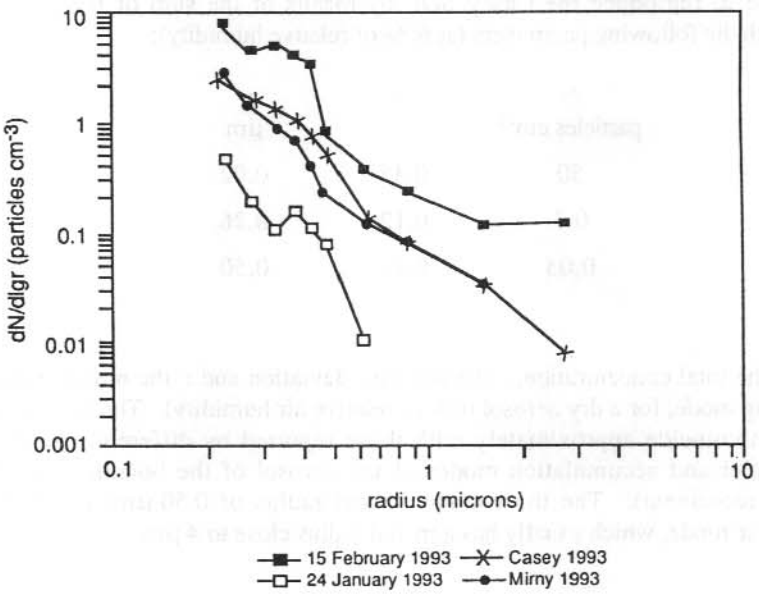

Figure 5. Size distribution functions for two selected days, the average for Casey (summer 1993) and for Mirny (summer 1983).

21.6 CONCLUSIONS

The experimental results confirm the main features of incoming solar fluxes and the content of aerosol particles in the Antarctic environment. The unusual low transparency of the total flux of direct solar radiation, about 70% against the normal value of ~83%, maybe related to the presence of volcanic dust in the stratosphere or to a high content of water vapour in the troposphere. Further analysis, based on the mixing water ratio vertical profiles provided by Neil Adams, Head of the Meteorological Station at Casey, will help to elucidate the causes of this result.

Of interest is the presence of a maximum in $\lambda \approx 0.4$ μm in the spectral distribution of the actinometric optical depth (see Figure 2) which suggests, according to Leyva and Vasilyev (1996) that the more optically active aerosol fraction has radii close to 0.25 μm, being such a fraction of the accumulation mode of the observed experimental aerosol.

Further experiments must include measurement of solar fluxes in narrow bands ($\Delta\lambda$ ~10 nm) in order to estimate the concentration and size distribution of the particles in the entire air column (Muhlia et al. 1989). The content of particles in the air vertical column

and in the air surface layer, are of great importance for the explanation of several climatic features of the region (Grass and Adriaansen 1985).

21.7 ACKNOWLEDGMENTS

The author expresses his thanks to Professor Patrick Quilty, Assistant Director Science, Australian Antarctic Division, for the invitation and encouragement to perform the experiment, which also would not have been possible without the invaluable support of colleagues in the Atmospheric and Space Physics group, headed by Dr Ray Morris. The author also expresses his gratitude to Mr Graeme Armstrong, Station Leader, and to all expeditioners at Casey during the 1992–93 summer .

The experiment was financially supported by the Ministry of Foreign Affairs, the National Council of Science and Technology and the National University of Mexico, and by the Australian Antarctic Division and the Australian Antarctic Foundation.

REFERENCES

Barteneva, O.D., Nikitinskaya, N.I., Sakunov, G.G. *and* Veselova, L.K. (1991). Transparency of the whole atmosphere in the visual and near infrared spectral ranges. Gidrotmet Publishing House, Leningrad. Pp. 227 (In Russian).

Gras, J.L. *and* Adriaansen, A. (1985). Concentration and size variation of condensation nuclei at Mawson, Antarctica. *Journal of Atmospheric Chemistry 3*:93–106.

Kondratyev, K.Ya. (1976). Radiation in the atmosphere. Academic Press, New York.

Leyva-Contreras, A. *and* Vasilyev, O.B. (1996). Report on the spectral and angular informative ranges of the aerosol radiative characteristics. Reportes Internos del Instituto de Geofisica, UNAM, Mexico.

Muhlia, A., Leyva, A. *and* Bravo, J.L. (1989). Actinometric method for the determination of the total number of aerosol particles in the vertical atmospheric column. *Geofisica International 28-1*:47–71.

APPENDIX 1

DIRECT SOLAR IRRADIANCES

hour	open	OG1	RG2	WG1	WG7	RG8	S/
			1 January 1993				
7 07	779.2	619.1	526.0	728.7	766.1	523.3	0
7 26	813.0	640.3	543.4	760.6	798.0	534.0	0
7 56	847.5	662.8	559.3	790.3	828.5	548.2	0
8 18	872.2	678.3	570.8	813.1	854.2	557.2	0
8 32	889.1	689.4	580.1	827.0	868.3	568.3	0
9 37	932.3	715.2	599.9	867.8	914.2	587.3	0
12 03	975.8	743.1	619.7	903.7	954.1	600.1	0
			3 January 1993				
7 44	828.4	658.5	556.9	778.1	817.2	546.8	0
8 08	860.9	673.1	567.1	804.0	844.7	556.5	0
8 22	877.6	683.1	575.5	816.2	858.4	561.5	0
8 43	893.0	694.2	582.1	830.1	874.1	568.0	0
9 08	912.2	703.9	588.7	847.9	892.8	576.4	0
9 58	933.5	712.8	594.3	866.9	913.8	582.4	0
10 28	946.8	721.8	601.5	875.8	925.1	585.9	0
11 27	959.6	728.5	606.6	888.6	939.6	591.2	0
14 04	957.5	727.5	606.9	887.0	936.2	589.4	0
15 34	923.9	706.9	590.4	856.5	903.7	578.0	0
17 02	859.1	667.8	561.0	799.6	839.4	544.2	0
17 26	831.7	650.0	547.2	774.6	812.7	535.3	0
17 58	791.7	621.7	525.1	737.9	773.2	517.5	0
18 12	769.2	610.5	516.5	718.1	752.7	508.5	0
18 22	755.0	601.9	510.3	705.3	740.8	504.0	0
18 32	739.3	589.1	502.0	691.1	722.3	493.4	0
18 47	712.0	572.2	487.8	664.6	694.5	480.0	0
19 10	666.0	540.4	463.1	623.2	649.9	457.7	0
19 30	617.7	506.7	436.8	577.1	601.3	430.3	0
20 02	543.0	454.8	395.7	509.3	530.0	392.4	0
20 36	446.2	381.8	337.7	418.1	433.2	338.1	0
21 02	366.4	320.2	287.6	343.8	356.1	290.4	0
			5 January 1993				
6 44	717.3	559.3	476.0	651.8	687.4	476.3	3
7 39	809.6	634.6	536.6	752.9	789.7	524.9	3
7 51	821.0	644.8	544.5	766.5	801.9	530.9	3
8 03	834.0	653.0	550.0	782.5	821.0	533.7	3
8 17	855.7	664.7	560.2	797.1	839.6	547.5	3

hour	open	OG1	RG2	WG1	WG7	RG8	S/
			9 January 1993				
7 57	819.8	643.9	542.3	769.2	806.2	530.0	3
8 18	837.8	649.7	544.7	775.0	815.3	530.7	3
8 32	853.1	657.5	552.5	796.3	836.5	540.2	3
8 47	879.1	678.0	569.6	817.2	863.8	560.0	3
9 07	838.4	657.0	548.0	773.1	807.2	517.1	3
9 22	855.1	657.0	544.7	793.0	836.6	533.9	3
9 48	776.1	591.4	487.7	690.3	754.7	494.8	3
12 23	971.7	738.3	610.6	902.8	953.2	589.4	3
15 23	943.2	721.6	600.5	874.7	924.1	576.8	3
16 38	887.0	685.9	570.8	825.4	868.8	552.7	3
17 23	848.8	661.7	553.0	790.8	831.2	538.9	3
17 44	821.8	644.8	541.9	767.6	805.2	528.4	3
18 17	785.4	623.1	526.2	732.7	767.5	512.6	0
18 32	756.6	605.1	512.8	707.2	739.6	499.0	0
18 47	733.4	589.4	500.9	685.8	716.2	489.2	0
19 02	703.7	570.3	485.8	658.9	688.3	474.1	0
19 27	650.6	534.1	458.6	611.4	637.3	449.5	0
19 42	616.0	510.1	438.7	578.5	602.5	432.5	0
			10 January 1993				
5 20	551.6	465.6	409.1	521.0	543.6	411.6	0
5 37	596.8	495.8	432.1	561.6	586.3	432.0	0
5 59	651.4	532.5	460.5	612.2	640.2	458.8	0
6 17	688.7	560.2	480.2	646.1	672.8	473.8	0
6 32	715.5	575.3	491.5	669.6	701.9	487.0	0
6 46	740.6	591.5	504.3	693.1	726.6	499.2	0
7 08	775.6	616.6	523.4	725.6	760.8	516.3	3
7 37	816.5	642.9	543.2	762.8	800.0	532.6	3
			18 January 1993				
6 23	628.4	512.4	438.8	591.7	617.7	438.1	0
6 38	657.6	530.7	452.8	617.4	646.3	449.6	0
7 02	707.4	564.5	478.2	662.7	694.0	470.9	0
7 17	734.2	581.4	492.0	686.7	723.0	483.4	0
7 32	760.6	599.5	505.6	712.0	746.8	495.8	0
7 47	782.8	615.7	517.9	733.6	769.5	508.1	0
8 02	803.2	628.6	526.9	749.1	787.4	513.7	0
8 27	833.4	646.8	542.7	776.5	817.3	529.1	0
8 53	860.3	664.2	555.1	800.4	842.6	539.8	0
10 13	917.4	699.0	584.2	851.9	898.2	565.3	0
10 57	933.4	710.0	589.9	867.4	914.7	573.6	0
15 00	927.2	707.6	586.9	859.0	906.4	569.0	0
16 09	887.4	682.6	568.9	824.5	868.3	551.0	0
16 47	859.8	666.2	556.6	800.5	841.6	538.8	0
17 38	802.0	630.3	528.9	747.9	784.5	513.2	3
17 57	777.3	614.4	516.9	726.8	762.0	502.9	3
18 17	745.9	592.5	500.0	697.3	729.7	488.9	3

hour	open	OG1	RG2	WG1	WG7	RG8	S/
			18 January 1993 Cont.				
18 31	718.3	574.7	486.0	673.2	703.7	475.8	0
18 47	688.5	555.4	471.5	645.3	675.6	461.5	0
19 03	655.2	532.2	454.1	615.5	641.8	447.7	0
19 16	627.9	514.2	440.5	590.1	615.1	432.3	0
			19 January 1993				
6 29	609.4	493.2	422.3	571.6	596.5	417.8	0
6 55	670.1	533.2	454.3	630.2	662.0	449.9	3
7 17	675.6	537.0	453.8	632.0	650.0	433.6	3
7 32	709.9	553.6	466.3	659.0	691.3	461.6	3
7 46	733.6	574.3	482.0	686.0	719.3	474.3	3
7 59	750.3	586.3	491.1	698.5	733.9	480.5	3
13 21	942.3	714.0	591.5	874.4	923.3	575.6	3
15 56	881.1	675.9	561.7	817.1	861.6	545.1	3
			20 January 1993				
4 46	322.7	276.6	253.5	303.8	317.8	269.1	0
4 56	344.3	301.9	272.2	331.3	347.7	288.4	0
5 22	441.6	373.3	331.4	417.2	435.3	339.0	0
5 52	531.5	440.4	384.0	500.4	521.9	386.4	0
6 31	633.6	513.4	441.0	594.0	621.3	439.7	3
6 42	658.8	531.5	455.5	617.0	645.4	451.4	0
6 56	690.2	552.1	472.8	645.8	676.5	468.0	0
7 18	738.0	585.7	498.4	689.2	722.7	491.7	3
8 32	830.9	647.0	544.2	774.4	814.6	531.7	0
10 07	901.6	689.3	579.0	837.5	883.6	564.2	0
10 58	920.0	699.8	584.6	852.7	901.6	571.9	0
15 06	902.8	689.1	591.7	838.2	884.8	562.0	0
16 32	846.5	654.6	550.2	787.8	828.7	536.5	0
17 31	781.7	615.8	521.0	731.4	766.6	510.0	0
17 52	755.3	596.0	506.8	705.4	739.3	498.6	0
18 01	744.7	590.8	502.4	695.4	728.9	497.6	0
18 26	701.4	561.3	480.0	657.4	686.5	471.2	0
18 58	639.4	519.2	445.7	599.9	625.3	440.7	0
19 16	601.1	493.9	426.5	563.9	587.5	421.7	0
19 31	560.3	465.2	404.6	525.9	548.2	402.2	0
19 51	505.5	426.2	373.4	474.8	493.7	373.0	0
			23 January 1993				
7 37	690.4	552.3	471.7	646.0	679.0	464.5	0
8 21	758.3	598.5	506.2	710.3	745.4	494.7	0
9 36	835.5	646.5	542.1	778.0	818.7	529.7	0
9 54	845.9	653.7	547.4	787.9	829.4	533.8	0
11 24	885.6	679.3	565.6	822.6	866.5	549.6	0

hour	open	OG1	RG2	WG1	WG7	RG8	S/
			1 February 1993				
8 35	774.5	605.8	510.3	723.8	760.1	503.7	0
8 52	799.7	619.9	524.9	749.1	786.5	516.4	0
9 17	823.9	638.8	535.6	767.8	806.0	522.4	0
9 30	834.4	645.8	540.9	776.4	815.6	527.6	0
9 47	849.1	656.1	547.6	789.7	829.5	532.9	0
10 11	866.4	666.3	556.1	805.7	847.5	540.7	0
10 38	882.0	673.9	562.5	820.9	863.6	547.6	0
11 10	896.8	684.2	571.1	834.1	879.1	554.7	0
13 38	918.5	702.0	584.4	852.2	899.7	564.4	3
15 03	899.9	690.4	576.1	835.9	879.8	560.5	3
17 01	753.3	601.2	501.0	693.6	725.3	473.7	3
17 17	718.3	570.7	486.0	673.0	711.7	470.2	3
17 32	522.0	422.2	347.9	463.2	487.7	325.5	3
17 39	459.0	364.0	308.4	424.4	442.8	296.5	3
17 58	486.5	416.5	348.6	440.9	455.9	305.0	3
18 46	287.3	243.7	208.8	286.2	299.5	214.6	3
			06 February 1993				
13 24	908.9	695.6	578.4	840.8	886.8	562.7	0
14 07	903.7	689.3	575.3	839.1	882.7	560.1	0
16 24	826.7	641.7	537.5	768.7	806.3	525.0	0
16 58	790.0	619.5	520.8	737.1	772.0	509.5	0
17 34	743.0	589.4	498.4	694.5	725.6	490.1	3
17 46	720.8	574.4	488.2	675.7	704.7	481.0	3
18 02	695.7	559.7	476.2	651.6	679.2	466.6	0
18 24	653.9	531.4	454.3	613.8	638.6	448.0	0
18 34	632.2	516.3	443.1	594.1	617.2	436.9	0
18 46	599.2	493.7	424.6	562.4	584.6	420.3	0
19 08	537.9	451.5	392.4	506.5	525.7	389.8	0
			17 February 1993				
15 55	787.6	608.6	511.1	733.6	769.3	509.9	0
16 14	764.4	598.0	504.9	713.7	747.3	496.8	0
16 32	748.6	587.7	497.4	698.4	730.5	487.2	0
16 46	723.6	572.6	485.3	676.6	706.0	475.2	0
16 56	716.3	567.6	482.0	669.4	699.6	471.4	0
17 12	689.1	549.8	467.5	644.6	672.3	457.8	0
17 22	675.1	541.0	461.5	630.4	658.0	452.7	0
17 50	626.0	508.2	435.7	586.4	610.6	430.2	0
19 24	299.5	267.2	243.1	281.5	290.7	247.8	0
19 41	269.5	242.6	222.7	252.7	261.2	228.0	0

hour	open	OG1	RG2	WG1	WG7	RG8	S/
			21 February 1993				
19 41	269.5	242.6	222.7	252.7	261.2	228.0	0
14 58	852.4	665.5	560.6	795.7	833.0	550.9	0
15 16	833.4	650.4	545.7	776.3	814.4	534.8	0
15 31	823.4	644.5	542.1	768.7	805.3	528.3	0
15 46	811.1	635.4	535.0	755.2	791.5	522.2	0
16 01	796.2	625.4	526.0	742.0	777.5	515.6	0
16 16	781.3	616.7	520.3	727.8	762.8	508.3	0
16 30	761.3	602.9	508.9	711.2	743.1	498.7	0
16 50	736.2	587.1	497.5	686.4	718.9	487.4	0
17 01	723.7	578.9	490.3	674.7	702.4	480.9	0
17 12	706.1	568.1	482.4	658.5	688.3	472.5	0
17 22	682.7	551.3	468.8	639.7	666.1	462.0	0
17 31	658.4	533.0	456.0	615.9	643.5	450.2	0

APPENDIX 2

AEROSOL INTEGRAL SIZE DISTRIBUTIONS

hour	1	2	3	4	5	6	7	8	9	10	V	D
						1 January 1993						
7 20	0.750	0.500	0.300	0.240	0.104	0.068	0.042	0.016	0.010	0.001	2	2
8 10	0.700	0.450	0.300	0.180	0.107	0.087	0.054	0.018	0.012	0.001	2	2
9 55	0.400	0.210	0.168	0.108	0.064	0.038	0.027	0.008	0.004	0.000	2	1
12 15	0.420	0.220	0.160	0.118	0.075	0.039	0.032	0.016	0.010	0.002	2	1
16 30	0.850	0.600	0.400	0.250	0.200	0.088	0.060	0.029	0.017	0.002	2	3
13 40	0.750	0.600	0.390	0.325	0.200	0.100	0.064	0.031	0.019	0.002	2	1
18 30	1.100	0.750	0.500	0.380	0.240	0.155	0.081	0.064	0.036	0.014	1	3
						2 January 1993						
7 45	1.000	0.600	0.450	0.300	0.220	0.190	0.072	0.039	0.014	0.001	3	1
6 08	0.800	0.600	0.380	0.220	0.154	0.084	0.062	0.022	0.008	0.001	1	1
10 22	0.600	0.450	0.300	0.200	0.120	0.089	0.057	0.023	0.014	0.002	1	3
13 22	0.550	0.320	0.220	0.175	0.088	0.052	0.037	0.013	0.007	0.000	1	3
17 48	0.500	0.350	0.220	0.143	0.092	0.064	0.045	0.022	0.007	0.000	2	3
						3 January 1993						
7 57	0.188	0.108	0.055	0.038	0.016	0.008	0.007	0.000	0.000	0.000	2	3
8 57	0.275	0.190	0.065	0.049	0.023	0.018	0.010	0.003	0.000	0.000	2	3
10 12	0.300	0.154	0.093	0.050	0.040	0.018	0.012	0.004	0.001	0.000	2	3
11 40	0.235	0.102	0.069	0.047	0.031	0.024	0.018	0.003	0.000	0.000	1	3
13 49	0.350	0.205	0.108	0.088	0.060	0.039	0.022	0.013	0.008	0.000	1	4
15 48	0.380	0.210	0.122	0.084	0.048	0.041	0.034	0.014	0.005	0.000	1	4
17 12	0.320	0.210	0.135	0.069	0.053	0.036	0.019	0.014	0.006	0.000	2	3
18 58	0.475	0.325	0.225	0.116	0.080	0.043	0.036	0.014	0.007	0.000	2	4
20 10	0.700	0.500	0.300	0.180	0.102	0.064	0.046	0.017	0.010	0.000	0	0
						4 January 1993						
6 19	1.200	0.775	0.525	0.400	0.219	0.143	0.100	0.045	0.019	0.000	1	1
8 12	1.400	0.950	0.650	0.450	0.320	0.183	0.104	0.051	0.023	0.000	1	1
15 08	0.950	0.550	0.360	0.260	0.124	0.090	0.049	0.012	0.005	0.000	1	2
16 36	0.950	0.650	0.450	0.325	0.139	0.102	0.043	0.020	0.015	0.000	2	2

hour	1	2	3	4	5	6	7	8	9	10	V	D
					5 January 1993							
5 20	1.600	1.000	0.825	0.625	0.400	0.221	0.148	0.044	0.012	0.000	1	2
6 26	0.850	0.550	0.350	0.223	0.122	0.111	0.051	0.020	0.006	0.000	1	2
7 28	0.850	0.550	0.315	0.188	0.127	0.076	0.041	0.025	0.008	0.000	2	2
14 13	1.050	0.750	0.525	0.285	0.168	0.148	0.079	0.046	0.018	0.000	3	1
15 58	0.875	0.600	0.450	0.290	0.168	0.103	0.060	0.022	0.014	0.000	1	3
17 23	1.500	1.150	0.725	0.550	0.370	0.240	0.135	0.055	0.032	0.003	1	3
18 35	1.050	0.750	0.450	0.350	0.240	0.140	0.073	0.034	0.015	0.000	2	3
					6 January 1993							
6 25	2.200	1.100	0.450	0.250	0.000	0.000	0.000	0.000	0.000	0.000	5	2
7 58	0.475	0.295	0.153	0.095	0.053	0.022	0.019	0.002	0.000	0.000	4	3
10 03	0.525	0.300	0.176	0.081	0.055	0.032	0.023	0.005	0.000	0.000	6	3
12 00	1.900	1.200	0.800	0.000	0.000	0.000	0.000	0.000	0.000	0.000	4	2
14 10	1.200	0.900	0.500	0.000	0.000	0.000	0.000	0.000	0.000	0.000	4	2
					9 January 1993							
8 08	0.121	0.092	0.045	0.026	0.019	0.004	0.000	0.000	0.000	0.000	1	2
9 38	0.176	0.118	0.071	0.059	0.024	0.018	0.007	0.001	0.000	0.000	1	1
12 08	0.166	0.094	0.070	0.039	0.029	0.009	0.008	0.003	0.000	0.000	2	3
15 38	0.179	0.120	0.068	0.050	0.033	0.017	0.013	0.008	0.000	0.000	1	3
17 38	0.355	0.220	0.143	0.088	0.069	0.050	0.033	0.018	0.007	0.002	1	3
19 18	0.525	0.375	0.360	0.123	0.088	0.066	0.039	0.015	0.008	0.001	1	1
20 03	0.450	0.350	0.220	0.118	0.073	0.048	0.030	0.022	0.010	0.002	1	4
					10 January 1993							
5 48	0.120	0.073	0.060	0.047	0.016	0.014	0.006	0.002	0.000	0.000	1	2
6 58	0.200	0.094	0.065	0.041	0.032	0.022	0.008	0.004	0.000	0.000	0	0
10 08	0.124	0.084	0.054	0.039	0.027	0.015	0.010	0.003	0.000	0.000	2	1
11 58	0.112	0.078	0.046	0.032	0.021	0.008	0.005	0.002	0.000	0.000	1	4
14 15	0.102	0.070	0.042	0.017	0.016	0.007	0.004	0.003	0.000	0.000	1	4
16 13	0.141	0.086	0.052	0.042	0.023	0.012	0.011	0.007	0.003	0.000	1	1
18 03	0.113	0.073	0.040	0.031	0.022	0.014	0.007	0.002	0.000	0.000	1	3
					14 January 1993							
13 08	0.500	0.325	0.197	0.134	0.078	0.060	0.046	0.018	0.013	0.002	2	3
14 52	0.800	0.550	0.375	0.200	0.150	0.092	0.057	0.037	0.028	0.001	3	4
16 10	0.700	0.500	0.260	0.195	0.158	0.121	0.086	0.052	0.013	0.003	3	4
18 00	1.633	1.267	0.867	0.667	0.390	0.292	0.177	0.061	0.031	0.001	3	4

hour	1	2	3	4	5	6	7	8	9	10	V	D
					14 January 1993 Cont.							
18 53	2.400	1.700	1.200	0.850	0.550	0.325	0.213	0.084	0.043	0.001	3	4
20 00	2.400	1.800	1.150	0.800	0.600	0.350	0.270	0.088	0.039	0.002	2	4
					15 January 1993							
7 38	0.123	0.075	0.066	0.044	0.022	0.012	0.008	0.003	0.000	0.000	1	3
8 02	0.140	0.093	0.067	0.041	0.018	0.012	0.004	0.000	0.000	0.000	2	3
10 18	0.600	0.350	0.250	0.154	0.118	0.074	0.044	0.022	0.006	0.002	3	3
12 03	0.675	0.450	0.300	0.164	0.116	0.075	0.046	0.017	0.011	0.000	2	3
14 43	1.150	0.950	0.675	0.450	0.330	0.185	0.116	0.053	0.021	0.000	4	2
16 04	0.900	0.700	0.500	0.380	0.164	0.113	0.098	0.044	0.020	0.003	2	2
18 03	1.050	0.750	0.550	0.350	0.210	0.145	0.098	0.048	0.032	0.002	1	1
19 03	1.050	0.800	0.600	0.350	0.183	0.145	0.095	0.054	0.026	0.001	1	3
					16 January 1993							
7 18	0.365	0.220	0.113	0.068	0.041	0.026	0.021	0.005	0.004	0.000	1	3
10 46	0.265	0.142	0.079	0.063	0.034	0.025	0.009	0.006	0.002	0.000	2	3
12 10	0.132	0.070	0.050	0.032	0.020	0.010	0.004	0.003	0.000	0.000	2	3
14 13	0.090	0.061	0.044	0.033	0.010	0.008	0.007	0.001	0.000	0.000	3	3
16 00	0.088	0.065	0.044	0.024	0.017	0.008	0.009	0.004	0.002	0.000	2	3
17 35	0.069	0.049	0.030	0.027	0.015	0.012	0.008	0.006	0.004	0.000	1	3
					17 January 1993							
4 30	0.071	0.043	0.026	0.011	0.007	0.003	0.000	0.000	0.000	0.000	1	3
7 15	0.046	0.024	0.013	0.006	0.004	0.002	0.000	0.000	0.000	0.000	2	3
10 23	0.425	0.300	0.200	0.102	0.059	0.049	0.031	0.018	0.005	0.000	3	3
13 58	0.650	0.275	0.200	0.124	0.080	0.029	0.025	0.016	0.006	0.000	3	1
15 48	1.050	0.650	0.425	0.300	0.140	0.110	0.064	0.019	0.014	0.000	2	1
18 33	0.450	0.300	0.220	0.124	0.094	0.061	0.048	0.018	0.017	0.001	3	2
					18 January 1993							
6 53	0.082	0.057	0.030	0.025	0.014	0.012	0.008	0.003	0.000	0.000	1	3
9 03	0.127	0.073	0.039	0.030	0.024	0.012	0.007	0.004	0.003	0.000	1	1
11 08	0.136	0.100	0.045	0.036	0.032	0.023	0.014	0.007	0.000	0.000	3	1
15 13	0.210	0.092	0.061	0.044	0.031	0.029	0.022	0.011	0.000	0.000	1	1
16 58	0.167	0.082	0.054	0.042	0.027	0.024	0.010	0.005	0.000	0.000	1	1

hour	1	2	3	4	5	6	7	8	9	10	V	D
						19 January 1993						
6 43	0.116	0.079	0.033	0.027	0.014	0.007	0.000	0.000	0.000	0.000	2	2
10 08	0.085	0.055	0.033	0.031	0.013	0.012	0.006	0.000	0.000	0.000	2	3
13 28	0.067	0.049	0.031	0.026	0.012	0.009	0.005	0.000	0.000	0.000	2	3
16 08	0.115	0.059	0.042	0.027	0.020	0.011	0.010	0.002	0.000	0.000	2	3
						20 January 1993						
5 06	0.575	0.450	0.325	0.180	0.105	0.078	0.057	0.025	0.009	0.000	3	1
7 43	0.200	0.086	0.057	0.039	0.027	0.012	0.010	0.008	0.002	0.000	4	1
11 13	0.225	0.098	0.054	0.032	0.013	0.008	0.006	0.001	0.000	0.000	4	2
14 58	0.200	0.109	0.067	0.056	0.026	0.022	0.012	0.006	0.000	0.000	0	0
18 35	0.200	0.112	0.074	0.044	0.022	0.011	0.010	0.002	0.000	0.000	3	1
						21 January 1993						
7 08	1.300	0.775	0.500	0.330	0.220	0.110	0.084	0.036	0.014	0.001	1	4
10 03	1.100	0.650	0.475	0.360	0.220	0.126	0.086	0.034	0.015	0.003	1	3
13 28	0.800	0.450	0.360	0.220	0.118	0.084	0.049	0.021	0.014	0.001	2	4
16 03	0.500	0.380	0.233	0.124	0.075	0.060	0.035	0.015	0.012	0.002	2	3
18 55	0.775	0.475	0.355	0.200	0.116	0.086	0.032	0.010	0.000	0.000	2	3
						22 January 1993						
6 10	0.220	0.115	0.089	0.081	0.052	0.022	0.020	0.007	0.004	0.001	1	1
						23 January 1993						
7 15	0.149	0.103	0.051	0.043	0.021	0.013	0.007	0.002	0.000	0.000	1	2
10 13	0.113	0.079	0.037	0.030	0.016	0.008	0.007	0.001	0.000	0.000	1	3
13 28	0.133	0.084	0.052	0.033	0.015	0.011	0.005	0.003	0.000	0.000	2	3
16 23	0.240	0.160	0.095	0.064	0.052	0.032	0.021	0.011	0.005	0.000	2	1
						24 January 1993						
7 13	0.118	0.067	0.039	0.028	0.013	0.005	0.000	0.000	0.000	0.000	4	2
10 20	0.054	0.016	0.013	0.010	0.007	0.004	0.002	0.000	0.000	0.000	2	3

hour	1	2	3	4	5	6	7	8	9	10	V	D
					25 January 1993							
7.00	0.950	0.700	0.500	0.325	0.235	0.160	0.103	0.049	0.036	0.002	9	2
					26 January 1993							
19 08	0.325	0.169	0.064	0.053	0.035	0.020	0.013	0.009	0.004	0.000	3	2
					27 January 1993							
9 48	0.600	0.425	0.220	0.153	0.082	0.063	0.042	0.012	0.009	0.005	5	3
12 12	0.600	0.275	0.220	0.105	0.074	0.051	0.035	0.018	0.010	0.000	5	3
					29 January 1993							
6 52	0.600	0.400	0.250	0.168	0.117	0.079	0.045	0.029	0.019	0.002	1	3
9 58	0.650	0.500	0.300	0.202	0.119	0.079	0.059	0.024	0.012	0.001	2	1
					30 January 1993							
6 58	0.169	0.094	0.072	0.039	0.029	0.011	0.006	0.000	0.000	0.000	1	2
10 16	0.390	0.094	0.072	0.039	0.029	0.011	0.006	0.000	0.000	0.000	1	2
10 16	0.290	0.142	0.065	0.049	0.034	0.022	0.013	0.004	0.000	0.000	1	2
13 06	0.300	0.220	0.105	0.072	0.046	0.027	0.013	0.007	0.000	0.000	1	4
16 05	0.300	0.220	0.103	0.059	0.034	0.029	0.014	0.008	0.000	0.000	1	3
18 36	0.300	0.200	0.101	0.082	0.052	0.031	0.021	0.006	0.000	0.000	2	3
					1 February 1993							
7 06	0.130	0.059	0.042	0.031	0.019	0.006	0.003	0.000	0.000	0.000	1	3
9 56	0.350	0.240	0.147	0.079	0.039	0.029	0.018	0.007	0.004	0.000	1	1
13 27	0.330	0.180	0.122	0.085	0.045	0.029	0.019	0.008	0.005	0.000	1	1
18 00	0.450	0.325	0.220	0.113	0.070	0.041	0.033	0.013	0.005	0.000	1	4
18 50	0.400	0.320	0.200	0.130	0.065	0.050	0.042	0.009	0.000	0.000	1	2
					2 February 1993							
6 57	0.240	0.160	0.093	0.057	0.028	0.018	0.006	0.000	0.000	0.000	1	2
10 00	0.172	0.089	0.062	0.040	0.017	0.011	0.008	0.000	0.000	0.000	2	3

hour	1	2	3	4	5	6	7	8	9	10	V	D
						5 February 1993						
6 00	1.050	0.750	0.425	0.325	0.180	0.113	0.063	0.016	0.011	0.001	1	1
8 52	1.700	1.250	0.750	0.500	0.375	0.230	0.096	0.024	0.012	0.001	1	1
19 00	0.110	0.078	0.059	0.038	0.016	0.010	0.006	0.003	0.000	0.000	2	3
20 00	0.170	0.079	0.053	0.039	0.026	0.014	0.011	0.003	0.000	0.000	1	3
						6 February 1993						
7 50	0.099	0.058	0.034	0.025	0.016	0.007	0.005	0.000	0.000	0.000	2	3
9 50	0.123	0.084	0.050	0.040	0.028	0.016	0.015	0.013	0.002	0.000	1	3
13 13	0.200	0.119	0.058	0.037	0.028	0.022	0.012	0.009	0.009	0.002	2	3
16 15	0.300	0.220	0.145	0.086	0.058	0.047	0.026	0.015	0.007	0.000	2	1
19 00	0.650	0.500	0.350	0.220	0.149	0.101	0.062	0.028	0.014	0.001	3	1
						7 February 1993						
10 00	0.500	0.325	0.225	0.130	0.074	0.055	0.038	0.029	0.015	0.002	2	1
13 09	0.700	0.450	0.350	0.263	0.151	0.079	0.064	0.026	0.023	0.001	2	4
15 55	0.850	0.525	0.350	0.260	0.170	0.089	0.071	0.032	0.018	0.001	3	1
18 53	0.800	0.500	0.400	0.245	0.161	0.106	0.067	0.033	0.017	0.001	3	1
						12 February 1993						
12 19	0.225	0.129	0.071	0.044	0.026	0.022	0.017	0.008	0.006	0.001	3	3
13 50	0.183	0.110	0.084	0.050	0.034	0.024	0.016	0.009	0.003	0.001	3	3
16 00	0.225	0.163	0.105	0.056	0.041	0.020	0.010	0.009	0.007	0.002	2	3
19 30	0.400	0.225	0.158	0.074	0.045	0.024	0.014	0.006	0.004	0.000	2	2
						15 February 1993						
11 40	2.000	1.200	0.800	0.450	0.300	0.173	0.123	0.053	0.037	0.015	3	2
13 50	2.000	1.300	1.000	0.700	0.400	0.200	0.180	0.130	0.092	0.050	3	2
						16 February 1993						
8 45	0.112	0.096	0.040	0.022	0.019	0.009	0.006	0.004	0.000	0.000	5	3
16 10	0.249	0.135	0.102	0.067	0.052	0.038	0.023	0.007	0.006	0.001	3	3
19 30	0.250	0.138	0.091	0.073	0.032	0.026	0.012	0.005	0.002	0.000	2	2

hour	1	2	3	4	5	6	7	8	9	10	V	D
						17 February 1993						
7 50	0.300	0.220	0.123	0.075	0.040	0.018	0.015	0.009	0.005	0.001	1	3
10 10	0.260	0.210	0.111	0.078	0.045	0.029	0.020	0.003	0.002	0.001	2	3
13 30	0.300	0.210	0.123	0.079	0.050	0.036	0.026	0.015	0.008	0.000	1	3
15 30	0.300	0.200	0.105	0.068	0.046	0.022	0.021	0.011	0.009	0.000	1	3
						18 February 1993						
7 50	1.350	1.050	0.750	0.550	0.425	0.275	0.157	0.091	0.049	0.004	4	1
10 40	1.000	0.700	0.475	0.350	0.213	0.152	0.114	0.057	0.030	0.003	1	1
13 30	1.000	0.750	0.550	0.400	0.208	0.157	0.109	0.058	0.024	0.007	3	1
16 10	0.900	0.650	0.450	0.300	0.157	0.118	0.092	0.041	0.025	0.000	2	1
19 40	0.525	0.375	0.225	0.147	0.101	0.068	0.059	0.026	0.015	0.002	3	4
						19 February 1993						
6 10	0.240	0.125	0.104	0.058	0.041	0.028	0.023	0.011	0.007	0.001	4	2
						21 February 1993						
7 30	1.000	0.800	0.600	0.375	0.260	0.154	0.129	0.058	0.035	0.002	5	4
12 40	1.275	0.875	0.650	0.450	0.330	0.208	0.117	0.054	0.024	0.001	5	4
14 35	0.700	0.525	0.350	0.220	0.158	0.096	0.057	0.031	0.016	0.000	6	4
16 40	0.700	0.450	0.300	0.220	0.157	0.098	0.075	0.047	0.019	0.001	4	4
16 10	0.600	0.400	0.300	0.211	0.150	0.115	0.080	0.050	0.021	0.000	2	4
						22 February 1993						
7 00	2.700	2.000	1.400	0.900	0.675	0.450	0.300	0.126	0.052	0.006	3	2
9 40	1.450	1.100	0.625	0.400	0.260	0.134	0.077	0.038	0.022	0.002	1	2
13 30	2.200	1.500	0.900	0.625	0.400	0.250	0.147	0.053	0.023	0.002	3	3
16 50	0.900	0.700	0.450	0.250	0.178	0.111	0.063	0.020	0.007	0.000	1	3
19 15	1.200	0.800	0.500	0.350	0.200	0.080	0.055	0.010	0.005	0.000	5	3

22. STRATEGIC PLAN FOR AUSTRALIAN ANTARCTIC MIDDLE AND UPPER ATMOSPHERIC PHYSICS

R.J. Morris

Atmospheric and Space Physics
Antarctic Division
Kingston Tasmania 7050
Australia

ABSTRACT

The distribution of Australian Antarctic and sub-Antarctic stations (Λ ~64.3 – 80.4°S) provides a unique platform for remote sensing the high-latitude middle and upper atmosphere. Following the recommendations of the Antarctic Science Advisory Committee (ASAC) review the Atmospheric and Space Physics (ASP) program has developed a strategic plan for monitoring the atmosphere from the ground to the thermosphere, initially over Davis. This program will address questions about climate change in Antarctica by focusing on measurements of the dynamics of ozone in the stratosphere, temperatures in the mesosphere, winds in the mesosphere and stratosphere, and plasma drift and energy deposition in the thermosphere. There are specific reasons why this should be achieved in Antarctica: in particular because of the influence of solar variability and the extreme cold temperatures in the Antarctic stratosphere and mesosphere. This paper presents an account of the strategic plan, with a brief overview of the scope of our Antarctic program, focusing on science of practical value and science relevant to global change (Morris et al. 1995). This work supports research programs of the Antarctic Division, Australian and international agencies. The program continues to seeks a better understanding of the Earth's upper atmosphere, the heliosphere and the local galactic region beyond.

22.1 STRATEGIC PLAN - MIDDLE AND UPPER ATMOSPHERE CLIMATE

22.1.1 *Objectives*

(i) To improve the understanding of coupling between the various thermal regions of the atmosphere and the role of the middle and upper atmosphere in relation to tropospheric climate and weather.

(ii) To monitor the physical structure of the middle and upper atmosphere on a long-term basis, focusing on the dynamics of stratospheric ozone, the temperature and dynamics of the mesopause region, and mechanisms related to climate change.

(iii) To understand the response of the middle and upper atmosphere to natural and human made perturbations.

22.1.2 *Approach*

In the past decade there has been increased effort to incorporate gravity-wave effects into numerical models. Observations of the gravity wave field in the lower atmosphere are crucial if gravity waves are to be properly initialised and constrained in model calculations. Temperature observations made by the radiosonde network operated by the Bureau of Meteorology are especially suitable for producing climatologies of gravity wave activity in the lower stratosphere. Wind and temperature observations can be combined to provide information on the vertical fluxes of horizontal momentum.

Understanding how energy of solar origin is injected and dispersed in the Earth system is vital to our understanding of the processes for natural climate change. Any investigation relating to global climatic change must incorporate solar variability and the subsequent coupling of solar energy through the troposphere to the stratosphere, mesosphere and thermosphere. While the atmosphere can conveniently be divided into a number of regions, these regions are not independent of each other and the coupling between them is of importance. At present the mechanism of how the upper atmosphere could modulate the tropospheric weather is not easily recognised, the opposite is not only possible but highly significant as the modulation may be a magnified signal. However a large temperature signal in the upper atmosphere is accompanied by correspondingly large noise.

The Atmospheric and Space Physics group of Antarctic Division will continue to support the operation of basic physics research projects (i.e. riometer, fluxgate and induction magnetometers, ionospheric sounders and receivers, photometers and auroral imagers) where facilities are *in situ* and expeditioner requirements to maintain them have been significantly reduced by recent technological upgrades (see Table 1). This caveat addresses ongoing Antarctic Division, external agencies and University upper atmospheric research endeavours, and moreover new installations must be developed and tested to Antarctic Division standards, inclusive of computer data acquisition. Furthermore such basic research should contribute where possible to a theoretical understanding of natural variability of global change in the upper atmosphere or be of practical value.

Davis has been nominated as the site for the middle and upper atmosphere refocussed program because of its unique geophysical location and moreover with consideration of the new laboratory which was commissioned in February 1992. This building was specifically designed to accommodate both the Fabry-Perot spectrometer and optical experiments. A Lidar module will be constructed in Australia prior to shipment to Davis. Lidar, radar, digisonde, interferometer, spectrometer, photometer, electric field observations and contemporary technologies will be used (see Table 1):

- To maintain ongoing basic information of the upper atmosphere as a contribution to national and international database archives, where this suite of data might be utilised as an indicator of natural global change, or of practical value to civilisation.

- To acquire baseline measurements of the nature of the high-latitude ionosphere utilising ionospheric sounders, where the data can of practical value (i.e. HF communication frequency forecasting) and/or as a baseline for evidence for global change in the ionosphere.

Table 1. Antarctic and sub-Antarctic experiments for 1996.

Experiment	Casey	Davis	Mawson	Mac. Is.	Research Agency
30 MHz Riometer	X	X	X	X	AD
Magnetometer	X	X	X	X	AD/AGSO/Nagoya U
Auroral Video Imager	X	X	X	X	AD
Induction Magnetometer	X	X	X	X	AD/Newcastle U/La Trobe U
Ionosondes		X	X	X	IPS Radio & Space Services
Magnetic Absolutes	X	X		X	AGSO
MFSA 2 MHz Radar		X			Adelaide U/AD
Fabry-Perot Spectrometer		X	X		La Trobe U/AD
3 Channel Photometer		X			La Trobe U/AD
Satellite Scintillations	X				La Trobe U/AD
2 Channel WA Photometer	X	X			AD
Cosmic Ray Observatory			X		AD/Tasmania U
Scanning Spectrometer		X			AD/Adelaide U
6 Channel Photometer		X			AD
Digital Portable Sounder	X	97/98!			AD/La Trobe U/IPS
Total Electron Content	X	X	X	X	AUSLIG/La Trobe U/AD
Ultra Violet Radiation B		X			ARL
Laboratory Computers/Time	X	X	X	X	AD
Proposed Experiments					
Imaging riometer		95/96			Newcastle U/Maryland U/AD
LIDAR		96/97			AD/Adelaide U
Ozone		96/97			AD/BoM
VHF radar		98/99			AD/BoM/Adelaide U

(AD – Antarctic Division, BoM – Bureau of Meteorology, AGSO – Australian Geological Survey Organisation, ARL – Australian Radiation Laboratories, U – University)

and to investigate:

- The climatology of the stratosphere, mesosphere and thermosphere regions of the atmosphere.

- The nature of stratospheric ozone and UVB radiation above Davis.

- Evidence of a sun-weather coupling mechanism in the near Earth atmospheric electric field.

- The annual and decadal trends in temperatures, winds and densities throughout the stratosphere, mesosphere and thermosphere, and can they provide evidence of global climate change, and indeed the rate of change.

- The present day structure and circulation of the middle and upper atmosphere and ionosphere, and the key physical and chemical processes that control these regions.

- What factors control the formation of polar mesospheric clouds in particular, is their existence related to global change and the impact of human endeavours on the atmosphere.

- How momentum is transferred from the lower atmosphere to the mesosphere and, in particular, what role does turbulence play.

22.1.3 *Milestones*

1995-2000	Installation of new experimental platforms at Davis to facilitate the refocus of the middle and upper atmosphere program directed at global change: ground ultra violet radiation instrument by 1994/95; ground ozone and lidar facility by 1997/98; digisonde by 1998/99; VHF radar by 1999/2000.
2000	Establish for one solar cycle a climatology of the middle atmosphere and correlate it against recorded tropospheric and solar irradiance.
1996-2000	Contribute to the database of national and international research programs, and to utilise these data sets for practical purposes (i.e., communications forecasting and magnetic field model improvements relevant to navigation).
1996	Contribute data as requested by SCAR on the basic atmospheric parameters recorded at ANARE stations.
1997	Complete the Australian contribution of data to the Solar Terrestrial Energy Program (STEP) so as to advance the quantitative understanding of energy coupling and transfer processes within the Earth's environment.
1998	Complete the installation of equipment at Davis in readiness for participation in the NASA Thermosphere-Ionosphere-Mesosphere Energetics and Dynamics (TIMED) mission, designed to study the atmosphere between 60 and 180 km.

1999 Utilise the unique location of Davis as the notional conjugacy to the northern hemisphere site of Svalbard. Invited ground based activities for (i) the EISCAT radar community, and (ii) the European Space Agency (ESA) with the four satellite CLUSTER mission are planned.

REFERENCES

Morris, R.J., Monselesan, D.P. *and* Klekociuk, A.R. (1995). Australian Antarctic middle and upper atmospheric physics - a new direction. *Advances in Space Physics 16*:151 – 162.

ANARE Strategic Plans 1995-2000. (internal publication).